Tgkgkghkhk

PhD

3rd CYCLE

FCUP
2025

Multifunctional nanomaterials and nanofoams: Novel materials for electrocatalytic oxygen reactions and supercapacitors

Hugo Duarte Capela Novais Teixeira

# Multifunctional nanomaterials and nanofoams: Novel materials for electrocatalytic oxygen reactions and supercapacitors

Hugo Duarte Capela Novais Teixeira
Doctoral Program in Sustainable Chemistry
Faculty of Sciences of the University of Porto

2025

# Multifunctional nanomaterials and nanofoams: Novel materials for electrocatalytic oxygen reactions and supercapacitors

Hugo Duarte Capela Novais Teixeira
Thesis carried out as part of the Doctoral Program in Sustainable Chemistry
Department of Chemistry and Biochemistry
2025

**Supervisor**
Diana Mónica Mesquita Sousa Fernandes, Assistant researcher, REQUIMTE/LAQV

**Co-supervisor**
Ana Cristina Freire, full professor, Faculty of Sciences of the University of Porto

**Co-supervisor**
Maria de Fátima Grilo da Costa Montemor, full professor, Higher Technical Institute

**Co-supervisor**
Maria Teresa Duarte, full professor, Higher Technical Institute






*À minha família*

# Acknowledgements

I would like to express my deepest gratitude to all the people and institutions that made this journey possible and fruitful.

To ChemMat Doctoral Programme and Fundação para a Ciência e Tecnologia (FCT) for the PhD grant PD/BD/143095/2018.

To Programa Doutoral em Química Sustentável for accepting me and my PhD project.

To REQUIMTE-LAQV, and Department of Chemistry and Biochemistry of the Faculty of Sciences, University of Porto, for providing me the conditions to develop this project.

To my supervisor, Doctor Diana Fernandes, for the guidance, dedication, critical suggestions, precious discussions, and for all the knowledge shared.

To Professor Pedro de Oliveira and Doctor Israël-Martyr Mbomekallé from Institut de Chimie-Physique (ICP), Université Paris-Saclay for their invaluable contributions to our discussions, for generously sharing their knowledge, and for inspiring me to pursue further learning and knowledge sharing.

To Professor Fátima Montemor from Centro de Química Estrutural, Departamento de Engenharia Química, Instituto Superior Técnico for kindly allowing me to use her laboratory facilities, for her constant availability, and for the helpful discussions.

To my co-supervisor, Professor Cristina Freire, for the opportunity to develop this project.

To Bruno Jarrais for his invaluable assistance in characterising the materials using XPS.

To Rui Rocha for the invaluable advice he provided on SEM analysis.

To the staff, colleagues, and Professors of the Inorganic Chemistry group their invaluable support, and I would like to extend my special thanks to Gabriela, Joana and Marlene for their commendable efforts in managing the crisis in the Electrochemistry lab.

To Malibu e Kimi, for everything.

To my friends, for the many happy memories that have enriched these years, especially Nina and Ana Branco, for the moments of support and enjoyment, for the dinners, parties and beers shared.

To my family, especially my brother Filipe and my parents, for their unwavering encouragement and support, which have been a constant source of inspiration for me.

To Patrícia, for her unconditional love, boundless patience, and unwavering support. I am very grateful to you for always being there for me and helping me to find my way. And of course, to our little one Duarte.

This work was financially supported by Fundação para a Ciência e Tecnologia (FCT) through the PhD grant PD/BD/143095/2018.

This work received financial support from the PT national funds (FCT/MECI, Fundação para a Ciência e Tecnologia and Ministério da Educação, Ciência e Inovação) through the project UID/50006 -Laboratório Associado para a Química Verde - Tecnologias e Processos Limpos.



# Resumo

A transição para sistemas energéticos sustentáveis e neutros em carbono requer o desenvolvimento de materiais avançados capazes de promover eficazmente as principais reacções electroquímicas. Entre elas, a reacção de redução de oxigénio (ORR) e as reacções de evolução de oxigénio e hidrogénio (OER e HER) são processos críticos que, juntamente com o armazenamento de energia de alto desempenho em supercondensadores, formam os pilares de tecnologias como células de combustível, electrolisadores e dispositivos híbridos de armazenamento de energia. Apesar dos progressos significativos registados nas últimas décadas, a viabilidade comercial destas tecnologias continua a ser prejudicada pela dependência de electrocatalisadores à base de metais nobres, que são dispendiosos, escassos e propensos à degradação. Esta tese propõe uma solução para estes desafios através da concepção, síntese e caracterização de novos electrocatalisadores híbridos, baseados principalmente em polioxometalatos (POM) e nanoestruturas de carbono, bem como nanoespumas bimetálicas 3D. O objectivo é melhorar a actividade catalítica, a selectividade, a estabilidade e a relação custo-eficácia em condições alcalinas.

O primeiro estudo analisa as propriedades electrocatalíticas dum POM distinto, designado 48-tungsto-8-fosfato $[H_7P_8W_{48}O_{184}]^{33-}$ ($P_8W_{48}$). Este foi imobilizado em diversos nanomateriais de carbono, incluindo flocos de grafeno (GF), nanotubos de carbono de parede simples (SWCNT), nanotubos de carbono de paredes múltiplas (MWCNT) e MWCNT dopados com azoto (N-MWCNT). A preparação e extensa caracterização destes materiais híbridos foi realizada utilizando várias técnicas analíticas, incluindo FTIR, XPS, SEM, EDX e métodos electroquímicos. A actividade ORR das amostras foi avaliada por voltametria de varrimento linear (LSV) em solução de KOH 0,1 mol·dm$^{-3}$ saturada com $O_2$. Entre os compostos estudados, o $P_8W_{48}$@N-MWCNT demonstrou o melhor desempenho para ORR, com um $E_{onset}$ de 0,94 V vs. RHE, comparável ao do catalisador comercial Pt/C ($E_{onset}$ = 0,94 V vs. RHE). Adicionalmente, foi observado que este composto apresentou a maior densidade de corrente limitante (-3,7 mA·cm$^{-2}$), o que representa uma melhoria em comparação com o desempenho do $P_8W_{48}$ combinado com outros suportes de carbono. Esta melhoria é atribuída à presença de dopantes de azoto, que potencialmente melhoram a adsorção de $O_2$ e modificam a estrutura electrónica da superfície catalítica. Foi observado que todos os híbridos seguiram um mecanismo misto de ORR, com números de transferência de electrões ($n_{O2}$) entre 2,2 e 3,0, indicando contribuições de mecanismos de 2 e 4 electrões, que corroboram os resultados de produção de $H_2O_2$. Adicionalmente,

todos os electrocatalisadores baseados em $P_8W_{48}$ apresentaram baixos declives de Tafel (43 a 82 $mV \cdot dec^{-1}$), indicando uma cinética favorável. Adicionalmente, os compostos evidenciaram uma excelente tolerância ao metanol, com uma retenção de corrente entre 91 - 93%, bem como uma boa estabilidade electroquímica, mantendo entre 67 - 82% da corrente inicial após 36000 segundos de operação contínua.

Num estudo subsequente, foi imobilizado um POM do tipo Wells–Dawson contendo ferro, $[P_2W_{17}FeO_{61}]^{7-}$ ($P_2W_{17}Fe$), em flocos de grafeno dopados com azoto e nanotubos de carbono dopados com azoto (MWCNT_N e GF-N). Os híbridos resultantes foram sujeitos a uma caracterização por FTIR, SEM, EDX, XPS e técnicas electroquímicas. Entre os materiais estudados, o $P_2W_{17}Fe$@MWCNT_N8 apresentou o desempenho mais promissor, com um $E_{onset}$ de 0,84 V vs. RHE e uma densidade de corrente limitante de -3,9 $mA \cdot cm^{-2}$. As análises de Koutecky–Levich e RRDE confirmaram um mecanismo misto de ORR, com $n_{O2}$ em torno de 3,4 e produção muito baixa de $H_2O_2$. Adicionalmente, o catalisador exibiu um declive de Tafel de 48 $mV \cdot dec^{-1}$ e demonstrou uma notável tolerância ao metanol, com 94% de retenção de corrente na sua presença. Testes cronoamperométricos de longa duração revelaram elevada estabilidade, com 88% de retenção após 36000 segundos de operação contínua. Estes resultados destacam o papel benéfico da substituição com ferro na melhoria das propriedades redox e da actividade do POM, e validam adicionalmente o suporte à base de carbono como uma plataforma de alto desempenho e baixo custo para a catálise ORR.

O terceiro estudo analisou o comportamento electrocatalítico de um POM do tipo Wells–Dawson com substituição por molibdénio, $[P_2W_{12}Mo_6]^{6-}$ ($P_2W_{12}Mo_6$), imobilizado numa variedade de nanomateriais de carbono dopados com azoto e enxofre, nomeadamente GF_S, MWCNT_S e MWCNT_N. Os suportes dopados foram preparados por moagem mecânica e tratamento térmico com melamina ou enxofre molecular como precursores, sendo a imobilização do POM realizada em meio ácido. Entre os híbridos obtidos, o $P_2W_{12}Mo_6$@MWCNT_N8 demonstrou actividade electrocatalítica mais elevada, com um $E_{onset}$ de 0,84 V vs. RHE e densidade de corrente limitante de -3,7 $mA \cdot cm^{-2}$. Adicionalmente, foi observado um aumento substancial da área de superfície electroquimicamente activa em comparação com o suporte não dopado, o que confirma a contribuição sinérgica da dopagem com heteroátomos. A reacção ORR ocorreu maioritariamente por via mista, com $n_{O2}$ próximo de 3,3 e baixa produção de peróxido de hidrogénio (34%). O catalisador demonstrou boa durabilidade

e resistência ao metanol, confirmando o seu potencial como electrocatalisador robusto e isento de metais nobres para ORR em meio alcalino.

Em última análise, a presente tese aborda o desenvolvimento de materiais energéticos multifuncionais, mediante a produção de nanoespumas tridimensionais de cobalto e níquel. Estas estruturas foram obtidas por deposição electroquímica assistida por modelo dinâmico de bolhas de hidrogénio (DHBT), resultando em redes metálicas porosas. Posteriormente, os materiais foram sujeitos a testes para avaliar a sua eficiência nas reacções de separação da água (HER e OER) e no desempenho em supercondensadores. A nanoespuma de Co demonstrou actividade HER superior, com um sobrepotencial de apenas 32 mV a 10 $mA \cdot cm^{-2}$, enquanto as nanoespumas de Co e Ni apresentaram desempenhos comparáveis na reacção OER, com sobrepotenciais de 321 e 323 mV, respectivamente. Os declives de Tafel variaram entre 98 e 156 $mV \cdot dec^{-1}$ (HER) e entre 102 e 204 $mV \cdot dec^{-1}$ (OER), indicando cinéticas favoráveis em ambas as reacções. Entre as composições bimetálicas, a nanoespuma CoNi-NF_75_OX, oxidada com $H_2O_2$ a 5%, apresentou a maior área de superfície electroquímica e desempenho capacitivo. Esta alcançou uma capacitância específica de 345,5 $F \cdot g^{-1}$ a 1 $A \cdot g^{-1}$ e manteve um desempenho estável até 3000 ciclos de carga/descarga. A redução de capacidade observada após este ponto foi atribuída principalmente ao destacamento mecânico parcial, e não à degradação irreversível do material. Estes resultados reforçam a interacção sinérgica entre o cobalto e o níquel na optimização do desempenho electrocatalítico e capacitivo, tornando estas nanoespumas candidatas promissoras para sistemas integrados de conversão e armazenamento de energia.

Em suma, a presente tese aborda uma investigação exaustiva sobre a conceção de electrocatalisadores híbridos POM-carbono e nanoarquitecturas tridimensionais para reações-chave em tecnologias energéticas sustentáveis. Os resultados contribuem de forma significativa para o desenvolvimento de alternativas economicamente viáveis, com elevado desempenho e estabilidade, em relação aos catalisadores baseados em metais nobres, impulsionando assim o avanço das células de combustível, dos eletrolisadores e dos dispositivos híbridos de armazenamento de energia, para um futuro energético mais sustentável.

Palavras-chave: Electrocatálise, Materiais de Carbono, Polioxometalatos, Conversão de Energia, Armazenamento de Energia, Supercondensadores, Nanoespumas de Cobalto-Níquel.

# Abstract

The transition towards sustainable and carbon-neutral energy systems necessitates the development of advanced materials capable of efficiently promoting key electrochemical reactions. Among these, the oxygen reduction reaction (ORR) and the oxygen and hydrogen evolution reactions (OER and HER) are critical processes, which along with high-performance energy storage in supercapacitors, form the pillars of technologies such as fuel cells, electrolysers, and hybrid energy storage devices. Despite significant progress in recent decades, the commercial viability of these technologies remains hindered by the reliance on noble metal-based electrocatalysts, which are costly, scarce, and prone to degradation. This thesis proposes a solution to these challenges through the design, synthesis, and characterisation of novel hybrid electrocatalysts, primarily based on polyoxometalates (POMs) and carbon nanostructures, as well as 3D bimetallic nanofoams. The objective is to enhance catalytic activity, selectivity, stability, and cost-effectiveness under alkaline conditions.

The conceptual journey of this work begins at the molecular level, leveraging the unique properties of polyoxometalates. POMs are discrete, anionic metal-oxide clusters known for their remarkable structural diversity and the ability to undergo fast, reversible multi-electron redox reactions without structural collapse. However, their high solubility in aqueous media and low electronic conductivity necessitate their immobilisation on conductive supports. The first stage of this research (Chapter 2) established a foundational synergy between POMs and carbon nanostructures. By selecting the wheel-shaped 48-tungsto-8-phosphate $[H_7P_8W_{48}O_{184}]^{33-}$ ($P_8W_{48}$) cluster, which has been immobilised on various carbon nanomaterials, including graphene flakes (GF), single-walled carbon nanotubes (SWCNT), multi-walled carbon nanotubes (MWCNT), and N-doped multi-walled carbon nanotubes (N-MWCNT). The preparation and extensive characterisation of these hybrid materials was conducted employing a range of techniques, including FTIR, XPS, SEM, EDX and electrochemical methods. The ORR activity of the samples was evaluated using linear sweep voltammetry (LSV) in $O_2$-saturated 0.1 mol·dm$^{-3}$ KOH solution. Among the composites that were studied, $P_8W_{48}$@N-MWCNT demonstrated the most effective ORR performance, with an $E_{onset}$ of 0.94 V vs. RHE, which is comparable to that of the commercial Pt/C catalyst ($E_{onset}$ = 0.94 V vs. RHE). It also demonstrated the highest limiting current density of −3.7 mA cm$^{-2}$, surpassing the performance of $P_8W_{48}$ combined with other carbon supports. This enhancement is attributed to the presence of nitrogen dopants, which likely improve $O_2$ adsorption and modulate the electronic structure of the catalyst surface. It was observed

that all hybrids followed a mixed ORR pathway, with electron transfer numbers ($n_{O2}$) ranging between 2.2 and 3.0, indicating contributions from both 2- and 4-electron mechanisms, supporting the results of % $H_2O_2$ production. In addition, all electrocatalysts based on $P_8W_{48}$ exhibited low Tafel slopes ranging from 43 to 82 mV·dec$^{-1}$, indicating favourable ORR kinetics. The composites also demonstrated excellent methanol tolerance, with current retentions of 91-93%, and good electrochemical stability, retaining 67-82% of their initial current after prolonged operation over 36000 seconds.

In a subsequent study, a Wells–Dawson-type iron-substituted POM, $[P_2W_{17}FeO_{61}]$7- ($P_2W_{17}Fe$), was immobilised onto nitrogen-doped graphene flakes and

nitrogen-doped carbon nanostructures (MWCNT_N and GF_N). The resulting hybrids were thoroughly characterised by FTIR, SEM, EDX, XPS, and electrochemical methods. Among them, $P_2W_{17}Fe$@MWCNT_N8 exhibited the most promising performance, with an onset potential of 0.84 V vs. RHE and a diffusion-limited current density of -3.9 mA·cm$^{-2}$. Koutecky–Levich and RRDE analyses confirmed a mixed ORR pathway, with $n_{O2}$ values of approximately 3.4 and very low %$H_2O_2$ production (34%). Furthermore, the catalyst demonstrated a Tafel slope of 48 mV·dec$^{-1}$ and excellent methanol tolerance, with 94% current retention in the presence of methanol. Long-term chronoamperometric tests also revealed high stability, with 88% retention after 36000 seconds of continuous operation. These results underscore the beneficial role of Fe substitution in enhancing the redox properties and activity of the POM, and further validate the carbon-based support as a low-cost, high-performance platform for ORR catalysis.

The third study investigated the electrocatalytic behaviour of a Mo-substituted Wells-Dawson POM, $[P_2W_{12}Mo_6O_{62}]^{6-}$ ($P_2W_{12}Mo_6$), immobilised on a range of nitrogen and sulphur doped carbon nanomaterials, namely GF_S, MWCNT_S and MWCNT_N. These doped supports were synthesised by ball milling and thermal treatment with melamine or molecular sulphur as precursor, and POM immobilisation was carried out in acidic aqueous medium. Among the resulting hybrids, $P_2W_{12}Mo_6$@MWCNT_N8 exhibited the highest electrocatalytic activity, with an onset potential of 0.84 V vs. RHE and a diffusion-limited current density of -3.7 mA cm$^{-2}$. This composite also showed a significant increase in electrochemical surface area compared to the undoped support, confirming the synergistic contribution of heteroatom doping. The ORR was predominantly via a mixed ORR pathway, with $n_{O2}$ values around 3.3 and a low hydrogen peroxide yield. The catalyst retained good durability and methanol resistance, confirming its potential as a robust noble metal-free ORR electrocatalyst in alkaline media.

Finally, the present thesis explores the development of multifunctional energy materials through the fabrication of 3D cobalt and nickel nanofoams. These structures were synthesised by dynamic hydrogen bubble templating (DHBT), resulting in porous metallic networks. The materials were then subjected to testing for both water splitting reactions (HER and OER) and supercapacitor performance. The Co-NF demonstrated optimal HER activity with an overpotential of 32 mV at 10 $mA \cdot cm^{-2}$, while for OER, the Co-NF and Ni-NF exhibited comparable performance with overpotentials of 321 and 323 mV, respectively. The Tafel slopes varied from 98 to 156 $mV \cdot dec^{-1}$ (HER) and 102 to 204 $mV \cdot dec^{-1}$ (OER), indicating favourable kinetics in both reactions.

Among the mixed-metal compositions, the CoNi-NF_75_OX nanofoam, oxidised with 5% $H_2O_2$, exhibited the highest electrochemical surface area and capacitive performance. The CoNi-NF_75_OX nanofoam exhibited high specific capacitance values, reaching 345.5 $F \cdot g^{-1}$ at 1 $A \cdot g^{-1}$, and demonstrated stable performance up to 3000 charge/discharge cycles. The decline in capacitance observed beyond this point was primarily attributed to minor mechanical detachment rather than irreversible degradation. These results emphasise the synergistic interaction between cobalt and nickel in optimising electrocatalytic and supercapacitor performance, making these nanofoams excellent candidates for integrated energy conversion and storage systems.

In summary, this thesis presents a comprehensive investigation into the design of POM-carbon hybrid electrocatalysts and 3D nanoarchitectures for key reactions in sustainable energy technologies. The findings contribute significantly to the development of cost-effective, high-performance, and stable alternatives to noble-metal-based catalysts, thereby supporting the advancement of fuel cells, electrolysers, and hybrid energy storage devices for a more sustainable energy future.

Keywords: Electrocatalysis, Carbon Materials, Polyoxometalates, Energy Conversion, Energy storage, Supercapacitors, Cobalt-Nickel Nanofoams.

# Contents

Acknowledgements ..... v

Resumo ..... vii

Abstract ..... xi

List of Tables ..... xix

List of Figures ..... xxi

**List of Abbreviations** ..... xxix

**Introduction** ..... 37

**1.1. Global Energy Challenger** ..... 37

**1.2. Electrochemical Oxygen Reduction and Evolution Reactions** ..... 44

**1.2.1. Oxygen Reduction Reaction** ..... 48

**1.2.2. Oxygen Evolution Reaction** ..... 50

**1.3. Electrocatalysts for Oxygen Reduction Reaction** ..... 55

**1.3.1. Carbon-based ORR electrocatalysts** ..... 58

**1.3.2. Polyoxometalates** ..... 59

**1.3.3. Polyoxometalate-Carbon Nanomaterials for the Oxygen Reduction Reaction (ORR)** ..... 62

**1.3.4. ORR electrocatalytic activity evaluation** ..... 64

**1.4. Electrochemical Capacitor** ..... 67

**1.4.1. Capacitors** ..... 67

**1.5. Mechanisms of Charge Storage** ..... 69

**1.5.1. Electrochemical double layer capacitor (EDLC)** ..... 73

**1.6. Metal Nanofoams for OER, HER and Supercapacitors Applications** ..... 77

**1.7. Electrodeposition of Metals using Dynamic Hydrogen Bubble Template (DHBT)** ..... 82

**1.8. References** ..... 85

**Electrocatalytic oxygen reduction reaction on 48-tungsto-8-phosphate wheel anchored on carbon** ..... 105

**2.1. Introduction** ..... 106

**2.2. Experimental section** ..... 108

**2.2.1 Materials preparation and characterisation methods** ..... 108

**2.3. Results and Discussion** ..... 109

**2.3.1. Materials characterisation** ..... 109

**2.4. Electrochemical performance towards ORR** ..... 116

**2.5. Conclusion** ..... 123

**2.6. Supporting information** ..... 123

**2.6.1. Materials and solvents** ..... 123

**2.6.2. Physicochemical characterisation** ..... 124

**2.6.3. ORR electrochemical tests** ..... 124

**2.6.4. Assessment of electrochemically active surface areas (ECSA)** ..... 126

**2.6.5. Figures** ..... 127

**2.7. Declarations** ..... 142

**Hybrids made of a Fe-containing Wells-Dawson polyoxometalate and carbon nanomaterials as promising electrocatalysts for the oxygen reduction reaction** 151

**3.1. Introduction** ..... 152

**3.2. Experimental section** ..... 154

**3.2.1 Materials preparation and characterisation methods** ..... 154

**3.3. Results and Discussion** ..... 155

**3.3.1. Materials characterisation** ..... 155

**3.4. Electrochemical performance towards ORR** ..... 162

**3.5. Conclusion** ..... 168

**3.6. Supporting information** ..... 169

**3.6.1. Materials and solvents** ..... 169

**3.6.2. Physicochemical characterization** ..... 169

**3.6.3. ORR electrochemical tests** ..... 170

**3.6.4. Assessment of electrochemically active surface areas (ECSA)** ..... 172

**3.6.5. Figures** ..... 173

**3.7. Declarations** ..... 184

**Enhanced Oxygen Reduction Reaction Activity of the Wells-Dawson Polyoxometalate $P_2W_{12}Mo_6$ Immobilised in Nitrogen and Sulphur-Doped Carbon Nanomaterials** ..... 193

**4.1. Introduction** ..... 194

**4.2. Experimental section** ..... 196

**4.2.1 Materials preparation and characterisation methods** ..... 196

**4.3. Results and Discussion** ..... 197

**4.3.1. Materials characterisation** ..... 197

**4.4. Electrochemical performance towards ORR** ..... 208

**4.5. Conclusion** ..... 216

**4.6. Supporting information** ..... 217

**4.6.1. Materials and solvents** ..... 217

**4.6.2. Physicochemical characterization** ..... 217

**4.6.3. ORR electrochemical tests** ..... 218

**4.6.4. Assessment of electrochemically active surface areas (ECSA)** ..... 220

**4.6.5. Figures** ..... 221

**4.7. Declarations** ..... 239

**Cobalt/Nickel Nanofoams: Potential application in Supercapacitors and OER/HER** ..... 249

**5.1. Introduction** ..... 250

**5.2. Experimental section** ..... 252

**5.2.1 Materials and solvents** ..... 252

**5.2.2 Synthesis of electrodeposited cobalt/nickel nanofoams composites on stainless steel** ..... 253

**5.2.3 Electrochemical study of CoNi nanofoams** ..... 254

**5.2.4 Characterisation techniques** ..... 255

**5.3. Results and discussion** ..... 256

**5.3.1 Materials characterisation** ..... 256

**5.4. Performance and evaluation of supercapacitors** ..... 261

**5.5. Electrochemical performance towards the OER and HER** ..... 270

**5.6. Conclusion** ..... 277

**5.7. Supporting information** ..... 279

**5.7.1. Figures** ..... 279

**General Conclusions and Future Perspectives** ..... 301

**6.1. Final conclusions** ..... 301

**6.2. Final perspectives** ..... 304

**Appendix A: Published Scientific Articles** ..... 309

# List of Tables

Table 2.1 - XPS surface atomic percentages for the pristine carbon materials and the prepared composites. ..... 111
Table 2.2 Onset Potentials ($E_{onset}$), diffusion-limiting current density values ($j_{L,0.26\ V,1600\ rpm}$) derived from the ORR polarization curves in $O_2$-purged 0.1 mol $dm^{-3}$ KOH solution for commercial Pt/C, carbon materials and composites prepared and Tafel and $n_{O2}$values. ..... 120
Table 2.3 Electrocatalytically active surface area (ECSA) values of the carbon supports and the corresponding POM-based composites..... 122
Table 3.1 - XPS surface atomic percentages for the pristine carbon materials, the doped carbon materials and the prepared composites..... 160
Table 3.2 - Main ORR parameters obtained from polarisation curves recorded in $O_2$-saturated 0.1 mol $dm^{-3}$ KOH solution for the different materials tested. ..... 166
Table 3.3 - Electrocatalytically active surface area (ECSA) values of the carbon supports and the corresponding POM-based composites..... 167
Table S3.1 - Relative atomic percentages of nitrogen presented in the XPS high-resolution N1s spectra of the prepared carbon materials. ..... 183
Table S3.2 - ORR performance of transition metal carbon hybrid electrocatalysts obtained from literature. ..... 183
Table 4.1 - XPS surface atomic percentages for the pristine carbon materials, the doped carbon materials and the prepared composites..... 201
Table 4.2 - Main ORR parameters obtained from polarisation curves recorded in $O_2$-saturated 0.1 mol $dm^{-3}$ KOH solution for the different materials tested. ..... 213
Table 4.3 - Electrocatalytically active surface area (ECSA) values of the carbon supports and the corresponding POM-based composites..... 214
Table 5.1 - Values of specific capacitance calculated current densities ranging from 1 to 5 A $g^{-1}$ for Ni-NF, Co-NF, CoNi-NF_25, CoNi-NF_50, CoNi-NF_75 and CoNi-NF_75_OX nanofoams. ..... 265
Table 5.2 - Fitted parameters obtained by numerical simulation of the EIS experimental data for CoNi-NF_75_OX composite material at 0 V potential. ..... 269
Table 5.3 - The OER performance parameters for Ni-NF, Co-NF, CoNi-NF_25, CoNi-NF_50 and CoNi-NF_75 nanofoams. ..... 273
Table 5.4 - The HER performance parameters for Ni-NF, Co-NF, CoNi-NF_25, CoNi-NF_50 and CoNi-NF_75 nanofoams. ..... 275
Table S5.1 - The performance for Ni-NF and Co-NF as OER/HER electrocatalysts compared with published work. ..... 287

Table S5.2 - The performance for Ni-NF and Co-NF as OER/HER electrocatalysts compared with published work. ..... 287
Table S5.3 - The performance for Ni-NF and Co-NF as OER/HER electrocatalysts compared with published work. ..... 288

# List of Figures

Figure 1.1 - Schematic representation of the ‘’Hydrogen Economy’’. Adapted from ref. [25] ..... 40
Figure 1.2 - The area of the circles represents reasonably assured recoverable reserves (RARs) from both finite and renewable resources over the next 30 years. These areas can be compared with the total demand (earth image) over that same ..... 42
Figure 1.3 – Illustration of the hydrogen and oxygen cycle for energy storage and conversion. Adapted from ref. [33] ..... 43
Figure 1.4 – Representation of the fuel cell mode and the electrolyser mode in alkaline electrolytes. Adapted from ref. [59] ..... 45
Figure 1.5 – Schematic of the overpotentials associated with hydrogen electrocatalysis (HER, HOR) and oxygen electrocatalysis (ORR, OER) and their overall reaction equations. Adapted from ref. [62] ..... 46
Figure 1.6 – HER mechanisms in acidic (A) and alkaline (B) media. Adapted from ref. [102] ..... 53
Figure 1.7 – Structures of (a) graphene, (b) graphitic, (c) carbon nanotube, and (d) fullerene. ..... 58
Figure 1.8 – Polyhedral representations of the structures of (a) Keggin-type and (b) Wells−Dawson heteropolyanions. Adapted from ref.[135] ..... 61
Figure 1.9 – Schematic view of a conventional capacitor. ..... 68
Figure 1.10– Schematic diagram of a supercapacitor cell. Adapted from ref. [158] ..... 71
Figure 1.11 – The schematic diagram (a, b, d, e, g, h) illustrates the cyclic voltammograms, while (c, f, i) show the corresponding galvanostatic discharge curves for various types of energy storage materials. A pseudocapacitive material will generally exhibit the electrochemical characteristics of one, or a combination, of the following categories: (b) surface redox materials (d) intercalation-type materials or (e) intercalation-type materials showing broad but electrochemically reversible redox peaks. Electrochemical responses in (g-i) correspond to battery-like materials. Adapted from [178]. ..... 76
Figure 1.12 – Electrodeposition of porous metal using dynamic hydrogen bubble template. ..... 82
Figure 2.1 - Overlaid FTIR spectra in the 4000–400 $cm^{-1}$ range of GF (black), KLi-$P_8W_{48}$ (red), and $P_8W_{48}$@GF composite (blue). ..... 110
Figure 2.2 - XPS deconvoluted spectra of corresponding elements in $P_8W_{48}$@N-MWCNT composite. ..... 113

Figure 2.3 - SEM images of $P_8W_{48}$@GF (a), $P_8W_{48}$@SWCNT (b), $P_8W_{48}$@MWCNT (c) and $P_8W_{48}$@N-MWCNT (d) at 50000× magnification. ..... 114
Figure 2.4 - SEM and EDX elemental mapping images of $P_8W_{48}$@GF, at 10000× magnification for the elements C (red), O (green), W (blue) and P (yellow). ..... 115
Figure 2.5 CVs of $P_8W_{48}$@GF (a), $P_8W_{48}$@SWCNT (b), $P_8W_{48}$@MWCNT (c) and $P_8W_{48}$@N-MWCNT (d) modified electrodes in $N_2$-purged (dash line) and $O_2$-purged (full line) 0.1 mol $dm^{-3}$ KOH solution at 0.005 V $s^{-1}$. ..... 116
Figure 2.6 - ORR LSV curves acquired using an RDE in $O_2$-purged KOH solution (0.1 mol $dm^{-3}$) at 1600 rpm and 0.005 V $s^{-1}$ of commercial Pt/C (20 wt %) and $P_8W_{48}$@CM composites (a); $n_{O2}$ at several potential values (b). ..... 118
Figure 2.7 - Estimated percentage of $H_2O_2$ produced with RRDE in $O_2$-purged 0.1 mol $dm^{-3}$ KOH solution, at 1600 rpm; the disk potential was swept at v = 0.005 V $s^{-1}$ and the ring potential was kept at $E$ = 0.2 V versus Ag/AgCl for $P_8W_{48}$@GF, $P_8W_{48}$@MWCNT, $P_8W_{48}$@SWCNT, $P_8W_{48}$@N-MWCNT and Pt/C (20 wt %). ..... 119
Figure 2.8 - ORR Tafel plots obtained from LSV data in Figure 2.7 where current densities are normalized to the mass of each ECs. ..... 121
Figure 2.9 - Chronoamperometric response of the ECs at 1600 rpm, in 0.1 mol $dm^{-3}$ $O_2$-purged KOH at: (a) $E$ = 0.46 V vs. RHE for 36000s and (b) $E$ = 0.46 V vs. RHE with the addition of 0.5 mol $dm^{-3}$ methanol after ≈ 500 s. ..... 122
Figure S2.1 - Infrared spectra in the range of 4000-400 $cm^{-1}$ for $P_8W_{48}$ (red), carbon material (black) and composite (blue) for: SWCNT (a), MWCNT (b) and N-MWCNT (c). ..... 127
Figure S2.2 - XPS deconvoluted spectra of corresponding elements in $P_8W_{48}$@GF composite. ..... 128
Figure S2.3 - XPS deconvoluted spectra of corresponding elements in $P_8W_{48}$@SWCNT composite. ..... 129
Figure S2.4 - XPS deconvoluted spectra of corresponding elements in $P_8W_{48}$@MWCNT composite. ..... 130
Figure S2.5 - XPS deconvoluted spectra of corresponding elements in GF composite. ..... 131
Figure S2.6 - XPS deconvoluted spectra of corresponding elements in SWCNT composite. ..... 132
Figure S2.7 - XPS deconvoluted spectra of corresponding elements in MWCNT composite. ..... 132
Figure S2.8 - XPS deconvoluted spectra of corresponding elements in N-MWCNT composite. ..... 132

Figure S2.9 - SEM and EDS elemental mapping images of $P_8W_{48}$@SWCNT at magnification 5000× for the elements C, O, W and P..... 133
Figure S2.10 - SEM and EDS elemental mapping images of $P_8W_{48}$@MWCNT at magnification 5000× for the elements C, O, W and P..... 134
Figure S2.11 - SEM and EDS elemental mapping images of $P_8W_{48}$@N-MWCNT at magnification 5000× for the elements C, O, W and P..... 135
Figure S2.12 - ORR polarization curves of $P_8W_{48}$@GF (a), $P_8W_{48}$@SWCNT (c), $P_8W_{48}$@MWCNT (e) and $P_8W_{48}$@N-MWCNT (g) at different rotation rates in $O_2$-saturated 0.1 mol $dm^{-3}$ KOH solution at 0.005 V $s^{-1}$ and the corresponding Koutecky-Levich (K-L) plots (b, d, f and h). ..... 137
Figure S2.13 - ORR polarization curves of GF (a), SWCNT (c), MWCNT (e) and N-MWCNT (g) modified electrodes, acquired at different rotation rates in $O_2$-saturated 0.1 mol $dm^{-3}$ KOH solution at 0.005 V $s^{-1}$ and the corresponding Koutecky-Levich (K-L) plots (b, d, f and h). ..... 138
Figure S2.14 - ORR polarization curves for Pt/C at different rotation rates in $O_2$-saturated 0.1 mol $dm^{-3}$ KOH solution at 0.005 V $s^{-1}$ (a) and the corresponding Koutecky-Levich (K-L) plots (b). ..... 139
Figure S2.15 - ORR LSV curves obtained in KOH (0.1 M) saturated with $O_2$ at 1600 rpm and 0.005 V $s^{-1}$ with current densities normalized to the respective double-layer capacitance values. ..... 139
Figure S2.16 - CVs at different scan rates for GF (a), SWCNT (b), MWCNT (c), N-MWCNT (d), $P_8W_{48}$@GF (e), $P_8W_{48}$@SWCNT (f), $P_8W_{48}$@MWCNT (g), $P_8W_{48}$@N-MWCNT (h) and Pt/C (i) in $N_2$-saturated KOH (0.1 M)..... 141
Figure S2.17 - Current density-scan rate linear fitting plots for all materials. Numeric values correspond to the double-layer capacitances ($C_{dl}$) for each material. ..... 142
Figure 3.1 - FTIR spectra in the 4000–500 $cm^{-1}$ range of $K_7[P_2W_{17}(FeOH_2)O_{61}]$ (black), and of the composites $P_2W_{17}$Fe@GF_N8 (red) and $P_2W_{17}$Fe@MWCNT_N8 (blue).. 156
Figure 3.2 - XPS deconvoluted spectra of corresponding elements in the $P_2W_{17}$Fe@MWCNT_N8 composite. ..... 159
Figure 3.3 - SEM images of $P_2W_{17}$Fe@MWCNT_N8 (a) and $P_2W_{17}$Fe@GF_N8 (b) at 50000× magnification..... 161
Figure 3.4 - SEM and EDX elemental mapping images of $P_2W_{17}$Fe@MWCNT_N8, at 5000× magnification for the elements C (red), O (green), W (blue), P (yellow) and Fe (purple). ..... 161
Figure 3.5 - CVs of $P_2W_{17}$Fe@MWCNT_N8 (a) and $P_2W_{17}$Fe@GF_N8 (b) modified electrodes in $N_2$-saturated (dash line) and $O_2$-saturated (full line) 0.1 mol $dm^{-3}$ KOH solution at 0.005 V $s^{-1}$. ..... 162

Figure 3.6 - ORR LSV curves acquired using an RDE in $O_2$-saturated KOH solution (0.1 mol $dm^{-3}$) at 1600 rpm and 0.005 V $s^{-1}$ of commercial Pt/C (20 wt %), $P_2W_{17}Fe$@CM nanocomposites and doped-nitrogen carbon materials (a); $n_{O2}$ at several potential values (b); estimated percentage of $H_2O_2$ produced with RRDE for $P_2W_{17}Fe$@CM and Pt/C (20 wt %) in $O_2$-saturated 0.1 mol $dm^{-3}$ KOH solution, at 1600 rpm; the disk potential was swept at v = 0.005 V $s^{-1}$ and the ring potential was kept at E = 0.2 V versus Ag/AgCl (c); ORR Tafel plots for $P_2W_{17}Fe$@CM obtained from LSV data in Figure 3.6 (a) where current densities are normalized to the mass of each ECs (d). ..... 165
Figure 3.7 - Chronoamperometric response of the ECs at 1600 rpm, in 0.1 mol $dm^{-3}$ $O_2$-saturated KOH at: E = 0.46 V vs. RHE for 36000s (a) and E = 0.46 V vs. RHE with the addition of 0.5 mol $dm^{-3}$ methanol after ≈ 500 s (b)..... 168
Figure 3S1 - FTIR spectra in the 4000–500 $cm^{-1}$ range of the nitrogen doped carbon materials GF_N8 (black) and MWCNT_N8 (red). ..... 173
Figure 3S2 - XPS deconvoluted spectra of corresponding elements of the GF_N8... 174
Figure 3S3 - XPS deconvoluted spectra of corresponding elements of the MWCNT_N8. ..... 175
Figure 3S4 - XPS deconvoluted spectra of corresponding elements in the $P_2W_{17}Fe$@GF_N8 composite. ..... 176
Figure 3S5 - SEM images of MWCNT_N8 (a) and GF_N8 (b) at 50000× magnification. ..... 177
Figure 3S6 - SEM and EDX elemental mapping images of $P_2W_{17}Fe$@GF_N8, at 5000× magnification for the elements C (red), O (green), W (blue), P (yellow) and Fe (purple). ..... 178
Figure 3S7 - CVs of MWCNT_N8 (a), GF_N8 (b) and Pt/C (20 wt. %) (c) modified electrodes in $N_2$-saturated (dash line) and $O_2$-saturated (full line) 0.1 mol $dm^{-3}$ KOH solution at 0.005 V. ..... 179
Figure 3S8 - ORR LSV polarization curves for Pt/C (20 wt. %) at different rotation rates in $O_2$-saturated 0.1 mol $dm^{-3}$ KOH solution at 0.005 V $s^{-1}$ (a), and the corresponding Koutecky-Levich (K-L) plots (b). ..... 179
Figure 3S9 - ORR LSV polarization curves for MWCNT_N8 at different rotation rates in $O_2$-saturated 0.1 mol $dm^{-3}$ KOH solution at 0.005 V $s^{-1}$ (a), and the corresponding Koutecky-Levich (K-L) plots (b). ..... 180
Figure 3S10 - ORR polarization curves for GF_N8 at different rotation rates in $O_2$-saturated 0.1 mol $dm^{-3}$ KOH solution at 0.005 V $s^{-1}$ (a), and the corresponding Koutecky-Levich (K-L) plots (b)..... 180

Figure 3S11 - ORR LSV polarization curves for $P_2W_{17}Fe$@MWCNT_N8 at different rotation rates in $O_2$-saturated 0.1 mol $dm^{-3}$ KOH solution at 0.005 V $s^{-1}$ (a), and the corresponding Koutecky-Levich (K-L) plots (b). ..... 180
Figure 3S12 - ORR LSV polarization curves for $P_2W_{17}Fe$@GF_N8 at different rotation rates in $O_2$-saturated 0.1 mol $dm^{-3}$ KOH solution at 0.005 V $s^{-1}$ (a), and the corresponding Koutecky-Levich (K-L) plots (b). ..... 181
Figure 3S13 - CVs at different scan rates for GF_N8 (a), MWCNT_N8 (b), $P_2W_{17}Fe$@GF_N8 (c), $P_2W_{17}Fe$@MWCNT_N8 (d) and Pt/C (e) in $N_2$-saturated KOH (0.1 M). ..... 182
Figure 3S14 - Current density-scan rate linear fitting plots for all materials. Numeric values correspond to the double-layer capacitances ($C_{dl}$) for each material. ..... 182
Figure 4.1 - FTIR spectra in the 4000–500 $cm^{-1}$ range of $K_6{\cdot}\alpha$-$[P_2W_{12}Mo_6O_{62}]{\cdot}19H_2O$ (black), and of the composites $P_2W_{12}Mo_6$@MWCNT_N6 (red), $P_2W_{12}Mo_6$@MWCNT_N8 (blue) (a) and $P_2W_{12}Mo_6$@MWCNT_S6 (green) and $P_2W_{12}Mo_6$@GF_S6 (purple) (b). ..... 200
Figure 4.2 - XPS deconvoluted spectra of the corresponding elements of $P_2W_{12}Mo_6$@MWCNT_N8. ..... 205
Figure 4.3 - SEM images of $P_2W_{12}Mo_6$@MWCNT_N8 (a), $P_2W_{12}Mo_6$@MWCNT_N6 (b), $P_2W_{12}Mo_6$@MWCNT_S6 (c) and $P_2W_{12}Mo_6$@GF_S6 (d) at 50000× magnification. .. 207
Figure 4.4 - SEM and EDX elemental mapping images of $P_2W_{12}Mo_6$@MWCNT_N8, at 5000× magnification for the elements C (red), O (green), W (blue), P (yellow) and Mo (purple). ..... 208
Figure 4.5 - CVs of $P_2W_{12}Mo_6$@MWCNT_N8 (a), $P_2W_{12}Mo_6$@MWCNT_N6 (b), $P_2W_{12}Mo_6$@MWCNT_S6 (c) and $P_2W_{12}Mo_6$@GF_S6 (d) modified electrodes in $N_2$-saturated (dash line) and $O_2$-saturated (full line) 0.1 mol $dm^{-3}$ KOH solution at 0.005 V $s^{-1}$. ..... 209
Figure 4.6 - ORR LSV curves acquired using an RDE in $O_2$-saturated KOH solution (0.1 mol $dm^{-3}$) at 1600 rpm and 0.005 V $s^{-1}$ of commercial Pt/C (20 wt %), $P_2W_{12}Mo_6$@CM nanocomposites and doped-nitrogen and sulphur carbon materials (a); $n_{O2}$ at several potential values (b); estimated percentage of $H_2O_2$ produced with RRDE for $P_2W_{12}Mo_6$@CM and Pt/C (20 wt %) in $O_2$-saturated 0.1 mol $dm^{-3}$ KOH solution, at 1600 rpm; the disk potential was swept at v = 0.005 V $s^{-1}$ and the ring potential was kept at E = 0.2 V versus Ag/AgCl (c); ORR Tafel plots for $P_2W_{12}Mo_6$@CM obtained from LSV data in Figure 4.6 (a) where current densities are normalised to the mass of each ECs (d). ..... 212

Figure 4.7 - Chronoamperometric response of the ECs at 1600 rpm, in 0.1 mol $dm^{-3}$ $O_2$-saturated KOH at: *E* = 0.46 V vs. RHE for 36000s (a) and *E* = 0.46 V vs. RHE with the addition of 0.5 mol $dm^{-3}$ methanol after ≈ 500 s (b). ..... 215
Figure 4S1 - FTIR spectra in the 4000–500 $cm^{-1}$ range of the nitrogen doped carbon materials MWCNT_N8 (black) and MWCNT_N6 (red). ..... 221
Figure 4S2 - FTIR spectra in the 4000–500 $cm^{-1}$ range of the sulphur-doped carbon materials MWCNT_S6 (black) and GF_S6 (red). ..... 221
Figure 4S3 - XPS deconvoluted spectra of the corresponding elements of MWCNT_N8. ..... 222
Figure 4S4 - XPS deconvoluted spectra of the corresponding elements of MWCNT_N6. ..... 223
Figure 4S5 - XPS deconvoluted spectra of the corresponding elements of MWCNT_S6. ..... 224
Figure 4S6 - XPS deconvoluted spectra of the corresponding elements of GF_S6... 225
Figure 4S7 - XPS deconvoluted spectra of the corresponding elements of $P_2W_{12}Mo_6$@MWCNT_N6. ..... 226
Figure 4S8 - XPS deconvoluted spectra of the corresponding elements of $P_2W_{12}Mo_6$@MWCNT_S6. ..... 227
Figure 4S9 - XPS deconvoluted spectra of the corresponding elements of $P_2W_{12}Mo_6$@GF_S6. ..... 228
Figure 4S10 - SEM images of MWCNT_N8 (a), MWCNT_N6 (b), MWCNT_S6 and GF_S6 at 50000× magnification. ..... 229
Figure 4S11 - SEM and EDX elemental mapping images of $P_2W_{12}Mo_6$@MWCNT_N6, at 5000× magnification for the elements C (red), O (green), W (blue), P (yellow) and Mo (purple). ..... 230
Figure 4S12 - SEM and EDX elemental mapping images of $P_2W_{12}Mo_6$@MWCNT_S6, at 5000× magnification for the elements C (red), O (green), W (blue), P (yellow) and Mo (purple). ..... 231
Figure 4S13 - SEM and EDX elemental mapping images of $P_2W_{12}Mo_6$@GF_S6, at 5000× magnification for the elements C (red), O (green), W (blue), P (yellow) and Mo (purple). ..... 232
Figure 4S14 - XRD spectra of $P_2W_{12}Mo_6$@GF_S6 (blue), $P_2W_{12}Mo_6$@MWCNT_S6 (red) and $P_2W_{12}Mo_6$@MWCNT_N8 (black). ..... 233
Figure 4S15 - CVs of MWCNT_N8 (a), MWCNT_N6 (b), MWCNT_S6 (c), GF_S6 (d) and Pt/C (20 wt. %) (e) modified electrodes in $N_2$-saturated (dash line) and $O_2$-saturated (full line) 0.1 mol $dm^{-3}$ KOH solution at 0.005 V. ..... 234

Figure 4S16 - ORR LSV polarization curves for Pt/C (20 wt. %) at different rotation rates in $O_2$-saturated 0.1 mol $dm^{-3}$ KOH solution at 0.005 V $s^{-1}$ (a), and the corresponding Koutecky-Levich (K-L) plots (b). ..... 235
Figure 4S17 - ORR LSV polarization curves for MWCNT_N8 at different rotation rates in $O_2$-saturated 0.1 mol $dm^{-3}$ KOH solution at 0.005 V $s^{-1}$ (a), and the corresponding Koutecky-Levich (K-L) plots (b). ..... 235
Figure 4S18 - ORR LSV polarization curves for MWCNT_N6 at different rotation rates in $O_2$-saturated 0.1 mol $dm^{-3}$ KOH solution at 0.005 V $s^{-1}$ (a), and the corresponding Koutecky-Levich (K-L) plots (b). ..... 235
Figure 4S19 - ORR LSV polarization curves for MWCNT_S6 at different rotation rates in $O_2$-saturated 0.1 mol $dm^{-3}$ KOH solution at 0.005 V $s^{-1}$ (a), and the corresponding Koutecky-Levich (K-L) plots (b). ..... 235
Figure 4S20 - ORR LSV polarization curves for GF_S6 at different rotation rates in $O_2$-saturated 0.1 mol $dm^{-3}$ KOH solution at 0.005 V $s^{-1}$ (a), and the corresponding Koutecky-Levich (K-L) plots (b). ..... 236
Figure 4S21 - CVs at different scan rates for MWCNT_N8 (a), MWCNT_N6 (b), MWCNT_S6 (c), GF_S6 (d), $P_2W_{12}Mo_6$@MWCNT_N8 (e), $P_2W_{12}Mo_6$@MWCNT_N6 (f), $P_2W_{12}Mo_6$@MWCNT_S6 (g), $P_2W_{12}Mo_6$@GF_S6 (h) and Pt/C (i) in $N_2$-saturated KOH (0.1 M). ..... 238
Figure 4S22 - Current density-scan rate linear fitting plots for all materials. Numeric values correspond to the double-layer capacitances ($C_{dl}$) for each material. ..... 239
Figure 5.1 - SEM images of the electrode materials electrodeposited on stainless steel at different magnifications: (a, d, g) at 1000×, showing overall morphology; (b, e, h) at 5000×, highlighting finer structural details; (c, f, i) at 25000×, revealing nanoscale features. ..... 257
Figure 5.2 - X-ray diffraction (XRD) patterns. (a) Patterns of (grey) stainless steel support, (black) Ni-NF, (blue) CoNi-NF_25, (green) CoNi-NF_50, (purple) CoNi-NF_75 and (yellow) CoNi-NF_75_OX; (b) Pattern (red) Co-NF; (c) Raman spectra for (black) Ni-NF, (red) Co-NF, (blue) CoNi-NF_25, (green) CoNi-NF_50, (purple) CoNi-NF_75 and (yellow) CoNi-NF_75_OX; (d) Atomic percentage of O, Co and Ni for each nanofoam. ..... 258
Figure 5.3 - CVs of (a) Ni-NF, (b) Co-NF, (c) CoNi-NF_25, (d) CoNi-NF_50, (e) CoNi-NF_75 and (f) CoNi-NF_75_OX nanofoams in $N_2$-saturated 0.1 mol $dm^{-3}$ KOH solution. ..... 262
Figure 5.4 - GCDs of (a) Ni-NF, (b) Co-NF, (c) CoNi-NF_25, (d) CoNi-NF_50, (e) CoNi-NF_75 and (f) CoNi-NF_75_OX nanofoams at current densities from 1 to 5 A $g^{-1}$ in 1 mol $dm^{-3}$ KOH solution. ..... 263

Figure 5.5 - Comparison of (a) specific capacitance and (b) capacitance retention obtained between CoNi-NF_75 and CoNi-NF_75_OX nanofoams in 1 mol $dm^{-3}$ KOH solution during cycling at 1 A $g^{-1}$ over 3500 cycles measured in 1 mol $dm^{-3}$ KOH solution. ..... 266
Figure 5.6 - (a and b) Bode, (c) Nyquist Electrochemical Impedance Spectra for CoNi-NF_75_OX composite material after 0 and 2000 cycles of Galvanostatic Charge Discharge at 1 A $g^{-1}$ for discharged (0 V) potential and (d) equivalent circuit model used in the fitting of the impedance spectra acquired for CoNi-NF_75_OX at 0V (discharged). ..... 268
Figure 5.7 - (a) OER LSV curves of Ni-NF, Co-NF, CoNi-NF_25, CoNi-NF_50, CoNi-NF_75 obtained in a 0.1 mol $dm^{-3}$ KOH electrolyte saturated in $N_2$, (b) the corresponding OER Tafel plots and (c) the chronoamperometric responses for 36000s. ..... 272
Figure 5.8 - (a) HER LSV curves of Ni-NF, Co-NF, CoNi-NF_25, CoNi-NF_50, CoNi-NF_75 obtained in a 0.1 mol $dm^{-3}$ KOH electrolyte saturated in $N_2$, (b) the corresponding HER Tafel plots. (c) and the chronoamperometric responses in 0.1 mol $dm^{-3}$ $N_2$–saturated KOH for 36000s. ..... 274
Figure 5S1 - SEM images of the electrode materials electrodeposited on stainless steel at different magnifications: (a, d, g) at 1000×, showing overall morphology; (b, e, h) at 5000×, highlighting finer structural details; (c, f, i) at 25000×, revealing nanoscale features..... 279
Figure 5S2 - SEM images of CoNi-NF_75_OX nanofoam at (a) 10000× and (b) 25000×. ..... 279
Figure 5S3 - EDX spectra of (a) Ni-NF, (b) Co-NF, (c) CoNi-NF_25, (d) CoNi-NF_50, (e) CoNi-NF_75, (f) CoNi-NF_75_OX and (g) stainless steel support..... 280
Figure 5S4 - Ni 2p XPS spectra of (a) Ni-NF, (b) CoNi-NF_25, (c) CoNi-NF_50, (d) CoNi-NF_75, (e) CoNi-NF_75_OX..... 281
Figure 5S5 - Co 2p XPS spectra of (a) Co-NF, (b) CoNi-NF_25, (c) CoNi-NF_50, (d) CoNi-NF_75, (e) CoNi-NF_75_OX..... 282
Figure 5S6 - O 1s XPS spectra of (a) Ni-NF, (b) Co-NF, (c) CoNi-NF_25, (d) CoNi-NF_50, (e) CoNi-NF_75 and (f) CoNi-NF_75_OX..... 283
Figure 5S7 - Specific capacitance versus current values for all nanofoams. ..... 284
Figure 5S8 – (a and b) Bode and (c) Nyquist Electrochemical Impedance Spectra for CoNi-NF_75 composite material after 0 and 2000 cycles of Galvanostatic Charge Discharge at 1 A $g^{-1}$ for discharged (0 V) potential. ..... 285
Figure 5S9 - Current density-scan rate linear fitting plots for all nanofoams. Numeric values correspond to the double-layer capacitances ($C_{dl}$) for each nanofoam..... 286

# List of Abbreviations

| | |
|---|---|
| 3D | THREE DIMENSIONAL |
| C | CAPACITANCE |
| $C_{DL}$ | DOUBLE LAYER CAPACITANCE |
| CNT | CARBON NANOTUBE |
| $C_{O2}$ | BULK CONCENTRATION OF $O_2$ |
| CPE | CONSTANT PHASE ELEMENT |
| $C_{REF}$ | REFERENCE CAPACITANCE VALUE PER UNIT AREA |
| CV | CYCLIC VOLTAMMETRY |
| DHBT | DYNAMIC HYDROGEN BUBBLE TEMPLATE |
| $D_{O2}$ | DIFFUSION COEFFICIENT OF $O_2$ |
| $E$ | ENERGY |
| EDX | ENERGY DISPERSIVE X-RAY SPECTROSCOPY |
| ECSA | ELECTROCHEMICAL ACTIVE SURFACE AREA |
| EDLC | ELECTROCHEMICAL DOUBLE LAYER CAPACITOR |
| EIS | ELECTROCHEMICAL IMPEDANCE SPECTROSCOPY |
| $E_{ONSET}$ | ONSET POTENTIAL |
| $E_{PA}$ | POTENTIAL OF THE ANODIC PEAK |
| $E_{PC}$ | POTENTIAL OF THE CATHODIC PEAK |
| $F$ | FARADAY'S CONSTANT |
| FTIR | FOURIER TRANSFORM INFRARED SPECTROSCOPY |
| GCD | GALVANOSTATIC CHARGE-DISCHARGE |
| GCE | GLASSY CARBON ELECTRODE |
| GF | GRAPHENE |
| HER | HYDROGEN EVOLUTION REACTION |
| HOR | HYDROGEN OXIDATION REACTION |
| $I_D$ | INTENSITY PRODUCED OF THE DISK |
| $I_{PA}$ | INTENSITY OF THE ANODIC PEAK |
| $I_{PC}$ | INTENSITY OF THE CATHODIC PEAK |
| $I_R$ | INTENSITY PRODUCED IN THE RING |
| $J$ | CURRENT DENSITY |
| $J_0$ | EXCHANGE CURRENT DENSITY |
| $J_K$ | KINETIC CURRENT DENSITY |
| $J_L$ | DIFFUSION LIMITING CURRENT DENSITY |
| K-L | KOUTECKY-LEVICH |
| LSV | LINEAR SWEEP VOLTAMMETRY |

| | |
|---|---|
| MWCNT | MULTI-WALLED NANOTUBE |
| N-FLG | NITROGEN-DOPED FEW LAYER GRAPHENE |
| $n_{O2}$ | NUMBER OF ELECTRONS TRANSFERRED PER $O_2$ MOLECULE |
| OER | OXYGEN EVOLUTION REACTION |
| ORR | OXYGEN REDUCTION REACTION |
| PEMFC | POLYMER ELECTROLYTE MEMBRANE FUEL CELL |
| POM | POLYOXOMETALATE |
| $R_T$ | TOTAL RESISTANCE |
| $R_S$ | SOLUTION RESISTENCE |
| RDE | ROTATING DISK ELECTRODE |
| RRDE | ROTATING RING-DISK ELECTRODE |
| RHE | REVERSIBLE HYDROGEN ELECTRODE |
| SEM | SCANNING ELECTRON MICROSCOPY |
| SWCNT | SINGLE-WALLED NANOTUBE |
| URFC | UNITIZED REGENERATIVE FUEL CELL |
| XPS | X-RAY PHOTOELECTRON SPECTROSCOPY |
| XRD | X-RAY DIFFRACTION SPECTROSCOPY |
| $W_R$ | WARBURG RESISTANCE |

# List of Papers

i. **Electrocatalytic Oxygen Reduction Reaction on 48-Tungsto-8-Phosphate Wheel Anchored on Carbon Nanomaterials**
Novais, H.C., Jarrais, B., Haider, A., Kortz, U., Guerrero-Ruiz, A., Rodríguez-Ramo, I., Freire, C.; Fernandes, D.M.
*Electrocatalysis* **14**, 294–305 (2023)
https://doi.org/10.1007/s12678-022-00792-w.

ii. **Hybrids Composed of an Fe-Containing Wells–Dawson Polyoxometalate and Carbon Nanomaterials as Promising Electrocatalysts for the Oxygen Reduction Reaction**
Novais, H.C.; Jarrais, B.; Mbomekallé, I.-M.; Teillout, A.-L.; Oliveira, P.d.; Freire, C.; Fernandes, D.M.
*Inorganics* **11**, 388, (2023)
https://doi.org/10.3390/inorganics11100388

iii. **Enhanced Oxygen Reduction Reaction Activity of the Wells-Dawson Polyoxometalate $P_2W_{12}Mo_6$ Immobilised in Nitrogen and Sulphur-Doped Carbon Nanomaterials**.
Novais, H.C.; Jarrais, B.; Mbomekallé, I.-M.; Teillout, A.-L.; Oliveira, P.d.; Freire, C.; Fernandes, D.M.
*Chemelectrochem* **11**, (2024)
https://doi.org/10.1002/celc.202300622

iv. **Cobalt/Nickel Nanofoams: Potential application in Supercapacitors and OER/HER**
Novais, H.C.; Montemor, M.F., Fernandes, A. J. S., Freire, C, Fernandes, D.M.
Scientific article submitted to the Journal of Power Sources

# Structure and Organization of this Thesis

This PhD thesis is divided into six chapters. Each chapter presents a significant research contribution, published or in preparation for publication, reflecting the overall objective of developing multifunctional nanomaterials and nanofoams for electrocatalytic energy conversion and storage applications.

**Chapter 1 - Introduction**

Provides a general overview of the scientific background to the thesis. It outlines the energy and environmental challenges driving the search for efficient, low-cost materials for electrochemical energy conversion and storage. The chapter introduces polyoxometalate@carbon-based electrocatalysts for ORR and metallic nanofoams for supercapacitor and water splitting applications.

**Chapter 2 - Electrocatalytic Oxygen Reduction Reaction on 48-Tungsto-8-Phosphate Wheel Anchored on Carbon Nanomaterials**

Focuses on the synthesis and characterisation of a POM-based composite using the 48-tungsto-8-phosphate polyoxometalate ($P_8W_{48}$) immobilised on different carbon nanomaterials (GF, SWCNT, MWCNT and N-MWCNT). The electrocatalytic performance towards the oxygen reduction reaction (ORR) in alkaline media is investigated and compared between the composites.

**Chapter 3 - Hybrids Composed of a Fe-containing Wells-Dawson Polyoxometalate and Carbon Nanomaterials as Promising Electrocatalysts for the ORR**

Describes the preparation of hybrid materials using a Wells-Dawson iron-substituted POM ($P_2W_{17}Fe$) anchored on nitrogen-doped graphene flakes and carbon nanotubes. The materials were thoroughly characterised and their electrocatalytic activity towards the ORR was evaluated, showing good performance and stability.

**Chapter 4 - Enhanced ORR activity of Wells-Dawson polyoxometalate $P_2W_{12}Mo_6$ immobilised on nitrogen and sulphur doped carbon nanomaterials**

Investigates the electrocatalytic behaviour of a molybdenum substituted Wells-Dawson POM ($P_2W_{12}Mo_6$) immobilised on nitrogen or sulphur doped carbon nanomaterials. The chapter explores the synergistic effect of heteroatom doping in improving ORR performance and catalyst durability.

**Chapter 5 - Cobalt/Nickel Nanofoams: Potential Application in Supercapacitors and OER/HER**

Presents the synthesis of Co, Ni and CoNi nanofoams via the Dynamic Hydrogen Bubble Template (DHBT) method. Their performance as electrode materials was evaluated for both supercapacitors and electrocatalysis, specifically the oxygen evolution and hydrogen evolution reactions (OER and HER). The influence of chemical activation and composition on their electrochemical behaviour is discussed in detail.

**Chapter 6 - General Conclusions and Future Perspectives**

Summarises the main findings of the thesis and discusses their implications for the development of advanced materials for energy conversion and storage. It also outlines possible directions for future research in this field.

Chapter 1

# Introduction

# 1

# Introduction

## 1.1. Global Energy Challenger

The world is currently at a critical juncture in its history. The relentless consumption of fossil fuels, driven by rapid industrialisation and population growth, has precipitated an unprecedented energy crisis.[1] This crisis is not merely a consequence of the depletion of non-renewable resources; it is also a consequence of the environmental impact of our energy consumption patterns.[2, 3] The burning of fossil fuels releases greenhouse gases into the atmosphere, contributing to global warming and climate change. These environmental changes present a significant threat to the future of our planet, affecting biodiversity, weather patterns and sea levels.[4] The implications of this crisis are far-reaching, affecting every aspect of our lives, from the air we breathe to the food we eat and the water we drink. It threatens our health, our economy, and our security. It exacerbates social and economic inequalities and fuels political instability. The environmental crisis affects us all, regardless of our geographical location or occupation.[5] However, the alarmism surrounding these issues can be counterproductive.[6, 7] While the challenges we face are real and serious, they are also manageable. Technological innovation, if allowed to continue and grow, will remedy environmental issues.[8, 9] In other words, we must avoid allowing environmental alarmism to hinder our progress. It is important to recognise that environmental problems are manageable, yet those who are most alarmist about environmental issues tend to oppose the most effective and readily available solutions to solve them. Some studies claim that the prospect of billions of deaths was causing widespread anxiety, including among adolescents.[10, 11] It is imperative that scientific evidence be distinguished from conjecture. Despite decades of news media coverage, a significant proportion of the population remains unaware of fundamental facts. Carbon emissions have reached a peak and have been in decline in most developed nations for over a decade.[12] The

number of deaths from extreme weather, even in developing countries, has decreased.[13]

The International Energy Agency (IEA) has stated in Key World Energy Statistics 2021 that 80.9% of the total primary energy supply came from fossil fuels.[14] Of this, 30% was based on oil, 26% was based on coal and 23.2% was based on natural gas. The remaining 19.1% was based on other sources, including nuclear, hydro, biofuels, waste and others. The IEA report on $CO_2$ emissions in 2023 indicates that global $CO_2$ emissions increased by 1.1% in 2023.[15] The report finds that clean energy growth has limited the rise in global emissions. Weather effects and continued reopening due to the ongoing impact of the Covid-19 pandemic played a significant role in driving emissions in 2023.[16] In contrast, advanced economies observed a record decline in their emissions, which have now returned to the level observed fifty years ago. In response to this crisis, governments and organisations worldwide have taken significant steps towards promoting sustainable energy. The European Union, for instance, has been actively promoting Europe's transition to a low-carbon society. Through the European energy union, the EU is ensuring there is greater coherence in all policy areas to meet the broad objectives of creating a reliable, affordable and sustainable energy system. The EU has also implemented the REPowerEU Plan, which is assisting the EU in reducing its energy consumption, increasing the production of clean energy, and diversifying its energy sources.[17] Similarly, the United States has taken decisive action to address the climate challenge. The Federal Sustainability Plan outlines a range of ambitious goals to deliver an emissions reduction pathway by 50–52 percent from 2005 levels by 2030.[18] The United States' Long-Term Strategy also delineates the manner in which the country can attain its ultimate objective of achieving net-zero emissions by no later than 2050.

The hydrogen economy represents a future in which hydrogen ($H_2$) serves as a key player in energy systems, acting as a sustainable energy carrier. Hydrogen's potential to decarbonise various sectors has positioned it as a critical element in achieving decarbonisation and energy sustainability goals. This economy promotes hydrogen as a fuel for transportation, for the energy needs of buildings and industry, and for portable electronic devices.

The current annual production of hydrogen ($H_2$) in 2022 is 87 million metric tons, which represents approximately 2.5% of the final energy demand in 2020.[19] Approximately three-quarters of this hydrogen is produced from natural gas through a

process known as steam-methane reforming (SMR), while the remaining quarter is produced from coal.[20] However, the SMR process is a significant source of carbon dioxide emissions, producing approximately 5 kg of $CO_2$ for every kilogram of $H_2$.[21] Furthermore, it is a fossil fuel-dependent industry. The $CO_2$ emissions associated with this production are about 800 megatonnes of carbon dioxide ($MtCO_2$/year), equivalent to almost 2.2% of the global energy-related $CO_2$ emissions.[19] The hydrogen is primarily utilised as a processing agent in a variety of industries, including oil refineries and chemical production processes, such as the ammonia and pharmaceutical industries.[22] Hydrogen can be employed throughout the energy system. However, the deployment of green hydrogen beyond the industrial sector necessitates the deployment of larger (renewable) capacities, greater investments and a more significant challenge to overcome. In certain applications, such as low- and medium-temperature heating or road transport, electrification is not only more efficient but also more cost-effective and can facilitate current decarbonisation with the available technologies.[23] Consequently, hydrogen is reserved for applications where electrification is limited or difficult, such as international sea and air transport, chemicals, steel and seasonal storage. For the majority of these applications, hydrogen itself is not the most cost-effective form of energy.

In recent years, there has been a significant increase in funding for research into sustainable methods of hydrogen production. This research is being conducted in several countries, including many in Europe, the United States, Japan, South Korea and China.[24] The concept of using hydrogen as a sustainable energy source, often referred to as the "Hydrogen Economy," was first proposed by Jules Verne in 1874. In his celebrated novel, *The Mysterious Island*, Jules Verne predicted the advent of hydrogen in response to the exhaustion of coal. He wrote, "I believe that water will one day be used as a fuel, that hydrogen and oxygen, which constitute it, used alone or simultaneously, will provide an inexhaustible source of heat and light of an intensity that coal cannot have." This concept has been further developed by numerous researchers since then. A schematic diagram illustrating the concept of the "Hydrogen Economy" is presented in Figure 1.1.

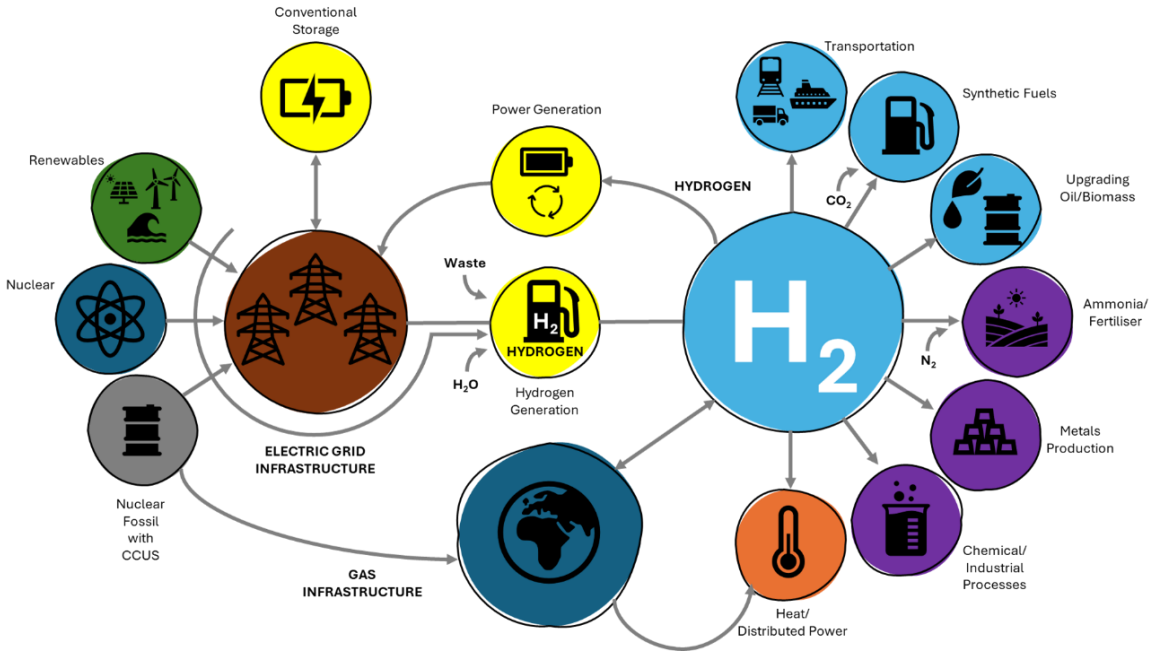



Figure 1.1 - Schematic representation of the ‘’Hydrogen Economy’’. Adapted from ref. [25]

In the transition towards a sustainable energy future, hydrogen is poised to play a pivotal role. Initially, hydrogen production will evolve from reliance on fossil fuels to be almost dependent on renewable energy.[26] As a versatile element, hydrogen is set to become a key player in energy storage and a carrier of clean energy. The transition to a hydrogen-centric economy promises numerous advantages, including the potential to bolster energy security by reducing the reliance on oil imports, to foster environmental health through the use of renewable sources, and to achieve a significant reduction in the emission of greenhouse gases and other pollutants. Economically, it has the potential to revolutionise the energy market landscape. The advent of decarbonisation is projected to result in a surge in hydrogen production, with an estimated increase of fivefold to meet 12% of global energy needs by 2050. This growth is anticipated to be fuelled by the industrial and transportation sectors, which could see a reduction in $CO_2$ emissions by approximately 12% and 26%, respectively.[19]

The integration of hydrogen into the energy system is a multifaceted endeavour. The expansion of green hydrogen usage beyond industrial applications necessitates significant enhancements to renewable energy capacity, substantial financial commitments, and the surmounting of considerable obstacles.[23] Nations and key industries, including the automotive sector with its substantial investments in hydrogen-

fuelled vehicles, have made noteworthy strides towards a hydrogen-centric economy. In particular, the Toyota Group and the Hyundai Motor Group have demonstrated a clear commitment to innovation and the implementation of this solution.[27] However, the path is obstructed by technological challenges. Currently, the techniques for producing green hydrogen are neither cost-effective nor efficient enough for broad industrial deployment.[28] Similarly, the existing methods for hydrogen's transport and storage present financial barriers to its adoption in energy infrastructures. Consequently, the shift towards a hydrogen-based economy is a formidable task, demanding extensive research and global collaboration. In order to address the escalating energy demands and harness the potential of hydrogen as an eco-friendly and appealing energy vector, the development of viable hydrogen production methodologies is imperative. One promising direction is the transformation of solar energy into hydrogen, a process that is entirely reliant on renewable sources.[29, 30] Solar energy, an immense and inexhaustible supply, bathes the Earth providing more energy in 1 hour to the earth than all of the energy consumed by humans in an entire year.[31] This staggering quantum of solar energy surpasses the total estimated reserves of fossil fuels, underscoring the plausibility of solar energy as a cornerstone for future energy systems.[32] Figure 1.2 present the reasonable assured recoverable reserves (RAR) estimates over the next 30 years.

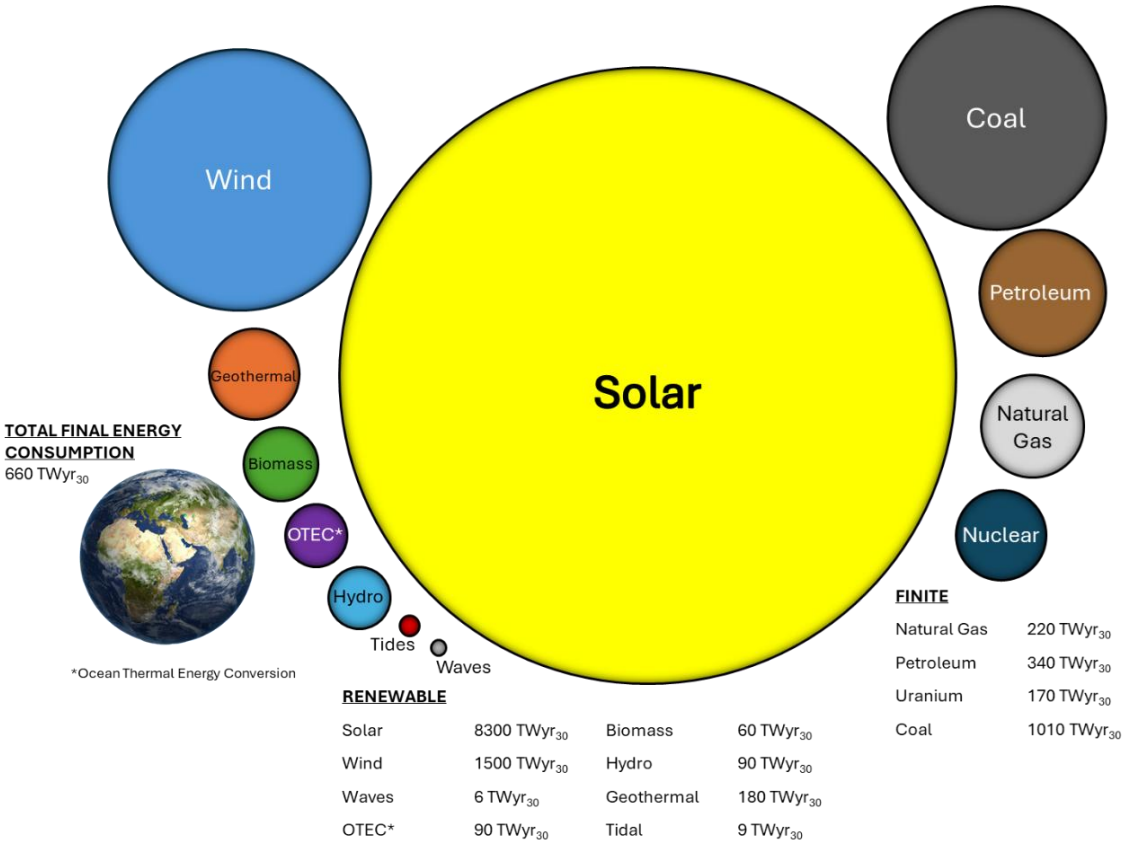



Figure 1.2 - The area of the circles represents reasonably assured recoverable reserves (RARs) from both finite and renewable resources over the next 30 years. These areas can be compared with the total demand (earth image) over that same time period.

The decentralised and intermittent nature of renewable energy sources represents a significant challenge to their widespread adoption. Since electricity demand fluctuates independently, there is often a mismatch between supply and demand. To address this issue, the integration of solar-based technologies with advanced electrochemical energy conversion and storage systems becomes crucial. In order to enhance energy efficiency and sustainability when the supply of solar energy exceeds demand, the surplus electricity can lead to non-spontaneous electrochemical reactions, such as water splitting, to produce molecular hydrogen. Conversely, in the event of a surplus, the stored chemical energy can be converted back into electricity through spontaneous electrochemical reactions, with water being the only by-product. This concept is illustrated in Figure 1.3. Furthermore, the development of electrochemical energy conversion and storage is essential for portable technologies and transport.

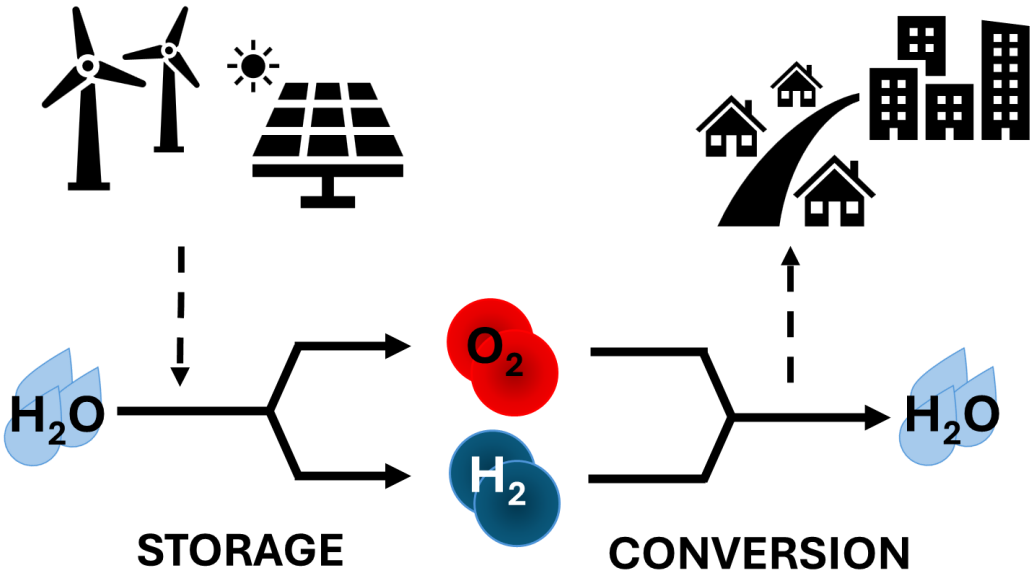



Figure 1.3 – Illustration of the hydrogen and oxygen cycle for energy storage and conversion. Adapted from ref. [33]

There is an urgent requirement for efficient energy storage solutions that can complement fuel cells and guarantee a stable energy supply.[34, 35] In the absence of effective storage, excess energy generated from renewable sources (and beyond) cannot be utilised during periods of high demand, thus limiting the scalability and reliability of hydrogen-based energy systems. In order to surmount the limitations of intermittent energy production, energy storage technologies such as batteries and supercapacitors play a pivotal role in ensuring a continuous supply of energy.[36, 37] Supercapacitors offer a complementary approach by storing energy either electrostatically (in electric double-layer capacitors, EDLCs) or through rapid surface redox reactions (in pseudocapacitors), enabling fast charge and discharge cycles.[38-40] The value of supercapacitors is particularly evident in applications requiring high power density and rapid response times, such as grid stabilisation, hybrid energy systems, and regenerative braking in electric vehicles.[41-44] Their capacity to store and release energy expeditiously renders them an optimal partner for fuel cells, which are susceptible to delays in energy release. For instance, although fuel cells provide an efficient means of energy conversion, they frequently necessitate energy storage systems, such as supercapacitors, to balance supply and demand.[45] The integration of both technologies enhances the overall efficiency of the energy system, ensuring more reliable energy collection and supply. There is also growing interest in the development of materials that can serve a dual role in both fuel cells and supercapacitors.[35]

Advanced carbon-based nanomaterials, metal oxides and hybrid structures have demonstrated potential for use in both fields, and the study of these multifunctional materials is a crucial step towards bridging the gap between energy conversion and storage, leading to more efficient and sustainable energy solutions.[46-49]

## 1.2. Electrochemical Oxygen Reduction and Evolution Reactions

The advancement of renewable energy technologies is contingent on the efficient conversion and storage of energy, which can be facilitated by means of fuel cells, electrolysers and metal-air batteries. These offer a sustainable pathway toward a cleaner energy future.[50-52] While the mechanisms governing these systems differ, their operation is fundamentally rooted in electrochemical reactions occurring at the electrode-electrolyte interfaces. In electrolysers, which facilitate hydrogen production via water splitting, the oxygen evolution reaction (OER) occurs at the anode, resulting in the oxidation of water molecules to release oxygen gas ($O_2$), protons ($H^+$), and electrons.[53] Concurrently, at the cathode, the hydrogen evolution reaction (HER) takes place, where protons gain electrons to form molecular hydrogen ($H_2$), which can be stored as a clean energy carrier.[53]

Conversely, in hydrogen-oxygen fuel cells, these reactions are reversed to facilitate energy conversion. The hydrogen oxidation reaction (HOR) occurs at the anode, where hydrogen molecules split into protons and electrons.[54] The electrons travel through an external circuit, generating electricity, while the protons migrate through an electrolyte membrane toward the cathode, where they participate in the oxygen reduction reaction (ORR). The result of this reaction is water ($H_2O$) which is formed as a byproduct.[55] As illustrated schematically in Figure 1.4, the fuel cell and electrolyser function through a series of reactions involving hydrogen and oxygen. Metal-air batteries, conversely, employ a metal as the energy carrier, facilitating the storage and conversion of energy through reactions that involve the formation and reduction of metal oxides.[56] Another promising technology in the field of clean energy storage and conversion devices is the unitised regenerative fuel cell (URFC). A URFC is a versatile and compact electrochemical system that has been designed to operate in two distinct modes: as an electrolyser for hydrogen production and as a fuel cell for energy generation. This dual functionality allows a single electrochemical cell to efficiently store excess energy by

producing hydrogen when surplus electricity is available and later convert the stored hydrogen into electrical power to meet varying energy demands. This seamless transition between storage and generation renders URFCs highly attractive for renewable energy integration and off-grid applications.[57, 58]

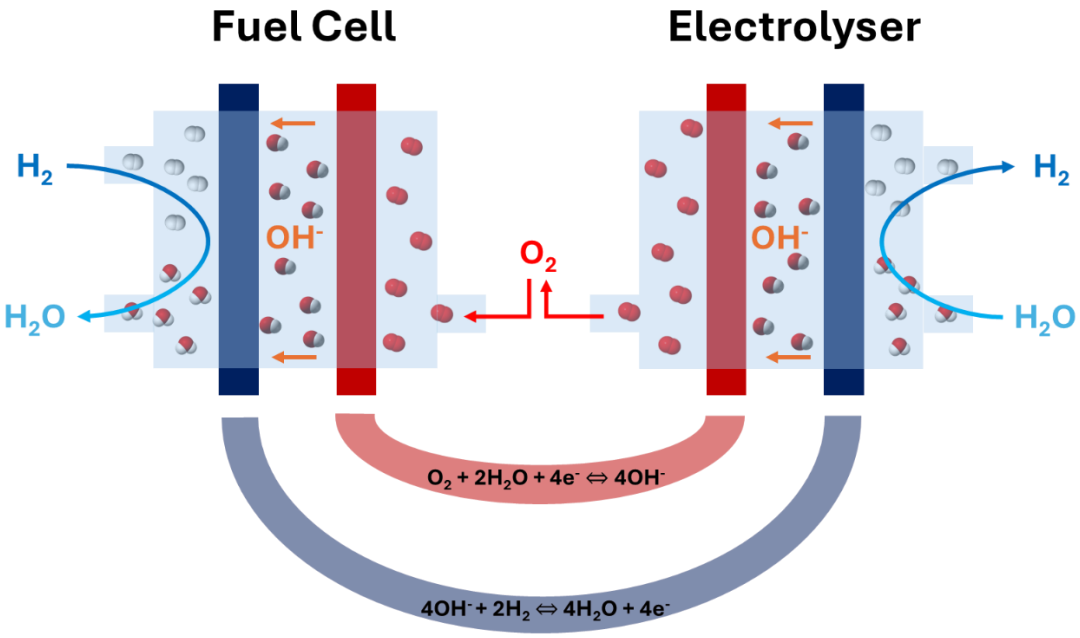



Figure 1.4 – Representation of the fuel cell mode and the electrolyser mode in alkaline electrolytes. Adapted from ref. [59]

The development of efficient bifunctional electrocatalysts is a pivotal challenge in advancing unitised regenerative fuel cells, as they must effectively catalyse both the oxygen reduction reaction and the oxygen evolution reaction. Given the alternating operational modes of a URFC, the cathodic and anodic reactions change depending on whether the device is functioning as a fuel cell or an electrolyser. In this dual mode of operation, the ORR and OER are particularly sluggish, with high overpotentials and slow reaction kinetics, which limits overall efficiency.[57, 58, 60] Figure 1.5 shows the overpotentials and overall reaction equations associated with reactions involving oxygen and hydrogen. It is clear that oxygen reactions require high overpotentials. This means that oxygen electrocatalysis limits the energy efficiency and the rate capability of electrochemical energy devices.[33] The kinetic behaviour of these four key electrochemical reactions plays a crucial role in determining the efficiency and performance of energy conversion and storage systems, yet sluggish reaction kinetics

can often hinder their overall effectiveness. Typically, the two-electron transfer processes involved in HER and HOR occur relatively quickly; in contrast, the multi-step proton-coupled electron transfer mechanisms governing the ORR and OER are inherently slow, creating a major bottleneck in these systems. For instance, the slow ORR kinetics is the primary source of energy loss in low-temperature hydrogen fuel cells, significantly affecting their efficiency.[61] Similarly, electrolysers and metal-air batteries suffer from comparable losses due to the kinetic constraints of the ORR, which limit their overall performance and energy output. Addressing these kinetic limitations through advanced electrocatalyst design is essential for enhancing the viability of these energy technologies.[33]

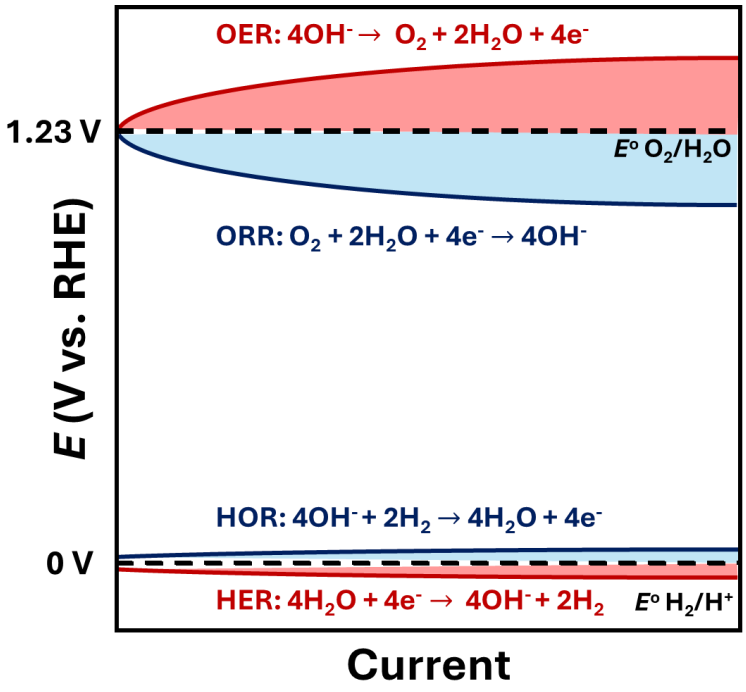



Figure 1.5 – Schematic of the overpotentials associated with hydrogen electrocatalysis (HER, HOR) and oxygen electrocatalysis (ORR, OER) and their overall reaction equations. Adapted from ref. [62]

A significant impediment to the extensive implementation of these technologies is the reliance on noble metal catalysts, including platinum (Pt), iridium (Ir), and ruthenium (Ru).[63] These elements are not only rare but also substantially elevate the cost of production, impeding large-scale commercialisation.[33] Consequently, there has been a concerted effort within the scientific community to explore alternative materials,

with a particular focus on non-precious metal catalysts (NPMCs).[64, 65] These catalysts have been shown to exhibit comparable activity to that of the traditional noble metals, while being more cost-effective and more abundant. Transition metal-based catalysts, particularly those involving iron (Fe), cobalt (Co), and nickel (Ni), have emerged as promising candidates due to their ability to catalyse both the ORR and the OER with efficiency.[66-68] The transition to anion-exchange membrane fuel cells (AEMFCs) signifies a shift away from the utilisation of noble metals, given the operational versatility of these systems within alkaline media, which allows for the employment of a more extensive range of catalyst materials.[69, 70] Carbon-based materials doped with heteroatoms such as nitrogen (N), phosphorus (P) and sulphur (S) have demonstrated considerable potential in enhancing catalytic performance.[71-73] Metal-organic frameworks (MOFs), perovskites and metal-nitrogen-carbon (M-N-C) catalysts have also demonstrated potential for high activity and durability under alkaline conditions.[63, 74, 75]

In addition to ORR and OER, HER and HOR are also crucial for hydrogen-based energy systems. The efficiency of HER depends a lot on the activity of the electrocatalyst, as it requires overcoming activation barriers for proton reduction and ensuring rapid electron transfer.[76] Platinum-based materials remain the most effective catalysts for HER due to their excellent hydrogen binding energy, but researchers are looking at cost-effective alternatives, such as transition metal phosphides, sulphides, and carbides.[77, 78] In contrast, HOR represents the fundamental reaction in hydrogen fuel cells, whereby hydrogen is oxidised at the anode to release electrons and protons, thereby driving the electrochemical generation of electricity. The sluggish kinetics of HOR in alkaline media have posed significant challenges for non-Pt-based catalysts, as platinum-free materials frequently exhibit lower intrinsic activity and higher overpotentials. In order to enhance HOR catalyst efficiency, various strategies are currently being explored, including bimetallic alloying, electronic structure modulation, and defect engineering.[79]

Even though there have been some great advancements in this area, more research is needed to make these alternative catalysts even better. Adding high-surface-area supports, making defects in the catalysts, and changing the electronic parts of the catalysts have all been shown to make them more efficient and stable.[80, 81] Furthermore, recent studies have explored single-atom catalysts (SACs), which offer well-defined active sites and exceptional catalytic activity, thereby narrowing the performance gap between noble metals and earth-abundant materials.[82-84]

A comprehensive understanding of the reaction mechanism is essential for the design of next-generation bifunctional catalysts. The ORR involves complex multi-step electron and proton transfer processes, and its sluggish kinetics result in significant overpotentials. Meanwhile, OER, which involves the oxidation of hydroxide ions or water molecules, also suffers from slow kinetics and energy losses. Similarly, HER and HOR require efficient catalysts to facilitate proton adsorption, charge transfer, and gas evolution while maintaining durability under electrochemical cycling. By elucidating the fundamental adsorption-desorption processes, intermediate species formation, and rate-determining steps, researchers can develop more efficient catalysts that enhance ORR, OER, HER, and HOR performance, ultimately improving the efficiency and commercial viability of regenerative fuel cells and electrolyser technologies.

### 1.2.1. Oxygen Reduction Reaction

The ORR mechanism can proceed via two distinct pathways. The first and most efficient route is the four-electron transfer mechanism, often referred to as the direct pathway.[85] This process facilitates the complete reduction of oxygen to either water or hydroxide ions, depending on the electrolyte medium, without generating undesirable intermediate species.[86] As a result, it minimises energy losses and enhances the overall efficiency of the reaction. This highly desirable mechanism is predominantly observed when employing platinum-based electrocatalysts, which exhibit exceptional catalytic activity and selectivity for the direct four-electron pathway.[87, 88] The ORR reaction in acidic and alkaline electrolytes can be described by Equations 1.1 and 1.2, respectively, which illustrate the fundamental electrochemical steps governing this process.

$$O_2 + 4H^+ + 4e^- \leftrightarrow 2H_2O \ (1.23 \text{ V vs RHE}) \quad (1.1)$$

$$O_2 + 2H_2O + 4e^- \leftrightarrow 4OH^- \ (0.40 \text{ V vs RHE}) \quad (1.2)$$

In the direct mechanism, two distinct pathways can be distinguished. The first is the associative mechanism, whereby molecular oxygen is adsorbed onto the catalyst surface and sequentially accepts four electrons and protons in an acidic medium or four electrons in an alkaline medium. This results in the complete reduction of oxygen to either water or hydroxide ions, depending on the electrolyte used. The alternative, the dissociative mechanism, involves the initial splitting of the $O_2$ molecule into two adsorbed

oxygen atoms ($O_{ads}$ or $OOH_{ads}$), followed by the reduction of each atom to form the final products. Notably, these mechanisms do not occur as a single step, but rather involve the formation of multiple intermediate species, which in turn influence the reaction kinetics and efficiency. During the initial stage of ORR, the active catalytic site (*) adsorbs an oxygen molecule ($O_2$), which may either dissociate into separate oxygen atoms (*-O) or remain intact (*-$O_2$) while undergoing further reduction. If the latter occurs, the oxygen molecule reacts with protons and electrons to form an intermediate peroxide species (*-OOH), which subsequently breaks down into surface-bound oxygen (*-O). Regardless of whether the reaction proceeds via the associative or dissociative mechanism, the remaining steps follow a similar pattern. Subsequent electron transfer and protonation steps lead to the formation of hydroxyl intermediates, which are then fully reduced to produce water or hydroxide ions. Consequently, the catalyst surface is regenerated, allowing it to facilitate further oxygen reduction reactions.

The production of hydrogen peroxide in the sluggish two-electron process (known as the indirect mechanism) is often detrimental in fuel cells due to its potential to corrode components and degrade the electrolyte membrane.[89] The ORR indirect mechanism in acidic or alkaline electrolytes can be expressed by Eq. 1.3-1.4 and 1.5-1.6, respectively.[90] However, in industrial settings, this pathway is exploited for hydrogen peroxide generation. The detailed ORR mechanism involves a complex interplay of multiple adsorbed intermediates, which are highly dependent on the surface properties of the electrode. The high energy required to break the oxygen-oxygen bond (498 kJ $mol^{-1}$) contributes to the sluggish nature of ORR, necessitating the application of high reduction potentials, which in turn lower the overall efficiency of energy devices.[91] To mitigate these limitations, the development of efficient ORR catalysts is critical.

$$O_2 + 2H^+ + 2e^- \leftrightarrow H_2O_2 \ (0.70 \text{ V vs RHE}) \quad (1.3)$$

$$H_2O_2 + 2H^+ + 2e^- \leftrightarrow 2H_2O_2 \ (1.78 \text{ V vs RHE}) \quad (1.4)$$

$$O_2 + H_2O + 2e^- \leftrightarrow HO_2^- + OH^- (-0.08 \text{ V vs RHE}) \quad (1.5)$$

$$HO_2^- + H_2O + 2e^- \leftrightarrow 3OH^- \ (0.88 \text{ V vs RHE}) \quad (1.6)$$

The electrochemical parameters that are used to evaluate the performance of ORR electrocatalysts are:

- **Onset potential ($E_{onset}$)** is the potential at which the reaction starts. It can be calculated by two different ways: 1) the potential at 5% of the maximum current ($j_{max}$) or 2) the potential at a current density ($j$) of -0.1 mA $cm^{-2}$.

- **Diffusion-limited current density (*j*L)** is the current density reached when the reaction at the electrode is totally controlled by mass transport (a plateau is reached and $j = j_L$).
- **Kinetic current density (*j*k)** is the current in the absence of mass-transfer limitations.
- **Number of electrons transferred per $O_2$ molecule ($n_{O2}$)** is determined through the Koutecky-Levich (K-L) equation, from the $j^{-1}$ vs. $\omega^{-1/2}$ plot's slope and provides information about the selectivity of the electrocatalyst (2-electron or 4-electron pathway).
- **Tafel slope** is usually employed to understand the reaction kinetics and mechanism, which is needed to compare the catalytic activities of different electrocatalysts.

An electrocatalyst with a good performance towards ORR is expected to have a less negative $E_{onset}$, high $j_L$ value, low Tafel slope and selectivity for the 2- or 4- electron pathway depending on the desired application.[92]

A range of catalysts have been the focus of study, with platinum nanoparticles supported on carbon materials (Pt/C) being regarded as the most effective for promoting ORR due to their low overpotential, high current densities, and selectivity towards the four-electron pathway. However, the need for high platinum loadings, typically between 40% and 80%, has led to concerns over cost and long-term stability. The decline in catalytic activity over time, in conjunction with the potential for deactivation due to carbon monoxide poisoning or methanol crossover, has prompted significant research endeavours into alternative materials.[93]

### 1.2.2. Oxygen Evolution Reaction

As a counter-reaction to the ORR, the OER is responsible for generating molecular oxygen from water by means of an anodic oxidation process. Despite its significance, the OER is intrinsically sluggish due to the complex multi-electron transfer steps involved, necessitating high overpotentials and efficient electrocatalysts to enhance reaction kinetics.[94] The OER is an anodic reaction that can be carried out in acid (equation 1.7) and alkaline (equation 1.8) media, releasing $O_2$ gas.

$$2H_2O \leftrightarrow 4H^+ + O_2 + 4e^- \quad (1.7)$$

$$4HO^- \leftrightarrow 2H_2O + O_2 + 4e^- \quad (1.8)$$

Under standard conditions, the equilibrium potential for the OER is approximately 1.23 V versus the reversible hydrogen electrode (RHE). However, achieving practical reaction rates requires the application of significant overpotentials (η), which are notably higher than those required for HER.[95] This discrepancy arises due to the inherently sluggish kinetics of OER, which stem from its complex four-electron, proton-coupled electron transfer mechanism. The stepwise nature of this reaction imposes a high activation energy barrier, making it one of the most kinetically challenging processes in electrochemical energy conversion systems.[95, 96] Furthermore, the kinetics of OER are highly dependent on pH, with a notable difference in performance between acidic and alkaline conditions. In acidic electrolytes, the reaction proceeds more slowly, necessitating a higher overpotential to reach the same current density compared to alkaline media.[95] This disparity in reaction rates can be attributed to the presence of distinct reaction pathways and the varying availability of reactant species in different pH environments. The necessity for elevated overpotentials in OERs represents a significant impediment to the efficiency of alkaline water electrolysis, metal-air batteries, and regenerative fuel cells.[95, 96] This is due to the fact that overpotentials are a fundamental component of these technologies. Consequently, elevated overpotentials contribute to augmented energy consumption. To mitigate the high overpotentials associated with this reaction, the implementation of electrocatalysts is employed to provide reduced activation energies, thereby enhancing the reaction kinetics.

In an acidic medium, the reaction commences when the active site (*) adsorbs a water molecule, facilitating the release of a proton and an electron, forming an *-OH intermediate. This is followed by a sequence of steps where additional protons and electrons are removed, progressively forming the next reaction intermediates. The transformation of *-OH leads to the formation of an *-O species, which subsequently interacts with another $H_2O$ molecule, resulting in the *-OOH intermediate. Finally, this intermediate undergoes further oxidation, producing molecular oxygen ($O_2$). The restoration of the active site to its initial state is pivotal for the continuation of the reaction.[97]

In an alkaline medium, the process follows a similar sequence, but involves hydroxide ions ($OH^-$) instead of water molecules. The active site initially binds $OH^-$, forming *-OH and releasing an electron. A second $OH^-$ then reacts with this intermediate, leading to the formation of *-O while simultaneously generating a water molecule and releasing another electron. The reaction continues with the addition of another hydroxide ion, resulting in the formation of a *-OOH intermediate and the release of an additional

electron. In the final step, the *-OOH intermediate undergoes further oxidation, producing $O_2$ along with the release of a water molecule and an electron, thereby regenerating the active site for further catalytic cycles. Apart from these stepwise processes, an alternative mechanism has also been suggested, wherein two neighbouring metal-oxo (M–O) species interact directly, enabling the formation of an $O_2$ molecule without passing through the conventional *-OOH intermediate. This pathway provides an alternative perspective on the oxygen evolution reaction, highlighting the complexity of the mechanistic landscape and the role of catalyst design in optimising efficiency.[97]

In order to perform an accurate assessment of the performance of OER electrocatalysts, it is common practice to employ several key kinetic parameters, such as[93]:

- **Overpotential ($\eta_{10}$)** is the difference between the potential at which a $j$ = 10 mA $cm^{-2}$ is obtained and the standard value of 1.23 V vs. RHE. The $j$ = 10 mA $cm^{-2}$ value usually used is the current density expected for a 12.3 % efficiency in solar to hydrogen devices, a requirement for cost-competitive photoelectrochemical water splitting.
- **Maximum current density ($j_{max}$)** is the potential at the last $E$ used.
- **Tafel slope**, as for the ORR is usually employed to understand the reaction kinetics and mechanism, which is needed to compare the catalytic activities of different electrocatalysts.

A lower Tafel slope is indicative of faster reaction kinetics and a more efficient catalytic process, thus making it a desirable feature in high-performance OER catalysts.[98] Additionally, a low overpotential is another key indicator of a highly active electrocatalyst, as it reflects the catalyst's ability to drive OER with minimal energy losses.[93]

Since OER is inherently a four-electron transfer process, it is characterised by slow reaction kinetics and high activation energy barriers, necessitating the development of efficient electrocatalysts to enhance reaction rates and reduce energy losses. The optimisation of these kinetic parameters is essential for advancing next generation catalysts capable of accelerating OER and improving the overall efficiency of electrochemical energy conversion systems.

### 1.2.3. Hydrogen Evolution Reaction

The HER is the cathodic process in water electrolysis, and it plays a crucial role in hydrogen production. However, the rate of the reaction varies significantly with pH; under acidic conditions, the HER exhibits faster reaction rates, whereas in alkaline and neutral environments, its kinetics are considerably slower – by approximately two to three orders of magnitude.[99, 100] This kinetic limitation poses a significant challenge for alkaline water electrolysis technologies, requiring highly active electrocatalysts to compensate for the sluggish reaction rates. The disparity in HER kinetics arises from differences in reaction mechanisms between acidic and alkaline/neutral media, as shown in Figure 1.6. Despite these challenges, alkaline electrolytes are often preferred over acidic ones due to economic and practical considerations, including the high cost of noble metal electrodes, such as platinum (Pt) and iridium (Ir), which are required for operation in acidic conditions, and the accelerated corrosion of equipment in acidic environments, reducing the operational lifespan of electrolysis systems.[101]

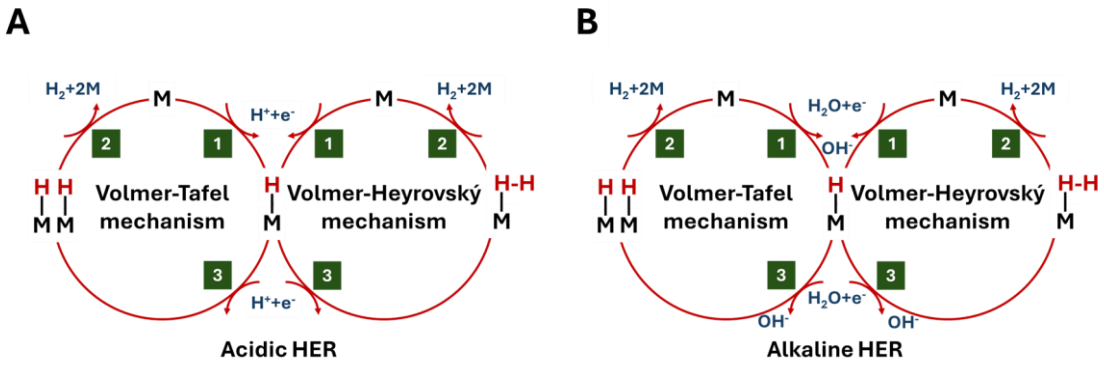



Figure 1.6 – HER mechanisms in acidic (A) and alkaline (B) media. Adapted from ref. [102]

In acidic electrolytes, protons ($H^+$) participate directly in the HER, while in alkaline or neutral media, water molecules serve as the proton source. This distinction is reflected in the fundamental reaction equations 1.9 and 1.10 for acidic and neutral/alkaline medium, respectively:

$$2H^+ + 2e^- \rightarrow H_2 \quad (1.9)$$

$$2H_2O + 2e^- \rightarrow H_2 + 2OH^- \quad (1.10)$$

From a mechanistic perspective, HER can be conceptualised as a two-electron transfer process, which imposes lower thermodynamic constraints and, consequently, a lower activation energy compared to the OER.[99, 103] Consequently, lower overpotentials are typically required to achieve efficient hydrogen production, provided that the catalyst facilitates favourable reaction kinetics.

Amongst all known HER electrocatalysts, platinum supported on carbon (Pt/C) remains the most effective, owing to its optimal hydrogen binding energy - neither too strong to hinder hydrogen desorption, nor too weak to limit adsorption.[99, 101] This balance places Pt/C near the top of the HER activity volcano plot, making it the benchmark for HER performance. Nevertheless, the high cost and limited availability of platinum severely restrict its use in scalable technologies. This has prompted extensive research into alternative electrocatalysts that are not only cost-effective and abundant but also exhibit comparable activity and stability. Particular attention has been given to materials based on early transition metals such as nickel (Ni), cobalt (Co), manganese (Mn), and copper (Cu), which show promising catalytic properties and structural tunability for alkaline HER applications.[104] These efforts reflect the ongoing pursuit of sustainable, efficient, and economically viable solutions for large-scale hydrogen production.

The performance of HER electrocatalysts is typically assessed using the following electrochemical parameters[105]:

- **Overpotential ($\eta_{10}$)** refers to the additional potential that must be applied, beyond the thermodynamic value (0 V vs. RHE), to drive the reaction at a practical rate. A frequently adopted benchmark is the overpotential required to reach a current density of 10 mA cm$^{-2}$ ($\eta_{10}$), which corresponds to the current density necessary for solar-to-hydrogen conversion efficiencies around 12.3%. Lower overpotentials reflect higher catalytic activity, and in some cases, overpotentials at 50 mA cm$^{-2}$ ($\eta_{50}$) are also reported to assess performance at higher operational rates.
- **Tafel slope** is a crucial metric in analysing the reaction kinetics and elucidating the underlying HER mechanism. It is extracted from the linear region of a plot of overpotential ($\eta$) versus the logarithm of the current density (log $j$). Typical values can provide insight into the rate-determining step: a slope around 120 mV dec$^{-1}$ suggests the Volmer step is limiting, whereas values near 30-40 mV dec$^{-1}$ indicate

Heyrovsky or Tafel steps. A lower Tafel slope is indicative of faster kinetics and more favourable charge transfer processes.

- **Exchange current density ($j_0$)** is intrinsic to the catalytic activity of the electrode at equilibrium conditions ($\eta$ = 0) and is calculated by extrapolating the Tafel plot to zero overpotential. A higher $j_0$ implies that the catalyst can drive HER efficiently even without external bias and is a direct indicator of the surface's electrocatalytic reactivity.

The consideration of these parameters in unison furnishes a comprehensive understanding of the intrinsic activity and operational behaviour of HER electrocatalysts.[106] While the overpotential and Tafel slope offer insight into the reaction kinetics and energy efficiency, the exchange current density reflects the catalyst's baseline reactivity.

The collective measurement of these parameters enables the rational screening and optimisation of materials, thus guiding the development of advanced electrocatalysts tailored for efficient and durable hydrogen production in water electrolysis systems. As research progresses, integrating these conventional metrics with in situ characterisation techniques and theoretical modelling will further enhance our ability to design catalysts with high activity, selectivity, and longevity across diverse electrochemical environments.

## 1.3. Electrocatalysts for Oxygen Reduction Reaction

The surface chemistry of an electrocatalyst is governed by a complex interplay of factors, including the applied potential, the stability of the surface structure, and the physicochemical properties of the surrounding electrolyte. These conditions can give rise to multiple competing pathways, side reactions, or intermediate species before the desired electrochemical transformation is achieved. The interpretation of the reaction mechanism is rendered particularly challenging when the catalyst exhibits inadequate structural stability or undergoes surface degradation during operation. In the context of ORR, as well as OER and HER, a high-performance electrocatalyst must fulfil a set of fundamental criteria, such as those outlined below[107, 108]:

- **Chemical stability:** Resistance to degradation under electrochemical conditions is a prerequisite for any electrocatalyst. Instability in aqueous environments, whether due to dissolution, surface reconstruction, or side reactions with the

electrolyte, can compromise both the accuracy of experimental results and the long-term viability of the material. It is imperative that catalysts maintain their structural and compositional integrity throughout the testing process to ensure the reliability of the data obtained and their practical applicability.

- **Density of active sites:** An effective electrocatalyst should exhibit a large number of accessible active sites to enhance the adsorption and conversion of reaction intermediates. The catalytic activity is often governed by the availability of these sites. To this end, a range of strategies are employed to increase surface area and active site density, including doping, alloying, defect engineering, heterostructure formation, hierarchical structuring, and metal decoration.
- **Electrochemical stability within the redox window:** It is imperative that the catalyst maintains electrochemically inert properties across the potential window applied during HER, OER, or ORR. Catalysts that undergo unwanted redox transitions during operation can yield misleading performance metrics, as the observed activity may stem from transient redox states rather than intrinsic catalytic properties. Indicators of such instability often include time-dependent shifts in the polarisation curve and the appearance of redox peaks during cycling. Consequently, the implementation of cycling tests in both acidic and alkaline media is a common practice to verify the electrochemical robustness of the catalyst.
- **Favourable adsorption energy for reaction intermediates:** The interaction between the catalyst surface and the key intermediates must be energetically optimised. In accordance with the Sabatier principle, the binding energy must be neither excessively weak (resulting in inadequate adsorption) nor excessively strong (impeding desorption and turnover). The most efficient catalysts exhibit intermediate adsorption energies and often appear near the peak of the well-known volcano plot, representing the best trade-off between activity and stability.

In summary, the rational design of HER, OER, and ORR electrocatalysts necessitates a holistic approach that balances structural stability, surface reactivity, and electrochemical robustness, whilst ensuring favourable adsorption energetics to facilitate the desired multistep transformations.

Noble metals and their alloys have long been regarded as benchmark materials for the ORR, playing a central role in a variety of electrochemical energy conversion and storage systems, including fuel cells and metal–air batteries. Among these, platinum-based catalysts are the most widely used for ORR due to their excellent activity and low

overpotential.[109-111] In addition, other precious metals, such as silver and gold, have been explored for their potential in the ORR, particularly in the context of bifunctional catalysts designed for both ORR and OER.[112] Notwithstanding their high performance, noble metal catalysts are encumbered by significant limitations that hinder their widespread deployment. These limitations primarily encompass the high cost and limited availability of the raw materials, in addition to concerns regarding long-term stability under operational conditions. Consequently, there is a pressing need to develop efficient, durable, and cost-effective alternatives based on earth-abundant elements to support the advancement of sustainable energy technologies.[113] In this regard, increasing attention has been directed towards transition metal-based materials as promising non-precious alternatives for ORR catalysis.

Transition metal oxides have attracted particular interest owing to their low cost, ease of synthesis, environmental compatibility, and chemical stability in alkaline media.[114, 115] The inherent property of transition metals to adopt multiple oxidation states renders their oxides especially suitable for use in redox processes such as ORR, where dynamic changes in valence states occur during operation. A prevalent structural motif among these materials is the spinel structure, which accommodates metal cations in both tetrahedral and octahedral coordination environments.[116] This structural flexibility can lead to adjustable electronic and catalytic properties, offering opportunities for optimising ORR activity. Cobalt, manganese, and nickel oxides are among the most extensively studied transition metal oxides for ORR applications in alkaline media.[113] While these materials exhibit catalytic behaviour that is promising, their activity still falls short of that achieved with platinum-based catalysts. Key limitations include their intrinsically low electrical conductivity, due to wide band gaps, and moderate chemical stability, both of which constrain their performance in practical applications.[117]

In order to address these challenges, significant efforts have been made to integrate metal oxide nanoparticles with highly conductive carbon-based supports, such as graphene and its derivatives.[118] The formation of such hybrid materials enables strong chemical and electronic coupling between the oxide phase and the carbon support, which can significantly improve electron transfer kinetics, enhance active site utilisation, and reinforce structural stability during prolonged operation.[119]

The rational design of metal oxide-carbon nanocomposites is therefore a promising strategy for developing next-generation ORR electrocatalysts that meet the

key requirements of activity, durability, and economic feasibility. This paves the way for their integration into large-scale, clean energy technologies.

### 1.3.1. Carbon-based ORR electrocatalysts

Carbon is an abundant and versatile element, renowned for its unique physicochemical properties that render it particularly well suited to electrochemical applications. Carbon-based materials exhibit high chemical and thermal stability, excellent electrical conductivity, and large surface areas with well-developed porosity.[86] A defining feature of carbon is its ability to exist in multiple allotropic forms, including graphite, diamond, fullerenes, carbon nanotubes (CNTs), and graphene (Figure 1.7).

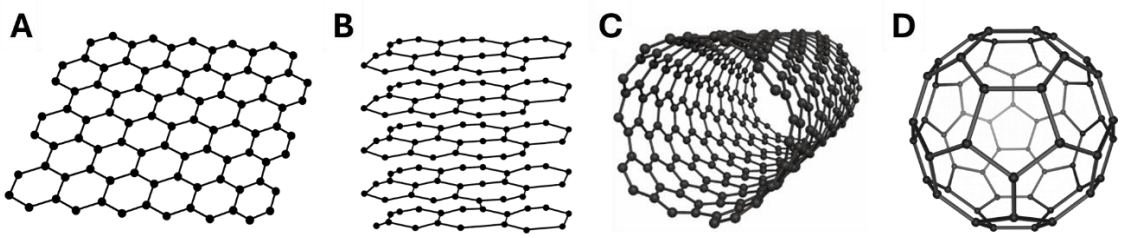



Figure 1.7 – Structures of (a) graphene, (b) graphitic, (c) carbon nanotube, and (d) fullerene.

With the exception of diamond, all other allotropes are fundamentally derived from graphene, which consists of a single, atomically thin sheet of carbon atoms arranged in a hexagonal honeycomb lattice via $sp^2$ hybridisation. Graphite consists of stacked layers of graphene in a crystalline arrangement, while carbon nanotubes are essentially rolled graphene sheets that form cylindrical structures. These can exist as single-walled (SWCNTs) or multi-walled (MWCNTs) nanotubes, typically a few nanometres in diameter and extending to several micrometres in length.[88]

These carbon nanostructures have been the focus of extensive research in the context of ORR, with particular attention paid to their utilisation as metal-free electrocatalysts and as conductive supports within functional hybrid materials.[46, 120-122] Among these, carbon materials doped with heteroatoms, such as nitrogen, phosphorus, or sulphur, have demonstrated particularly promising performance.[123, 124] These dopants introduce electronic modifications and active sites into the carbon

lattice, enhancing durability and catalytic activity, often outperforming some traditional metal-based catalysts. Nitrogen-doped graphene, in particular, has emerged as one of the most effective metal-free ORR electrocatalysts.

In contrast, undoped or non-functionalised carbon materials have been observed to favour the less desirable two-electron pathway, which results in the formation of hydrogen peroxide as a by-product.[86, 125] Activated carbon, a disordered amorphous form of carbon with a high surface area and a random microstructure, has also been employed as an ORR catalyst. Its well-developed pore network facilitates electrolyte access to active sites, thereby improving electrocatalytic activity.

In addition to their role as active catalysts, carbon materials serve as ideal supports in composite electrocatalysts.[125, 126] Their conductive nature, high surface area, and structural stability contribute to improved dispersion of active sites, enhanced charge transfer, and better interaction with reactants, ultimately boosting overall catalytic performance and longevity.

Carbon nanotubes (CNTs) and graphene-based supports, despite being more expensive than carbon black, typically enable higher catalyst utilisation due to their high degree of crystallinity, conductivity, and surface area. These materials have been successfully incorporated into various composite systems that include conducting polymers, non-precious metals, metal oxides, and metal complexes. Among metal oxides, polyoxometalates (POMs) are of particular interest as ORR catalysts, due to their ability to mediate electron, proton, and oxygen transfer processes.[127, 128] When immobilised onto conductive carbon scaffolds, POMs contribute both redox activity and molecular-level tunability, rendering them promising components of advanced hybrid electrocatalysts.

### 1.3.2. Polyoxometalates

Polyoxometalates (POMs) represent a fascinating and structurally diverse class of inorganic metal-oxygen clusters within the broad domain of coordination chemistry. Typically, they consist of early transition metal centres, most commonly molybdenum ($Mo^{VI}$), tungsten ($W^{VI}$) or vanadium ($V^{V}$), referred to as addenda atoms, which are coordinated by bridging and terminal oxygen atoms to form discrete polyanionic frameworks. The general formula for a POM can be represented as $(MO_x)_n$, where x

typically ranges from 4 to 7.[129] These fundamental units can assemble in various ways to yield a vast array of compounds, with some POMs containing as few as six and others up to 368 metal centres within a single molecule. The size of POMs is monodisperse, varying from a few angstroms up to around 10 nanometres.[130]

Structurally, POMs are broadly categorised into three principal families: isopolyanions ($[M_xO_y]^{m-}$), heteropolyanions ($[X_zM_xO_y]^{n-}$), and reduced molybdenum species such as molybdenum blues and browns.[131] Of these, heteropolyanions are the most extensively studied, owing to their adjustable chemical properties and structural versatility. In these species, the heteroatom X plays an essential role in stabilising the polyanionic framework and cannot typically be substituted or removed without disrupting the overall structure. In certain instances, the presence of secondary heteroatoms is also observed, which are less firmly bound and can be selectively removed without causing the collapse of the entire cluster.

One of the most recognised heteropolyanion structures is the Keggin-type anion, which has the general formula $[XM_{12}O_{40}]^{n-}$. This structure comprises four $M_3O_{13}$ units, each formed by three edge-sharing $MO_6$ octahedra. These units are linked via corner-sharing to form a symmetrical cage that encapsulates the central heteroatom within a tetrahedral cavity. Another common class is the Wells–Dawson structure, which consists of a more elongated arrangement of addenda atoms. These frameworks offer structural integrity and enable a wide range of redox behaviours, which are particularly attractive in electrochemical applications.

The electrochemical properties of Keggin-type POMs (Figure 1.8A), for instance, have been the subject of extensive investigation in aqueous media using techniques such as cyclic voltammetry.[132, 133] These anions typically undergo multiple fast, reversible one- and two-electron reduction processes, followed by irreversible multi-electron reductions that may lead to partial decomposition. In many cases, the POM structure remains largely intact during the initial few electron transfers, up to four electrons for heteropolytungstates and up to six for heteropolymolybdates, beyond which structural changes may occur.[134] The Wells–Dawson structure (Figure 1.8B). represents a well-established class of heteropolyanions within the polyoxometalate family, frequently represented by the general formula $[X_2M_{18}O_{62}]^{n-}$. This structure is distinguished from the more symmetrical Keggin-type in terms of size and geometry, exhibiting an elongated, ellipsoidal shape rather than a tetrahedral framework.[135] The Wells–Dawson anion consists of eighteen $MO_6$ octahedra, arranged into two fused

groups of nine.[136] The resulting architecture exhibits D3h symmetry and is structurally more flexible than the Keggin analogue, allowing for a broader range of chemical modifications.

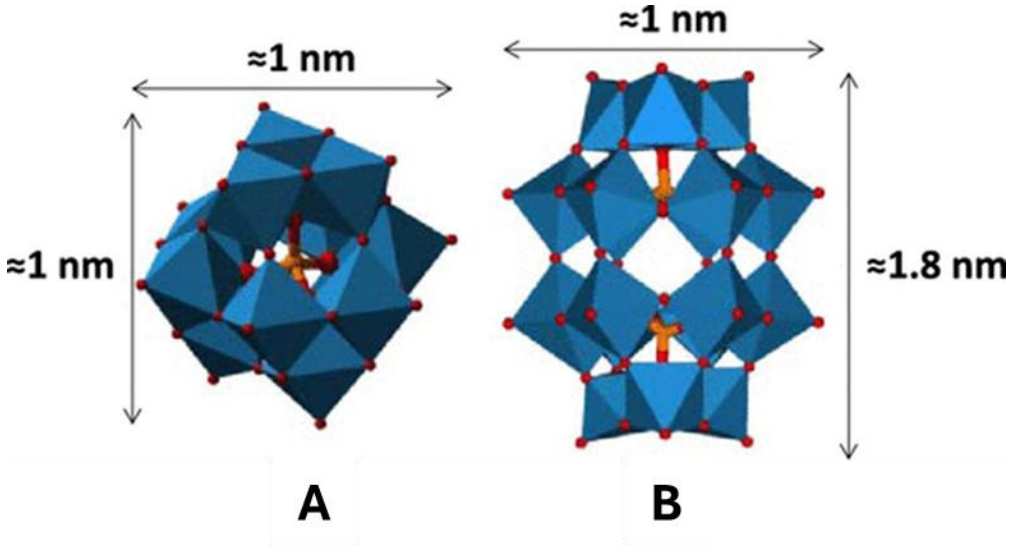



Figure 1.8 – Polyhedral representations of the structures of (a) Keggin-type and (b) Wells−Dawson heteropolyanions. Adapted from ref.[135]

The increased number of accessible redox states that this structure generally possesses, due to its extended structure and larger number of addenda atoms, makes it particularly attractive in redox catalysis, electrocatalysis, and energy-related applications. In a manner analogous to Keggin-type POMs, the electrochemical behaviour of Wells–Dawson species can be tuned through partial substitution of addenda atoms or by incorporating transition metals with varying oxidation states, thereby adjusting their redox potential and electron transfer capabilities.

It is imperative to acknowledge the pivotal role of the pH of the medium in dictating the redox behaviour of POMs. A linear correlation is generally observed between the redox potentials of the addenda atoms and the pH, owing to the protonation and deprotonation of the reduced species.[137] The slope of the potential versus pH plot is observed to vary depending on the number of protons and electrons involved in the redox transitions and can be altered when the $pK_a$ values of the oxidised and reduced forms differ significantly.

Furthermore, the redox potential and electronic properties of POMs can be tuned by partial substitution of the addenda atoms. To illustrate this, the replacement of some $Mo^{VI}$ or $W^{VI}$ ions with other transition metals, such as $V^{V}$, can result in the formation of mixed-addenda POMs, which exhibit enhanced redox activity. The oxidising strength of POMs can be modulated accordingly, with the general order of increasing oxidising power being $W^{VI} < Mo^{VI} < V^{V}$.[138]

Despite their numerous advantages, POMs are sometimes limited in their practical applications due to their relatively low surface area and solubility in aqueous media. In order to overcome these challenges, immobilisation onto high-surface-area conductive supports, such as carbon-based materials (e.g., graphene, carbon nanotubes, or activated carbon), has been explored. The development of such hybrid systems has been shown to enhance the processability and mechanical stability of POMs, whilst concomitantly improving their electrochemical properties and electrocatalytic performance. This strategy facilitates the effective integration of POMs into advanced devices for applications such as ORR, energy storage, and electrosensing.

### 1.3.3. Polyoxometalate-Carbon Nanomaterials for the Oxygen Reduction Reaction (ORR)

Polyoxometalates have emerged as versatile redox active materials with promising catalytic properties for a wide range of electrochemical applications. Of these, ORR has attracted considerable attention due to its pivotal role in fuel cells and metal-air batteries. POMs offer several advantages, including well-defined molecular structures, tunable redox potentials, thermal stability, and the possibility of incorporating catalytically active metal centres such as Co, Fe, or Ni. However, their application as standalone ORR catalysts are hindered by poor electrical conductivity, relatively low surface area, and susceptibility to leaching in aqueous environments. To overcome these limitations, recent research has focused on developing hybrid materials that integrate POMs with carbon-based nanostructures. Such as, graphene, carbon nanotubes and their doped derivatives provide high surface area, excellent electrical conductivity and mechanical stability, all of which contribute to improved electrochemical performance. Furthermore, the interaction between the POMs and carbon supports has been shown to mitigate the issue of catalyst dissolution and improve dispersion of the active

species.[139] The doping of the carbon matrix with heteroatoms such as nitrogen, sulphur, or phosphorus has proven to be a particularly effective strategy, as it enables the modification of the electronic properties of the support and the creation of active sites that synergistically enhance the ORR activity of the immobilised POMs.

A number of studies have demonstrated the effectiveness of such hybrids in alkaline media. For instance, Ji *et al.*, the combination of POMs and nanocarbons leads to synergistic effects that significantly enhance ORR activity. The carbon matrix functions as both an electron conductive scaffold and a high surface area support, thereby facilitating efficient electrical "wiring" of the otherwise insulating POMs. Furthermore, the interactions between POMs and the carbon substrate have been shown to modulate the electronic structure of the POM clusters, thereby enabling enhanced catalytic behaviour.[140] As reported by Fernandes *et al.* investigated the ORR performance of a cobalt-based sandwich-type POM, $(TBA)_7H_3[Co_4(H_2O)_2(PW_9O_{34})_2]$, supported on various carbon nanostructures, including SWCNTs, GF, N-CNTs and N-FLG. Among these, the $Co_4(PW_9)_2$@N-CNT hybrid exhibited the most promising results, with an onset potential of 0.90 V vs. RHE, a Tafel slope of 68 mV $dec^{-1}$ and an electron transfer number approaching 4, indicating a near complete 4-electron pathway. In addition, this composite demonstrated superior methanol tolerance and cyclic durability when compared to commercial Pt/C catalysts. In the study by Limani *et al.*, a series of Co-POMs anchored on doped carbon materials (MWCNT_N8_Co4, GF_N8_Co4, GF_ND8_Co4, and GF_NS8_Co4) were prepared and their performance for ORR and OER at alkaline conditions (0.1 M KOH) was tested. The materials exhibited onset potentials within the range of 0.83 - 0.85 V vs. RHE, Tafel slopes ranging from 40 to 90 mV $dec^{-1}$, and a number of transferred electrons ranging from 3.2 to 3.7. The materials were also found to demonstrate good stability properties and high methanol crossover tolerance, indicating their durability.

POM-carbon nanomaterial hybrids represent an attractive class of non-precious ORR electrocatalysts. Continued innovation in the design, synthesis and characterisation of materials is expected to further advance their performance and enable their integration into practical energy conversion devices.

### 1.3.4. ORR electrocatalytic activity evaluation

Linear sweep voltammetry (LSV) is a technique that is frequently utilised for the purpose of evaluating the electrocatalytic performance of materials with regard to ORR. It provides a direct means of evaluating activity under controlled electrochemical conditions. In order to provide further insight, cyclic voltammetry (CV) is frequently utilised to investigate the redox behaviour of the electrocatalyst, particularly in the presence of oxygen or other species that may interact with or poison the catalyst.

In the process of evaluating candidate materials in relation to the contemporary Pt/C electrocatalyst, there are several key electrochemical parameters that are generally taken into consideration. These include the onset potential ($E_{onset}$), the diffusion-limited current density ($j_L$), and the number of electrons transferred per $O_2$ molecule ($n_{O2}$).[141] These parameters are generally extracted from LSV measurements conducted using a rotating disk electrode (RDE), which enables the precise control of mass transport conditions. The onset potential ($E_{onset}$) is defined as the potential at which the ORR starts, thus providing an indication of the catalyst's activation energy.[142] The limiting current density ($j_L$) is observed when the reaction becomes entirely mass transport-limited; that is, when the supply of reactant ($O_2$) to the electrode surface via diffusion becomes the rate-determining factor. At this point, the current reaches a plateau and is no longer dependent on further increases in applied potential. Conversely, the kinetic current density ($j_k$) denotes the current that would be observed in the absence of any diffusion limitations, reflecting the intrinsic catalytic activity of the material.

LSV data are analysed through Koutecky-Levich (K-L), equation (1.11)[143, 144]:

$$\frac{1}{j} = \frac{1}{j_L} + \frac{1}{j_k} = \frac{1}{B\omega^{1/2}} + \frac{1}{j_k} \qquad (1.11)$$

where $j$ is the experimentally measured current density, $j_k$ is kinetic current density, and ω is the angular velocity; $B$ is related to the diffusion limiting density, as expressed by the equation (1.12):

$$B = 0.2 n_{O2} F (D_{O2})^{\frac{2}{3}} v^{-\frac{1}{6}} C_{O2} \qquad (1.12)$$

where $F$ is the Faraday constant (96 485 C $mol^{-1}$), $D_{O2}$ = $O_2$ diffusion coefficient, $v$ is the electrolyte kinematic viscosity and $C_{O2}$ = $O_2$ bulk concentration. For rotation speeds in

rpm is adopted a constant 0.2. Additionally, in the electrolyte used KOH (0.1 mol $dm^{-3}$): $D_{O2}$ = 1.95×$10^{-5}$ $cm^2$ $s^{-1}$, $v$ = 0.008977 $cm^2$ $s^{-1}$ and $C_{O2}$ = 1.15×$10^{-3}$ mol $dm^{-3}$. $j_k$ and $n_{O2}$ can be determined from the intercept and the slope of the plot of $j^{-1}$ vs. $\omega^{-1/2}$, respectively.[141, 145]

The value of $n_{O2}$, representing the number of electrons transferred per oxygen molecule, offers crucial insight into the selectivity of an electrocatalyst towards ORR. In this context, a value of $n_{O2}$ = 2 corresponds to the partial reduction of $O_2$ to hydrogen peroxide ($H_2O_2$), characteristic of the two-electron pathway. Conversely, $n_{O2}$ = 4 denotes the complete four-electron reduction of $O_2$ to water ($H_2O$), which is the more favourable pathway for high-performance energy conversion systems. Electrocatalysts exhibiting higher ORR activity are typically associated with a more positive (less negative) onset potential ($E_{onset}$) and higher diffusion-limited current densities. However, it should be noted that the limiting current density is directly influenced by the number of electrons transferred. Therefore, a lower $j_L$ does not necessarily imply inferior catalytic activity. For instance, a catalyst may display high intrinsic activity yet favour the two-electron pathway, leading to a lower current output despite its efficiency in catalysing the reduction of oxygen.[141] Consequently, a comprehensive and precise interpretation of electrocatalytic performance necessitates a multifaceted evaluation that incorporates both kinetic parameters and selectivity profiles.

The kinetics of ORR can be assessed through the analysis of Tafel plots. These plots offer valuable insights into the rate-determining steps and the overall efficiency of the electrocatalyst. An effective ORR electrocatalyst is characterised by its ability to minimise the overpotential ($\eta$), defined as the difference between the applied potential and the thermodynamic equilibrium potential, required to drive the reaction at a given rate. In circumstances where the current is governed purely by the kinetics of the electrode process (i.e. in the absence of mass transport limitations), the relationship between overpotential and current density is described by the Tafel equation (equation 1.13). This equation is a fundamental tool for quantifying electrocatalytic activity.[146, 147]

$$|\eta| = \frac{2.3RT}{\alpha n F} log \frac{j}{j_0} \quad (1.13)$$

Where $j_0$ is the exchange current density, α is the transfer coefficient, n is the number of electrons involved in the electrode reaction, $T$ is the temperature and $R$ is the gas constant. The slop of the $\eta$ vs. log $j$ plot (2.3$RT$/α$nF$) is called the Tafel slope.[148]

In order to achieve high current densities at low overpotentials in an electrochemical reaction, it is essential that the system exhibits a low Tafel slope, as this reflects efficient reaction kinetics. In addition to demonstrating promising activity towards ORR, an ideal electrocatalyst must also demonstrate excellent stability and durability, along with resistance to carbon monoxide (CO) poisoning and tolerance to fuel crossover, such as methanol in the case of direct methanol fuel cells.

The long-term stability of an electrocatalyst can be gauged by monitoring the loss in current density over time, typically through chronoamperometric measurements. Another common approach involves the recording of cyclic voltammograms over a large number of cycles and the subsequent evaluation of significant changes in the electrochemical response, which could indicate catalyst degradation.

It is imperative to discern between two facets of catalyst stability: physical and chemical. Physical stability refers to the retention of the catalyst's structural integrity under varying electrochemical or environmental conditions. Conversely, chemical stability pertains to the preservation of functional groups and surface chemistry, which may otherwise be compromised through processes such as oxidation or protonation. Ensuring the long-term viability of electrocatalysts in practical applications necessitates a focus on both components.

The rotating ring–disk electrode (RRDE) technique is a powerful and widely adopted electrochemical method for investigating the reaction mechanisms of electrocatalytic processes, particularly in ORR. Utilising a bipotentiostat configuration, this technique facilitates the concurrent regulation and measurement of current at both the disk and ring electrodes. This capability enables the detection of intermediates and products that are formed during the electrochemical reaction.

In conventional RRDE experiments, the disk electrode (typically made of glassy carbon) is modified with the electrocatalyst of interest and functions as the primary surface where the ORR occurs. When the electrode is rotated at a constant speed (e.g., 1600 rotations per minute), a well-defined hydrodynamic flow is established. This facilitates the controlled delivery of dissolved $O_2$ from the bulk electrolyte to the catalyst surface, ensuring reproducible mass transport conditions. The applied potential at the disk is swept cathodically, and the resulting current provides information on the overall electrocatalytic activity of the material. This enables the quantification of partially reduced oxygen species, thereby offering insight into the selectivity of the catalyst towards the desired 4-electron pathway ($O_2 \rightarrow H_2O$) versus the 2-electron pathway ($O_2 \rightarrow H_2O_2$).

By simultaneously monitoring the currents at both the disk ($I_D$) and the ring ($I_R$), the fraction of peroxide generated during the ORR can be calculated using the following expression[149]:

$$\%H_2O_2 = 200 \times \frac{\frac{i_R}{N}}{i_D + \frac{i_R}{N}} \quad (1.14)$$

where N is the collection efficiency of the RRDE setup, a geometric factor. This parameter accounts for the proportion of species produced at the disk that are successfully intercepted and detected at the ring. The RRDE technique has been shown to provide both quantitative and mechanistic insight into electrocatalytic performance by distinguishing between competing ORR pathways. It is especially valuable for evaluating the selectivity and efficiency of novel electrocatalysts under conditions relevant to alkaline fuel cells and metal–air batteries.

## 1.4. Electrochemical Capacitor

Electrochemical capacitors (ECs), more commonly referred to as ‘’supercapacitors’’, represent a class of energy storage devices that combine the fast charge-discharge characteristics of conventional capacitors with significantly higher energy storage capabilities. In order to contextualise their operation and performance, it is essential to first understand the principles underpinning traditional (electrostatic) capacitors.

### 1.4.1. Capacitors

A capacitor constitutes a passive electrical component that stores energy in the form of an electrostatic field, in contradistinction to chemical storage in batteries. It consists of two conductive plates (electrodes) separated by a dielectric material, which is an electrically insulating substance such as air, mica, plastic, or metal oxide (Figure 1.9). When a voltage is applied between the electrodes, positive and negative charges accumulate on opposing plates, thereby generating an electric field across the dielectric. This charge separation enables the capacitor to store potential energy.[150]

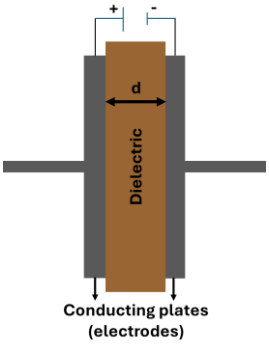



Figure 1.9 – Schematic view of a conventional capacitor.

The quantity of charge (*Q*) stored in the capacitor is directly proportional to the applied voltage (*U*), in volts (V), as described by the following equation[151]:

$$Q = CU \tag{1.15}$$

where *C* is the capacitance, expressed in farad (F). The capacitance itself is a geometric and material-dependent property, defined by[150]:

$$C = \frac{A\varepsilon_r\varepsilon_0}{d} \tag{1.16}$$

Here, *A* is the surface area of each electrode, *d* is the distance between the plates, $\varepsilon_0$ is the permittivity of dielectric material in vacuum, and $\varepsilon_r$ is the relative permittivity of the dielectric. It is evident from this relationship that the increase in capacitance is directly proportional to the increase in electrode area and the decrease in dielectric thickness. The energy (*E*) stored in a capacitor is given by:

$$E = \frac{1}{2}QU = \frac{1}{2}CU^2 \tag{1.17}$$

Whilst conventional capacitors can withstand high voltages (up to several kilovolts), their low capacitance values, typically ranging from picofarad (pF) to microfarad (μF), result in limited energy storage. Consequently, they are more appropriate for applications requiring brief periods of high power output than for those requiring continuous energy supply.

A defining characteristic of capacitors is their high power density. The release of energy is governed by the capacitor's rate of energy release, which is quantified by:

$$P = \frac{E}{t} = \frac{1}{2}UI = \frac{U^2}{4ESR} \quad (1.18)$$

where *t* is a discharge time, *I* is the amount of current flowing through a capacitor and *ESR* denotes the equivalent series resistance of the device. A lower *ESR* facilitates faster energy delivery and reduced energy loss, thus rendering it a critical parameter in performance assessment. Furthermore, the virtually unlimited cycle life of capacitors, owing to their physical, rather than chemical, mode of energy storage, render them particularly attractive for long-term repetitive charge-discharge applications.

The normalisation of capacitance, energy, and power can be expressed in terms of mass (specific capacitance, energy or power), volume (volumetric density), or surface area (areal capacitance or energy). Despite their advantages in terms of power density and cycle life, conventional capacitors are inherently limited by their low energy density, which constrains their use in applications requiring substantial energy storage. The development of supercapacitors represents a significant advancement in this field, offering an advanced class of electrochemical devices that integrate the high power capability of capacitors with substantially enhanced energy storage capacity.

## 1.5. Mechanisms of Charge Storage

Supercapacitors have attracted considerable attention as a promising class of energy storage devices that bridge the gap between conventional dielectric capacitors and rechargeable batteries. These devices offer remarkably high power densities (reaching up to 10000 $W \cdot kg^{-1}$), rapid charge-discharge capabilities, and exceptional cyclability (often exceeding one million cycles), underscoring their strategic importance in modern energy storage systems.[152] Their operational characteristics position them as an optimal solution for applications necessitating rapid and frequent energy delivery, such as in regenerative braking systems, start-stop automotive technologies, emergency backup, renewable energy smoothing, and portable/wearable electronics.[153] In contradistinction to conventional capacitors, which rely on electrostatics to store energy across a dielectric, or to batteries, which rely on bulk redox processes involving ion diffusion, supercapacitors utilise surface-confined or near-surface electrochemical mechanisms for charge storage.[154]

A conventional supercapacitor cell consists of two electrodes, a separator, an electrolyte, and current collectors. The electrodes are immersed in an electrolyte, which facilitates ion movement during charging and discharging cycles. The separator, which is typically a porous, ion-permeable membrane, fulfils two functions: firstly, it prevents electrical short-circuiting, and secondly, it allows for the flow of ions. Figure 1.10 provides a schematic representation of a complete supercapacitor cell, highlighting the various components and their interactions during operation. The performance of a supercapacitor is critically dependent on the compatibility between the electrolyte and the electrode material, the effective surface area of the electrodes, the pore distribution and accessibility, and the conductivity of all cell components.[155]

In terms of structural design, supercapacitors bear a resemblance to batteries, comprising two electrodes, a separator, and an electrolyte. However, their operational principle diverges fundamentally: in contrast to batteries, which store energy through bulk-phase chemical transformations often accompanied by significant structural and compositional changes, supercapacitors rely predominantly on highly reversible surface or near-surface processes.[156] This key distinction endows supercapacitors with considerably higher specific power, as their performance is not constrained by the inherently slower kinetics of diffusion-controlled redox reactions characteristic of batteries. Furthermore, supercapacitors exhibit outstanding cycling stability, often exceeding hundreds of thousands of cycles with minimal degradation, making them highly suitable for applications requiring rapid and repetitive charge–discharge operations.[157]

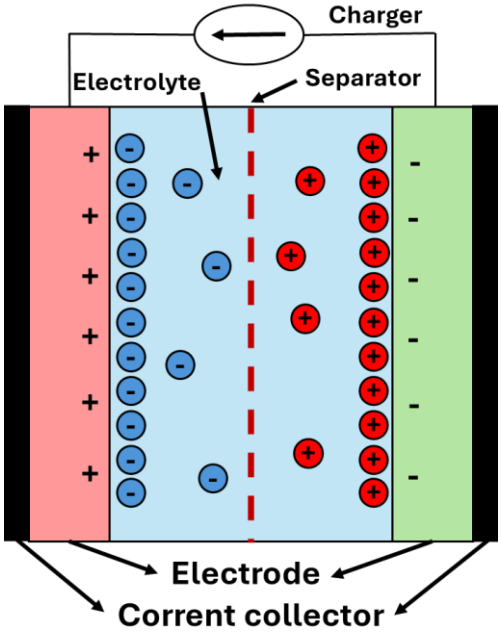



Figure 1.10– Schematic diagram of a supercapacitor cell. Adapted from ref. [158]

While supercapacitors generally exhibit lower specific energy compared to batteries, they demonstrate superior performance in comparison to conventional dielectric capacitors.[159] This enhancement can be ascribed to the utilisation of high surface area carbon-based electrodes or redox-active materials in conjunction with liquid or gel electrolytes, thereby facilitating the more effective utilisation of the electrode-electrolyte interface. The charge storage mechanism in supercapacitors is fundamentally dependent on this interface and can be classified as either non-faradaic, such as electric double-layer (EDL) formation on porous carbons, or faradaic, involving fast and reversible redox reactions on pseudocapacitive materials.[160] Through the judicious selection and tuning of electrode and electrolyte materials, it is possible to engineer supercapacitors with tailored performance characteristics across a wide range of power and energy demands. This design flexibility enhances their technological versatility and positions supercapacitors as a compelling alternative to traditional capacitors and batteries in numerous energy storage applications.

Supercapacitors are a diverse class of electrochemical energy storage devices that can be classified according to both their charge storage mechanism and their electrode configuration. Basically, two main mechanisms govern charge storage in supercapacitors: electrical double layer capacitance and pseudocapacitance. Devices

that operate by electrostatic charge accumulation at the electrode-electrolyte interface, without any electron transfer or chemical transformation, are classified as electrical double layer capacitors (EDLCs). In contrast, pseudocapacitors, also known as redox supercapacitors, rely on fast and reversible faradaic redox reactions at or near the surface of the electrode material to store charge. These mechanisms differ significantly in terms of kinetics, energy density and electrode material requirements, but both can deliver high power and fast response times.[161]

In addition to their function in charge storage, supercapacitors are distinguished by the symmetry of their electrodes.[162] Symmetrical supercapacitors utilise the same material for both the positive and negative electrodes, typically porous carbonaceous substances in the case of EDLCs. This configuration is the most widely commercialised due to its structural simplicity and cost-effectiveness. Conversely, asymmetrical supercapacitors employ distinct materials for the cathode and anode, frequently integrating an EDLC-type carbon electrode with a pseudocapacitive or battery-type counterpart. This configuration has been demonstrated to expand the operating voltage window and enhance specific energy, rendering it particularly attractive for advanced applications that demand higher energy densities.

The electrolyte plays a pivotal role in determining the electrochemical performance and voltage stability of supercapacitors. A wide variety of electrolytes, encompassing both aqueous (e.g., potassium hydroxide, sulphuric acid) and organic (e.g., acetonitrile, propylene carbonate) types, find application in these devices. Aqueous systems offer superior ionic conductivity and environmental friendliness; however, their narrow electrochemical stability window, is a limitation. In contrast, organic electrolytes, despite being more expensive and flammable, are predominantly employed in commercial supercapacitors because they enable significantly broader voltage ranges, thereby increasing the device's energy density.[163]

Asymmetric pseudocapacitors are currently emerging as a promising solution for next-generation energy storage, particularly in the context of electric mobility and grid-scale buffering systems.[38, 164] These systems combine the fast charge-discharge capabilities and cycling durability of capacitors with improved energy density that approaches that of batteries. The combination of these features, coupled with the development of electrode materials and electrolyte engineering, positions asymmetric supercapacitors as a competitive and scalable alternative for sustainable energy storage solutions.

### 1.5.1. Electrochemical double layer capacitor (EDLC)

Electrical double layer capacitors (EDLCs), regarded as the inaugural generation of electrochemical capacitors, operate through the absorption of energy via non-Faradaic electrostatic processes.[165] In contradistinction to batteries, which rely on bulk redox reactions, or traditional dielectric capacitors that accumulate charge across an insulating layer, EDLCs utilise the reversible adsorption of ions at the electrode-electrolyte interface, forming what is termed the electric double layer.[166] This phenomenon enables EDLCs to store and release energy rapidly and efficiently, making them particularly valuable in high-power applications that demand short charge-discharge cycles and exceptional cycling stability.

The charge storage mechanism in EDLCs is governed by the formation of the electric double layer at the electrode-electrolyte interface.[166] This process was first proposed by Helmholtz[167] in 1853 and later refined by the Gouy-Chapman[168, 169] and Stern-Graham[170, 171] models. The contemporary Stern-Graham model posits that the double layer consists of two distinct regions:

- **the compact Helmholtz layer** (also termed the Stern layer) comprising solvated ions adsorbed specifically onto the electrode surface.
- **the diffuse Gouy–Chapman layer**, which contains mobile ions dispersed in the electrolyte.

Within the Helmholtz layer, two sub-planes can be identified: the Inner Helmholtz Plane (IHP), where partially or unsolvated ions reside, and the Outer Helmholtz Plane (OHP), where fully solvated ions accumulate. When a potential is applied across the EDLC, a migration of electrons occurs from one electrode to the other through an external circuit. Concurrently, electrolyte ions undergo a reorganisation, with cations moving towards the negatively charged electrode and anions towards the positively charged one. This charge separation at the interface gives rise to a high specific capacitance, without any chemical transformation of the active materials. It is noteworthy that the electrolyte composition remains unaltered during this process.

The total double-layer capacitance ($C_{dl}$) is derived from the Helmholtz and diffuse layer capacitances as follows[150]:

$$\frac{1}{C_{dl}} = \frac{1}{C_H} + \frac{1}{C_{diff}} \tag{1.19}$$

The relationship between these variables demonstrates that the overall capacitance is dominated by the smaller of the two component values. For a complete EDLC cell consisting of two electrodes, the total capacitance ($C_T$) is expressed analogously:

$$\frac{1}{C_T} = \frac{1}{C_{dl(+)}} + \frac{1}{C_{dl(-)}} \tag{1.20}$$

It can thus be concluded that capacitance is directly dependent on the accessible surface area of the electrodes and the effective ionic environment of the electrolyte.

### 1.5.2. Pseudocapacitors

Pseudocapacitors represent a critical class of electrochemical capacitors that complement the performance limitations of EDLCs, particularly in terms of energy density. While EDLCs are able to store energy through non-faradaic electrostatic adsorption of ions at the electrode-electrolyte interface, pseudocapacitors harness fast and reversible faradaic processes, specifically redox reactions, that occur either at the surface or within the near-surface region of the active electrode materials. The resultant faradaic reactions within these electrodes yield a substantially higher specific capacitance and energy density than those observed in EDLCs.[172] However, these electrodes retain analogous benefits in terms of power density and cycling stability.

The concept of pseudocapacitance, first introduced in the 1970s, was coined to describe a class of materials whose electrochemical response mimics that of ideal capacitors, despite being governed by charge transfer processes.[173] In a pseudocapacitor, energy is stored via a sequence of fast, reversible redox reactions that occur either at the electrode surface or within its bulk structure. These reactions are accompanied by charge transfer across the electric double layer, distinguishing them from the purely electrostatic mechanism of EDLCs.

There are two principal mechanisms that are now widely accepted as contributing to pseudocapacitance:

- **Surface Redox Reactions:** These involve electrochemical adsorption and desorption of electroactive species on the surface or subsurface of the electrode. Such processes are typified by materials such as $RuO_2$, which has been

extensively studied due to its high electrical conductivity and the presence of multiple oxidation states that facilitate rapid redox cycling.[174, 175]

- **Intercalation pseudocapacitance:** In this mechanism, ions are absorbed and inserted into the crystal lattice of the electrode material without triggering a phase transformation. In contradistinction to conventional battery materials, where intercalation leads to volumetric and structural changes, pseudocapacitive intercalation is characterised by a continuous and reversible insertion process, thereby maintaining structural integrity even after extensive cycling.[175]

The distinguishing feature of both mechanisms is the capacitive-like electrochemical behaviour they exhibit, which differentiates them from traditional faradaic processes. In CV, pseudocapacitive materials typically display broad, quasi-rectangular curves, without the pronounced peaks that are characteristic of faradaic redox reactions. Furthermore, galvanostatic charge-discharge (GCD) profiles demonstrate nearly linear potential-time curves, contrasting with the plateaus typically observed in battery-type materials.[176]

The categorisation of pseudocapacitive materials is predicated on the basis of two distinct classifications: namely, intrinsic and extrinsic. This categorisation is informed by the nature of their respective pseudocapacitive responses:

- **Intrinsic pseudocapacitors** demonstrate pseudocapacitive behaviour irrespective of particle size or morphology. Their electrochemical response is governed by inherent properties such as electronic structure, redox activity, and ionic diffusion pathways. Examples of intrinsic pseudocapacitive materials include transition metal oxides such as $RuO_2$ and $MnO_2$, as well as certain conducting polymers.[174, 175]
- **Extrinsic pseudocapacitors** manifest pseudocapacitive behaviour exclusively under specific nanostructured or low-dimensional conditions. When employed in bulk, these materials tend to follow battery-like, diffusion-limited redox reactions rather than exhibiting the capacitive traits seen in their nanoscale counterparts. The enhanced pseudocapacitance in such materials is often attributed to increased surface area, shortened diffusion paths, and enhanced accessibility of active sites when confined to the nanoscale.[174, 175]

Although pseudocapacitive processes are fundamentally faradaic in nature, their electrochemical signatures are distinct from those of conventional battery-type systems.[177] Conversely, CV measurements demonstrate that pseudocapacitive

materials yield smooth, almost rectangular current-potential curves, which is indicative of a continuous redox process with minimal kinetic hindrance (Figure 1.11). This is in marked contrast to the sharp redox peaks observed in battery electrodes, which correspond to discrete redox transitions. Furthermore, in GCD tests, the voltage-time curves of pseudocapacitors exhibit a linear slope, deviating only slightly from the ideal triangular profiles seen in EDLCs. The absence of voltage plateaus further distinguishes pseudocapacitors from battery materials and confirms the capacitive nature of the charge storage mechanism.

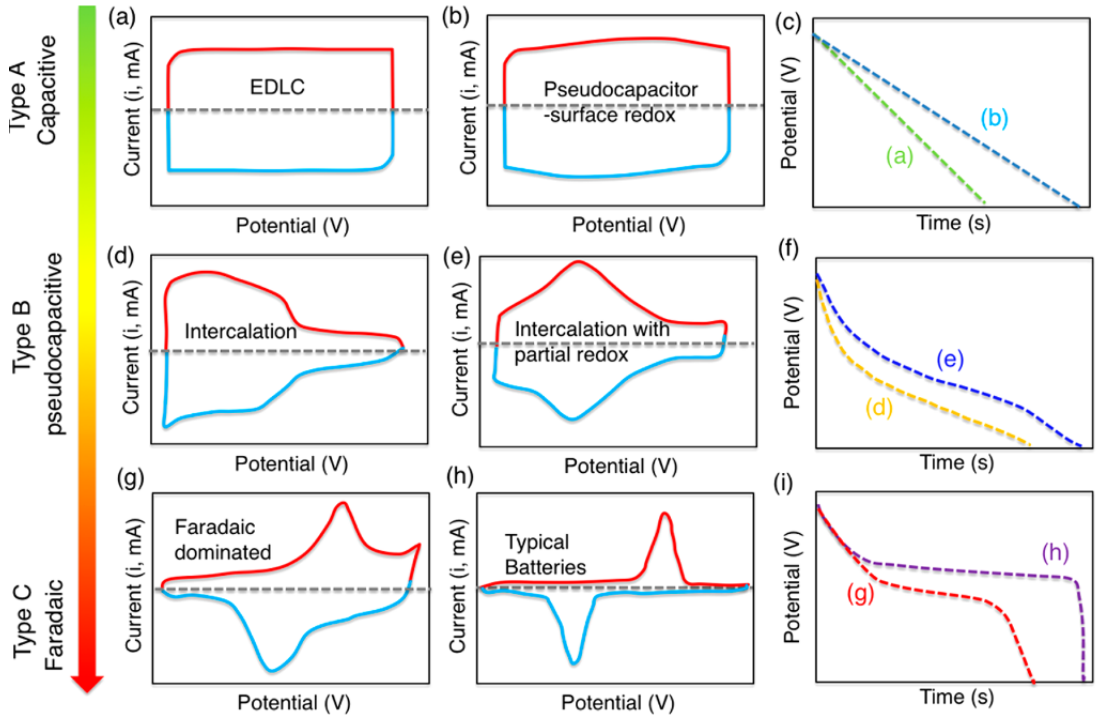



Figure 1.11 – The schematic diagram (a, b, d, e, g, h) illustrates the cyclic voltammograms, while (c, f, i) show the corresponding galvanostatic discharge curves for various types of energy storage materials. A pseudocapacitive material will generally exhibit the electrochemical characteristics of one, or a combination, of the following categories: (b) surface redox materials (d) intercalation-type materials or (e) intercalation-type materials showing broad but electrochemically reversible redox peaks. Electrochemical responses in (g-i) correspond to battery-like materials. Adapted from [178].

These features enable pseudocapacitors to combine the advantages of both capacitors and batteries, offering high power density due to rapid kinetics and enhanced energy density resulting from faradaic reactions.[177] The energy stored ($E$) in such devices is governed by the equation 1.17. However, the effective capacitance ($C$) can

be significantly higher than that of an EDLC due to the contribution from redox-active sites.

## 1.6. Metal Nanofoams for OER, HER and Supercapacitors Applications

Transition metal-based nanofoams have emerged as multifunctional materials of great interest in the field of electrochemical energy technologies. The unique combination of high surface area, interconnected porous architecture, electrical conductivity, and mechanical robustness renders them highly suitable for a range of applications, including HER and OER, and charge storage in supercapacitors. Fabricated through templating techniques such as dynamic hydrogen bubble templating (DHBT), these materials exhibit a foam-like morphology that enables rapid mass and charge transport, efficient gas release, and extended electroactive interfaces.

### 1.6.1. Metal Nanofoam for OER

The development of highly active and durable electrocatalysts for OER is pivotal to the advancement of a wide range of electrochemical energy conversion technologies, notably water electrolysis.[179, 180] In this context, metal nanofoams have emerged as a class of electrode materials that show promise, offering a combination of favourable structural and electronic properties, as well as versatility in compositional engineering.[181, 182] Metal nanofoams are 3D porous structures characterised by high surface area, hierarchical pore networks, and good electrical conductivity.[183, 184] These attributes contribute to an enhanced number of exposed active sites and improved mass transport, factors that are critical in optimising OER performance.[185, 186] In comparison to conventional flat or planar electrodes, nanofoams provide a structure that supports high density catalytic sites and allows rapid electrolyte penetration, facilitating both charge transfer and interdiffusion.[182] Additionally, the inherent robustness and electrical conductivity of the metallic framework eliminate the necessity for binders or conductive additives, which are frequently employed in powder-based systems.[187] Despite the long-standing utilisation of metal foams, including nickel and stainless steel,

as electrode substrates, their use as active catalysts, particularly in the form of engineered nanofoams for OER, has only gained significant attention in recent years.[184] The transition from utilising foams solely as passive supports to the precise tailoring of their nanoarchitecture to function as active electrocatalytic surfaces signifies a pivotal advancement in this field. This transformation has been catalysed by the development of synthesis strategies such as the dynamic hydrogen bubble template (DHBT) method, dealloying, hydrothermal treatments, and glucose-blowing approaches, which allow for precise control over pore size, ligament thickness, and compositional homogeneity.[188-190]

The use of metal nanofoams as electrocatalysts for OER has gained considerable attention in recent years, based on these structural and functional advantages. A substantial literature demonstrates not only their intrinsic electrocatalytic activity, but also their adaptability to a wide range of compositional and architectural modifications. Yang *et al.* showed that a multilayered NiFeCo nanofoam is better than $IrO_2$ when used in an alkaline anion exchange membrane water electrolyser (AEMWE), getting current densities of over 2.0 $A \cdot cm^{-2}$ at 1.7 V in diluted KOH.[181] In this work, trimetallic nanofoams have been synthesised with layered structures, where each layer exhibits a distinct chemical composition. This layered design facilitates enhanced cooperation among the different metals, thereby optimising the material's capacity to bind the molecules involved in the OER, resulting in a substantial enhancement in overall catalytic performance. Łuba *et al.* investigates the effect of modifying commercial nickel foam through the electrodeposition of cobalt and molybdenum nanoparticles, with the aim of enhancing its electrocatalytic performance for OER under alkaline conditions.[185] Therefore a key advantage of nanofoam structures is their capacity to serve as substrates for subsequent functionalisation processes. In a recent published study by Lytvynenko *et al.*, silver nanofoams were synthesised by DHBT-assisted electrodeposition from acidic $AgNO_3$ solutions.[188] The study systematically varied deposition parameters and demonstrated precise control over foam morphology, including crater and filament sizes. Although the electrocatalytic tests focused on the debromination of bromobenzene, the structural characteristics, namely high porosity, abundant edge sites and hierarchical texture are directly applicable in OER systems. The literature also includes foam-based systems designed for trifunctional activity. $RuCoO_x$ nanofoam, developed by Zhou *et al.*, has demonstrated high performance not only for OER but also for HER and ORR.[191].

Despite their recent introduction to the field of electrocatalysis for OER, current studies have demonstrated their considerable potential as both active materials and functional supports. Advances in nanoarchitectural design continue to drive the growth of this field, with metal nanofoams emerging as a particularly promising class of electrocatalysts for the oxygen evolution reaction. These catalysts offer a unique combination of structural and compositional tunability, high surface area, and excellent conductivity.

### 1.6.2. Metal Nanofoam for HER

Following the demonstration of their efficacy in OER catalysis, metal nanofoams have also exhibited considerable potential in the HER, the complementary half-reaction in water electrolysis.[192, 193] While the underlying reaction mechanisms and optimal catalytic conditions differ, the structural and electronic characteristics that render nanofoams effective for OER, namely, high surface area, interconnected porosity, and excellent electrical conductivity, are equally advantageous for HER applications.[194] However, the focus of HER-oriented nanofoam research has shifted towards tailoring the surface chemistry and electronic properties of these frameworks to facilitate proton reduction and hydrogen adsorption-desorption processes.[195] Transition metal-based nanofoams, particularly those composed of nickel, copper and iron, have attracted considerable attention in the field of HER electrocatalysis due to several factors. Firstly, they are abundant in nature, which makes them a cost-effective solution.[182] Secondly, their catalytic properties are favourable. These elements exhibit inherent activity towards HER and can be utilised not only as mechanically robust electrode supports, but also as catalytically active substrates.[196, 197] Moreover, oxides, sulphides, phosphides, and carbides derived from Ni, Cu, Fe, Co, Mo, and W have been successfully integrated into foam architectures, often through direct growth or surface modification, to produce enhanced electrocatalytic behaviour.[198]

A seminal study by Santos *et al.* demonstrated that Ni-Cu nanofoams fabricated via DHBT exhibit notable HER performance in alkaline media, maintaining low overpotentials and stable activity under prolonged operation.[196] An earlier study by Zhang *et al.* had already reported the successful synthesis of Cu-Ni nanofoam films using the DHBT method, showing enhanced HER activity in 1 M KOH. Their findings emphasised the significance of bimetallic synergy and hierarchical porosity in enhancing

HER efficiency.[199] The findings of Cardoso *et al.* corroborated these results, demonstrating that deposition parameters have a significant impact on the morphology and catalytic performance of the resulting materials.[197] Recent efforts have focused on multimetallic nanofoams and composite systems. Cui *et al.* introduced a trimetallic NiCoCuP foam prepared by combining DHBT deposition with low temperature phosphorisation; the resulting electrode displayed excellent HER activity across a wide pH range, achieving relevant current densities with strong operational stability.[198] Chaitoglou *et al* embedded tungsten carbide nanoparticles into carbon nanofoam matrices, thereby producing a catalyst with superior conductivity and mechanical integrity. Their tungsten carbide-carbon composite demonstrated high HER activity in acidic media, supported by prolonged stability at elevated current densities. The optimisation of morphology remains a pivotal aspect in the design of nanofoams. In a related study, Siwek *et al.* demonstrated that by varying the electrolyte composition during DHBT synthesis, it was possible to precisely tune the microstructure of Ni foams. Dendritic structures were found to exhibit superior catalytic performance due to increased active site.[200]

Together, these advancements exemplify the maturing sophistication and adaptability of metal nanofoams in the context of HER electrocatalysis. The field has evolved from an exploratory phase to one of performance optimisation, mechanistic understanding, and device integration. As a result, metal nanofoams are now recognised as legitimate alternatives to precious metals in alkaline and acidic water electrolysis.

### 1.6.3. Metal Nanofoam for Supercapacitors

Following their demonstrated efficacy in electrocatalytic processes such as the oxygen and hydrogen evolution reactions, metal nanofoams have also gained considerable attention as promising electrode materials for electrochemical energy storage devices, most notably supercapacitors. The integration of metal nanofoams within supercapacitors serves to address the limitations observed in conventional capacitors and batteries, thereby offering high power density, rapid charge-discharge capability, and long cycle life. The performance of these devices is governed by the architecture of the electrodes, which must facilitate rapid ion transport, efficient charge accumulation, and robust cycling stability. In this context, metal nanofoams, with their 3D porous architecture, high electrical conductivity, and mechanical robustness, are ideal

candidates for use as supercapacitor electrode platforms. Whilst carbon-based materials, including activated carbon, carbon nanotubes and graphene, are frequently utilised in EDLCs, metal nanofoams exhibit particular advantages in pseudocapacitive systems due to their capacity to accommodate transition metal oxides, hydroxides and other redox-active species, thereby substantially enhancing the capacitance. The superiority of metal nanofoams in this context is attributable to three key factors. Firstly, their high surface area, interconnected porous network and excellent electrical pathways support enhanced electrochemical activity and high mass loading of active materials without compromising conductivity. Additionally, the open structure of nanofoams facilitates rapid electrolyte diffusion, which is essential for maintaining high capacitance at elevated current densities.

A representative study by Siwek *et al.* involved the electrodeposition of hydrated manganese oxide ($MnOx \cdot nH_2O$) onto DHBT-fabricated nickel nanofoam.[201] The composite electrode demonstrated a specific capacitance of up to 1700 F $g^{-1}$ and retained between 73 - 90% of its capacity after 5000 cycles. The success of this system was attributed to the uniform coating of MnOx, which formed a conformal thin film around the high surface area Ni framework, thus maximising the utilisation of active material. Subsequent research by the same group (Siwek *et al.*) investigated the deposition of MnOx onto bimetallic NiCo foams, determining that the deposition current density significantly influenced the morphology and electrochemical performance of the material.[202] It was found that foams coated at lower currents exhibited superior rate capabilities and structural uniformity. In a further development of the approach, Shi *et al.* incorporated NiMn-LDH (layered doubles hydroxides) nanosheets into DHBT-fabricated Ni nanofoams via electrodeposition.[203] The composite that resulted from this process exhibited a capacitance of 2755 F $g^{-1}$ at 1 A $g^{-1}$, which is noteworthy. Furthermore, it demonstrated a capacitance retention of 71.25% after 5000 cycles. In addition, hierarchical nanofoam composites have been investigated as a route to improve pseudocapacitance and rate performance. In a study by *Cong et al.*, a multi-layered structure comprising $MnO_2/ZnCo_2O_4$/graphene, grown on Ni foam, was reported.[204] This architecture was found to achieve a specific capacitance of 3405 F $g^{-1}$ 2 A $g^{-1}$and an energy density of 46.85 Wh $kg^{-1}$, with 91.2% retention after 5000 cycles.

In conclusion, metal nanofoams provide a structurally and functionally versatile platform for the development of next generation supercapacitor electrodes. The 3D architecture of these materials, in conjunction with their high conductivity and adaptability

to a range of active materials, facilitates superior energy storage performance, particularly with regard to rate capability, energy density, and long-term stability.

## 1.7. Electrodeposition of Metals using Dynamic Hydrogen Bubble Template (DHBT)

The development of advanced nanostructured materials with tunable porosity and high surface area has become a focal point in materials science, particularly in the context of electrochemical energy storage devices such as supercapacitors. Among the various strategies employed for fabricating such materials, electrochemical deposition offers a simple, cost-effective, and highly controllable route. A particularly versatile and efficient approach is the dynamic hydrogen bubble template (DHBT) method, which leverages the hydrogen evolution reaction during electrodeposition to generate porous metallic architectures (Figure 1.12).[205-207]

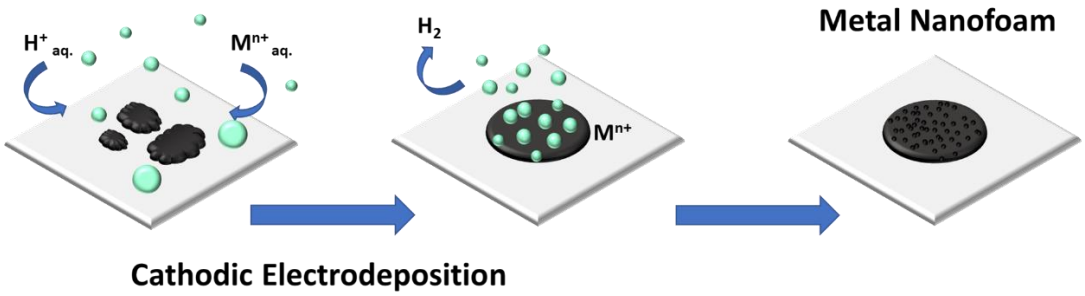



Figure 1.12 – Electrodeposition of porous metal using dynamic hydrogen bubble template.

It was originally considered a hindrance in conventional electrodeposition due to its interference with uniform metal growth; however, hydrogen evolution has been repurposed in DHBT as a powerful templating mechanism for forming hierarchical porous metal foams. The DHBT method is predicated on the continuous generation of hydrogen gas bubbles at elevated cathodic overpotentials.[205] These bubbles act as dynamic templates that obstruct uniform metal deposition, thereby enabling the formation of a porous, three dimensional (3D) metallic framework. In contradistinction to conventional electrodeposition, where the objective is to achieve smooth and dense metallic coatings, the DHBT approach fosters the deliberate disruption of film growth through the vigorous

evolution of hydrogen gas. This results in metallic foams with interconnected pores, large surface areas, and complex internal geometries that are highly favourable for electrochemical applications.[208]

The DHBT process is comprised of three sequential stages: nucleation, growth, and detachment of hydrogen bubbles. During the initial nucleation phase, hydrogen ions (protons) are reduced at the cathodic surface via HER[207]:

$$2H^+(aq) + 2e^- \rightarrow H_2(g) \quad (1.22)$$

Simultaneously, metal cations $M^{n+}$ present in the electrolyte are reduced and deposited onto the electrode surface as solid metal:

$$M^{n+}(aq) + ne^- \rightarrow M(s) \quad (1.23)$$

Concurrently, metal cations present in the electrolyte undergo electrochemistry and begin to deposit onto the aforementioned active sites. Concurrent nucleation of both metal and hydrogen bubbles establishes the foundation for the formation of the porous structure. As the deposition progresses into the growth phase, the hydrogen bubbles expand in size due to the continued influx of hydrogen gas. These growing bubbles act as physical barriers that displace the electrolyte locally and inhibit metal deposition beneath them, leading to a non-uniform current distribution. Consequently, the current lines concentrate around the periphery of the bubbles, resulting in preferential metal growth in those regions. Once the hydrogen bubbles reach a critical size, they detach from the electrode surface due to buoyancy forces and the decreasing contact angle with the substrate. The departure of these particles results in the formation of voids or pores within the metal matrix.[208] The morphology of these pores, which may vary in shape and size, is contingent on the deposition parameters, the nature of the electrolyte, and the properties of the metal being deposited. The dynamic process of bubble generation and detachment leads to a continuous restructuring of the electrode surface, contributing to the formation of a highly porous, interconnected metallic network.

The structure and porosity of metal foams made using DHBT are very sensitive to a range of deposition parameters. These factors influence how quickly hydrogen bubbles are produced, how close together metal and hydrogen bubbles are at first, and how much the bubbles stick together. This all affects the final structure of the foam. The most important factors are:

- **Current Density and Overpotential:** Elevated current densities or more negative potentials have been shown to enhance the rate of hydrogen evolution,

thereby promoting the formation of smaller, more numerous bubbles. This phenomenon results in an increased density of pores and the formation of finer microstructures. However, excessive hydrogen evolution can result in unstable deposition and loss of mechanical integrity due to uncontrolled bubble detachment or excessive gas formation.

- **Electrolyte composition:** The supporting electrolyte fulfils a dual role in modulating the ionic conductivity and influencing the HER. For instance, acidic electrolytes containing $H_2SO_4$, $NH_4Cl$, or $HNO_3$ promote vigorous hydrogen evolution, facilitating the formation of more pronounced porous features. Conversely, alkaline or neutral electrolytes have been observed to suppress bubble formation, leading to the formation of more compact deposits.
- **Metal Ion Concentration:** A higher concentration of electroactive metal ions competes with hydrogen ions for electron uptake, reducing the extent of HER and leading to less porous structures. Conversely, lower metal ion concentrations favour hydrogen evolution and the development of more porous morphologies, albeit at the cost of reduced deposition efficiency.
- **The duration of electrodeposition:** The time of electrodeposition governs the thickness of the deposited film and the extent of structural evolution. Shorter deposition times may result in insufficient foam formation, while extended deposition promotes bubble coalescence and hierarchical porosity. However, prolonged deposition can also lead to the collapse of fragile pore structures if not carefully optimised.

Notwithstanding the numerous advantages of the DHBT method, there are challenges associated with its implementation. The uniformity of bubble distribution and detachment remains a critical issue, as random or excessive coalescence can lead to heterogeneous structures or collapse of the foam.

## 1.8. References

[1] Farhidi F. Impact of fossil fuel transition and population expansion on economic growth. Environment, Development and Sustainability. 2023;25:2571-609.
[2] Yu C, Moslehpour M, Tran TK, Trung LM, Ou JP, Tien NH. Impact of non-renewable energy and natural resources on economic recovery: Empirical evidence from selected developing economies. Resources Policy. 2023;80:103221.
[3] Mufutau Opeyemi B. Path to sustainable energy consumption: The possibility of substituting renewable energy for non-renewable energy. Energy. 2021;228:120519.
[4] Rahmstorf S, Box JE, Feulner G, Mann ME, Robinson A, Rutherford S, et al. Exceptional twentieth-century slowdown in Atlantic Ocean overturning circulation. Nature Climate Change. 2015;5:475-80.
[5] Kumar A, Nagar S, Anand S. 1 - Climate change and existential threats. In: Singh S, Singh P, Rangabhashiyam S, Srivastava KK, editors. Global Climate Change: Elsevier; 2021. p. 1-31.
[6] Bradley RL. Climate alarmism reconsidered. Institute of Economic Affairs Monographs, Forthcoming. 2023.
[7] Risbey JS. The new climate discourse: Alarmist or alarming? Global environmental change. 2008;18:26-37.
[8] Huang Y. Technology innovation and sustainability: challenges and research needs. Clean Technologies and Environmental Policy. 2021;23:1663-4.
[9] Weng S, Tao W, Lu Y. Unlocking the carbon emission efficiency improvement path of technological innovation: a perspective on industrial restructuring and R&D element flows. Environmental Science and Pollution Research. 2024;31:21189-207.
[10] Cianconi P, Betrò S, Janiri L. The impact of climate change on mental health: a systematic descriptive review. Frontiers in psychiatry. 2020;11:490206.
[11] Charlson F, Ali S, Benmarhnia T, Pearl M, Massazza A, Augustinavicius J, et al. Climate Change and Mental Health: A Scoping Review. International Journal of Environmental Research and Public Health. 2021;18:4486.
[12] Levin K, Rich D. Turning points: trends in countries' reaching peak greenhouse gas emissions over time. World Resources Institute. 2017.
[13] European Environment A. Economic losses from weather and climate-related extremes in Europe reached around half a trillion euros over past 40 years: Publications Office of the European Union; 2022.

[14] Key World Energy Statistics. International Energy Agency2021.
[15] CO2 Emissions in 2023. International Energy Agency2023.
[16] Zhao J, Dong K, Dong X, Shahbaz M. How renewable energy alleviate energy poverty? A global analysis. Renewable Energy. 2022;186:299-311.
[17] European C, Directorate-General for C. REPowerEU Actions: Publications Office of the European Union; 2022.
[18] Officer OotFCS. Federal Sustainability Plan: Catalyzing America's Clean Energy Industries and Jobs2021.
[19] Agency IRE. Global Hydrogen Trade to Meet the 1.5°C Climate Goal: Trade outlook for 2050 and way forward: International Renewable Energy Agency; 2022.
[20] Navas-Anguita Z, García-Gusano D, Dufour J, Iribarren D. Revisiting the role of steam methane reforming with CO2 capture and storage for long-term hydrogen production. Science of the total Environment. 2021;771:145432.
[21] Navarro RM, Alvarez-Galvan MC, De La Mano JAV, Al-Zahrani SM, Fierro JLG. A framework for visible-light water splitting. Energy & Environmental Science. 2010;3:1865-82.
[22] Osman AI, Mehta N, Elgarahy AM, Hefny M, Al-Hinai A, Al-Muhtaseb AaH, et al. Hydrogen production, storage, utilisation and environmental impacts: a review. Environmental Chemistry Letters. 2022:1-36.
[23] Knobloch F, Hanssen SV, Lam A, Pollitt H, Salas P, Chewpreecha U, et al. Net emission reductions from electric cars and heat pumps in 59 world regions over time. Nature Sustainability. 2020;3:437-47.
[24] Thomas JM, Edwards PP, Dobson PJ, Owen GP. Decarbonising energy: The developing international activity in hydrogen technologies and fuel cells. Journal of Energy Chemistry. 2020;51:405-15.
[25] Feldmann J, Byrum Z, Cyrs T. Clean hydrogen: Outlook for freight transport in the United States. 2023.
[26] Amin M, Shah HH, Fareed AG, Khan WU, Chung E, Zia A, et al. Hydrogen production through renewable and non-renewable energy processes and their impact on climate change. International Journal of Hydrogen Energy. 2022;47:33112-34.
[27] Low JM, Haszeldine RS, Mouli-Castillo J. Refuelling infrastructure requirements for renewable hydrogen road fuel through the energy transition. Energy Policy. 2023;172:113300.
[28] Squadrito G, Maggio G, Nicita A. The green hydrogen revolution. Renewable Energy. 2023;216:119041.

[29] Hosseini SE, Wahid MA. Hydrogen from solar energy, a clean energy carrier from a sustainable source of energy. International Journal of Energy Research. 2020;44:4110-31.
[30] Hassan Q, Abdulateef AM, Hafedh SA, Al-samari A, Abdulateef J, Sameen AZ, et al. Renewable energy-to-green hydrogen: A review of main resources routes, processes and evaluation. International Journal of Hydrogen Energy. 2023;48:17383-408.
[31] Lewis NS, Nocera DG. Powering the planet: Chemical challenges in solar energy utilization. Proceedings of the National Academy of Sciences. 2006;103:15729-35.
[32] Perez M, Perez R. Update 2022 – A fundamental look at supply side energy reserves for the planet. Solar Energy Advances. 2022;2:100014.
[33] Hong WT, Risch M, Stoerzinger KA, Grimaud A, Suntivich J, Shao-Horn Y. Toward the rational design of non-precious transition metal oxides for oxygen electrocatalysis. Energy & Environmental Science. 2015;8:1404-27.
[34] Yadlapalli RT, Alla RR, Kandipati R, Kotapati A. Super capacitors for energy storage: Progress, applications and challenges. Journal of Energy Storage. 2022;49:104194.
[35] Islam MS, Shudo Y, Hayami S. Energy Conversion and Storage in Fuel Cells and Super-Capacitors from Chemical Modifications of Carbon Allotropes: State-of-Art and Prospect. Bulletin of the Chemical Society of Japan. 2021;95:1-25.
[36] Njema GG, Ouma RBO, Kibet JK. A Review on the Recent Advances in Battery Development and Energy Storage Technologies. Journal of Renewable Energy. 2024;2024:2329261.
[37] Dutta A, Mitra S, Basak M, Banerjee T. A comprehensive review on batteries and supercapacitors: Development and challenges since their inception. Energy Storage. 2023;5:e339.
[38] Olabi AG, Abbas Q, Al Makky A, Abdelkareem MA. Supercapacitors as next generation energy storage devices: Properties and applications. Energy. 2022;248:123617.
[39] Bhojane P. Recent advances and fundamentals of Pseudocapacitors: Materials, mechanism, and its understanding. Journal of Energy Storage. 2022;45:103654.
[40] Ashritha MG, Hareesh K. Chapter 9 - Electrode materials for EDLC and pseudocapacitors. In: Hussain CM, Ahamed MB, editors. Smart Supercapacitors: Elsevier; 2023. p. 179-98.
[41] Vladimir P, Iurii P. Supercapacitor Energy Storages in Hybrid Power Supplies for Frequency-Controlled Electric Drives: Review of Topologies and Automatic Control Systems. Energies. 2023;16:3287.

[42] Lemian D, Bode F. Battery-Supercapacitor Energy Storage Systems for Electrical Vehicles: A Review. Energies. 2022;15:5683.
[43] Pershaanaa M, Bashir S, Ramesh S, Ramesh K. Every bite of Supercap: A brief review on construction and enhancement of supercapacitor. Journal of Energy Storage. 2022;50:104599.
[44] Xu H, Shen M. The control of lithium-ion batteries and supercapacitors in hybrid energy storage systems for electric vehicles: A review. International Journal of Energy Research. 2021;45:20524-44.
[45] Mounica V, Obulesu Y. Hybrid power management strategy with fuel cell, battery, and supercapacitor for fuel economy in hybrid electric vehicle application. Energies. 2022;15:4185.
[46] Hu C, Paul R, Dai Q, Dai L. Carbon-based metal-free electrocatalysts: from oxygen reduction to multifunctional electrocatalysis. Chemical Society Reviews. 2021;50:11785-843.
[47] Lichchhavi, Kanwade A, Shirage PM. A review on synergy of transition metal oxide nanostructured materials: Effective and coherent choice for supercapacitor electrodes. Journal of Energy Storage. 2022;55:105692.
[48] Araújo H, Šljukić B, Gago S, Santos DMF. The current state of transition metal-based electrocatalysts (oxides, alloys, POMs, and MOFs) for oxygen reduction, oxygen evolution, and hydrogen evolution reactions. Frontiers in Energy Research. 2024;12.
[49] Fu Z, Zhuo H, Liu X, Li W, Song H, Shi Z, et al. Fe/Co Bimetal-Containing Carbon Prepared from a 2D Metalloporphyrin-Based MOF for the Optimal ORR/OER Bifunction and Its Application in Zn–Air Batteries. ACS Applied Energy Materials. 2025;8:1051-9.
[50] Arfeen ZA, Abdullah MP, Hassan R, Othman BM, Siddique A, Rehman AU, et al. Energy storage usages: Engineering reactions, economic-technological values for electric vehicles—A technological outlook. International Transactions on Electrical Energy Systems. 2020;30:e12422.
[51] Olabi AG, Sayed ET, Wilberforce T, Jamal A, Alami AH, Elsaid K, et al. Metal-Air Batteries—A Review. Energies. 2021;14:7373.
[52] Wang Y, Pang Y, Xu H, Martinez A, Chen KS. PEM Fuel cell and electrolysis cell technologies and hydrogen infrastructure development – a review. Energy & Environmental Science. 2022;15:2288-328.
[53] Tsai F-T, Deng Y-T, Pao C-W, Chen J-L, Lee J-F, Lai K-T, et al. The HER/OER mechanistic study of an FeCoNi-based electrocatalyst for alkaline water splitting. Journal of Materials Chemistry A. 2020;8:9939-50.

[54] Cao L, Soto FA, Li D, Deng T, Hu E, Lu X, et al. Pd-Ru pair on Pt surface for promoting hydrogen oxidation and evolution in alkaline media. Nature Communications. 2024;15:7245.
[55] Yang Y, Peltier CR, Zeng R, Schimmenti R, Li Q, Huang X, et al. Electrocatalysis in Alkaline Media and Alkaline Membrane-Based Energy Technologies. Chemical Reviews. 2022;122:6117-321.
[56] Cao R, Lee JS, Liu M, Cho J. Recent progress in non-precious catalysts for metal-air batteries. Advanced Energy Materials. 2012;2:816-29.
[57] Sadhasivam T, Dhanabalan K, Roh S-H, Kim T-H, Park K-W, Jung S, et al. A comprehensive review on unitized regenerative fuel cells: Crucial challenges and developments. International Journal of Hydrogen Energy. 2017;42:4415-33.
[58] Wang Y, Leung DYC, Xuan J, Wang H. A review on unitized regenerative fuel cell technologies, part-A: Unitized regenerative proton exchange membrane fuel cells. Renewable and Sustainable Energy Reviews. 2016;65:961-77.
[59] Chen D, Chen C, Baiyee ZM, Shao Z, Ciucci F. Nonstoichiometric Oxides as Low-Cost and Highly-Efficient Oxygen Reduction/Evolution Catalysts for Low-Temperature Electrochemical Devices. Chemical Reviews. 2015;115:9869-921.
[60] Dutta K, Rana D, Han HS, Kundu PP. Unitized Regenerative Fuel Cells: A Review on Developed Catalyst Systems and Bipolar Plates. Fuel Cells. 2017;17:736-51.
[61] Di Noto V, Negro E, Patil B, Lorandi F, Boudjelida S, Bang YH, et al. Hierarchical metal–[carbon nitride shell/carbon core] electrocatalysts: A promising new general approach to tackle the ORR bottleneck in low-temperature fuel cells. ACS catalysis. 2022;12:12291-301.
[62] Devi Renuka K, Bhat SD, Unni SM. Unitized Regenerative Fuel Cells: Future of Renewable Energy Research. Renewable Energy Technologies2022. p. 375-402.
[63] Adegoke KA, Ogunjinmi OE, Adegoke OR, Bello OS. Bifunctional two-dimensional metal organic frameworks for oxygen reaction and water splitting. Nano Energy. 2024;128:109897.
[64] Xie X, Du L, Yan L, Park S, Qiu Y, Sokolowski J, et al. Oxygen evolution reaction in alkaline environment: material challenges and solutions. Advanced Functional Materials. 2022;32:2110036.
[65] Sarapuu A, Lilloja J, Akula S, Zagal JH, Specchia S, Tammeveski K. Recent Advances in Non-Precious Metal Single-Atom Electrocatalysts for Oxygen Reduction Reaction in Low-Temperature Polymer-Electrolyte Fuel Cells. ChemCatChem. 2023;15:e202300849.

[66] Zhang K, Zou R. Advanced transition metal-based OER electrocatalysts: current status, opportunities, and challenges. Small. 2021;17:2100129.
[67] Li L, Cao X, Huo J, Qu J, Chen W, Liu C, et al. High valence metals engineering strategies of Fe/Co/Ni-based catalysts for boosted OER electrocatalysis. Journal of Energy Chemistry. 2023;76:195-213.
[68] Lang P, Yuan N, Jiang Q, Zhang Y, Tang J. Recent advances and prospects of metal-based catalysts for oxygen reduction reaction. Energy Technology. 2020;8:1900984.
[69] Das G, Choi J-H, Nguyen PKT, Kim D-J, Yoon YS. Anion exchange membranes for fuel cell application: a review. Polymers. 2022;14:1197.
[70] Hren M, Božič M, Fakin D, Kleinschek KS, Gorgieva S. Alkaline membrane fuel cells: anion exchange membranes and fuels. Sustainable Energy & Fuels. 2021;5:604-37.
[71] Huang K, Xu YY, Song YP, Wang RY, Wei HH, Long YZ, et al. NiPS<sub>3</sub> quantum sheets modified nitrogen-doped mesoporous carbon with boosted bifunctional oxygen electrocatalytic performance. Journal of Materials Science & Technology. 2021;65:1-6.
[72] Jia Y, Yao XD. Defects in Carbon-Based Materials for Electrocatalysis: Synthesis, Recognition, and Advances. Accounts of Chemical Research. 2023;56:948-58.
[73] Wang J, Kong H, Zhang JY, Hao Y, Shao ZP, Ciucci F. Carbon-based electrocatalysts for sustainable energy applications. Progress in Materials Science. 2021;116.
[74] Beall CE, Fabbri E, Schmidt TJ. Perovskite Oxide Based Electrodes for the Oxygen Reduction and Evolution Reactions: The Underlying Mechanism. Acs Catalysis. 2021;11:3094-114.
[75] Artyushkova K, Serov A, Rojas-Carbonell S, Atanassov P. Chemistry of Multitudinous Active Sites for Oxygen Reduction Reaction in Transition Metal-Nitrogen-Carbon Electrocatalysts. Journal of Physical Chemistry C. 2015;119:25917-28.
[76] Tong L, Duan L, Zhou A, Thummel RP. First-row transition metal polypyridine complexes that catalyze proton to hydrogen reduction. Coordination Chemistry Reviews. 2020;402:213079.
[77] Feidenhans'l AA, Regmi YN, Wei C, Xia D, Kibsgaard J, King LA. Precious metal free hydrogen evolution catalyst design and application. Chemical Reviews. 2024;124:5617-67.
[78] Johnson D, Pranada E, Yoo R, Uwadiunor E, Ngozichukwu B, Djire A. Review and perspective on transition metal electrocatalysts toward carbon-neutral energy. Energy & Fuels. 2023;37:1545-76.

[79] An L, Zhao X, Zhao T, Wang D. Atomic-level insight into reasonable design of metal-based catalysts for hydrogen oxidation in alkaline electrolytes. Energy & Environmental Science. 2021;14:2620-38.

[80] Ahsan MA, He T, Eid K, Abdullah AM, Curry ML, Du A, et al. Tuning the Intermolecular Electron Transfer of Low-Dimensional and Metal-Free BCN/C60 Electrocatalysts via Interfacial Defects for Efficient Hydrogen and Oxygen Electrochemistry. Journal of the American Chemical Society. 2021;143:1203-15.

[81] Wei C, Rao RR, Peng JY, Huang BT, Stephens IEL, Risch M, et al. Recommended Practices and Benchmark Activity for Hydrogen and Oxygen Electrocatalysis in Water Splitting and Fuel Cells. Advanced Materials. 2019;31.

[82] Yang XY, Lin L, Guo XY, Zhang SL. Design of Multifunctional Electrocatalysts for ORR/OER/HER/HOR: Janus Makes Difference. Small. 2024.

[83] Zhang QQ, Guan JQ. Single-Atom Catalysts for Electrocatalytic Applications. Advanced Functional Materials. 2020;30.

[84] Li J, Chen C, Xu L, Zhang Y, Wei W, Zhao E, et al. Challenges and Perspectives of Single-Atom-Based Catalysts for Electrochemical Reactions. JACS Au. 2023;3:736-55.

[85] Wang Z, Cao C, Zheng Y, Chen S, Zhao F. Abiotic oxygen reduction reaction catalysts used in microbial fuel cells. ChemElectroChem. 2014;1:1813-21.

[86] Wang D-W, Su D. Heterogeneous nanocarbon materials for oxygen reduction reaction. Energy & Environmental Science. 2014;7:576-91.

[87] Figueiredo JL. Nanostructured porous carbons for electrochemical energy conversion and storage. Surface and Coatings Technology. 2018;350:307-12.

[88] Wu Z, Song M, Wang J, Liu X. Recent progress in nitrogen-doped metal-free electrocatalysts for oxygen reduction reaction. Catalysts. 2018;8:196.

[89] Ge X, Sumboja A, Wuu D, An T, Li B, Goh FT, et al. Oxygen reduction in alkaline media: from mechanisms to recent advances of catalysts. Acs Catalysis. 2015;5:4643-67.

[90] Ma R, Lin G, Zhou Y, Liu Q, Zhang T, Shan G, et al. A review of oxygen reduction mechanisms for metal-free carbon-based electrocatalysts. npj Computational Materials. 2019;5:78.

[91] Shi H, Shen Y, He F, Li Y, Liu A, Liu S, et al. Recent advances of doped carbon as non-precious catalysts for oxygen reduction reaction. Journal of Materials Chemistry A. 2014;2:15704-16.

[92] Seh ZW, Kibsgaard J, Dickens CF, Chorkendorff I, Nørskov JK, Jaramillo TF. Combining theory and experiment in electrocatalysis: Insights into materials design. Science. 2017;355:eaad4998.

[93] Freire C, Fernandes DM, Nunes M, Abdelkader VK. POM & MOF-based Electrocatalysts for Energy-related Reactions. ChemCatChem. 2018;10:1703-30.
[94] Liang Q, Brocks G, Bieberle-Hütter A. Oxygen evolution reaction (OER) mechanism under alkaline and acidic conditions. Journal of Physics: Energy. 2021;3:026001.
[95] Chatenet M, Pollet BG, Dekel DR, Dionigi F, Deseure J, Millet P, et al. Water electrolysis: from textbook knowledge to the latest scientific strategies and industrial developments. Chemical society reviews. 2022;51:4583-762.
[96] Tahir M, Pan L, Idrees F, Zhang X, Wang L, Zou J-J, et al. Electrocatalytic oxygen evolution reaction for energy conversion and storage: A comprehensive review. Nano Energy. 2017;37:136-57.
[97] Suen N-T, Hung S-F, Quan Q, Zhang N, Xu Y-J, Chen HM. Electrocatalysis for the oxygen evolution reaction: recent development and future perspectives. Chemical Society Reviews. 2017;46:337-65.
[98] Li S, Thomas A. Emerged carbon nanomaterials from metal-organic precursors for electrochemical catalysis in energy conversion. Advanced nanomaterials for electrochemical-based energy conversion and storage: Elsevier; 2020. p. 393-423.
[99] Chatenet M, Pollet BG, Dekel DR, Dionigi F, Deseure J, Millet P, et al. Water electrolysis: from textbook knowledge to the latest scientific strategies and industrial developments. Chemical Society Reviews. 2022;51:4583-762.
[100] Pratama DSA, Haryanto A, Lee CW. Heterostructured mixed metal oxide electrocatalyst for the hydrogen evolution reaction. Frontiers in Chemistry. 2023;11:1141361.
[101] Zeb Z, Huang Y, Chen L, Zhou W, Liao M, Jiang Y, et al. Comprehensive overview of polyoxometalates for electrocatalytic hydrogen evolution reaction. Coordination Chemistry Reviews. 2023;482:215058.
[102] Yan Z, Liu H, Hao Z, Yu M, Chen X, Chen J. Electrodeposition of (hydro)oxides for an oxygen evolution electrode. Chemical Science. 2020;11:10614-25.
[103] Horn MR, Singh A, Alomari S, Goberna-Ferrón S, Benages-Vilau R, Chodankar N, et al. Polyoxometalates (POMs): from electroactive clusters to energy materials. Energy & Environmental Science. 2021;14:1652-700.
[104] Ďurovič M, Hnát J, Bouzek K. Electrocatalysts for the hydrogen evolution reaction in alkaline and neutral media. A comparative review. Journal of Power Sources. 2021;493:229708.
[105] Raveendran A, Chandran M, Dhanusuraman R. A comprehensive review on the electrochemical parameters and recent material development of electrochemical water splitting electrocatalysts. RSC advances. 2023;13:3843-76.

[106] Wang S, Lu A, Zhong C-J. Hydrogen production from water electrolysis: role of catalysts. Nano Convergence. 2021;8:4.
[107] Liu Q, Ranocchiari M, van Bokhoven JA. Catalyst overcoating engineering towards high-performance electrocatalysis. Chemical Society Reviews. 2022;51:188-236.
[108] Liu X, Zhang G, Wang L, Fu H. Structural Design Strategy and Active Site Regulation of High-Efficient Bifunctional Oxygen Reaction Electrocatalysts for Zn–Air Battery. Small. 2021;17:2006766.
[109] Bhuvanendran N, Ravichandran S, Lee S, Sanij FD, Kandasamy S, Pandey P, et al. Recent progress in Pt-based electrocatalysts: a comprehensive review of supported and support-free systems for oxygen reduction. Coordination Chemistry Reviews. 2024;521:216191.
[110] Zhang C, Shen X, Pan Y, Peng Z. A review of Pt-based electrocatalysts for oxygen reduction reaction. Frontiers in Energy. 2017;11:268-85.
[111] Li C, Baek J-B. Recent Advances in Noble Metal (Pt, Ru, and Ir)-Based Electrocatalysts for Efficient Hydrogen Evolution Reaction. ACS Omega. 2020;5:31-40.
[112] Amin HMA, Zan L, Baltruschat H. Boosting the bifunctional catalytic activity of Co3O4 on silver and nickel substrates for the alkaline oxygen evolution and reduction reactions. Surfaces and Interfaces. 2024;54:105218.
[113] Wang X, Li Z, Qu Y, Yuan T, Wang W, Wu Y, et al. Review of Metal Catalysts for Oxygen Reduction Reaction: From Nanoscale Engineering to Atomic Design. Chem. 2019;5:1486-511.
[114] Huang X, Shen T, Zhang T, Qiu H, Gu X, Ali Z, et al. Efficient oxygen reduction catalysts of porous carbon nanostructures decorated with transition metal species. Advanced Energy Materials. 2020;10:1900375.
[115] Bhoyate SD, Kim J, de Souza FM, Lin J, Lee E, Kumar A, et al. Science and engineering for non-noble-metal-based electrocatalysts to boost their ORR performance: A critical review. Coordination Chemistry Reviews. 2023;474:214854.
[116] Wei C, Feng Z, Scherer GG, Barber J, Shao-Horn Y, Xu ZJ. Cations in octahedral sites: a descriptor for oxygen electrocatalysis on transition-metal spinels. Advanced Materials. 2017;29:1606800.
[117] Li H, Kelly S, Guevarra D, Wang Z, Wang Y, Haber JA, et al. Analysis of the limitations in the oxygen reduction activity of transition metal oxide surfaces. Nature Catalysis. 2021;4:463-8.
[118] Ahmed MS, Choi B, Kim Y-B. Development of Highly Active Bifunctional Electrocatalyst Using Co3O4 on Carbon Nanotubes for Oxygen Reduction and Oxygen Evolution. Scientific Reports. 2018;8:2543.

[119] Noor T, Yaqoob L, Iqbal N. Recent advances in electrocatalysis of oxygen evolution reaction using noble-metal, transition-metal, and carbon-based materials. ChemElectroChem. 2021;8:447-83.
[120] Shen A, Zou Y, Wang Q, Dryfe RAW, Huang X, Dou S, et al. Oxygen Reduction Reaction in a Droplet on Graphite: Direct Evidence that the Edge Is More Active than the Basal Plane. Angewandte Chemie International Edition. 2014;53:10804-8.
[121] Bouleau L, Pérez-Rodríguez S, Quílez-Bermejo J, Izquierdo MT, Xu F, Fierro V, et al. Best practices for ORR performance evaluation of metal-free porous carbon electrocatalysts. Carbon. 2022;189:349-61.
[122] Liang J, Yuan Q. Effects of graphitic-and pyridinic-N co-doping on structure regulation and ORR activity of N-doped graphene. Applied Surface Science. 2024;648:159025.
[123] Feng X, Bai Y, Liu M, Li Y, Yang H, Wang X, et al. Untangling the respective effects of heteroatom-doped carbon materials in batteries, supercapacitors and the ORR to design high performance materials. Energy & Environmental Science. 2021;14:2036-89.
[124] Gao Y, Wang Q, Ji G, Li A, Niu J. Doping strategy, properties and application of heteroatom-doped ordered mesoporous carbon. RSC advances. 2021;11:5361-83.
[125] Byeon A, Yun WC, Kim JM, Lee JW. Recent progress in heteroatom-doped carbon electrocatalysts for the two-electron oxygen reduction reaction. Chemical Engineering Journal. 2023;456:141042.
[126] Tang Z, Li H, Jia X, Lin F, Li K. Recovery of Waste-Activated Carbon for Synthesizing High-Efficiency ORR Electrocatalyst. Energies. 2025;18:1666.
[127] Araújo H, Šljukić B, Santos DM. POM-based Electrocatalysts for Oxygen Reduction Reactions. Applied Polyoxometalate-based Electrocatalysis. 2025:263-82.
[128] Araújo H, Šljukić B, Gago S, Santos DM. The current state of transition metal-based electrocatalysts (oxides, alloys, POMs, and MOFs) for oxygen reduction, oxygen evolution, and hydrogen evolution reactions. Frontiers in Energy Research. 2024;12:1373522.
[129] Long D-L, Burkholder E, Cronin L. Polyoxometalate clusters, nanostructures and materials: From self assembly to designer materials and devices. Chemical Society Reviews. 2007;36:105-21.
[130] Liu S, Tang Z. Polyoxometalate-based functional nanostructured films: Current progress and future prospects. Nano Today. 2010;5:267-81.
[131] Long DL, Tsunashima R, Cronin L. Polyoxometalates: building blocks for functional nanoscale systems. Angewandte Chemie International Edition. 2010;49:1736-58.

[132] Fernandes DM, Simões SM, Carapuça HM, Cavaleiro AM. Functionalisation of glassy carbon electrodes with deposited tetrabutylammonium microcrystalline salts of lacunary and metal-substituted α-Keggin-polyoxosilicotungstates. Electrochimica acta. 2008;53:6580-8.

[133] Fernandes DM, Freire C. Carbon nanomaterial–phosphomolybdate composites for oxidative electrocatalysis. ChemElectroChem. 2015;2:269-79.

[134] Keita B, Zhang G, Dolbecq A, Mialane P, Sécheresse F, Miserque F, et al. MoV−MoVI Mixed Valence Polyoxometalates for Facile Synthesis of Stabilized Metal Nanoparticles: Electrocatalytic Oxidation of Alcohols. The Journal of Physical Chemistry C. 2007;111:8145-8.

[135] García-López EI, Marcì G, Krivtsov I, Casado Espina J, Liotta LF, Serrano A. Local Structure of Supported Keggin and Wells–Dawson Heteropolyacids and Its Influence on the Catalytic Activity. The Journal of Physical Chemistry C. 2019;123:19513-27.

[136] Fernandes DM. Applied Polyoxometalate-Based Electrocatalysis: John Wiley & Sons; 2024.

[137] Couto FA, Cavaleiro AM, de Jesus JDP, Simão JE. Study of polyoxotungstates with the Keggin structure by cyclic voltammetry. Inorganica chimica acta. 1998;281:225-8.

[138] Sadakane M, Steckhan E. Electrochemical properties of polyoxometalates as electrocatalysts. Chemical reviews. 1998;98:219-38.

[139] Dehghani Sanij F, Balakrishnan P, Su H, Khotseng L, Xu Q. Fabrication of polyoxometalate-modified palladium–nickel/reduced graphene oxide alloy catalysts for enhanced oxygen reduction reaction activity. RSC Advances. 2021;11:39118-29.

[140] Ji Y, Huang L, Hu J, Streb C, Song Y-F. Polyoxometalate-functionalized nanocarbon materials for energy conversion, energy storage and sensor systems. Energy & Environmental Science. 2015;8:776-89.

[141] Daems N, Sheng X, Vankelecom IF, Pescarmona PP. Metal-free doped carbon materials as electrocatalysts for the oxygen reduction reaction. Journal of Materials Chemistry A. 2014;2:4085-110.

[142] Hoang S, Guo S, Hahn NT, Bard AJ, Mullins CB. Visible light driven photoelectrochemical water oxidation on nitrogen-modified TiO2 nanowires. Nano letters. 2012;12:26-32.

[143] Chen P, Wang L-K, Wang G, Gao M-R, Ge J, Yuan W-J, et al. Nitrogen-doped nanoporous carbon nanosheets derived from plant biomass: an efficient catalyst for oxygen reduction reaction. Energy & Environmental Science. 2014;7:4095-103.

[144] Liu F, Peng H, You C, Fu Z, Huang P, Song H, et al. High-performance doped carbon catalyst derived from nori biomass with melamine promoter. Electrochimica Acta. 2014;138:353-9.
[145] Tuci G, Zafferoni C, Rossin A, Milella A, Luconi L, Innocenti M, et al. Chemically Functionalized Carbon Nanotubes with Pyridine Groups as Easily Tunable N-Decorated Nanomaterials for the Oxygen Reduction Reaction in Alkaline Medium. Chemistry of Materials. 2014;26:3460-70.
[146] Bard AJ, Faulkner LR, White HS. Electrochemical methods: fundamentals and applications: John Wiley & Sons; 2022.
[147] Faber MS, Jin S. Earth-abundant inorganic electrocatalysts and their nanostructures for energy conversion applications. Energy & Environmental Science. 2014;7:3519-42.
[148] Jiao Y, Zheng Y, Jaroniec M, Qiao SZ. Design of electrocatalysts for oxygen-and hydrogen-involving energy conversion reactions. Chemical Society Reviews. 2015;44:2060-86.
[149] Muthuswamy N, Buan ME, Walmsley JC, Rønning M. Evaluation of ORR active sites in nitrogen-doped carbon nanofibers by KOH post treatment. Catalysis Today. 2018;301:11-6.
[150] Conway B. Behavior of Dielectrics in Capacitors and Theories of Dielectric Polarization. Electrochemical Supercapacitors: Scientific Fundamentals and Technological Applications: Springer; 1999. p. 87-104.
[151] Hampson J, Hanssen S. Electrical Trade Principles 5th Edition: Cengage Learning Australia; 2019.
[152] Jose R, Krishnan S, Vidyadharan B, Misnon I, Harilal M, Aziz R, et al. Supercapacitor electrodes delivering high energy and power densities. Materials Today: Proceedings. 2016;3:S48-S56.
[153] Naseri F, Farjah E, Ghanbari T. An Efficient Regenerative Braking System Based on Battery/Supercapacitor for Electric, Hybrid, and Plug-In Hybrid Electric Vehicles With BLDC Motor. IEEE Transactions on Vehicular Technology. 2017;66:3724-38.
[154] Pholauyphon W, Charoen-amornkitt P, Suzuki T, Tsushima S. Guidelines for supercapacitor electrochemical analysis: A comprehensive review of methodologies for finding charge storage mechanisms. Journal of Energy Storage. 2024;98:112833.
[155] Liu M, Liu J-C, Zhang Y, Han X, Li H, Huang Z-H, et al. Current Collectors for Supercapacitors: Objectives, Modification Methods and Challenges. ChemElectroChem. 2025;12:e202400513.

[156] Shao Y, El-Kady MF, Sun J, Li Y, Zhang Q, Zhu M, et al. Design and mechanisms of asymmetric supercapacitors. Chemical reviews. 2018;118:9233-80.
[157] Pameté E, Köps L, Kreth FA, Pohlmann S, Varzi A, Brousse T, et al. The many deaths of supercapacitors: degradation, aging, and performance fading. Advanced Energy Materials. 2023;13:2301008.
[158] Bose S, Kuila T, Mishra AK, Rajasekar R, Kim NH, Lee JH. Carbon-based nanostructured materials and their composites as supercapacitor electrodes. Journal of Materials Chemistry. 2012;22:767-84.
[159] Sun J, Luo B, Li H. A review on the conventional capacitors, supercapacitors, and emerging hybrid ion capacitors: past, present, and future. Advanced Energy and Sustainability Research. 2022;3:2100191.
[160] Patra A, Namsheer K, Jose JR, Sahoo S, Chakraborty B, Rout CS. Understanding the charge storage mechanism of supercapacitors: in situ/operando spectroscopic approaches and theoretical investigations. Journal of Materials Chemistry A. 2021;9:25852-91.
[161] Schötz T, Gordon LW, Ivanov S, Bund A, Mandler D, Messinger RJ. Disentangling faradaic, pseudocapacitive, and capacitive charge storage: a tutorial for the characterization of batteries, supercapacitors, and hybrid systems. Electrochimica Acta. 2022;412:140072.
[162] Choudhary N, Li C, Moore J, Nagaiah N, Zhai L, Jung Y, et al. Asymmetric supercapacitor electrodes and devices. Advanced Materials. 2017;29:1605336.
[163] Liu J-C, Huang Z-H, Ma T-Y. Aqueous Supercapacitor with Ultrahigh Voltage Window Beyond 2.0 Volt. Small Structures. 2020;1:2000020.
[164] Sun J, Wu C, Sun X, Hu H, Zhi C, Hou L, et al. Recent progresses in high-energy-density all pseudocapacitive-electrode-materials-based asymmetric supercapacitors. Journal of Materials Chemistry A. 2017;5:9443-64.
[165] Pandolfo AG, Hollenkamp AF. Carbon properties and their role in supercapacitors. Journal of Power Sources. 2006;157:11-27.
[166] Miller JR. Introduction to electrochemical capacitor technology. IEEE Electrical Insulation Magazine. 2010;26:40-7.
[167] Helmholtz Hv. Ueber einige Gesetze der Vertheilung elektrischer Ströme in körperlichen Leitern, mit Anwendung auf die thierisch-elektrischen Versuche (Schluss.). Annalen der Physik. 1853;165:353-77.
[168] Gouy M. Sur la constitution de la charge électrique à la surface d'un électrolyte. J Phys Theor Appl. 1910;9:457-68.

[169] Chapman DL. LI. A contribution to the theory of electrocapillarity. The London, Edinburgh, and Dublin philosophical magazine and journal of science. 1913;25:475-81.
[170] Stern O. Zur theorie der elektrolytischen doppelschicht. Zeitschrift für Elektrochemie und angewandte physikalische Chemie. 1924;30:508-16.
[171] Grahame DC. The electrical double layer and the theory of electrocapillarity. Chemical reviews. 1947;41:441-501.
[172] Chen GZ. Supercapacitor and supercapattery as emerging electrochemical energy stores. International Materials Reviews. 2017;62:173-202.
[173] Huang H, Niederberger M. Towards fast-charging technologies in Li+/Na+ storage: from the perspectives of pseudocapacitive materials and non-aqueous hybrid capacitors. Nanoscale. 2019;11:19225-40.
[174] Simon P, Gogotsi Y. Materials for electrochemical capacitors. Nature materials. 2008;7:845-54.
[175] Conway B. Electrochemical capacitors based on pseudocapacitance. Electrochemical supercapacitors: scientific fundamentals and technological applications: Springer; 1999. p. 221-57.
[176] Eftekhari A, Mohamedi M. Tailoring pseudocapacitive materials from a mechanistic perspective. Materials Today Energy. 2017;6:211-29.
[177] Conway B, Pell W. Double-layer and pseudocapacitance types of electrochemical capacitors and their applications to the development of hybrid devices. Journal of Solid State Electrochemistry. 2003;7:637-44.
[178] Gogotsi Y, Penner RM. Energy Storage in Nanomaterials – Capacitive, Pseudocapacitive, or Battery-like? ACS Nano. 2018;12:2081-3.
[179] Cheng Y, Wang H, Qian T, Yan C. Interfacial engineering of carbon-based materials for efficient electrocatalysis: Recent advances and future. EnergyChem. 2022;4:100074.
[180] Seh ZW, Kibsgaard J, Dickens CF, Chorkendorff I, Nørskov JK, Jaramillo TF. Combining theory and experiment in electrocatalysis: Insights into materials design. Science. 2017;355.
[181] Yang X, Liang J, Shi Q, Zachman MJ, Kabir S, Liang J, et al. Regulating the Third Metal to Design and Engineer Multilayered NiFeM (M: Co, Mn, and Cu) Nanofoam Anode Catalysts for Anion-Exchange Membrane Water Electrolyzers. Advanced Energy Materials. 2024;14:2400029.
[182] Hu X, Tian X, Lin Y-W, Wang Z. Nickel foam and stainless steel mesh as electrocatalysts for hydrogen evolution reaction, oxygen evolution reaction and overall water splitting in alkaline media. RSC advances. 2019;9:31563-71.

[183] Zhou C, Zhao S, Meng H, Han Y, Jiang Q, Wang B, et al. RuCoO(x) Nanofoam as a High-Performance Trifunctional Electrocatalyst for Rechargeable Zinc-Air Batteries and Water Splitting. Nano Lett. 2021;21:9633-41.
[184] Zheng W, Liu M, Lee LYS. Best practices in using foam-type electrodes for electrocatalytic performance benchmark. ACS Energy Letters. 2020;5:3260-4.
[185] Łuba M, Mikołajczyk T, Kuczyński M, Pierożyński B, Kowalski IM. Enhancing the Effectiveness of Oxygen Evolution Reaction by Electrodeposition of Transition Metal Nanoparticles on Nickel Foam Material. Catalysts. 2021;11:468.
[186] Adak MK, Basak HK, Kumar S, Chakraborty B. Detection of a Nickel-Oxide Nanolayer During Mild Acid Treatment of Nickel Foam and Its Effect on Alkaline Oxygen Evolution and Ammonia Oxidation Reactions. ACS Applied Nano Materials. 2024;7:8329-40.
[187] Santos AL, Cebola MJ, Antunes J, Santos DMF. Insights on the Performance of Nickel Foam and Stainless Steel Foam Electrodes for Alkaline Water Electrolysis. Sustainability. 2023;15:11011.
[188] Lytvynenko AS, Brzózka A, Mishura AM, Kolotilov SV, Sulka GD. Control of Ag nanofoam structure and its electrocatalytic performance in bromobenzene reductive debromination via variation of electrodeposition conditions. Applied Surface Science. 2022;579:152131.
[189] Woo J, Moon BC, Lee U, Oh H-S, Chae KH, Jun Y, et al. Collaborative electrochemical oxidation of the alcohol and aldehyde groups of 5-hydroxymethylfurfural by NiOOH and Cu (OH) 2 for superior 2, 5-furandicarboxylic acid production. ACS Catalysis. 2022;12:4078-91.
[190] Sun S, Zheng M, Cheng P, Wu F, Xu L. Porous bimetallic cobalt-iron phosphide nanofoam for efficient and stable oxygen evolution catalysis. J Colloid Interface Sci. 2022;626:515-23.
[191] Zhou C, Zhao S, Meng H, Han Y, Jiang Q, Wang B, et al. RuCoOx Nanofoam as a High-Performance Trifunctional Electrocatalyst for Rechargeable Zinc–Air Batteries and Water Splitting. Nano Letters. 2021;21:9633-41.
[192] Zhou C, Zhao S, Meng H, Han Y, Jiang Q, Wang B, et al. RuCoO x nanofoam as a high-performance trifunctional electrocatalyst for rechargeable zinc–air batteries and water splitting. Nano Letters. 2021;21:9633-41.
[193] Yang X, Liang J, Shi Q, Zachman MJ, Kabir S, Liang J, et al. Regulating the Third Metal to Design and Engineer Multilayered NiFeM (M: Co, Mn, and Cu) Nanofoam Anode Catalysts for Anion-Exchange Membrane Water Electrolyzers. Advanced Energy Materials. 2024;14:2400029.

[194] Zheng Z, Yu L, Gao M, Chen X, Zhou W, Ma C, et al. Boosting hydrogen evolution on MoS2 via co-confining selenium in surface and cobalt in inner layer. Nature communications. 2020;11:3315.
[195] Ren G, Liu B, Xu X, Jing P, Wu J, Zhang J. Heterojunction engineering via in-situ electrochemical reconstruction for boosting electrocatalytic biomass upgrading-coupled hydrogen production. Nano Today. 2024;56:102315.
[196] Santos DM, Eugenio S, Sequeira CA, Montemor MF. Transition metal foam electrocatalysts for hydrogen evolution reaction. ECS Transactions. 2015;64:9.
[197] Cardoso D, Eugénio S, Silva T, Santos D, Sequeira C, Montemor M. Hydrogen evolution on nanostructured Ni–Cu foams. RSC Advances. 2015;5:43456-61.
[198] Cui P, Wang T, Zhang X, Ba C, Wu Y, Peng K, et al. NiCoCuP foam with a 3D hierarchical porous structure as all-pH efficient and stable HER electrocatalyst. International Journal of Hydrogen Energy. 2023;48:16725-32.
[199] Zhang J, Baró MD, Pellicer E, Sort J. Electrodeposition of magnetic, superhydrophobic, non-stick, two-phase Cu–Ni foam films and their enhanced performance for hydrogen evolution reaction in alkaline water media. Nanoscale. 2014;6:12490-9.
[200] Siwek K, Eugénio S, Santos D, Silva M, Montemor M. 3D nickel foams with controlled morphologies for hydrogen evolution reaction in highly alkaline media. International journal of hydrogen energy. 2019;44:1701-9.
[201] Siwek KI, Eugénio S, Silva TM, Montemor MF. Electrochemical performance of MnOx·nH2O@Ni composite foam electrodes for energy storage in KOH media. Electrochimica Acta. 2018;281:39-47.
[202] Siwek KI, Eugénio S, Silva TM, de Fatima Montemor M. Electrodeposited Manganese Oxide on Tailored 3D Bimetallic Nanofoams for Energy Storage Applications. Energy Technology. 2019;7:1801139.
[203] Shi Y, Xue J, Yu Y, Liu N, Tang C. Construction of binder-free 3-D porous NiMn LDH electrode materials for high performance asymmetric supercapacitors using dynamic hydrogen bubbles as template. Journal of Alloys and Compounds. 2024;970:172513.
[204] Cong W, Miao R, Tao B, Miao F. MnO2/ZnCo2O4 with binder-free arrays on nickel foam loaded with graphene as a high performance electrode for advanced asymmetric supercapacitors. RSC Advances. 2019;9:32889-97.
[205] Feng C, Zhang J, He Y, Zhong C, Hu W, Liu L, et al. Sub-3 nm Co3O4 nanofilms with enhanced supercapacitor properties. ACS nano. 2015;9:1730-9.

[206] Popov KI, Djokić SS, Nikolić ND, Jović VD, Popov KI, Djokić SS, et al. Electrodeposition of Metals with Hydrogen Evolution. Morphology of Electrochemically and Chemically Deposited Metals. 2016:171-203.
[207] Plowman BJ, Jones LA, Bhargava SK. Building with bubbles: the formation of high surface area honeycomb-like films via hydrogen bubble templated electrodeposition. Chemical Communications. 2015;51:4331-46.
[208] Popov KI, Djokić SS, Nikolić ND, Jović VD. Morphology of electrochemically and chemically deposited metals: Springer; 2016.

Chapter 2

# Electrocatalytic oxygen reduction reaction on 48-tungsto-8-phosphate wheel anchored on carbon nanomaterials

# 2

# Electrocatalytic oxygen reduction reaction on 48-tungsto-8-phosphate wheel anchored on carbon[1,2]

Following the theoretical concepts of electrocatalysis and energy conversion established in the introductory chapter, this chapter marks the beginning of the practical investigation into carbon-based materials and polyoxometalates. The motivation for choosing the wheel-shaped 48-tungsto-8-phosphate ($P_8W_{48}$) cluster at this stage lies in its unique structural properties and its potential for synergistic interaction with carbon nanostructures. The primary objective to achieve with this novel material is its effective immobilisation onto various carbon supports (such as graphene flakes and carbon nanotubes) to evaluate how this combination enhances the electrocatalytic activity for the oxygen reduction reaction (ORR) in an alkaline medium.

[1] Novais, H.C., Jarrais, B., Haider, A. *et al.* Electrocatalytic Oxygen Reduction Reaction on 48-Tungsto-8-Phosphate Wheel Anchored on Carbon Nanomaterials. *Electrocatalysis* **14**, 294–305 (2023). https://doi.org/10.1007/s12678-022-00792-w.

[2] Hugo C. Novais' contribution to the publication: synthesis and characterisation of composite materials, electrocatalytic experiments and responsible for writing up the manuscript.

## Abstract

Regardless of great efforts, the development of novel low cost electrocatalysts with high electrocatalytic activity for the oxygen reduction reaction (ORR) remains a real challenge. This is a setback for the mass commercialization of one of the eco-friendliest alternative power sources: fuel cells (FCs). Thus, this work describes the preparation of four composites based on the 48-tungsto-8-phosphate polyanion salt $K_{28}Li_5[H_7P_8W_{48}O_{184}]\cdot 92H_2O$ (KLi-$P_8W_{48}$) immobilized on four distinct carbon materials, namely graphene flakes (GF), single-walled carbon nanotubes (SWCNT), multi-walled carbon nanotubes (MWCNT), and N-doped multi-walled carbon nanotubes (N-MWCNT), and their application as ORR electrocatalysts. In alkaline medium, all composites exhibited electrocatalytic activity with onset potentials between 0.71 and 0.94 V *vs.* RHE, whilst $P_8W_{48}$@N-MWCNT presented superior current density (-3.3 mA $cm^{-2}$). A mixed electron process of 2- and 4-electrons is observed for all the composites, supporting the results of % $H_2O_2$ production. Additionally, low Tafel slopes were obtained (43–82 mV $dec^{-1}$) for all composites. The electrocatalysts also showed excellent tolerance to methanol, with current retentions of 91 – 93%, and good electrochemical stability with current retentions between 67 and 82% after 36000s.

## 2.1. Introduction

In the last decades, the abrupt growth of world population and industrial processes has had a profound impact on the environment and health, increasing the urgency to substitute the use of fossil fuels with alternative energy sources and conversion devices.[1] One of the most common eco-friendly options are fuel cells (FCs), which commercialization is on hold due to the high cost of hydrogen storage and noble metal-based state-of-the-art electrocatalysts. The current use of precious Pt and Pd-based electrocatalysts is a major drawback for the economic viability of most fuel cells.[2] Proton exchange membrane (PEM) systems despite being the most technologically mature, rely on expensive acid membranes and ionomers [3] and platinum group metal-based electrocatalysts which are expensive, have restricted durability, and scarce availability.[4] To increase the oxygen reduction reaction (ORR) performance, Pt and Pd have been combined with other transition metals, such as Ru[5], Ni[6], Ag[6] or Co[7, 8]. In the case of anion exchange membrane fuel cells (AEMFCs), their intrinsically noncorrosive environment allows the use of less noble ORR electrocatalysts than Pt.[9] Therefore, materials from families of base metal oxides ($MnO_x$, mixed oxides,

spinels)[10], M–N–Cs (where M = Fe, Co, Mn)[11], and Ni-based materials[12] have been extensively studied as ORR electrocatalysts in alkaline media with some excellent results. For example, pyrolyzed M–N–Cs electrocatalysts have shown ORR activities comparable to that of Pt-based catalysts in basic media.[9] As the ORR has a crucial function as the cathode reaction in these energy-converting systems, it is imperative to find new electrocatalysts with high performance and at the same time less expensive.[13-16]

Polyoxometalates (POMs) exhibit a wide range of chemical and electrochemical properties that make them promising electrocatalysts for replacing platinum in the ORR. With a wide variety of sizes, compositions and shapes, POMs have the ability to undergo reversible multi-electron reductions/oxidations leading to the formation of mixed-valence species. Moreover, POMs have electron and proton transfer capabilities, and therefore, can act as acceptors/donors of a large number of electrons, without any significant structural changes.

Due to the high surface area, stability, and conductivity, combined with low cost, carbon materials have been the subject of several studies such as the degradation of organic pollutants,[17] hydrogen storage,[18] supercapacitors,[19] batteries[20, 21] as well as their application in ORR.[22, 23] It is imperative to find and choose carbon materials that have additional anchoring positions where other active materials can be attached. For applications such as ORR, several carbon–based materials, such as graphene,[24-26] carbon nanotubes,[27] and respective doped carbon materials[28] have been proposed. One way to improve the electrocatalytic performance of carbon materials is through doping with different elements, nitrogen being one of the most used and with the most potential.[29-31] It has been shown that nitrogen-doped carbon materials show an increase in electrocatalytic activity towards ORR.[32, 33] Different forms of nitrogen species can be incorporated on the graphitic network, such as, pyridinic, pyrrolic, graphitic (quaternary) and oxidized nitrogen.[34]

The individual use of polyoxometalates has not been very promising for reactions related to energy applications.[35, 36] However, these materials show higher performances when coupled with carbon supports.[37-39] Taking advantage of their high stability, good redox properties, and the ability to transfer electrons, POMs are excellent candidates to be coupled with carbon materials for subsequent application as ORR electrocatalysts.[39, 40]

Herein we report on the preparation of composites based on the incorporation of the 48-tungsto-8-phosphate $[H_7P_8W_{48}O_{184}]^{33-}$ ($P_8W_{48}$) onto four distinct carbon materials: graphene flakes (GF), single-walled carbon nanotubes (SWCNT), multi-walled carbon

nanotubes (MWCNT), and N-doped multi-walled carbon nanotubes (N-MWCNT), and their application as ORR electrocatalysts.

## 2.2. Experimental section

### 2.2.1 Materials preparation and characterisation methods

The materials and solvents used in the preparation of the composites and in the ORR studies are described in detail in the Supplementary Information (SI). All carbon materials used in the preparation of the composites were commercially available, and used as received, with the exception of N-MWCNT, which was produced by catalytic chemical vapour decomposition using a previously described method.[41] The nitrogen content (4.1%) was determined by elemental analysis using a LECO CHNS-932 equipment. The rest of the N-MWCNT characterisation is described elsewhere.[41]

The composites were prepared using an adapted procedure.[42] An aqueous dispersion of the selected carbon material (15 mL $H_2SO_4$, pH=1.0, 3.3 mg $mL^{-1}$) was mixed with a solution of $P_8W_{48}$ ($0.5 \times 10^{-3}$ mol $dm^{-3}$ in 15 mL $H_2SO_4$, pH=1.0) using an ultrasonic homogenizer for 15 min. Then, the grafting of $P_8W_{48}$ onto the carbon materials was achieved through controlled potential coulometry at -0.65 V *vs.* SCE. For this purpose, a conventional three-electrode compartment cell was used, comprising of: a glassy carbon electrode (GCE, 3 mm diameter, ALS Co., Ltd) as working electrode, a platinum wire with a large surface area as the auxiliary electrode, and a purged calomel electrode (SCE) as reference electrode, with the latter two separated from the electrolyte by a glass frit. The electrolyte was purged with ultrahigh-purity $N_2$ for at least 30 min and kept under a positive pressure of this gas during the experiments. In the end, the suspension obtained was filtered and washed with ultra-pure water and the composites were dried in an oven overnight at 80 ºC.

Prior to their use in the electrocatalytic studies, all composites prepared ($P_8W_{48}$@GF, $P_8W_{48}$@SWCNT, $P_8W_{48}$@MWCNT and $P_8W_{48}$@N-MWCNT) were characterised by different techniques: Fourier-transformed infrared spectroscopy (FTIR), scanning electron microscopy (SEM), energy dispersive X-ray spectroscopy (EDS) and X-ray photoelectron spectroscopy (XPS). The methods and equipment used are detailed in the SI. Electrocatalytic performances towards ORR were evaluated using a PGSTAT 302N potentiostat (Metrohm Autolab B.V., Utrecht, The Netherlands) controlled by

NOVA 2.1 and using a conventional 3-electrode system. For all details regarding electrodes, electrode conditioning and modification, see the SI.

## 2.3. Results and Discussion

### 2.3.1. Materials characterisation

The infrared spectra for all prepared composites can be observed in Figures 2.1 and 2S1 (SI). Figure 2.1 shows, as an example, the FTIR spectra for $P_8W_{48}$@GF, $P_8W_{48}$ and GF. The FTIR spectrum of $P_8W_{48}$ shows the typical POM vibrational bands between 1150 and 500 $cm^{-1}$. The two bands at 1134 and 1081 $cm^{-1}$ are attributed to the splitting of the $\nu_{as}$P-O stretching vibration. The $\nu_{as}W=O_t$ vibration band is detected at 1017 $cm^{-1}$ and the vibrational bands at 929 and 803 $cm^{-1}$ are assigned to $\nu_{as}W-O_b-W$ and $\nu_{as}W-O_c-W$ stretching modes, respectively.[42, 43]

The FTIR spectrum of GF (Figure 2.1, black) reveals some vibrational bands at 3433, 2921, 2853, 1633, 1580, 1384, 1165 and 1059 $cm^{-1}$, but some of the vibration bands are very weak and poorly resolved. The representative vibrational bands of OH groups are observed at 3433 and 1384 $cm^{-1}$, which are due to O-H stretching and bending modes, respectively from residual adsorbed water and to the hydroxyl groups.[44, 45] At 1580 and 1165 $cm^{-1}$, the bands are assigned to the C=C stretching mode of skeletal vibrations from non-oxidized domains and to the influence of phenolic groups vibration modes, respectively.[44, 46, 47] The two bands at 2921 and 2853 $cm^{-1}$ correspond, respectively, to the C-H stretching modes that can be due to the existence of defects in the $sp^2$ hybridized domains, and the band at 1633 $cm^{-1}$ can be assigned to the C=O stretching mode of carboxylic acid, carbonyl, ketone and quinone groups.[44, 45] The band at 1059 $cm^{-1}$ is assigned to C-O-C and C-O stretching modes and C-O-H bending mode.[44, 46, 47]

The vibrational spectra of single- and multi-walled were very identical (Figure 2S1 blue line) with weak bands. However, the SWCNT spectrum shows bands assigned to O-H stretching and bending modes at ~ 3437 and 1384 $cm^{-1}$, respectively.[44, 45] The band corresponding to the C=C stretching vibrations of the aromatic carbon is found at 1579 $cm^{-1}$, the band at 1628 $cm^{-1}$ is attributed to C=O stretching vibration, and the band at 1383 $cm^{-1}$ to the phenol groups.[45] Finally, the band at 1174 $cm^{-1}$ is assigned to the C-O stretching vibrations of oxygen groups.[39]

The vibrational bands of N-MWCNT (Figure 2S1 (c)) can be observed at 3422, 1565, 1383 and 1118 $cm^{-1}$, corresponding to the O-H groups stretching vibrations, the stretching vibrations of C=N and C=C, and the C-N and C-O stretching vibrations, respectively.[48, 49]

The FTIR spectra of $P_8W_{48}$@carbon materials (CM) shown in Figure 2.1 for $P_8W_{48}$@GF and in Figure 2S1 for the other three composites show very week and poorly resolved bands sill it confirms the immobilization of the POM onto the carbon materials, as it exhibits the typical bands from the POM in addition to the bands from the carbon material. After adsorption of the $P_8W_{48}$ onto the carbon materials, the positions of the vibration modes are slightly shifted to lower wavenumbers. Reported changes are likely to reflect weakening bonds.[50, 51] Similar results were observed for the other three composites.

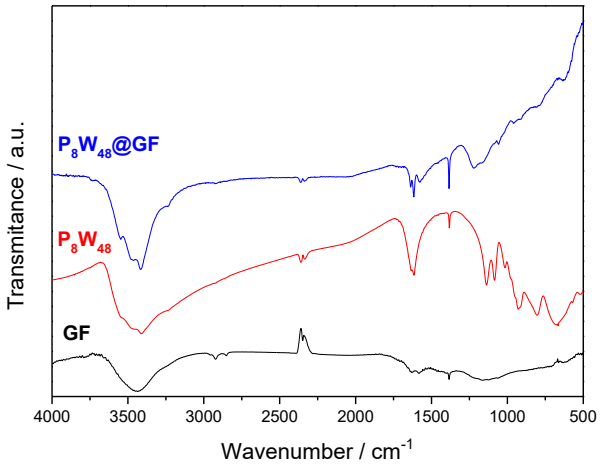



Figure 2.1 - Overlaid FTIR spectra in the 4000–400 cm-1 range of GF (black), KLi-P8W48 (red), and P8W48@GF composite (blue).

All composites were characterised by XPS, and the surface atomic percentages are summarised in Table 2.1. This technique was used to probe the chemical environments of the elemental surface species, showing that the immobilization of the POM (O, P and W elements) onto the carbon materials was successful. The atomic ratios obtained for $P_8W_{48}$@N-MWCNT and $P_8W_{48}$@MWCNT of 1:6 (P/W) suggest that the POM structured is maintained as this value is equal to the theoretical one. Still, for the other two materials prepared, namely for $P_8W_{48}$@GF and $P_8W_{48}$@SWCNT the ratios are

close (1:3 and 1:3.5, respectively). In Figures 2S2-2S8, all the deconvoluted XPS spectra are shown.

Table 2.1 - XPS surface atomic percentages for the pristine carbon materials and the prepared composites.

| Material | XPS Atomic %[a] | | | | |
|---|---|---|---|---|---|
| | C1s | O1s | N1s | P2p | W4f |
| **GF** | 96.8 | 3.2 | - | - | - |
| **SWCNT** | 98.4 | 1.6 | - | - | - |
| **MWCNT** | 98.9 | 1.1 | - | - | - |
| **N-MWCNT** | 90.4 | 5.2 | 4.4 | - | - |
| **$P_8W_{48}$@GF** | 92.2 | 6.8 | 0.6 | 0.1 | 0.3 |
| **$P_8W_{48}$@SWCNT** | 89.9 | 8.5 | 0.7 | 0.2 | 0.7 |
| **$P_8W_{48}$@MWCNT** | 87.6 | 10.6 | 1.1 | 0.1 | 0.6 |
| **$P_8W_{48}$@N-MWCNT** | 78.6 | 15.3 | 4.0 | 0.3 | 1.8 |

[a] Determined by the areas of the respective bands in the high-resolution XPS spectra.

Figure 2.2 (a) shows the C1s high-resolution spectra of $P_8W_{48}$@N-MWCNT, fitted with seven peaks: a main peak at 284.6 eV assigned to the graphitic structure ($sp^2$, C=C), a peak at approximately 285.6 eV attributed to a $sp^3$ hybridized carbon and C-N bonding, a peak at 285.9 eV assigned to C-N and C-OH bonding, a peak at approximately 286.9 eV attributed to C-O-C groups, a peak at 288.2 eV assigned to C=O groups (ketones, quinones, aldehydes), a peak at ~289.3 eV ascribed to COOH (carboxylic acids, esters), and a peak at 291.0 eV attributed to π–π* transitions.[52] The C1s high-resolution spectra of the remaining composites and pristine carbon materials are similar to that for $P_8W_{48}$@N-MWCNT, as can be seen in the SI file.

The N1s XPS spectrum (Figure 2.2 (b)) was deconvoluted onto two main peaks at 398.5 eV and 401.6 eV, attributed to pyridinic and quaternary N, respectively. This is consistent with the results obtained for the pristine N-MWCNT, which also contains a peak corresponding to pyridinic N. Different sets of peaks are observed for the other N-containing compounds, which show additional peaks referring to pyrrolic and quaternary

N at 400.1 eV and 401.6 eV, respectively.[53-55] The rest of the starting carbon materials do not show any presence of nitrogen, as expected. Nevertheless, it is possible to see a small amount of nitrogen in the rest of the composites (Table 2.1). This is explained from the alkaline degradation in the presence of amine to obtain the polyoxometalate salt throughout the synthesis of the POM.[56]

In the high resolution O1s spectra (Figure 2.2(c)), the peak at 530.7 eV is ascribed to oxygen in C=O (ketones, quinones, aldehydes), and COOH groups (carboxylic acids, esters) and oxygen atoms belonging to the POM. The peak at 532.8 eV is attributed to O in HO-C groups (phenols).[57, 58] These two peaks are observed throughout all materials, with material MWCNT having an extra peak from O of water at 536.0 eV, due to fortuitous contamination.[55]

The P2p high-resolution spectra of $P_8W_{48}$@GF is shown in Figure 2.2 (d) and the observed peaks can be resolved as $2p_{3/2}$ and $2p_{1/2}$ doublets at 133.4 and 134 eV, respectively. Finally, in Figure 2.2 (e), the peaks found in the high-resolution spectra of W4f are attributed to $4f_{7/2}$ (35.4 eV) and $4f_{5/2}$ (37.6 eV), due to spin-orbital coupling.

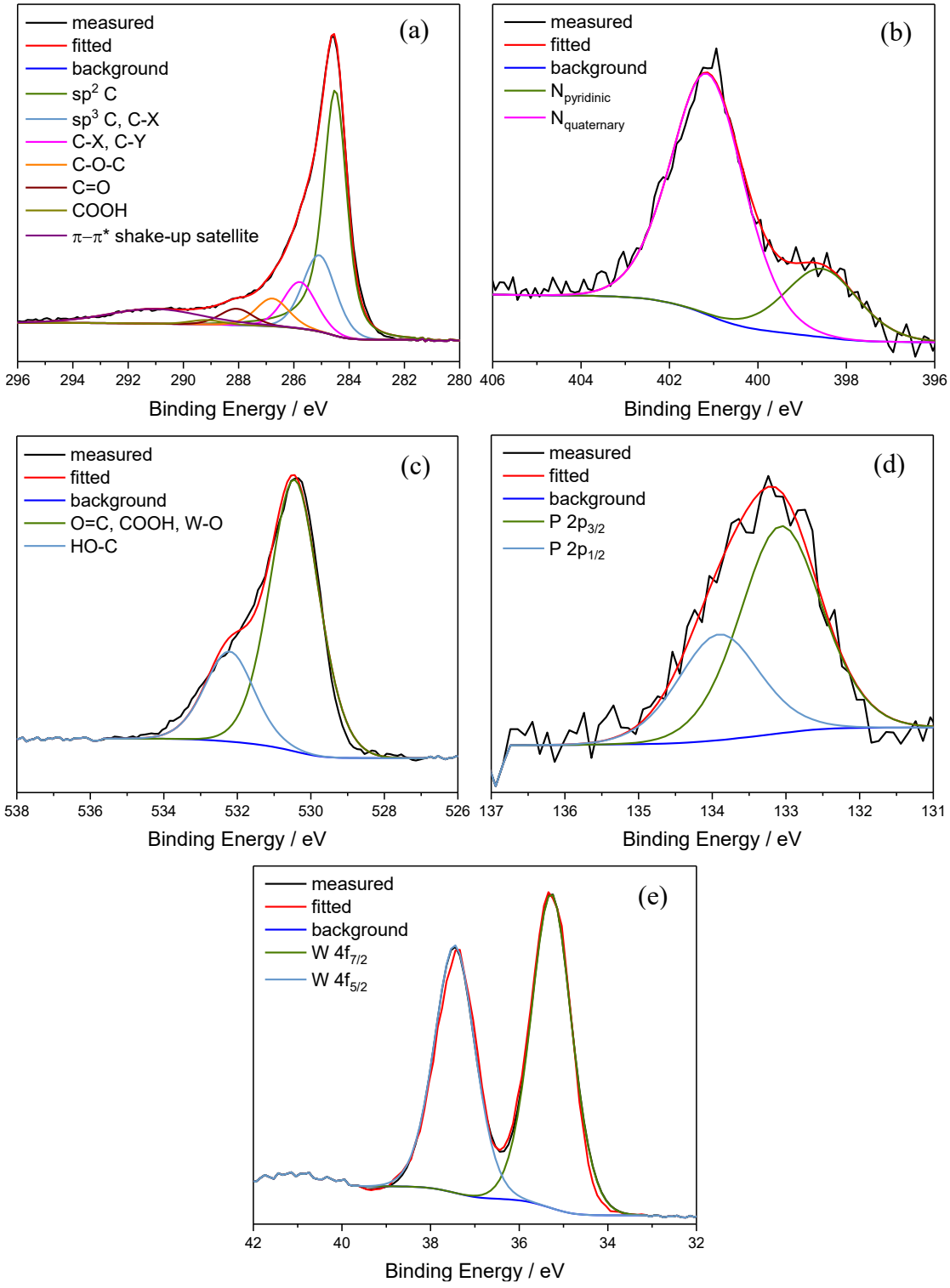



Figure 2.2 - XPS deconvoluted spectra of corresponding elements in $P_8W_{48}$@N-MWCNT composite.

The morphology of all composites was assessed by SEM and Figure 2.3 shows the SEM images for $P_8W_{48}$@GF(a), $P_8W_{48}$@SWCNT (b), $P_8W_{48}$@MWCNT (c), and

$P_8W_{48}$@N-MWCNT (d). In Figure 2.3 (a) it is possible to observe the folded graphene sheets completely covered with $P_8W_{48}$ clusters which leads to this roughened texture. For the other three images the morphology is quite different, being possible to observe the carbon nanotubes with diverse widths. The measured diameter of the nanotubes is approximately $d$ = 12 nm for the single-walled, and between $d$ = 12 – 22 nm for the multi-walled nanotubes. The N-MWCNTs are much larger in size, with diameters ranging from 90 - 190 nm. A possible reason for such a large difference in diameter is the fact that the MWCNT were commercially available while the N-MWCNT were prepared by chemical vapour decomposition (CVD). This can lead to different sizes and shapes.

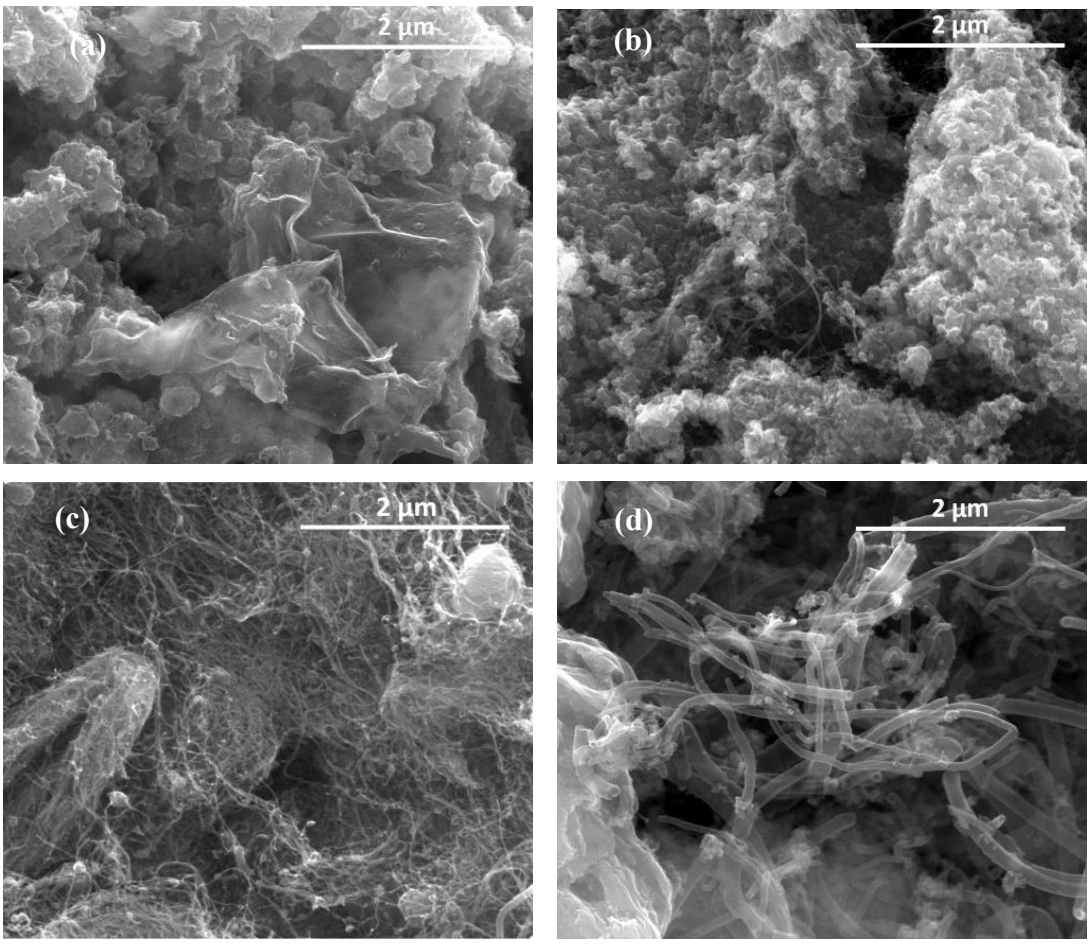



Figure 2.3 - SEM images of $P_8W_{48}$@GF (a), $P_8W_{48}$@SWCNT (b), $P_8W_{48}$@MWCNT (c) and $P_8W_{48}$@N-MWCNT (d) at 50000× magnification.

EDX analysis was conducted to assess the distribution of $P_8W_{48}$ throughout the carbon materials. Figure 2.4 shows the SEM and EDX elemental mapping images for $P_8W_{48}$@GF, while the images for the other composites can be found in Figures 2S5 to

2S7. The EDX spectra of the composites show the presence of C and O from the carbon materials, and P, W and O from the POMs. The elemental mapping analysis also revealed a homogeneous distribution of all the elements throughout the sample, which indicates that the $P_8W_{48}$ polyanions are well distributed throughout the carbon materials.

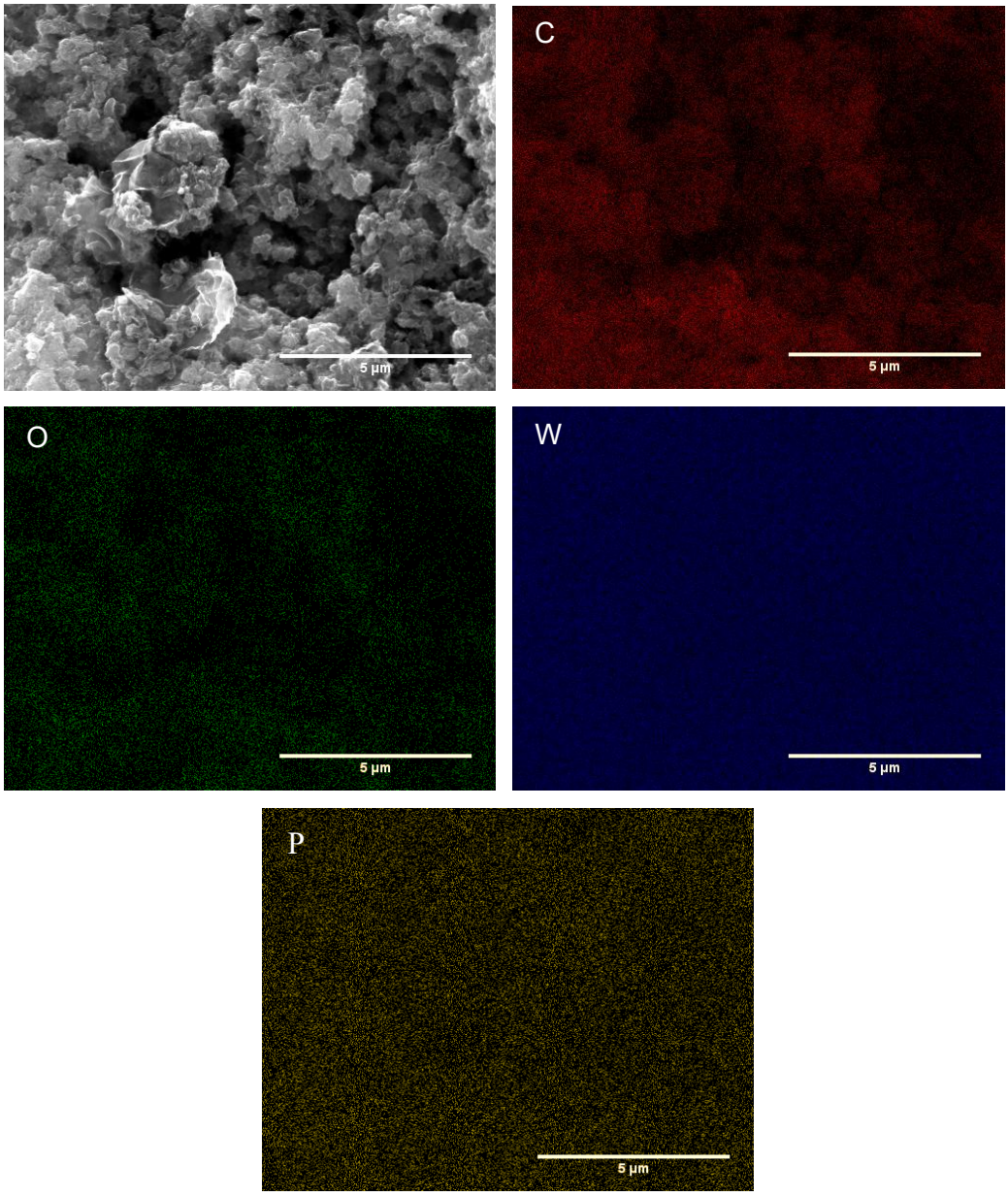



Figure 2.4 - SEM and EDX elemental mapping images of $P_8W_{48}$@GF, at 10000× magnification for the elements C (red), O (green), W (blue) and P (yellow).

## 2.4. Electrochemical performance towards ORR

The electrocatalytic activity of all composites prepared was evaluated by cyclic voltammetry (CV) in $N_2$- and $O_2$-satured KOH solution (0.1 mol $dm^{-3}$) and the CVs obtained are shown in Figure 2.5. In $N_2$-purged electrolyte no peaks are observed except for $P_8W_{48}$@MWCNT where two pairs of peaks can be identified at $E_{pc1}$ = 0.79 V, $E_{pa1}$ = 0.90 V, $E_{pc2}$ = 0.46 V, and $E_{pa2}$ = 0.51 V, corresponding to the two consecutive 4-electron redox processes of tungsten.[42] In $O_2$-purged electrolyte, all composites exhibit an irreversible reduction peak corresponding to oxygen reduction at $E_{pc}$ = 0.72, 0.70, 0.69 and 0.83 V vs. RHE for $P_8W_{48}$@GF, $P_8W_{48}$@SWCNT, $P_8W_{48}$@MWCNT and $P_8W_{48}$@N-MWCNT, respectively. The Pt/C (20 wt. %) was also evaluated in the same experimental conditions (Figure 2S8 (a) in the SI) and it presented an $E_{pc}$ = 0.86 V vs. RHE.

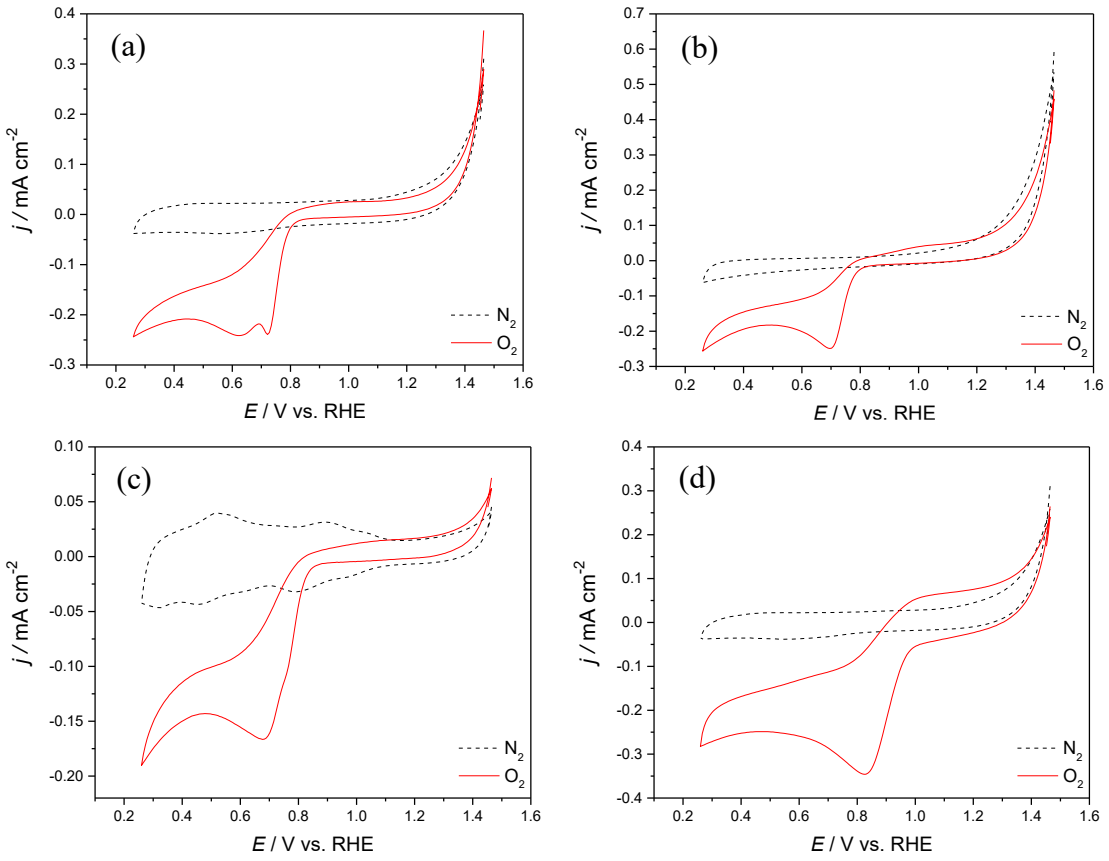



Figure 2.5 - CVs of $P_8W_{48}$@GF (a), $P_8W_{48}$@SWCNT (b), $P_8W_{48}$@MWCNT (c) and $P_8W_{48}$@N-MWCNT (d) modified electrodes in $N_2$-purged (dash line) and $O_2$-purged (full line) 0.1 mol $dm^{-3}$ KOH solution at 0.005 V $s^{-1}$.

Linear sweep voltammetry (LSV) at different rotation speeds was further used to evaluate the performance of the composites prepared (Figure 2S12). For comparison, the LSV studies were also performed for the carbon supports (GF, SWCNT, MWCNT

and N-MWCNT) in order to determine their contribution to the overall ORR electroactivity (Figure 2S13) and for Pt/C (Figure 2S14). The LSV curves of the composites, obtained at 1600 rpm in $O_2$-purged KOH solution (0.1 mol $dm^{-3}$), are shown in Figure 2.6 and Table 2.2 presents the main ORR parameters obtained - onset potential ($E_{onset}$), diffusion-limiting current density values ($j_{L,\ 0.26\ V,\ 1600\ rpm}$), Tafel slopes (TS) and the number of electrons transferred per oxygen molecule ($n_{O2}$).

The results obtained for the carbon supports show that all materials present similar $E_{onset}$ values (between 0.72 and 0.69 V vs RHE) except for N-MWCNT that presented an $E_{onset}$ value of 0.90 V vs RHE being just 0.04 V lower than that obtained for Pt/C. Moreover, N-MWCNT presented the highest $j_L$ value (-3.2 mA $cm^{-2}$) compared with the other carbon supports where $-2.6 \geq j_L \geq 2.0$ mA $cm^{-2}$. In the same condition, Pt/C presented a $j_L$ = -4.7 mA $cm^{-2}$. The doping process of MWCNT led to an improvement of ORR electrocatalytic activity owing to the presence of nitrogen atoms, which is in agreement with several already reported works[39, 59] where N-doping led to an enhancement of ORR electrocatalytic activity. After doping, the $E_{onset}$ value of MWCNT shifted 21 mV to more positive potentials, and the $j_L$ increases 60%.

Then the ORR performance of the POM-based composites was evaluated. It can be clearly seen that the immobilization of $P_8W_{48}$ onto the different carbon nanomaterials leads to an improvement of the ORR electrocatalytic performance (more positive $E_{onset}$ values and higher $j_L$). It is also possible to observe that $P_8W_{48}$@GF, $P_8W_{48}$@SWCNT and $P_8W_{48}$@MWCNT composites present a similar behaviour with comparable $E_{onset}$ values (0.75, 0.76, 0.77 respectively). However, $P_8W_{48}$@N-MWCNT presents an $E_{onset}$ value shifted to more positive potentials (0.94 V vs. RHE) which is equal to the value obtained for Pt/C. This suggests an enhancement of the ORR electrocatalytic performance for the $P_8W_{48}$@N-MWCNT composite. This is also confirmed by the higher value of $j_L$ obtained for the later composite (-3.7 mA $cm^{-2}$) compared to those obtained for the other composites (-3.0, -3.0 and -2.4 mA $cm^{-2}$ for $P_8W_{48}$ @GF, SWCNT and MWCNT, respectively).

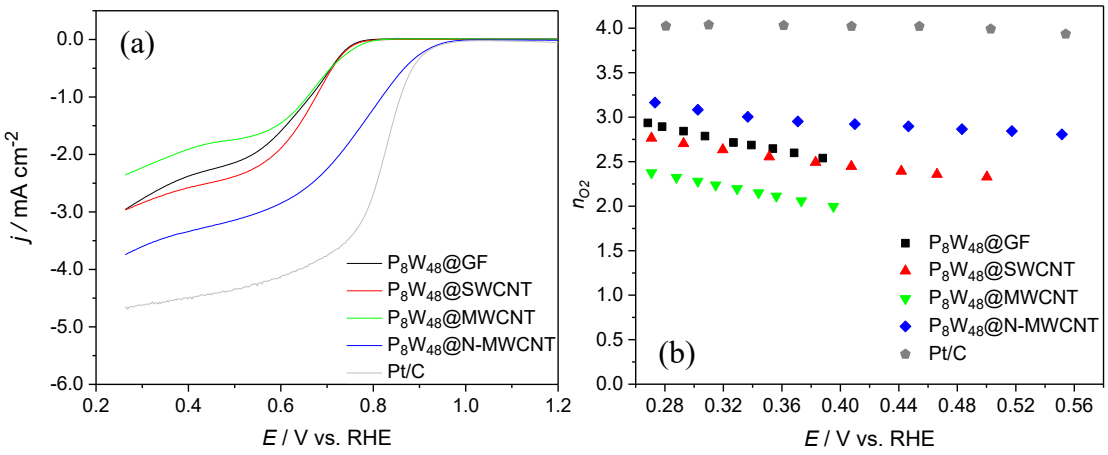



Figure 2.6 - ORR LSV curves acquired using an RDE in $O_2$-purged KOH solution (0.1 mol $dm^{-3}$) at1600 rpm and 0.005 V $s^{-1}$ of commercial Pt/C (20 wt %) and $P_8W_{48}$@CM composites (a); $n_{O2}$ at several potential values (b).

This behaviour might be explained because of the nitrogen atom presence leading to a better electrocatalytic performance.[60] Due to its high electronegativity, it may be allowing greater interaction between $O_2$ molecules and thus restructuring the electronic structure of neighbouring atoms, promoting the ORR mechanism.[61] Hereupon, all the composites are implicated in a mixed electron process of 2- and 4-electrons, confirmed by the $n_{O2}$ values occurred between 2.2 and 3.0 (Figure 2.6 (b)).

Using Eq. 2.4 (SI) the percentage of $H_2O_2$ produced was calculated and is shown in Figure 2.7 at various potential values. Thus, as expected, $P_8W_{48}$@N-MWCNT got the lowest percentage of $H_2O_2$ among the analysed composites. This behaviour was anticipated[62] towards ORR applications once this composite got the highest number of transferred electrons ($n_{O2}$ = 3.0). The composites $P_8W_{48}$@GF, $P_8W_{48}$@SWCNT and $P_8W_{48}$@MWCNT with the lowest number of transferred electrons feature a higher production of $H_2O_2$ obtaining respectively, 52, 86 and 58% in about the same potential range.

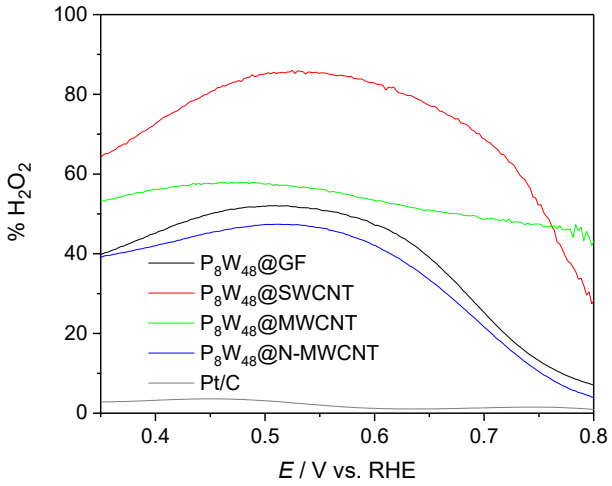



Figure 2.7 - Estimated percentage of $H_2O_2$ produced with RRDE in $O_2$-purged 0.1 mol $dm^{-3}$ KOH solution, at 1600 rpm; the disk potential was swept at v = 0.005 V $s^{-1}$ and the ring potential was kept at E = 0.2 V versus Ag/AgCl for $P_8W_{48}$@GF, $P_8W_{48}$@MWCNT, $P_8W_{48}$@SWCNT, $P_8W_{48}$@N-MWCNT and Pt/C (20 wt %).

Table 2.2 Onset Potentials ($E_{onset}$), diffusion-limiting current density values ($j_{L,0.26\ V,1600\ rpm}$) derived from the ORR polarization curves in $O_2$-purged 0.1 mol $dm^{-3}$ KOH solution for commercial Pt/C, carbon materials and composites prepared and Tafel and $n_{O2}$values.

| Samples | $E_{onset}$vs RHE | $j_L$ (mA $cm^{-2}$) | Tafel (mV $dec^{-1}$) | $n_{O2}$ |
|---|---|---|---|---|
| Pt/C | 0.94 | -4.7 | 89 | 4.0 |
| GF | 0.72 | -2.0 | 63 | 2.4 |
| SWCNT | 0.72 | -2.6 | 60 | 3.0 |
| MWCNT | 0.69 | -2.0 | 54 | 2.1 |
| N-MWCNT | 0.90 | -3.2 | 125 | 2.5 |
| $P_8W_{48}$@GF | 0.75 | -3.0 | 44 | 2.7 |
| $P_8W_{48}$@SWCNT | 0.76 | -3.0 | 48 | 2.7 |
| $P_8W_{48}$@MWCNT | 0.77 | -2.4 | 47 | 2.2 |
| $P_8W_{48}$@N-MWCNT | 0.94 | -3.7 | 72 | 3.0 |

The Tafel plots of the prepared electrocatalysts and of the Pt/C reference were obtained from the LSV curves in $O_2$-purged KOH at 1600 rpm and are shown in Figure 2.8. $P_8W_{48}$@GF, $P_8W_{48}$@MWCNT and $P_8W_{48}$@SWCNT showed very similar Tafel slopes between 44 and 48 mV $dec^{-1}$ while $P_8W_{48}$@N-MWCNT slightly higher value (72 mV $dec^{-1}$). The proposed mechanism for all compounds suggests the overall reaction rate is probably determined by the elementary step that involves the conversion the intermediate surface adsorbed specie $MOO^-$ to MOOH (M is an empty site on the electrocatalyst surface).[63]

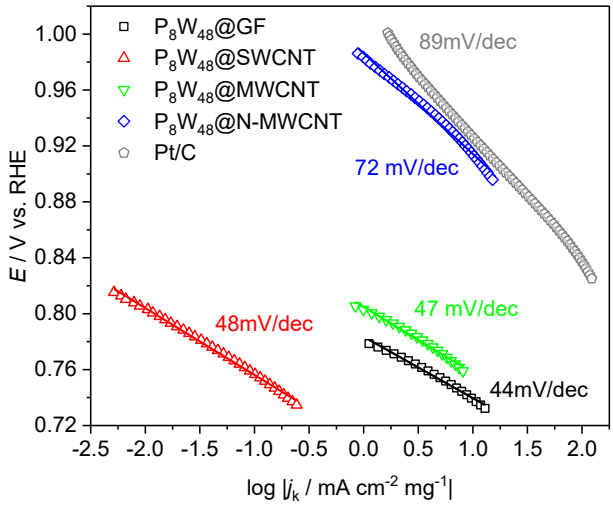



Figure 2.8 - ORR Tafel plots obtained from LSV data in Figure 2.7 where current densities are normalized to the mass of each ECs.

To get more information about the effect of POM immobilization onto the carbon supports used on the intrinsic ORR performance, the current values were normalized to the double-layer capacitances ($C_{dl}$) used as an approximated estimation of the electrochemically active surface areas (ECSAs) (Figure 2S15). This is only possible due to the similar nature of the materials tested and the proportional relationship between $C_{dl}$ and ECSAs[59, 64].

The $C_{dl}$ values were determined by performing CV measurements at increasing scan rates (see full details in SI file and Figures 2S16). So, $C_{dl}$ values were calculated from the slopes of the linear fittings of CV current densities (measured at the same potential of 1.13V vs. RHE) reached at different scan rates (Figure 2S17. However, as some faradaic contributions can be seen in the CV plots of the charge-discharge tests, these calculated capacitance values must be seen as estimated values. Therefore, the $C_{dl}$ can be considered as an estimate of the number of electrocatalytically accessible sites for a given electrocatalyst.[65] Results show that there is a significant increase in the number of active sites after the immobilization of POM for GF and a less significant one for MWCNT. For SWCNT and N-MWCNT the number of active sites decreases after POM immobilization. As can be observed in Figure 2S15, the electroactive surface area has a significant impact on the ORR performance with $P_8W_{48}$@SWCNT and $P_8W_{48}$@MWCNT showing the best ORR intrinsic activity. Results also show that apparent better performance of N-MWCNT (nominal activity) is due to the higher number of active sites when compared with the other composites.

Table 2.3 Electrocatalytically active surface area (ECSA) values of the carbon supports and the corresponding POM-based composites.

| CM support | $C_{dl}$ mF cm$^{-2}$ | Composite | $C_{dl}$ mF cm$^{-2}$ | Composite/Carbon Support $C_{dl}$ Ratio |
|---|---|---|---|---|
| GF | 0.0048 | $P_8W_{48}$@GF | 0.0762 | 15.8 |
| SWCNT | 0.0039 | $P_8W_{48}$@SWCNT | 0.0032 | 0.813 |
| MWCNT | 0.0023 | $P_8W_{48}$@MWCNT | 0.0035 | 1.53 |
| N-MWCNT | 0.0685 | $P_8W_{48}$@N-MWCNT | 0.0609 | 0.889 |

Another crucial parameter when assessing potential electrocatalysts for ORR is their stability. Therefore, chronoamperometric studies were performed at $E$ = 0.46 V vs. RHE for 36000s at 1600 rpm, in oxygen-purged alkaline electrolyte (Figure 2.9 (a)). The composite that shows better stability is $P_8W_{48}$@N-MWCNT with a current retention of 82%, while the other electrocatalysts showed slightly lower values, of 75%, 67% and 69% for $P_8W_{48}$@GF, $P_8W_{48}$@SWCNT and $P_8W_{48}$@MWCNT, respectively. The higher current retention obtained for $P_8W_{48}$@N-MWCNT may be due to the stronger interaction between the POM and this particular carbon material as a result of N-doping process. Still, the decrease in stability for all composites may be a consequence of depletion of catalyst from the electrode surface over time. Nevertheless, the value obtained for the $P_8W_{48}$@N-MWCNT is very close to that obtained by us for commercial Pt/C catalysts (87%) which is consistent with the literature.[39]

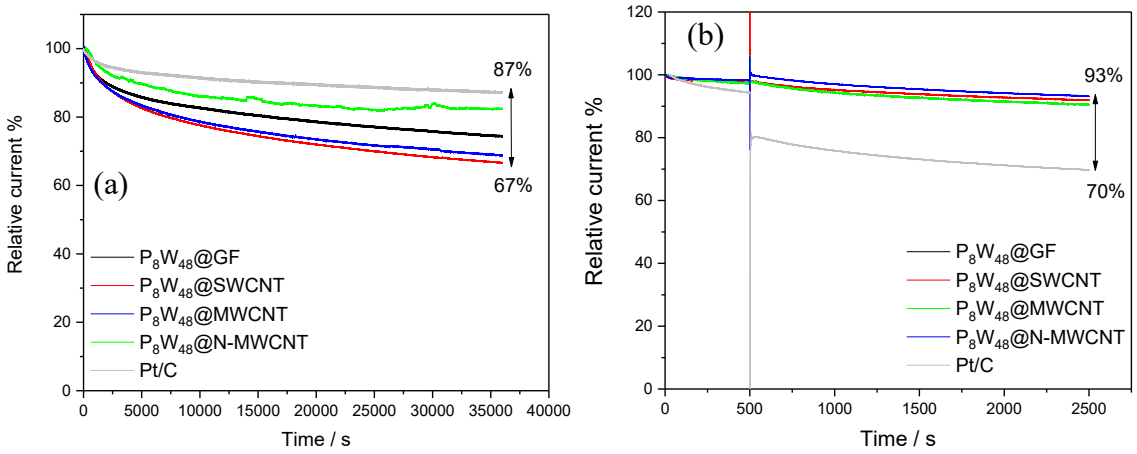



Figure 2.9 - Chronoamperometric response of the ECs at 1600 rpm, in 0.1 mol dm$^{-3}$ $O_2$-purged KOH at: (a) E = 0.46 V vs. RHE for 36000s and (b) E = 0.46 V vs. RHE with the addition of 0.5 mol dm$^{-3}$ methanol after ≈ 500 s.

In methanol fuel cells, the study of the methanol tolerance is very important because it can lead to a drastic drop in cathodic performance if the electrocatalysts are sensitive to it.[66] For this reason, chronoamperometry (CA) was evaluated for the methanol tolerance of $P_8W_{48}$@CM composites. CA were obtained in $O_2$-purged 0.1mol $dm^{-3}$ KOH (0.1 mol $dm^{-3}$), in presence of methanol (0.5 mol $dm^{-3}$) for Pt/C and $P_8W_{48}$@CM composites (Figure 2.9 (b)) during 2500s. The methanol was added after 500s since the beginning of the CA. The Pt/C electrocatalyst retains ~70% of its current density. On the other hand, the composites retain between ~91-93% of their initial current density.

## 2.5. Conclusion

This work introduces $P_8W_{48}$/carbon-based nanomaterials as alternative electrocatalysts for ORR with good activity and stability, including high selectivity towards the ORR in the presence of methanol. Throughout various characterisation techniques such as FTIR, XPS and SEM analysis, it was proven that all composites ($P_8W_{48}$@GF, $P_8W_{48}$@SWCNT, $P_8W_{48}$@MWCNT, $P_8W_{48}$@N-MWCNT) were successfully synthesized. All nanocomposites showed ORR electroactivity in alkaline medium with onset potential values ranging from 0.71 and 0.94 V *vs.* RHE, low Tafel slopes (44 – 72 mV $dec^{-1}$), good $j_L$ values (-2.4 – -3.7 mA $cm^{-2}$), and a mixed electron process of 2- and 4-electrons confirmed by the results of $\%H_2O_2$ production. Still, the $P_8W_{48}$@N-MWCNT showed the best ORR out of all materials prepared. Additionally, all nanocomposites showed robust electrocatalytic performance over 36000 s, exhibiting high current retention values (~91-93%) and excellent methanol tolerance, suggesting high selectivity to ORR, overcoming one of the major limitations of the Pt/C electrocatalyst. Globally, this study is a step forward towards novel cheap and durable electrocatalysts, which are noble metal-free and offer great potential for energy-related reactions.

## 2.6. Supporting information

### 2.6.1. Materials and solvents

The POM salt $K_{28}Li_5[H_7P_8W_{48}O_{184}]\cdot 92H_2O$ was prepared according to the reported procedure.[56]

Potassium hydroxide (> 99%, Sigma-Aldrich), Nafion® at 5 wt. % (lower aliphatic alcohols and water, Sigma-Aldrich), isopropanol (99.5 %, Sigma-Aldrich), sulfuric acid (95–97 %, Merck), platinum 20 % on carbon black (Pt/C, HiSPEC® 3000, Alfa Aesar). The N-MWCNT were produced by catalytic chemical vapour decomposition using a previously described method and its full characterisation can be found elsewhere.[41] Multi-walled carbon nanotubes (MWCNT, Nanocyl S.A., Ref. 3100,>95% carbon purity, 9.5 nm average diameter), single-walled carbon nanotubes, SWCNT (Nanoledge, Batch P0329A), and graphene flakes, GF (Graphene Technologies, Lot GTX-7/6−10.4.13) were used as received. For electrolyte and composites preparation ultrapure water (18.2 MΩ cm at 25ºC, Interlab) was always used.

### 2.6.2. Physicochemical characterisation

A Jasco FT/IR-460 Plus spectrophotometer was used to acquire the Fourier-transformed infrared (FTIR) spectra (64 scans, resolution of 4 $cm^{-1}$, between 400 and 4000 cm-1). The spectra were obtained for samples dispersed (0.2 wt. %) in KBr pellets (spectroscopic grade, Merck).

X-ray photoelectron spectroscopy (XPS) measurements were performed at “Centro de Materiais da Universidade do Porto” (CEMUP), Portugal, in a VG Scientific ESCALAB 200A spectrometer with non-monochromatized Al Kα radiation (1486.6 eV). Potential deviations induced by electric charge of the samples were corrected using the C 1s band at 284.6 eV as an internal standard. The high-resolution spectra analysis and deconvolution was performed with CasaXPS software.

The SEM/EDX (scanning electron microscopy/energy-dispersive X-ray spectroscopy) images were acquired using a high resolution (Schottky) environmental SEM with X-ray microanalysis and electron backscattered diffraction analysis (Quanta 400 FEG ESEM/EDAX Genesis X4M), in high-vacuum conditions, at CEMUP.

### 2.6.3. ORR electrochemical tests

An Autolab PGSTAT 302N (EcoChimie B.V.) potentiostat/galvanostat, controlled by the NOVA v2.0 software was employed for the cyclic voltammetry (CV) and linear sweep voltammetry (LSV) experimentations. The working electrode was a modified glassy carbon rotating disk electrode, RDE (Metrohm, 3 mm diameter) whilst as reference and counter electrodes were used Ag/AgCl (Metrohm, 3 M KCl) and a carbon

rod (Metrohm, 2 mm diameter), respectively. Prior to modification, the RDE was cleaned with diamond polishing pastes of 6, 3 and 1 μM (Buehler) on a MicroCloth polishing pad (BAS), followed by washing with ultra-pure water. Next, a 4 × 2.5 μL drop of selected electrocatalyst (EC) dispersion was deposited onto the RDE and left to dry under an air flux.

For the RDE modification, 1 mg of EC ($P_8W_{48}$@CM or Pt/C) and a mixture of 125 μL of isopropanol, 125 μL of ultrapure water and 20 μL of Nafion (5 wt%) were ultrasonically dispersed for 20 min.

The CV measurements were performed at 0.005 V $s^{-1}$ and the LSV ones at 0.005 V $s^{-1}$ with rotation speeds in the range 400 - 3000 rpm. The ORR current obtained in $N_2$-saturated KOH (0.1 mol $dm^{-3}$) was subtracted from that obtained in $O_2$-saturated KOH. The chronoamperometry (CA) tests were done at a potential (*E*) of 0.5 V vs. RHE and a rotation speed of 1600 rpm for 36000 s. Resistance to methanol was evaluated by CA at *E* = 0.5 V vs. RHE and 1600 rpm for 2500 s.

The onset potential ($E_{onset}$) is defined as the potential at which the reduction of $O_2$ begins and it was determined as described in literature. [49] The electrochemical potentials and the $E_{onset}$ values determined vs. Ag/AgCl were converted to the reversible hydrogen electrode (RHE) using the following equation:

$$E_{(RHE)} = E_{(Ag/AgCl)} + 0.059\,pH + E^{\circ}_{(Ag/AgCl)} \quad (2.1)$$

where $E_{(RHE)}$ is the potential vs. RHE, $E^{o}_{(Ag/AgCl)}$ = 0.1976 V (25 °C) and $E_{(Ag/AgCl)}$ is the potential measure vs. Ag/AgCl.[67]

To analyse the LSV data and the number of electrons transferred per $O_2$ molecule ($n_{O2}$) in the oxygen reduction reaction the Koutecky-Levich (K-L) equation was used (2.2):

$$\frac{1}{j} = \frac{1}{j_L} + \frac{1}{j_k} = \frac{1}{B\omega^{1/2}} + \frac{1}{j_k} \quad (2.2)$$

Here, *j* = current density measured, $j_L$ = diffusion-limiting current density, $j_k$ = kinetic current density and ω= angular velocity. The parameter *B* is associated to the diffusion limiting current density expressed by the Equation (2.3):

$$B = 0.2 n_{O2} F (D_{O2})^{\frac{2}{3}} v^{-\frac{1}{6}} C_{O2} \quad (2.3)$$

with *F* = 96 485 C $mol^{-1}$, $D_{O2}$ = $_{O2}$ diffusion coefficient, *v* = electrolyte kinematic viscosity and $C_{O2}$ = $O_2$ bulk concentration. For rotation speeds in rpm is adopted a constant 0.2. Additionally, in the electrolyte used KOH (0.1 mol $dm^{-3}$): $D_{O2}$ = 1.95×$10^{-5}$ $cm^2$ $s^{-1}$, *v* =0.008977 $cm^2$ $s^{-1}$ and $C_{O2}$ = 1.15×$10^{-3}$ mol $dm^{-3}$. [68]

Tafel plots ($E_{(RHE)}$ vs. log $j_k$) were obtained after the measured LSV currents were rectified for diffusion to yield the corresponding kinetic current values. The $j_L$ parameter, determined combining equations (2.2) and (2.3), was used to make the mass transport correction. The values of *j*k obtained were normalized for the total deposited mass of EC.

Tests with rotating ring disk electrode (RRDE) were performed as well for a more complete examination of the ECs. The electrode was polished for 15 min with aluminium oxide 0.3 μm and washed with ultrapure water. The LSV experiments were conducted at 0.005 V $s^{-1}$ and1600 rpm in $O_2$-saturated KOH. A constant potential of 1.2 V vs RHE was applied at the Pt ring electrode. The percentage of $H_2O_2$ produced was calculated from Eq. 2.4, using the current produced in the ring ($i_R$), in the disk ($i_D$) and the current collection efficiency of the ring.[69]

$$\%H_2O_2 = 200 \times \frac{\frac{i_R}{N}}{i_D + \frac{i_R}{N}} \tag{2.4}$$

### 2.6.4. Assessment of electrochemically active surface areas (ECSA)

ECSA values exhibited by electrocatalysts are usually calculated by using the equation 2.1:

$$ECSA = \frac{C_{dl}}{C_{ref}} \tag{2.5}$$

where $C_{dl}$ stands for the double-layer capacitance and $C_{ref}$ for the reference capacitance value per unit area. Due to the impossibility of knowing the exact $C_{ref}$ value for specific and structurally complex materials, reliable ECSA values cannot be obtained frequently. However, the linear proportional relation between ECSA and the double-layer capacitance allows performing a relative comparison for similar electrocatalysts. Taking advantage of this fact, in the present work, $C_{dl}$ values have been directly employed as approximated ECSA estimations to assess the surface effects on the OER performances. Thus, $C_{dl}$ values were calculated for all materials via a standard double-layer charging test, namely, the acquisition of consecutive CV plots at different scan rates (from 20 to 160 mV $s^{-1}$), being the double-layer capacitance estimated from the slope of a linear-fitted plot of current density at 1.15 V vs. RHE (non-faradaic region) versus the scan rate.

## 2.6.5. Figures

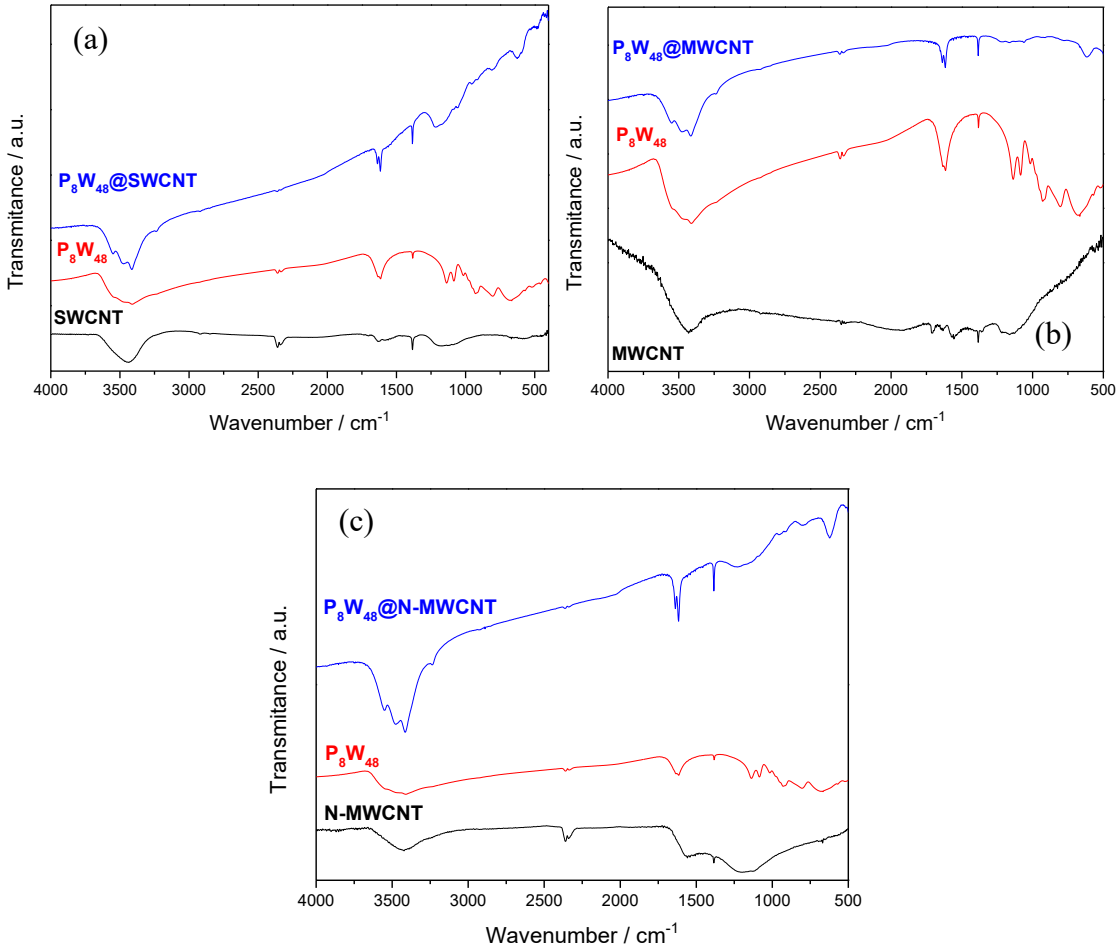



Figure 2S1 - Infrared spectra in the range of 4000-400 $cm^{-1}$ for $P_8W_{48}$ (red), carbon material (black) and composite (blue) for: SWCNT (a), MWCNT (b) and N-MWCNT (c).

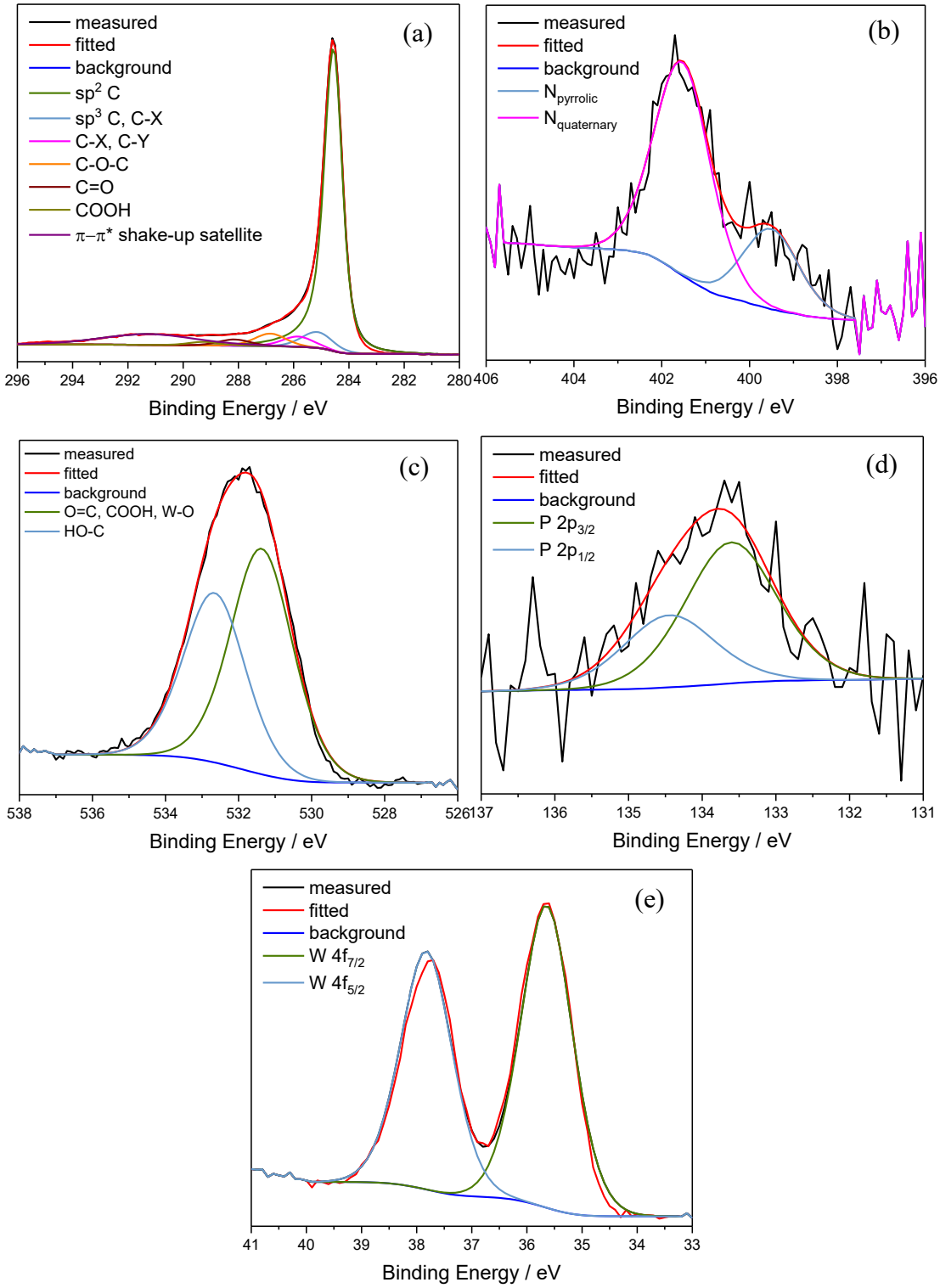



Figure 2S2 - XPS deconvoluted spectra of corresponding elements in $P_8W_{48}$@GF composite.

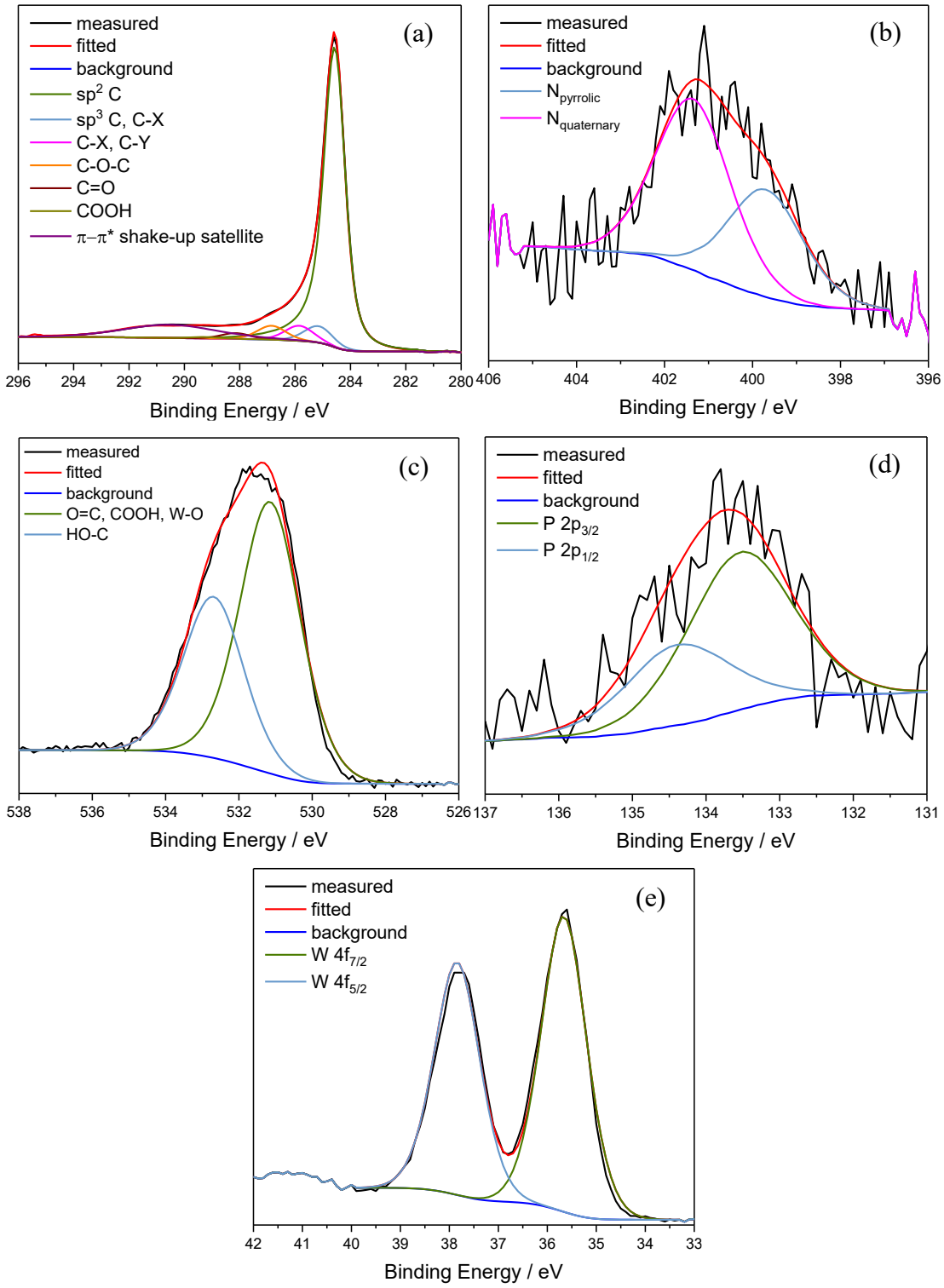



Figure 2S3 - XPS deconvoluted spectra of corresponding elements in $P_8W_{48}$@SWCNT composite.

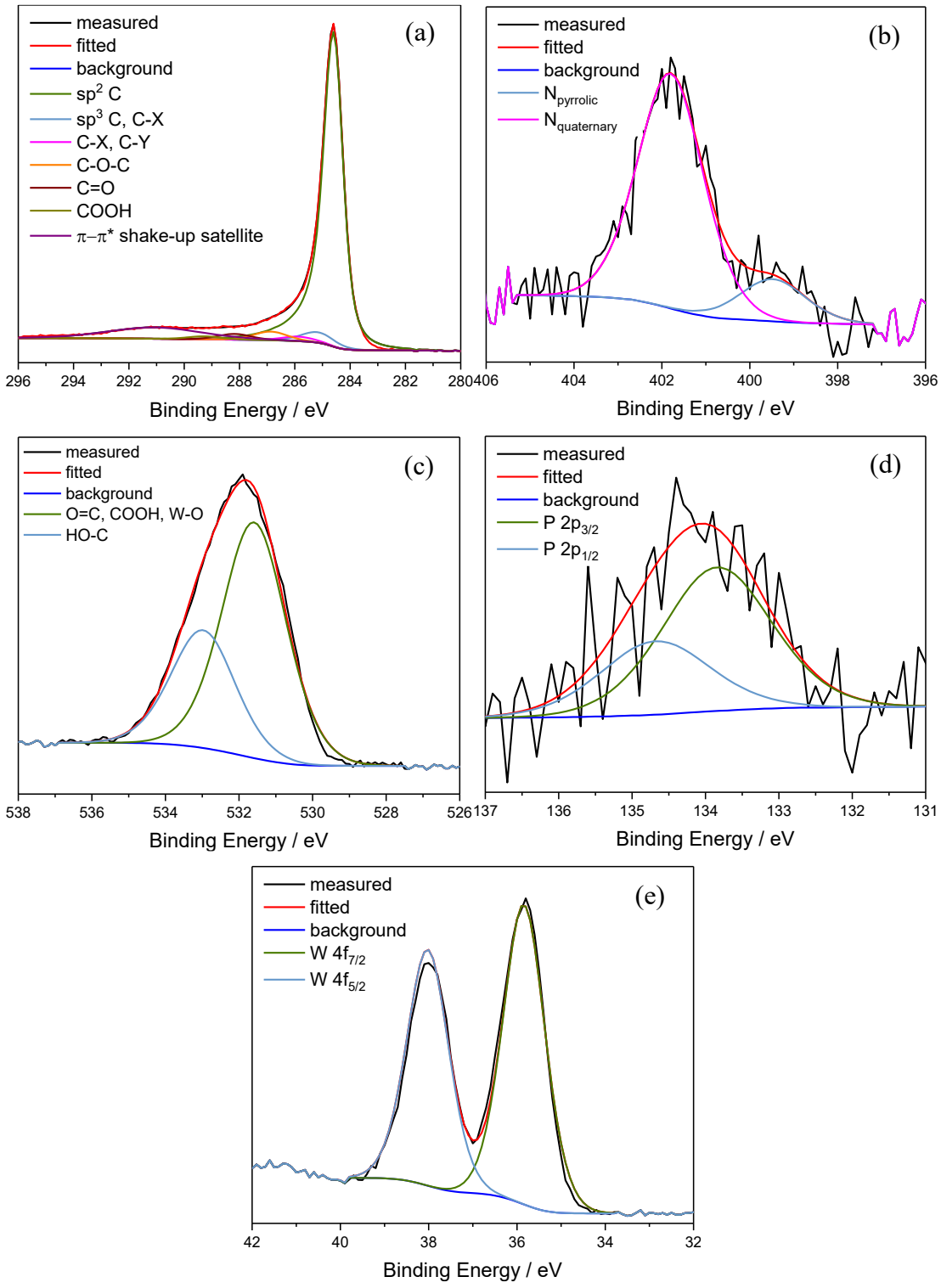



Figure 2S4 - XPS deconvoluted spectra of corresponding elements in $P_8W_{48}$@MWCNT composite.

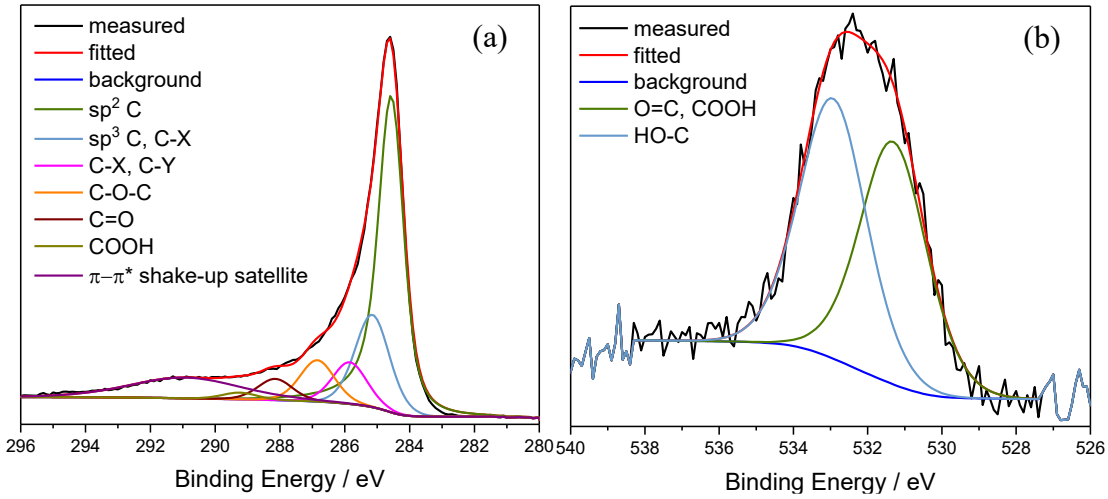



Figure 2S5 - XPS deconvoluted spectra of corresponding elements in GF composite.

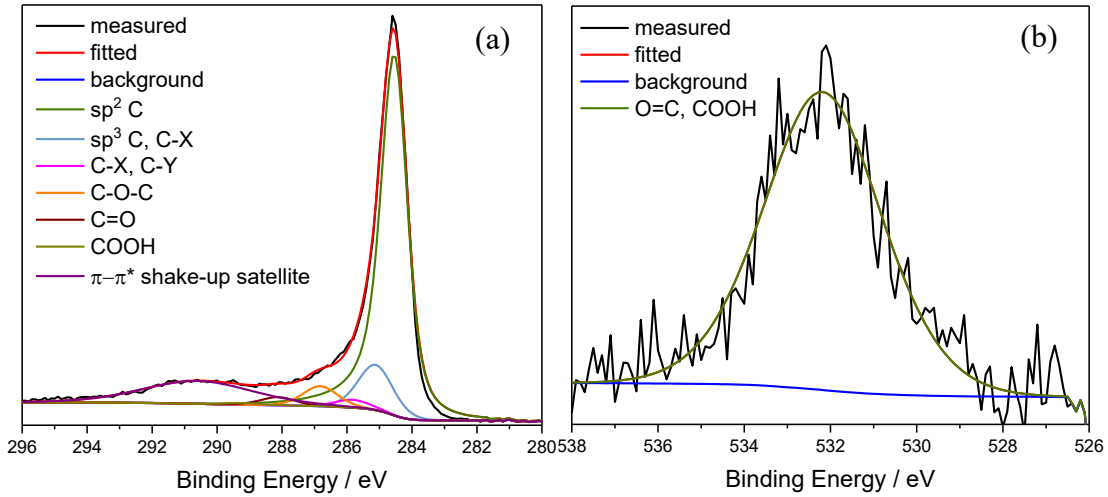



Figure 2S6 - XPS deconvoluted spectra of corresponding elements in SWCNT composite.

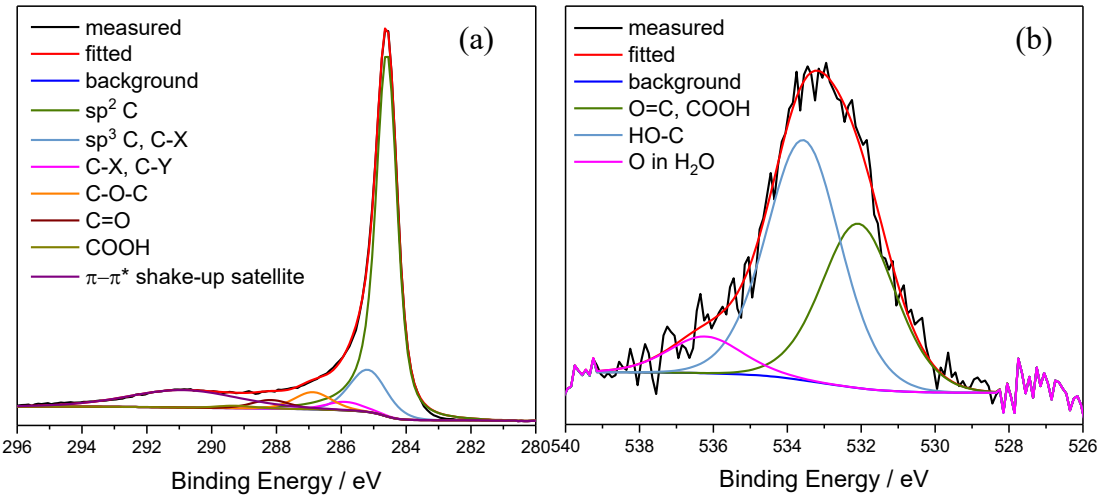



Figure 2S7 - XPS deconvoluted spectra of corresponding elements in MWCNT composite.

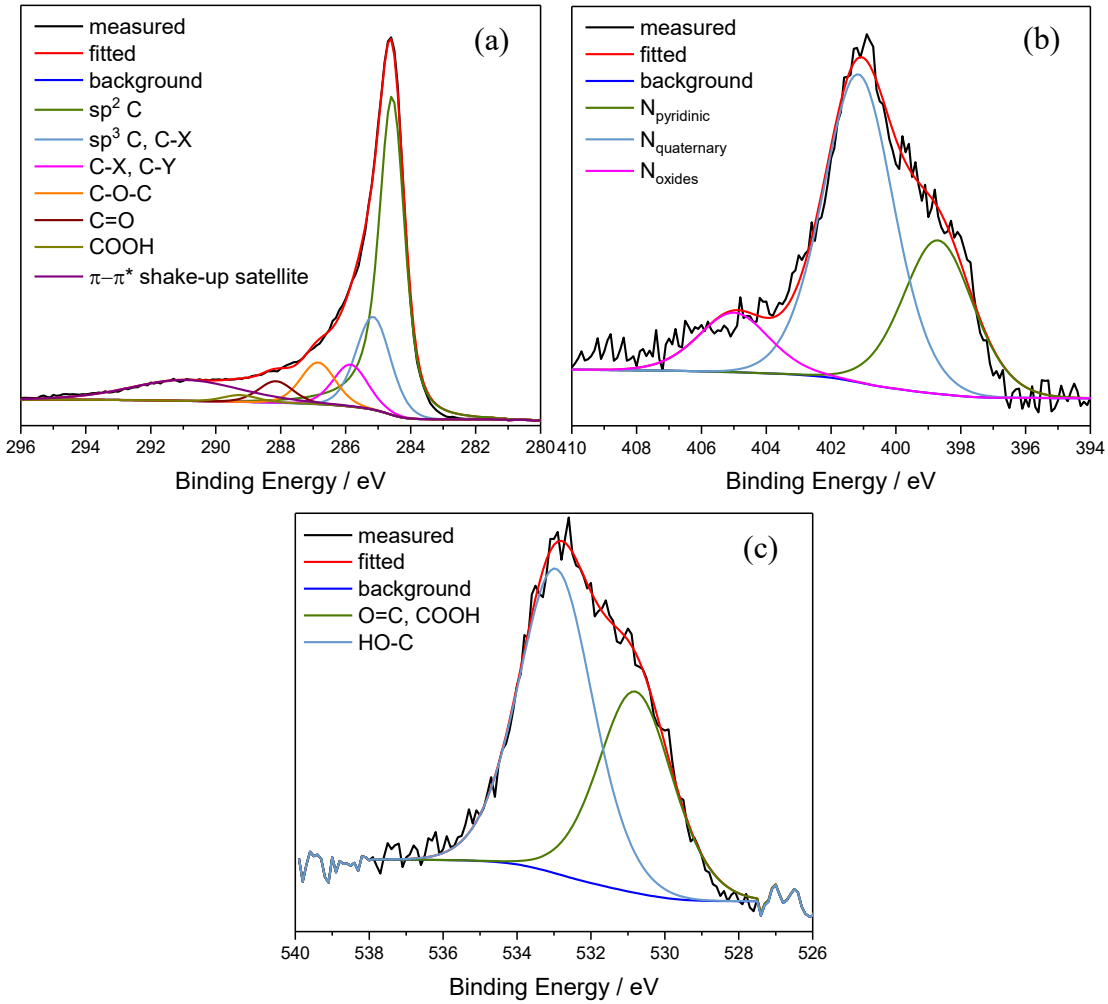



Figure 2S8 - XPS deconvoluted spectra of corresponding elements in N-MWCNT composite.

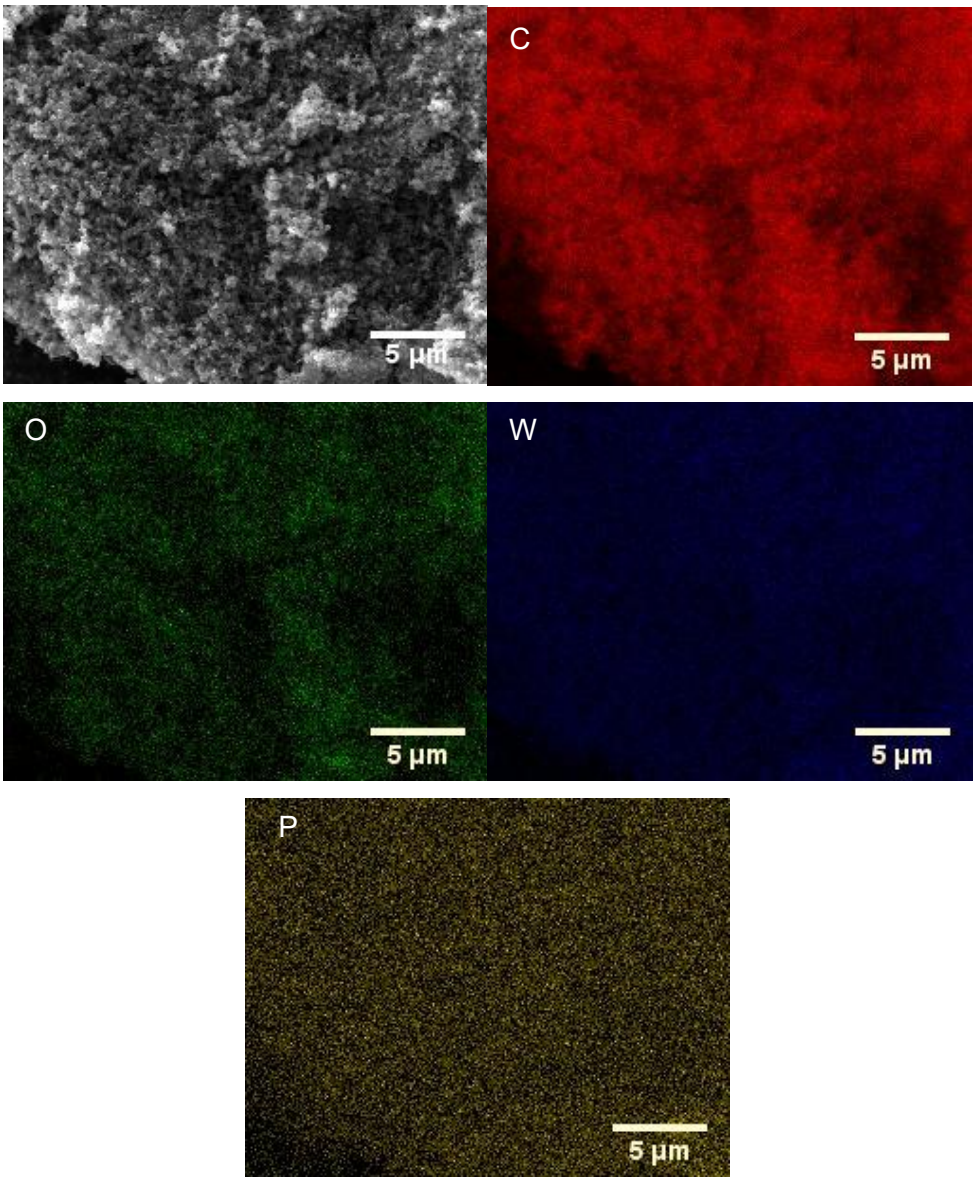



Figure 2S9 - SEM and EDS elemental mapping images of $P_8W_{48}$@SWCNT at magnification 5000× for the elements C, O, W and P.

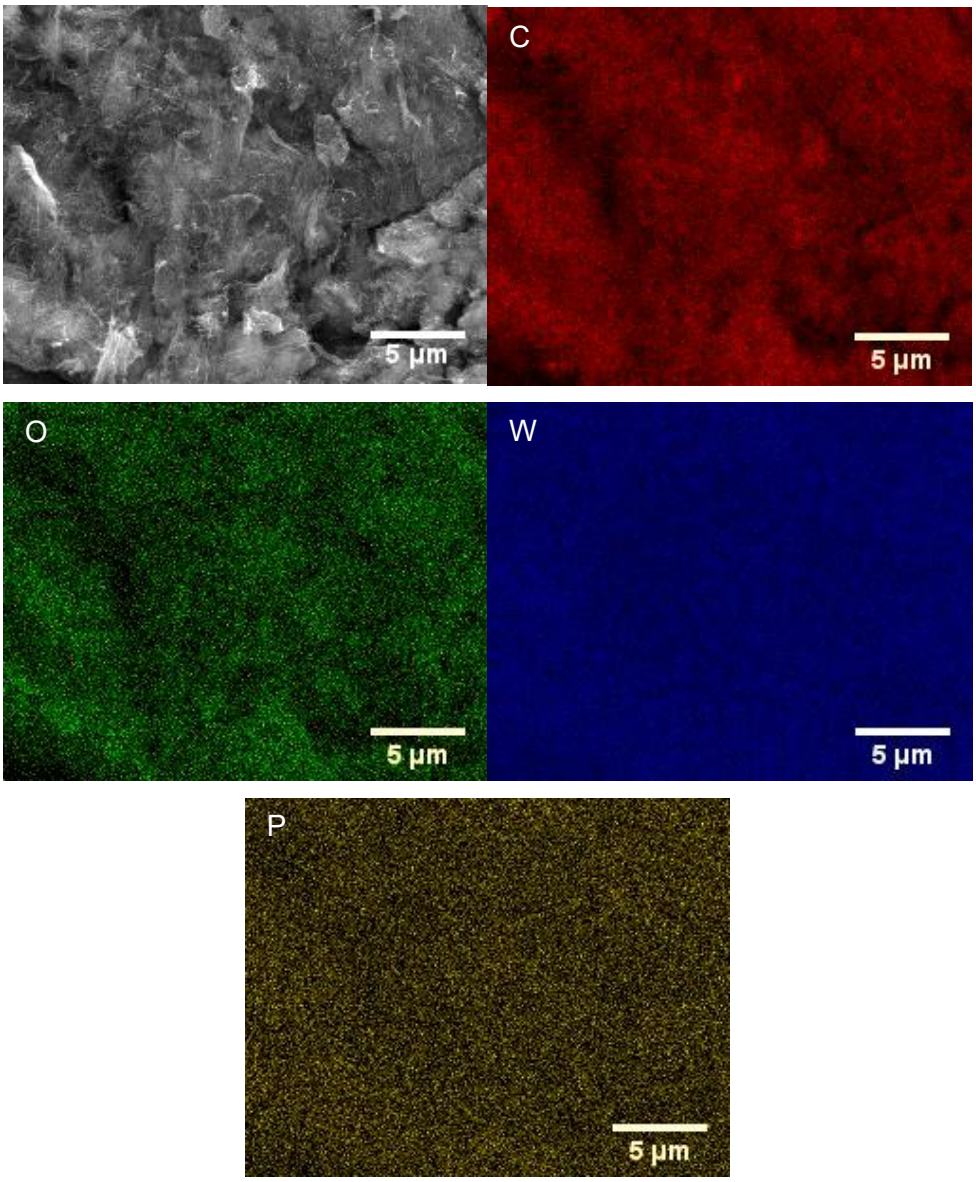



Figure 2S10 - SEM and EDS elemental mapping images of $P_8W_{48}$@MWCNT at magnification 5000× for the elements C, O, W and P.

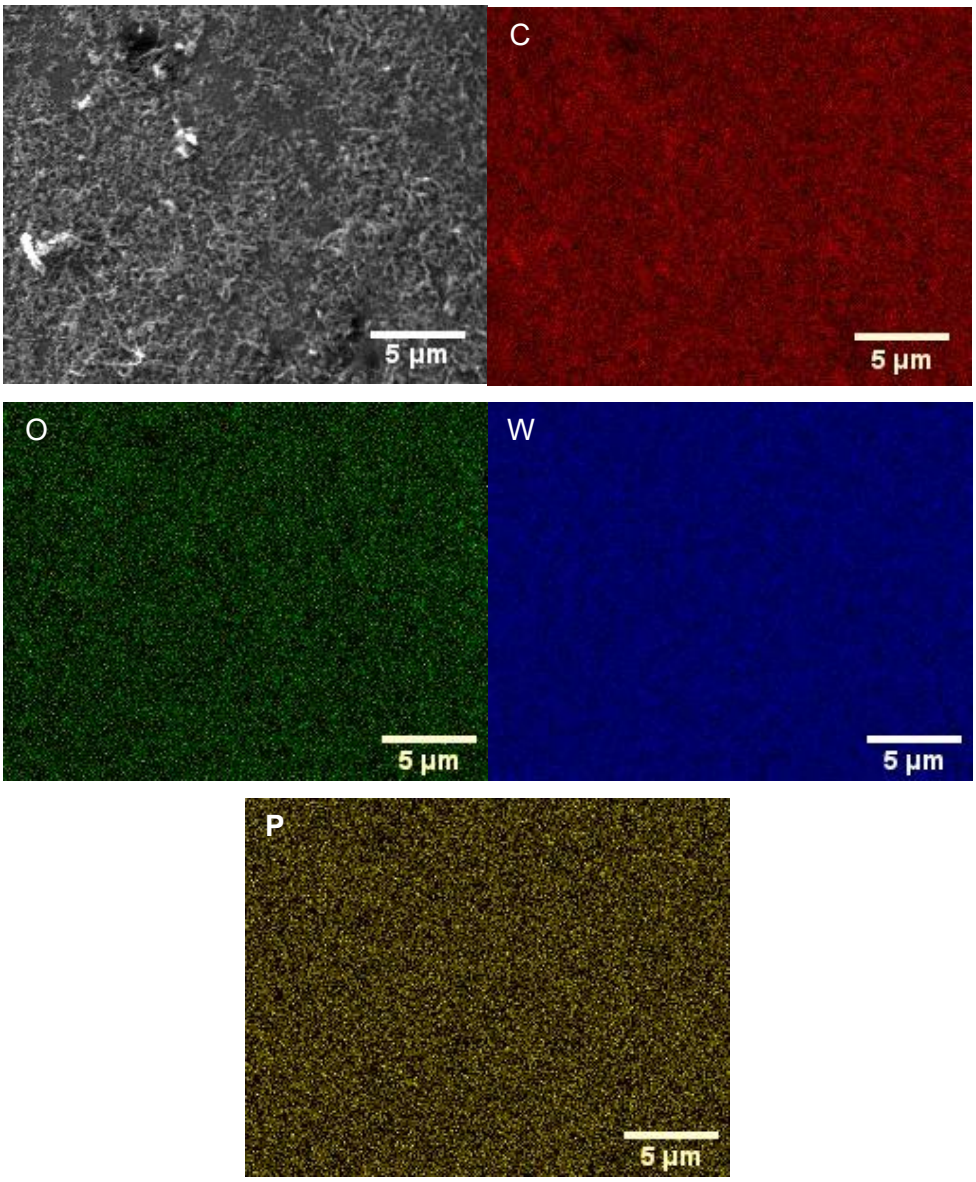
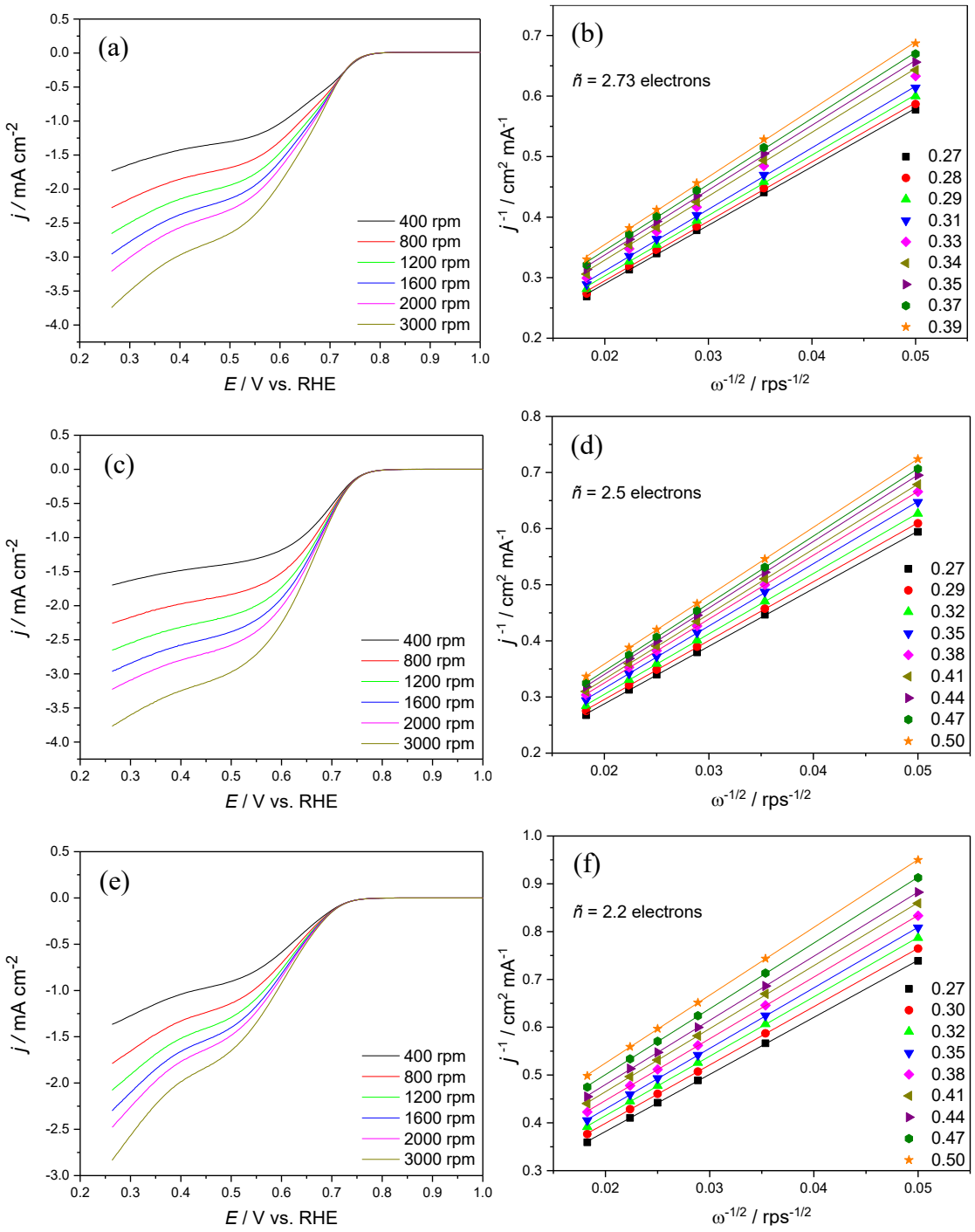



Figure 2S11 - SEM and EDS elemental mapping images of $P_8W_{48}$@N-MWCNT at magnification 5000× for the elements C, O, W and P.


(a)
j / mA cm-2
E / V vs. RHE
400 rpm
800 rpm
1200 rpm
1600 rpm
2000 rpm
3000 rpm
(b)
ñ = 2.73 electrons
j-1 / cm2 mA-1
ω-1/2 / rps-1/2
0.27
0.28
0.29
0.31
0.33
0.34
0.35
0.37
0.39
(c)
(d)
ñ = 2.5 electrons
0.27
0.29
0.32
0.35
0.38
0.41
0.44
0.47
0.50
(e)
(f)
ñ = 2.2 electrons
0.27
0.30
0.32
0.35
0.38
0.41
0.44
0.47
0.50

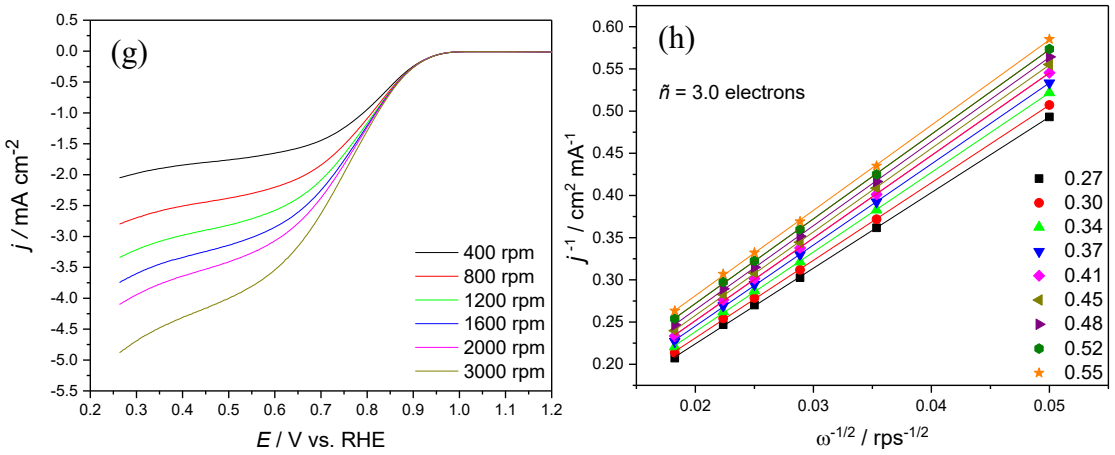
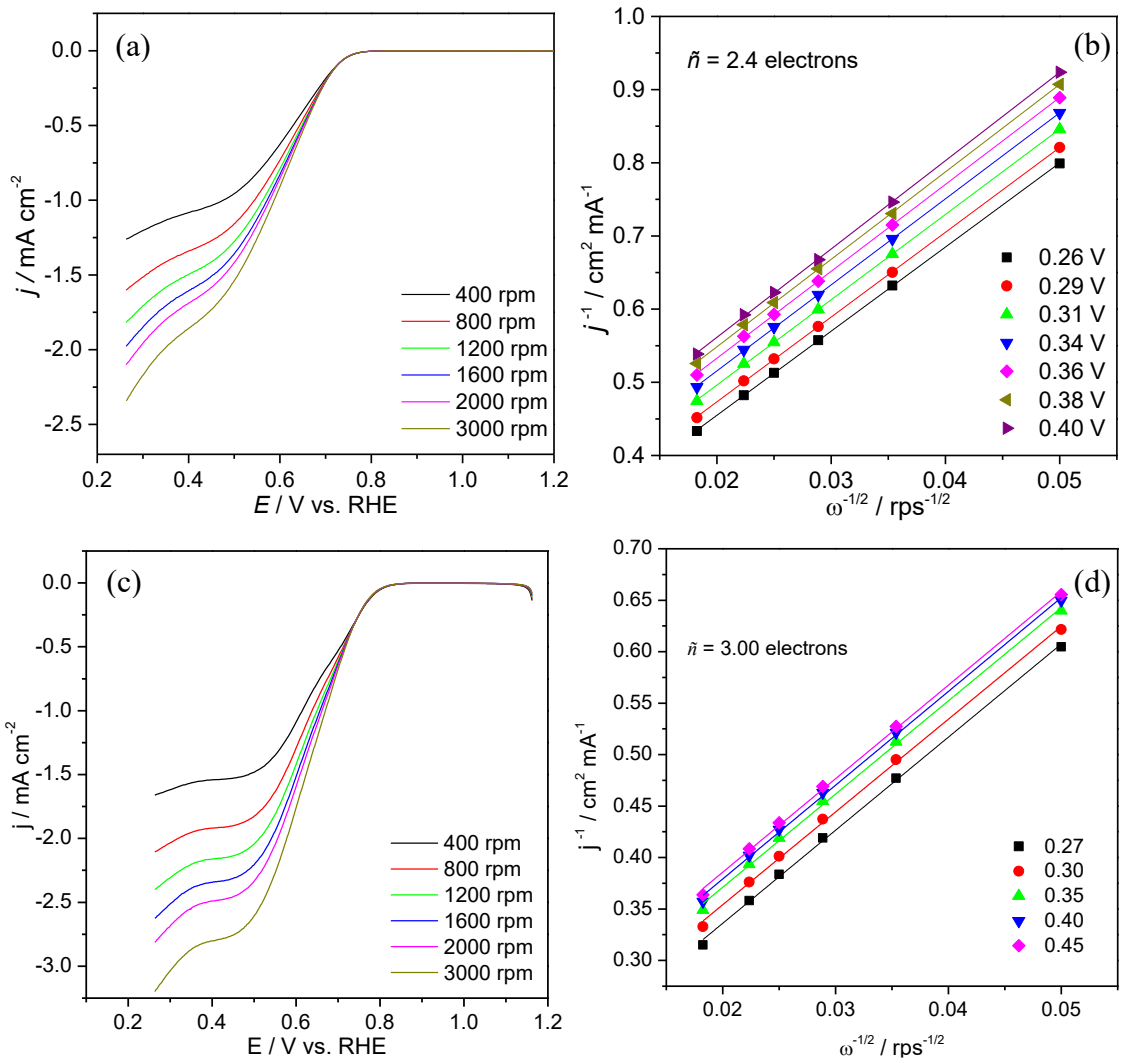



Figure 2S12 - ORR polarization curves of $P_8W_{48}$@GF (a), $P_8W_{48}$@SWCNT (c), $P_8W_{48}$@MWCNT (e) and $P_8W_{48}$@N-MWCNT (g) at different rotation rates in $O_2$-saturated 0.1 mol $dm^{-3}$ KOH solution at 0.005 V $s^{-1}$ and the corresponding Koutecky-Levich (K-L) plots (b, d, f and h).



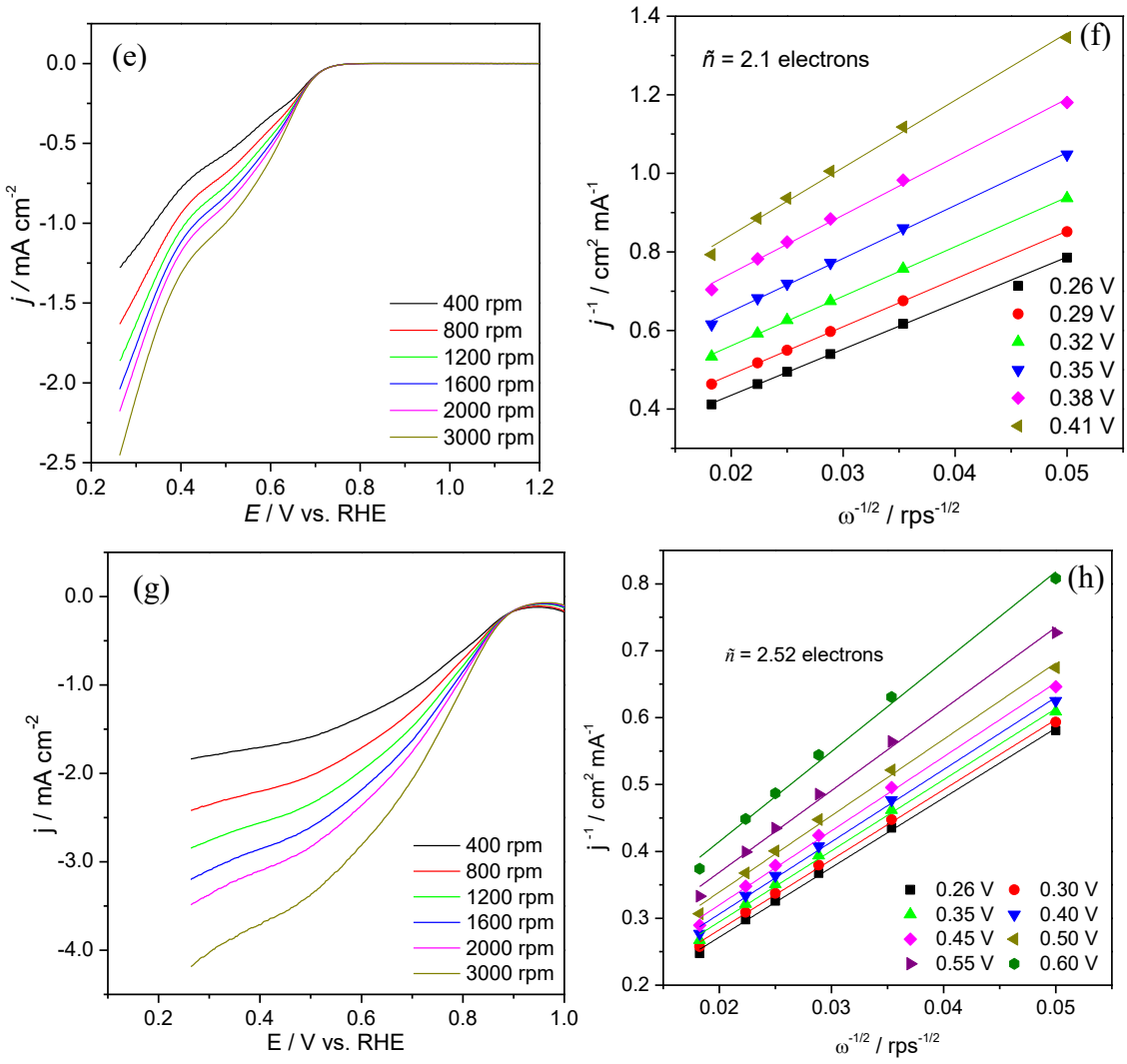



Figure 2S13 - ORR polarization curves of GF (a), SWCNT (c), MWCNT (e) and N-MWCNT (g) modified electrodes, acquired at different rotation rates in $O_2$-saturated 0.1 mol $dm^{-3}$ KOH solution at 0.005 V $s^{-1}$ and the corresponding Koutecky-Levich (K-L) plots (b, d, f and h).

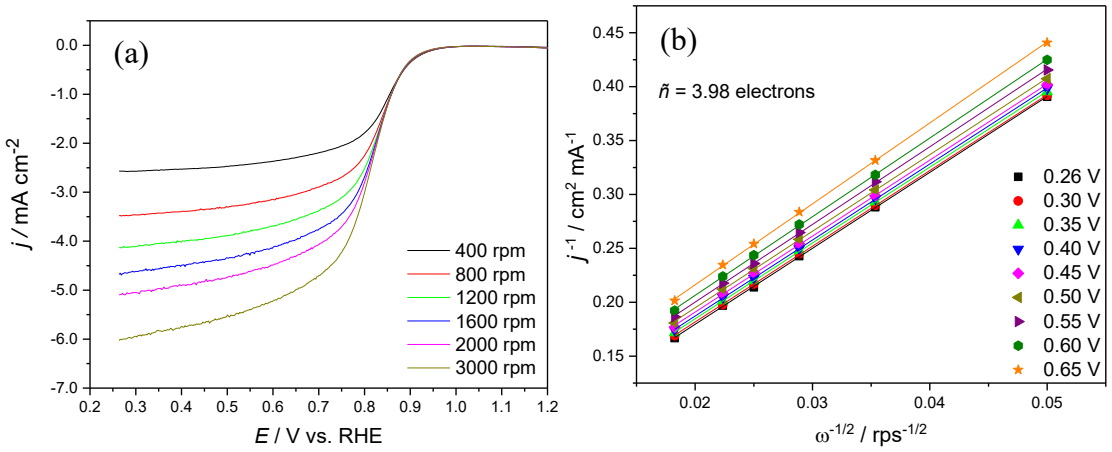



Figure 2S14 - ORR polarization curves for Pt/C at different rotation rates in $O_2$-saturated 0.1 mol $dm^{-3}$ KOH solution at 0.005 V $s^{-1}$ (a) and the corresponding Koutecky-Levich (K-L) plots (b).

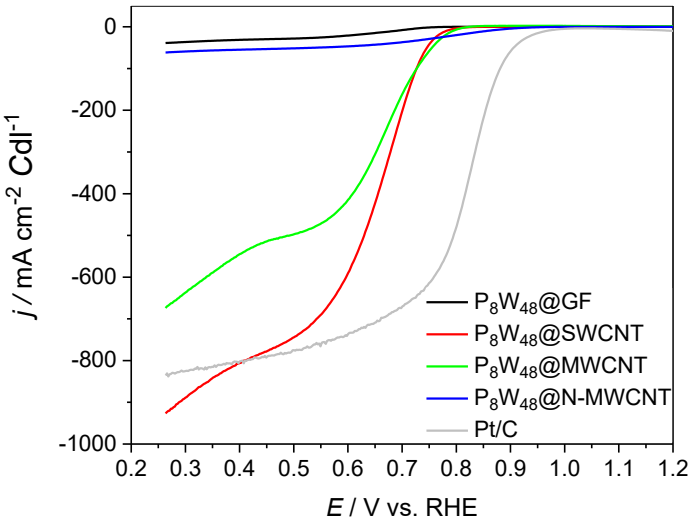
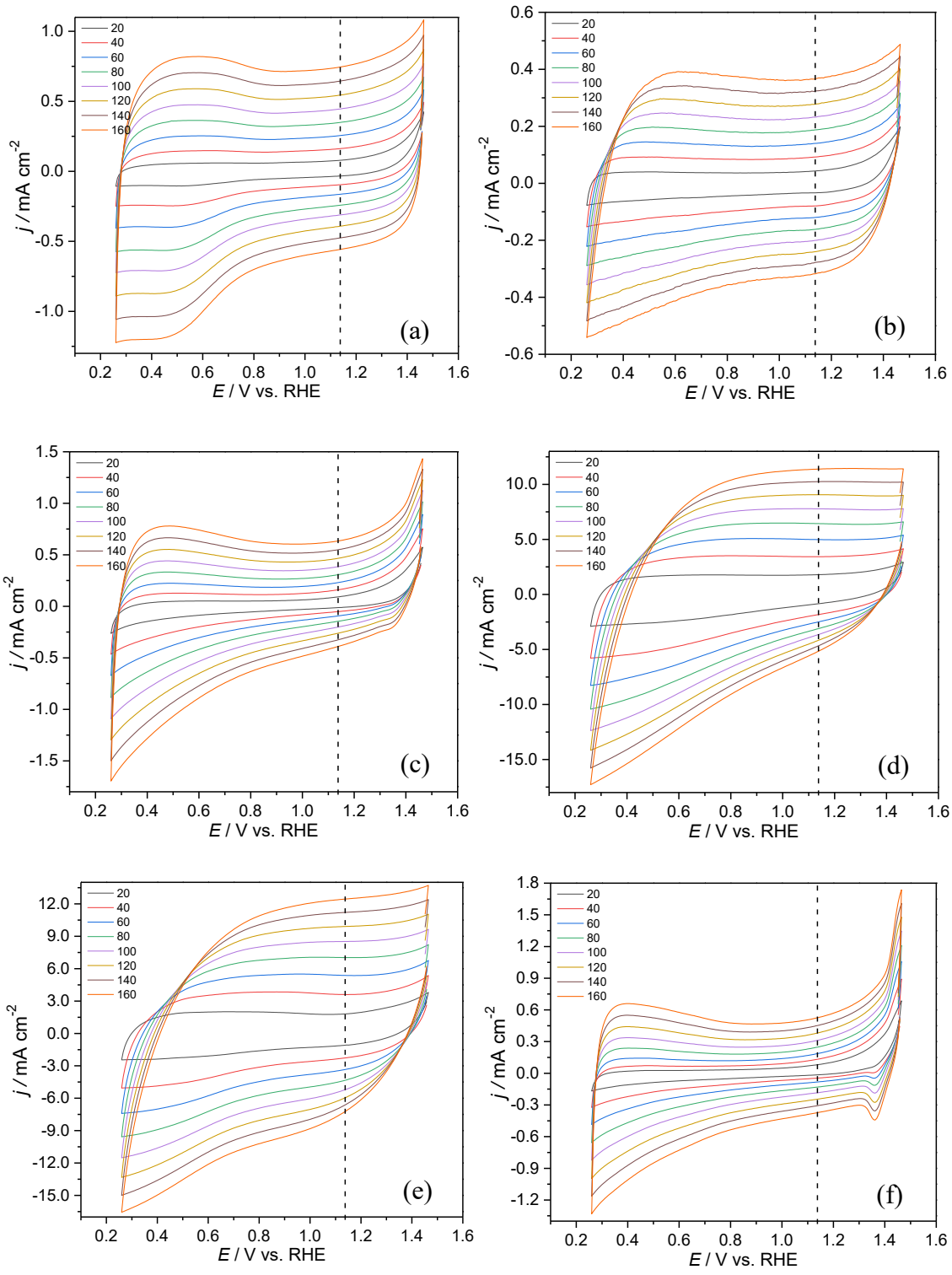



Figure 2S15 - ORR LSV curves obtained in KOH (0.1 M) saturated with $O_2$ at 1600 rpm and 0.005 V $s^{-1}$ with current densities normalized to the respective double-layer capacitance values.


20
40
60
80
100
120
140
160
j / mA cm-2
E / V vs. RHE
(a)
(b)
(c)
(d)
(e)
(f)

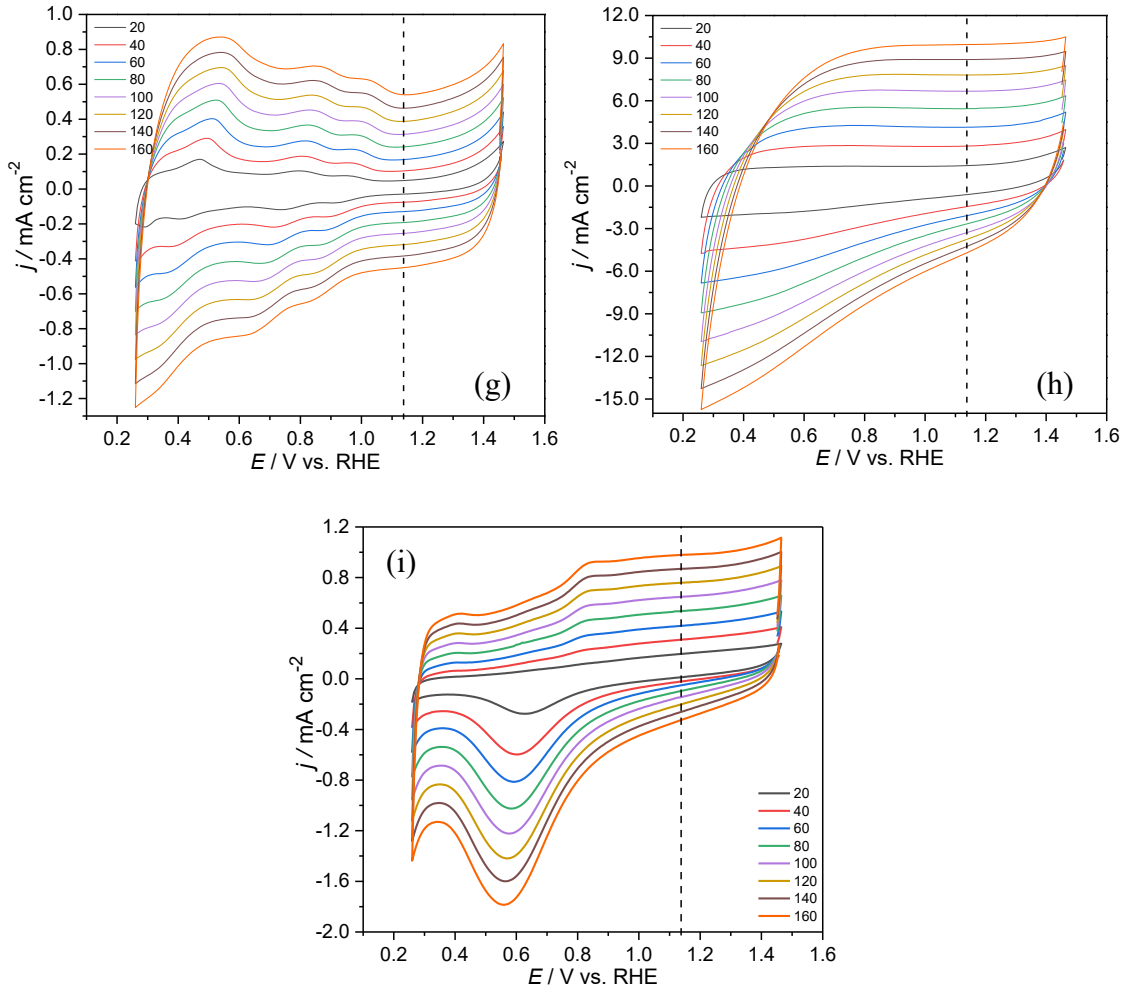
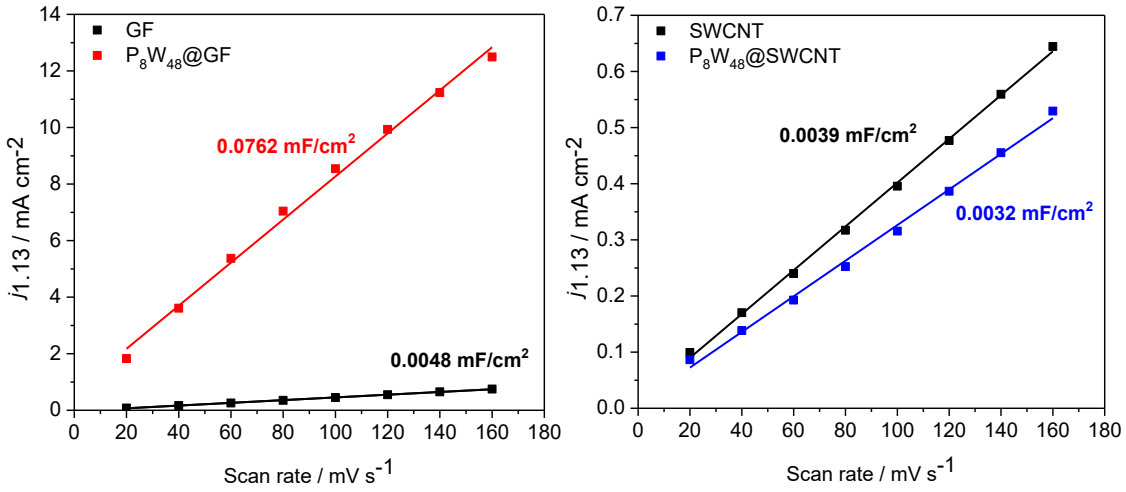



Figure 2S16 - CVs at different scan rates for GF (a), SWCNT (b), MWCNT (c), N-MWCNT (d), $P_8W_{48}$@GF (e), $P_8W_{48}$@SWCNT (f), $P_8W_{48}$@MWCNT (g), $P_8W_{48}$@N-MWCNT (h) and Pt/C (i) in $N_2$-saturated KOH (0.1 M).



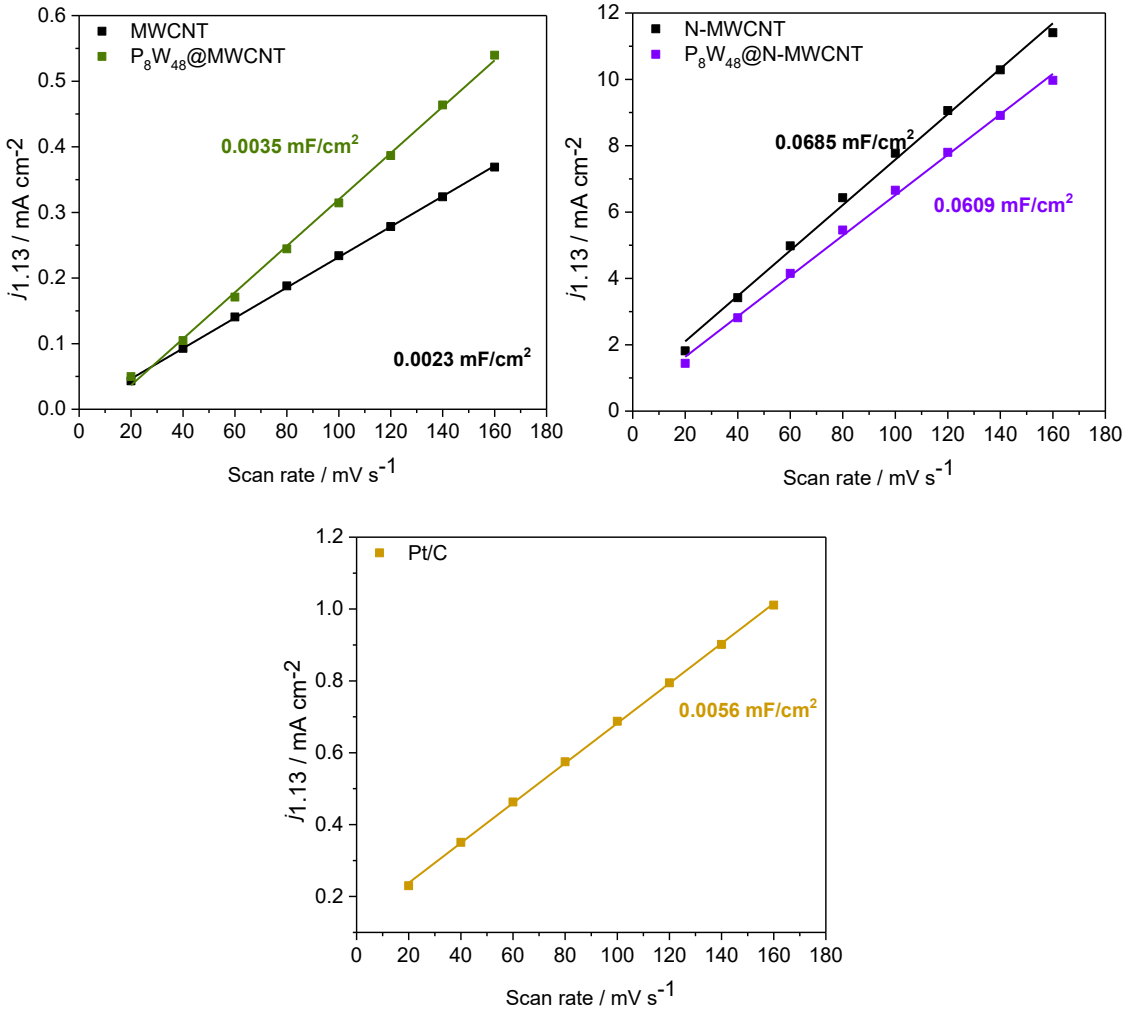



Figure 2S17 - Current density-scan rate linear fitting plots for all materials. Numeric values correspond to the double-layer capacitances ($C_{dl}$) for each material.

## 2.7. Declarations

**Authors' contributions:** The synthesis and characterisation of: POM was performed by A.H., N-MWCNT by A.G-R and I.R-R, composite materials by D.M.F, H.C.N and B.J. The electrocatalytic experiments were conducted by H.C.N. The research was supervised by D.M.F., U.K. and C.F. and H.C.N was responsible for writing up the manuscript, which was proofread by D.M.F and U.K..

**Funding:** This work was financially supported by: Project FOAM4NER (PTDC/QUI-ELT/28299/2017) (FOAM4NER) funded by (FCT/MCTES, Fundação para a Ciência e

Tecnologia and Ministério da Ciência, Tecnologia e Ensino Superior) through national funds.

**Acknowledgments:** Thanks are also due to PT national funds FCT/MCTES through the projects UIDB/50006/2020 and UIDP/50006/2020. HCN thanks FCT through ChemMat program for his PhD grant PD/BD/143095/2018. DMF thanks FCT/MCTES for funding through the Individual Call to Scientific Employment Stimulus (2021.00771.CEECIND/CP1662/CT0007). UK thanks the German Science Foundation (DFG) and Jacobs University for support.

**Conflict of interest:** The authors declare that they have no conflict of interest.

## 2.8. References

[1] F Perera (2018) International journal of environmental research and public health 15: 16.

[2] M Kuang, G Zheng (2016) Small 12: 5656.

[3] AM Samsudin, M Bodner, V Hacker (2022) Polymers 14: 3565.

[4] DM Fernandes, AF Peixoto, C Freire (2019) Dalton Transactions 48: 13508.

[5] EH Yu, K Scott, RW Reeve (2003) Fuel Cells 3: 169. Doi:https://doi.org/10.1002/fuce.200330129

[6] H Yin, S Liu, C Zhang, et al. (2014) ACS Applied Materials & Interfaces 6: 2086. Doi:10.1021/am405164f

[7] FHB Lima, EA Ticianelli (2004) Electrochimica Acta 49: 4091. Doi:https://doi.org/10.1016/j.electacta.2004.04.002

[8] N Todoroki, T Wadayama (2018) Electrochemistry advpub. Doi:10.5796/electrochemistry.18-00024

[9] M Hren, M Božič, D Fakin, KS Kleinschek, S Gorgieva (2021) Sustainable Energy & Fuels 5: 604.

[10] JS Spendelow, A Wieckowski (2007) Physical Chemistry Chemical Physics 9: 2654. Doi:10.1039/B703315J

[11] MM Hossen, K Artyushkova, P Atanassov, A Serov (2018) Journal of Power Sources 375: 214. Doi:https://doi.org/10.1016/j.jpowsour.2017.08.036

[12] X Song, D Zhang (2014) Energy 70: 223. Doi:https://doi.org/10.1016/j.energy.2014.03.116

[13] AS Arico, P Bruce, B Scrosati, J-M Tarascon, W Van Schalkwijk (2011) Materials for sustainable energy: a collection of peer-reviewed research and review articles from Nature Publishing GroupWorld Scientific,

[14] C Freire, DM Fernandes, M Nunes, VK Abdelkader (2018) ChemCatChem 10: 1703. Doi:10.1002/cctc.201701926

[15] H Qin, Y Wang, B Wang, et al. (2021) Journal of Energy Chemistry 53: 77. Doi:https://doi.org/10.1016/j.jechem.2020.05.015

[16] C-X Zhao, B-Q Li, J-N Liu, J-Q Huang, Q Zhang (2019) Chinese Chemical Letters 30: 911. Doi:https://doi.org/10.1016/j.cclet.2019.03.026

[17] A Rodríguez, G Ovejero, JL Sotelo, M Mestanza, J García (2010) Industrial & Engineering Chemistry Research 49: 498. Doi:10.1021/ie901212m

[18] M Mohan, VK Sharma, EA Kumar, V Gayathri (2019) Energy Storage 1: e35. Doi:https://doi.org/10.1002/est2.35

[19] Y Gong, Q Fu, C Pan (2017) MRS Advances 2: 3283. Doi:10.1557/adv.2017.385

[20] J Lach, K Wróbel, J Wróbel, P Podsadni, A Czerwiński (2019) Journal of Solid State Electrochemistry 23: 693. Doi:10.1007/s10008-018-04174-5

[21] W Yuan, Y Zhang, L Cheng, H Wu, L Zheng, D Zhao (2016) Journal of Materials Chemistry A 4: 8932. Doi:10.1039/C6TA01546H

[22] L Yang, J Shui, L Du, et al. (2019) Advanced Materials 31: 1804799.

[23] Q Wu, L Yang, X Wang, Z Hu (2017) Accounts of chemical research 50: 435.

[24] Y Liang, H Wang, J Zhou, et al. (2012) Journal of the American Chemical Society 134: 3517.

[25] Y Liang, Y Li, H Wang, et al. (2011) Nature materials 10: 780.

[26] MP Araújo, M Nunes, IM Rocha, M Pereira, C Freire (2018) ChemistrySelect 3: 10064.

[27] Y Liang, H Wang, P Diao, et al. (2012) Journal of the American Chemical Society 134: 15849.

[28] G Zhang, C Li, J Liu, et al. (2014) Journal of Materials Chemistry A 2: 8184.

[29] A Sarapuu, E Kibena-Põldsepp, M Borghei, K Tammeveski (2018) Journal of Materials Chemistry A 6: 776.

[30] J Masa, W Xia, M Muhler, W Schuhmann (2015) Angewandte Chemie International Edition 54: 10102.

[31] Z Yang, H Nie, X Chen, S Huang (2013) Journal of Power Sources 236: 238.

[32] N-T Suen, S-F Hung, Q Quan, N Zhang, Y-J Xu, HM Chen (2017) Chemical Society Reviews 46: 337.

[33] X Wang, X Fan, H Lin, et al. (2016) RSC Advances 6: 37965. Doi:10.1039/C6RA04771H

[34] M Vikkisk, I Kruusenberg, S Ratso, et al. (2015) RSC Advances 5: 59495.

[35] E Naseri, R Khoshnavazi (2018) RSC advances 8: 28249.

[36] Y Ji, L Huang, J Hu, C Streb, Y-F Song (2015) Energy & Environmental Science 8: 776.

[37] M Skunik, B Baranowska, D Fattakhova, et al. (2006) Journal of Solid State Electrochemistry 10: 168.

[38] S Aguado-Ureta, J Rodríguez-Hernández, A Del Campo, et al. (2018) Nanomaterials 8: 142.

[39] DM Fernandes, HC Novais, R Bacsa, et al. (2018) Langmuir 34: 6376. Doi:10.1021/acs.langmuir.8b00299

[40] TC Nagaiah, D Gupta, SD Adhikary, A Kafle, D Mandal (2021) Journal of Materials Chemistry A 9: 9228. Doi:10.1039/D0TA10423J

[41] L Faba, YA Criado, E Gallegos-Suárez, et al. (2013) Applied Catalysis A: General 458: 155.

[42] R Liu, G Zhang, H Cao, et al. (2016) Energy & Environmental Science 9: 1012. Doi:10.1039/C5EE03503A

[43] DM Fernandes, MP Araújo, A Haider, et al. (2018) ChemElectroChem 5: 273. Doi:10.1002/celc.201701210

[44] A Navaee, A Salimi, S Soltanian, P Servati (2015) Journal of Power Sources 277: 268. Doi:https://doi.org/10.1016/j.jpowsour.2014.11.117

[45] B Olalde, JM Aizpurua, A García, I Bustero, I Obieta, MJ Jurado (2008) The Journal of Physical Chemistry C 112: 10663. Doi:10.1021/jp800266j

[46] DW Lee, L De Los Santos V, JW Seo, et al. (2010) The Journal of Physical Chemistry B 114: 5723. Doi:10.1021/jp1002275

[47] AR Kumarasinghe, L Samaranayake, F Bondino, et al. (2013) The Journal of Physical Chemistry C 117: 9507. Doi:10.1021/jp402428j

[48] DM Fernandes, C Freire (2015) ChemElectroChem 2: 269. Doi:10.1002/celc.201402271

[49] N Daems, X Sheng, IFJ Vankelecom, PP Pescarmona (2014) Journal of Materials Chemistry A 2: 4085. Doi:10.1039/C3TA14043A

[50] M Skunik, M Chojak, IA Rutkowska, PJ Kulesza (2008) Electrochimica Acta 53: 3862.

[51] N Mizuno, K Katamura, Y Yoneda, M Misono (1983) Journal of Catalysis 83: 384.

[52] H Estrade-Szwarckopf (2004) Carbon 42: 1713.

[53] W Ai, Z Luo, J Jiang, et al. (2014) Advanced Materials 26: 6186.

[54] Y Liu, Y Qiao, G Wei, et al. (2018) Energy Storage Materials 11: 274.

[55] B Jarrais, A Guedes, C Freire (2018) ChemistrySelect 3: 1737. Doi:https://doi.org/10.1002/slct.201702706

[56] R Contant, A Teze (1985) Inorganic Chemistry 24: 4610. Doi:10.1021/ic00220a036

[57] DM Fernandes, HC Novais, R Bacsa, et al. (2018) Langmuir 34: 6376.

[58] ME Lipińska, SL Rebelo, MFR Pereira, J Gomes, C Freire, J Figueiredo (2012) Carbon 50: 3280.

[59] N Limani, IS Marques, B Jarrais, AJS Fernandes, C Freire, DM Fernandes (2022) Catalysts 12: 357.

[60] L Dai, Y Xue, L Qu, H-J Choi, J-B Baek (2015) Chemical Reviews 115: 4823. Doi:10.1021/cr5003563

[61] S Ni, Z Li, J Yang (2012) Nanoscale 4: 1184. Doi:10.1039/C1NR11086A

[62] X Wang, H Fu, W Li, J Zheng, X Li (2014) RSC Advances 4: 37779. Doi:10.1039/C4RA05961A

[63] T Shinagawa, AT Garcia-Esparza, K Takanabe (2015) Scientific Reports 5: 13801. Doi:10.1038/srep13801

[64] IS Marques, B Jarrais, I-M Mbomekallé, et al. (2022) Catalysts 12: 440.

[65] VK Abdelkader-Fernández, DM Fernandes, SS Balula, L Cunha-Silva, C Freire (2020) Journal of Materials Chemistry A 8: 13509. Doi:10.1039/D0TA03898A

[66] C Lo Vecchio, D Sebastián, M Lázaro, A Aricò, V Baglio (2018) Catalysts 8: 650.

[67] S Hoang, S Guo, NT Hahn, AJ Bard, CB Mullins (2012) Nano Letters 12: 26. Doi:10.1021/nl2028188

[68] G Tuci, C Zafferoni, A Rossin, et al. (2014) Chemistry of Materials 26: 3460. Doi:10.1021/cm500805c

[69] N Muthuswamy, MEM Buan, JC Walmsley, M Rønning (2018) Catalysis Today 301: 11. Doi:https://doi.org/10.1016/j.cattod.2017.03.045

Chapter 3

# Hybrids made of a Fe-containing Wells-Dawson polyoxometalate and carbon nanomaterials as promising electrocatalysts for the oxygen reduction reaction

# 3

# Hybrids made of a Fe-containing Wells-Dawson polyoxometalate and carbon nanomaterials as promising electrocatalysts for the oxygen reduction reaction[3,4]

Having demonstrated the successful immobilisation of polyoxometalates on carbon nanomaterials in the previous chapter, it became evident that introducing specific heteroatoms and metal substitutions could offer significant advantages. The motivation for transitioning to a Wells-Dawson-type polyoxometalate containing iron ($P_2W_{17}Fe$) stems from the ability of transition metals to tune the redox properties and improve the catalytic activity of the system. The objective for this new hybrid material is to exploit the synergy between the iron centre of the POM and nitrogen-doped carbon nanostructures, aiming to develop a low-cost ORR electrocatalyst with superior performance, high stability, and remarkable methanol tolerance.

[3] Novais, H.C.; Jarrais, B.; Mbomekallé, I.-M.; Teillout, A.-L.; Oliveira, P.d.; Freire, C.; Fernandes, D.M. Hybrids Composed of an Fe-Containing Wells–Dawson Polyoxometalate and Carbon Nanomaterials as Promising Electrocatalysts for the Oxygen Reduction Reaction. *Inorganics* **11**, 388, (2023). https://doi.org/10.3390/inorganics11100388.

[4] Hugo C. Novais' contribution to the publication: synthesis and characterisation of composite materials, electrocatalytic experiments and responsible for writing up the manuscript.

## Abstract

The abrupt growth of world population and industrial processes has had a profound impact on the environment and health, increasing the urgency on substituting the burn of fossil fuels with alternative energy sources. The oxygen reduction reaction (ORR) has a crucial function as the cathodic reaction in energy-converting systems, such as fuel cells (FCs), which contributes to a sustainable energy supply. Thus, it is of utmost importance to develop cost-effective and efficient electrocatalysts (ECs) without noble metals to substitute the Pt-based ones. This work reports the preparation and application of POM-based electrocatalysts for the ORR. A Wells-Dawson POM salt $K_7[P_2W_{17}(FeOH_2)O_{61}].20H_2O$ was immobilized onto graphene flakes and multi-walled carbon nanotubes doped with nitrogen, denominated as $P_2W_{17}Fe$@GF_N8 and $P_2W_{17}Fe$@MWCNT_N8. The successful preparation of the composites was proved by various characterisation techniques such as FTIR, XPS and SEM analysis. Both materials showed good ORR performance in alkaline medium with similar potential onset values of ~0.84 V vs. RHE and diffusion-limiting current densities of -3.9 and -3.3 mA $cm^{-2}$ for $P_2W_{17}Fe$@MWCNT_N8 and $P_2W_{17}Fe$@GF_N8, respectively. Furthermore, both composites presented low Tafel slopes (48 – 58 mV $dec^{-1}$). Chronoamperometric tests revealed that the as-prepared nanocomposites rendered a significant improvement achieving between 90 – 94% of current retention in tolerance to methanol in comparison with Pt/C, and moderate to good long-term electrochemical stability with current retentions comprised between 68 – 88%.

This work reinforces the use of POMs as important electroactive species for the preparation of alternative electrocatalysts for the ORR, exhibiting good activity and stability, including good selectivity towards the ORR in the presence of methanol.

## 3.1. Introduction

The increase in the world population has led to a steep rise in energy demand which has raised concerns about the security of our energy supplies in the mid-term future. It is therefore of the highest urgency to develop sustainable alternative energy sources and conversion devices in order to reduce carbon emissions.[1] Fuel cells (FCs) present themselves as one of the most promising green options and sustainable technologies available. A key feature of these systems is the oxygen reduction reaction (ORR) that occurs at the cathode and generally exhibits slow kinetics.[2-4] Electrocatalysts (ECs) play a major role in most energy conversion devices, including

FCs because they increase the efficiency and selectivity of the chemical reactions involved. So far the most active ECs for ORR are based on noble metals such as platinum and palladium.[5] The latter have several disadvantages, such as high cost, low abundance and intolerance to fuel crossover (methanol and CO).[5] Since the discovery of the ORR in fuel cells, researchers have been working to improve the efficiency and stability of the electrocatalysts used in this process. In recent years, there have been significant advances in the development of ORR electrocatalysts, particularly in the use of iron-based catalysts.[6] Also, surface science studies have been conducted to better understand the electronic structure, stability, and electrocatalytic properties of various catalysts.[7, 8] In addition, computational methods have been developed to aid in the design of solid catalysts, which has opened up new possibilities for ORR electrocatalyst research.[9] Over the last years, several studies have been conducted aiming at designing efficient ECs based on earth-abundant elements to overcome the referred limitations associated with Pt and Pd-based electrocatalysts.[2, 4, 10] The development of efficient and cost-effective catalysts for the ORR is of critical importance for the widespread adoption of fuel cells. Plus, significant progress has been made towards the design of ORR catalysts based on earth-abundant elements.[11] However, despite these advances, the search for efficient and stable ORR catalysts remains a topic of active research. One of the first catalysts tested for ORR was cobalt phthalocyanine (CoPc).[11] Jasinski's seminal work published in Nature in 1964 demonstrated that CoPc can catalyze ORR in acidic media. This work laid the foundation for the development of metal-phthalocyanine-based catalysts for fuel cells. Currently, the FCs that have received the most attention are proton exchange membrane fuel cells (PEMFCs).[12] These systems, despite being the most technologically mature, rely on expensive acid membranes and ionomers[13], and on platinum group metal-based electrocatalysts which are expensive, show restricted durability, and have scarce availability.[14] In order to enhance the electrocatalytic behaviour of the ORR, Pt and Pd have been incorporated with several transition metals such as Ru[15], Ni[16], Ag[16] or Co[17, 18].

Carbon nanomaterials (CMs) such as graphene (GF) and carbon nanotubes (CNT) have emerged as promising ORR electrocatalysts considering their low cost, high surface area, great conductivity, and high stability.[19] These materials have shown high chemical and thermal stability, good electrical properties, high porosity and a large surface area.[20] Nanotubes and graphene are among the most widely applied materials in the ORR, both as metal-free ECs in alkaline media and as electrocatalyst supports in hybrid nanocomposites.[21-23] In addition, their electrocatalytic activity may still be improved by doping with different heteroatoms such as nitrogen, sulphur and

phosphorus.[21, 22, 24-27] Regarding nitrogen species, different forms can be incorporated on the graphitic network, such as pyridinic, pyrrolic, graphitic (quaternary), and oxidized nitrogen and these can have a significant impact on the electrocatalytic performance of the material. Artyushkova et al. showed that pyridinic and graphitic (quaternary) nitrogen species can act as highly active sites for the ORR due to their ability to stabilize the adsorption of reaction intermediates.[27] On the other hand, pyrrolic and oxidized nitrogen species have been found to exhibit lower activity for the ORR. Therefore, it is important to carefully consider the type and concentration of nitrogen species when designing doped carbon catalysts for the ORR. The incorporation of nitrogen in the $sp^2$ carbon allows the improvement of electronic properties of pristine carbons, which gives rise to an enhanced electrocatalytic performance towards the ORR.[21, 22, 28, 29].[30] Over the years, several studies have reported progress in the performance of pyrolyzed catalysts for ORR.[31, 32] In 2009, Lefèvre et al. reported the use of polymers as carbon-nitrogen sources for the synthesis of ORR catalysts.[33] The sacrificial support method (SSM) has also been shown to be an effective strategy for the preparation of ORR catalysts.[34] In 2011, Zelenay reported a significant improvement in the durability of ORR catalysts based on non-precious metals.[35]

Furthermore, the design and preparation of composite electrocatalysts which combine the excellent properties of carbon nanomaterials with the high stability and rich redox features of polyoxometalates (POMs) has been suggested as a possible way to increase the efficiency of different energy-related reactions.[29, 36-39] The POM used in this work belongs to the Wells-Dawson family ($[(P_2W_{17}O_{61})Fe^{III}(H_2O)]^{7-}$). The iron-substituted POMs are of particular interest as they may act either as oxidation or as reduction electrocatalysts.[12]

Herein, we report on the preparation of composites based on the incorporation of the Wells-Dawson POM's salt $K_7[P_2W_{17}(FeOH_2)O_{61}].20H_2O$ onto two distinct nitrogen-doped carbon materials (nitrogen-doped graphene flakes - GF_N8, nitrogen-doped multi-walled carbon nanotubes - MWCNT_N8) and their application as ORR electrocatalysts.

## 3.2. Experimental section

### 3.2.1 Materials preparation and characterisation methods

The materials and solvents used in the preparation of the composites and in the ORR studies are described in detail in the Supplementary Information (SI).

Nitrogen doping of the carbon materials (0.60 g) was achieved by mechanical ball milling treatment during 5 h at a constant frequency of 15 vibrations $s^{-1}$ with a Retsch MM200 equipment using melamine (0.26 g) as a precursor. Then, the resulting materials were subjected to a thermal treatment under $N_2$ flow (100 $cm^3$ $min^{-1}$), at a rate of 10 ˚C $min^{-1}$ until reaching the final temperature of 800 ºC, and kept at these temperature during 1 h, cooled to room temperature under nitrogen atmosphere and stored in a desiccator.[40] The $P_2W_{17}Fe$@CM composites were then prepared through the immobilization of $P_2W_{17}Fe$ onto previously prepared MWCNT_N8 and GF_N8. The immobilization of POM was achieved as follows: a 5 mL acetate buffer solution (pH = 4.0) containing 50 mg of $P_2W_{17}Fe$ was added to a 20 mL acetate buffer solution (pH = 4.0) containing 25 mg of CM. The mixture was dispersed 15 min in an ultrasonic bath and then left to stir for 2h at 400 rpm. Then, the resulting composites were filtered, washed and left to dry at 60 ºC under vacuum overnight. The composites were labelled as $P_2W_{17}Fe$@GF_N8 and $P_2W_{17}Fe$@MWCNT_N8.

Prior to their use in the electrocatalytic studies, the composites prepared were characterized by different techniques: Fourier-transformed infrared spectroscopy (FTIR), scanning electron microscopy (SEM), energy dispersive X-ray spectroscopy (EDS) and X-ray photoelectron spectroscopy (XPS). The methods and equipment used are detailed in the SI. Electrocatalytic performances towards the ORR were evaluated using a PGSTAT 302N potentiostat (Metrohm Autolab B.V., Utrecht, The Netherlands) controlled by the NOVA 2.1 software and using a conventional 3-electrode system. For all details regarding electrodes, electrode conditioning and modification, see the SI.

## 3.3. Results and Discussion

### 3.3.1. Materials characterisation

All the prepared materials were initially characterized by infrared spectroscopy (Figure 3.1). The FTIR spectra of the nitrogen-doped carbon materials are shown in Figure 3S1. The MWCNT_N8 spectrum reveals several vibrational bands at 3436, 2928, 2846, 1641, 1383 and 1124 $cm^{-1}$, but some of these bands are very weak and poorly resolved. This may arise from the low loading of POMs onto the carbon material or their interaction with the graphene and carbon nanotube matrix that hinders their identification.

The vibrational bands of the OH groups can be observed at 3436 $cm^{-1}$, and are due to the O-H stretching and bending modes from the adsorbed residual water and hydroxyl groups.[41, 42] The C-N stretching vibration band is shown at 1383 $cm^{-1}$.[43, 44] The band at 1124 $cm^{-1}$ is assigned to the phenolic groups' vibration modes.[41, 45, 46] Lastly, the two bands at 2928 and 2846 $cm^{-1}$ correspond, respectively, to the C-H stretching modes that may be due to the existence of defects in the $sp^2$ hybridised domains, and the band at 1641 $cm^{-1}$ can be attributed to the C=N and the C=O stretching mode of the carboxylic acid, carbonyl, ketone and quinone groups.[41, 43-46] The vibrational spectra of GF_N8 is similar (Figure 3S1 black line), showing vibrational bands assigned to O-H stretching and bending modes at ~ 3410 and 1386 $cm^{-1}$, respectively.[41, 42] The C=N and the C=O stretching vibrations are observed at 1630 $cm^{-1}$, the phenol groups at 1387 $cm^{-1}$ and the C-O stretching vibrations of oxygen groups at 1142 $cm^{-1}$.[41-44] [39] Finally, the band assigned to the C-O-C and the C-O stretching modes, and the C-O-H bending mode is observed at 1070 $cm^{-1}$.[41, 45, 46]

Figure 3.1 (black) shows the FTIR spectrum of $P_2W_{17}Fe$ where the typical vibrational bands of POMs can be observed between 1100 and 700 $cm^{-1}$. The band at 1085 $cm^{-1}$ is assigned to the splitting of the $\nu_{as}$P-O stretching vibration and the three vibration bands at 947, 917 and 793 $cm^{-1}$ are assigned to the $\nu_{as}W{=}O_t$, $\nu_{as}W\text{-}O_b\text{-}W$ and $\nu_{as}W\text{-}O_c\text{-}W$ stretching modes (corner and edge sharing W-O-W), respectively.[47, 48] The infrared spectra of the composites $P_2W_{17}Fe$@GF_N8 (red) and $P_2W_{17}Fe$@MWCNT_N8 (blue) show weaker bands when compared with the spectrum of the POM, still it is possible to confirm its immobilization onto the carbon materials. Additionally, the bands arising from the nitrogen-doped carbon materials are also observed. After the immobilization of $P_2W_{17}Fe$ onto the carbon materials it can be verified a small shift in the position of the characteristic bands of the POM to shorter wavelengths. The reported changes are likely to reflect the weakening (stretching) of the W-O bonds as a result of possible changes in electron densities (or strengthening of repulsive interactions between oxygen atoms), following the adsorption of the POM on the surfaces of the carbon materials.[29, 49]

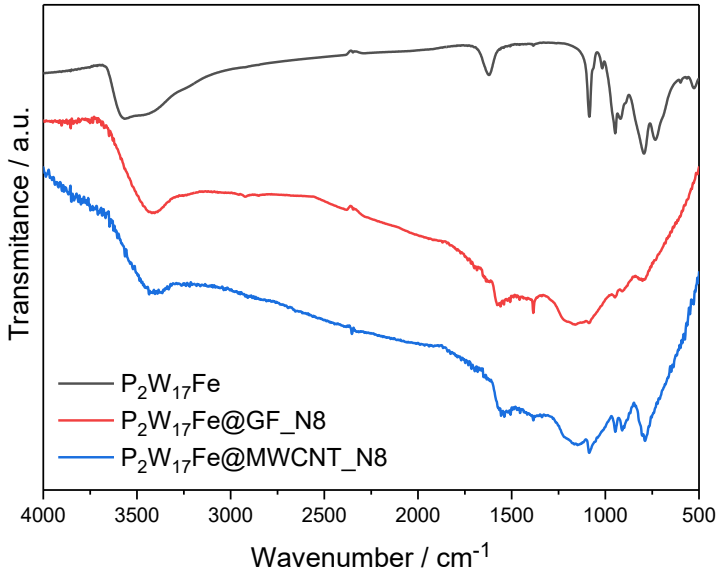



Figure 3.1 - FTIR spectra in the 4000–500 $cm^{-1}$ range of $K_7[P_2W_{17}(FeOH_2)O_{61}]$ (black), and of the composites $P_2W_{17}Fe$@GF_N8 (red) and $P_2W_{17}Fe$@MWCNT_N8 (blue).

The XPS characterisation of the starting nitrogen-doped materials GF_N8 and MWCNT_N8 has already been published by Bruno Jarrais et al[40]. Still, for a proper comparison with the composite materials, the main peaks are recalled here. Both composites were also characterised by XPS to assess their composition. The relative amounts of the different elements were calculated through the peak areas and are presented in Table 3.1.

As can be seen in Figure 3S2 (a) and 3S3 (a) in the SI file, the presence of nitrogen in the heteroatom-doped carbon materials (GF_N8 and MWCNT_N8) was found, which suggests that the doping procedure was successful. The XPS N1s spectra of the N-doped carbon materials were deconvoluted into three main peaks that are assigned to pyridinic N at 398.2 eV, pyrrolic N at 399.6 eV, and quaternary N at 401.0 eV.[50, 51] For the MWCNT_N8, a fourth peak at 404.1 eV was found and attributed to nitrogen oxide and/or nitrate species.[50, 52] For both N-doped materials, the relative amounts of N-functionalities show the same pattern, increasing in the same order: [quaternary N] < [pyrrolic N] < [pyridinic N]. The C1s high resolution spectra (Figure 3S2 (b) and S3 (b)) were fitted with 7 peaks: one at 284.6 eV attributed to the graphitic structure ($sp^2$, C=C), $sp^3$ hybridized carbon and C-N bonding at 285.2 eV, C-N and C-OH bonding at 285.9 eV, C-O-C groups at 286.9 eV, C=O groups (ketones, quinones, aldehydes) at 288.2 eV, COOH (carboxylic acids, esters) at 289.3 eV, and a peak at 291.0 eV attributed to π–π* transitions[40, 53]. The O1s high-resolution spectra of the

GF_N8 (Figure 3S2(c)) were fitted with one peak at 531.9 eV attributed to C=O and COOH. However, the MWCNT_N8 (Figure 3S3 (c)) upon deconvolution presents two peaks, one at 531.7 eV assigned to C=O and COOH, and another at 533.1 eV attributed to HO-C[39, 40, 54].

The N1s XPS spectrum of the $P_2W_{17}Fe$@MWCNT_N8 composite (Figure 3.2 (a)) has 4 main peaks at 398.5, 399.8, 401 and 402.2 eV attributed to pyridinic, pyrrolic, quaternary N and to nitrogen oxide and/or nitrate species, respectively.[40, 51, 55, 56] The XPS fitting of the N1s spectrum for the composite $P_2W_{17}Fe$@GF_N8 (Figure 3S2 (a)) is very similar to that of GF_N8, presenting peaks at 398.1, 399.8 and 401.1 eV corresponding to pyridinic, pyrrolic, and quaternary N, respectively.

The C1s high-resolution XPS spectrum of the $P_2W_{17}Fe$@MWCNT_N8 composite is shown in Figure 3.2 (b). Overall it has 7 peaks, a main peak at 284.6 eV assigned to the graphitic structure ($sp^2$, C=C), a peak at approximately 285.1 eV attributed to a $sp^3$ hybridized carbon and C-N bonding, a peak at 285.8 eV assigned to C-N and C-OH bonding, a peak at approximately 286.8 eV attributed to C-O-C groups, a peak at 288.1 eV assigned to C=O groups (ketones, quinones, aldehydes), a peak at ~289.2 eV ascribed to COOH (carboxylic acids, esters), and a peak at 291.0 eV attributed to π–π* transitions.[40, 53] The fitting of the C1s XPS spectrum of $P_2W_{17}Fe$@GF_N8 was very similar as can be seen in Figure 3S4 (a) of the SI file.

Figure 3.2 (c) shows the high resolution O1s spectrum for $P_2W_{17}Fe$@MWCNT_N8 which was deconvoluted into two main peaks: one at 530.7 eV assigned to oxygen in C=O (ketones, quinones, aldehydes) and COOH (carboxylic acids, esters) groups and oxygen atoms belonging to the POM, and another at 532.6 eV attributed to O in HO-C groups (phenols).[39, 40, 54] These two peaks are observed for the MWCNT_N8 and in the O1s spectrum of $P_2W_{17}Fe$@GF_N8. It is important to refer that, after the immobilisation of the POM on the carbon materials, there was a significant increase (about 3-fold) in the percentage of oxygen O1s in the final composites. This is due to a contribution of the POM to the O1s percentages of the composite.

The P2p high-resolution spectra of $P_2W_{17}Fe$@CM are shown in Figure 3.2 (d) and Figure 3S4 (d). The observed peaks can be resolved as $2p_{3/2}$ and $2p_{1/2}$ doublets at ~133.4 and ~134.2 eV, respectively.[57] In Figure 3.2 (e) and Figure 3S4 (e), the peaks found in the high-resolution spectra of W4f are attributed to $4f_{7/2}$ (~35.6 eV) and $4f_{5/2}$ (~37.8 eV), due to spin-orbital coupling.[57] Finally, in Figure 3.2 (f) and Figure 3S4 (f) the Fe2p can be divided into Fe $2p_{3/2}$ and Fe $2p_{1/2}$ with the binding energies of ~711.6 eV and ~724.7 eV associated with $Fe^{3+}$.[58, 59]

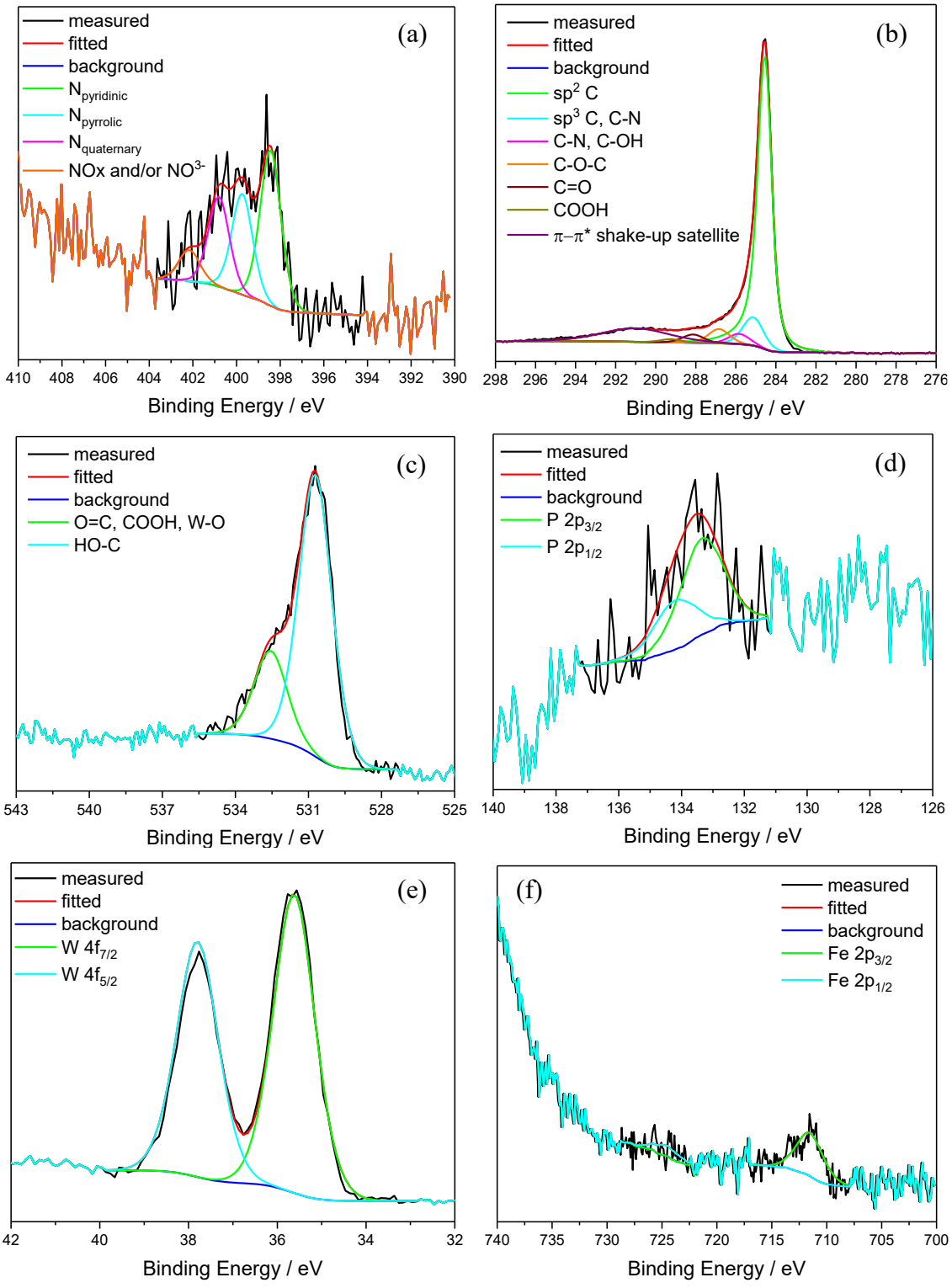



Figure 3.2 - XPS deconvoluted spectra of corresponding elements in the $P_2W_{17}Fe$@MWCNT_N8 composite.

Assuming that XPS is a surface technique that scans sample depths down to 10 nm, this may have prevented from reaching the expected P/W ratio. Still, the

experimental value of the P/W ratio of both composites is very close to the theoretical value, thus confirming the preservation of the polyoxometalate structure.

Table 3.1 - XPS surface atomic percentages for the pristine carbon materials, the doped carbon materials and the prepared composites.

| Material | XPS Atomic %[a] | | | | | |
|---|---|---|---|---|---|---|
| | C1s | O1s | N1s | P2p | W4f | Fe 2p |
| **GF** | 96.8 | 3.2 | - | - | - | -- |
| **MWCNT** | 98.9 | 1.1 | - | - | - | - |
| **GF_N8** | 97.0 | 2.0 | 1.0 | - | - | - |
| **MWCNT_N8** | 98.0 | 1.0 | 1.0 | - | - | - |
| **$P_2W_{17}Fe$@GF_N8** | 92.6 | 6.0 | 0.62 | 0.10 | 0.61 | 0.16 |
| **$P_2W_{17}Fe$@MWCNT_N8** | 95.0 | 3.4 | 0.68 | 0.12 | 0.63 | 0.12 |

[a] Determined by the areas of the respective bands in the high-resolution XPS spectra.

The morphology of all materials was assessed by scanning electron microscopy (SEM), and Figure 3.3 shows the SEM images for $P_2W_{17}Fe$@MWCNT_N8 (a) and $P_2W_{17}Fe$@GF_N8 (b) at a 50,000× magnification. As can be seen, the morphologies of $P_2W_{17}Fe$@MWCNT_N8 and $P_2W_{17}Fe$@GF_N8 differ significantly. $P_2W_{17}Fe$@MWCNT_N8 exhibits a needle-like structure characteristic of multi-walled carbon nanotubes, whereas $P_2W_{17}Fe$@GF_N8 shows a thin and flat flakes of carbon layers. Both composites are decorated lighter microsized spots that correspond to $P_2W_{17}Fe$ clusters which leads to this roughened texture. In Figure 3.3 (a), the widths of the carbon nanotubes show clear uniformity with a range of diameters between 8 - 20 nm wide. In Figure 3.3 (b) it is possible to observe folded graphene sheets and a less rough texture. SEM images of MWCNT_N8 and GF_N8, exhibiting the same morphological characteristics as described above, are shown in Figure 3S5.

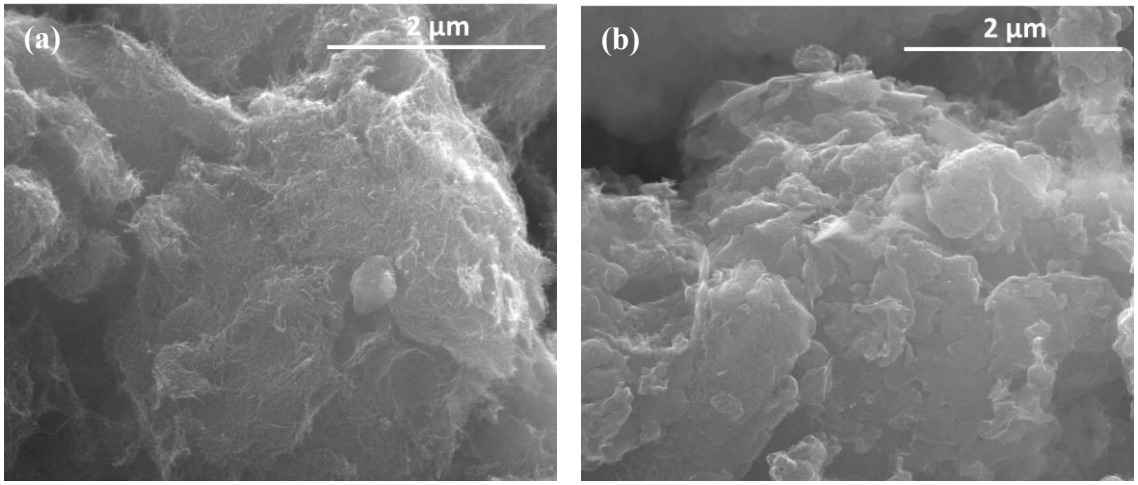



Figure 3.3 - SEM images of $P_2W_{17}Fe$@MWCNT_N8 (a) and $P_2W_{17}Fe$@GF_N8 (b) at 50000× magnification.

EDX analysis was conducted to assess the distribution of $P_2W_{17}Fe$ throughout the composites. Figure 3.4 shows the SEM and EDX elemental mapping images for $P_2W_{17}Fe$@MWCNT_N8, while the images of $P_2W_{17}Fe$ @GF_N8 composite can be found in Figure 3S6. The elemental analysis mapping shows, in general, a homogenous distribution of the POM elements (W, P, Fe and O), suggesting that the POM has been uniformly immobilized throughout the carbon material. The lighter shades on the EDX elemental mapping images of the W, P, Fe and O elements refer to the POM clusters.

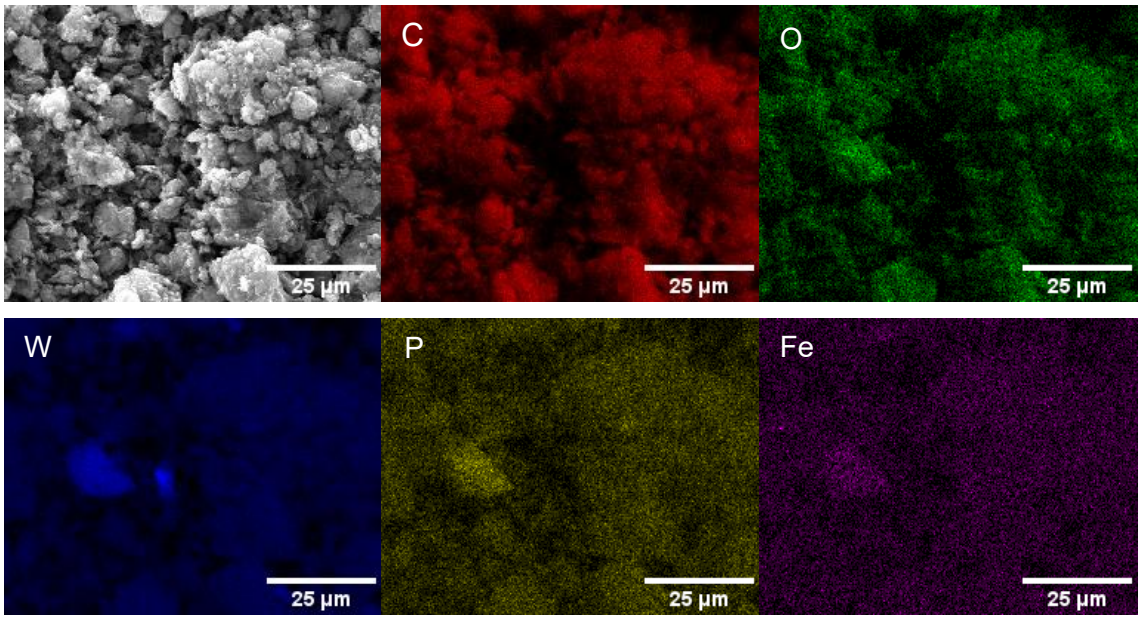



Figure 3.4 - SEM and EDX elemental mapping images of $P_2W_{17}Fe$@MWCNT_N8, at 5000× magnification for the elements C (red), O (green), W (blue), P (yellow) and Fe (purple).

## 3.4. Electrochemical performance towards ORR

The electrocatalytic activity towards the ORR of both composites prepared was firstly studied by cyclic voltammetry (CV) in $N_2$- and $O_2$-saturated KOH solutions (0.1 mol $dm^{-3}$). The N-doped carbon materials were also evaluated in the same experimental conditions for comparison. Figure 3.5 presents the CVs in $N_2$- and $O_2$-saturated solutions for the two nanocomposites prepared, where it can be clearly observed that in $N_2$-saturated electrolyte, no peak is detected, while in the $O_2$-purged electrolyte, both composites exhibit an irreversible peak corresponding to the reduction of oxygen at $E_{pc}$ = 0.82 and 0.79 V vs. RHE for $P_2W_{17}Fe$@MWCNT_N8 and $P_2W_{17}Fe$@GF_N8, respectively. The electrochemical study of the starting nitrogen-doped materials - GF_N8 and MWCNT_N8 - was published by Limani et. al.[52], but was replicated here for comparison. The MWCNT_N8 and GF_N8 were evaluated in the same experimental conditions (Figure 3S7 (a) and (b) in the SI) and they exhibit reduction peaks at $E_{pc}$ = 0.74 and 0.80 V vs. RHE, respectively. The performance of Pt/C (20 wt %) was also measured in the same experimental conditions (Figure 3S7 (c)) exhibiting the ORR peak at $E_{pc}$ = 0.86 V vs. RHE.

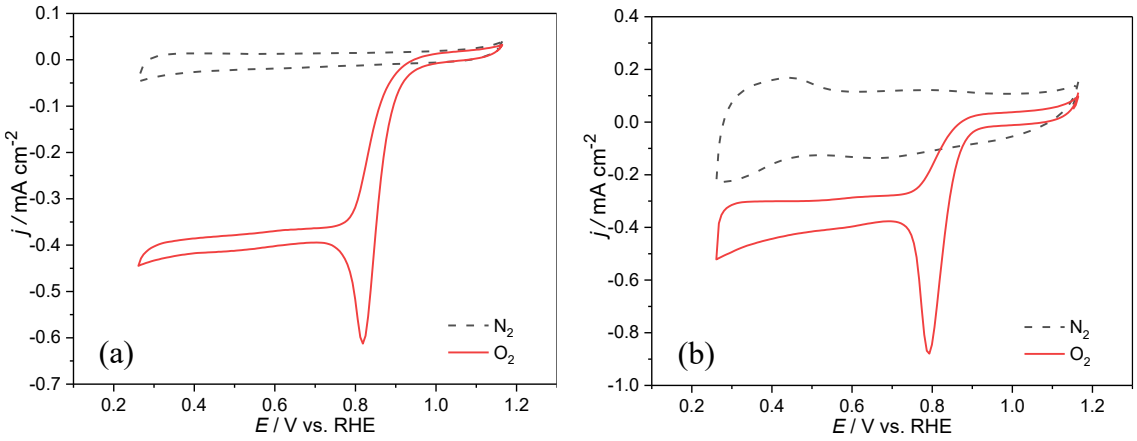



Figure 3.5 - CVs of $P_2W_{17}Fe$@MWCNT_N8 (a) and $P_2W_{17}Fe$@GF_N8 (b) modified electrodes in $N_2$-saturated (dash line) and $O_2$-saturated (full line) 0.1 mol $dm^{-3}$ KOH solution at 0.005 V $s^{-1}$.

To gain further insights into the electrocatalytic performance of $P_2W_{17}Fe$@CM nanocomposites towards the ORR, linear sweep voltammetry (LSV) was carried out at 1600 rpm in $O_2$-saturated KOH solution (0.1 mol $dm^{-3}$). The LSV curves shown in Figure 3.6 (a) were obtained after subtraction of the blanks (the latter recorded in $N_2$-saturated

KOH solution) from the ones saved in $O_2$-saturated KOH. Table 3.2 presents the main ORR parameters acquired – the onset potential ($E_{onset}$), the diffusion-limiting current density values ($j_{L,\ 0.26\ V,\ 1600\ rpm}$), the Tafel slopes (TS) and the number of electrons transferred per oxygen molecule ($n_{O2}$).

The $E_{onset}$ values of the $P_2W_{17}Fe$@CM nanocomposites and N-doped carbon materials are very similar, ranging from 0.83 to 0.84 V vs RHE. The $P_2W_{17}Fe$@MWCNT_N8 has the closest $E_{onset}$ value to the one obtained for Pt/C (0.94 V vs. RHE). Furthermore, all electrocatalysts showed $j_L$ values between −4.0 and −3.3 mA $cm^{-2}$, but do not reach the value obtained for Pt/C (−4.7 mA $cm^{-2}$). Still, these nanocomposites performed well compared to other similar electrocatalysts as it can be observed in Table 3S2. It is also important to highlight that the ORR electrocatalytic activity of the pristine carbon materials is greatly improved after nitrogen doping, which agrees with various studies that have reported an enhancement of the ORR electrocatalytic performance after N-doping of similar carbon materials.[52, 57, 60, 61] After N-doping, the $E_{onset}$ value of MWCNT shifted 14 mV to positive potentials and the $j_L$ value doubled, whereas GF presented a positive shift of 11 mV and a $j_L$ 1.3 times higher (in magnitude of $j_L$). As nitrogen atoms have a high electronegativity, there may be an increased favourable interaction between $O_2$ molecules promoting the ORR mechanism through a rearrangement of the electronic structure of the neighbouring atoms.[62]

Considering the XPS results in Table 3.1, we cannot directly relate the better performance of MWCNT_N8 with the N%, as both the nitrogen-doped carbon materials present the same total percentage. Therefore, in Table 3S1 are presented the relative atomic percentages of nitrogen of the prepared carbon materials. According to literature, the most active N species for ORR are the pyridinic and quaternary ones. Pyridinic N atoms, due to the electron donated to the conjugated p bond of graphene and to the lone pair of electrons, are known to facilitate reductive oxygen adsorption and thus have been reported to behave as electroactive sites for ORR.[62, 63] Quaternary N is also known to be an electroactive site for ORR.[63, 64] Even though our previous work[65] has shown that the amount of pyridinic nitrogen is positively correlated with the ORR activity in nitrogen-doped carbon materials here it seems that quaternary is more relevant. If we compare MWCNT_N8 and GF_N8, the best performing electrocatalysts is the former presenting higher quaternary- N (16.9%). The same applies for the composite material.

On the other hand, we have the incorporation of POMs which are known for their excellent ORR activity. POMs have multiple redox-active sites that can facilitate electron transfer during ORR. In previous studies, including ours, POMs have been suggested to

interact with nitrogen-doped carbon materials to form composite catalysts that exhibit enhanced ORR activity.

Figure 3.6 (b) depicts the number of electrons transferred per oxygen molecule for the N-doped CM and the respective composites. The results obtained with $P_2W_{17}Fe$@MWCNT_N8 and MWCNT_N8 suggest that the redox processes are very close to being 4-electron ones. On the other hand, $P_2W_{17}Fe$@GF_N8 and GF_N8 participate in a mixed redox process involving 2- and 4-electrons, as confirmed by the $n_{O2}$ values. Based on these parameters, the behaviour after POM immobilization appears to be very similar to the doped-nitrogen carbon materials. A possible explanation is that the active sites arising from the POM immobilisation do not compensate for the eventual loss of N-induced active sites.[39, 52]

In alkaline medium, the oxygen reduction reaction can take either an indirect (2-electron) pathway which involves the reduction of $O_2$ to $HO_2^-$ and then the reduction of the intermediate to $H_2O/HO^-$, or a more desirable process where $O_2$ is directly reduced to $H_2O/HO^-$.[66] Thus, for a more complete examination of the ECs, it is of utmost importance to estimate the percentage of $H_2O_2$ produced during the ORR process. The percentage of $H_2O_2$ produced was calculated using Eq. 4 (SI) at several potential values (Figure 3.6 (c)). The $P_2W_{17}Fe$@MWCNT_N8 composite showed the lowest percentage of $H_2O_2$ produced (33%), which is in accordance with the $n_{O2}$ value obtained ($n_{O2}$ = 3.4). For the $P_2W_{17}Fe$@GF_N8 composite, the values of $H_2O_2$ produced (40%) are also in accordance with the $n_{O2}$ value obtained (3.1). Despite the agreement of the results, care should be taken when a direct comparison between these two methods is made, as both present limitations.[60, 67-70] Firstly, the oxidation process of hydrogen peroxide on the platinum electrocatalyst is not a mass-transfer limited process. And secondly, as can be seen in the SEM images, these prepared electrocatalysts present a rough structure of the support material and a heterogeneity of clusters of the immobilised POM. This may alter the electrode geometry and introduce turbulence in the electrolyte flow, leading to estimated $n_{O2}$ values that may not reflect the actual electrocatalytic performance of the ORR.[52]

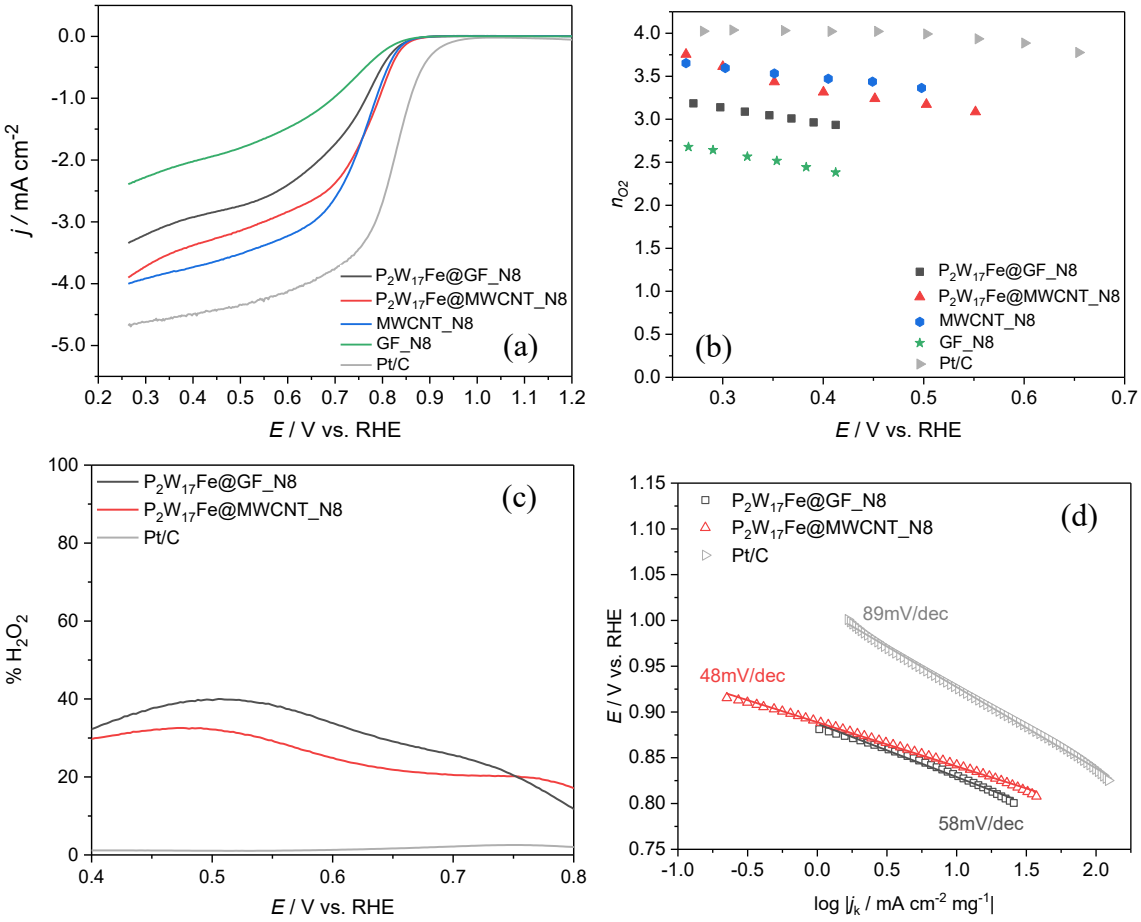



Figure 3.6 - ORR LSV curves acquired using an RDE in $O_2$-saturated KOH solution (0.1 mol $dm^{-3}$) at 1600 rpm and 0.005 V $s^{-1}$ of commercial Pt/C (20 wt %), $P_2W_{17}Fe$@CM nanocomposites and doped-nitrogen carbon materials (a); $n_{O2}$ at several potential values (b); estimated percentage of $H_2O_2$ produced with RRDE for $P_2W_{17}Fe$@CM and Pt/C (20 wt %) in $O_2$-saturated 0.1 mol $dm^{-3}$ KOH solution, at 1600 rpm; the disk potential was swept at v = 0.005 V $s^{-1}$ and the ring potential was kept at E = 0.2 V versus Ag/AgCl (c); ORR Tafel plots for $P_2W_{17}Fe$@CM obtained from LSV data in Figure 3.6 (a) where current densities are normalized to the mass of each ECs (d).

Table 3.2 - Main ORR parameters obtained from polarisation curves recorded in $O_2$-saturated 0.1 mol dm$^{-3}$ KOH solution for the different materials tested.

| Samples | $E_{onset}$ vs RHE (V) | $j_L$ (mA cm$^{-2}$) | Tafel slope (mV dec$^{-1}$) | $n_{O2}$ |
|---|---|---|---|---|
| Pt/C | 0.94 | -4.7 | 89 | 4.0 |
| GF | 0.72 | -2.0 | 63 | 2.4 |
| MWCNT | 0.69 | -2.0 | 54 | 2.1 |
| GF_N8 | 0.83 | -3.3 | 70 | 2.5 |
| MWCNT_N8 | 0.83 | -4.0 | 47 | 3.5 |
| $P_2W_{17}Fe$@GF_N8 | 0.83 | -3.3 | 58 | 3.1 |
| $P_2W_{17}Fe$@MWCNT_N8 | 0.84 | -3.9 | 48 | 3.4 |

In order to get more information about the kinetics of the reaction, the Tafel plots of the prepared nanocomposites and of the Pt/C reference were obtained from the LSV curves in $O_2$-saturated KOH at 1600 rpm and are shown in Figure 3.6 (d). The nanocomposite $P_2W_{17}Fe$@GF_N8 has a slightly higher Tafel slope value (58 mV dec$^{-1}$) when compared with $P_2W_{17}Fe$@MWCNT_N8 (48 mV dec$^{-1}$), but both nanocomposites showed a lower Tafel slope compared with Pt/C (89 mV dec$^{-1}$). These results indicate that oxygen molecules can be easily adsorbed and activated at the surface of these materials. In general, ORR process can follow different mechanisms at high-pH environment. One is the well-known electrocatalytic inner-sphere electron transfer mechanism, where molecular $O_2$ undergoes direct chemisorption on catalyst site leading to a direct/series 4e$^-$ pathway without the desorption of reaction intermediates (such as peroxide) from the surface.[71-73] Normally, on metal-containing materials proceeds through a dissociative 4-electron pathway, due to the adequate adsorption ability for $O_2$. Through this mechanism, $O_2$ is initially adsorbed, followed by the O-O bond break and formation of adsorbed O* species ($O_2 + 2^* \rightarrow 2O^*$, where $^*$ represents a surface catalytic site). Then the specie gains two electrons and two protons and form directly the final product $OH^-$ ($2O^* + 2e^- + 2H_2O \rightarrow 2OH^* + 2OH^-$; $2OH^* + 2e^- \rightarrow 2OH^- + 2^*$).[74]

Our Tafel slope values suggest that for $P_2W_{17}Fe$@CM the global reaction rate is ruled by the conversion of a species $MOO^-$ to MOOH (M is an empty site on the electrocatalyst surface) or by the first discharge step.[39, 52]

The proportional relationship between the double layer capacitance ($C_{dl}$) and the electrochemically active surface areas (ECSA), as well as the similarity between the electrocatalysts used in this study, allows a direct comparison of the obtained $C_{dl}$ values of the composites.[75-78] By performing CV measurements at increasing scan rates, it was possible to estimate $C_{dl}$ values from the slopes of the linear fittings of the CV current densities (measured at the same potential of 1.13 V vs. RHE in a non-faradaic region) reached at different scan rates for the composites and their nitrogen-doped carbon materials (see experimental details in SI file section 1.4 and Figures 3S13 and 3S14). Still, the $C_{dl}$ should be interpreted as an estimation of the number of accessible electrocatalytically active sites for a specific electrocatalyst.[79] Table 3.3 clearly shows an increase in the number of active sites after the immobilization of the POM ($P_2W_{17}Fe$) for both nitrogen-doped carbon materials. This increase is higher for the $P_2W_{17}Fe$@MWCNT_N8 composite, with a composite/carbon support $C_{dl}$ ratio of 3.98 vs. 1.39 for the $P_2W_{17}Fe$@GF_N8.

Table 3.3 - Electrocatalytically active surface area (ECSA) values of the carbon supports and the corresponding POM-based composites.

| CM support | $C_{dl}$ (mF cm$^{-2}$) | Composite | $C_{dl}$ (mF cm$^{-2}$) | Composite/Carbon Support $C_{dl}$ Ratio |
|---|---|---|---|---|
| GF_N8 | 0.0228 | $P_2W_{17}Fe$@GF_N8 | 0.0317 | 1.39 |
| MWCNT_N8 | 0.0203 | $P_2W_{17}Fe$@MWCNT_N8 | 0.0808 | 3.98 |

When evaluating the potential of an electrocatalyst for the ORR, it is of utmost importance to assess its stability. This was carried out by chronoamperometry (CA) at $E$ = 0.46 V vs. RHE for 36000s at 1600 rpm, in oxygen-saturated alkaline electrolyte (Figure 3.7 (a)). The nanocomposite $P_2W_{17}Fe$@MWCNT_N8 showed the best stability with a current retention of 88%, surpassing the value obtained for commercial Pt/C (86%), while $P_2W_{17}Fe$@GF_N8 showed a lower current retention value (68%). The higher current retention obtained for $P_2W_{17}Fe$@MWCNT_N8 may be due to the stronger interaction between the POM and its highly ordered nitrogen-doped MWCNT. Still, the good stability of the composites is mainly due to the trapping of the POM particles in the nano-networks of the carbon materials, avoiding (or at least limiting) their migration, aggregation, and leaching towards the electrolyte, not affecting adversely the corresponding support stabilities. In addition, the high degree of graphitisation and/or ordered wall structure of

carbon materials will reduce a possible degradation of the composite, which can be another cause of the increased durability.[80-82]

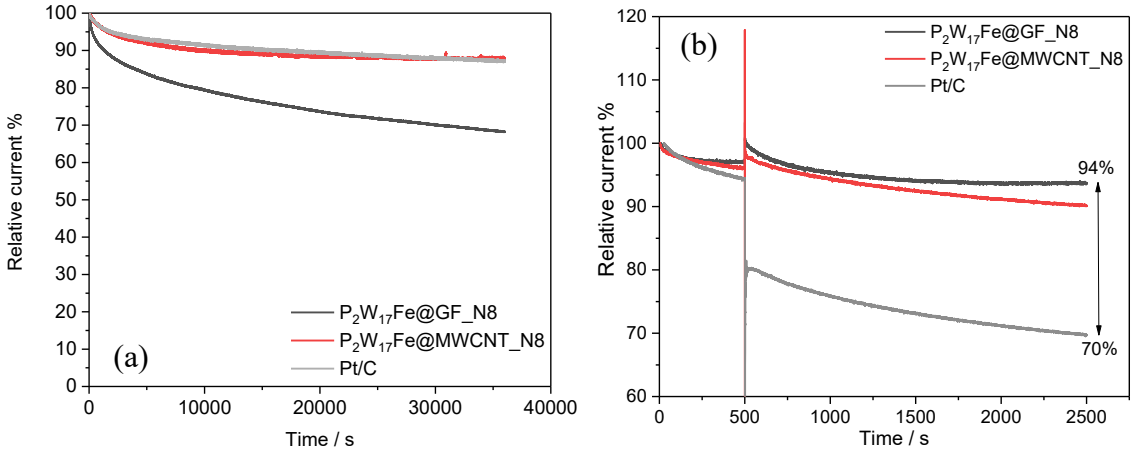



Figure 3.7 - Chronoamperometric response of the ECs at 1600 rpm, in 0.1 mol $dm^{-3}$ $O_2$-saturated KOH at: E = 0.46 V vs. RHE for 36000s (a) and E = 0.46 V vs. RHE with the addition of 0.5 mol $dm^{-3}$ methanol after ≈ 500 s (b).

Methanol is an excellent hydrogen carrier fuel and can also be produced from sustainable and green pathways to allow it to be a carrier of low carbon, and potentially carbon-neutral hydrogen.[83, 84] As such, the study of methanol tolerance of electrocatalysts in methanol fuel cells is extremely important, since the methanol crossover from the anode to the cathode can lead to a drastic drop in the cathodic performance, if the electrocatalysts is sensitive to it.[85] The Pt-based materials have the disadvantage of being highly responsive to the methanol oxidation reaction, despite their better performance in alkaline medium than most of the studied electrocatalysts.[86] This situation affects their performance in the ORR, lowering the current density obtained. Thus, the tolerance of methanol was evaluated by chronoamperometry in $O_2$-saturated 0.1mol $dm^{-3}$ KOH, in the presence of methanol (0.5 mol $dm^{-3}$) for Pt/C and $P_2W_{17}Fe$@CM composites during 2500s (Figure 3.7 (b)). Methanol was added 500s after the beginning of the CA. The Pt/C electrocatalyst retains only ~70% of its initial current density, whereas the composites retain between ~90-94%, being one of the advantages of using this type of materials.

## 3.5. Conclusion

In this work, it was possible to immobilise successfully the Wells-Dawson POM $[P_2W_{17}(FeOH_2)O_{61}]^{7-}$ onto graphene flakes and carbon nanotubes doped with nitrogen

($P_2W_{17}Fe$@GF_N8 and $P_2W_{17}Fe$@MWCNT_N8) without the need for linker molecules. It was proven that both composites were successfully synthesised by several characterisation techniques such as FTIR, XPS, and SEM analysis. The prepared composites showed intrinsic electroactivity towards the ORR in alkaline medium, with onset potential values ranging from 0.83 and 0.84 V *vs.* RHE, low Tafel slopes (47 – 70 mV $dec^{-1}$), and good $j_L$ values (-3.3 – -4.0 mA $cm^{-2}$). Analysis of Koutecky−Levich plots revealed that the ORR process occurs through a mixed electron process for $P_2W_{17}Fe$@GF_N8 and a process involving 4-electrons for $P_2W_{17}Fe$@MWCNT_N8, also confirmed by the results of $\%H_2O_2$ production. The composite $P_2W_{17}Fe$@MWCNT_N8 has demonstrated a sturdy electrocatalytic performance over 36000 s, revealing a high retention value of 88% - surpassing the commercial Pt/C which achieved 86%. Additionally, both composites have an excellent methanol tolerance (90-94%), evincing high selectivity for the ORR, and overcoming one of the major limitations of the Pt/C electrocatalyst. Globally, this study is a step forward towards novel, cheap, and durable electrocatalysts, which are noble metal-free and offer great potential for energy-related reactions.

## 3.6. Supporting information

### 3.6.1. Materials and solvents

The POM salt $K_7[P_2W_{17}(FeOH_2)O_{61}].20H_2O$ was prepared according to the reported procedure.[47]

Potassium hydroxide (> 99%, Sigma-Aldrich), Nafion® at 5 wt. % (lower aliphatic alcohols and water, Sigma-Aldrich), isopropanol (99.5 %, Sigma-Aldrich), sulfuric acid (95–97 %, Merck), platinum 20 % on carbon black (Pt/C, HiSPEC® 3000, Alfa Aesar) were used as received from the suppliers. Commercial graphene (sample denoted as GF) was from Graphene Technologies (Lot #GTX-7/6-10.4.13). Multi-walled carbon nanotubes (sample denoted as MWCNT) were commercially obtained from Nanocyl S.A., Ref. 3100 MWCNT (>95% carbon purity; 9.5 nm average diameter). For electrolyte and composites preparation, ultrapure water (18.2 MΩ cm at 25ºC, Interlab) was always used.

### 3.6.2. Physicochemical characterization

A Jasco FT/IR-460 Plus spectrophotometer was used to acquire the Fourier-transformed infrared (FTIR) spectra (64 scans, resolution of 4 $cm^{-1}$, between 400 and 4000 $cm^{-1}$). The spectra were obtained for samples dispersed (0.2 wt. %) in KBr pellets (spectroscopic grade, Merck).

X-ray photoelectron spectroscopy (XPS) measurements were performed at "Centro de Materiais da Universidade do Porto" (CEMUP), Portugal, in a VG Scientific ESCALAB 200A spectrometer with non-monochromatized Al Kα radiation (1486.6 eV). Potential deviations induced by electric charge of the samples were corrected using the C 1s band at 284.6 eV as an internal standard. The high-resolution spectra analysis and deconvolution was performed with the CasaXPS software.

The scanning electron microscopy/energy-dispersive X-ray spectroscopy (SEM/EDX) images were acquired using a high resolution (Schottky) environmental SEM with X-ray microanalysis and electron backscattered diffraction analysis (Quanta 400 FEG ESEM/EDAX Genesis X4M), in high-vacuum conditions, at CEMUP.

### 3.6.3. ORR electrochemical tests

An Autolab PGSTAT 302N (EcoChimie B.V.) potentiostat/galvanostat, controlled by the NOVA v2.1 software was employed for the cyclic voltammetry (CV) and linear sweep voltammetry (LSV) studies. The experiments were carried out at room temperature using a conventional three-electrode compartment cell.

A modified glassy carbon rotating disk electrode, RDE (Metrohm, 3 mm diameter) was used as the working electrode while an Ag/AgCl (Metrohm, 3 M KCl) and a carbon rod (Metrohm, 2 mm diameter) were used as reference and counter electrodes, respectively. Prior to modification of the bare electrodes, the RDE was polished with 6, 3 and 1 μM diamond polishing pastes (Buehler) on a MicroCloth polishing pad (BAS), followed by washing with ultrapure water. Then, a 2 × 2.5 μL drop of selected electrocatalyst dispersion was deposited on the RDE and left to dry under an airflow.

For the RDE modification, 1 mg of EC ($P_2W_{17}Fe$@CM or Pt/C) and a mixture of 125 μL of isopropanol, 125 μL of ultrapure water and 20 μL of Nafion (5 wt%) were ultrasonically dispersed for 20 min. The electrochemical tests were carried out in $N_2$- or $O_2$-saturated KOH (0.1 mol $dm^{-3}$). To achieve this, the electrolyte was bubbled for 40 min with the selected gas.

The CV measurements were performed at 0.005 V $s^{-1}$ and the LSV ones at 0.005 V $s^{-1}$ with rotation speeds in the range 400 - 3000 rpm. The ORR current obtained in $N_2$-saturated KOH (0.1 mol $dm^{-3}$) was subtracted from that obtained in $O_2$-saturated KOH.

The chronoamperometry (CA) tests were done at a potential ($E$) of 0.5 V vs. RHE and a rotation speed of 1600 rpm for 36000 s. Resistance to methanol was evaluated by CA at $E$ = 0.5 V vs. RHE and 1600 rpm for 2500 s.

The onset potential ($E_{onset}$) is defined as the potential at which the reduction of $O_2$ begins and it was determined as described in the literature. [44] The electrochemical potentials and the $E_{onset}$ values determined vs. Ag/AgCl were converted to the reversible hydrogen electrode (RHE) using the following equation:

$$E_{(RHE)} = E_{(Ag/AgCl)} + 0.059\,pH + E^{o}_{(Ag/AgCl)} \quad (3.1)$$

where $E_{(RHE)}$ is the potential vs. RHE, $E^{o}_{(Ag/AgCl)}$ = 0.1976 V (25 ºC) and $E_{(Ag/AgCl)}$ is the potential measured vs. Ag/AgCl.[87]

To analyse the LSV data and the number of electrons transferred per $O_2$ molecule ($n_{O2}$) in the oxygen reduction reaction the Koutecky-Levich (K-L) equation was used:

$$\frac{1}{j} = \frac{1}{j_L} + \frac{1}{j_k} = \frac{1}{B\omega^{1/2}} + \frac{1}{j_k} \quad (3.2)$$

Here, $j$ is the current density measured, $j_L$ the diffusion-limiting current density, $j_k$ the kinetic current density and ω the angular velocity. The parameter $B$ is associated to the diffusion limiting current density expressed by the following equation:

$$B = 0.2 n_{O2} F (D_{O2})^{\frac{2}{3}} v^{-\frac{1}{6}} C_{O2} \quad (3.3)$$

with $F$ = 96 485 C mol$^{-1}$, $D_{O2}$ the $O_2$ diffusion coefficient, $v$ the electrolyte kinematic viscosity and $C_{O2}$ the $O_2$ bulk concentration. For rotation speeds in rpm is adopted a constant 0.2. Additionally, in the electrolyte used KOH (0.1 mol dm$^{-3}$): $D_{O2}$ = 1.95×10$^{-5}$ cm$^2$ s$^{-1}$, $v$ = 0.008977 cm$^2$ s$^{-1}$ and $C_{O2}$ = 1.15×10$^{-3}$ mol dm$^{-3}$. [88]

Tafel plots ($E_{(RHE)}$ vs. log $j_k$) were obtained after the measured LSV currents were rectified for diffusion to yield the corresponding kinetic current values. The $j_L$ parameter, determined combining equations (3.2) and (3.3), was used to make the mass transport correction. The values of $j$k obtained were normalized for the total deposited mass of EC.

Tests with a rotating ring disk electrode (RRDE) were performed as well for a more complete examination of the ECs. The electrode was polished for 15 min with aluminium oxide 0.3 μm and washed with ultrapure water. The LSV experiments were conducted at 0.005 V s$^{-1}$ and1600 rpm in $O_2$-saturated KOH. A constant potential of 1.2 V vs RHE was applied at the Pt ring electrode. The percentage of $H_2O_2$ produced was calculated from Eq. 3.4 below, using the currents measured on the ring ($i_R$) and on the disk ($i_D$) electrodes, and the current collection efficiency of the ring ($N$).[89]

$$\%H_2O_2 = 200 \times \frac{\frac{i_R}{N}}{i_D + \frac{i_R}{N}} \quad (3.4)$$

### 3.6.4. Assessment of electrochemically active surface areas (ECSA)

ECSA values exhibited by electrocatalysts are usually calculated by using the following equation:

$$ECSA = \frac{C_{dl}}{C_{ref}} \quad (3.5)$$

where $C_{dl}$ stands for the double-layer capacitance and $C_{ref}$ for the reference capacitance value per unit area. Due to the impossibility of knowing the exact $C_{ref}$ value for specific and structurally complex materials, reliable ECSA values cannot be obtained easily. However, the linear proportional relation between ECSA and the double-layer capacitance allows performing a relative comparison for similar electrocatalysts. Taking advantage of this fact, in the present work, $C_{dl}$ values have been directly employed as approximated ECSA estimations to assess the surface effects on the ORR performances. Thus, $C_{dl}$ values were calculated for all materials via a standard double-layer charging test, namely, the acquisition of consecutive CV plots at different scan rates (from 20 to 160 mV $s^{-1}$), being the double-layer capacitance estimated from the slope of a linear-fitted plot of current density at 1.13 V vs. RHE (non-faradaic region) versus the scan rate.

## 3.6.5. Figures

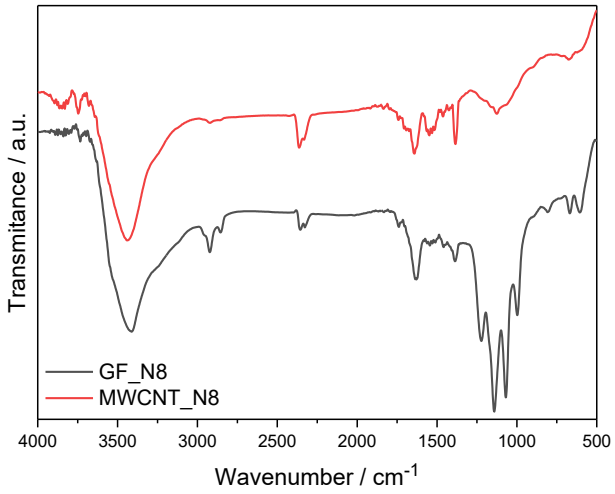



Figure 3S1 - FTIR spectra in the 4000–500 $cm^{-1}$ range of the nitrogen doped carbon materials GF_N8 (black) and MWCNT_N8 (red).

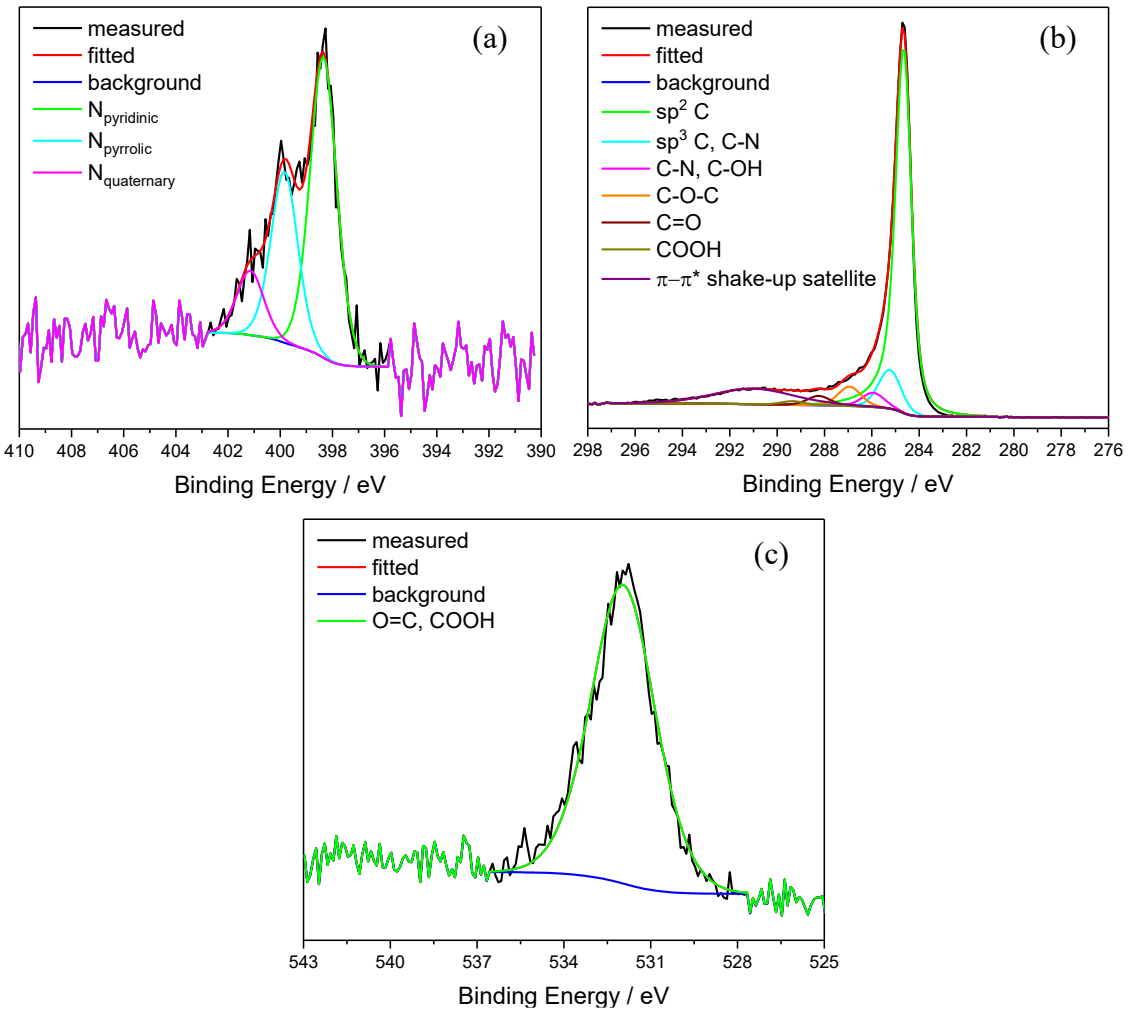



Figure 3S2 - XPS deconvoluted spectra of corresponding elements of the GF_N8.

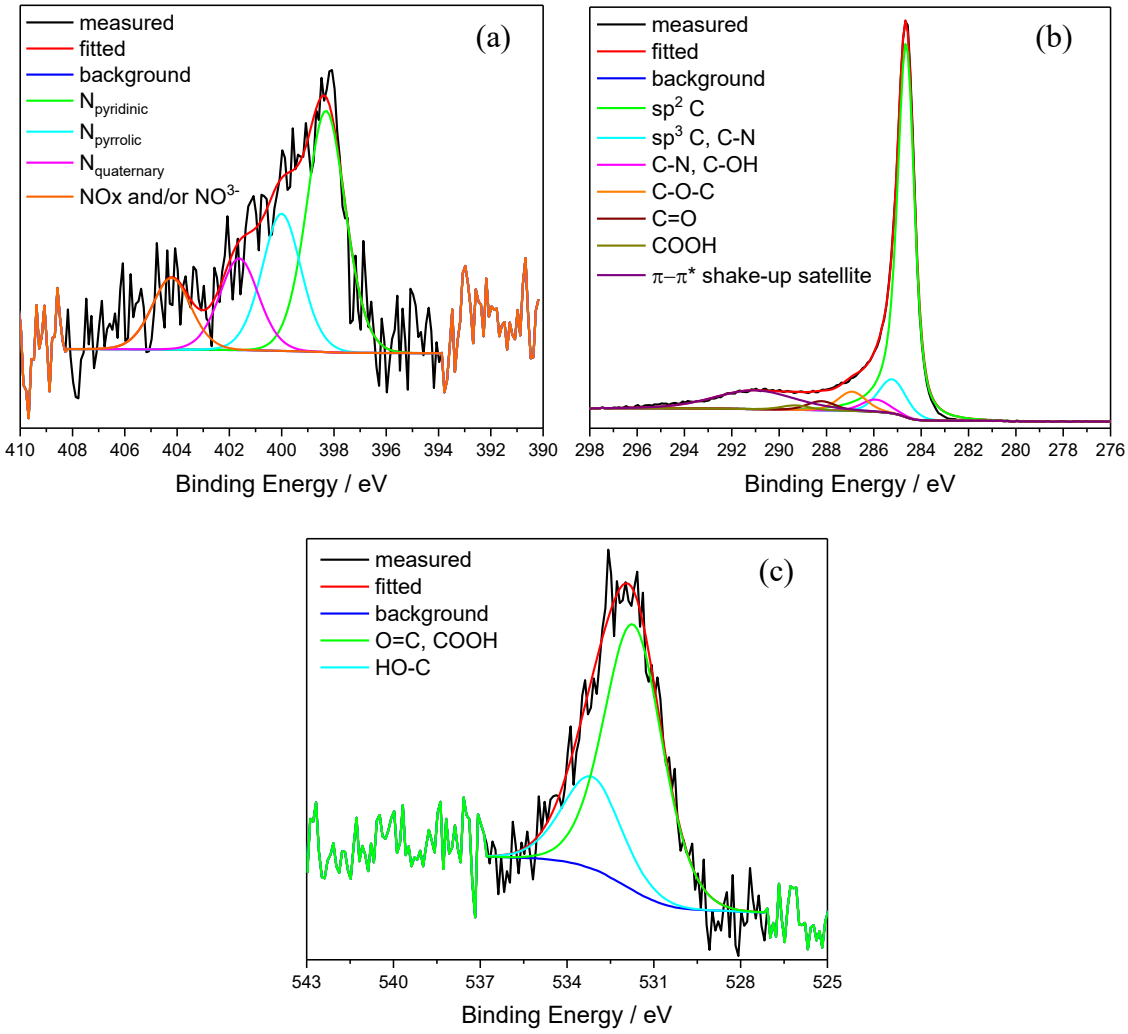



Figure 3S3 - XPS deconvoluted spectra of corresponding elements of the MWCNT_N8.

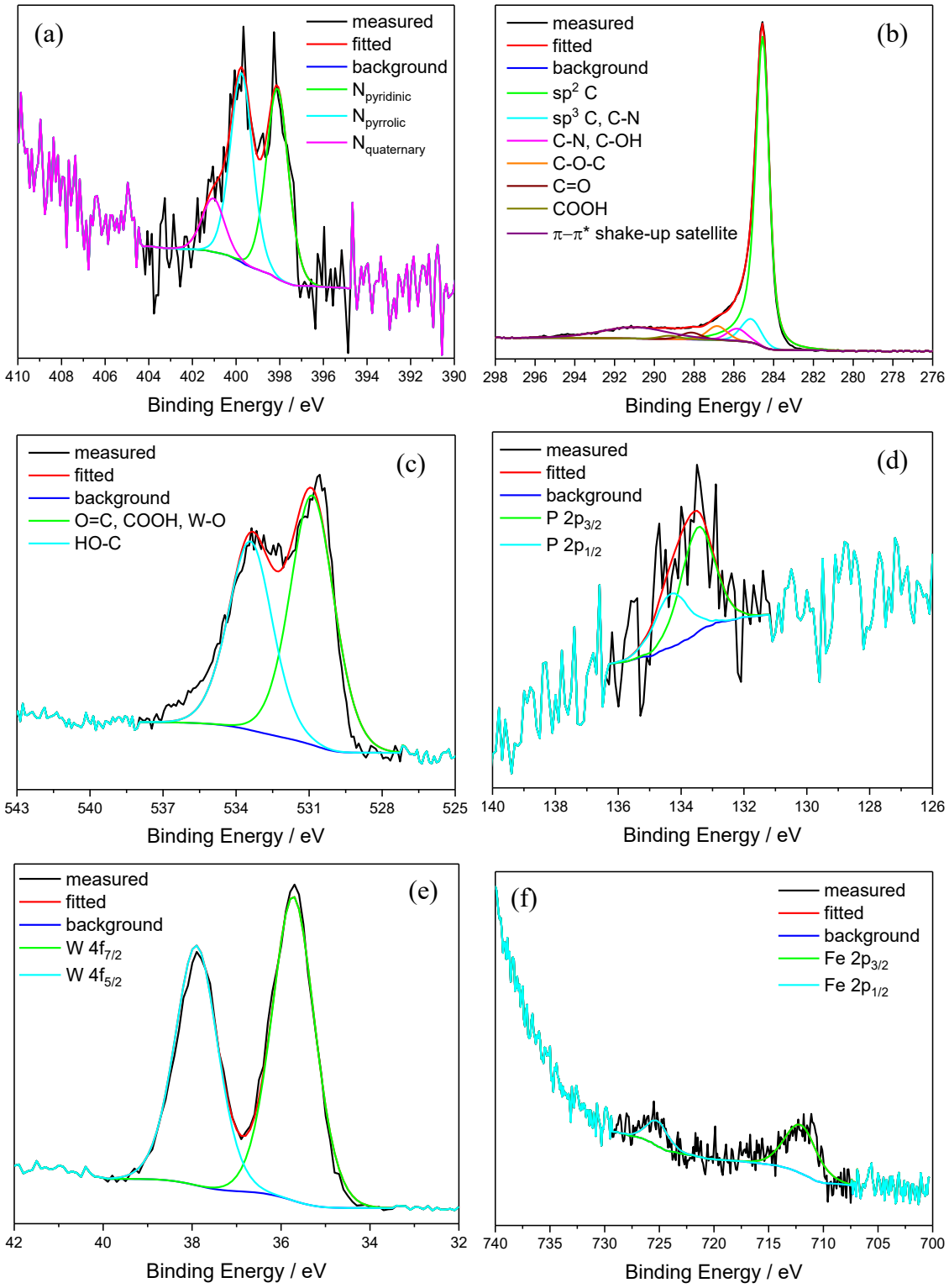



Figure 3S4 - XPS deconvoluted spectra of corresponding elements in the $P_2W_{17}Fe$@GF_N8 composite.

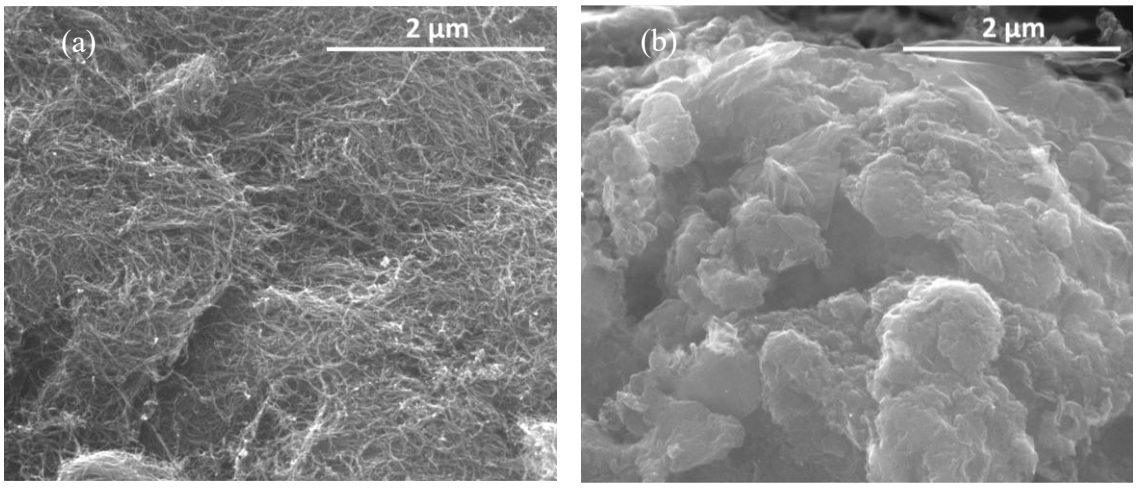



Figure 3S5 - SEM images of MWCNT_N8 (a) and GF_N8 (b) at 50000× magnification.

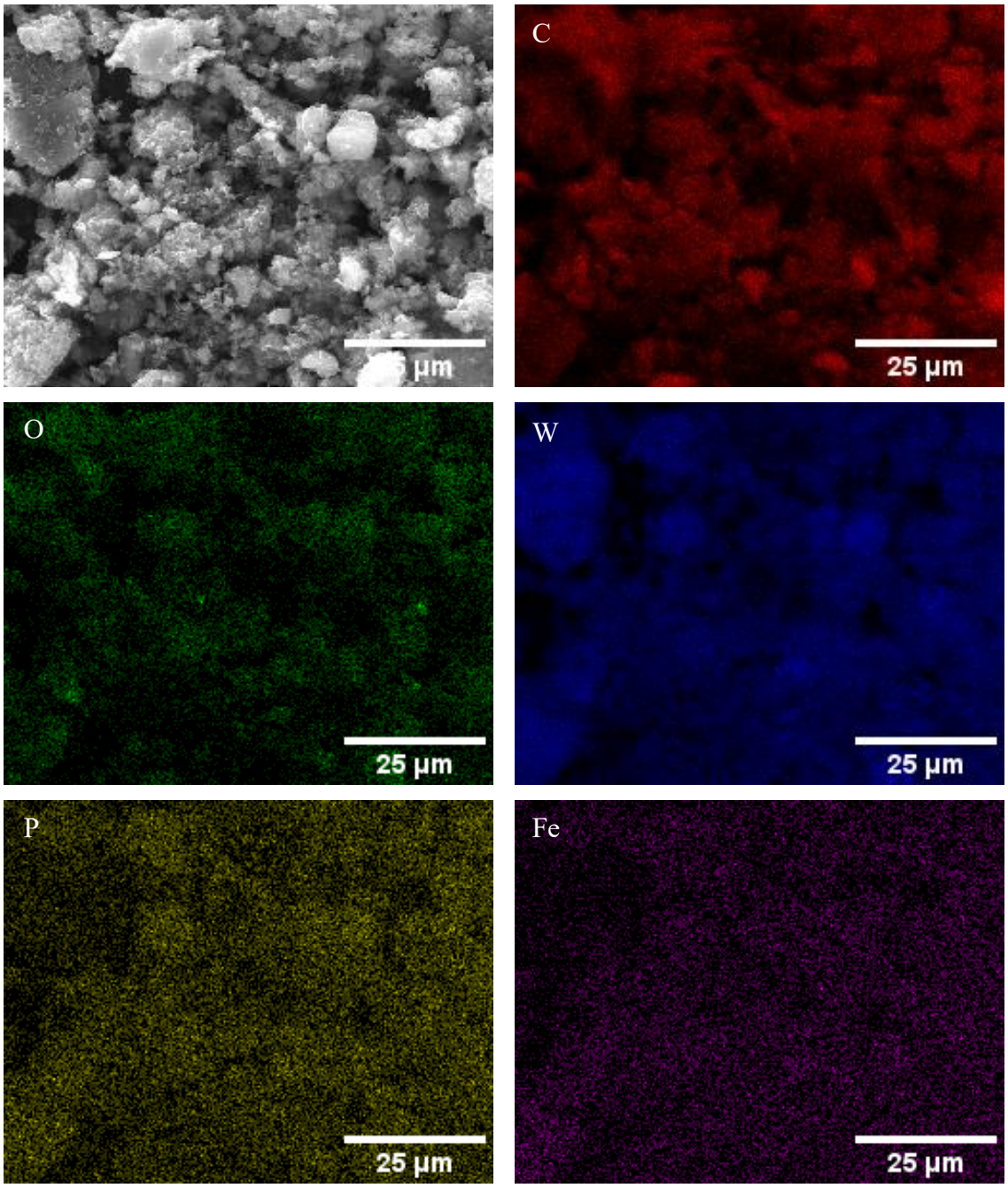



Figure 3S6 - SEM and EDX elemental mapping images of $P_2W_{17}Fe$@GF_N8, at 5000× magnification for the elements C (red), O (green), W (blue), P (yellow) and Fe (purple).

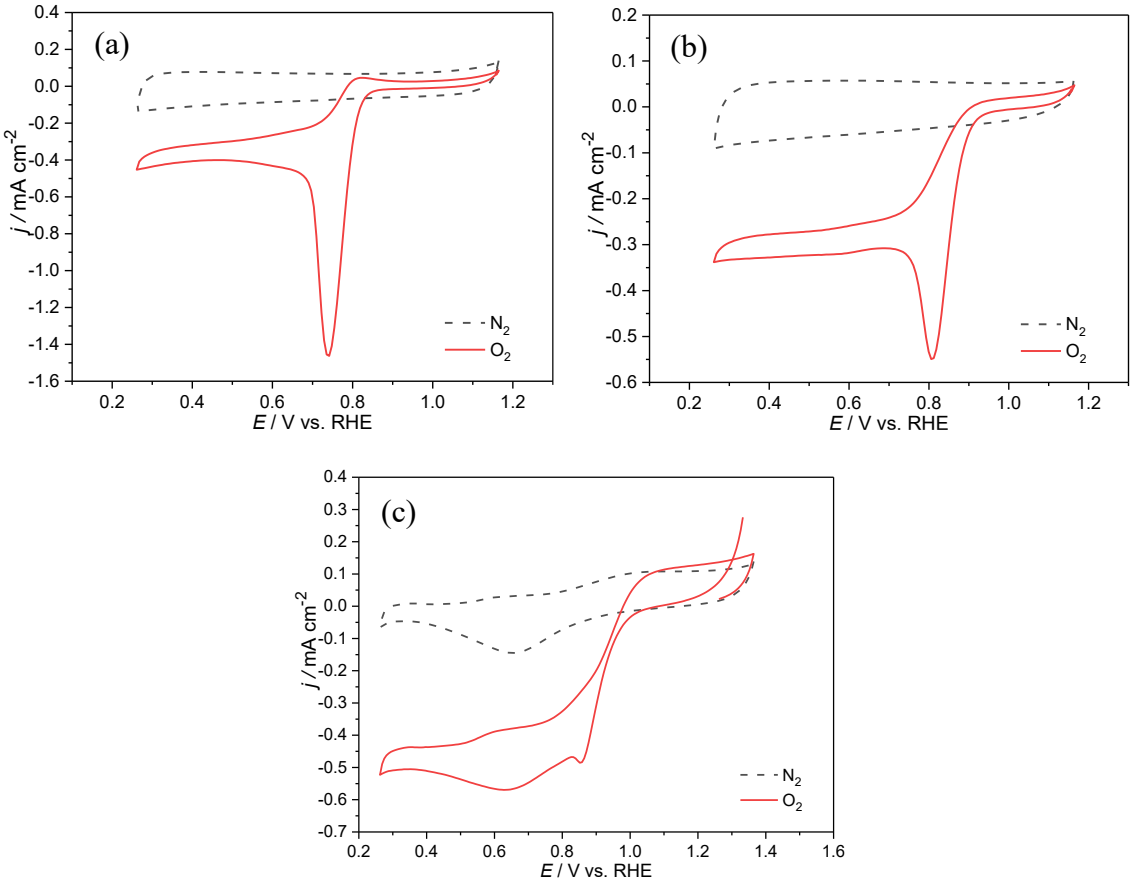



Figure 3S7 - CVs of MWCNT_N8 (a), GF_N8 (b) and Pt/C (20 wt. %) (c) modified electrodes in $N_2$-saturated (dash line) and $O_2$-saturated (full line) 0.1 mol $dm^{-3}$ KOH solution at 0.005 V.

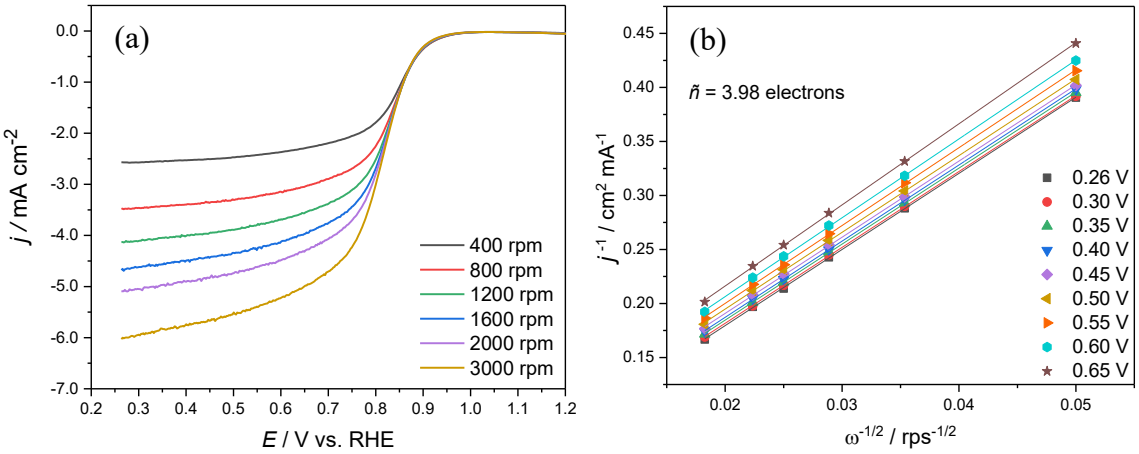



Figure 3S8 - ORR LSV polarization curves for Pt/C (20 wt. %) at different rotation rates in $O_2$-saturated 0.1 mol $dm^{-3}$ KOH solution at 0.005 V $s^{-1}$ (a), and the corresponding Koutecky-Levich (K-L) plots (b).

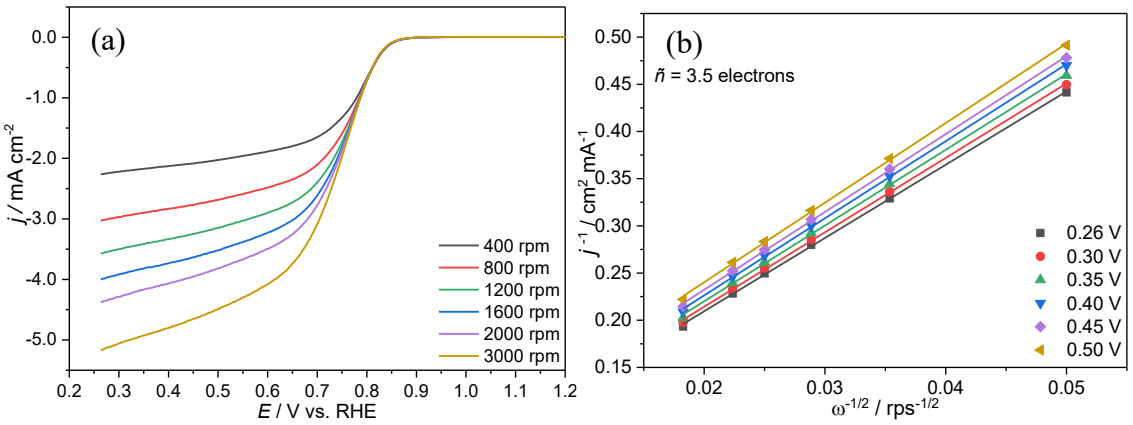



Figure 3S9 - ORR LSV polarization curves for MWCNT_N8 at different rotation rates in $O_2$-saturated 0.1 mol $dm^{-3}$ KOH solution at 0.005 V $s^{-1}$ (a), and the corresponding Koutecky-Levich (K-L) plots (b).

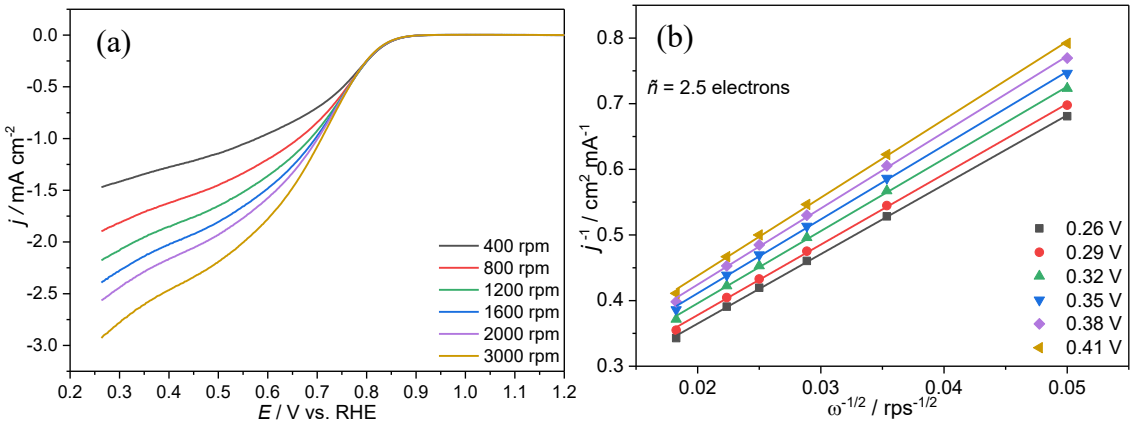



Figure 3S10 - ORR polarization curves for GF_N8 at different rotation rates in $O_2$-saturated 0.1 mol $dm^{-3}$ KOH solution at 0.005 V $s^{-1}$ (a), and the corresponding Koutecky-Levich (K-L) plots (b).

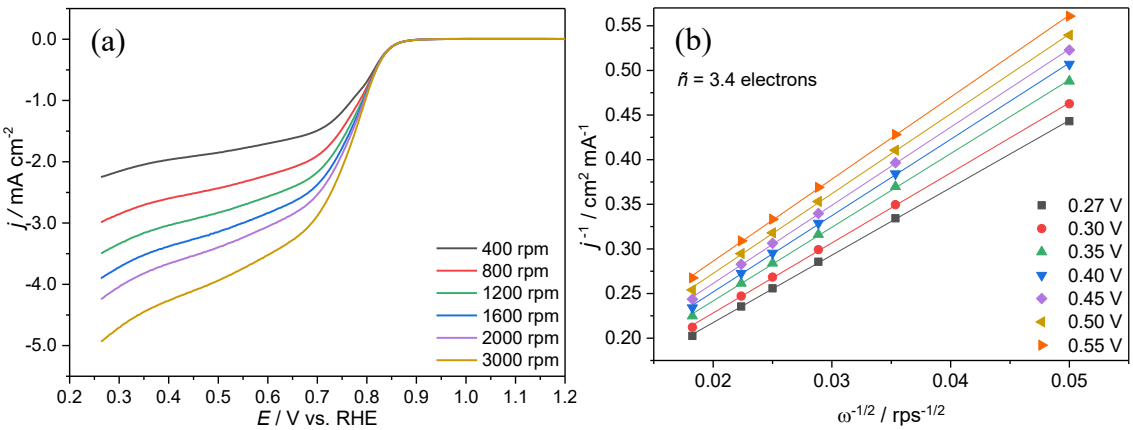



Figure 3S11 - ORR LSV polarization curves for $P_2W_{17}Fe$@MWCNT_N8 at different rotation rates in $O_2$-saturated 0.1 mol $dm^{-3}$ KOH solution at 0.005 V $s^{-1}$ (a), and the corresponding Koutecky-Levich (K-L) plots (b).

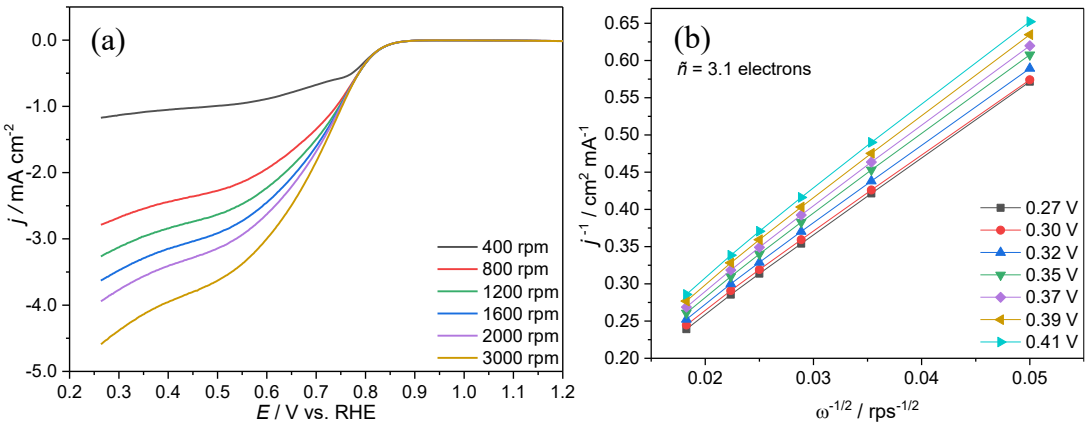
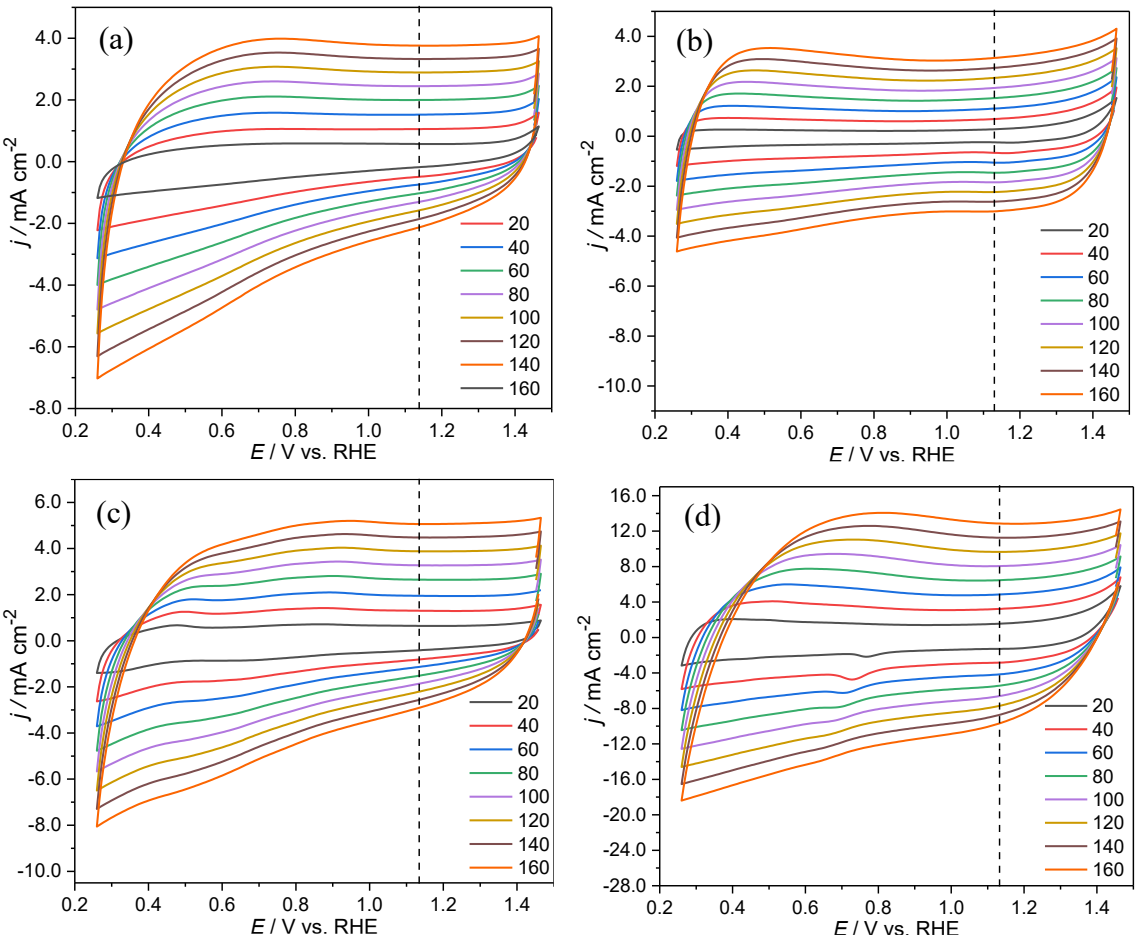



Figure 3S12 - ORR LSV polarization curves for $P_2W_{17}Fe$@GF_N8 at different rotation rates in $O_2$-saturated 0.1 mol $dm^{-3}$ KOH solution at 0.005 V $s^{-1}$ (a), and the corresponding Koutecky-Levich (K-L) plots (b).



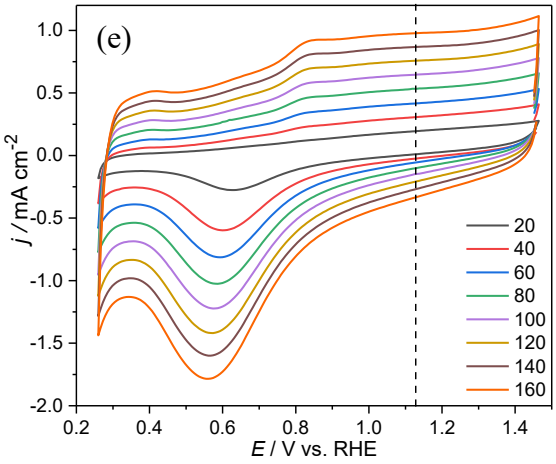



Figure 3S13 - CVs at different scan rates for GF_N8 (a), MWCNT_N8 (b), $P_2W_{17}Fe$@GF_N8 (c), $P_2W_{17}Fe$@MWCNT_N8 (d) and Pt/C (e) in $N_2$-saturated KOH (0.1 M).

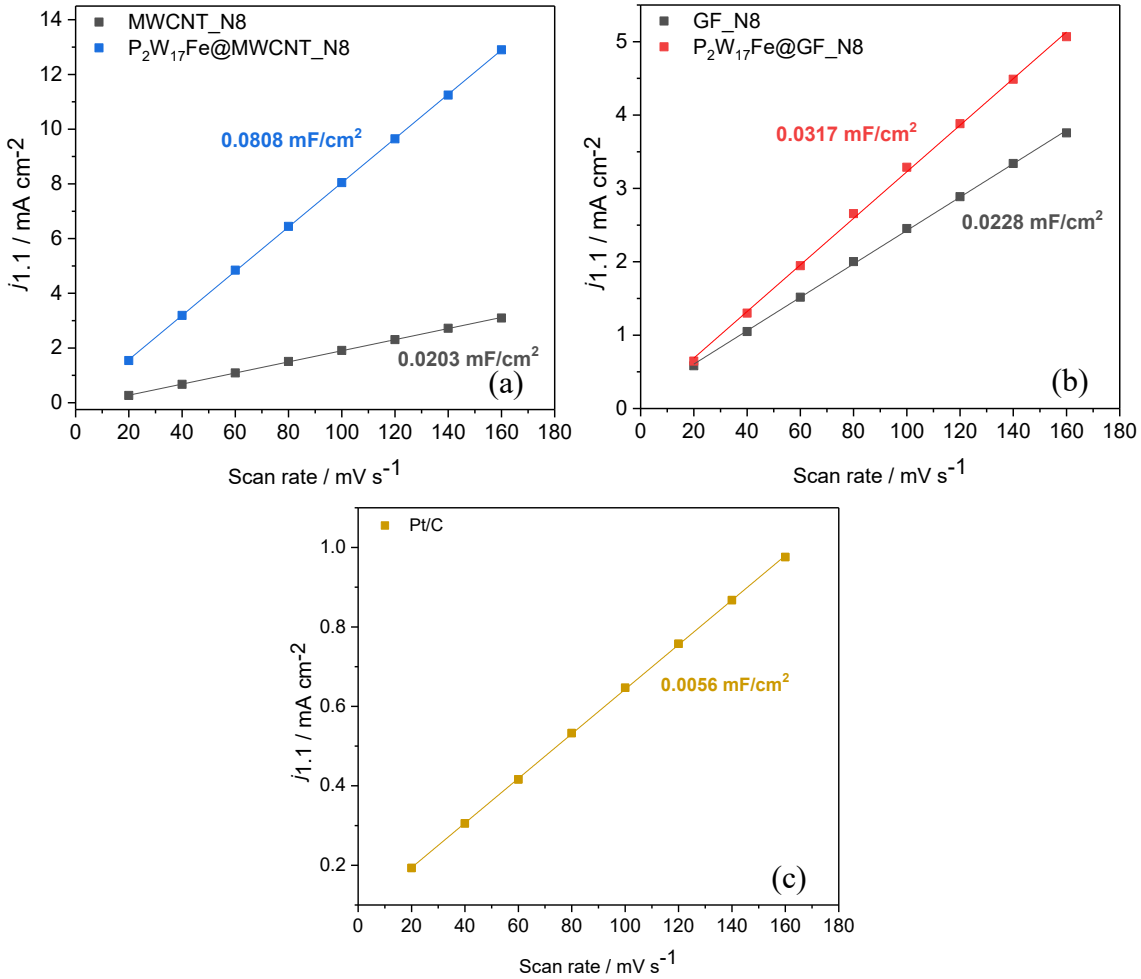



Figure 3S14 - Current density-scan rate linear fitting plots for all materials. Numeric values correspond to the double-layer capacitances ($C_{dl}$) for each material.

Table S3.1 - Relative atomic percentages of nitrogen presented in the XPS high-resolution N1s spectra of the prepared carbon materials.

| **Material** | **% N** | | | |
|---|---|---|---|---|
| | **398.5 eV (pyridinic N)** | **400.1 eV (pyrrolic N)** | **401.6 eV (quaternary N)** | **404.1 eV (N in N-oxides)** |
| **GF_N8** | 56.1 | 31.9 | 12.0 | - |
| **MWCNT_N8** | 44.6 | 25.3 | 16.9 | 13.2 |
| **$P_2W_{17}Fe$@GF_N8** | 44.0 | 43.6 | 12.4 | - |
| **$P_2W_{17}Fe$ @MWCNT_N8** | 41.2 | 26.7 | 23.8 | 8.3 |

Table S3.2 - ORR performance of transition metal carbon hybrid electrocatalysts obtained from literature.

| Catalyst | $E_{onset}$ (mV vs. RHE) | $j_L$ (mA/cm$^2$) | TS (mV/dec) | Stability[a] | Reference |
|---|---|---|---|---|---|
| $P_8W_{48}$@N-MWCNT | 0.94 | -3.7 | 72 | 82% (10h) | [65] |
| $Co_4(PW_9)_2$@N-CNT | 0.90 | -8.5 | 96 | 78% (5.5h) | [90] |
| N-PC[b] | 0.94 | - | 63 | 81.4% (10h) | [91] |
| CoPOM@C | 1.00 | -4.2 | 65 | - | [92] |
| $AC_1$[c] | 0.84 | -3.12 | 250 | ~80% (5.5h) | [93] |
| $PMo_{11}V$@GF | 0.80 | -1.60 | 177 | - | [94] |
| MWCNT_N8_$Co_4$ | 0.85 | -3.52 | 41 | ~75% (5.5h) | [95] |
| $Fe_3O_4$/N/C | 0.92 | - | - | 90% (2.8h) | [96] |
| $NiCo_2O_4$/NrGO | 0.88 | - | - | 87% (2h) | [97] |
| $FeP/Fe_2P/Fe_2P_2O_7$/C | 0.86 | - | - | 87% (12h) | [98] |
| $CuCo_2O_4$/NrGO | 0.89 | - | - | 85% (5.6h) | [99] |
| Fe-N-C | 0.96 | - | - | - | [100] |
| Fe-bNCNT/NC-900 | 1.02 | - | 57 | 89% (11.1h) | [101] |
| $P_2W_{17}Fe$@GF_N8 | 0.83 | -3.3 | 58 | 68% (10h) | This work |
| $P_2W_{17}Fe$@MWCNT_N8 | 0.84 | -3.9 | 48 | 88% (10h) | This work |

[a] The percentages are of current retention and between bracket is the time; [b] N-doped porous carbon; [c]Biomass residue (Agave sisalana).

## 3.7. Declarations

**Authors' contributions:** The synthesis and characterisation of the POM was performed by I.-M.M. and A.-L.T., MWCNT_N8 and GF_N8 by B.J., composite materials by H.C.N., D.M.F, and B.J. The electrocatalytic experiments were conducted by H.C.N. The research was supervised by D.M.F. and C.F.. H.C.N was responsible for writing up the manuscript, which was proofread by D.M.F and P.d.O. All authors have read and agreed to the published version of the manuscript.

**Funding:** This work was financially supported by: Project UNIRCELL POCI-01-0145-FEDER-16422, funded by FEEI through Programa operacional Competitividade e Internacionalização-COMPETE2020 and by national funds through FCT - Fundação para a Ciência e a Tecnologia, I.P.

**Acknowledgments:** Thanks are also due to PT national funds FCT/MCTES through the projects UIDB/50006/2020, UIDP/50006/2020 as well as to Campus France—project PHC Pessoa 42341RM (O2@nanoCPOM). Thanks are also due to the FCT project FOAM4ENER PTDC/QUI-ELT/28299/2017. H.C.N. thanks the FCT through ChemMat program for his PhD grant PD/BD/143095/2018. D.M.F. thanks FCT/MCTES for funding through the Individual Call to Scientific Employment Stimulus (2021.00771.CEECIND/CP1662/CT0007). I.-M M., A.-L.T. and P.d.O. thank the CNRS (namely its IEA programme) and the Université Paris-Saclay for financial support.

**Conflict of interest:** The authors declare that they have no conflict of interest.

## 3.8. References

[1] F Perera (2018) International journal of environmental research and public health 15: 16.

[2] Y Nie, L Li, Z Wei (2015) Chemical Society Reviews 44: 2168. Doi:10.1039/C4CS00484A

[3] J Stacy, YN Regmi, B Leonard, M Fan (2017) Renewable and Sustainable Energy Reviews 69: 401. Doi:https://doi.org/10.1016/j.rser.2016.09.135

[4] W Xia, A Mahmood, Z Liang, R Zou, S Guo (2016) Angewandte Chemie International Edition 55: 2650. Doi:https://doi.org/10.1002/anie.201504830

[5] M Kuang, G Zheng (2016) Small 12: 5656.

[6] M Lefèvre, E Proietti, F Jaouen, J-P Dodelet (2009) science 324: 71.

[7] VR Stamenkovic, BS Mun, KJJ Mayrhofer, PN Ross, NM Markovic (2006) Journal of the American Chemical Society 128: 8813. Doi:10.1021/ja0600476

[8] NM Marković, PN Ross (2002) Surface Science Reports 45: 117. Doi:https://doi.org/10.1016/S0167-5729(01)00022-X

[9] JK Nørskov, T Bligaard, J Rossmeisl, CH Christensen (2009) Nature Chemistry 1: 37. Doi:10.1038/nchem.121

[10] R Cao, J-S Lee, M Liu, J Cho (2012) Advanced Energy Materials 2: 816. Doi:https://doi.org/10.1002/aenm.201200013

[11] R Jasinski (1964) Nature 201: 1212. Doi:10.1038/2011212a0

[12] M-C Kuo, RJ Stanis, JR Ferrell Iii, JA Turner, AM Herring (2007) Electrochimica Acta 52: 2051. Doi:https://doi.org/10.1016/j.electacta.2006.08.015

[13] AM Samsudin, M Bodner, V Hacker (2022) Polymers 14: 3565.

[14] DM Fernandes, AF Peixoto, C Freire (2019) Dalton Transactions 48: 13508. Doi:10.1039/C9DT01691K

[15] EH Yu, K Scott, RW Reeve (2003) Fuel Cells 3: 169. Doi:https://doi.org/10.1002/fuce.200330129

[16] H Yin, S Liu, C Zhang, et al. (2014) ACS Applied Materials & Interfaces 6: 2086. Doi:10.1021/am405164f

[17] FHB Lima, EA Ticianelli (2004) Electrochimica Acta 49: 4091. Doi:https://doi.org/10.1016/j.electacta.2004.04.002

[18] N Todoroki, T Wadayama (2018) Denki kagaku oyobi kōgyō butsuri kagaku 86: 243. Doi:10.5796/electrochemistry.18-00024

[19] S-A Wohlgemuth, RJ White, M-G Willinger, M-M Titirici, M Antonietti (2012) Green Chemistry 14: 1515. Doi:10.1039/C2GC35309A

[20] Y Zheng, Y Jiao, M Jaroniec, Y Jin, SZ Qiao (2012) Small 8: 3550. Doi:https://doi.org/10.1002/smll.201200861

[21] L Qu, Y Liu, J-B Baek, L Dai (2010) ACS Nano 4: 1321. Doi:10.1021/nn901850u

[22] Z Chen, D Higgins, Z Chen (2010) Carbon 48: 3057. Doi:https://doi.org/10.1016/j.carbon.2010.04.038

[23] M Nunes, DM Fernandes, IM Rocha, et al. (2016) ChemistrySelect 1: 6257. Doi:https://doi.org/10.1002/slct.201601370

[24] MK Debe (2012) Nature 486: 43. Doi:10.1038/nature11115

[25] BCH Steele, A Heinzel (2001) Nature 414: 345. Doi:10.1038/35104620

[26] HA Gasteiger, SS Kocha, B Sompalli, FT Wagner (2005) Applied Catalysis B: Environmental 56: 9. Doi:https://doi.org/10.1016/j.apcatb.2004.06.021

[27] H Wang, LR Grabstanowicz, HM Barkholtz, et al. (2019) ACS Energy Letters 4: 2500. Doi:10.1021/acsenergylett.9b01740

[28] X Wang, X Fan, H Lin, et al. (2016) RSC Advances 6: 37965. Doi:10.1039/C6RA04771H

[29] C Freire, DM Fernandes, M Nunes, VK Abdelkader (2018) ChemCatChem 10: 1703. Doi:10.1002/cctc.201701926

[30] M Vikkisk, I Kruusenberg, S Ratso, et al. (2015) RSC Advances 5: 59495.

[31] H Jahnke, M Schönborn, G Zimmermann (1976) Top Curr Chem 61: 133. Doi:10.1007/BFb0046059

[32] S Gupta, D Tryk, I Bae, W Aldred, E Yeager (1989) J Appl Electrochem 19: 19. Doi:Doi 10.1007/Bf01039385

[33] M Lefèvre, E Proietti, F Jaouen, JP Dodelet (2009) Science 324: 71. Doi:10.1126/science.1170051

[34] S Pylypenko, S Mukherjee, TS Olson, P Atanassov (2008) Electrochimica Acta 53: 7875. Doi:https://doi.org/10.1016/j.electacta.2008.05.047

[35] G Wu, KL More, CM Johnston, P Zelenay (2011) Science 332: 443. Doi:10.1126/science.1200832

[36] H Lin, J-W Wang, X-W Guo, et al. (2018) Journal of Materials Chemistry A 6: 24479. Doi:10.1039/C8TA09240K

[37] S Zhang, O Oms, L Hao, et al. (2017) ACS Applied Materials & Interfaces 9: 38486. Doi:10.1021/acsami.7b10989

[38] DM Fernandes, MP Araújo, A Haider, et al. (2018) ChemElectroChem 5: 273. Doi:10.1002/celc.201701210

[39] DM Fernandes, HC Novais, R Bacsa, et al. (2018) Langmuir 34: 6376. Doi:10.1021/acs.langmuir.8b00299

[40] B Jarrais, A Guedes, C Freire (2018) ChemistrySelect 3: 1737. Doi:https://doi.org/10.1002/slct.201702706

[41] A Navaee, A Salimi, S Soltanian, P Servati (2015) Journal of Power Sources 277: 268. Doi:https://doi.org/10.1016/j.jpowsour.2014.11.117

[42] B Olalde, JM Aizpurua, A García, I Bustero, I Obieta, MJ Jurado (2008) The Journal of Physical Chemistry C 112: 10663. Doi:10.1021/jp800266j

[43] DM Fernandes, C Freire (2015) ChemElectroChem 2: 269. Doi:10.1002/celc.201402271

[44] N Daems, X Sheng, IFJ Vankelecom, PP Pescarmona (2014) Journal of Materials Chemistry A 2: 4085. Doi:10.1039/C3TA14043A

[45] DW Lee, L De Los Santos V, JW Seo, et al. (2010) The Journal of Physical Chemistry B 114: 5723. Doi:10.1021/jp1002275

[46] AR Kumarasinghe, L Samaranayake, F Bondino, et al. (2013) The Journal of Physical Chemistry C 117: 9507. Doi:10.1021/jp402428j

[47] DK Lyon, WK Miller, T Novet, et al. (1991) Journal of the American Chemical Society 113: 7209. Doi:10.1021/ja00019a018

[48] A Amiri, HR Saadati-Moshtaghin, FM Zonoz, A Targhoo (2017) Journal of Chromatography A 1483: 64. Doi:https://doi.org/10.1016/j.chroma.2016.12.083

[49] AS Aricò, P Bruce, B Scrosati, J-M Tarascon, W van Schalkwijk (2005) Nature Materials 4: 366. Doi:10.1038/nmat1368

[50] M-C Huang, H Teng (2003) Carbon 41: 951. Doi:https://doi.org/10.1016/S0008-6223(02)00436-0

[51] K Artyushkova, A Serov, S Rojas-Carbonell, P Atanassov (2015) The Journal of Physical Chemistry C 119: 25917. Doi:10.1021/acs.jpcc.5b07653

[52] N Limani, IS Marques, B Jarrais, AJS Fernandes, C Freire, DM Fernandes (2022) Catalysts 12: 357.

[53] H Estrade-Szwarckopf (2004) Carbon 42: 1713. Doi:https://doi.org/10.1016/j.carbon.2004.03.005

[54] ME Lipińska, SLH Rebelo, MFR Pereira, JANF Gomes, C Freire, JL Figueiredo (2012) Carbon 50: 3280. Doi:https://doi.org/10.1016/j.carbon.2011.12.018

[55] W Ai, Z Luo, J Jiang, et al. (2014) Advanced Materials 26: 6186. Doi:https://doi.org/10.1002/adma.201401427

[56] Y Liu, Y Qiao, G Wei, et al. (2018) Energy Storage Materials 11: 274.

[57] HC Novais, B Jarrais, A Haider, et al. (2022) Electrocatalysis. Doi:10.1007/s12678-022-00792-w

[58] S Imar, M Yaqub, C Maccato, et al. (2015) Electrochimica Acta 184: 323. Doi:https://doi.org/10.1016/j.electacta.2015.10.082

[59] X-H Li, W-L Chen, P He, et al. (2019) Inorganic Chemistry Frontiers 6: 3315. Doi:10.1039/C9QI01093A

[60] L Dai, Y Xue, L Qu, H-J Choi, J-B Baek (2015) Chemical Reviews 115: 4823. Doi:10.1021/cr5003563

[61] IM Rocha, OSG Soares, DM Fernandes, C Freire, JL Figueiredo, MFR Pereira (2016) ChemistrySelect 1: 2522.

[62] S Ni, Z Li, J Yang (2012) Nanoscale 4: 1184. Doi:10.1039/C1NR11086A

[63] NP Subramanian, X Li, V Nallathambi, et al. (2009) Journal of Power Sources 188: 38. Doi:https://doi.org/10.1016/j.jpowsour.2008.11.087

[64] DM Fernandes, P Mathumba, AJS Fernandes, EI Iwuoha, C Freire (2019) Electrochimica Acta 319: 72. Doi:https://doi.org/10.1016/j.electacta.2019.06.175

[65] HC Novais, B Jarrais, A Haider, et al. (2023) Electrocatalysis 14: 294.

[66] K Kakaei, MD Esrafili, A Ehsani (2019) in Kakaei K, Esrafili MD, Ehsani A (eds)Interface Science and TechnologyElsevier,

[67] Y Zheng, Y Jiao, L Ge, M Jaroniec, SZ Qiao (2013) Angewandte Chemie 125: 3192.

[68] VK Abdelkader-Fernández, DM Fernandes, L Cunha-Silva, AJ Fernandes, C Freire (2021) Electrochimica Acta 389: 138719.

[69] M Mamlouk, SS Kumar, P Gouerec, K Scott (2011) Journal of Power Sources 196: 7594.

[70] R Zhou, Y Zheng, M Jaroniec, S-Z Qiao (2016) Acs Catalysis 6: 4720.

[71] N Ramaswamy, S Mukerjee (2012) Advances in Physical Chemistry 2012.

[72] S Fletcher (2009) Journal of Solid State Electrochemistry 13: 537. Doi:10.1007/s10008-008-0670-8

[73] C Zúñiga, C Candia-Onfray, R Venegas, et al. (2019) Electrochemistry Communications 102: 78. Doi:https://doi.org/10.1016/j.elecom.2019.04.005

[74] Y Jiao, Y Zheng, M Jaroniec, SZ Qiao (2015) Chemical Society Reviews 44: 2060. Doi:10.1039/C4CS00470A

[75] X Liu, Y Liu, L-Z Fan (2017) Journal of Materials Chemistry A 5: 15310. Doi:10.1039/C7TA04662F

[76] S Liu, Z Wang, S Zhou, et al. (2017) Advanced Materials 29: 1700874.

[77] J Lach, K Wróbel, J Wróbel, P Podsadni, A Czerwiński (2019) Journal of Solid State Electrochemistry 23: 693. Doi:10.1007/s10008-018-04174-5

[78] Y Liang, H Wang, J Zhou, et al. (2012) Journal of the American Chemical Society 134: 3517.

[79] MP Araújo, M Nunes, IM Rocha, MFR Pereira, C Freire (2018) ChemistrySelect 3: 10064. Doi:https://doi.org/10.1002/slct.201802108

[80] Z Lei, W Feng, C Feng, W Zhou, C Wei, X Wang (2017) Journal of Materials Chemistry A 5: 2012. Doi:10.1039/C6TA09887H

[81] Z Wang, Y Lu, Y Yan, et al. (2016) Nano Energy 30: 368. Doi:https://doi.org/10.1016/j.nanoen.2016.10.017

[82] S Xia, W Guo, N Cai, et al. (2021) Fuel Processing Technology 224: 107028. Doi:https://doi.org/10.1016/j.fuproc.2021.107028

[83] GA Olah (2013) Angewandte Chemie International Edition 52: 104. Doi:https://doi.org/10.1002/anie.201204995

[84] A Kumar, P Daw, D Milstein (2022) Chemical Reviews 122: 385. Doi:10.1021/acs.chemrev.1c00412

[85] C Lo Vecchio, D Sebastián, MJ Lázaro, AS Aricò, V Baglio (2018) Catalysts 8: 650.

[86] P Mathumba, DM Fernandes, R Matos, EI Iwuoha, C Freire (2020) Materials 13: 1562.

[87] S Hoang, S Guo, NT Hahn, AJ Bard, CB Mullins (2012) Nano Letters 12: 26. Doi:10.1021/nl2028188

[88] G Tuci, C Zafferoni, A Rossin, et al. (2014) Chemistry of Materials 26: 3460. Doi:10.1021/cm500805c

[89] N Muthuswamy, MEM Buan, JC Walmsley, M Rønning (2018) Catalysis Today 301: 11. Doi:https://doi.org/10.1016/j.cattod.2017.03.045

[90] DM Fernandes, HC Novais, R Bacsa, et al. (2018) Langmuir 34: 6376.

[91] X Chen, W Zhang, Y Qu, X Chen, Y Liu, C Lu (2022) Journal of Electroanalytical Chemistry 926: 116909.

[92] S Ingavale, I Patil, K Prabakaran, A Swami (2021) International Journal of Energy Research 45: 7366.

[93] DM Fernandes, AS Mestre, A Martins, N Nunes, AP Carvalho, C Freire (2020) Catalysis Today 357: 269.

[94] M Nunes, DM Fernandes, IM Rocha, et al. (2016) ChemistrySelect 1: 6257.

[95] N Limani, IS Marques, B Jarrais, AJ Fernandes, C Freire, DM Fernandes (2022) Catalysts 12: 357.

[96] Y Su, H Jiang, Y Zhu, et al. (2014) Journal of Materials Chemistry A 2: 7281.

[97] H Zhang, H Li, H Wang, et al. (2015) Journal of Power Sources 280: 640.

[98] Z Yang, J Wu, X Zheng, Z Wang, R Yang (2015) Journal of Power Sources 277: 161.

[99] R Ning, J Tian, AM Asiri, AH Qusti, AO Al-Youbi, X Sun (2013) Langmuir 29: 13146.

[100] MM Hossen, K Artyushkova, P Atanassov, A Serov (2018) Journal of Power Sources 375: 214.

[101] F Lu, K Fan, L Cui, et al. (2022) Applied Catalysis B: Environmental 313: 121464. Doi:https://doi.org/10.1016/j.apcatb.2022.121464

Chapter 4

# Enhanced Oxygen Reduction Reaction Activity of the Wells-Dawson Polyoxometalate $P_2W_{12}Mo_6$ Immobilised in Nitrogen and Sulphur-Doped Carbon Nanomaterials

# 4

# Enhanced Oxygen Reduction Reaction Activity of the Wells-Dawson Polyoxometalate $P_2W_{12}Mo_6$ Immobilised in Nitrogen and Sulphur-Doped Carbon Nanomaterials[5,6]

Building upon the benefits of the iron-substituted Wells-Dawson POM hybrids established in the preceding chapter, the next logical step is to expand the complexity of both the polyoxometalate and the doped support. The choice of material for this chapter is motivated by the selection of a molybdenum-substituted POM ($P_2W_{12}Mo_6$), paired with carbon nanomaterials doped with both nitrogen and sulphur. The objective in utilising these new composites is to understand how multi-heteroatom doping alters the electronic environment and synergistic contribution of the support, seeking to maximise the electrochemically active surface area and enhance the overall efficiency during the ORR.

[5] Novais, H.C.; Jarrais, B.; Mbomekallé, I.-M.; Teillout, A.-L.; Oliveira, P.d.; Freire, C.; Fernandes, D.M. Enhanced Oxygen Reduction Reaction Activity of the Wells-Dawson Polyoxometalate P2W12Mo6 Immobilised in Nitrogen and Sulphur-Doped Carbon Nanomaterials. *Chemelectrochem* **11**, (2024). https://doi.org/10.1002/celc.202300622.

[6] Hugo C. Novais' contribution to the publication: synthesis and characterisation of composite materials, electrocatalytic experiments and responsible for writing up the manuscript.

## Abstract

As the world faces an escalating energy crisis, the necessity of adopting alternative energy sources becomes increasingly evident. Despite challenges, the imperative to prioritise these eco-friendly alternatives remains paramount in paving the way for a more sustainable and resilient future for our planet and its inhabitants. The pursuit of sustainable energy sources has brought the oxygen reduction reaction (ORR) into the spotlight as a crucial cathodic reaction in energy-converting systems, notably fuel cells (FCs). These FCs hold tremendous promise in providing an eco-friendly and efficient energy supply. However, the widespread implementation of FCs is hindered by their reliance on expensive and scarce noble metal catalysts, such as platinum (Pt), which pose economic and environmental challenges. Hence, this work reports the preparation, characterisation (FTIR, XPS, SEM and EDX) and application of four composites based on doped-carbon materials (CM) and on the Wells-Dawson POM salt $K_6 \cdot \alpha\text{-}[P_2W_{12}Mo_6O_{62}] \cdot 19H_2O$ ($P_2W_{12}Mo_6$@MWCNT_N8, $P_2W_{12}Mo_6$@MWCNT_N6, $P_2W_{12}Mo_6$@MWCNT_S6, and $P_2W_{12}Mo_6$@GF_S6) as ORR electrocatalysts in alkaline medium (pH = 13). The successful doping of the carbon materials with nitrogen (N) and sulphur (S) and the incorporation of the polyoxometalate were verified through comprehensive structural characterisation. Overall, $P_2W_{12}Mo_6$@MWCNT_N8 exhibited favourable onset potentials of 0.84 V vs. RHE, highlighting its high catalytic activity. Additionally, the catalyst showed excellent tolerance to methanol crossover, retaining 91% of initial current, which is crucial for practical fuel cell applications. Furthermore, the $P_2W_{12}Mo_6$@MWCNT_N8 catalyst showed commendable stability, retaining 81% of its initial current after 36000 seconds at an operating potential of $E$ = 0.46 V vs. RHE. These encouraging results denote the significant potential of this electrocatalyst in advancing sustainable energy conversion technologies.

## 4.1. Introduction

There is an increasing need for sustainable and ecologically friendly energy sources with a more balanced and practical approach to tackling environmental difficulties as civilisations around the world struggle with the repercussions of global environmental concerns.[1, 2] The exploration of alternative clean energy technologies has been sparked by the depletion of traditional fossil fuels and the unfavourable consequences of energy consumption, which emphasise the need to take into account human welfare, economic development, and the potential benefits of technology in

environmental solutions.[3] Among these, fuel cells have emerged as a promising avenue for clean energy conversion, offering a viable solution to mitigate the negative environmental impacts associated with traditional energy sources. The cathode's oxygen reduction reaction stands out as a critical feature of FCs. However, the reaction kinetics are typically slow, presenting a challenge that requires resolution.[4-7] Fuel cells and other energy conversion devices, rely heavily on electrocatalysts (ECs) because they greatly improve the selectivity and efficiency of critical chemical reactions. The ORR's most active ECs, however, are mostly dependent on noble metals like platinum and palladium.[8] While effective, these ECs have several drawbacks, including high cost, low abundance and intolerance to fuel crossover (such as methanol and CO).[8] Therefore, it is imperative to search for other electrocatalysts that can lessen these drawbacks and provide more practical and affordable options. Moreover, the emergence of computational methods has revolutionised the field of solid catalyst design, offering exciting prospects for advancing research in ORR electrocatalysts.[9]

The molybdenum (Mo) based electrocatalyst has shown great promise as a viable alternative to address the sluggish ORR at the cathode, leading to significant improvements in overall ORR performance. However, its use in ORR has been limited by the unfavourable energy level of the Mo d-band for this particular reaction, as well as the lack of a suitable coordination environment.[10] In ORR catalytic activity, the process involves the activation of $O_2$ and the adsorption of reaction intermediates onto the electrocatalyst surface. These interactions are strongly influenced by the geometric and electronic structures of the catalyst.[9,11] The strength of adsorption of oxygen-containing intermediates (O*, OH*, and OOH*) is particularly crucial and depends on the position of the d-band centre for the transition metal in the catalyst.[12-14] The design and employment of composite electrocatalysts has been proposed as a promising way to improve the efficiency of various energy-related reactions. These hybrids combine the exceptional properties of carbon nanomaterials with the high stability and rich redox properties of polyoxometalates (POMs).[15-19] The specific POM used belongs to the Wells-Dawson family ($[(P_2W_{12}Mo_6O_{62})^{6-}$). In particular, the molybdenum-substituted POMs have attracted considerable interest due to their dual ability to act as either oxidation or reduction electrocatalysts.[10]

Promising ORR electrocatalysts have emerged in the form of carbon nanomaterials (CMs), including graphene (GF) and carbon nanotubes (CNT). These materials have remarkable properties such as low cost, high surface area, excellent conductivity, and superior stability.[20] In particular, they have high chemical and thermal stability, desirable electrical properties, significant porosity, and large surface area. Both

nanotubes and graphene have found widespread applications in ORR, serving as metal-free electrocatalysts in alkaline media and as supports for electrocatalysts in hybrid nanocomposites.[15,21-23] In addition, their electrocatalytic activity can be further enhanced by doping with various heteroatoms such as nitrogen, sulphur, and phosphorus.[21, 22, 24-27] By introducing nitrogen and sulphur into the $sp^2$ carbon structure, the electronic properties of the original carbons can be enhanced, resulting in improved electrocatalytic performance for ORR.[28,29] Various nitrogen and sulphur species can be incorporated into the graphitic network, including pyridinic, pyrrolic, graphitic (quaternary) and thiol groups, further enhancing their catalytic activity.[19, 30-34]

Following the pioneering work of Hu e*t al*.[35] and Girault *et al*.[12] our group have demonstrated that hybrids composed of the molybdotungstophosphate polyoxometalate ($P_2W_{12}Mo_6$) considered in this work immobilised in nitrogen and sulphur-doped carbon nanomaterials are active catalysts for the oxygen reduction reaction on modified electrodes. Herein, we report on the preparation of composites based on the incorporation of the Wells-Dawson POM's salt $K_6 \cdot \alpha\text{-}[P_2W_{12}Mo_6O_{62}] \cdot 19H_2O$ onto distinct nitrogen and sulphur-doped carbon materials (sulphur-doped graphene flakes and multi-walled carbon nanotubes, nitrogen-doped multi-walled carbon nanotubes) and their application as ORR electrocatalysts.

## 4.2. Experimental section

### 4.2.1 Materials preparation and characterisation methods

A full description of the materials and solvents used in the preparation of the composites and in the ORR studies can be found in the Supplementary Information (SI). A mixture of 0.60 g of the carbon materials (multi-walled carbon nanotubes and graphene flakes) and 0.26 g of the doping element was prepared using an appropriate precursor (melamine as nitrogen precursor and molecular sulphur as sulphur precursor) via a 5-hour mechanical ball milling procedure utilizing a Retsch MM200 apparatus operating at a consistent frequency of 15 vibrations per second. In the next step, the materials were exposed to a thermal process with a nitrogen flow rate of 100 $cm^3\ min^{-1}$. The temperature was subsequently raised by 10ºC per minute until it reached 800ºC for MWCNT_N8 preparation and 600ºC for MWCNT_N6, MWCNT_S6 and GF_S6 preparation. The attained temperature was then sustained for an hour before the materials were cooled

down to room temperature in a nitrogen atmosphere. Finally, the components were preserved in a desiccator. The $P_2W_{12}Mo_6$@CM composites were then prepared by immobilising $P_2W_{12}Mo_6$ onto previously prepared MWCNT_N8, MWCNT_N6, MWCNT_S6, and GF_S6. The immobilisation of POM was accomplished by mixing a 5 mL $H_2SO_4/Na_2SO_4$ solution (pH = 2.0) containing 50 mg of $P_2W_{12}Mo_6$ with 50 mg of CM in 20 mL of the same solution. The mixture was dispersed for 15 minutes in an ultrasonic bath and then stirred for 2 hours at 400 rpm. The resulting composites were subsequently filtered, washed, and dried at 60°C under vacuum overnight. The composites were labelled as $P_2W_{12}Mo_6$@MWCNT_N8, $P_2W_{12}Mo_6$@MWCNT_N6, $P_2W_{12}Mo_6$@MWCNT_S6, and $P_2W_{12}Mo_6$@GF_S6.

Prior to their utilization in electrocatalytic studies, the composites were characterized using Fourier-transformed infrared spectroscopy (FTIR), scanning electron microscopy (SEM), energy-dispersive X-ray spectroscopy (EDS), and X-ray photoelectron spectroscopy (XPS). The methodologies and instrumentation used for the characterization are expounded in the SI. Electrochemical performances towards ORR were assessed using a conventional 3-electrode system with a PGSTAT 302N potentiostat (Metrohm Autolab B.V., Utrecht, The Netherlands) controlled by NOVA 2.1. Complete details of the electrodes, electrode conditioning, and modification are provided in the SI.

## 4.3. Results and Discussion

### 4.3.1. Materials characterisation

The prepared composite materials were subjected to initial characterisation via infrared spectroscopy, as depicted in Figure 4.1. The nitrogen-doped multi-walled carbon nanotubes synthesised at two different calcination temperatures of 600 and 800ºC (MWCNT_N6 and MWCNT_N8, respectively) as well as sulphur-doped multi-walled carbon nanotubes (MWCNT_S6) and sulphur-doped graphene (GF_S6) at 600ºC were also characterised by FTIR and the spectra are presented in Figure 4S1 (N-doped) and Figure 4S2 (S-doped).

The spectrum of MWCNT_N8 displayed several vibrational bands at 3436, 2928, 2846, 1641, 1383, and 1124 $cm^{-1}$, even though some of these bands were weak and poorly resolved. This may be attributed to the low loading of POMs on the carbon material or their interaction with the graphene and carbon nanotube matrix, which may impede

their detection. The OH groups' vibrational bands appeared at 3436 $cm^{-1}$, resulting from the O-H stretching and bending modes from adsorbed residual water and hydroxyl groups.[36, 37] The C-N stretching vibration band appeared at 1383 $cm^{-1}$ [38, 39], and the band at 1124 $cm^{-1}$ was assigned to the phenolic groups' vibration modes.[39, 41] The bands at 2928 and 2846 $cm^{-1}$ corresponded, respectively, to the C–H stretching modes, which may be attributed to the presence of defects in the $sp^2$ hybridised domains. Additionally, the band at 1641 $cm^{-1}$ could be attributed to the C=N and the C=O stretching mode of the carboxylic acid, carbonyl, ketone, and quinone groups.[36, 38, 41] Our results show that MWCNTs doped with nitrogen at 600°C (MWCNT_N6) exhibit similar vibrational bands to those of MWCNTs doped with nitrogen at 800°C (MWCNT_N8). However, it is observed mainly two additional vibrational bands in the spectra of MWCNT_N6: a C=O stretching mode at 1710 $cm^{-1}$ and a C-N stretching mode at 1224 $cm^{-1}$. The presence of the C=O stretching mode in the spectrum of MWCNT_N6 indicates the presence of carboxylic acid, carbonyl, ketone or quinone groups.[36, 42] The C-N stretching mode at 1224 $cm^{-1}$ suggests the presence of amine or amide groups, which are also likely introduced during the nitrogen doping process.[36, 42]

In the FTIR analysis of sulphur-doped carbon nanomaterials, it is important to consider the potential overlap of vibrational bands associated with sulphur and carbon bonds. Due to the presence of sulphur atoms in the carbon nanotube structure, certain vibrational modes may exhibit overlapping peaks, making it challenging to directly assign specific bands to either sulphur or carbon bonds based solely on their positions. The FTIR spectrum of sulphur-doped multi-walled carbon nanotubes (MWCNT_S6), as such, is expected to show similar vibrational bands as those of nitrogen-doped MWCNTs, but with some differences due to the presence of sulphur. MWCNT_S6 (Figure 4S2 black line) shows vibrational bands assigned to O-H stretching and bending modes at ~ 3436 and 1363 $cm^{-1}$, respectively.[36, 43, 44] The presence of peaks between 1122 and 1515 $cm^{-1}$ in the FTIR spectrum of sulphonated multi-walled carbon nanotubes can be attributed to the C–S (carbon-sulphur), S=O (sulphone/sulphite) and S–O stretching bonds.[45] Figure 4S2 also shows an intense band at a wavelength of 1224 $cm^{-1}$ which corresponds to the presence of the S–O vibration related to the absorption of sulphonate.[46] Nevertheless, the band at 1118 $cm^{-1}$ may be assigned to the phenolic groups' vibration modes[39, 41], and the two bands at 2921 and 2853 $cm^{-1}$ correspond, respectively, to the C–H stretching modes, the band at 1641 $cm^{-1}$ can be attributed to the C=N and the C=O stretching mode of the carboxylic acid, carbonyl, ketone, and quinone groups.[36, 38, 41] Both GF_S6 and MWCNT_S6 exhibit similar vibrational bands related to the presence of sulphur in the nanomaterial and its carbon structure. In

the infrared spectrum of GF_S6 (Figure 4S2 red line), prominent bands are observed at 3434, 2922, 2856, 1639, 1387, and 1135 $cm^{-1}$, which can be attributed to specific molecular vibrations. The O–H stretching and bending modes are observed at approximately 3410 $cm^{-1}$ and 1386 $cm^{-1}$, respectively.[36, 43] The presence of C=N and the C=O stretching vibrations are observed at 1630 $cm^{-1}$, the phenol groups at 1387 $cm^{-1}$ and the C-O stretching vibrations of oxygen groups at 1142 $cm^{-1}$.[36, 38, 43, 47, 48] Furthermore, a band assigned to the C-O-C and C-O stretching modes, along with the C-O-H bending mode, is observed at 1070 $cm^{-1}$.[36, 49, 50] Notably, these bands closely resemble the corresponding bands in the infrared spectrum of MWCNT_S6. The resemblance in the infrared spectra of GF_S6 and MWCNT_S6 suggests the presence of similar sulphur-related functional groups in both materials. These functional groups may include sulphur-oxygen (S=O/S–O) bonds or sulphur-carbon (S–C) bonds.

Figure 4.1 depicts the FTIR spectrum of $P_2W_{12}Mo_6$ (black), wherein the typical vibrational bands associated with polyoxometalates are evident within the range of 1100 to 700 $cm^{-1}$. The band observed at 1088 $cm^{-1}$ is attributed to the splitting of the $\nu_{as}$P-O stretching vibration, while the three vibration bands located at 955, 910, and 781 $cm^{-1}$ correspond to the $\nu_{as}W{=}O_t$, $\nu_{as}W\text{-}O_b\text{-}W$ and $\nu_{as}W\text{-}O_c\text{-}W$ stretching modes (corner and edge sharing W-O-W), respectively.[51, 52] In the infrared spectra of the composites $P_2W_{12}Mo_6$@MWCNT_N6 (red line), $P_2W_{12}Mo_6$@MWCNT_N8 (blue line) and $P_2W_{12}Mo_6$@MWCNT_S6 (green line) and $P_2W_{12}Mo_6$@GF_S6 (purple line), the intensity of the bands appears weaker compared to that of the pure POM spectrum. However, the immobilisation of $P_2W_{12}Mo_6$ onto the carbon materials can still be confirmed. Notably, the bands arising from the nitrogen-doped carbon materials are also observed. Interestingly, the characteristic bands of the POM experience a small shift in the position towards shorter wavelengths upon immobilisation, suggesting potential changes in electron densities or increased repulsive interactions between oxygen atoms on the carbon material surfaces likely to reflect the weakening (stretching) of the W-O bonds.[19, 53, 54]

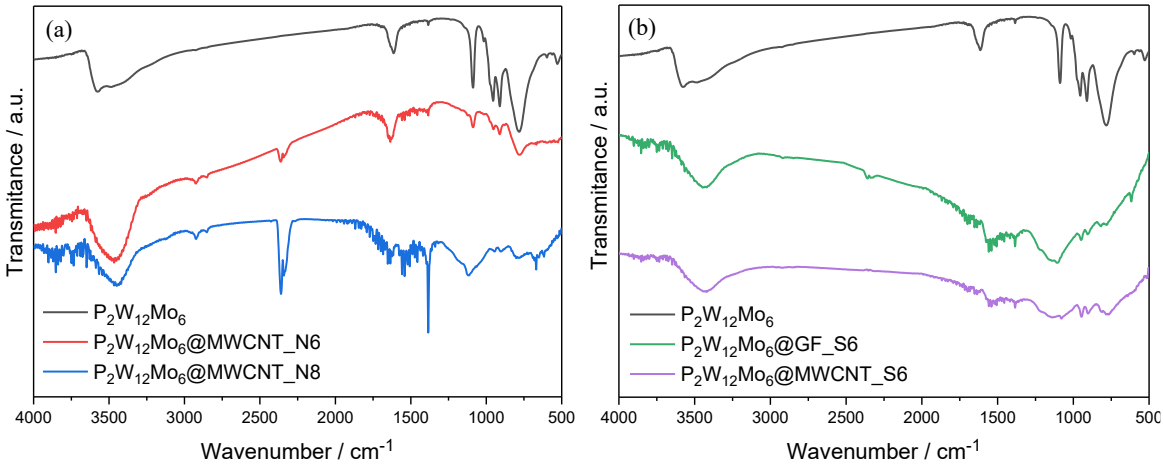



Figure 4.1 - FTIR spectra in the 4000–500 $cm^{-1}$ range of $K_6$·α-[$P_2W_{12}Mo_6O_{62}$]·19$H_2O$ (black), and of the composites $P_2W_{12}Mo_6$@MWCNT_N6 (red), $P_2W_{12}Mo_6$@MWCNT_N8 (blue) (a) and $P_2W_{12}Mo_6$@MWCNT_S6 (green) and $P_2W_{12}Mo_6$@GF_S6 (purple) (b).

The XPS characterisation of the initial nitrogen-doped materials, MWCNT_N8 and MWCNT_N6, as well as the sulphur-doped materials, MWCNT_S6 and GF_S6, has been previously reported by Bruno Jarrais et al..[55] However, to facilitate a comprehensive comparison with the composite materials, we present a concise summary of the main peaks observed in the XPS spectra. The relative amounts of the different elements were calculated through the peak areas and are presented in Table 4.1.

The successful incorporation of nitrogen and sulphur in the N, S-doped materials (MWCNT_N6, MWCNT_N8, GF_S6, and MWCNT_S6) was confirmed, validating the effectiveness of the doping procedure. The analysis of the atomic percentages of the composite materials further demonstrated the presence of the POM. Substantial increase in the oxygen percentage was observed following the immobilisation of the POM, providing strong evidence for its presence in the composite materials. Furthermore, following the immobilisation of the POM, the composite materials containing sulphur ($P_2W_{12}Mo_6$@GF_S6 and $P_2W_{12}Mo_6$@MWCNT_S6) exhibited a marginal change in the atomic percentages of S2p, falling well within the range of experimental uncertainty. The observed increase of sulphur in the sample could potentially be linked to its surface heterogeneity, which allowed for the detection of areas with varying concentrations that may have hindered sulphur detection. The coexistence of overlapping N1s and Mo3p peaks presents a notable obstacle in precisely discerning the individual contributions of nitrogen in the XPS analysis. Therefore, discrepancies may

arise in the atomic percentage of nitrogen in the resulting composites when compared to the nitrogen content in the initial materials due to the surface limit of XPS analysis, which analyses depths up to 10 nm.

Table 4.1 - XPS surface atomic percentages for the pristine carbon materials, the doped carbon materials and the prepared composites.

| Material | XPS Atomic %[a] | | | | | | |
|---|---|---|---|---|---|---|---|
| | C1s | O1s | N1s | S2p | P2p | W4f | Mo3d |
| **GF** | 96.8 | 3.2 | - | - | - | - | -- |
| **MWCNT** | 98.9 | 1.1 | - | - | - | - | - |
| **MWCNT_N6** | 94.9 | 3.3 | 1.8 | - | - | - | - |
| **MWCNT_N8** | 98.0 | 1.0 | 1.0 | - | - | - | - |
| **GF_S6** | 96.2 | 2.0 | - | 0.8 | - | - | - |
| **MWCNT_S6** | 98.6 | 0.7 | - | 0.7 | - | - | - |
| **$P_2W_{12}Mo_6$@MWCNT_N6** | 90.2 | 6.1 | 2.7 | - | 0.1 | 0.6 | 0.3 |
| **$P_2W_{12}Mo_6$@MWCNT_N8** | 86.1 | 10.9 | 1.7 | - | 0.2 | 0.6 | 0.5 |
| **$P_2W_{12}Mo_6$@GF_S6** | 91.6 | 6.1 | - | 1.0 | 0.2 | 0.8 | 0.4 |
| **$P_2W_{12}Mo_6$@MWCNT_S6** | 94.2 | 3.9 | - | 0.9 | 0.1 | 0.6 | 0.3 |

[a] Determined by the areas of the respective bands in the high-resolution XPS spectra.

In the Supplementary Information (SI), Figure 4S3 to 4S6 (a) clearly demonstrate the presence of nitrogen and sulphur in the heteroatom-doped carbon materials (MWCNT_N8, MWCNT_N6, MWCNT_S6, and GF_S6). This observation strongly indicates the successful implementation of the doping procedure. The XPS spectra of the nitrogen-doped carbon materials revealed distinct peaks corresponding to different nitrogen functionalities. Deconvolution of the N1s spectra resulted in three prominent peaks assigned to specific nitrogen species: pyridinic N at ~ 398.3 eV, pyrrolic N at ~ 400.0 eV, and quaternary N at ~ 401.6 eV.[19, 56, 57] Additionally, a fourth peak observed at 404.2 eV was attributed to nitrogen oxide and/or nitrate species.[19, 33, 56] The relative quantities of these nitrogen functionalities followed a consistent trend across

both N-doped materials (MWCNT_N8 and MWCNT_N6), with increasing proportions in the order: [quaternary N] < [pyrrolic N] < [pyridinic N]. The deconvolution analysis of the S-doped carbon materials, MWCNT_S6 and GF_S6, revealed the presence of characteristic peaks common to both samples. In particular, two peaks observed at ~ 164.1 and ~ 165.3 eV assigned to the doublet of $S2p_{3/2}$ and $S2p_{1/2}$ in thiophene-S, indicating the presence of thiophene-like sulphur functionalities.[55, 58-60] Additionally, a peak identified at ~ 162.3 eV was assigned to thiol groups.[55, 58-60] For material GF_S6, a fourth peak at 166.7 eV was found, which corresponds to sulphate species.[61] These results provide clear evidence of the successful incorporation of sulphur into the carbon matrix of the composite materials, highlighting the specific sulphur species present and their respective chemical environments. The C1s high-resolution spectra (Figure 4S3 to 4S6 (b)) were also subjected to fitting analysis, resulting in the identification of seven distinct peaks. At 284.6 eV, a peak corresponding to the graphitic structure ($sp^2$, C=C) was observed. Then, $sp^3$ hybridised carbon and C-N bonding at ~ 285.2 eV indicated the incorporation of nitrogen in the materials, as seen in MWCNT_N8 and MWCNT_N6, as well the presence of C-S bonding in MWCNT_S6 and GF_S6, alongside the C-N bonding, with additionally peaks at ~ 285.9 eV attributed to C-N/C-S and C-OH bonding. The presence of C-O-C groups was indicated by a peak at ~ 286.9 eV, C=O groups at ~ 288.2 eV encompassing ketones, quinones, and aldehydes, the occurrence of COOH functional groups, including carboxylic acids and esters, was observed at ~ 289.3 eV, and finally, a peak at ~ 291.0 eV was attributed to π–π* transitions.[19, 55, 62] The high-resolution O1s spectra of MWCNT_N6 (Figure 4S4 (c)) did not allow for precise peak deconvolution. However, the peak observed at ~ 532.7 eV was attributed to the contributions of oxygen in the form of C=O, COOH, and C-OH groups.[19] In contrast, the O1s spectra of MWCNT_N8, MWCNT_S6, and GF_S6 (Figure 4S3 (c), 4S5 (c), and 4S6 (c)) showed a distinct two-peak structure upon deconvolution. The first peak, located at ~ 531.7 eV, was attributed to C=O and COOH functionalities and a second peak at ~ 533.1 eV could be attributed to the presence of HO-C species.[19, 38, 55, 63]

The N1s XPS spectrum of the $P_2W_{12}Mo_6$@MWCNT_N8 composite (Figure 4.2 (a)) exhibits four prominent peaks at 398.3, 399.8, 400.0, and 405.2 eV, which are assigned to pyridinic, pyrrolic, quaternary N, and nitrogen oxide and/or nitrate species, respectively.[19, 55, 57, 64, 65] Similarly, the N1s spectrum fitting of the $P_2W_{12}Mo_6$@MWCNT_N6 composite (Figure 4S7 (a)) shows peaks at 398.5, 400.4, 402.8, and 406.3 eV, corresponding to pyridinic, pyrrolic, quaternary N, and nitrogen

oxide and/or nitrate species, respectively. The S2p XPS spectrum of the $P_2W_{12}Mo_6$@MWCNT_S6 composite (Figure 4S8 (a)) reveals distinct peaks at 163.8 and 165.0 eV, corresponding to the $S2p_{3/2}$ and $S2p_{1/2}$ doublet, which can be attributed to the presence of sulphur in thiophene-S.[55, 58-60] Additionally, a peak at 169.0 eV is observed, which corresponds to sulphate species.[61] Similarly, in the case of the $P_2W_{12}Mo_6$@GF_S6 composite (Figure 4S9 (a)), the deconvolution of the S2p spectrum exhibits peaks at 163.9 and 165.1 eV, representing the $S2p_{3/2}$ and $S2p_{1/2}$ doublet, associated with thiophene-S. Furthermore, as for the previous composite, a distinct peak at 168.6 eV is observed, indicative of the presence of sulphate species.

The C1s high-resolution XPS spectra of the $P_2W_{12}Mo_6$@MWCNT_N8, $P_2W_{12}Mo_6$@MWCNT_N6, $P_2W_{12}$Mo6@MWCNT_S6, and $P_2W_{12}Mo_6$@GF_S6 composites are depicted in Figure 4.2 (b) and Figures 4S7-4S9 (b), respectively. Each spectrum displays a total of seven distinct peaks, with the main peak observed at 284.6 eV representing the graphitic structure ($sp^2$, C=C), a peak at around 285.1 eV attributed to $sp^3$ hybridised carbon and C-N bonding, a peak at 285.8 eV assigned to C-N and C-OH bonding, a peak at approximately 286.8 eV attributed to C-O-C groups, a peak at 288.1 eV assigned to C=O groups including ketones, quinones, and aldehydes, a peak at 289.2 eV corresponding to COOH functional groups, namely carboxylic acids and esters, and a peak at 291.0 eV ascribed to π–π* transitions.[19, 55, 62] The similarity between the C1s XPS spectra of $P_2W_{12}Mo_6$@MWCNT_N8, $P_2W_{12}Mo_6$@MWCNT_N6, $P_2W_{12}$Mo6@MWCNT_S6, and $P_2W_{12}Mo_6$@GF_S6 indicates consistent carbon functionalisation patterns in these composite materials.

Figure 4.2 (c) and Figures 4S7-4S9 (c) display the high-resolution O1s spectra for $P_2W_{12}Mo_6$@CM, which has been deconvoluted into two primary peaks: one at 530.7 eV assigned to oxygen in C=O (ketones, quinones, aldehydes) and COOH (carboxylic acids, esters) groups, along with oxygen atoms originating from the POM, and another at 532.7 eV attributed to O in HO-C groups (phenols).[19, 38, 55, 63] These two peaks are also evident in the remaining composites. It is noteworthy that the immobilisation of the POM on the carbon materials led to a significant increase in the percentage of O1s in the final composites. This increase can be attributed to the contribution of the POM to the O1s percentages of the composite materials. The P2p high-resolution spectra of $P_2W_{12}Mo_6$@CM are depicted in Figure 4.2 (d) and Figures 4S7-4S9 (d). The observed peaks exhibit distinct $2p_{3/2}$ and $2p_{1/2}$ doublets, with energies approximately at ~ 133.5 and ~ 134.4 eV, respectively.[19] In Figure 4.2 (e) and Figures 4S7-4S9 (e) the peaks observed in the high-resolution spectra of W4f are attributed to $4f_{7/2}$ (~ 35.6 eV) and $4f_{5/2}$

(~ 37.8 eV), resulting from spin-orbital coupling.[19, 66] Lastly, in Figure 4.2 (f) and Figures 4S7-4S9 (f), the Mo3d spectrum can be divided into $Mo3d_{5/2}$ and $Mo3d_{3/2}$ regions. The dominant doublet (with higher intensity) at ~ 233.0 and ~ 235.7 eV corresponds to the $Mo^{6+}$ oxidation state, while the minor doublet (with lower intensity) at ~ 231.5 and ~ 234.2 eV corresponds to the $Mo^{5+}$ oxidation state.[67,70]

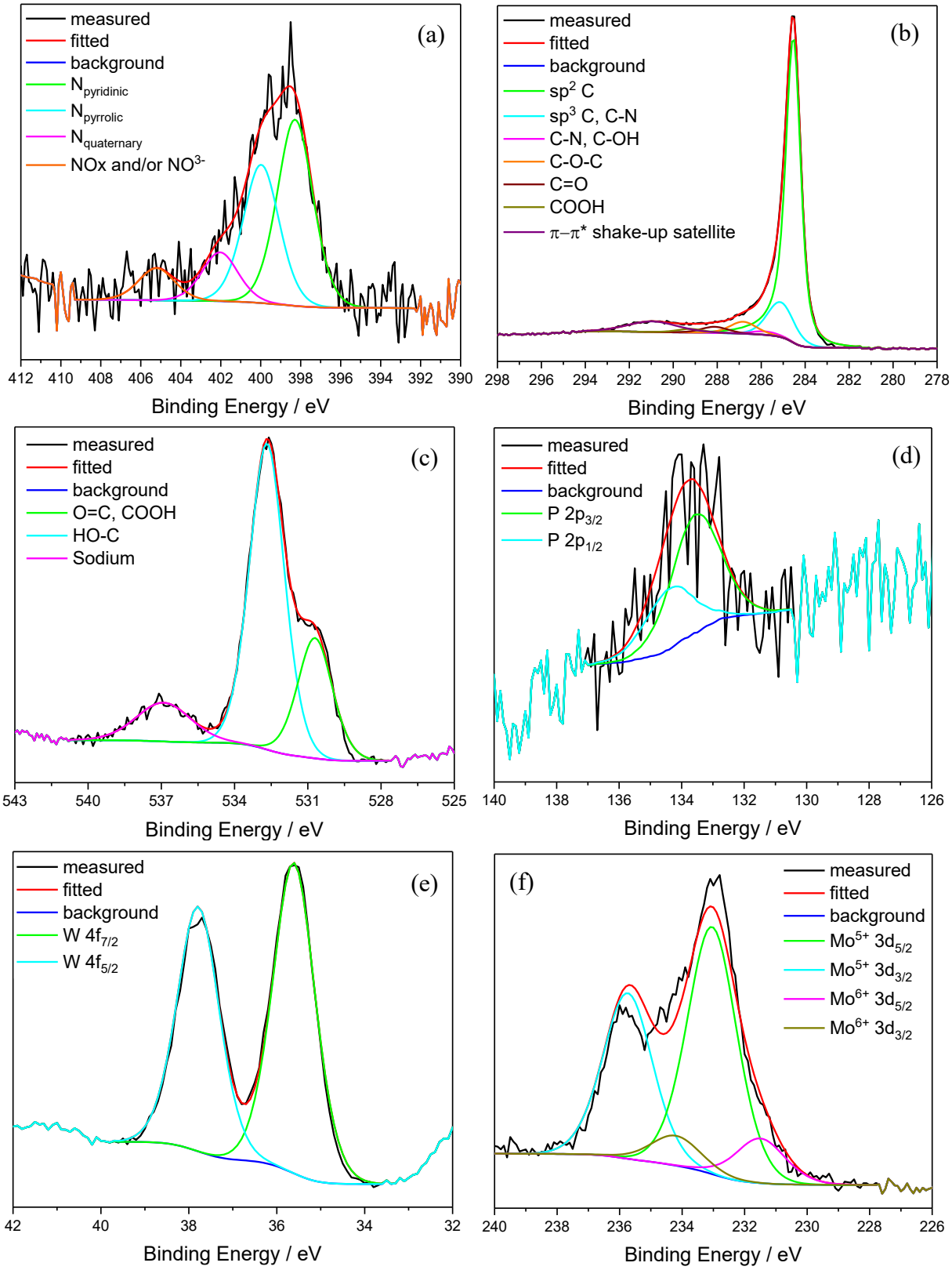



Figure 4.2 - XPS deconvoluted spectra of the corresponding elements of $P_2W_{12}Mo_6$@MWCNT_N8.

The morphology of all the materials was examined using scanning electron microscopy (SEM), and Figure 4.3 displays the SEM images for $P_2W_{12}Mo_6$@MWCNT_N8 (a), $P_2W_{12}Mo_6$@MWCNT_N6 (b), $P_2W_{12}Mo_6$@MWCNT_S6 (c), and $P_2W_{12}Mo_6$@GF_S6 (d) at a magnification of 50,000×. As observed, the morphologies of the composites containing carbon nanotubes ($P_2W_{12}Mo_6$@MWCNT_N8, $P_2W_{12}Mo_6$@MWCNT_N6, and $P_2W_{12}$Mo6@MWCNT_S6) differ significantly from the composite containing graphene ($P_2W_{12}Mo_6$@GF_S6). Those containing carbon nanotubes exhibit a needle-like structure characteristic of multi-walled carbon nanotubes, whereas $P_2W_{12}$Mo6@GF_S6 shows thin and flat flakes of carbon layers. In all composites, lighter micro-sized spots are visible, corresponding to $P_2W_{12}Mo_6$ clusters, contributing to the overall roughened texture. Figure 4.3 (a-c) demonstrate a clear uniformity in the widths of the carbon nanotubes, with diameters ranging between 5 - 22 nm. In Figure 4.3 (d), folded graphene sheets and a smoother texture can be observed. Supplementary Figure 4S10 displays SEM images of MWCNT_N8, MWCNT_N6, MWCNT_S6, and GF_S6, exhibiting similar morphological characteristics as described above.

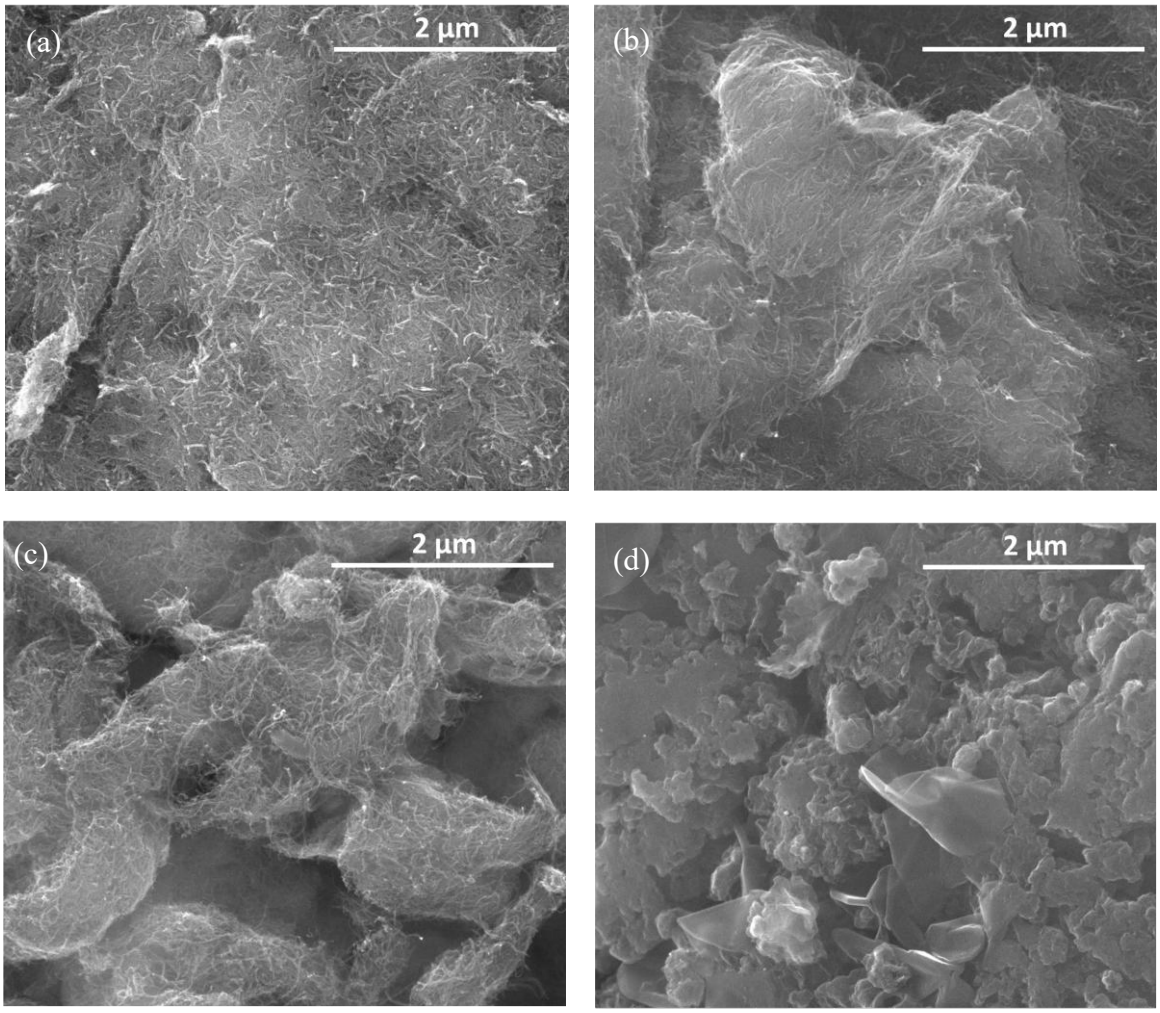



Figure 4.3 - SEM images of $P_2W_{12}Mo_6$@MWCNT_N8 (a), $P_2W_{12}Mo_6$@MWCNT_N6 (b), $P_2W_{12}Mo_6$@MWCNT_S6 (c) and $P_2W_{12}Mo_6$@GF_S6 (d) at 50000× magnification.

EDX elemental mapping was employed to investigate the spatial distribution of $P_2W_{12}Mo_6$ within the composite materials. Figure 4.4 presents the SEM and corresponding elemental mapping images specifically for $P_2W_{12}Mo_6$@MWCNT_N8, while Supplementary Figures 4S11, 4S12, and 4S13 showcase the mapping images for the $P_2W_{12}Mo_6$@MWCNT_N6, $P_2W_{12}Mo_6$@MWCNT_S6, and $P_2W_{12}Mo_6$@GF_S6 composites, respectively. The elemental mapping analysis revealed a homogeneous dispersion of the POM elements (W, P, Mo, and O) throughout the carbon matrix, indicating the successful immobilisation of the POM species. The brighter regions observed in the elemental mapping images correspond to the localised accumulation of $P_2W_{12}Mo_6$ clusters.

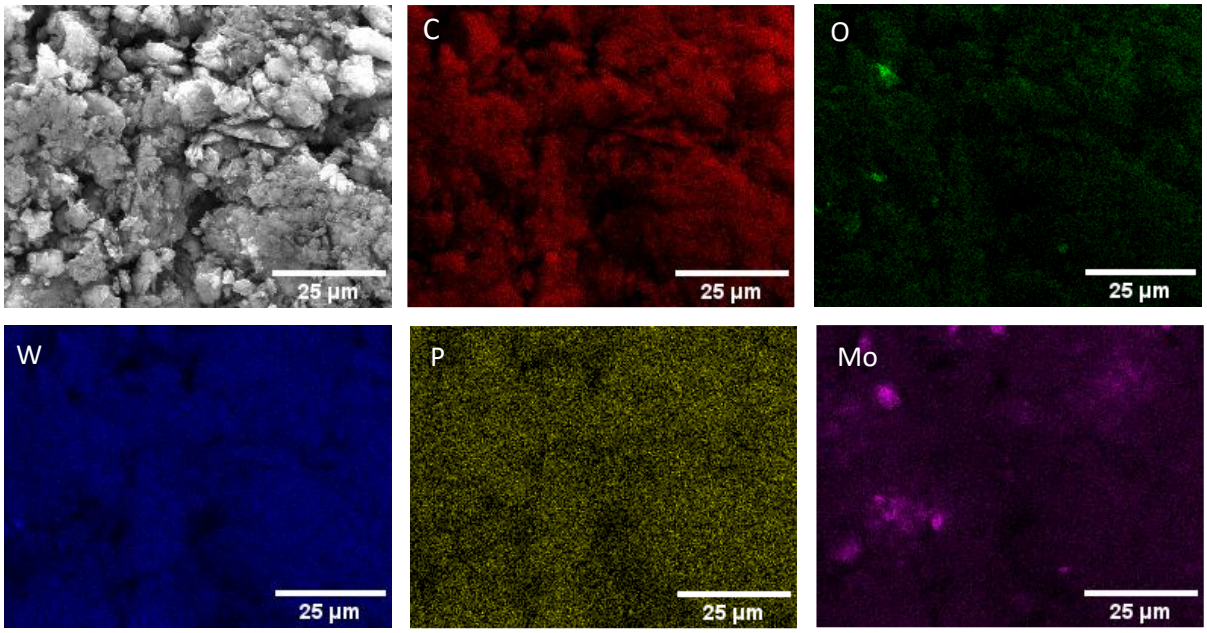



Figure 4.4 - SEM and EDX elemental mapping images of $P_2W_{12}Mo_6$@MWCNT_N8, at 5000× magnification for the elements C (red), O (green), W (blue), P (yellow) and Mo (purple).

The composites were also characterized by XRD (Figure 4S14). The analyzed composites present peaks at a 25.8º angle corresponding to (002) planes of graphitic framework and at 43.1º which are indexed to the 002 graphite planes. The narrower and more prominent peak displayed in GF_S6 may indicate a higher level of crystallinity in the graphitic framework, as anticipated, contrasted with MWCNT_N8 and MWCNT_S6.

## 4.4. Electrochemical performance towards ORR

The electrocatalytic activity towards the ORR of the prepared composites was initially investigated using cyclic voltammetry (CV) in $N_2$- and $O_2$-saturated KOH solutions (0.1 M). The N and S-doped carbon materials were also examined under identical experimental conditions for comparative analysis. Figure 4.5 illustrates the CVs obtained in $N_2$- and $O_2$-saturated electrolytes for the prepared nanocomposites. It is evident that in the $N_2$-saturated electrolyte, no reduction peak associated with oxygen reduction is observed. However, in the $O_2$-saturated electrolyte, all four composites exhibit an irreversible peak corresponding to the reduction of oxygen. Specifically, the reduction peaks are observed at $E_{pc}$ = 0.81, 0.79, 0.70, and 0.71 V vs. RHE for

$P_2W_{12}Mo_6$@MWCNT_N8, $P_2W_{12}Mo_6$@MWCNT_N6, $P_2W_{12}Mo_6$@MWCNT_S6, and $P_2W_{12}Mo_6$@GF_S6, respectively. The CVs for MWCNT_N8, MWCNT_N6, MWCNT_S6, and GF_S6 in the same experimental conditions are shown in Figure 4S15 (a-d) in the supplementary information. These materials exhibit ORR peaks at $E_{pc}$ values of 0.79, 0.77, 0.70, and 0.72 V vs. RHE, respectively. Furthermore, the performance of Pt/C (20 wt %) was evaluated and found to closely resemble that of the composites ($E_{pc}$ = 0.86 V vs. RHE) (Figure 4S15 (e)).

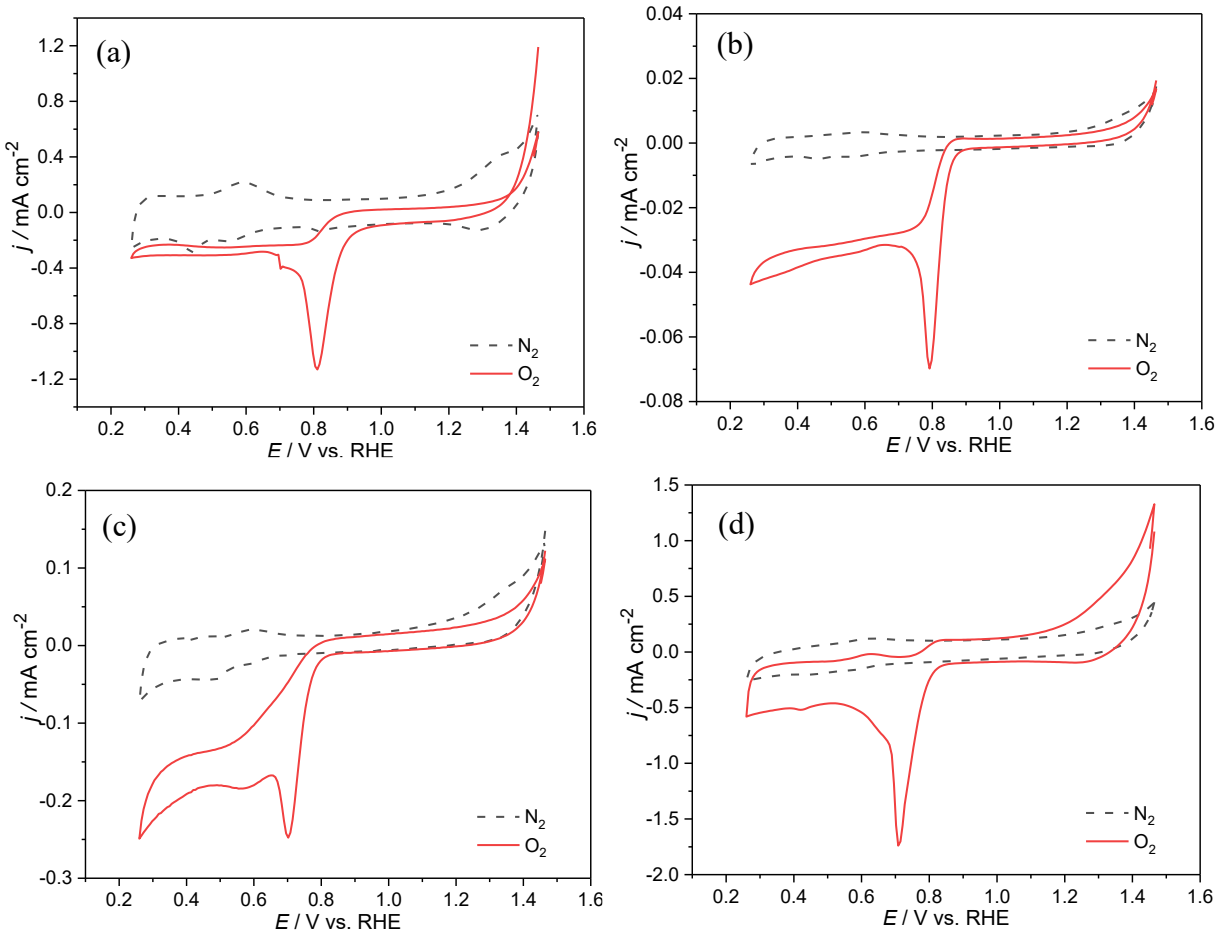



Figure 4.5 - CVs of $P_2W_{12}Mo_6$@MWCNT_N8 (a), $P_2W_{12}Mo_6$@MWCNT_N6 (b), $P_2W_{12}Mo_6$@MWCNT_S6 (c) and $P_2W_{12}Mo_6$@GF_S6 (d) modified electrodes in $N_2$-saturated (dash line) and $O_2$-saturated (full line) 0.1 mol $dm^{-3}$ KOH solution at 0.005 V $s^{-1}$.

In order to gain deeper insights into the electrocatalytic performance of all carbon materials and $P_2W_{12}Mo_6$@CM nanocomposites towards the ORR, linear sweep voltammetry (LSV) was performed at 1600 rpm in an $O_2$-saturated KOH solution (0.1 mol $dm^{-3}$). The LSV curves, as depicted in Figure 4.6 (a), were obtained after subtracting the

blanks (obtained in $N_2$-saturated KOH solution) from the corresponding $O_2$-saturated KOH curves. Table 4.2 presents the key ORR parameters acquired, including the onset potential ($E_{onset}$), the half-wave potential ($E_{1/2}$), the Tafel slopes (TS), and the number of electrons transferred per oxygen molecule ($n_{O2}$). Even though a diffusion-limiting current density plateau was not reached for our materials, we measured the values of current density obtained at 0.26 V vs RHE for a rotation speed of 1600 rpm ($j_{L,0.26\ V,\ 1600\ rpm}$). These are also included in Table 4.2. The electrocatalytic activity of the pristine carbon materials is significantly enhanced upon nitrogen and sulphur doping, corroborating the findings from various studies that have reported improved ORR performance upon N- and S-doping of similar carbon materials.[19, 32, 33, 71-74] This observed enhancement underscores the potential of N- and S-doping as effective strategies for enhancing the ORR electrocatalytic performance of carbon-based materials. Upon N-doping, both MWCNT_N8 and MWCNT_N6 exhibited a positive shift of $E_{onset}$ by 14 mV and 12 mV, respectively, compared to pristine carbon materials. Additionally, the diffusion-limiting current density doubled for MWCNT_N8 and increased by 1.35 times for MWCNT_N6. These enhancements suggest that the incorporation of nitrogen atoms introduced favourable interactions with $O_2$ molecules, thereby promoting the ORR mechanism through rearrangement of the neighbouring atoms' electronic structure.[75] For all of the N-doped materials tested, the proportion of N-functionalities increases in a consistent order: [N-oxides/nitrates] < [quaternary N] < [pyrrolic N] < [pyridinic N]. Nitrogen species, especially pyridinic and quaternary ones, are involved in ORR. Our previous research has demonstrated a positive correlation between the quantity of pyridinic nitrogen and ORR activity in carbon materials doped with nitrogen.[19, 23] Similarly, S-doping resulted in significant improvements in ORR performance. Both MWCNT_S6 and GF_S6 exhibited an $E_{onset}$ value of 0.77 V, indicating a substantial positive shift compared to the pristine materials (80 and 50 mV, respectively). A significant increase in the magnitude of the limiting current density was observed (65 % for MWCNT_S6 and 85% for GF_S6), with values of 3.3 and 3.7 mA $cm^{-2}$ for MWCNT_S6 and GF_S6, respectively. The electronegativity of sulphur being close to that of carbon had a lesser influence on the charge density of the carbon framework after doping. Species containing sulphur, such as thiophene S or sulphur oxide, positioned at the boundaries of carbon structures, exhibit electrocatalytic activity, especially in the context of GF_S6. Nevertheless, the introduction of sulphur doping triggers modifications in the spin density of carbon materials, thereby generating active sites for the chemisorption of $O_2$. This leads to an enhancement in the performance of the ORR.[32, 65, 73, 74]

The $P_2W_{12}Mo_6$@CM doped with nitrogen-based nanocomposites displayed good electrocatalytic activity. Among the $P_2W_{12}Mo_6$@CM derivatives, $P_2W_{12}Mo_6$@MWCNT_N6 and $P_2W_{12}Mo_6$@MWCNT_N8 exhibited particularly encouraging results, with $E_{onset}$ values of 0.79 V and 0.84 V vs. RHE, respectively, being the closest to the reference $E_{onset}$ value of 0.94 V vs. RHE observed for Pt/C. The difference is even smaller if the $E_{1/2}$ values are compared with 0.76 V and 0.79 V for $P_2W_{12}Mo_6$@MWCNT_N6 and $P_2W_{12}Mo_6$@MWCNT_N8 and 0.82 V for Pt/C. Moreover, among the investigated materials, $P_2W_{12}Mo_6$@MWCNT_N6 demonstrated the highest $j_L$ value of -5.1 mA $cm^{-2}$, surpassing even the Pt/C value of -4.7 mA $cm^{-2}$. This indicates its superior ability to facilitate the ORR process and sustain high current densities, thereby outperforming the benchmark catalyst in this regard. $P_2W_{12}Mo_6$@MWCNT_N8 and $P_2W_{12}Mo_6$@GF_S6 also exhibited noteworthy $j_L$ values of -3.7 mA $cm^{-2}$ and -3.2 mA $cm^{-2}$, respectively, further highlighting their good ORR activity. Finally, $P_2W_{12}Mo_6$@MWCNT_S6 showed the lowest $j_L$ value of -2.4 mA $cm^{-2}$. Figure 4.6 (b) shows the number of electrons transferred per oxygen molecule for the N and S-doped CMs and their respective composites. These results were obtained by applying the Koutecky-Levich (K-L) equation to the LSVs ate different rotation speeds (see Figures 4S16 to 4S20 and section 4.6.3 in SI file for more details). The data obtained for $P_2W_{12}Mo_6$@MWCNT_N8 and MWCNT_N8 indicate that the redox processes are nearly 4-electrons. Conversely, $P_2W_{12}Mo_6$@MWCNT_N6 and MWCNT_N6 show a mixed redox process involving 2- and 4-electrons, as confirmed by the $n_{O2}$ values. Interestingly, the POM immobilisation improved the $n_{O2}$ value in the MWCNT_N6 composite, implying an enhancement in its electrocatalytic performance. The behaviour of the doped-nitrogen carbon materials after POM immobilisation appears to be similar, with the active sites arising from the POM immobilisation possibly compensating for the loss of N-induced active sites.[19, 33, 38] Contrary to expectations, the immobilisation of $P_2W_{12}Mo_6$ did not lead to the expected improvement in the electrochemical parameters of GF_S6 and MWCNT_S6. This observation suggests that the immobilisation process may not have resulted in effective interactions between $P_2W_{12}Mo_6$ and the composites, potentially hindering their catalytic activity as electrocatalysts.

In an alkaline medium, the oxygen reduction reaction can proceed through either an indirect (2-electron) pathway involving the reduction of $O_2$ to $HO_2^-$ and subsequent reduction to $H_2O/HO^-$, or a more desirable direct pathway where $O_2$ is directly reduced to $H_2O/HO^-$.[76] To assess comprehensively the ECs, it is crucial to determine the percentage of $H_2O_2$ produced during the ORR process. The percentage of $H_2O_2$ was calculated using Eq. 4.4 (see SI) at various potential values (Figure 4.6 (c)). Among the

composites studied, $P_2W_{12}Mo_6$@MWCNT_N8 showed the lowest percentage of $H_2O_2$ produced (17.7%), which aligns with its $n_{O2}$ value ($n_{O2}$ = 3.3). $P_2W_{12}Mo_6$@MWCNT_N6, $P_2W_{12}Mo_6$@MWCNT_S6 and $P_2W_{12}Mo_6$@GF_N6 showed percentages of 32.0%, 42.4% and 36.0% respectively. While the results are consistent, caution must be exercised when directly comparing these two methods, as both have limitations.[72, 77, 78] Firstly, the oxidation process of hydrogen peroxide on the platinum electrocatalyst is not a mass-transfer limited process. Secondly, the SEM images reveal a rough structure of the support material and a heterogeneity of clusters of the immobilised POM in the prepared electrocatalysts. This structural variability may alter the electrode geometry and introduce turbulence in the electrolyte flow, leading to estimated $n_{O2}$ values that may not fully reflect the actual electrocatalytic performance of the ORR.[33]

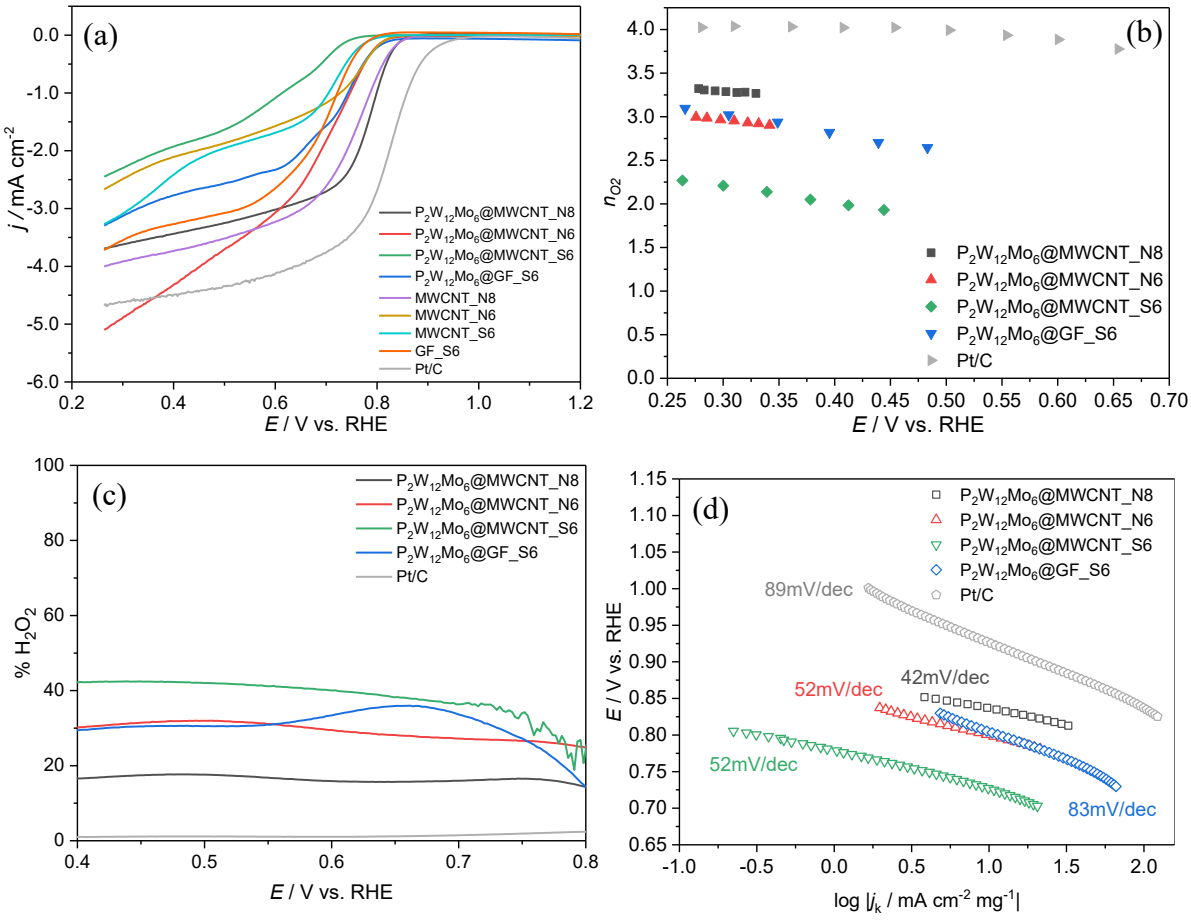



Figure 4.6 - ORR LSV curves acquired using an RDE in $O_2$-saturated KOH solution (0.1 mol $dm^{-3}$) at 1600 rpm and 0.005 V $s^{-1}$ of commercial Pt/C (20 wt %), $P_2W_{12}Mo_6$@CM nanocomposites and doped-nitrogen and sulphur carbon materials (a); $n_{O2}$ at several potential values (b); estimated percentage of $H_2O_2$ produced with RRDE for $P_2W_{12}Mo_6$@CM and Pt/C (20 wt %) in $O_2$-saturated 0.1 mol $dm^{-3}$ KOH solution, at 1600 rpm; the disk potential was swept at v = 0.005 V $s^{-1}$ and

the ring potential was kept at E = 0.2 V versus Ag/AgCl (c); ORR Tafel plots for $P_2W_{12}Mo_6$@CM obtained from LSV data in Figure 4.6 (a) where current densities are normalised to the mass of each ECs (d).

To gain deeper insights into the reaction kinetics, Tafel plots of the prepared nanocomposites and the Pt/C reference were derived from the LSV curves in $O_2$-saturated KOH at 1600 rpm, as shown in Figure 4.6(d). Remarkably, all the investigated materials exhibited lower Tafel slopes when compared to Pt/C (89 mV $dec^{-1}$), with $P_2W_{12}Mo_6$@MWCNT_N8 displaying the most favourable Tafel value (42 mV $dec^{-1}$). These results suggest that oxygen molecules undergo facile adsorption and activation at the surface of the nanocomposites, indicating efficient catalytic sites for the ORR. The lower Tafel slopes in the prepared nanocomposites imply enhanced reaction kinetics, favouring either the conversion of $MOO^-$ species to MOOH (where M represents an empty site on the electrocatalyst surface) or the initial discharge step.[23, 33, 38]

Table 4.2 - Main ORR parameters obtained from polarisation curves recorded in $O_2$-saturated 0.1 mol $dm^{-3}$ KOH solution for the different materials tested.

| Samples | $E_{onset}$ vs RHE (V) | $j_L$ (mA $cm^{-2}$) | Tafel slope (mV $dec^{-1}$) | $n_{O2}$ | $E_{1/2}$ (V) |
|---|---|---|---|---|---|
| Pt/C | 0.94 | -4.7 | 89 | 4.0 | 0.82 |
| GF | 0.72 | -2.0 | 63 | 2.4 | 0.60 |
| MWCNT | 0.69 | -2.0 | 54 | 2.1 | 0.57 |
| GF_S6 | 0.77 | -3.7 | 50 | 4.0 | 0.68 |
| MWCNT_S6 | 0.77 | -3.3 | 49 | 3.0 | 0.62 |
| MWCNT_N6 | 0.81 | -2.7 | 37 | 2.3 | 0.67 |
| MWCNT_N8 | 0.83 | -4.0 | 47 | 3.5 | 0.74 |
| $P_2W_{12}Mo_6$@GF_S6 | 0.73 | -3.2 | 83 | 2.9 | 0.70 |
| $P_2W_{12}Mo_6$@MWCNT_S6 | 0.74 | -2.4 | 52 | 2.1 | 0.73 |
| $P_2W_{12}Mo_6$@MWCNT_N6 | 0.79 | -5.1 | 52 | 3.0 | 0.76 |
| $P_2W_{12}Mo_6$@MWCNT_N8 | 0.84 | -3.7 | 42 | 3.3 | 0.79 |

The linear relationship between the double layer capacitance ($C_{dl}$) and the electrochemically active surface area (ECSA), coupled with the similar nature of the electrocatalysts used in this investigation, facilitates a direct comparison of the $C_{dl}$ values obtained for the composites.[79-82] By performing CV measurements at varying scan rates, we estimated the $C_{dl}$ values from the slopes of the linear fittings of the CV current densities (measured at the same potential of 1.13 V vs. RHE in a non-faradaic region) obtained at different scan rates for both the composites and their corresponding nitrogen and sulphur-doped carbon materials (for experimental details, see SI file section 4.6.4 and Figures 4S21 and 4S22). However, it is important to note that the $C_{dl}$ should be interpreted as an estimate of the number of electrocatalytically active sites accessible to a specific electrocatalyst.[83] As shown in Table 4.3, a noticeable increase in the number of active sites was observed upon immobilisation of the POM ($P_2W_{12}Mo_6$) for all the composites. The extent of this increase was most pronounced for the $P_2W_{12}Mo_6$@MWCNT_N8 composite, with a composite/carbon support $C_{dl}$ ratio of 2.00. These findings suggest the enhanced accessibility and availability of electrocatalytically active sites resulting from the incorporation of $P_2W_{12}Mo_6$ into the nanocomposite structures.

Table 4.3 - Electrocatalytically active surface area (ECSA) values of the carbon supports and the corresponding POM-based composites.

| CM support | $C_{dl}$ (mF cm$^{-2}$) | Composite | $C_{dl}$ (mF cm$^{-2}$) | Composite/Carbon Support $C_{dl}$ Ratio |
|---|---|---|---|---|
| MWCNT_N8 | 0.0203 | $P_2W_{12}Mo_6$@MWCNT_N8 | 0.0411 | 2.00 |
| MWCNT_N6 | 0.0108 | $P_2W_{12}Mo_6$@MWCNT_N6 | 0.0105 | 0.97 |
| MWCNT_S6 | 0.0054 | $P_2W_{12}Mo_6$@MWCNT_S6 | 0.0092 | 1.80 |
| GF_S6 | 0.0138 | $P_2W_{12}Mo_6$@GF_S6 | 0.0254 | 1.70 |

In the evaluation of an electrocatalyst's potential for ORR, assessing its stability is of paramount importance. To investigate thoroughly this aspect, chronoamperometry (CA) was performed at E = 0.46 V vs. RHE for 36000 s at 1600 rpm in an oxygen-saturated alkaline electrolyte (Figure 4.7 (a)). Among the nanocomposites studied, $P_2W_{12}Mo_6$@MWCNT_N8 showed the highest stability, with a current retention of 81%. Following closely, both $P_2W_{12}Mo_6$@MWCNT_N6 and $P_2W_{12}Mo_6$@GF_S6 showed

identical current retention values of 76%. In contrast, $P_2W_{12}Mo_6$@MWCNT_S6 exhibited a slightly lower current retention of 63%. This variation in stability could be attributed to the distinct interactions between the POM and its respective doped carbon supports. Still, the good stability of most composites can be attributed to the effective trapping of POM particles within the nano-networks of the carbon materials, effectively preventing (or at least limiting) their migration, aggregation, and leaching into the electrolyte. This, in turn, ensures that the stability of the corresponding support materials remains unaffected. Additionally, the high degree of graphitisation and/or ordered wall structure of the carbon materials contributes to the reduced likelihood of composite degradation, further enhancing their durability and long-term stability.[84, 86]

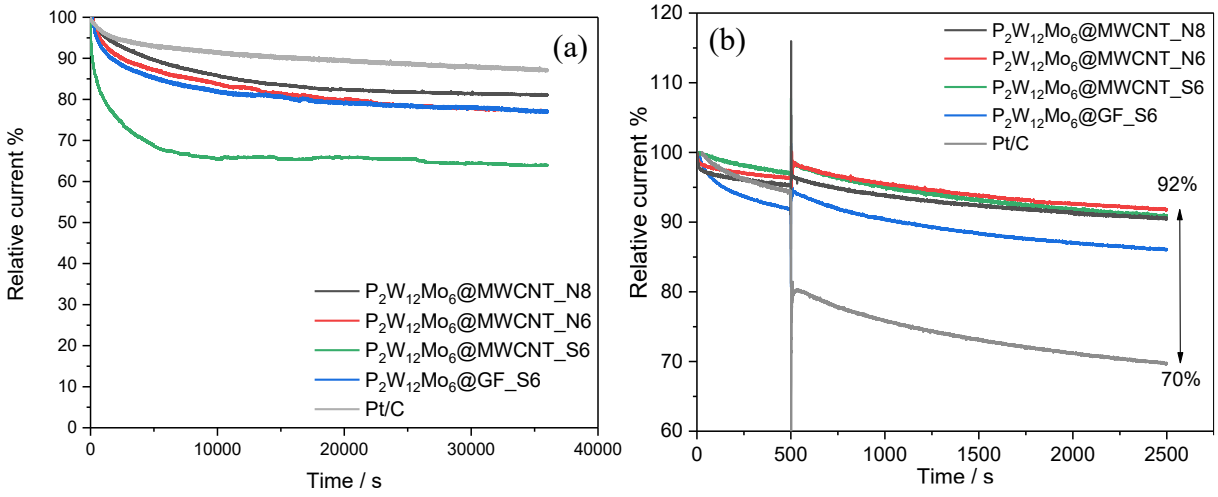



Figure 4.7 - Chronoamperometric response of the ECs at 1600 rpm, in 0.1 mol $dm^{-3}$ $O_2$-saturated KOH at: E = 0.46 V vs. RHE for 36000s (a) and E = 0.46 V vs. RHE with the addition of 0.5 mol $dm^{-3}$ methanol after ≈ 500 s (b).

Methanol, an excellent hydrogen carrier fuel with potential for sustainable and low-carbon pathways, holds promise as a carrier of carbon-neutral hydrogen.[87] Consequently, studying the methanol tolerance of electrocatalysts in methanol fuel cells assumes paramount importance. Methanol crossover from the anode to the cathode can severely compromise cathodic performance if the electrocatalysts are sensitive to it.[88] Although Pt-based materials offer superior performance in alkaline media compared to most electrocatalysts studied, they suffer from a significant drawback: heightened responsiveness to methanol oxidation reactions.[89] This vulnerability negatively impacts their ORR performance, leading to reduced current density outputs. Therefore, evaluating the methanol tolerance of the electrocatalysts becomes essential for their practical application. To assess methanol tolerance, CA was performed in $O_2$-saturated

0.1 mol $dm^{-3}$ KOH, in the presence of methanol (0.5 mol $dm^{-3}$) for both Pt/C and $P_2W_{12}Mo_6$@CM composites, over a period of 2500 s (Figure 4.7 (b)). Notably, methanol was introduced 500 s after the onset of CA. The results revealed a significant difference in methanol tolerance between Pt/C and the composites. While Pt/C retained only approximately 70% of its initial current density, the composites exhibited higher retention rates, ranging from ~86% to ~92%. This enhanced methanol tolerance represents a key advantage of using this kind of composites. The improved methanol tolerance of $P_2W_{12}Mo_6$@CM composites holds significant implications for their application in methanol fuel cells. By minimising the detrimental impact of methanol crossover on the cathodic performance, these materials pave the way for more efficient and reliable fuel cell technologies. The ability to retain higher current densities in the presence of methanol bodes well for the practical implementation of these composites in real-world energy conversion devices.

## 4.5. Conclusion

The study involved the immobilisation of the POM ($P_2W_{12}Mo_6$) onto nitrogen-doped multi-walled carbon nanotubes (MWCNT_N8 and MWCNT_N6), sulphur-doped multi-walled carbon nanotubes (MWCNT_S6), and sulphur-doped graphene (GF_S6) at varying calcination temperatures. The materials were extensively characterised using various analytical techniques, including FTIR, XPS, SEM, and EDX mapping proving that all composites were successfully synthesised. Electrochemical performance towards the ORR was investigated using cyclic voltammetry and linear sweep voltammetry in $O_2$-saturated KOH solution. The nanocomposites displayed excellent electrocatalytic activity for the ORR, with some composites approaching the performance of the Pt/C catalyst. $P_2W_{12}Mo_6$@MWCNT_N8 and $P_2W_{12}Mo_6$@MWCNT_N6 showed particularly encouraging results, with onset potentials close to Pt/C, significantly high diffusion-limiting current densities and low Tafel slopes. The nitrogen and sulphur-doped carbon materials demonstrated enhanced ORR performance compared to the pristine carbon materials, validating the effectiveness of N- and S-doping strategies. Through the analysis of Koutecky-Levich plots, it was determined that the ORR follows a mixed electron process, a conclusion further supported by the $\%H_2O_2$ production results. The composite $P_2W_{12}Mo_6$@MWCNT_N8 exhibited an enduring electrocatalytic performance over 36000 seconds, retaining a high value of 81%. This achievement is quite close to

the performance of the commercial Pt/C catalyst, which reached 86% retention. These findings underscore the robustness of the $P_2W_{12}Mo_6$@MWCNT_N8 composite and its potential as a viable alternative to traditional Pt/C in electrocatalytic applications. Moreover, the composites display remarkable methanol tolerance (86-92%), demonstrating a high selectivity for the ORR. This accomplishment addresses a significant limitation of the Pt/C electrocatalyst, marking a substantial advancement. The study's findings represent a significant step forward in the development of novel, cost-effective, and long-lasting electrocatalysts that are free of noble metals.

## 4.6. Supporting information

### 4.6.1. Materials and solvents

The POM salt $K_6 \cdot \alpha$-$[P_2W_{12}Mo_6O_{62}] \cdot 19H_2O$ was prepared according to the reported procedure.[1]

Potassium hydroxide (> 99%, Sigma-Aldrich), Nafion® at 5 wt. % (lower aliphatic alcohols and water, Sigma-Aldrich), isopropanol (99.5 %, Sigma-Aldrich), sulfuric acid (95–97 %, Merck), sodium sulphate anhydrous (99+ %, labkem), platinum 20 % on carbon black (Pt/C, HiSPEC® 3000, Alfa Aesar). Commercial graphene (sample denoted as GF) was from Graphene Technologies (Lot #GTX-7/6-10.4.13). Multi-walled carbon nanotubes (sample denoted as MWCNT) were commercially obtained from Nanocyl S.A., Ref. 3100 MWCNT (>95% carbon purity; 9.5 nm average diameter). For electrolyte and composites preparation, ultrapure water (18.2 MΩ cm at 25ºC, Interlab) was always used.

### 4.6.2. Physicochemical characterization

A Jasco FT/IR-460 Plus spectrophotometer was used to acquire the Fourier-transformed infrared (FTIR) spectra (64 scans, resolution of 4 $cm^{-1}$, between 400 and 4000 $cm^{-1}$). The spectra were obtained for samples dispersed (0.2 wt. %) in KBr pellets (spectroscopic grade, Merck).

X-ray photoelectron spectroscopy (XPS) measurements were performed at “Centro de Materiais da Universidade do Porto” (CEMUP), Portugal, in a VG Scientific ESCALAB 200A spectrometer with non-monochromatised Al Kα radiation (1486.6 eV).

Potential deviations induced by electric charge of the samples were corrected using the C 1s band at 284.6 eV as an internal standard. The high-resolution spectra analysis and deconvolution was performed with the CasaXPS software.

The SEM/EDX (scanning electron microscopy/energy-dispersive X-ray spectroscopy) images were acquired using a high resolution (Schottky) environmental SEM with X-ray microanalysis and electron backscattered diffraction analysis (Quanta 400 FEG ESEM/EDAX Genesis X4M), in high-vacuum conditions, at CEMUP.

The structural characterization of the materials was performed by XRD using a Rigaku SmartLabSe diffractometer (Cu Kα radiation – 1.5406 Å, 40 kV, 30 mA). The XRD patterns were collected in the range 10° < 2θ < 80°, with a scan speed of 3° min−1 and a step of 0.02°.

### 4.6.3. ORR electrochemical tests

An Autolab PGSTAT 302N (EcoChimie B.V.) potentiostat/galvanostat, controlled by the NOVA v2.0 software was employed for the cyclic voltammetry (CV) and linear sweep voltammetry (LSV) studies. The experiments were carried out at room temperature using a conventional three-electrode compartment cell.

A modified glassy carbon rotating disk electrode, RDE (Metrohm, 3 mm diameter) was used as the working electrode while an Ag/AgCl (Metrohm, 3 M KCl) and a carbon rod (Metrohm, 2 mm diameter) were used as reference and counter electrodes, respectively. Prior to modification of the bare electrodes, the RDE was cleaned with 6, 3 and 1 μm diamond polishing pastes (Buehler) on a MicroCloth polishing pad (BAS), followed by washing with ultrapure water. Then, a 2 × 2.5 μL drop of selected electrocatalyst dispersion was deposited on the RDE and left to dry under an airflow.

For the RDE modification, 1 mg of EC ($P_2W_{12}Mo_6$@CM or Pt/C) and a mixture of 125 μL of isopropanol, 125 μL of ultrapure water and 20 μL of Nafion (5 wt%) were ultrasonically dispersed for 20 min. The electrochemical tests were carried out in $N_2$- or $O_2$-saturated KOH (0.1 mol $dm^{-3}$). To achieve this, the electrolyte was degassed for 40 min with the selected gas.

The CV measurements were performed at 0.005 V $s^{-1}$ and the LSV ones at 0.005 V $s^{-1}$ with rotation speeds in the range 400 - 3000 rpm. The ORR current obtained in $N_2$-saturated KOH (0.1 mol $dm^{-3}$) was subtracted from that obtained in $O_2$-saturated KOH. The chronoamperometry (CA) tests were done at a potential (*E*) of 0.5 V vs. RHE and a rotation speed of 1600 rpm for 36000 s. Resistance to methanol was evaluated by CA at *E* = 0.5 V vs. RHE and 1600 rpm for 2500 s.

The onset potential ($E_{onset}$) is defined as the potential at which the reduction of $O_2$ begins and it was determined as described in the literature.[39] The electrochemical potentials and the $E_{onset}$ values determined vs. Ag/AgCl were converted to the reversible hydrogen electrode (RHE) using the following equation:

$$E_{(RHE)} = E_{(Ag/AgCl)} + 0.059\,pH + E^{o}_{(Ag/AgCl)} \quad (4.1)$$

where $E_{(RHE)}$ is the potential vs. RHE, $E^{o}_{(Ag/AgCl)}$ = 0.1976 V (25 ºC) and $E_{(Ag/AgCl)}$ is the potential measured vs. Ag/AgCl.[91]

To analyse the LSV data and the number of electrons transferred per $O_2$ molecule ($n_{O2}$) in the oxygen reduction reaction the Koutecky-Levich (K-L) equation was used (4.2):

$$\frac{1}{j} = \frac{1}{j_L} + \frac{1}{j_k} = \frac{1}{B\omega^{1/2}} + \frac{1}{j_k} \quad (4.2)$$

Here, $j$ = current density measured, $j_L$ = diffusion-limiting current density, $j_k$ = kinetic current density and ω= angular velocity. The parameter $B$ is associated to the diffusion limiting current density expressed by the Equation (4.3):

$$B = 0.2 n_{O2} F (D_{O2})^{\frac{2}{3}} v^{-\frac{1}{6}} C_{O2} \quad (4.3)$$

with $F$ = 96 485 C mol$^{-1}$, $D_{O2}$ = $O_2$ diffusion coefficient, $v$ = electrolyte kinematic viscosity and $C_{O2}$ = $O_2$ bulk concentration. For rotation speeds in rpm is adopted a constant 0.2. Additionally, in the electrolyte used KOH (0.1 mol dm$^{-3}$): $D_{O2}$ = 1.95×10$^{-5}$ cm$^2$ s$^{-1}$, $v$ =0.008977 cm$^2$ s$^{-1}$ and $C_{O2}$ = 1.15×10$^{-3}$ mol dm$^{-3}$.[92]

Tafel plots ($E_{(RHE)}$ vs. log $j_k$) were obtained after the measured LSV currents were rectified for diffusion to yield the corresponding kinetic current values. The $j_L$ parameter, determined combining equations (4.2) and (4.3), was used to make the mass transport correction. The values of $j_k$ obtained were normalised for the total deposited mass of EC.

Tests with a rotating ring disk electrode (RRDE) were performed as well for a more complete examination of the ECs. The electrode was polished for 15 min with aluminium oxide 0.3 μm and washed with ultrapure water. The LSV experiments were conducted at 0.005 V s$^{-1}$ and1600 rpm in $O_2$-saturated KOH. A constant potential of 1.2 V vs RHE was applied at the Pt ring electrode. The percentage of $H_2O_2$ produced was calculated from Eq. 4.4, using the current produced in the ring ($i_R$), in the disk ($i_D$) and the current collection efficiency of the ring.[93]

$$\%H_2O_2 = 200 \times \frac{\frac{i_R}{N}}{i_D + \frac{i_R}{N}} \quad (4.4)$$

### 4.6.4. Assessment of electrochemically active surface areas (ECSA)

ECSA values exhibited by electrocatalysts are usually calculated by using the equation (4.5):

$$ECSA = \frac{C_{dl}}{C_{ref}} \quad (4.5)$$

where $C_{dl}$ stands for the double-layer capacitance and $C_{ref}$ for the reference capacitance value per unit area. Due to the impossibility of knowing the exact $C_{ref}$ value for specific and structurally complex materials, reliable ECSA values cannot be obtained frequently. However, the linear proportional relation between ECSA and the double-layer capacitance allows performing a relative comparison for similar electrocatalysts. Taking advantage of this fact, in the present work, $C_{dl}$ values have been directly employed as approximated ECSA estimations to assess the surface effects on the ORR performances. Thus, $C_{dl}$ values were calculated for all materials via a standard double-layer charging test, namely, the acquisition of consecutive CV plots at different scan rates (from 20 to 160 mV $s^{-1}$), being the double-layer capacitance estimated from the slope of a linear-fitted plot of current density at 1.13 V vs. RHE (non-faradaic region) versus the scan rate.

## 4.6.5. Figures

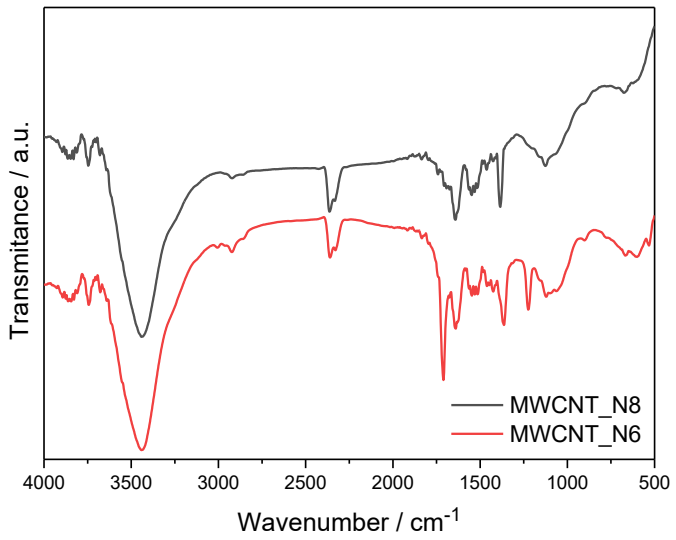



Figure 4S1 - FTIR spectra in the 4000–500 $cm^{-1}$ range of the nitrogen doped carbon materials MWCNT_N8 (black) and MWCNT_N6 (red).

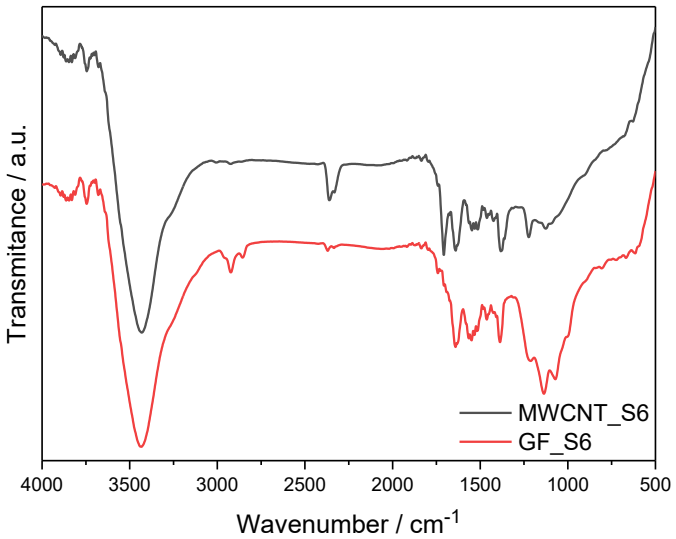



Figure 4S2 - FTIR spectra in the 4000–500 $cm^{-1}$ range of the sulphur-doped carbon materials MWCNT_S6 (black) and GF_S6 (red).

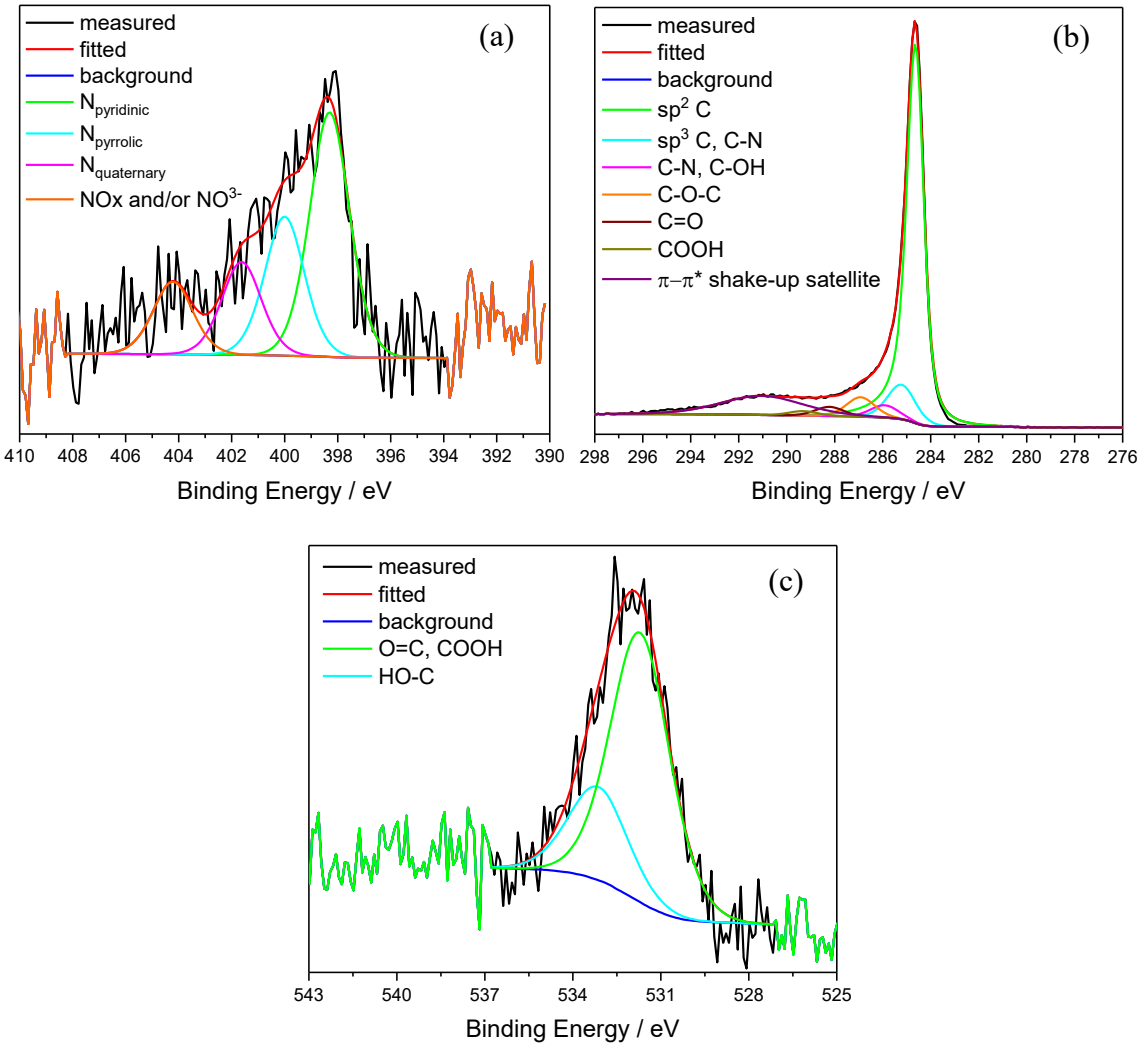



Figure 4S3 - XPS deconvoluted spectra of the corresponding elements of MWCNT_N8.

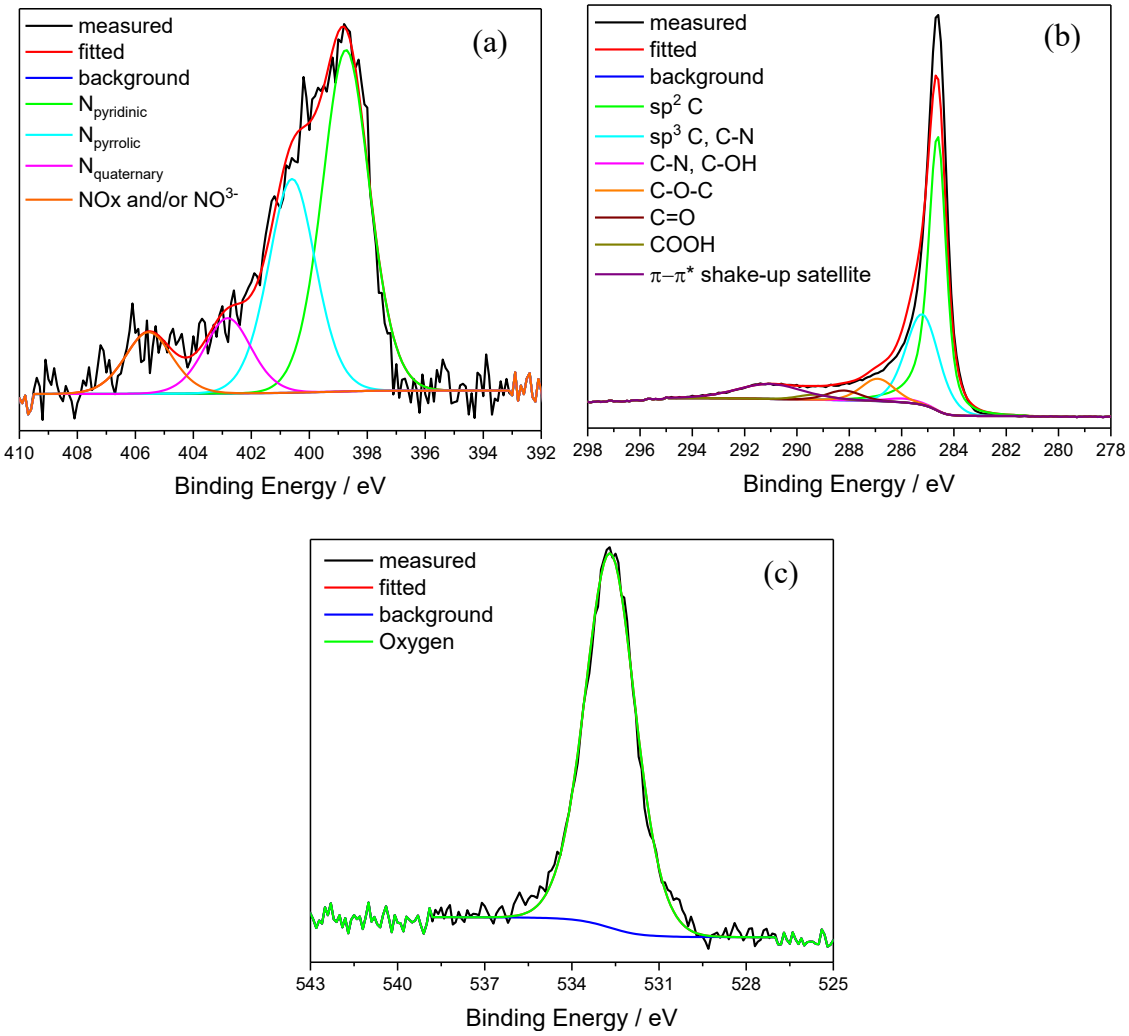



Figure 4S4 - XPS deconvoluted spectra of the corresponding elements of MWCNT_N6.

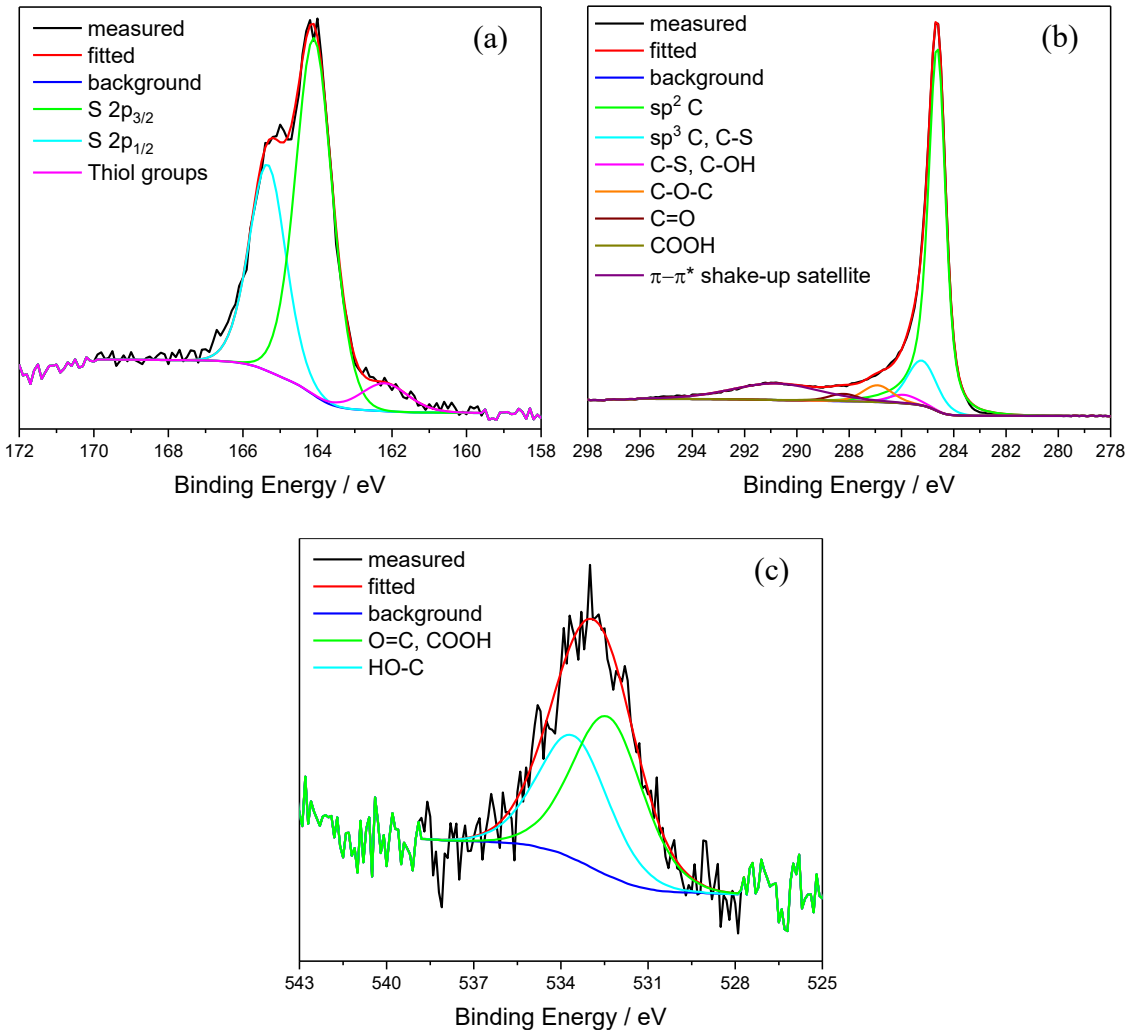



Figure 4S5 - XPS deconvoluted spectra of the corresponding elements of MWCNT_S6.

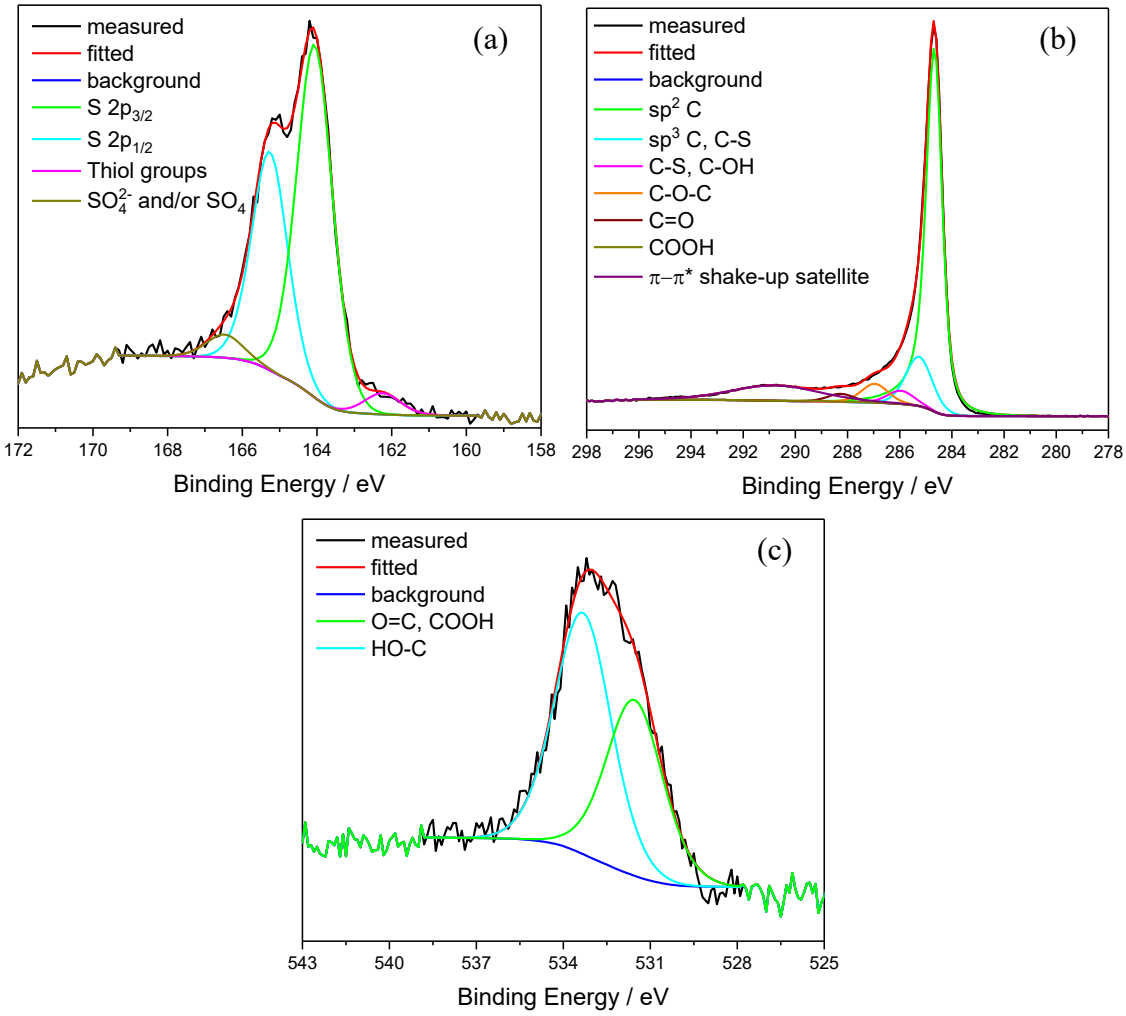



Figure 4S6 - XPS deconvoluted spectra of the corresponding elements of GF_S6.

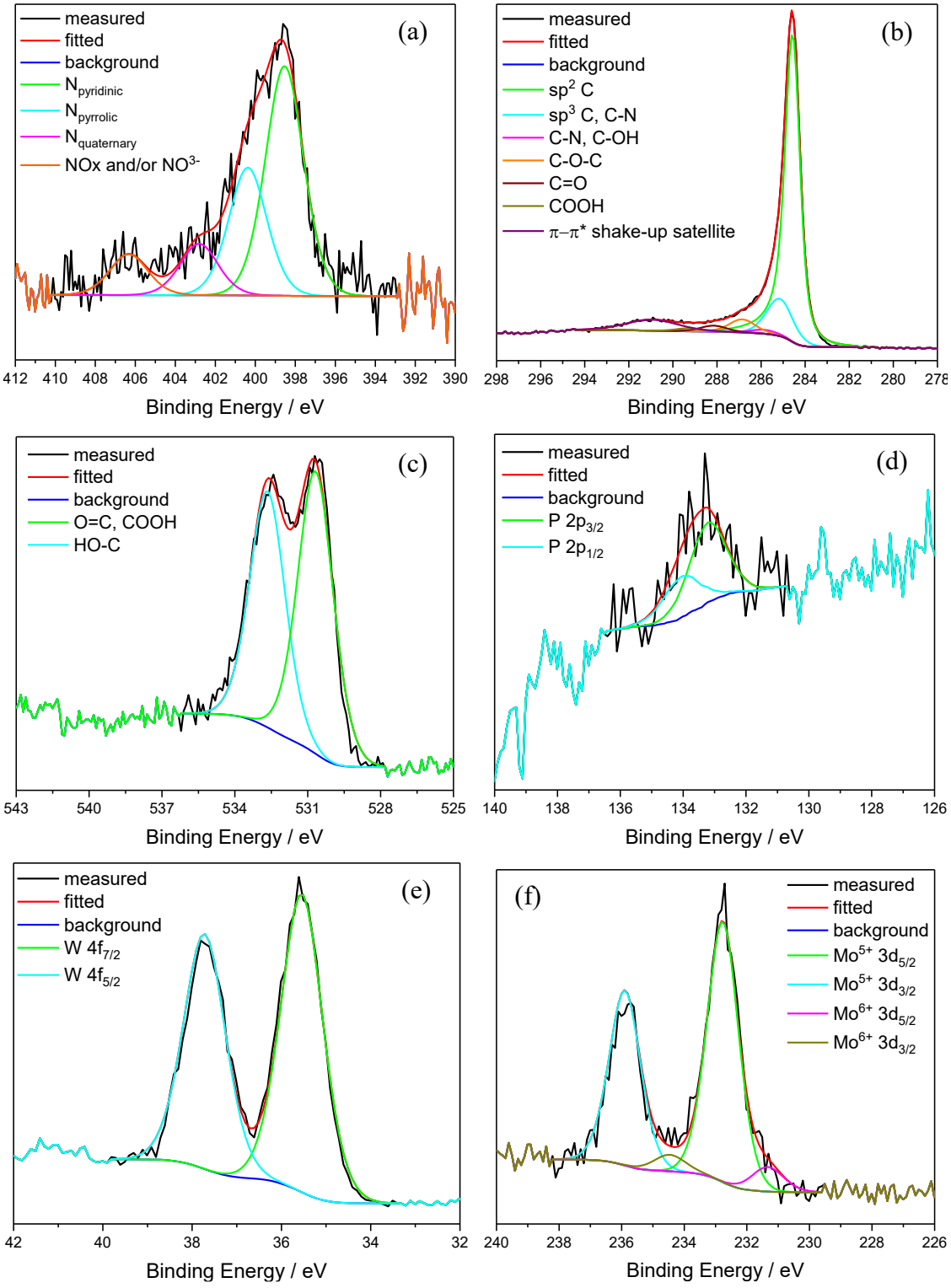



Figure 4S7 - XPS deconvoluted spectra of the corresponding elements of $P_2W_{12}Mo_6$@MWCNT_N6.

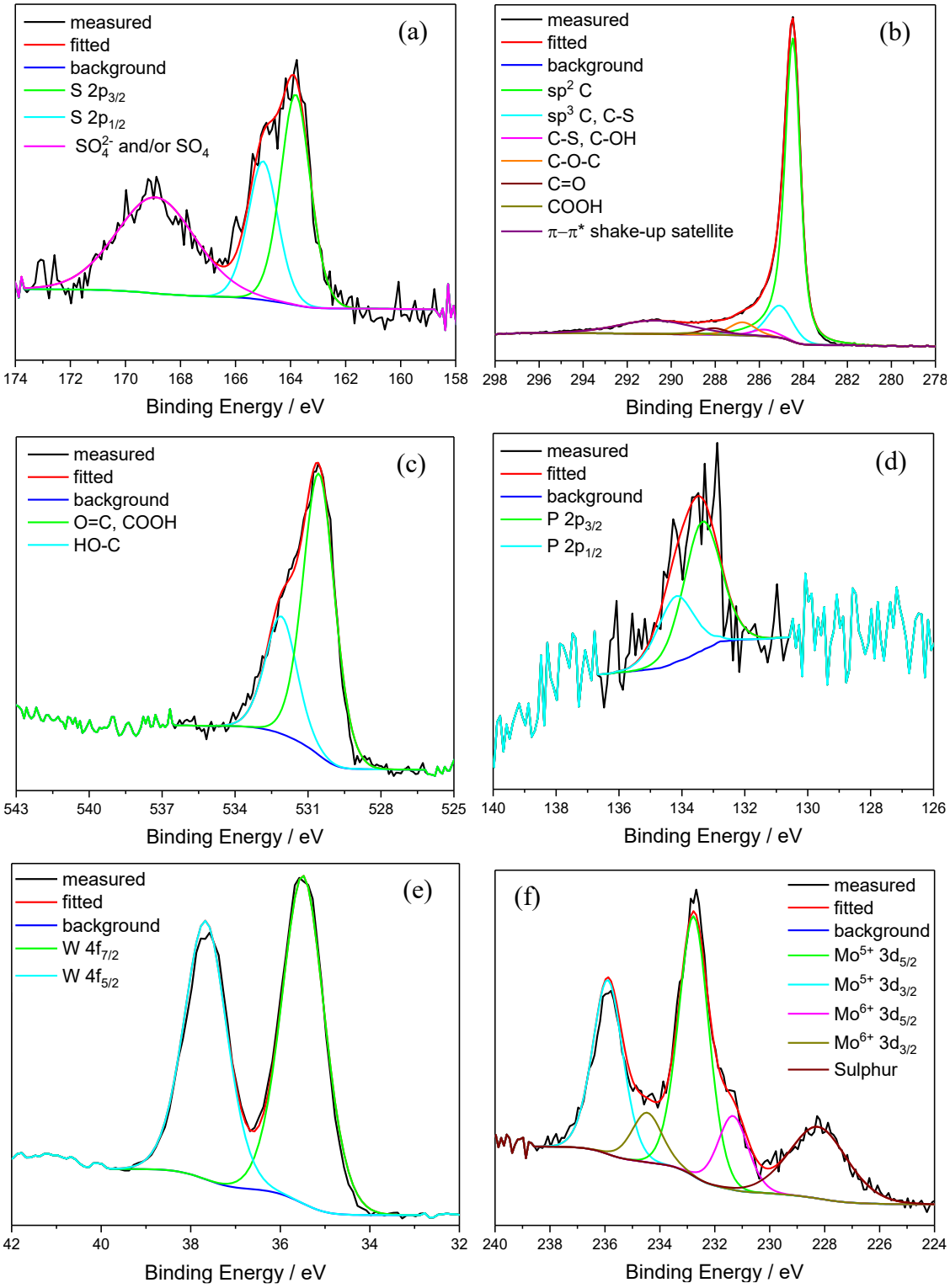



Figure 4S8 - XPS deconvoluted spectra of the corresponding elements of $P_2W_{12}Mo_6$@MWCNT_S6.

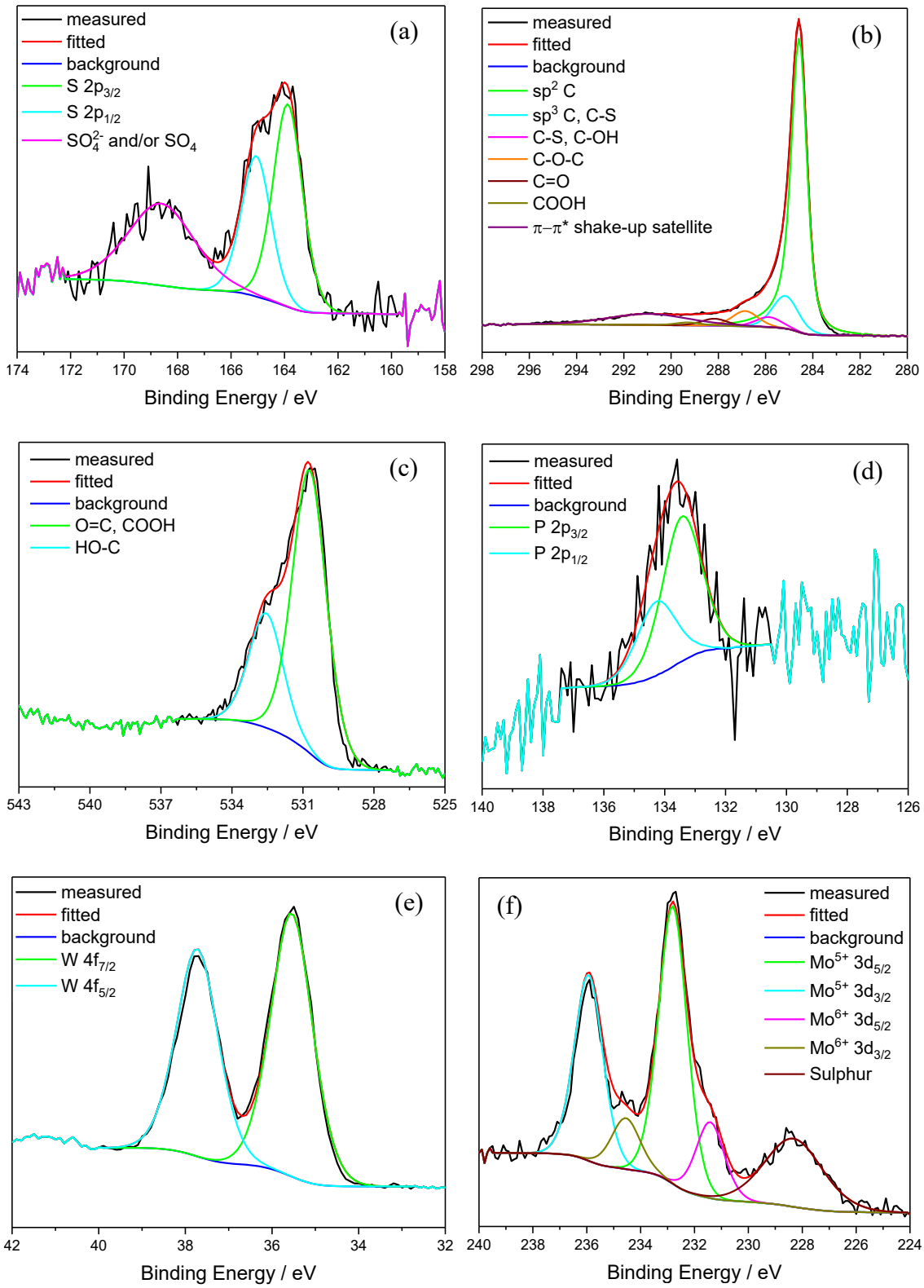



Figure 4S9 - XPS deconvoluted spectra of the corresponding elements of $P_2W_{12}Mo_6$@GF_S6.

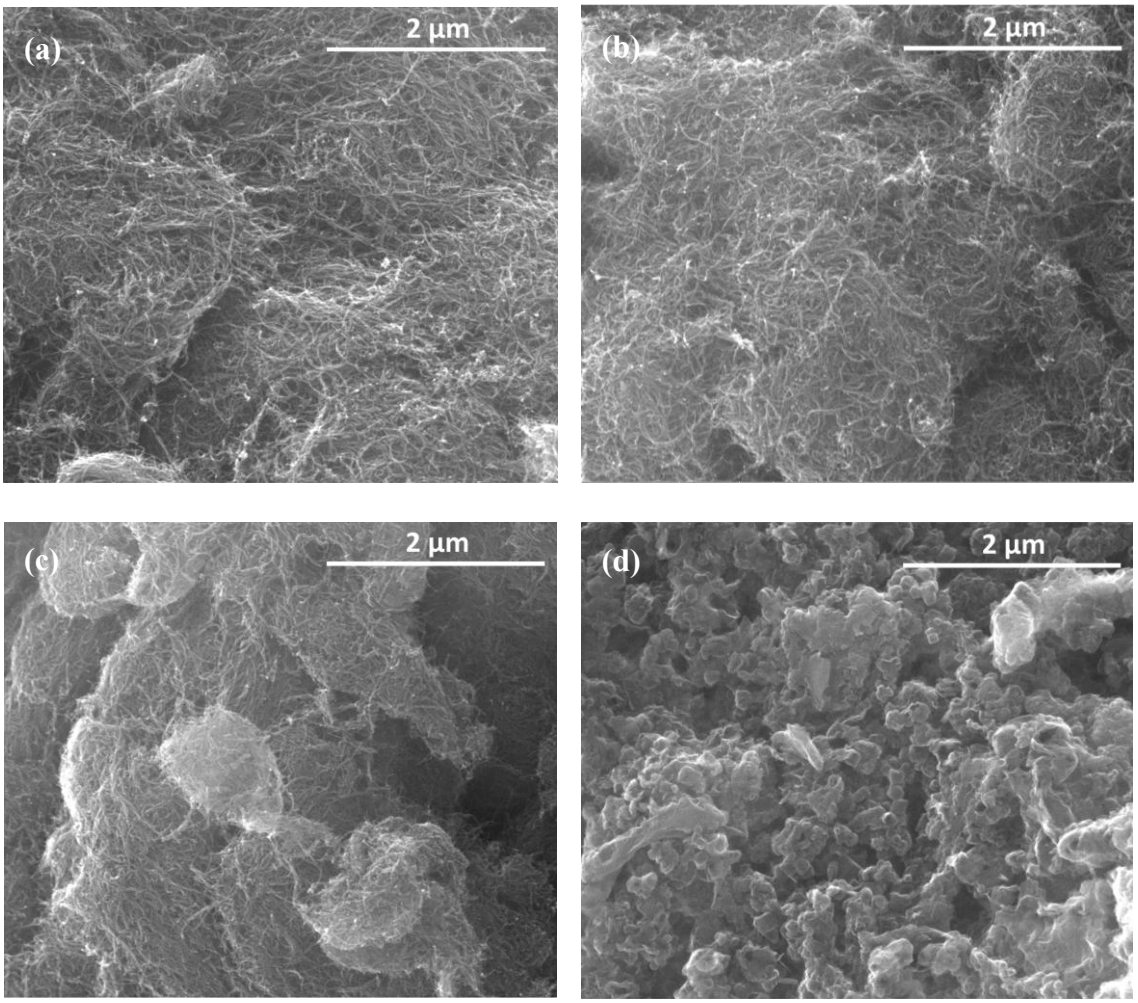



Figure 4S10 - SEM images of MWCNT_N8 (a), MWCNT_N6 (b), MWCNT_S6 and GF_S6 at 50000× magnification.

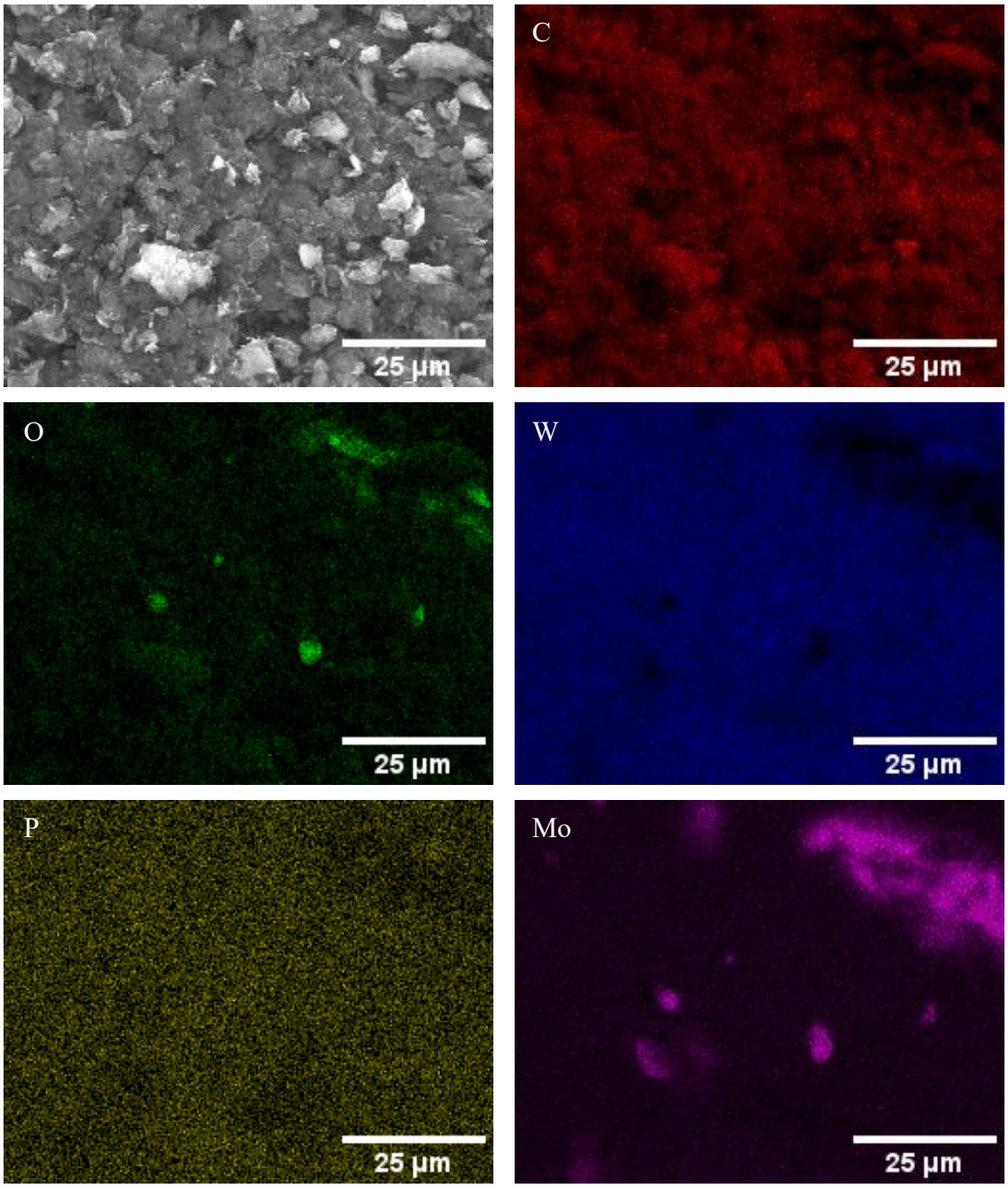



Figure 4S11 - SEM and EDX elemental mapping images of $P_2W_{12}Mo_6$@MWCNT_N6, at 5000× magnification for the elements C (red), O (green), W (blue), P (yellow) and Mo (purple).

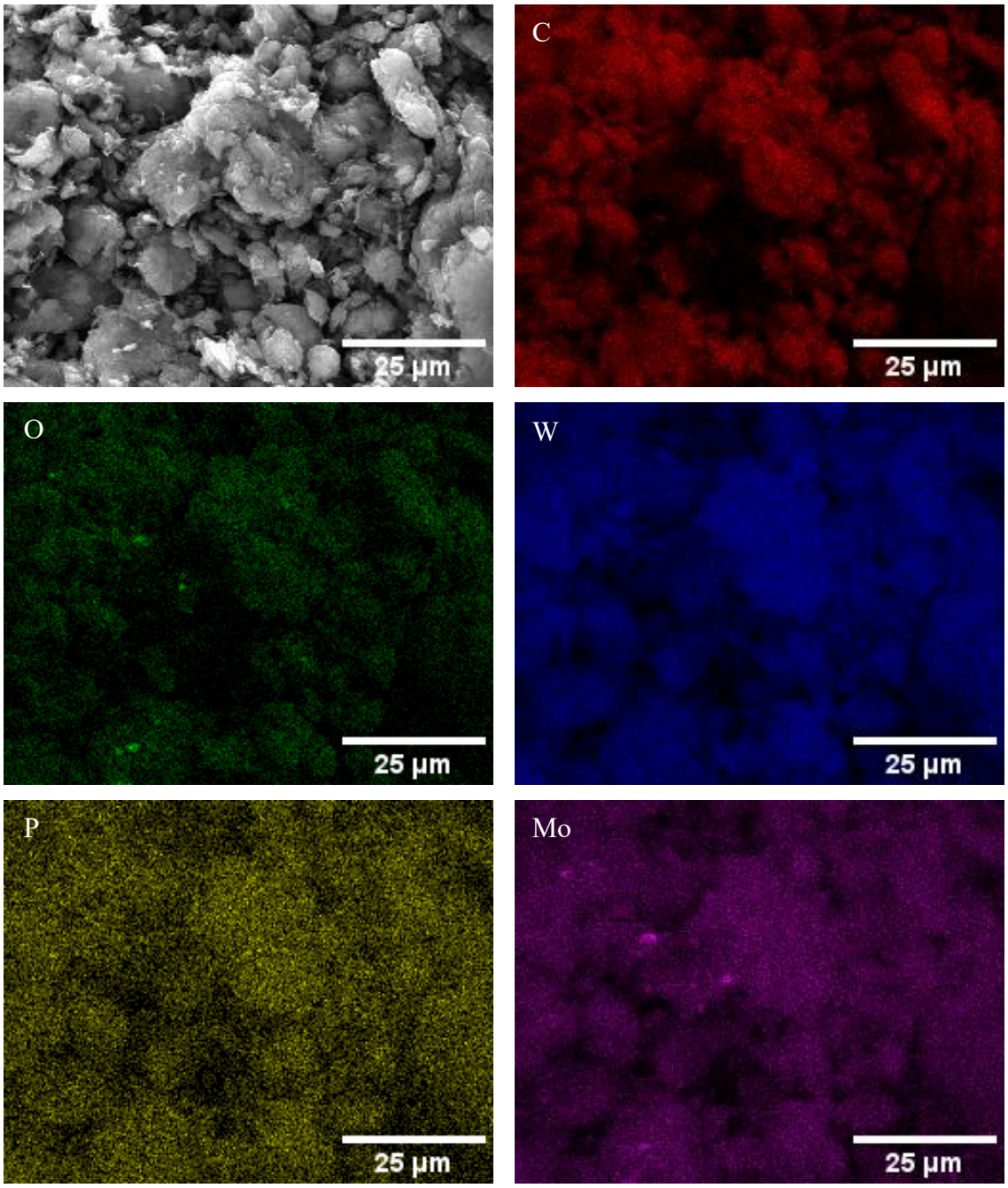



Figure 4S12 - SEM and EDX elemental mapping images of $P_2W_{12}Mo_6$@MWCNT_S6, at 5000× magnification for the elements C (red), O (green), W (blue), P (yellow) and Mo (purple).

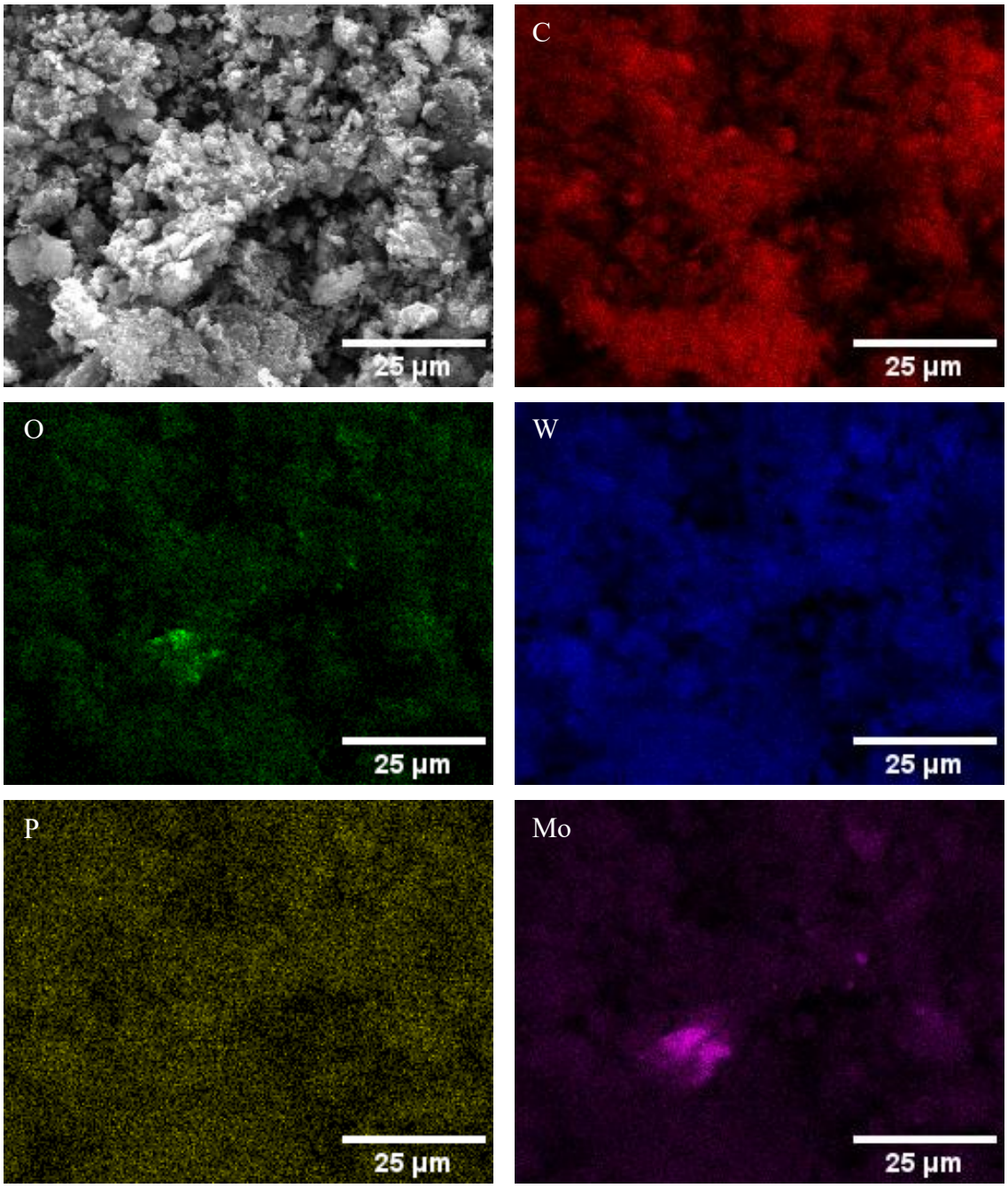



Figure 4S13 - SEM and EDX elemental mapping images of $P_2W_{12}Mo_6$@GF_S6, at 5000× magnification for the elements C (red), O (green), W (blue), P (yellow) and Mo (purple).

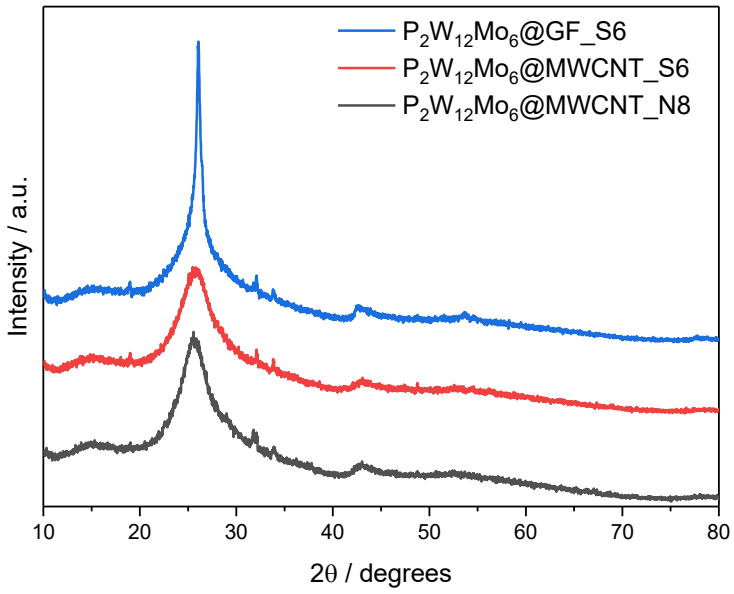



Figure 4S14 - XRD spectra of $P_2W_{12}Mo_6$@GF_S6 (blue), $P_2W_{12}Mo_6$@MWCNT_S6 (red) and $P_2W_{12}Mo_6$@MWCNT_N8 (black).

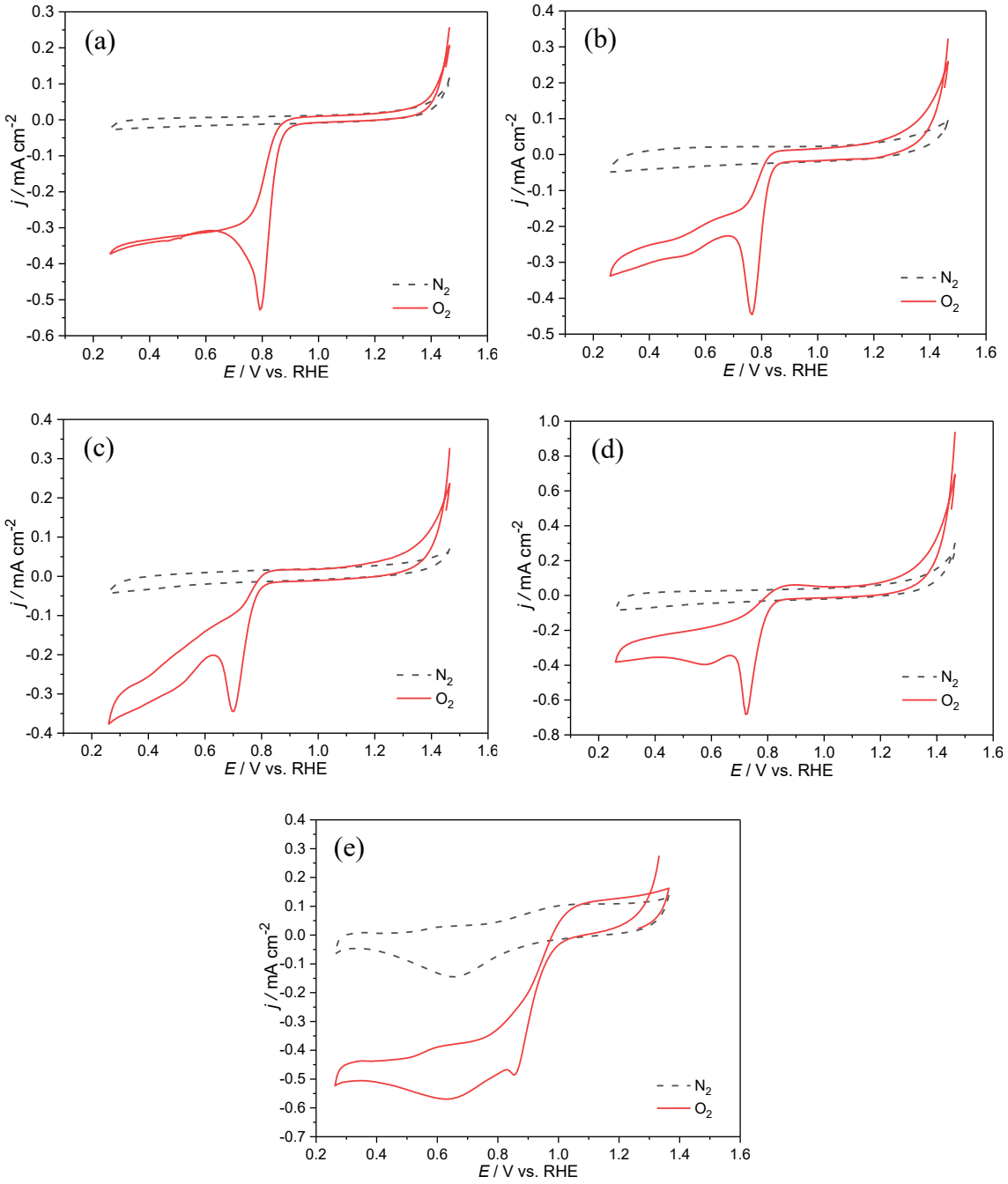



Figure 4S15 - CVs of MWCNT_N8 (a), MWCNT_N6 (b), MWCNT_S6 (c), GF_S6 (d) and Pt/C (20 wt. %) (e) modified electrodes in $N_2$-saturated (dash line) and $O_2$-saturated (full line) 0.1 mol $dm^{-3}$ KOH solution at 0.005 V.

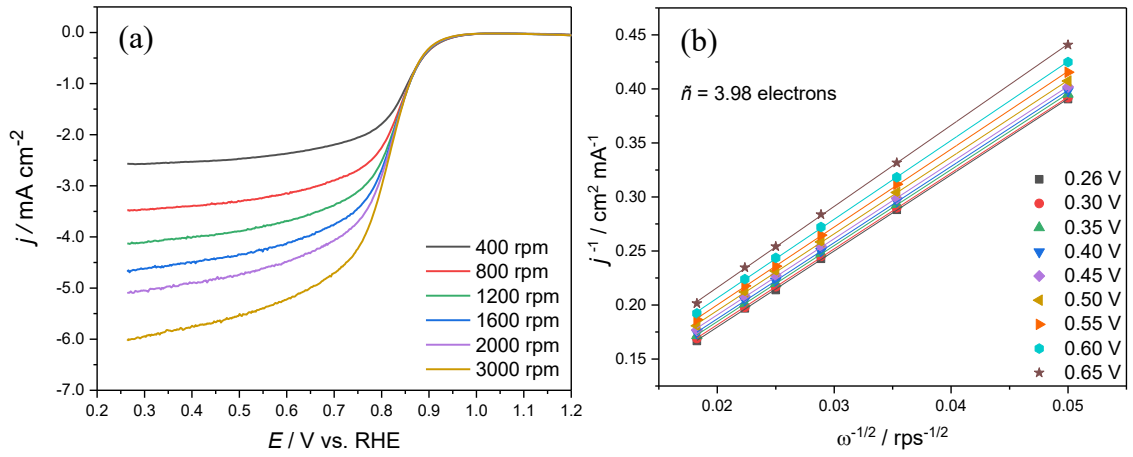



Figure 4S16 - ORR LSV polarization curves for Pt/C (20 wt. %) at different rotation rates in $O_2$-saturated 0.1 mol $dm^{-3}$ KOH solution at 0.005 V $s^{-1}$ (a), and the corresponding Koutecky-Levich (K-L) plots (b).

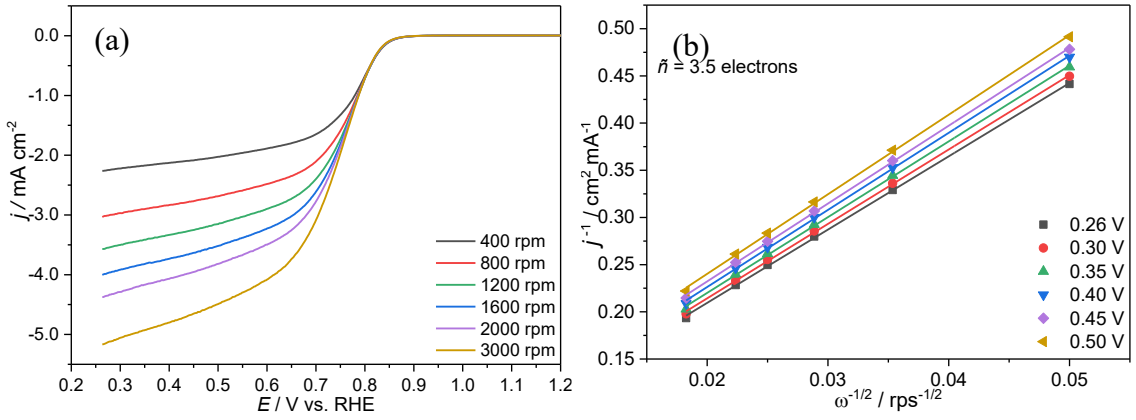



Figure 4S17 - ORR LSV polarization curves for MWCNT_N8 at different rotation rates in $O_2$-saturated 0.1 mol $dm^{-3}$ KOH solution at 0.005 V $s^{-1}$ (a), and the corresponding Koutecky-Levich (K-L) plots (b).

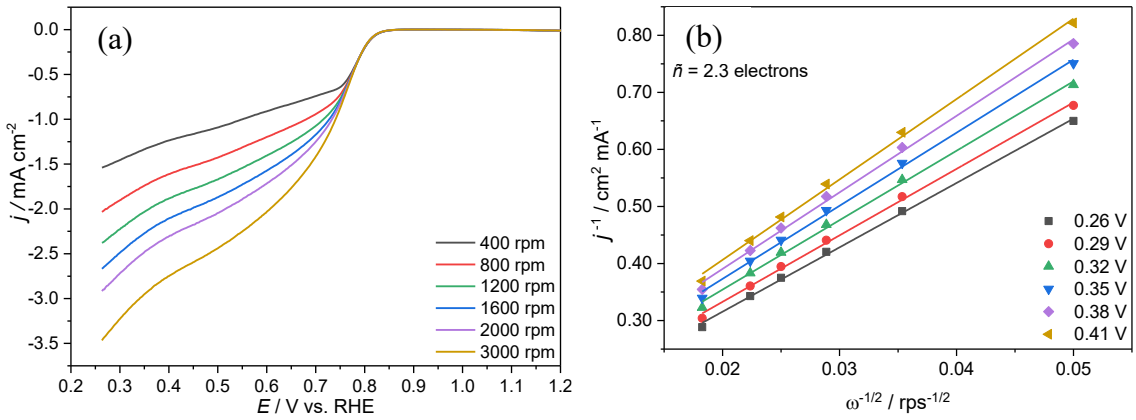



Figure 4S18 - ORR LSV polarization curves for MWCNT_N6 at different rotation rates in $O_2$-saturated 0.1 mol $dm^{-3}$ KOH solution at 0.005 V $s^{-1}$ (a), and the corresponding Koutecky-Levich (K-L) plots (b).

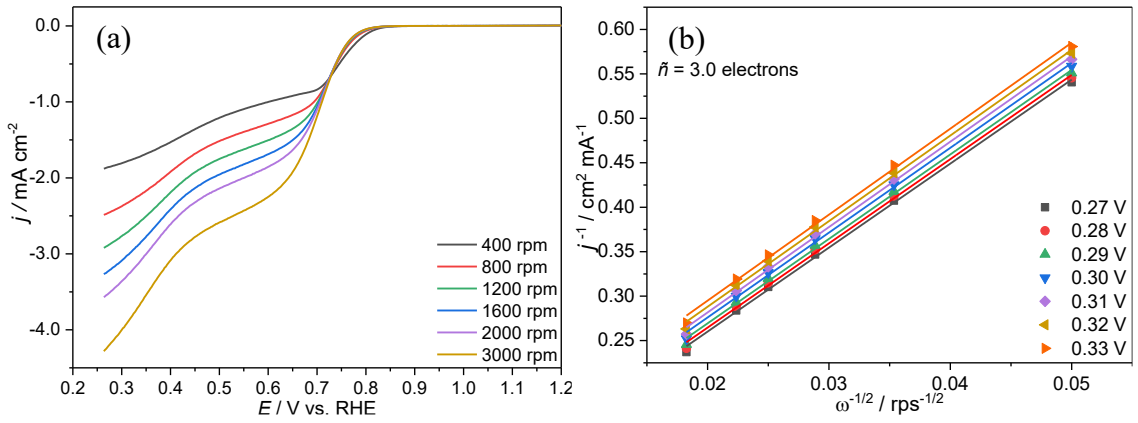



Figure 4S19 - ORR LSV polarization curves for MWCNT_S6 at different rotation rates in $O_2$-saturated 0.1 mol $dm^{-3}$ KOH solution at 0.005 V $s^{-1}$ (a), and the corresponding Koutecky-Levich (K-L) plots (b).

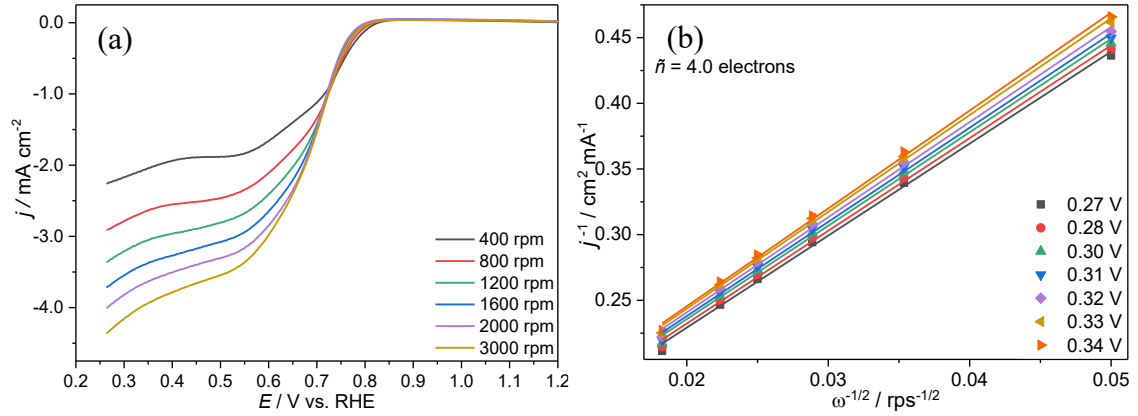
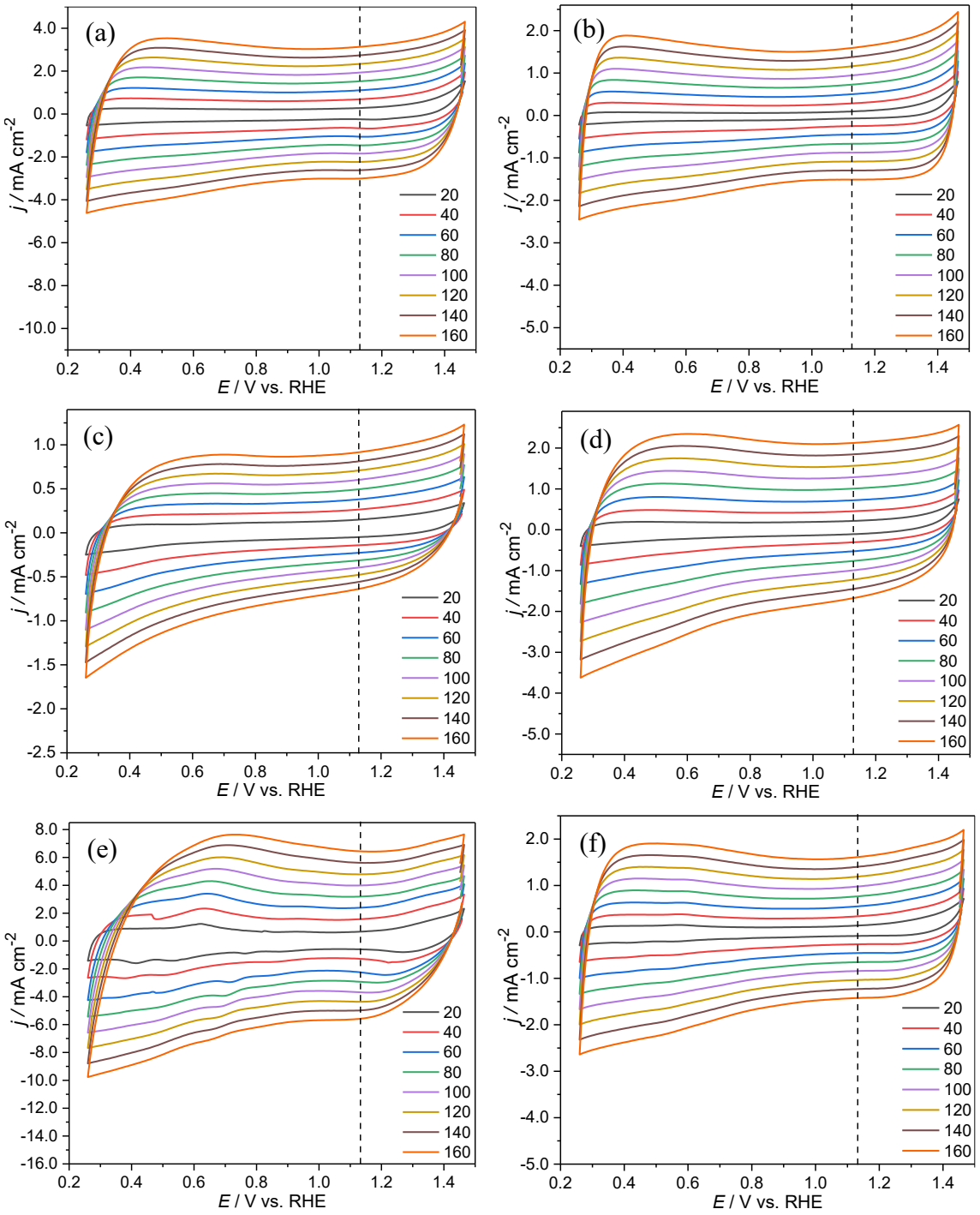



Figure 4S20 - ORR LSV polarization curves for GF_S6 at different rotation rates in $O_2$-saturated 0.1 mol $dm^{-3}$ KOH solution at 0.005 V $s^{-1}$ (a), and the corresponding Koutecky-Levich (K-L) plots (b).


(a)
(b)
(c)
(d)
(e)
(f)
j / mA cm-2
E / V vs. RHE
20
40
60
80
100
120
140
160

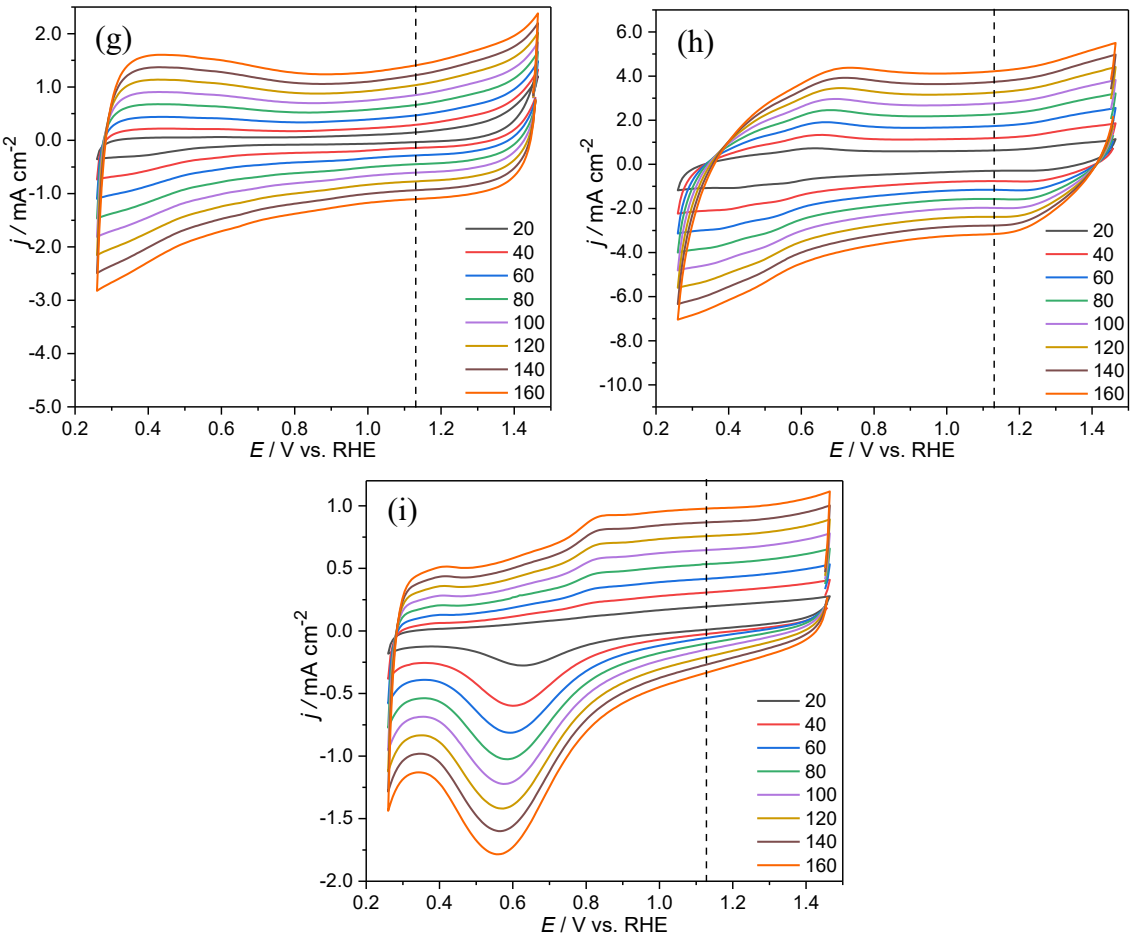
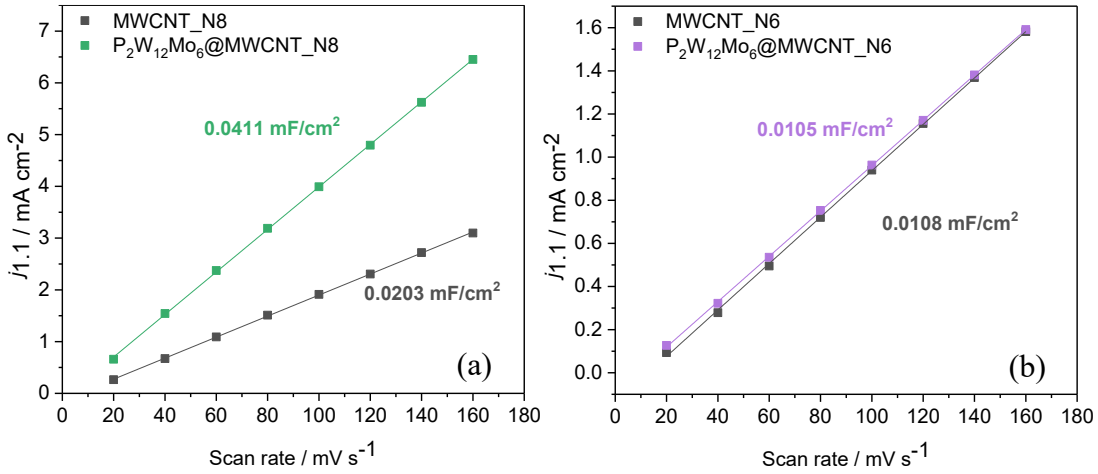



Figure 4S21 - CVs at different scan rates for MWCNT_N8 (a), MWCNT_N6 (b), MWCNT_S6 (c), GF_S6 (d), $P_2W_{12}Mo_6$@MWCNT_N8 (e), $P_2W_{12}Mo_6$@MWCNT_N6 (f), $P_2W_{12}Mo_6$@MWCNT_S6 (g), $P_2W_{12}Mo_6$@GF_S6 (h) and Pt/C (i) in $N_2$-saturated KOH (0.1 M).



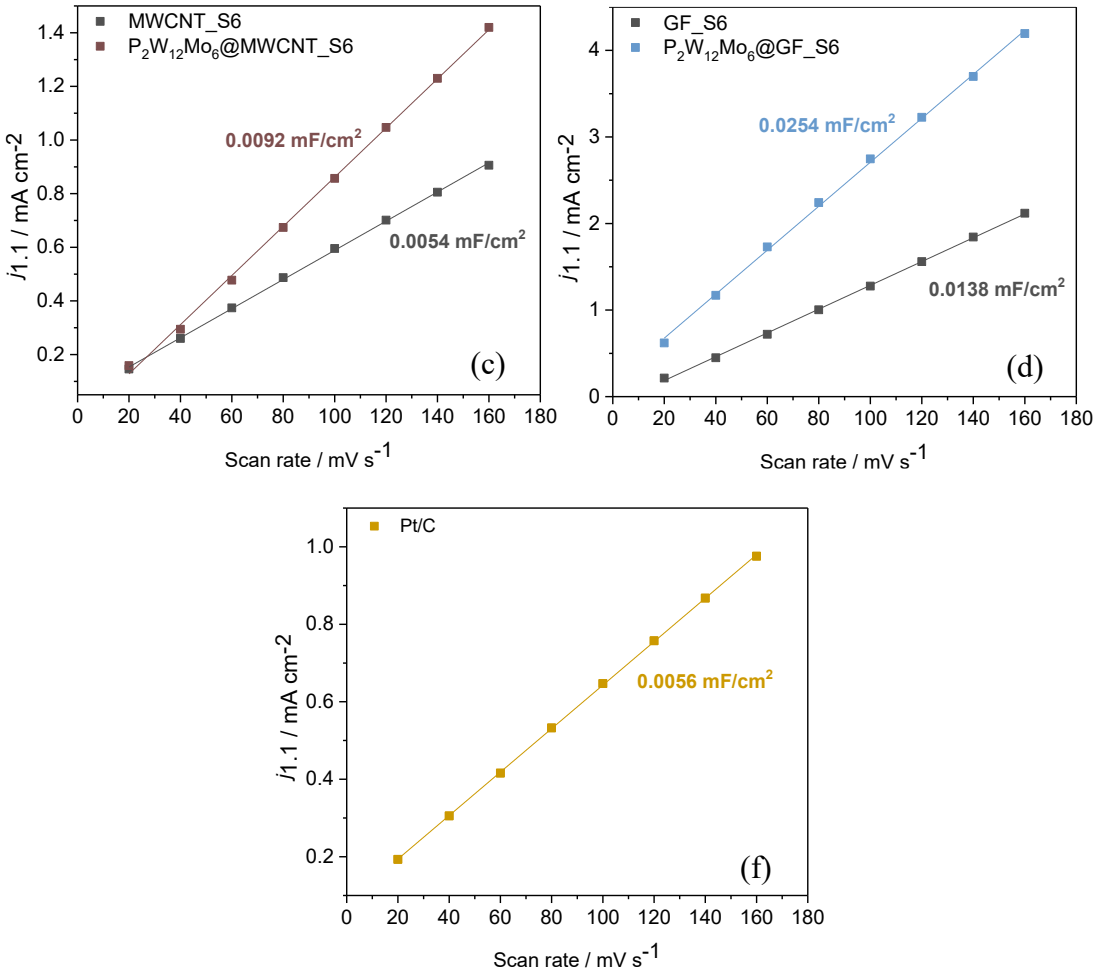



Figure 4S22 - Current density-scan rate linear fitting plots for all materials. Numeric values correspond to the double-layer capacitances ($C_{dl}$) for each material.

## 4.7. Declarations

**Funding:** This work was financially supported by: Project UNIRCELL POCI-01-0145-FEDER-16422, funded by FEEI through Programa operacional Competitividade e Internacionalização-COMPETE2020 and by national funds through FCT - Fundação para a Ciência e a Tecnologia, I.P.

**Acknowledgments:** Thanks are also due to PT national funds FCT/MCTES through the projects UIDB/50006/2020, UIDP/50006/2020 as well as to Campus France—project PHC Pessoa 42341RM (O2@nanoCPOM). Thanks are also due to the FCT project FOAM4ENER PTDC/QUI-ELT/28299/2017. H.C.N. thanks the FCT through ChemMat

program for his PhD grant PD/BD/143095/2018. D.M.F. thanks FCT/MCTES for funding through the Individual Call to Scientific Employment Stimulus (2021.00771.CEECIND/CP1662/CT0007). I.-M M., A.-L.T. and P.d.O. thank the CNRS (namely its IEA programme) and the Université Paris-Saclay for financial support.

**Conflict of interest:** The authors declare that they have no conflict of interest.

## 4.8. References

[1] F. Perera, *Int. J. Environ. Res. Public Health*, **2018**, 15, 16.

[2] F. Dawood, M. Anda and G. Shafiullah, *Int. J. Hydrogen Energ*, **2020**, 45, 3847-3869.

[3] K. Alanne and S. Cao, *Applied Energy*, **2019**, 238, 284-302.

[4] Y. Nie, L. Li and Z. Wei, *Chem. Soc. Rev.*, **2015**, 44, 2168-2201.

[5] J. Stacy, Y. N. Regmi, B. Leonard and M. Fan, *Renewable and Sustainable Energy Reviews*, **2017**, 69, 401-414.

[6] W. Xia, A. Mahmood, Z. Liang, R. Zou and S. Guo, *Angew. Chem. Int. Ed.*, **2016**, 55, 2650-2676.

[7] F. Guo, M. Zhang, S. Yi, X. Li, R. Xin, M. Yang, B. Liu, H. Chen, H. Li and Y. Liu, *Nano Research Energy*, **2022**, 1, 9120027.

[8] M. Kuang and G. Zheng, *Small*, **2016**, 12, 5656-5675.

[9] J. K. Nørskov, T. Bligaard, J. Rossmeisl and C. H. Christensen, *Nature chemistry*, **2009**, 1, 37-46.

[10] C. Wang, D. Wang, S. Liu, P. Jiang, Z. Lin, P. Xu, K. Yang, J. Lu, H. Tong, L. Hu, W. Zhang and Q. Chen, *Journal of Catalysis*, **2020**, 389, 150-156.

[11] V. Stamenkovic, B. S. Mun, K. J. J. Mayrhofer, P. N. Ross, N. M. Markovic, J. Rossmeisl, J. Greeley and J. K. Nørskov, *Angew. Chem. Int. Ed.*, **2006**, 45, 2897-2901.

[12] L. Liao, X. Bian, J. Xiao, B. Liu, M. D. Scanlon and H. H. Girault, *Phys. Chem. Chem. Phys.*, **2014**, 16, 10088-10094.

[13] F. H. B. Lima, J. Zhang, M. H. Shao, K. Sasaki, M. B. Vukmirovic, E. A. Ticianelli and R. R. Adzic, *J. Phys. Chem. C*, **2007**, 111, 404-410.

[14] Y. Cheng, H. Wang, H. Song, K. Zhang, G. I. N. Waterhouse, J. Chang, Z. Tang and S. Lu, *Nano Research Energy*, **2023**, 2, e9120082.

[15] C. Freire, D. M. Fernandes, M. Nunes and V. K. Abdelkader, *ChemCatChem*, **2018**, 10, 1703-1730.

[16] H. Lin, J.-W. Wang, X.-W. Guo, S. Yao, M. Liu, Z.-M. Zhang and T.-B. Lu, *J. Mater. Chem. A*, **2018**, 6, 24479-24485.

[17] S. Zhang, O. Oms, L. Hao, R. Liu, M. Wang, Y. Zhang, H.-Y. He, A. Dolbecq, J. Marrot and B. Keita, *ACS Appl. Mater. Interfaces*, **2017**, 9, 38486-38498.

[18] D. M. Fernandes, M. P. Araujo, A. Haider, A. S. Mougharbel, A. J. Fernandes, U. Kortz and C. Freire, *ChemElectroChem*, **2018**, 5, 273-283.

[19] H. C. Novais, B. Jarrais, A. Haider, U. Kortz, A. Guerrero-Ruiz, I. Rodríguez-Ramos, C. Freire and D. M. Fernandes, *Electrocatalysis*, **2023**, 14, 294-305.

[20] S.-A. Wohlgemuth, R. J. White, M.-G. Willinger, M.-M. Titirici and M. Antonietti, *Green Chemistry*, **2012**, 14, 1515-1523.

[21] L. Qu, Y. Liu, J.-B. Baek and L. Dai, *ACS nano*, **2010**, 4, 1321-1326.

[22] Z. Chen, D. Higgins and Z. Chen, *Carbon*, **2010**, 48, 3057-3065.

[23] H. C. Novais, B. Jarrais, I.-M. Mbomekallé, A.-L. Teillout, P. d. Oliveira, C. Freire and D. M. Fernandes, *Inorganics*, **2023**, 11, 388.

[24] M. K. Debe, *Nature*, **2012**, 486, 43-51.

[25] B. C. Steele and A. Heinzel, *Nature*, **2001**, 414, 345-352.

[26] H. A. Gasteiger, S. S. Kocha, B. Sompalli and F. T. Wagner, *Applied Catalysis B: Environmental*, **2005**, 56, 9-35.

[27] H. Wang, L. R. Grabstanowicz, H. M. Barkholtz, D. Rebollar, Z. B. Kaiser, D. Zhao, B.-H. Chen and D.-J. Liu, *ACS Energy Lett.*, **2019**, 4, 2500-2507.

[28] J. Yan, F. Ye, Q. Dai, X. Ma, Z. Fang, L. Dai and C. Hu, *Nano Research Energy*, **2023**, 2, e9120047.

[29] W. Zhang, W. Pu, Y. Qu, H. Yang and Y. Liu, *Electrochimica Acta*, **2023**, 462, 142800.

[30] I. Kone, A. Xie, Y. Tang, Y. Chen, J. Liu, Y. Chen, Y. Sun, X. Yang and P. Wan, *ACS Appl. Mater. Interfaces*, **2017**, 9, 20963-20973.

[31] D. Xu and W. D. Wu, in *Chalcogen Chemistry*, IntechOpen, **2018**.

[32] E. M. Macias, A. M. Valenzuela-Muñiz, G. Alonso-Núñez, M. H. F. Sánchez, R. Gauvin and Y. V. Gómez, *Diamond and Related Materials*, **2020**, 103, 107671.

[33] N. Limani, I. S. Marques, B. Jarrais, A. J. Fernandes, C. Freire and D. M. Fernandes, *Catalysts*, **2022**, 12, 357.

[34] P. M. Gíslason and E. Skúlason, *Nanoscale*, **2019**, 11, 18683-18690.

[35] H. Vrubel and X. Hu, *Angew. Chem. Int. Ed.*, **2012**, 51, 12703-12706.

[36] A. Navaee, A. Salimi, S. Soltanian and P. Servati, *Journal of Power Sources*, **2015**, 277, 268-276.

[37] B. Olalde, J. M. Aizpurua, A. García, I. Bustero, I. Obieta and M. J. Jurado, *J. Phys. Chem. C*, **2008**, 112, 10663-10667.

[38] D. M. Fernandes and C. Freire, *ChemElectroChem*, 2015, 2, 269-279.

[39] N. Daems, X. Sheng, I. F. Vankelecom and P. P. Pescarmona, *J. Mater. Chem. A*, **2014**, 2, 4085-4110.

[40] D. Lee, L. De Los Santos V, J. Seo, L. L. Felix, A. Bustamante D, J. Cole and C. Barnes, *J. Phys. Chem. B*, **2010**, 114, 5723-5728.

[41] A. Kumarasinghe, L. Samaranayake, F. Bondino, E. Magnano, N. Kottegoda, E. Carlino, U. Ratnayake, A. De Alwis, V. Karunaratne and G. A. Amaratunga, *J. Phys. Chem. C*, **2013**, 117, 9507-9519.

[42] A. Misra, P. K. Tyagi, M. K. Singh and D. S. Misra, *Diamond and Related Materials*, **2006**, 15, 385-388.

[43] B. Olalde, J. M. Aizpurua, A. García, I. Bustero, I. Obieta and M. J. Jurado, *J. Phys. Chem. C*, **2008**, 112, 10663-10667.

[44] Z. Tian, J. Li, G. Zhu, J. Lu, Y. Wang, Z. Shi and C. Xu, *Phys. Chem. Chem. Phys.*, 2016, 18, 1125-1130.

[45] M. M. Doroodmand, S. Sobhani and A. Ashoori, *Canadian Journal of Chemistry*, **2012**, 90, 701-707.

[46] Y. Lou, H. Cai, X. Liu, S. Tu, K. Pei, Y. Zhao, G. Cao, S. Li, K. Qin and B. Cai, *Pharmacognosy Magazine*, **2014**, 10, S30.

[47] N. Daems, X. Sheng, I. F. J. Vankelecom and P. P. Pescarmona, *J. Mater. Chem. A*, **2014**, 2, 4085-4110.

[48] D. M. Fernandes, H. C. Novais, R. Bacsa, P. Serp, B. Bachiller-Baeza, I. Rodríguez-Ramos, A. Guerrero-Ruiz and C. Freire, *Langmuir*, **2018**, 34, 6376-6387.

[49] D. W. Lee, L. De Los Santos V, J. W. Seo, L. L. Felix, A. Bustamante D, J. M. Cole and C. H. W. Barnes, *J. Phys. Chem. B*, **2010**, 114, 5723-5728.

[50] A. R. Kumarasinghe, L. Samaranayake, F. Bondino, E. Magnano, N. Kottegoda, E. Carlino, U. N. Ratnayake, A. A. P. de Alwis, V. Karunaratne and G. A. J. Amaratunga, *J. Phys. Chem. C*, **2013**, 117, 9507-9519.

[51] R. Guerroudj, L. Dermeche, L. Mouheb, T. Mazari and C. Rabia, *The Eurasia Proceedings of Science Technology Engineering and Mathematics*, **2022**, 20, 1-9.

[52] M. R. Guerroudj, L. Dermeche, L. Mouheb, T. Mazari, S. Benadji and C. Rabia, *Bull. Chem. React. Eng. Catal*, **2019**, 14, 283-293.

[53] A. S. Aricò, P. Bruce, B. Scrosati, J.-M. Tarascon and W. van Schalkwijk, *Nature Materials*, **2005**, 4, 366-377.

[54] C. Freire, D. M. Fernandes, M. Nunes and V. K. Abdelkader, *ChemCatChem*, **2018**, 10, 1703-1730.

[55] B. Jarrais, A. Guedes and C. Freire, *ChemistrySelect*, 2018, 3, 1737-1748.

[56] M.-C. Huang and H. Teng, *Carbon*, **2003**, 41, 951-957.

[57] K. Artyushkova, A. Serov, S. Rojas-Carbonell and P. Atanassov, *J. Phys. Chem. C*, **2015**, 119, 25917-25928.

[58] A. M. El-Sawy, I. M. Mosa, D. Su, C. J. Guild, S. Khalid, R. Joesten, J. F. Rusling and S. L. Suib, *Adv. Energy Mater.*, **2016**, 6, 1501966.

[59] M. Waqas, L. Wu, H. Tang, C. Liu, Y. Fan, Z. Jiang, X. Wang, J. Zhong and W. Chen, *ACS Appl. Nano Mater.*, **2020**, 3, 4788-4798.

[60] J.-J. Fan, Y.-J. Fan, R.-X. Wang, S. Xiang, H.-G. Tang and S.-G. Sun, *J. Mater. Chem. A,* **2017**, 5, 19467-19475.

[61] Y. Wang, B. Zhang, M. Xu and X. He, *RSC advances*, **2015**, 5, 86746-86753.

[62] H. Estrade-Szwarckopf, *Carbon*, **2004**, 42, 1713-1721.

[63] M. E. Lipińska, S. L. Rebelo, M. F. R. Pereira, J. Gomes, C. Freire and J. Figueiredo, *Carbon*, **2012**, 50, 3280-3294.

[64] W. Ai, Z. Luo, J. Jiang, J. Zhu, Z. Du, Z. Fan, L. Xie, H. Zhang, W. Huang and T. Yu, *Adv. Mater.*, **2014**, 26, 6186-6192.

[65] Y. Liu, Y. Qiao, G. Wei, S. Li, Z. Lu, X. Wang and X. Lou, *Energy Storage Materials*, **2018**, 11, 274-281.

[66] H. C. Novais, D. M. Fernandes and C. Freire, *Applied Surface Science*, **2015**, 347, 40-47.

[67] K. Zilberberg, H. Gharbi, A. Behrendt, S. Trost and T. Riedl, *ACS Appl. Mater. Interfaces*, **2012**, 4, 1164-1168.

[68] R. Amin, M. A. Hossain and Y. Zakaria, *ACS Appl. Mater. Interfaces*, **2018**, 10, 13509-13518.

[69] H. N. Tran, S. Park, F. T. A. Wibowo, N. V. Krishna, J. H. Kang, J. H. Seo, H. Nguyen-Phu, S. Y. Jang and S. Cho, *Adv Sci (Weinh)*, **2020**, 7, 2002395.

[70] H. Wu and K. Lian, *ECS Transactions*, **2014**, 58, 67.

[71] I. M. Rocha, O. S. G. Soares, D. M. Fernandes, C. Freire, J. L. Figueiredo and M. F. R. Pereira, *ChemistrySelect*, **2016**, 1, 2522-2530.

[72] L. Dai, Y. Xue, L. Qu, H.-J. Choi and J.-B. Baek, *Chemical reviews*, **2015**, 115, 4823-4892.

[73] G. Rambabu, Z. Turtayeva, F. Xu, G. Maranzana, M. Emo, S. Hupont, M. Mamlouk, A. Desforges and B. Vigolo, *J. Mater. Sci.*, **2022**, 57, 16739-16754.

[74] N. Yang, L. Li, J. Li, W. Ding and Z. Wei, *Chemical science*, 2018, 9, 5795-5804.

[75] S. Ni, Z. Li and J. Yang, *Nanoscale*, **2012**, 4, 1184-1189.

[76] K. Kakaei, M. D. Esrafili and A. Ehsani, in *Interface Science and Technology*, eds. K. Kakaei, M. D. Esrafili and A. Ehsani, Elsevier, **2019**, vol. 27, pp. 203-252.

[77] Y. Zheng, Y. Jiao, L. Ge, M. Jaroniec and S. Z. Qiao, *Angew. Chem. Int. Ed.*, **2013**, 52, 3110-3116.

[78] R. Zhou, Y. Zheng, M. Jaroniec and S.-Z. Qiao, *Acs Catalysis*, **2016**, 6, 4720-4728.

[79] X. Liu, Y. Liu and L.-Z. Fan, *J. Mater. Chem. A*, **2017**, 5, 15310-15314.

[80] S. Liu, Z. Wang, S. Zhou, F. Yu, M. Yu, C. Y. Chiang, W. Zhou, J. Zhao and J. Qiu, *Adv. Mater.*, **2017**, 29, 1700874.

[81] J. Lach, K. Wróbel, J. Wróbel, P. Podsadni and A. Czerwiński, *J. Solid State Electrochem.*, **2019**, 23, 693-705.

[82] Y. Liang, H. Wang, J. Zhou, Y. Li, J. Wang, T. Regier and H. Dai, *J. Am. Chem. Soc.*, **2012**, 134, 3517-3523.

[83] M. P. Araújo, M. Nunes, I. M. Rocha, M. Pereira and C. Freire, *ChemistrySelect*, **2018**, 3, 10064-10076.

[84] Z. Lei, W. Feng, C. Feng, W. Zhou, C. Wei and X. Wang, *J. Mater. Chem. A*, **2017**, 5, 2012-2020.

[85] Z. Wang, Y. Lu, Y. Yan, T. Y. P. Larissa, X. Zhang, D. Wuu, H. Zhang, Y. Yang and X. Wang, *Nano Energy*, **2016**, 30, 368-378.

[86] S. Xia, W. Guo, N. Cai, L. Sun, H. Zhou, W. Lu, X. Chen, J. Zhang, Y. Chen and H. Yang, *Fuel Processing Technology*, **2021**, 224, 107028.

[87] G. A. Olah, *Angew. Chem. Int. Ed.*, 2013, 52, 104-107.

[88] C. Lo Vecchio, D. Sebastián, M. J. Lázaro, A. S. Aricò and V. Baglio, *Catalysts*, **2018**, 8, 650.

[89] P. Mathumba, D. M. Fernandes, R. Matos, E. I. Iwuoha and C. Freire, *Materials*, **2020**, 13, 1562.

[90] DK Lyon, WK Miller, T Novet, et al., **1991,** Journal of the American Chemical Society 113: 7209.

[91] S Hoang, S Guo, NT Hahn, AJ Bard, CB Mullins, **2012,** Nano Letters 12: 26.

[92] G Tuci, C Zafferoni, A Rossin, et al., **2014,** Chemistry of Materials 26: 3460.

[93] N Muthuswamy, MEM Buan, JC Walmsley, M Rønning, **2018**, Catalysis Today 301: 11.

Chapter 5

# Cobalt/Nickel Nanofoams: Potential application in Supercapacitors and OER/HER

# 5

# Cobalt/Nickel Nanofoams: Potential application in Supercapacitors and OER/HER[7,8]

While the preceding chapters focused on overcoming the kinetic barriers of the ORR using POM-carbon hybrids, a fully integrated energy conversion system requires equally robust solutions for water splitting reactions and energy storage. Departing from the previous molecular approach, the motivation for exploring three-dimensional cobalt and nickel nanofoams is driven by their highly porous metallic networks, which enable rapid mass transport and offer excellent electrical conductivity. The ultimate objective for this new class of material is to demonstrate its multifunctionality, proving that these bimetallic nanofoams can serve as highly efficient electrocatalysts for both the oxygen and hydrogen evolution reactions (OER and HER), as well as act as high-performance electrodes for supercapacitors.

[7] Scientific article submitted to the Journal of Power Sources.
Novais, H.C.; Montemor, M.F., Fernandes, A. J. S., Freire, C, Fernandes, D.M. Cobalt/Nickel Nanofoams: Potential application in Supercapacitors and OER/HER.

[8] Hugo C. Novais' contribution to the publication: synthesis and characterisation of the foams, electrocatalytic experiments and responsible for writing up the manuscript.

## Abstract

With the global energy crisis growing, the demand for alternative energy sources is more pressing than ever. Transition-metal nanofoams show great promise as materials for supercapacitors and electrocatalysts. However, their development in various fields is hindered by poor electrical conductivity and a lack of sufficient active sites. This study presents the successful synthesis of bi-metal (Cobalt and Nickel) nanofoams (CoNi-NF) using the hydrogen bubble template (DHBT) technique. The resulting foam-like structure exhibits a 3D porous architecture. The nanofoams' elemental composition was determined through EDX, confirming that each atomic percentages correspond to the Co/Ni ratio predetermined during synthesis.

Cyclic voltammetry (CV) and galvanostatic charge–discharge (GCD) measurements were used to assess the electrochemical performance of the nanofoams before and after activation in 5% $H_2O_2$. The bi-metal nanofoams showed higher specific capacitance values compared to the single metal nickel and cobalt nanofoams. The specific capacitance value of the oxidised nanofoam (CoNi-NF_75_OX) increased due to surface oxidation and activation by the 5% $H_2O_2$ chemical treatment, enhancing its capacitive response without degrading its morphology. The stability of CoNi-NF_75_OX nanofoam was good, maintaining its specific capacitance up to the 3000th cycle, which is a significant improvement over the as produced nanofoam (CoNi-NF_75). The electrochemical performance of cobalt-nickel, single cobalt foam and single nickel foam nanofoams was tested for both oxygen evolution reaction (OER) and hydrogen evolution reaction (HER). The high surface area of the nanofoams provides more active sites for the reaction, potentially enhancing electrocatalytic activity. Although the single Co nanofoam has a low overpotential (32 mV at 10 mA $cm^{-2}$) for HER, it is less stable compared to the mixed nanofoams. This research provides valuable insights into the synthesis and characterisation of Co and Ni nanofoams and their potential as promising materials for use in electrochemical energy storage and conversion systems, specifically supercapacitors.

## 5.1. Introduction

The need for improved electrochemical energy storage and conversion solutions is driven by the escalating issues of energy scarcity and environmental degradation. Therefore, there is a growing interest in supercapacitors and electrocatalysts for comprehensive water splitting.[1-5] Electrode materials that are high performance,

economically viable and environmentally friendly are critical to the advancement of more efficient electrochemical energy storage systems. These electrode materials can be classified into different groups based on their electrochemical behaviour, such as electrodes that behave like batteries, capacitive electrodes, and electrodes that exhibit an intermediate response (such as supercapacitors, etc.).[6-8] A variety of materials are currently being investigated as potential options for the next generation of electrochemical energy storage devices. Supercapacitors have recently received significant research attention as energy storage devices due to their high power density, fast charge/discharge rates, and robust cycle stability.[9-11] However, their practical advancement has been limited by the issue of low energy density.[12] Electrocatalysis for comprehensive water splitting is typically divided into two reactions: the Oxygen Evolution Reaction (OER) and the Hydrogen Evolution Reaction (HER). Pt-based materials for HER and $RuO_2$ and $IrO_2$ for OER, are commonly recognised as the most efficient electrocatalysts.[13] However, their high cost hinders widespread commercial use. Therefore, there is a need to investigate cost-effective materials with high performance to address the challenge of sluggish kinetics.[14-18] In this context, we focus on cobalt, nickel and cobalt/nickel nanofoams. These materials offer several advantages that make them promising candidates for OER and HER and supercapacitor applications. Co and Ni are considered to be cost-effective alternatives to the more expensive precious metal electrocatalysts.[1, 3, 18-20] However, despite considerable research, their performance in OER and HER applications requires further improvement. In addition to inherent material properties, other critical aspects of catalytic materials include a large surface area and a tailored morphology. A porous structure promotes efficient material utilisation and improves reactant accessibility, while the presence of intricate nanostructures can influence the electrocatalytic activity for OER and HER.[18, 21-25] Electrode materials that are often examined for supercapacitors applications include mixed metal oxides and hydroxides. Cobalt-nickel oxides, in particular, are gaining attention due to their lower cost in comparison with noble metal-based materials , recyclability, robust redox activity, and reliable electrochemical response.[10, 26, 27] The Dynamic Hydrogen Bubble Template (DHBT) is a technique suggested for fabricating porous nanofoams.[1, 28-30] The process of electrodeposition takes place amidst vigorous evolution of hydrogen bubbles, which forms a dynamic template leading to a deposit with high porosity. The size of the pores or cavities is dictated by the size of the emerging hydrogen bubbles. The morphology of the film depends on the metal's nucleation and growth mechanism and can vary from dendritic to resembling a cauliflower.[1, 31] Changes in hydrodynamic conditions during deposition can cause

changes in morphology. By adjusting the applied current density and deposition duration, the film can be tailored. The mechanical stability of the deposit can be influenced by the concentration and composition of the electrolyte.

This research explores materials suitable for supercapacitor applications, specifically the synthesis of 3D nanofoams composed of Co, Ni, and a CoNi nanofoams. In contrast to previous work of our research team (by *P. Arévalo-Cid et al.*)[32], which mainly focused on the structural and morphological characterisation of cobalt nanofoams, this study emphasises the electrochemical performance of Co, Ni and CoNi nanofoams. It introduces a detailed evaluation using cyclic voltammetry (CV), galvanostatic charge-discharge (GCD), electrochemical impedance spectroscopy (EIS), and electrochemically active surface area (ECSA) analysis. In addition, an $H_2O_2$ oxidation treatment was applied to enhance the redox activity and capacity. A comprehensive X-ray photoelectron spectroscopy (XPS) analysis was also carried out to investigate the oxidation states and their influence on the electrochemical behaviour. These were affixed onto a stainless steel base using the galvanostatic deposition process, steered by the DHBT method. The study aims to assess the electrochemical attributes of the nanofoams. GCD tests were performed to evaluate the electrochemical behaviour of the CoNi nanofoams as potential materials for supercapacitors. The degradation pattern of the bi metallic foams was also examined using EIS, providing insights into the capacity loss during extended usage. A thorough examination of the composition and morphology of these nanofoams was conducted. This enabled an understanding of their electrocatalytic performance, particularly in the context of OER and HER. Furthermore, their overall stability in alkaline media for energy conversion purposes was evaluated.

## 5.2. Experimental section

### 5.2.1 Materials and solvents

Stainless steel, AISI 304 (Goodfellow) 0.914 mm thick, was used as current collector for the metal foam deposition. The substrates were 2.5 cm × 2.5 cm with an area of about ~6.25 $cm^2$. They were initially polished with SiC abrasive paper from Buehler® of P360 and P600 grit to achieve a uniform, smooth, and clean surface. After polishing, the substrates were rinsed with distilled water and acetone, respectively. They were then dried with compressed air and in an oven at 40-50°C for at least 2 hours.

Finally, the weight of each substrate was measured using the Pioneer™ Semi-Micro PD225D balance with an accuracy of 0.001mg. $NiCl_2 \cdot 6H_2O$, $CoCl_2 \cdot 6H_2O$ and $NH_4Cl$ were obtained from Fluka Analytical. Finally, KOH was used as testing electrolyte. For that purpose, potassium hydroxide purchased from Sigma-Aldrich (> 99%) was used.

For electrolyte and metal foams preparation, ultrapure water (18.2 MΩ cm at 25ºC, Interlab) was always used.

### 5.2.2 Synthesis of electrodeposited cobalt/nickel nanofoams composites on stainless steel

The synthesis methodology employed for the electrodeposited cobalt/nickel nanofoam composites on stainless steel was developed based on the optimised procedures outlined in the study by *P. Arévalo-Cid et al*.[32] An aqueous solution of 0.1M $CoCl_2 \cdot {}_6H_2O$ and 2M $NH_4Cl$ (the total concentration of metallic ions has to be maintained, although the Co:Ni ratio can be altered, for example to 0.075 M and 0.025 M Co:Ni) was prepared for foam deposition. The foam deposition was galvanostatically deposited using the hydrogen bubble template (DHBT) technique in a two-electrode electrochemical cell connected to a BK Precision® 1667 DC power supply. AISI 304 stainless steel was the working electrode and Pt was used as a counter electrode of the electrochemical cell. The cylindrical cell was about 7 cm of height and about 4 cm of diameter. A lateral hole with a diameter of 0.7854 cm where the working electrode attached contains an O-ring to prevent the leakage of the electrolyte. A current density of -3.72 A $cm^{-2}$ (this implies -1.8 A in the current source) was applied for 30 seconds. After the foam deposition, the samples were rinsed respectively with distilled water and ethanol followed by drying with compressed air. Finally, the samples were dried at room temperature and the weight of the active material was carefully measured. Five samples were synthesised: single Ni nanofoams (Ni-NF), single cobalt nanofoams (Co-NF), 25% cobalt and 75% nickel foam (CoNi-NF_25), 50% cobalt and 50% nickel nanofoam CoNi-NF_50 and 75% cobalt and 25% nickel nanofoam CoNi-NF_75. The number on the sample indicates the percentage of cobalt present. Additionally, the CoNi-NF_75 sample underwent chemical treatment in a 5% hydrogen peroxide solution for 24 hours.

A thin Stainless steel current collector was chosen since it does not increase porosity, has no impact on the final electrochemical response, does not introduce relevant resistance, and is corrosion resistant.

### 5.2.3 Electrochemical study of CoNi nanofoams

An Autolab PGSTAT 302N (EcoChimie B.V.) potentiostat/galvanostat, controlled by the NOVA v2.1.6 software was employed for the cyclic voltammetry (CV), linear sweep voltammetry (LSV) and electrochemical impedance spectroscopy (EIS) studies. The experiments were carried out at room temperature.

The tests were conducted in a three-electrode electrochemical cell using 1 M KOH as the electrolyte for supercapacitor tests and 0.1 M KOH for energy conversion tests. The cell used for electrochemical measurements consisted of 3 electrodes: a modified stainless steel electrode as working electrode (2.5 cm × 2.5 cm with 0.7854 $cm^2$ of modified area, Ag/AgCl electrode (Metrohm, 3 mol $dm^{-3}$ KCl) as the reference and a carbon rod (Metrohm, 2 mm of diameter) for HER or a platinum wire (d = 0.6 mm, 0.5 m, 99.99 +%, Goodfellow) for OER and supercapacitors tests as counter electrodes.

The electrochemical response of the materials was studied using CV, GCD, EIS, and capacity retention with GCD cycling. The CV measurements were performed at 0.002, 0.005, 0.010, 0.020, 0.030, 0.040 and 0.050 V $s^{-1}$ (vs. Ag/AgCl 3 mol $dm^{-3}$ KCl) and the LSV ones at 0.005 V $s^{-1}$ (vs. RHE). The OER and HER electrochemical experiments were performed in nitrogen-saturated KOH (0.1 mol $dm^{-3}$). The electrolyte was bubbled with the desired gas for at least 30 min. LSVs were obtained by sweeping the potential from 1.0 V to 1.8 V vs. RHE for OER and from 0.2 V to -0.8 V vs. RHE with a scan rate of 0.005 V $s^{-1}$. All presented LSV tests were performed with $i_R$-compensation, via previous calculation of the uncompensated resistance (Ru) of the circuit by using *i*-interrupt approach, and finally, applying an $i_R$-compensation value equal to 0.90×Ru to the LSV measurement. Tafel slopes were determined by linear fitting of LSV data to the following equation:

$$\eta = a + b \times \log|j| \tag{5.1}$$

where $\eta$ is the overpotential, b is the Tafel slope, and $j$ is the current density. Stability tests were evaluated by chronoamperometry in $N_2$-saturated KOH for 36 000s.

The GCD was performed at various current values ranging from 0.1 to 5 A $g^{-1}$ within the potential range of 0 V to 0.45 V. The specific capacitance (C) of the electrodes (measured in F $g^{-1}$) was calculated from galvanostatic discharge curves obtained at different discharge currents (from 0.1 A $g^{-1}$ to 5 A $g^{-1}$) according to the equation:

$$C = \frac{i(A) \times \Delta t}{m \times \Delta V} \tag{5.2}$$

where i(A) is the constant discharging current, $\Delta$t (s) is the discharge time, m (g) the mass of electrodeposited nanofoam and $\Delta V$(V) is the potential drop at constant discharge current.

The EIS was conducted at two different potentials, corresponding to two different charge states of the material: discharged at 0 V and charged at 0.45 V. A voltage of interest was applied for 120 seconds as a conditioning pre-step. Then, EIS was measured by applying a sinusoidal perturbation with 10 mV of amplitude (rms) in the frequency range of 0.01–$10^5$ Hz. Finally, capacity retention testing was performed for the cobalt-nickel oxide materials by charging and discharging the material 3500 times at a current density of 1 A $g^{-1}$.

### 5.2.4 Characterisation techniques

The surface morphology and chemical composition of the various materials were analysed using scanning electron microscopy (SEM) for direct imaging, energy dispersive X-ray spectroscopy (EDX), X-ray diffraction (XRD) and Raman spectroscopy.

The SEM/EDX images were acquired using a high resolution (Schottky) environmental SEM with X-ray microanalysis and electron backscattered diffraction analysis (Quanta 400 FEG ESEM/EDAX Genesis X4M), in high-vacuum conditions, at Centro de Materiais da Universidade do Porto (CEMUP). Raman spectra were recorded using a Jobin Yvon Horiba Labram HR-800 micro-spectrometer, excited with a He-Cd laser at the 442nm line. The diffraction grating used was 600 lines/mm. Spectra were collected with a 100x objective (Olympus, NA=0.9, focus point ~1micrometer), with acquisition times of 10s in 10 accumulations (total time of 100s per spectrum). Given the sensitivity of the samples to radiation, a neutral density filter was used to keep the excitation power below ~1 mW at the sample.

The XRD was used to study the structure and composition of the nanofoams. The nanofoams materials were characterised by X-Ray diffraction on a Rigaku SmartLabSe diffractometer equipped with Cu Kα radiation (λ = 1.5418 Å). Wide-angle diffractograms were collected over the range 10º < 2θ < 80º with a step size of 0.02◦ and counting time of 10 s.

The XPS spectra were obtained on Thermo Fisher Scientific K-Alpha spectrometer with monochromatized Al Kα radiation (1486.6 eV), at CACTI - Servicio Nanotecnología y Análisis de Superficies, Universidade de Vigo, Spain. The binding energies were calibrated using the C 1s peak at 284.60 eV as internal reference. The CasaXPS software was used to deconvolute the XPS spectra, employing a non-linear

least square fitting routine after a Shirley-type background subtraction. Surface atomic percentages were calculated from the corresponding peak areas upon spectra deconvolution and using the sensitivity factors provided by the manufacturer.

## 5.3. Results and discussion

### 5.3.1 Materials characterisation

Scanning Electron Microscopy (SEM) was used to examine the morphology of all synthesised materials. Figure 5.1 presents SEM images that reveal the nanofoams' structure at magnifications of 1000×, 5000×, and 25000×. The materials exhibit a foam-like structure with a three-dimensional (3D) porous architecture. The SEM images demonstrate that the nanofoams have a highly porous, honeycomb-like morphology with both regular and irregular voids. The presence of voids within the surface voids indicates a highly porous structure with interconnected channels. Some of these irregular channels, which connect the voids, result from coalescence during the galvanotactic deposition process, specifically the DHBT technique. The samples show void diameters ranging from 2 μm to 15 μm. The nickel nanofoam has a continuous structure, in contrast to the cobalt-containing nanofoams, which exhibit cracks connecting the voids. Figure 5.1 (c) shows the cauliflower-shaped agglomerates of the Ni-NF sample, while Figures 5.1 (f) and Figures 5S1 (c, f and h) show dendritic-shaped agglomerates in the Co-containing samples. This difference is due to the electrodeposition of 3D Ni foams, resulting in the formation of a compact, cauliflower-shaped morphology around the voids.[1] This deposit type has a smaller surface area than dendrites. Figure 5.1 (i) shows the CoNi-NF_75_OX sample, which has cauliflower-like agglomerates. However, there is a significant change in the agglomerate morphology. The nanofoam surface is covered by a cloudy layer, causing further agglomeration of the cauliflower-like nanostructures.[20, 33] This layer comprises of CoOOH and NiOOH nanosheets that grow almost perpendicularly on the substrate and interconnect to form a network. The small spike-like features within the cauliflower clusters, which are the vertices of the nanosheets, are revealed in Figure 5S2. These films are likely formed through instantaneous nucleation followed by growth.[34]

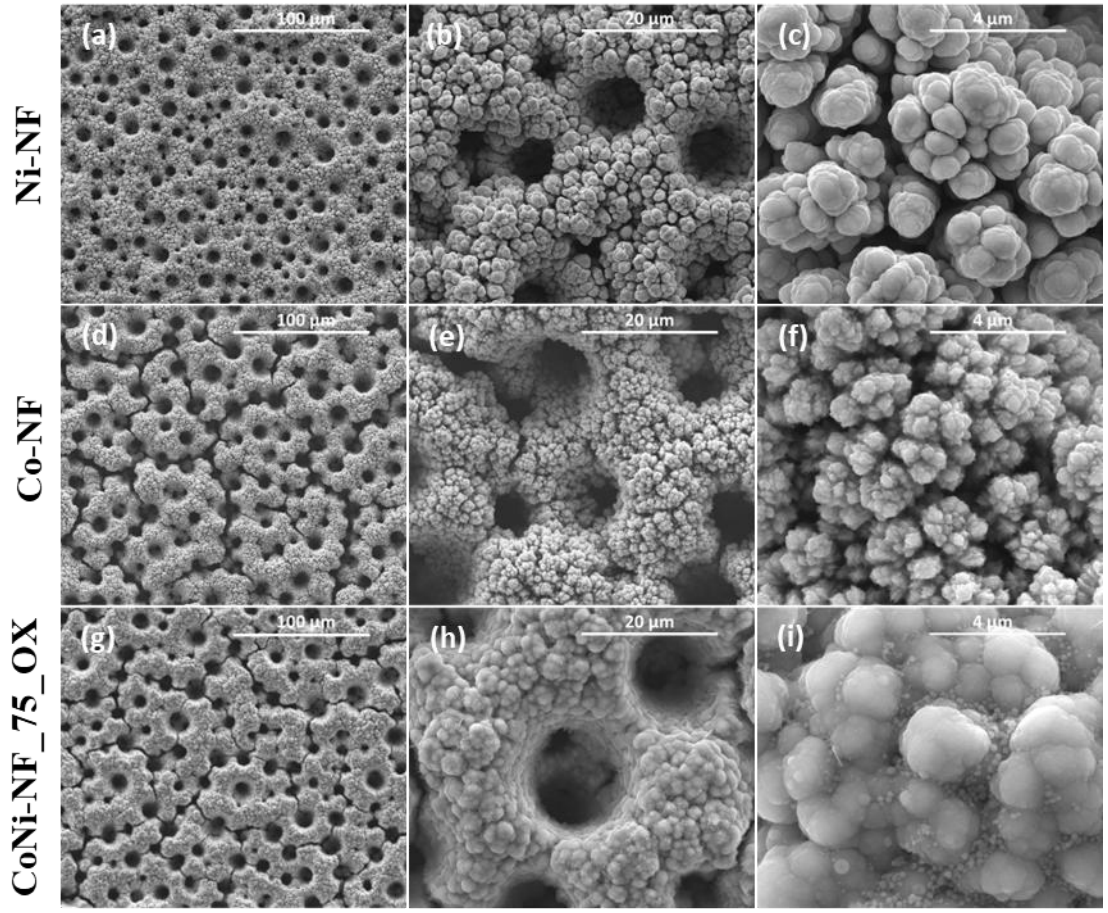



Figure 5.1 - SEM images of the electrode materials electrodeposited on stainless steel at different magnifications: (a, d, g) at 1000×, showing overall morphology; (b, e, h) at 5000×, highlighting finer structural details; (c, f, i) at 25000×, revealing nanoscale features.

X-ray diffraction (XRD) diffractograms were obtained to determine the crystalline phase of the nanofoams. All samples showed a consistent pattern, indicating the preservation of their chemical composition, except for the Co-NF nanofoam. The diffraction facets (111), (200), and (220) associated with face-centred cubic Ni (ICDD: 01-087-0712) (Figure 5.2 (a)) showed varying intensity ratios and slightly shifted peaks across the different nanofoams.[1] Figure 5.2 (b) shows the diffractogram obtained for a cobalt nanofoam. Broad diffraction peaks are visible at 41.9º, 44.4º, 47.2º, and 50.2º, corresponding to the reflection planes (100), (111), (101), and (200), respectively. The peaks observed in the X-ray diffraction pattern can be attributed to the cubic crystalline system of metallic cobalt (ICDD: 00-001-1259).[20, 35] The high fluorescence of cobalt under copper X-rays is the cause of the low signal-to-noise ratio. For purposes of comparison, the XRD pattern of the substrate has also been included in Figure 5.2 (a).

The XRD results of the stainless steel indicate the presence of austenite (γ-Fe) and ferrite (α-Fe). Therefore, the XRD results are in accordance with the EDS results. The XRD phase analysis confirmed the diffraction planes for face-centred cubic (FCC) austenite and body-centred cubic (BCC) ferrite. The peaks characteristic of FCC austenite were (111)γ, (200)γ and (220)γ, while the peaks characteristic of BCC ferrite appeared at (110)α and (200)α.[36-40]

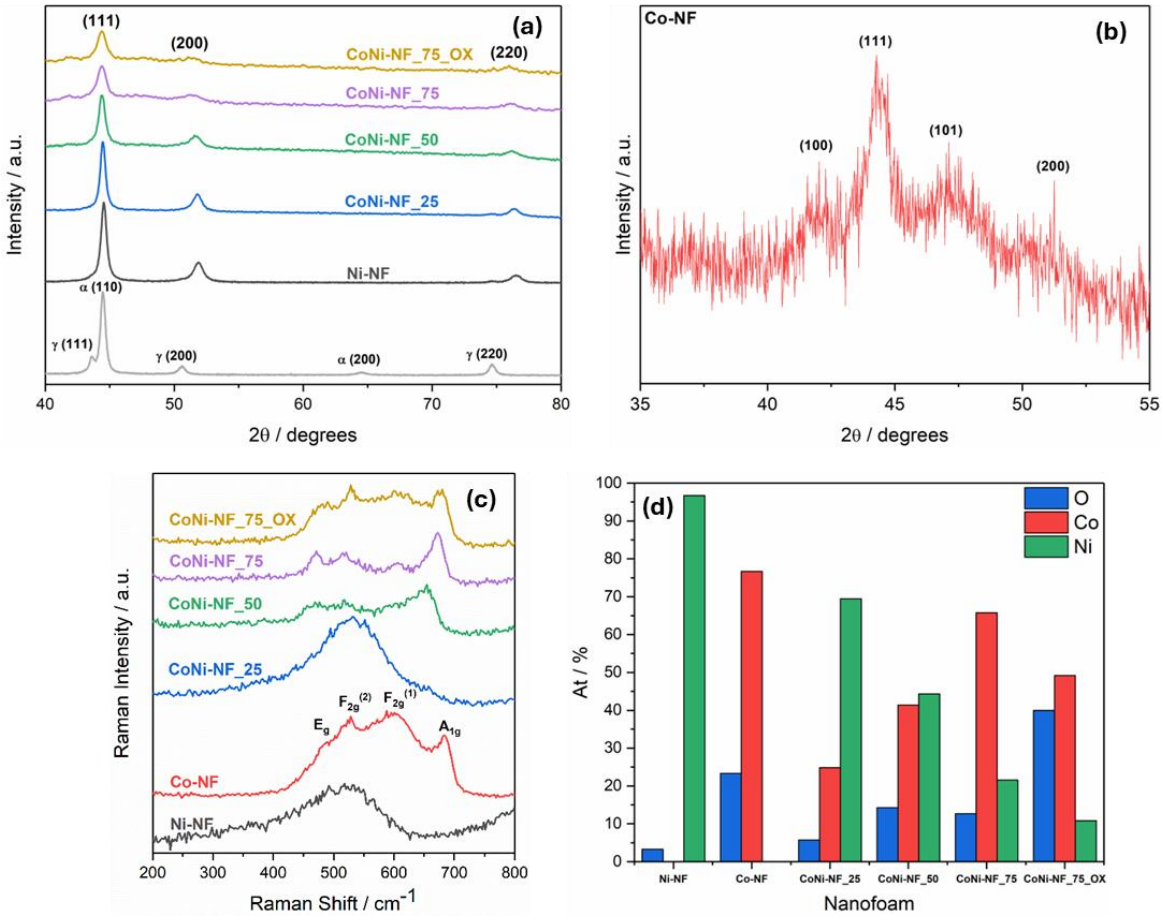



Figure 5.2 - X-ray diffraction (XRD) patterns. (a) Patterns of (grey) stainless steel support, (black) Ni-NF, (blue) CoNi-NF_25, (green) CoNi-NF_50, (purple) CoNi-NF_75 and (yellow) CoNi-NF_75_OX; (b) Pattern (red) Co-NF; (c) Raman spectra for (black) Ni-NF, (red) Co-NF, (blue) CoNi-NF_25, (green) CoNi-NF_50, (purple) CoNi-NF_75 and (yellow) CoNi-NF_75_OX; (d) Atomic percentage of O, Co and Ni for each nanofoam.

Raman spectroscopy is commonly used to characterise carbon forms, but it can also identify certain bands related to hydroxides and metal oxides, as supported by the literature.[10] Raman spectroscopy is a widely used technique for assessing structural defects and disturbances.[26] Figure 5.2 (c) shows the Raman spectra obtained for the

different nanofoams. All the peaks observed in the spectra, which are associated with nickel and cobalt, have low Raman shifts. Cobalt displays four signals at 490, 528, 600, and 683 $cm^{-1}$, which correspond to Co-O vibrations and can be assigned to the $E_g$, $F_{2g}^{(2)}$, $F_2g^{(1)}$, and $A_{1g}$ bands.[26, 41, 42] The peak at 525 $cm^{-1}$ in the Ni-NF sample is attributed to the characteristic vibrational modes of the Ni-O crystal lattice in the 3D nickel nanofoam.[26, 43] For mixed CoNi nanofoams, an increase in cobalt content results in intensified cobalt peaks. This effect is particularly noticeable in the CoNi-NF_25 nanofoam, where the broad nickel peak is significantly reduced.

The elemental composition of the fabricated nanofoams was ascertained through Energy Dispersive X-ray Spectroscopy (EDX), a semi-quantitative chemical technique, as depicted in Figure 5.2 (d). The EDX analysis reveals that the atomic percentages of each nanofoam align with the Co/Ni ratio predetermined during synthesis. This outcome suggests that the co-deposition of Ni and Co is consistent under the experimental conditions employed in this study. The CoNi-NF_75_OX nanofoam exhibits a high percentage of oxygen, attributable to the oxidation process conducted with 5% $H_2O_2$. The EDX results, presented in Figure 5S3 and Figure 5.2 (d), corroborate the formation of a metal oxide foam. Consequently, it can be concluded that metal nanofoams are successfully synthesised via galvanostatic electroplating using the HDBT method.

The surface chemistry and oxidation states of the samples, Ni-NF, Co-NF, CoNi-NF_25, CoNi-NF_50, CoNi-NF_75, and CoNi-NF_75_OX, were thoroughly investigated using X-ray photoelectron spectroscopy (XPS). This analysis was crucial in understanding the oxidation states of nickel and cobalt, as well as identifying the types of oxygen species present in the materials. The XPS results provided valuable insights into the chemical environment of these elements, shedding light on the composition and oxidation treatment of the nanofoams. To obtain a complete understanding of the oxidation behaviour, the Ni 2p, Co 2p, and O 1s photoionisations were systematically analysed. The results obtained from this analysis revealed a progressive evolution in oxidation states across the different compositions. It was observed that there was an increase in higher oxidation states in samples with greater cobalt content, as well as those subjected to oxidative treatment. Furthermore, the O 1s photoionization deconvolution confirmed the presence of multiple oxygen species, including lattice oxygen ($O^{2-}$), hydroxides ($OH^-$), and oxyhydroxides ($OOH^-$). These oxygen species play a crucial role in defining the chemical stability and electrochemical properties of the materials.

The Ni 2p photoionization of the Ni-NF sample (Figure 5S4 (a)) reveals two primary ionisations at ~854.9 eV (Ni $2p_{3/2}$) and ~872.6 eV (Ni $2p_{1/2}$), which are

characteristic of $Ni^{2+}$ species.[44, 45] Furthermore, the presence of a higher binding energy feature at ~856.5 eV (Ni $2p_{3/2}$) and ~874.1 eV (Ni $2p_{1/2}$), suggests a contribution from $Ni^{3+}$ species, indicative of NiOOH formation.[44, 45] This suggests that the sample contains a mixture of $Ni^{2+}$ and $Ni^{3+}$, primarily in the form of NiO, $Ni(OH)_2$, and possibly NiOOH. In the CoNi nanofoam series, the Ni2p and Co2p photoionisations (Figure 5S4 (b, c and d)) evidenced an increasing cobalt content, with the $Ni^{2+}$ signature at ~855.5 eV remaining dominant in all cases, suggesting the presence of NiO and $Ni(OH)_2$. However, a gradual increase in intensity around 856.5–857.1 eV, corresponding to $Ni^{3+}$ species, was observed as the cobalt content increased. This suggests that the incorporation of cobalt into the nanofoam structure promotes the stabilisation of higher nickel oxidation states, likely due to electronic interactions between Ni and Co in the mixed-metal system. A noteworthy observation in these samples was the presence of the Ni LMM Auger peak (~776–780 eV), which overlapped with the Co $2p_{3/2}$ region.[46, 47] This overlap required careful spectral deconvolution to ensure accurate quantification of the Co and Ni contributions. The interaction between Ni and Co in these materials highlights the complex nature of electronic transitions within bimetallic oxide systems. Upon subjecting the CoNi-NF_75_OX sample (Figure 5S4 (e)) to oxidation treatment, a significant increase in the $Ni^{3+}$ component of the Ni 2p spectrum was observed, pointing out the formation of NiOOH. The shift towards higher oxidation states suggests that the oxidative treatment facilitated the transformation of $NiO/Ni(OH)_2$ into NiOOH. The increase in $Ni^{3+}$ has been well-documented in analogous systems, where surface oxidation leads to the formation of oxyhydroxide species, which are known to enhance electrocatalytic performance.[48-50]

The Co 2p photoionisation of the Co-NF sample (Figure 5S5 (a)) exhibited two primary ionisations at ~780.2 eV (Co $2p_{3/2}$) and ~795.6 eV (Co $2p_{1/2}$).[51] These were accompanied by shake-up satellites, which appeared ~5–6 eV above the main peaks. The fitting of these photoionisations revealed contributions from both $Co^{2+}$ and $Co^{3+}$ oxidation states, probably corresponding to CoO, $Co(OH)_2$, and CoOOH. The coexistence of $Co^{2+}$ and $Co^{3+}$ species in the Co-NF sample suggests a mixed oxidation state system, which is crucial for redox processes and catalytic activity. As the cobalt content increased in the CoNi nanofoam series (Figure 5S5 (b, c, and d)), the $Co^{3+}$ peak (~781.7 eV) became increasingly more intense relative to the $Co^{2+}$ peak (~780.4 eV). This progression indicates a higher proportion of CoOOH in samples with greater Co content, suggesting that the Co-Ni interaction facilitates oxidation. The shake-up satellites remained consistent across the samples. The overlap with the Ni LMM Auger peak (~776–780 eV) in the Co $2p_{3/2}$ photoionization was observed in the CoNi-NF_25

sample, necessitating careful peak separation. In the oxidised CoNi-NF_75_OX sample (Figure 5S5(e)), a significant increase in the $Co^{3+}$ component was observed, indicating the formation of CoOOH. This increase in $Co^{3+}$ suggests a transition towards higher oxidation states, which is consistent with the observed increase in $Ni^{3+}$ in the Ni 2p s photoionization.

The O 1s photoionization of the samples (Figure 5S6 (a, b, c, d, e, f)) exhibited variations in the number and intensity of peaks, indicating different oxygen environments depending on composition and oxidation state. Two to three primary peaks were identified: $O^{2-}$ (~529.3–530.3 eV), corresponding to lattice oxygen in metal oxides (NiO, CoO), and $OH^-$ (~531.1–531.4 eV), associated with hydroxyl groups in $Ni(OH)_2$ and $Co(OH)_2$.[51-53] In certain samples, a third peak, designated as $OOH^-$ (~532.4–533.4 eV) and adsorbed water, was identified, suggesting the presence of oxyhydroxides (NiOOH, CoOOH) or adsorbed water species. A discernible trend emerged across the Co-Ni series: in samples with higher cobalt content, the $OOH^-$ peak became more pronounced, confirming an increasing proportion of oxyhydroxides (CoOOH, NiOOH). However, in samples such as Ni-NF, only two peaks were observed, suggesting a limited presence of oxyhydroxides.[53] Conversely, in samples exhibiting a greater degree of oxidation, such as CoNi-NF_75_OX, the presence of all three oxygen species was distinctly evident, thereby supporting the formation of higher oxidation state oxyhydroxides.

## 5.4. Performance and evaluation of supercapacitors

A thorough evaluation of the studied supercapacitors was carried out using various metrics and methodologies, including an assessment of their capacitance and cycling stability. These performance attributes are crucial for their use in energy storage devices.[10, 35, 54]

Cyclic voltammetry (CV) is a crucial measurement technique for evaluating the electrochemical behaviour of materials intended for use in electrochemical energy storage and conversion systems.[20, 55] CV results, procured at varying scanning speeds (vs. Ag/AgCl), for all the fabricated nanofoams in in $N_2$-saturated 0.1 M KOH are depicted in Figure 5.3. Galvanostatic charge-discharge (GCD) measurements in 1 M KOH electrolyte are presented in Figure 5.4. The curves exhibit redox peaks attributable to reactions (1), (2), (3), and (4) [1, 10]:

$$Ni(OH)_2 + OH^- \leftrightarrow NiOOH + H_2O + e^- \quad (1)$$

$$NiO + OH^- \leftrightarrow NiO(OH) + e^- \quad (2)$$

$$Co(OH)_2 + OH^- \leftrightarrow CoOOH + H_2O + e^- \quad (3)$$

$$CoOOH + OH^- \leftrightarrow CoO_2 + H_2O + e^- \quad (4)$$

It is crucial to underscore that these reactions do not represent the precise stoichiometry but are merely illustrative of the variation in the oxidation state of nickel and cobalt during the charge-discharge process. The cyclic voltammograms reveal that the redox peaks tend to diverge from each other and, in the case of the mixed nanofoams, even vanish. This phenomenon could be attributed to the polarisation of the electrodes at higher scanning rates and the augmented resistance of the electrode, resulting in these reactions exhibiting markedly slow kinetics. However, this behaviour is to be expected, as reported in the literature.[20, 26, 55] The area beneath the CV curve of the CoNi-NF_75_OX electrode surpassed that of all the other electrodes studied, suggesting its superior charge storage capacity.[19]

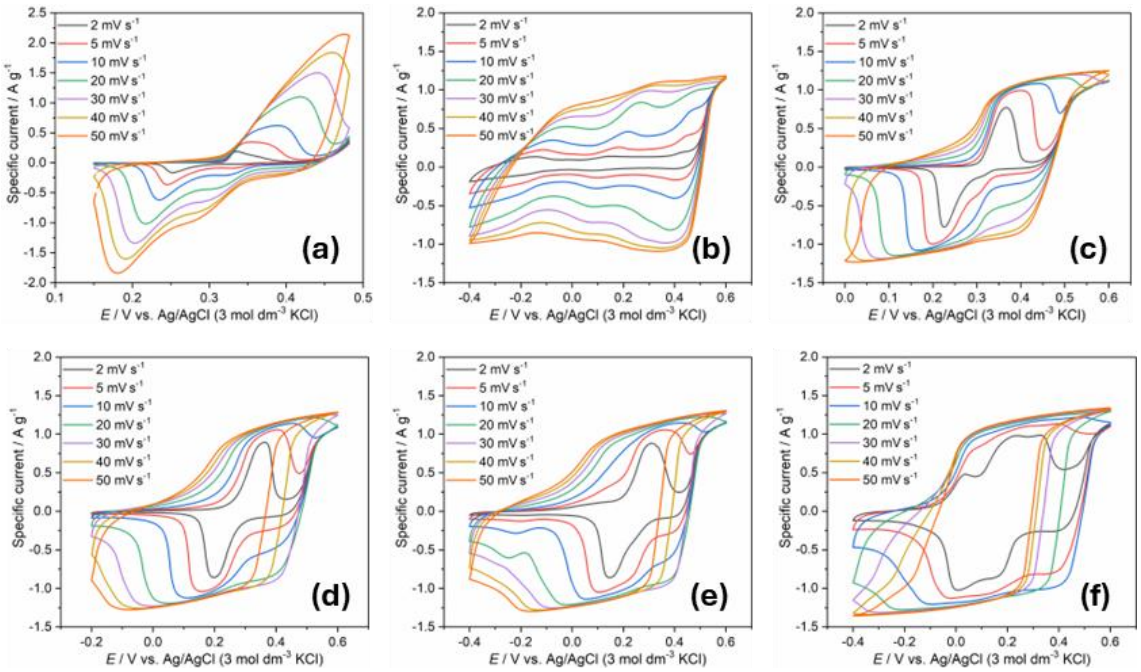



Figure 5.3 - CVs of (a) Ni-NF, (b) Co-NF, (c) CoNi-NF_25, (d) CoNi-NF_50, (e) CoNi-NF_75 and (f) CoNi-NF_75_OX nanofoams in $N_2$-saturated 0.1 mol $dm^{-3}$ KOH solution.

The Ni-NF nanofoam CVs, shown in Figure 5.3 (a), display a battery-like response with distinct and sharp redox peaks indicating significant Faradaic reactions.[55] Figure 5.4 (a) presents the GCD curve for the Ni-NF nanofoam, which

shows a flat charge/discharge plateau at a constant voltage level. In contrast, the CVs of the Co-NF nanofoam, as shown in Figure 5.3 (b), exhibit an integrated pseudocapacitive behaviour with partial slower redox participation.[8] This is supported by the shape of the GCDs in Figure 5.4 (b). However, the current-voltage relationship mirrors that of Electric Double Layer Capacitor (EDLC) materials, assuming a pseudo-rectangular CV shape and a triangular-shaped GCD curve. For the mixed CoNi materials (CoNi-NF_25, CoNi-NF_50, CoNi-NF_75, and CoNi-NF_75_OX), as shown in Figures 5.3 (c, d, e, and f) and Figures 5.4 (c, d, e, and f), the electrochemical characteristics exhibit well-defined separated peaks in the CV curves and a relatively flat charge/discharge plateau in the GCD curve. Consequently, they should be categorised as materials behaving as a Faradic rather than pseudocapacitive electrodes.[8, 55]

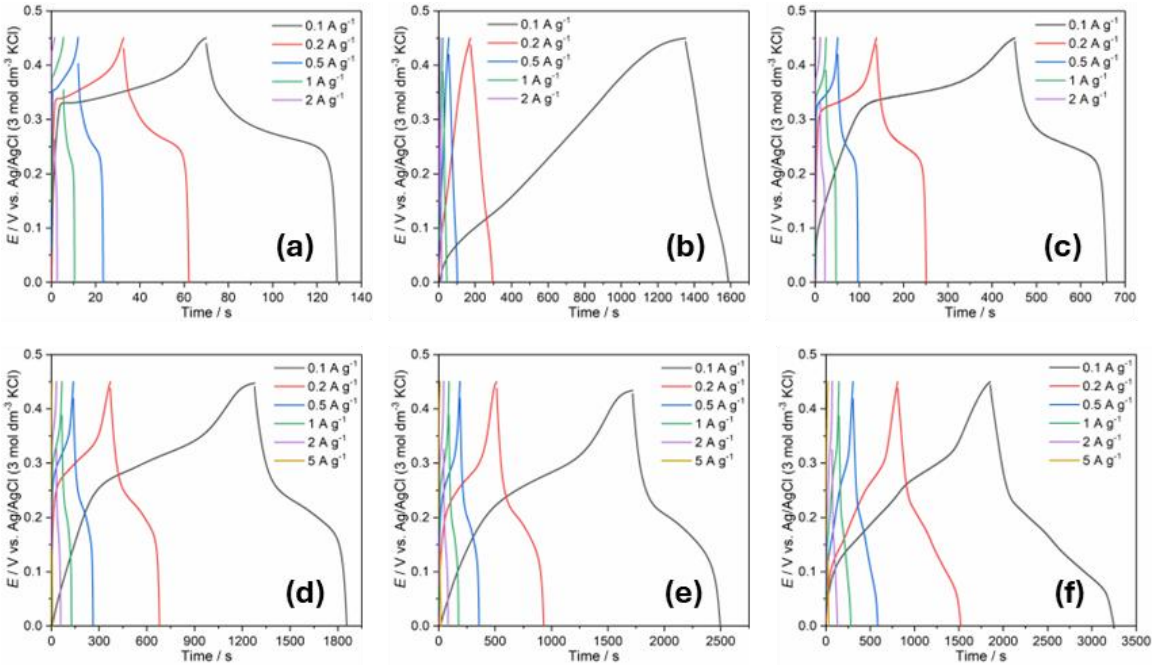



Figure 5.4 - GCDs of (a) Ni-NF, (b) Co-NF, (c) CoNi-NF_25, (d) CoNi-NF_50, (e) CoNi-NF_75 and (f) CoNi-NF_75_OX nanofoams at current densities from 1 to 5 A $g^{-1}$ in 1 mol $dm^{-3}$ KOH solution.

The specific capacitance values derived from the discharge curves in 1 M KOH (as shown in Figures 5.4 (a, b, c, d, e and f)) are presented in Table 5.1, calculated according to Equation 5.2. The potential windows used to measure the specific capacitance values of each nanofoam were optimised to bypass the potential range that minimally contributes to the specific capacitance in the corresponding nanofoams. The specific capacitance values at 1 A $g^{-1}$ are 14.2 F $g^{-1}$, 53.6 F $g^{-1}$, 57.7 F $g^{-1}$, 155.0 F $g^{-1}$,

215.4 F $g^{-1}$ and 345.5 F $g^{-1}$ for the Ni-NF, Co-NF, CoNi-NF_25, CoNi-NF_50, CoNi-NF_75 and CoNi-NF_75_OX nanofoams respectively. The specific capacitance of the mixed nanofoams shows an increase compared to the single metal nickel nanofoam and cobalt nanofoam due to the presence of synergistic redox reactions. The increased specific capacitance value observed for the CoNi-NF_75_OX nanofoam is due to the contribution of surface oxidation and activation by the 5% $H_2O_2$ chemical treatment. This chemical oxidation treatment of the nanofoam allows the sample to undergo oxidation without degrading its morphology, thereby improving its capacitive response. In fact, a capacitance increase of approximately 160% at 1 A $g^{-1}$ is achieved when the CoNi-NF_75 nanofoam is chemically treated with 5% $H_2O_2$, demonstrating a high charge storage capacity. In our experiments, we encountered difficulties in calculating the specific capacitance for Ni-NF, Co-NF and CoNi-NF_25 at a high current density of 5 A $g^{-1}$. This was due to the rapid charge/discharge process induced by such a high current density, which exceeded the response time of our measurement system. Consequently, it was challenging to accurately capture the specific capacitance under these conditions. In particular, the response time of these nanofoams dropped to zero when a specific current of 5 $Ag^{-1}$ was applied. The specific capacitance varies with the specific current applied, as shown in Figure 5S7. The results demonstrate capacitance retentions of 66%, 93%, 137%, 128%, 134%, and 130% when the current increases from 0.1 A $g^{-1}$ to 2 A $g^{-1}$ for Ni-NF, Co-NF, CoNi-NF_25, CoNi-NF_50, CoNi-NF_75, and CoNi-NF_75_OX, respectively. The specific capacitance values at 0.1 A $g^{-1}$ are lower than those at 2 A $g^{-1}$ except for single-metal nanofoams. This suggests that single-metal nanofoams may have limitations in rate capability, ion diffusion, ohmic losses at higher currents and/or the result of less accessible active sites at higher rates.[8, 55] The specific capacitance values varied with the applied current. Notably, the mixed-metal nanofoams exhibited higher specific capacitance values at 2 A $g^{-1}$ compared to 0.1 A $g^{-1}$. Thorough investigation is warranted into faradaic efficiency, a critical characteristic. Upon evaluating the charge versus discharge time ($t_{discharge}/t_{charge}$) for the composite materials at 1 A $g^{-1}$, we obtained ratios of 0.92, 0.89, 0.92, 0.92, 0.84, and 0.91 for the Ni-NF, Co-NF, CoNi-NF_25, CoNi-NF_50, CoNi-NF_75, and CoNi-NF_75_OX nanofoams, respectively. These nanofoams exhibit high faradaic efficiency values, surpassing those of cobalt/nickel metal oxides optimised with carbon materials. The treatment of the CoNi-NF_75 nanofoam with 5% $H_2O_2$ resulted in an increase in faradaic efficiency from 0.84 to 0.91. This enhancement could be attributed to improved electron transfer, as the chemical treatment can augment electron conduction, thereby bolstering reaction reversibility.

Table 5.1 - Values of specific capacitance calculated current densities ranging from 1 to 5 A $g^{-1}$ for Ni-NF, Co-NF, CoNi-NF_25, CoNi-NF_50, CoNi-NF_75 and CoNi-NF_75_OX nanofoams.

| Current Density (A $g^{-1}$) | Ni-NF | Co-NF | CoNi-NF_25 | CoNi-NF_50 | CoNi-NF_75 | CoNi-NF_75_OX |
|---|---|---|---|---|---|---|
| | F $g^{-1}$ | | | | | |
| 0.1 | 13.4 | 53.0 | 46.7 | 131.4 | 181.4 | 314.3 |
| 0.2 | 13.7 | 55.5 | 51.4 | 141.1 | 190.4 | 325.1 |
| 0.5 | 14.0 | 55.7 | 54.4 | 147.9 | 201.8 | 334.3 |
| 1 | 14.2 | 53.6 | 57.7 | 155.0 | 215.4 | 345.5 |
| 2 | 8.9 | 49.3 | 63.9 | 168.4 | 242.7 | 366.0 |
| 5 | - | - | - | 184.8 | 299.0 | 407.1 |

To assess the durability of the nanofoams, it was calculated the retention of specific capacitance from the discharge curves at 1 A $g^{-1}$ over 3500 charge/discharge cycles for the two most promising nanofoams. Figure 5.5 (a) and (b) illustrates the stability of specific capacitance for CoNi-NF_75 and CoNi-NF_75_OX nanofoams. The specific capacitance of the CoNi-NF_75 nanofoam rapidly increases within the first 600 cycles and then reaches a plateau. In contrast, the CoNi-NF_75_OX nanofoam exhibits exceptional stability for the initial 1100 cycles, which is almost double that of the CoNi-NF_75 nanofoam. However, it then experiences a significant increase. This sudden surge in specific capacitance is due to the time required for the electrolyte to permeate all the pores within the nanofoams. The complete potential of the nanofoam is only realised once the electrolyte has reached all the pores, including more constrained ones. After complete wetting of the foam, the specific capacitance values regain stability. However, the CoNi-NF_75 nanofoam exhibits a decline in capacitance from the 2200th cycle onwards. In contrast, the CoNi-NF_75_OX nanofoam maintains stability up to the 3000th cycle, after which it begins to show a drop in specific capacitance values. This decrease is primarily attributed to minor detachment of the nanofoam from the stainless steel substrate, rather than the irreversibility of the reaction.

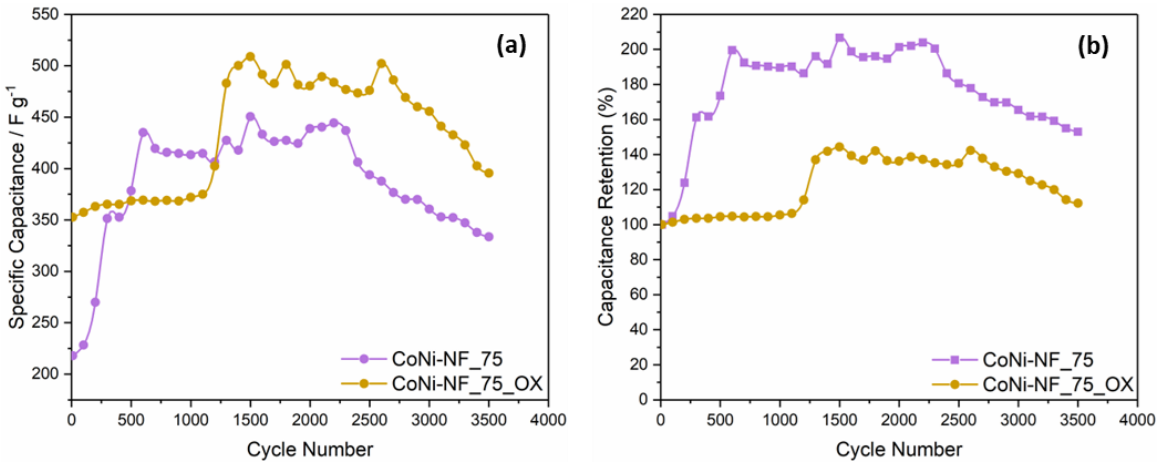



Figure 5.5 - Comparison of (a) specific capacitance and (b) capacitance retention obtained between CoNi-NF_75 and CoNi-NF_75_OX nanofoams in 1 mol $dm^{-3}$ KOH solution during cycling at 1 A $g^{-1}$ over 3500 cycles measured in 1 mol $dm^{-3}$ KOH solution.

Electrochemical Impedance Spectroscopy (EIS) was employed to assess the electrochemical performance and stability of the CoNi-NF_75_OX composite following prolonged cycling. EIS measurements were conducted at 0 V (discharged state) following 0 and 2000 cycles of galvanostatic charge-discharge (GCD) at 1 A $g^{-1}$ (Figure 5.6). Measurements were conducted at a discharged potential of 0 V to circumvent interference from the oxygen evolution reaction (OER) at higher potentials, which could obfuscate the impedance response. Consequently, the analysis at 0 V provides a more accurate reflection of the material's stability and impedance behaviour, uncontaminated by OER-related artefacts. The Bode and Nyquist plots presented in Figures 5.6 (a), 5.6 (b), and 5.6 (c) offer insights into the impedance characteristics of CoNi-NF_75_OX under cycling conditions. Figure 5.6 (a) show the magnitude Bode plot, which represents the impedance magnitude (|Z|) as a function of frequency. The CoNi-NF_75_OX nanofoam exhibits low |Z| values at high frequencies and elevated values at low frequencies, which is characteristic of a system that behaves like a capacitor at high frequencies and a resistor at low frequencies.[10, 26] However, after 2000 cycles, there is a noticeable increase in impedance values across all frequencies, reflecting a possible rise in internal resistance due to changes in the electrode's surface or due to modifications in the surface structure as a result of cycling. The phase angle in EIS represents the change in phase when the input and output signals are overlapped in time. In an ideal capacitor the phase angle is -90 degrees, and in an ideal resistor, it is 0 degrees.[56] The phase angle plot (Figure 5.6 (b)) further supports the Bode plot

observation. Initially, the CoNi-NF_75_OX composite exhibits a high phase angle at low frequencies, approaching ideal capacitive behaviour. However, after 2000 cycles, there is a reduction in the phase angle, indicating a deviation from ideal capacitance. This shift in phase angle suggests that the material's electrochemical characteristics are affected by cycling, potentially due to structural degradation or surface passivation, which impacts its ability to store charge efficiently.[56]

The Nyquist plots, in Figure 5.6 (c), for the initial and cycled states of CoNi-NF_75_OX show a near-vertical slope at low frequencies in the fresh electrode, consistent with a good capacitive response. In an ideal capacitor, the impedance diminishes as the frequency increases, represented by a vertical line in the Nyquist plot.[54] The near-vertical lines in the plot indicate that the system is behaving very much like an ideal capacitor [54] However, with an increase in the number of cycles, the angle of the Nyquist line exhibits a decrease, means that the system is shifting away from ideal capacitive behaviour. The value of Z' is greater at low and high frequencies as the cycles increase, suggesting that the equivalent series resistance of the system or impedance is increasing with the number of cycles at low and high frequencies. This may be due to changes, such as pores blocking or formation of parasitic and irreversible species in the electrode surface over the cycles.

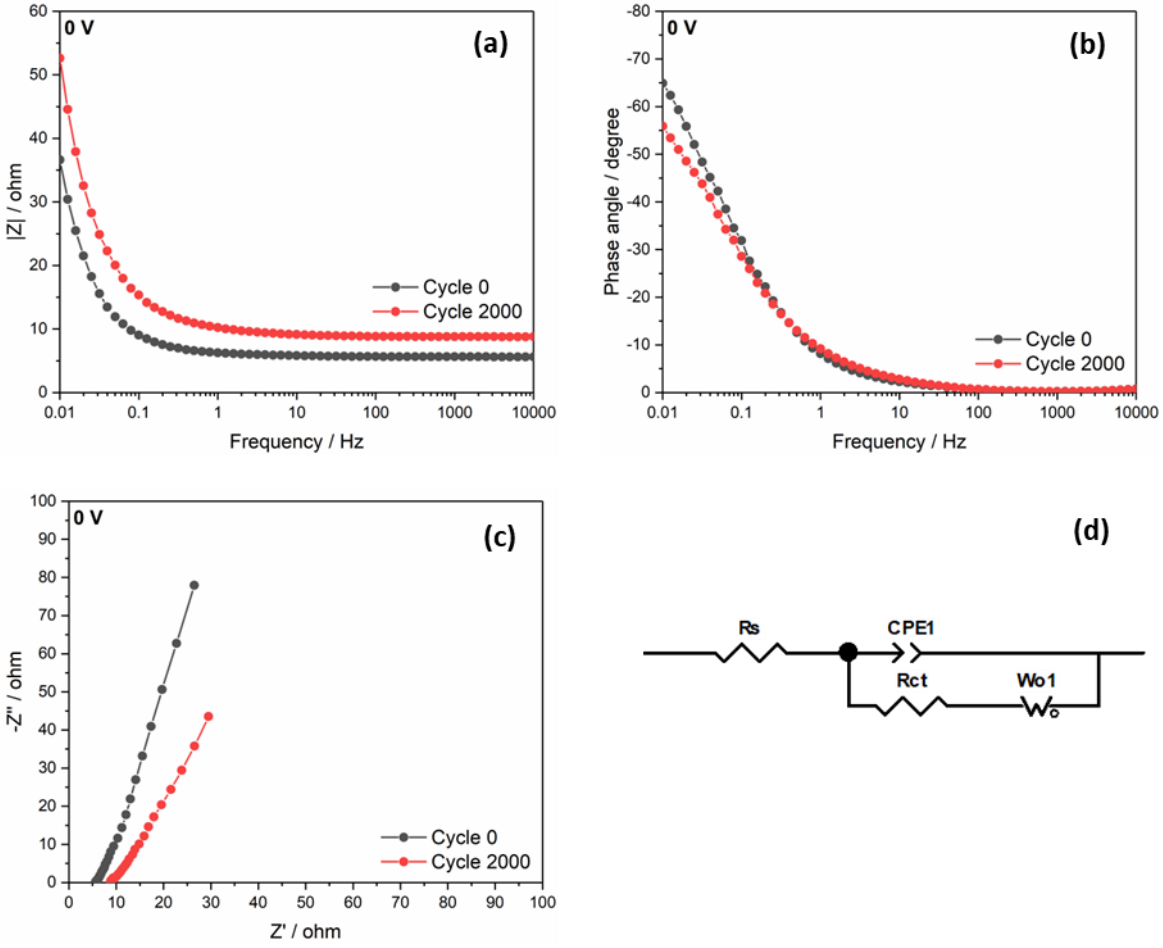



Figure 5.6 - (a and b) Bode, (c) Nyquist Electrochemical Impedance Spectra for CoNi-NF_75_OX composite material after 0 and 2000 cycles of Galvanostatic Charge Discharge at 1 A $g^{-1}$ for discharged (0 V) potential and (d) equivalent circuit model used in the fitting of the impedance spectra acquired for CoNi-NF_75_OX at 0V (discharged).

To further analyse these changes quantitatively, the EIS data were fitted to an equivalent circuit model (Figure 5.6 (d)), comprising a solution resistance ($Rs$), a constant phase element (CPE1) representing the double-layer capacitance at the electrode/electrolyte interface, a charge-transfer resistance ($Rct$), and a Warburg impedance (Wo1) to account for diffusion processes within the electrode material. The fitting parameters for the initial and 2000-cycle states are presented in Table 5.2.

The initial solution resistance ($R_s$) was found to be 5.66 Ω, which subsequently increased to 8.79 Ω following the completion of 2000 cycles. This increase in *Rs* indicates a potential rise in the electrolyte's resistance, which is likely due to degradation in the ionic conductivity of the electrolyte or changes in the electrode's surface properties that restrict ion access to the electrode. Furthermore, the increase in solution resistance also

suggests possible structural or compositional degradation within the electrode itself. Additionally, the Constant Phase Element (CPE) parameters suggest a reduction in capacitive behaviour. The initial CPE value of 0.140 $\Omega^{-1}$ $cm^{-2}$ $s^n$ decreased to 0.097 $\Omega^{-1}$ $cm^{-2}$ $s^n$, while the CPE exponent (n) decreased from 0.803 to 0.656, indicating that the material deviates further from a capacitive response after 2000 cycles. This shift is likely to be a consequence of alterations to the electrode surface or structure, including electroconductivity which have the effect of reducing its effective charge-storage capacity. The initial values reflect near-ideal capacitive behaviour at the electrode-electrolyte interface, which points out higher capacitance values.

Table 5.2 - Fitted parameters obtained by numerical simulation of the EIS experimental data for CoNi-NF_75_OX composite material at 0 V potential.

| | CoNi-NF_75_OX | |
|---|---|---|
| | (cycle 0) | (cycle 2000) |
| $R_S$ ($\Omega$ $cm^2$) | 5.66 | 8.79 |
| $R_{ct}$ ($\Omega$ $cm^2$) | 0.078 | 0.417 |
| $R_{total}$ ($\Omega$ $cm^2$) | 5.74 | 9.20 |
| $W_R$ ($\Omega$ $cm^2$) | 9.73 | 20.5 |
| CPE ($\Omega^{-1}$ $cm^{-2}$ $s^n$) | 0.140 | 0.097 |
| n | 0.803 | 0.656 |
| $\chi^2$ Chi-Squared | 0.00037 | 0.00012 |

Additionally, the very low charge-transfer resistance ($R_{ct}$) exhibits a pronounced rise, from 0.078 Ω initially to 0.417 Ω after 2000 cycles. This suggests a reduction in the electrode's charge-transfer efficiency. This increase in $R_{ct}$ may be attributed to the formation of resistive features, surface passivation or insulating layers on the electrode, which can impede electron transport at the electrode/electrolyte interface. The total resistance, $R_{total}$, was found to increase from 5.74 Ω $cm^2$ up to 9.20 Ω $cm^2$ after 2000 cycles of charge-discharge, as illustrated in Table 5.2. This increase in $R_{total}$ suggests a cumulative rise in resistive losses within the system, which is likely due to surface changes and degradation that restrict electron transfer and ion diffusion and. The Warburg impedance ($W_R$), which accounts for mass transfer within the electrode, demonstrates significant alterations following the cycling process. The Warburg resistance ($W_R$) exhibited an increase from 9.73 Ω initially to 20.5 Ω after 2000 cycles,

indicating a potential slowing of ion diffusion within the electrode structure. Finally, the low chi-squared ($\chi^2$) values confirm that the equivalent circuit model effectively captures the electrochemical behaviour of the CoNi-NF_75_OX composite, both initially and after prolonged cycling. The chi-squared parameter provides an indication of the goodness of fit between the experimental data and the equivalent circuit model.

## 5.5. Electrochemical performance towards the OER and HER

The electrochemical performance of electrocatalysts in the OER and the HER can be affected by various factors, including material conductivity, surface area, porosity, and the presence of active sites. These factors significantly impact the performance of electrocatalysts in these reactions. [18, 57] These reactions are integral processes in water splitting, which is a promising avenue for sustainable hydrogen production. Therefore, a comprehensive understanding of supercapacitor performance can provide valuable insights for optimising OER and HER processes. To demonstrate their multifunctional catalytic activity, the electrochemical performance of the cobalt-nickel and nickel-cobalt nanofoams was tested for both OER and HER.

The electrochemical performance of the Ni-NF, Co-NF, CoNi-NF_25, CoNi-NF_50, and CoNi-NF_75 nanofoams was tested for OER. Figure 5.7 (a) displays the LSV curves, and Table 5.3 presents the key parameters. The electrocatalytic activities of the Ni-NF, Co-NF, CoNi-NF_25, CoNi-NF_50, and CoNi-NF_75 nanofoams were measured in a three-electrode system using 0.1 mol $dm^{-3}$ KOH. It is clear that the peak between 1.1 V and 1.2 V vs RHE refers to cobalt. The oxidation peaks observed between 1.3 V and 1.5 V vs RHE are attributed to nickel. These peaks can be used to predict OER performance.[18] One of the parameters typically determined to assess the performance of the OER electrocatalyst is the potential required to reach $j$ = 10 mA $cm^{-2}$, which corresponds to the current density expected at the electrode in a solar water-splitting device (under sunlight) with an efficiency of 10%.[14] The reference point for overpotential ($\eta_{10}$) at $j$ = 10 mA $cm^{-2}$ is generally taken. However, the oxidative peaks of the nanofoams make it somewhat difficult to obtain the overpotential value. The $\eta_{10}$ values for Ni-NF, Co-NF, CoNi-NF_25, CoNi-NF_50 and CoNi-NF_75 are relatively low, with values of 0.323, 0.321, 0.333, 0.347 and 0.362, respectively. It appears that the initial nanofoams, Ni-NF and Co-NF, achieve a higher current density value. In the context of OER, the nanofoams' high surface area provides more active sites for the

reaction, potentially enhancing electrocatalytic activity. Furthermore, the good electrical conductivity of Ni and Co nanofoams can facilitate electron transfer during OER, which is crucial for efficient energy conversion. However, the performance of a Co/Ni nanofoams can vary depending on its specific composition and structure. The morphology of the material is altered by the interaction between Ni and Co in the nanofoam, which can affect its electrocatalytic performance in OER, as seen in Figure 5.1. It is crucial to note that the electrocatalyst's performance can also be influenced by the specific conditions under which OER is carried out. Therefore, while Ni and Co nanofoams may perform better under certain conditions, a Co/Ni nanofoam may be more effective under different conditions. These findings suggest that there is no potential synergistic impact in the combined nanofoams under these conditions.

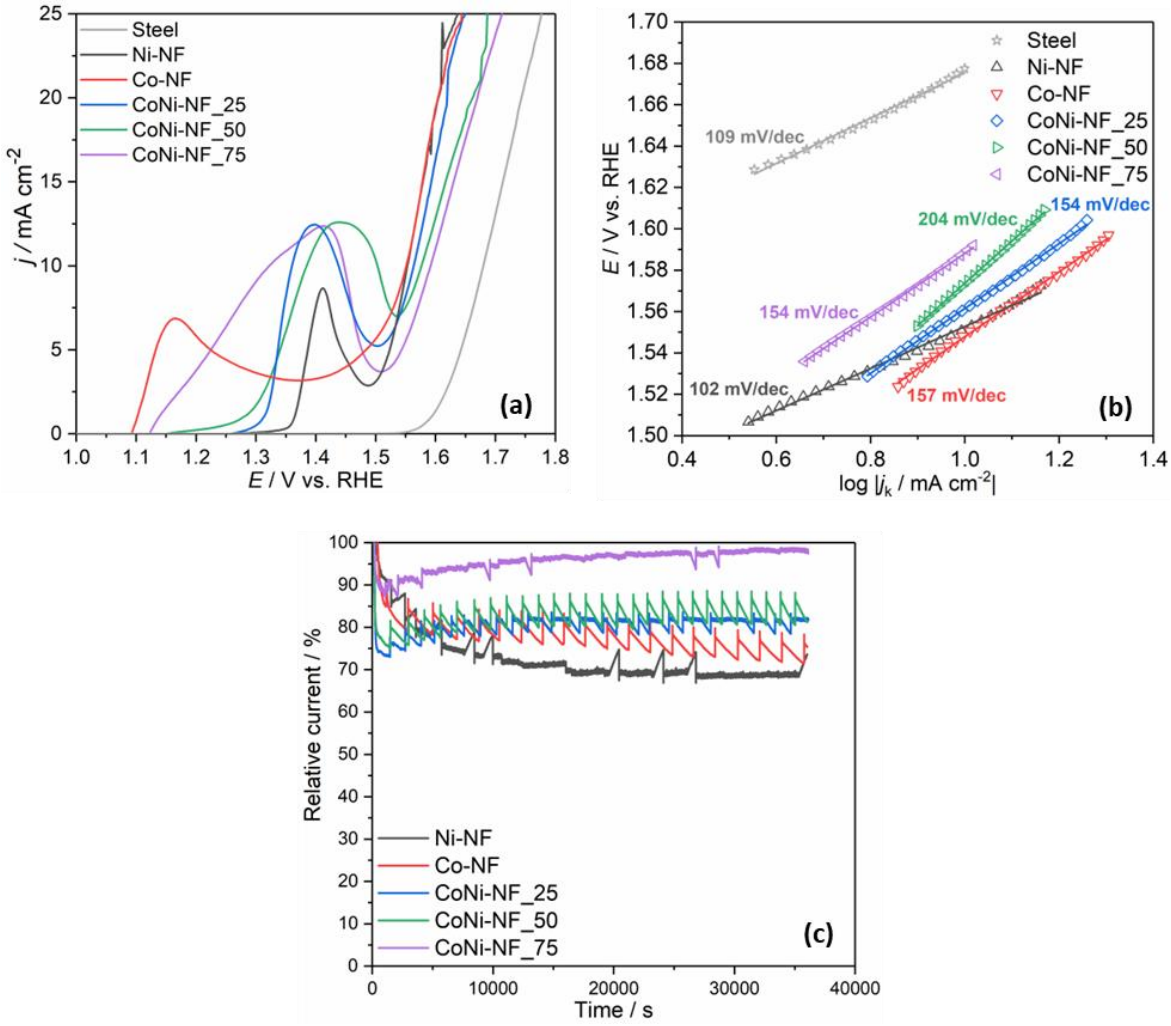



Figure 5.7 - (a) OER LSV curves of Ni-NF, Co-NF, CoNi-NF_25, CoNi-NF_50, CoNi-NF_75 obtained in a 0.1 mol $dm^{-3}$ KOH electrolyte saturated in $N_2$, (b) the corresponding OER Tafel plots and (c) the chronoamperometric responses for 36000s.

Figure 5.7 (b) shows the Tafel analysis of the cobalt/nickel nanofoams in an OER context. The Tafel slopes range from 102 to 204 mV/dec, which is typical for this type of material.[58] Among the analysed nanofoams, the Ni-NF nanofoam exhibited the best slope value, demonstrating its superior efficiency for OER. Additionally, Figure 5.7 (c) presents the results of the long-term stability tests for OER. During the chronoamperometric stability test, all of the nanofoams produced positive results. Notably, the CoNi-NF_75 nanofoam demonstrated exceptional performance, retaining 98.2% of its current after 10 hours. The remaining nanofoams achieved retention rates of 68.7%, 75.7%, 82%, and 86.4% for Ni-NF, Co-NF, CoNi-NF_25, and CoNi-NF_50, respectively. The graph illustrates the drops in local current density caused by the

formation of oxygen bubbles on the electrode surface. Although the previous current density values are partially recovered with the release of the bubbles.

Table 5.3 - The OER performance parameters for Ni-NF, Co-NF, CoNi-NF_25, CoNi-NF_50 and CoNi-NF_75 nanofoams.

| **Sample** | $E_{10}$ **V vs RHE** | $\eta_{10}$ ($j$ **=10 mA cm$^{-2}$**) | **Tafel (mV dec$^{-1}$)** |
|---|---|---|---|
| Ni-NF | 1.553 | 0.323 | 102 |
| Co-NF | 1.551 | 0.321 | 157 |
| CoNi-NF_25 | 1.563 | 0.333 | 154 |
| CoNi-NF_50 | 1.577 | 0.347 | 204 |
| CoNi-NF_75 | 1.592 | 0.362 | 154 |

The electrocatalytic properties of the nanofoams for HER were evaluated in a 0.1 mol dm$^{-3}$ KOH solution. Figure 5.8 (a) shows the polarisation curves obtained through LSV for Ni-NF, Co-NF, CoNi-NF_25, CoNi-NF_50, and CoNi-NF_75. To assess the performance of HER electrocatalysts, it is crucial to consider the potential value corresponding to a current density of $j$ = 10 mA cm$^{-2}$, which is referred to as the overpotential ($\eta_{10}$). This parameter is crucial because hydrogen evolution devices, when coupled with sunlight, typically operate at current densities of 10 - 20 mA cm$^{-2}$ under standard conditions (AM 1.5, 1 sun). [59] The cobalt nanofoam exhibited superior performance among the tested materials, achieving an overpotential of $\eta_{10}$ = 32 mV. The overpotentials for CoNi-NF_75, CoNi-NF_50, CoNi-NF_25, and Ni-NF nanofoams were $\eta_{10}$ = 68 mV, 95 mV, 120 mV, and 142 mV, respectively. These results suggest that a better performance is achieved for the nanofoams with higher content of cobalt as the overpotential value increases with lower cobalt content in the nanofoam. No synergistic interaction between Co and Ni was observed in these nanofoams for this reaction, similar to the OER tests.

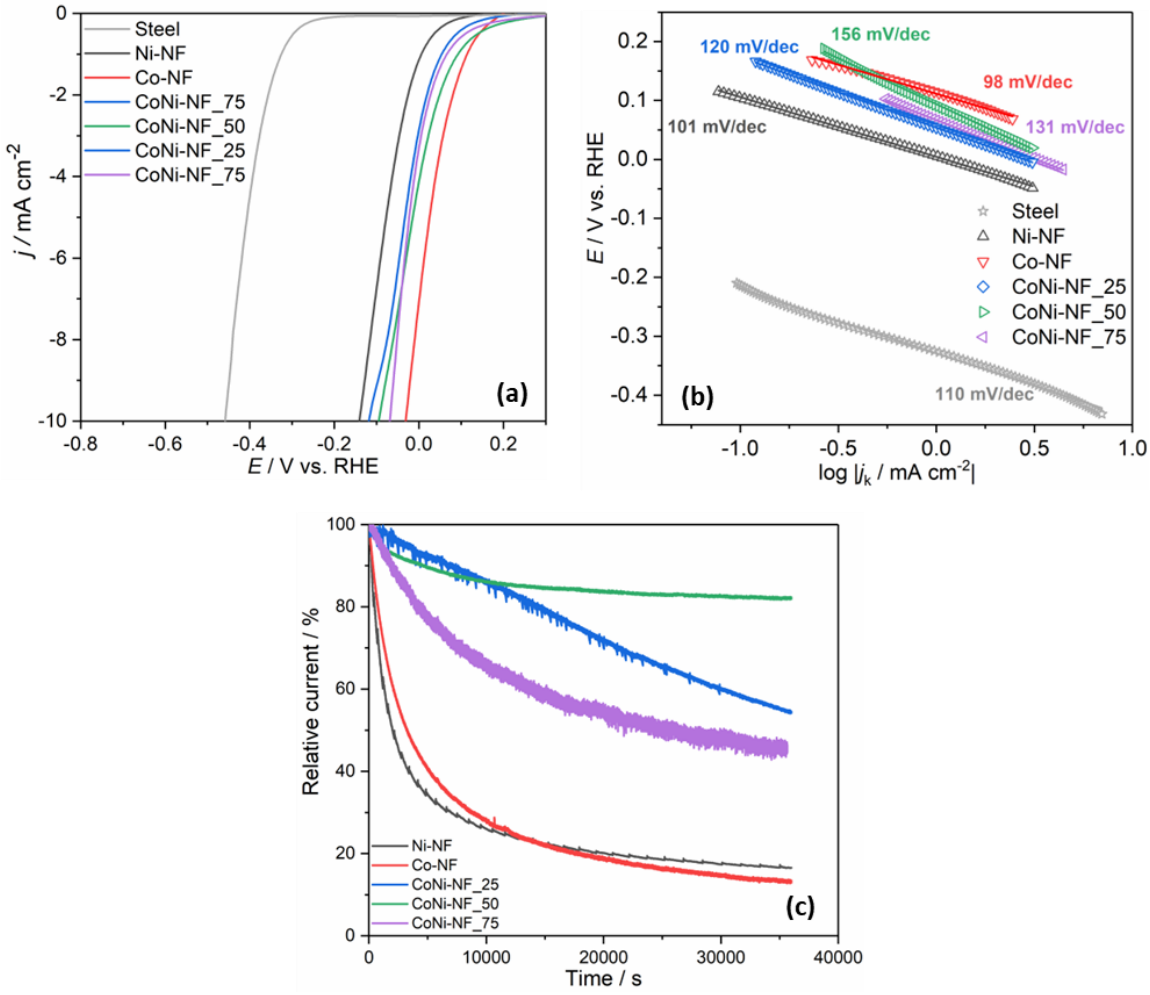



Figure 5.8 - (a) HER LSV curves of Ni-NF, Co-NF, CoNi-NF_25, CoNi-NF_50, CoNi-NF_75 obtained in a 0.1 mol $dm^{-3}$ KOH electrolyte saturated in $N_2$, (b) the corresponding HER Tafel plots. (c) and the chronoamperometric responses in 0.1 mol $dm^{-3}$ $N_2$–saturated KOH for 36000s.

In an effort to delve deeper into the kinetics of the HER, it was scrutinised the Tafel plot depicted in Figure 5.8 (b). In the context of the HER mechanism, the Tafel slopes serve as a pivotal tool in discerning the rate-determining step and the prospective HER reaction pathway. The HER can be explained via two mechanisms [60-62], each involving an initial phase of hydrogen adsorption, known as the Volmer step, followed by either an electrochemical desorption, referred to as the Heyrovsky step, or a chemical recombination, termed the Tafel step. In this particular instance, HER is occurring within the porous matrix of the nanofoam. Given the intricate nature of the electrode structure, it is commonplace to observe deviations from the standard Tafel slope values. [1, 62] Remarkably, Co-NF demonstrated a lower Tafel slope (98 mV $dec^{-1}$) compared to the

other nanofoams. The Tafel values obtained for Ni-NF, CoNi-NF_25, CoNi-NF_50, and CoNi-NF_75 were 101, 120, 156, and 131 mV $dec^{-1}$, respectively. The nanofoams, namely Co-NF, Ni-NF and CoNi-NF_25, show an intermediate slope ranging from 40 to 120 mV $dec^{-1}$. This range is expected for the Volmer and Heyrovsky reaction mechanism. The above range includes the Tafel slope values found for these nanofoams, but not for the nanofoams CoNi-NF_50 and CoNi-NF_75. It is important to note that higher Tafel slope values have been documented for other porous materials [1, 63-65], which are in agreement with the previously mentioned deviating values. Additionally, it was conducted a chronoamperometric test at a constant potential value, as depicted in Figure 5.8 (c). The results show that all samples experienced a decrease in current density over a 10 hour period. At the end of the test, the mixed nanofoams displayed the most favourable current density values. These observations indicate that while the individual Co and Ni tested have a low overpotential for HER, they exhibit less stability compared to the mixed nanofoams.

Table 5.4 - The HER performance parameters for Ni-NF, Co-NF, CoNi-NF_25, CoNi-NF_50 and CoNi-NF_75 nanofoams.

| **Sample** | **$\eta_{10}$ (mV vs. RHE)** | **Tafel (mV $dec^{-1}$)** | **% Current Retention** |
|---|---|---|---|
| Ni-NF | 142 | 101 | 16.6 |
| Co-NF | 32 | 98 | 13.1 |
| CoNi-NF_25 | 120 | 120 | 54.3 |
| CoNi-NF_50 | 95 | 156 | 82.1 |
| CoNi-NF_75 | 68 | 131 | 45.6 |

In order to further investigate the electrochemical performance of the nanofoam samples, the electrochemically active surface area (ECSA) was determined for Ni-NF, Co-NF, CoNi-NF_25, CoNi-NF_50, CoNi-NF_75, and CoNi-NF_75_OX. The ECSA is a crucial parameter in evaluating the intrinsic activity of electrocatalysts, as it provides insights into the available electrochemical sites that contribute to catalytic reactions. The

results obtained from the ECSA measurements reveal significant variations across the different compositions, reflecting the influence of material composition and oxidation treatment on electrochemical properties. The ECSA values for the nanofoam electrocatalysts were estimated using the following relationship:

$$ECSA = \frac{C_{dl}}{C_{ref}} \tag{5.3}$$

where $C_{dl}$ is the double-layer capacitance and $C_{ref}$ is the specific capacitance value per unit area. The impossibility of knowing the exact $C_{ref}$ value for specific and structurally complex materials means that reliable ECSA values cannot be obtained frequently. However, given the direct proportionality of ECSA to $C_{dl}$, a reliable relative comparison of the similar electrocatalysts compositions can be made based on $C_{dl}$ values. In this study, the double-layer capacitance of Ni-NF, Co-NF and CoNi nanofoams was determined through CV measurements conducted in a non-faradaic potential region. The double-layer capacitance was estimated by acquiring consecutive CV scans at different scan rates (from 5 to 50 mV $s^{-1}$) and extracting the slope from a linear fit of current density versus scan rate. The non-faradaic potential regions were selected based on the electrochemical stability of each sample, with capacitance values estimated at 0.27 V vs. Ag/AgCl for Ni-NF, -0.87 V for Co-NF, and -0.07 V for the CoNi nanofoams. The Ni-NF specimen (Figure 5S9 (a)) demonstrated a moderate ECSA, indicative of the electrochemical accessibility of nickel oxide/hydroxide species. The presence of $Ni^{2+}$ (NiO, $Ni(OH)_2$) and minor contributions from $Ni^{3+}$ (NiOOH) result in a stable, redox-active surface, thereby facilitating charge transfer. However, the relatively lower intrinsic conductivity of Ni-based oxides compared to cobalt-rich samples may limit its overall electrochemical activity. As demonstrated in Figure 5S9 (b), the Co-NF specimen exhibited a greater ECSA in comparison to the Ni-NF specimen, thus indicating an augmented number of active sites available for the purpose of electrochemical reactions. The presence of $Co^{2+}$ and $Co^{3+}$ species (CoO, $Co(OH)_2$ and CoOOH) has been demonstrated to enhance charge transport, a phenomenon attributable to the superior conductivity of cobalt-based oxides in comparison to nickel oxides. Moreover, the formation of CoOOH in alkaline conditions has been shown to contribute to an enhanced redox response, a process which results in a further increase in the active surface area.[66] The ECSA of the CoNi mixed-metal samples (Figure 5S9 (c and d)) exhibited a progressive increase with rising cobalt content; the CoNi-NF_25 sample (75% Ni and 25% Co) showed a higher ECSA than the Ni-NF sample, suggesting that cobalt incorporation enhances electrochemical accessibility. As the cobalt content increased to 50% (CoNi-NF_50), the ECSA further increased, indicating an optimised balance

between Ni and Co species. This enhancement can be attributed to synergistic electronic interactions between Ni and Co, which promote charge transfer and increase the density of accessible active sites. The CoNi-NF_75, Figure 5S9 (e), and CoNi-NF_75_OX sample, Figure 5S9 (f), containing 75% Co and 25% Ni, demonstrated the highest ECSA among the as-prepared samples. The enhanced cobalt content results in a greater proportion of CoOOH, which is recognised for its high electrocatalytic activity in alkaline media.[67, 68] The presence of oxyhydroxide species is critical in OER and other electrocatalytic processes, as they provide highly active redox sites.[69, 70] Additionally, the increased oxidation state may result in structural modifications that improve electrolyte accessibility to the active surface.

## 5.6. Conclusion

Metal nanofoams were successfully synthesised by galvanostatic electroplating using the DHBT method in this study. The SEM analysis revealed that the synthesised materials have a foam-like structure with a three-dimensional porous architecture. The nanofoams exhibit a highly porous, honeycomb-like morphology with both regular and irregular voids, indicating a highly porous structure with interconnected channels. The nanofoams' elemental composition was determined through EDX, indicating that the atomic percentages of each nanofoam correspond to the Co/Ni ratio predetermined during synthesis. This finding suggests that the co-deposition of Ni and Co is consistent under the experimental conditions employed in this study. The nanofoams' electrochemical performance was assessed using CV and GCD measurements. The results show that the mixed-metal nanofoams have higher specific capacitance values than the single metal nickel nanofoam and cobalt nanofoam due to the presence of synergistic redox reactions. The specific capacitance value of the CoNi-NF_75_OX nanofoam is increased due to the contribution of surface oxidation and activation by the 5% $H_2O_2$ chemical treatment. The chemical oxidation treatment of the nanofoam enables oxidation without degrading its morphology, thereby enhancing its capacitive response. The CoNi-NF_75_OX nanofoam demonstrated good stability in terms of durability, maintaining its specific capacitance up to the 3000th cycle. This is a significant improvement over the CoNi-NF_75 nanofoam, which exhibited a decline in capacitance from the 2200th cycle onwards. The equivalent circuit analysis facilitated a more profound comprehension of the electrochemical behaviour of the nanofoams. At the outset, at 0 V, the Nyquist plot indicated a solution resistance ($R_s$) of 5.66 Ω·cm² and a

low charge-transfer resistance ($R_{ct}$ = 0.078 Ω·cm²), thereby suggesting efficient charge transfer at the electrode surface. The Warburg resistance ($W_R$) was found to be 9.73 Ω·cm², indicating minimal diffusion impedance and consistent with a material that facilitates efficient ion transport. However, following 2000 cycles, the solution resistance increased to 8.79 Ω·cm², and the charge-transfer resistance rose to 0.417 Ω·cm². This increase in resistance is indicative of the electrolyte resistance and potential degradation in the electrode structure over the course of extended cycling. The decline in the CPE phase constant (n) from 0.803 to 0.656 provides further evidence of a loss of ideal capacitive behaviour, which is likely attributable to surface passivation or structural alterations. The electrochemical performance of cobalt-nickel and nickel-cobalt nanofoams was tested for both OER and HER. The results indicate that the high surface area of the nanofoams provides more active sites for the reaction, potentially enhancing electrocatalytic activity. The electrochemical performance of the nanofoams was tested for both OER and HER. The study indicates that although the individual Co and Ni tested have a low overpotential for HER, they are less stable compared to the mixed nanofoams. The ECSA analysis demonstrates that augmenting the cobalt content and implementing oxidative treatment substantially enhance electrochemical accessibility, thus establishing CoNi-NF_75_OX as the most electrochemically active sample. This enhancement in ECSA is ascribed to the formation of higher oxidation state species, specifically CoOOH and NiOOH, which are recognised for their exceptional electrocatalytic activity. The research provides valuable insights into the synthesis and characterization of metal nanofoams and their potential as promising materials for use in electrochemical energy storage and conversion systems. The nanofoams' successful synthesis and promising electrochemical performance highlight their potential for sustainable hydrogen production through water splitting. Their superior charge storage capacity, faradaic efficiency, and durability make them ideal candidates for further exploration and optimisation.

# 5.7. Supporting information

## 5.7.1. Figures

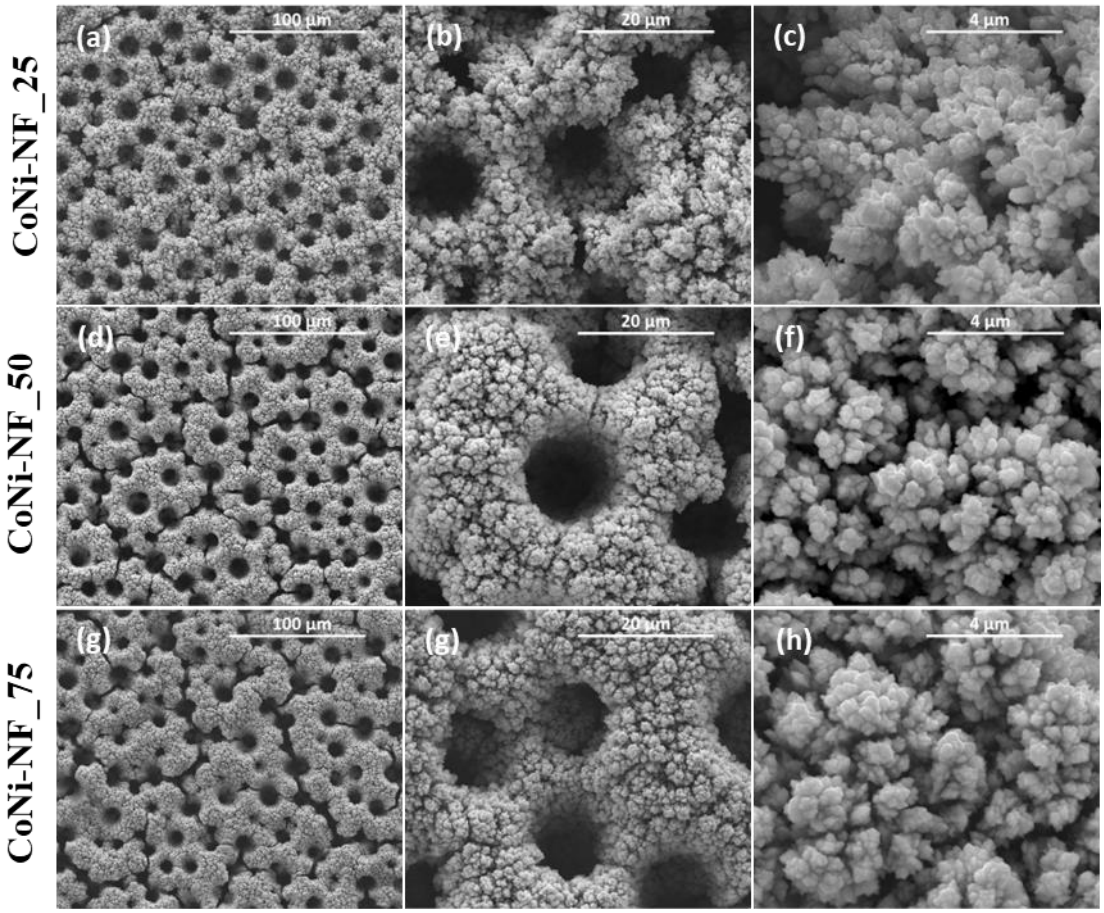



Figure 5S1 - SEM images of the electrode materials electrodeposited on stainless steel at different magnifications: (a, d, g) at 1000×, showing overall morphology; (b, e, h) at 5000×, highlighting finer structural details; (c, f, i) at 25000×, revealing nanoscale features.

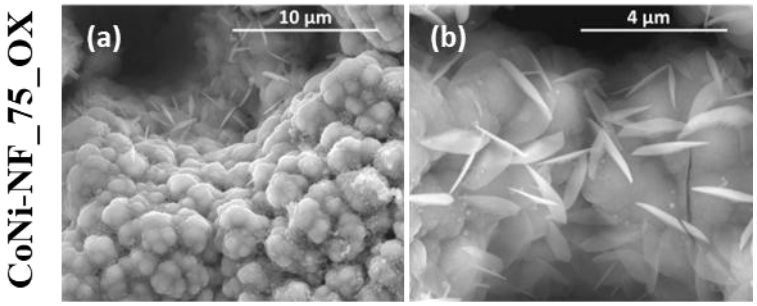



Figure 5S2 - SEM images of CoNi-NF_75_OX nanofoam at (a) 10000× and (b) 25000×.

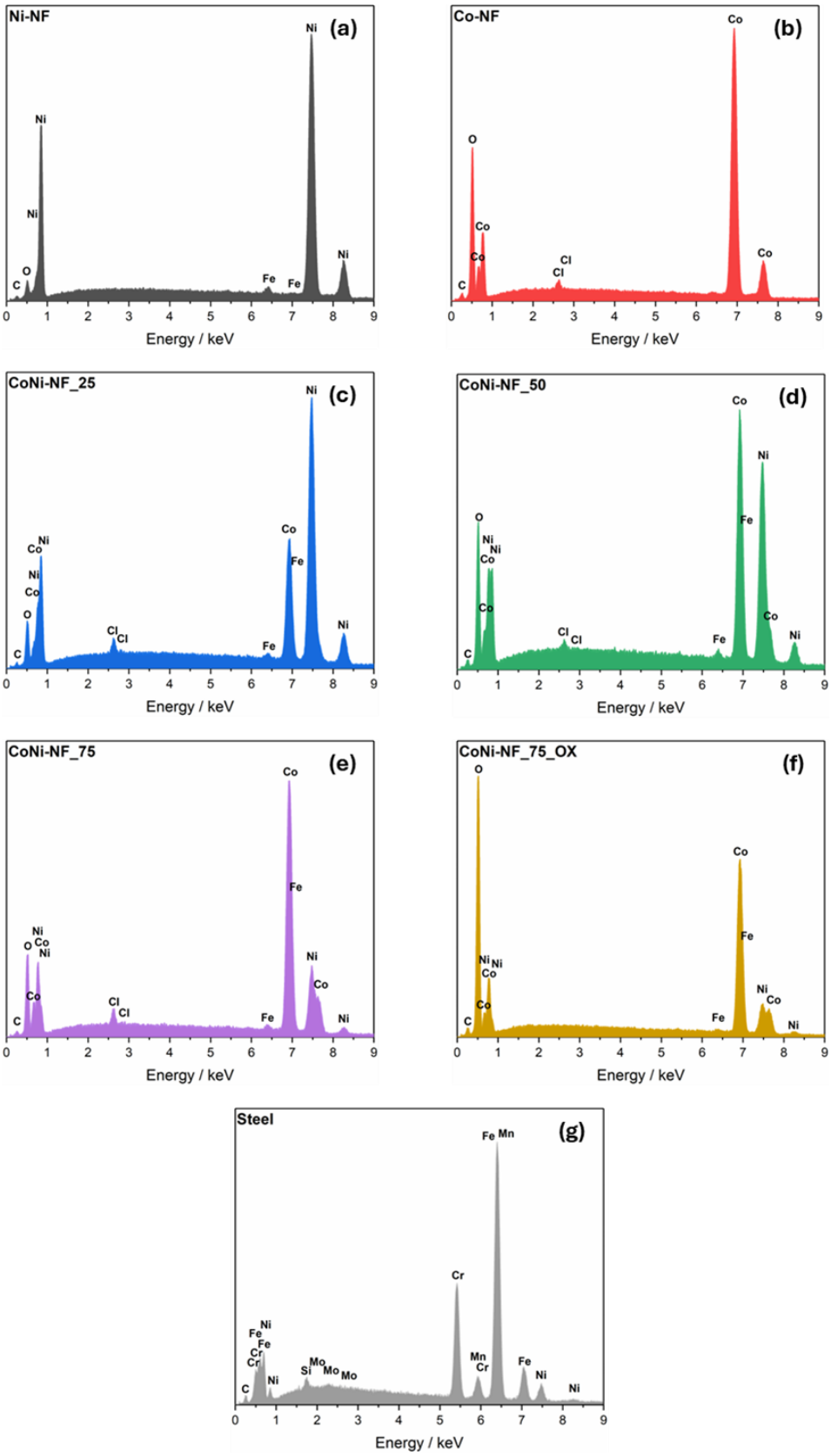



Figure 5S3 - EDX spectra of (a) Ni-NF, (b) Co-NF, (c) CoNi-NF_25, (d) CoNi-NF_50, (e) CoNi-NF_75, (f) CoNi-NF_75_OX and (g) stainless steel support.

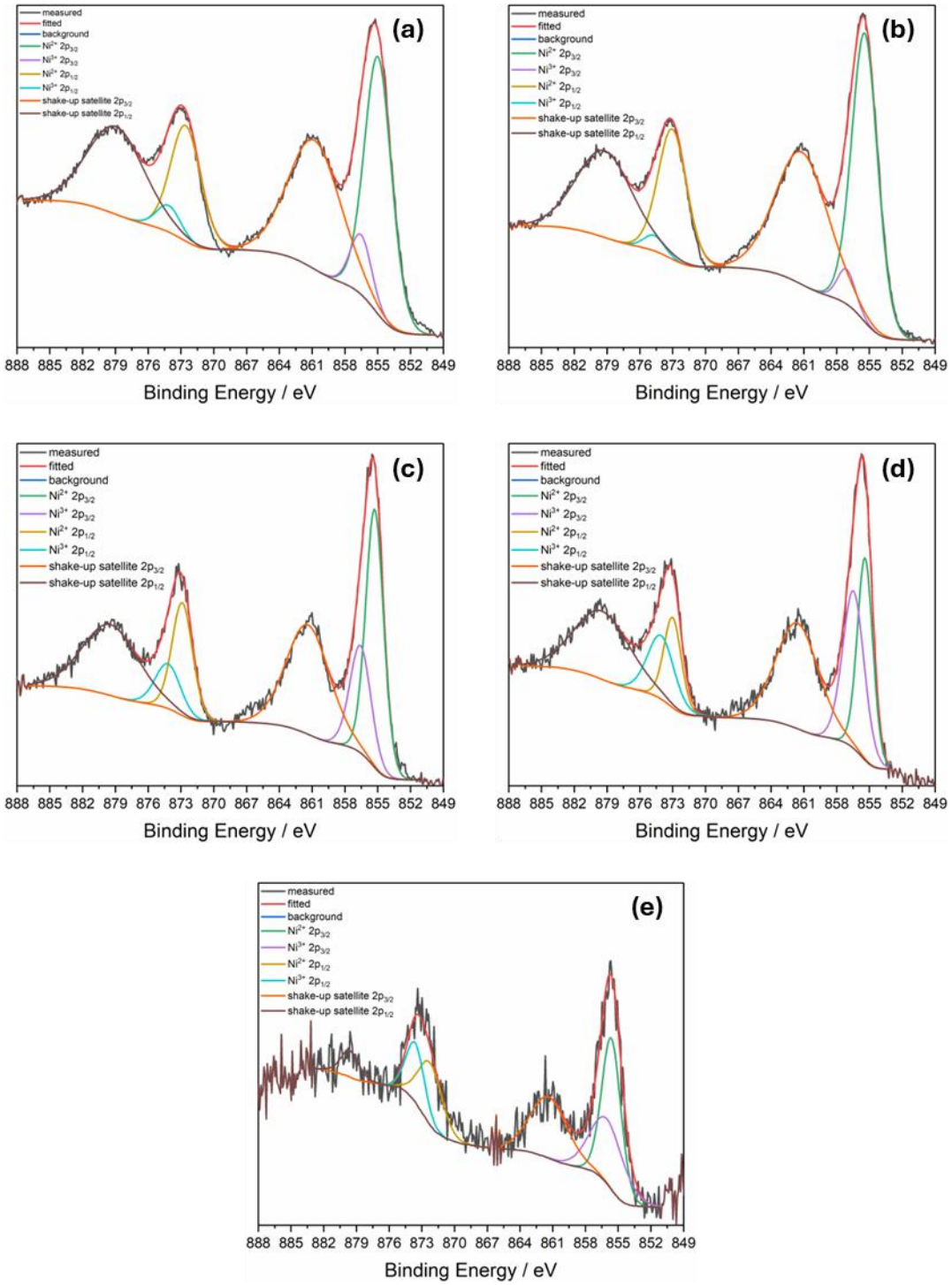



Figure 5S4 - Ni 2p XPS spectra of (a) Ni-NF, (b) CoNi-NF_25, (c) CoNi-NF_50, (d) CoNi-NF_75, (e) CoNi-NF_75_OX.

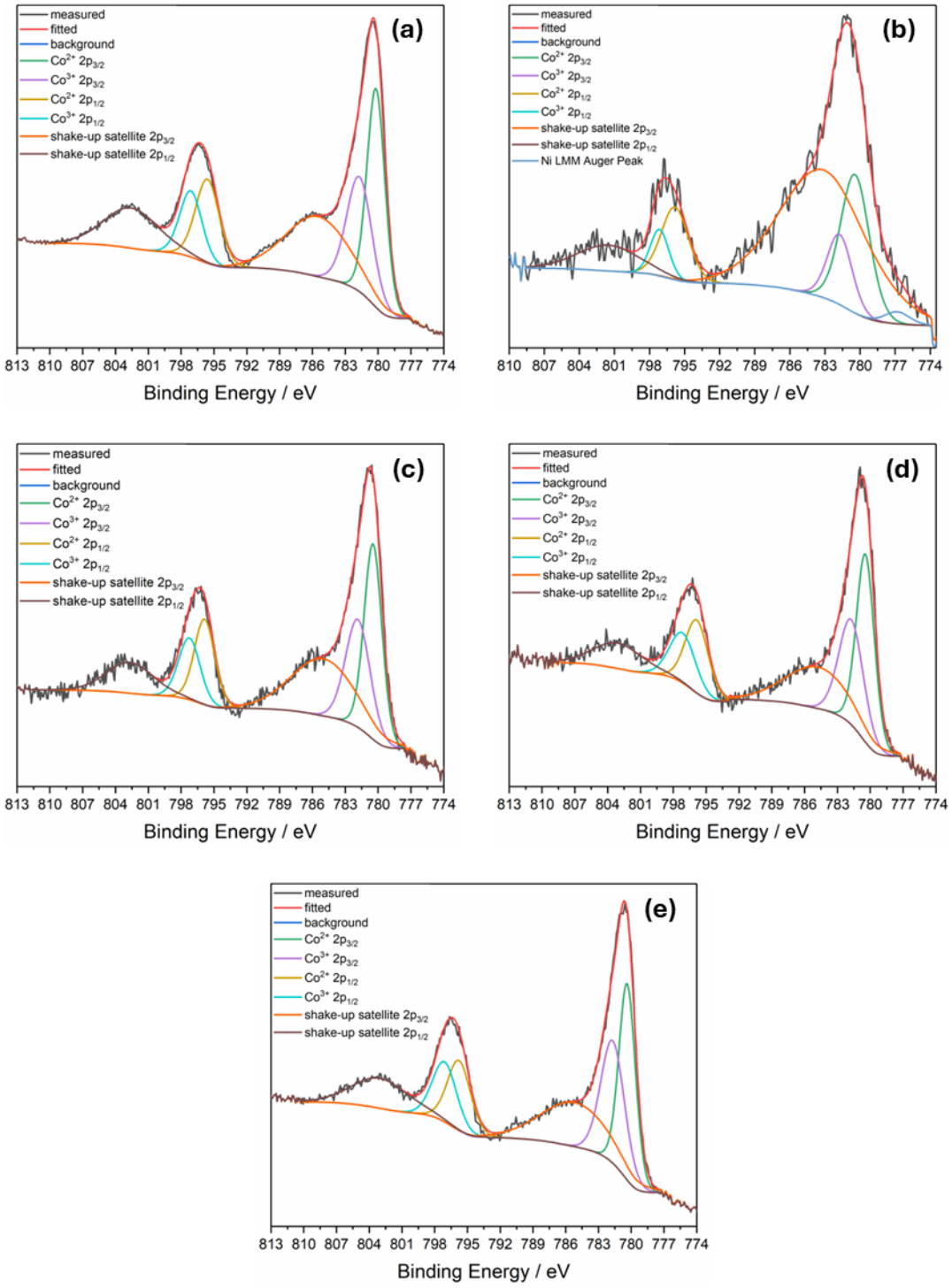



Figure 5S5 - Co 2p XPS spectra of (a) Co-NF, (b) CoNi-NF_25, (c) CoNi-NF_50, (d) CoNi-NF_75, (e) CoNi-NF_75_OX.

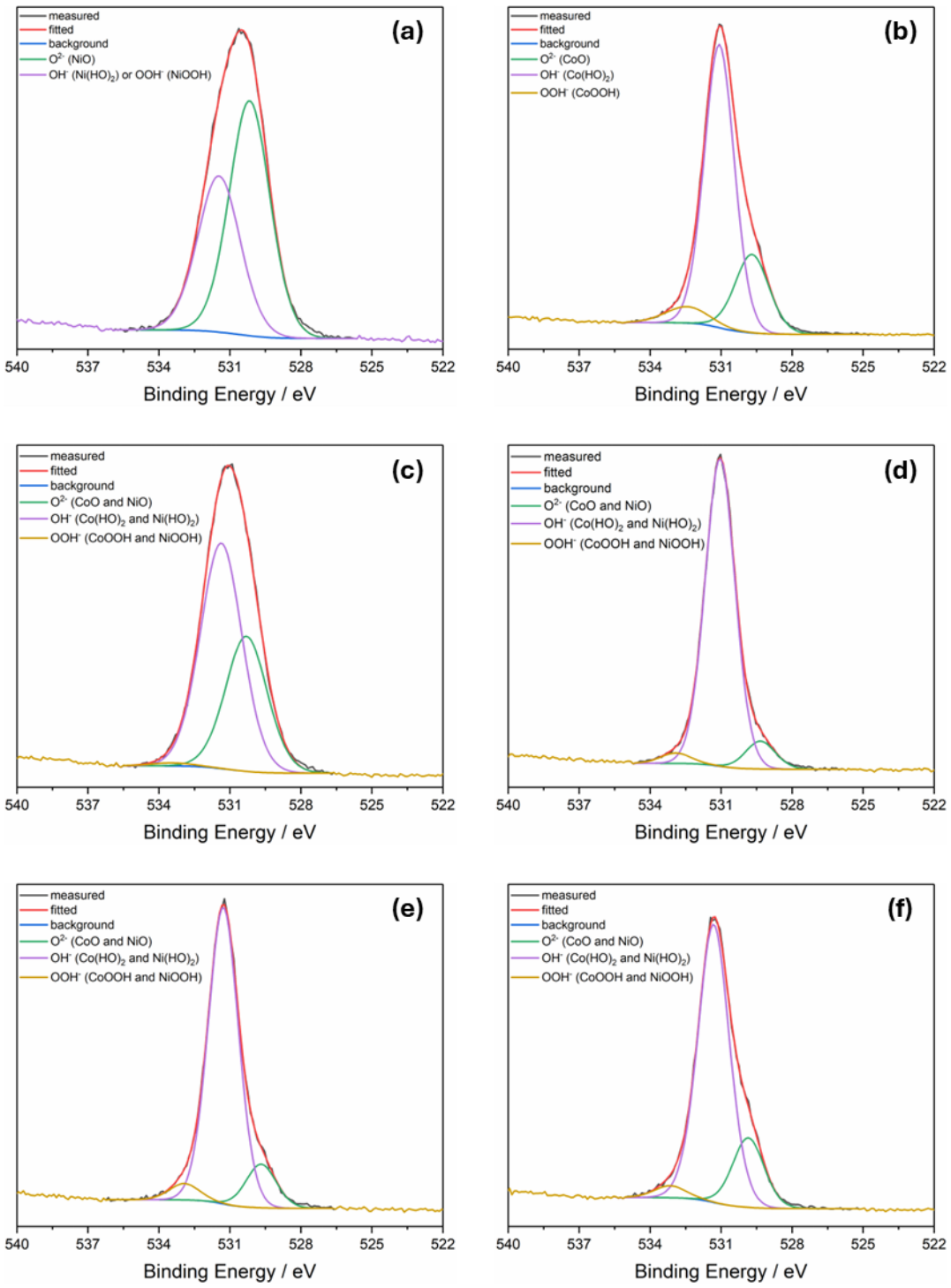



Figure 5S6 - O 1s XPS spectra of (a) Ni-NF, (b) Co-NF, (c) CoNi-NF_25, (d) CoNi-NF_50, (e) CoNi-NF_75 and (f) CoNi-NF_75_OX.

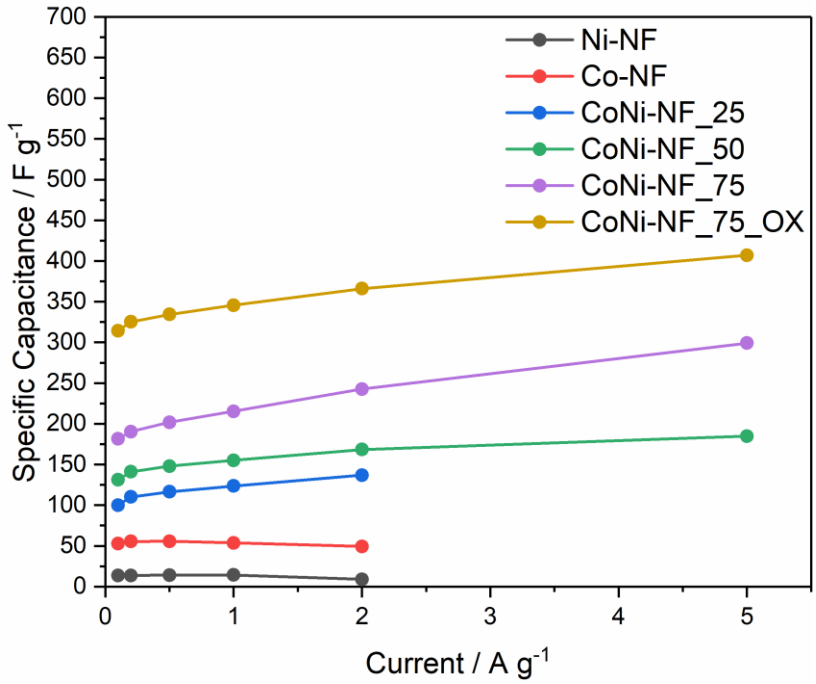



Figure 5S7 - Specific capacitance versus current values for all nanofoams.

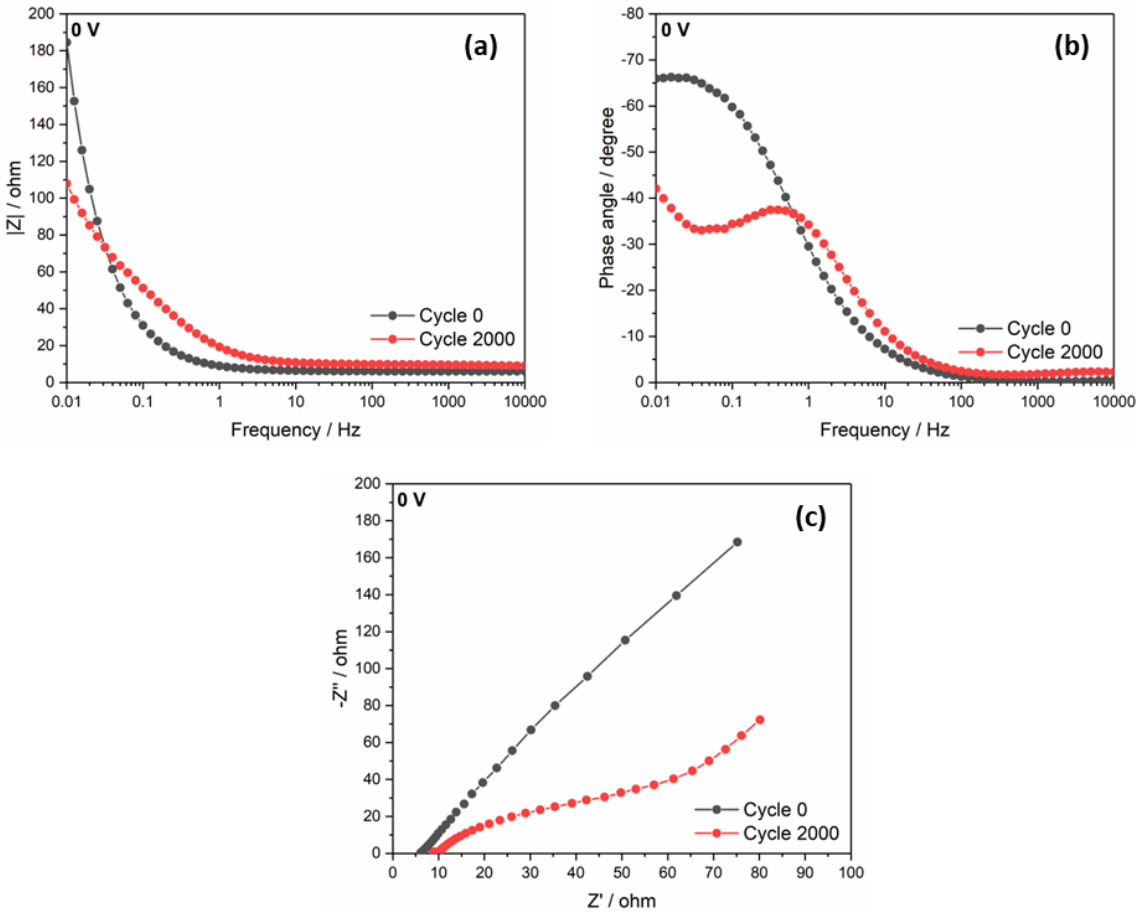



Figure 5S8 – (a and b) Bode and (c) Nyquist Electrochemical Impedance Spectra for CoNi-NF_75 composite material after 0 and 2000 cycles of Galvanostatic Charge Discharge at 1 A $g^{-1}$ for discharged (0 V) potential.

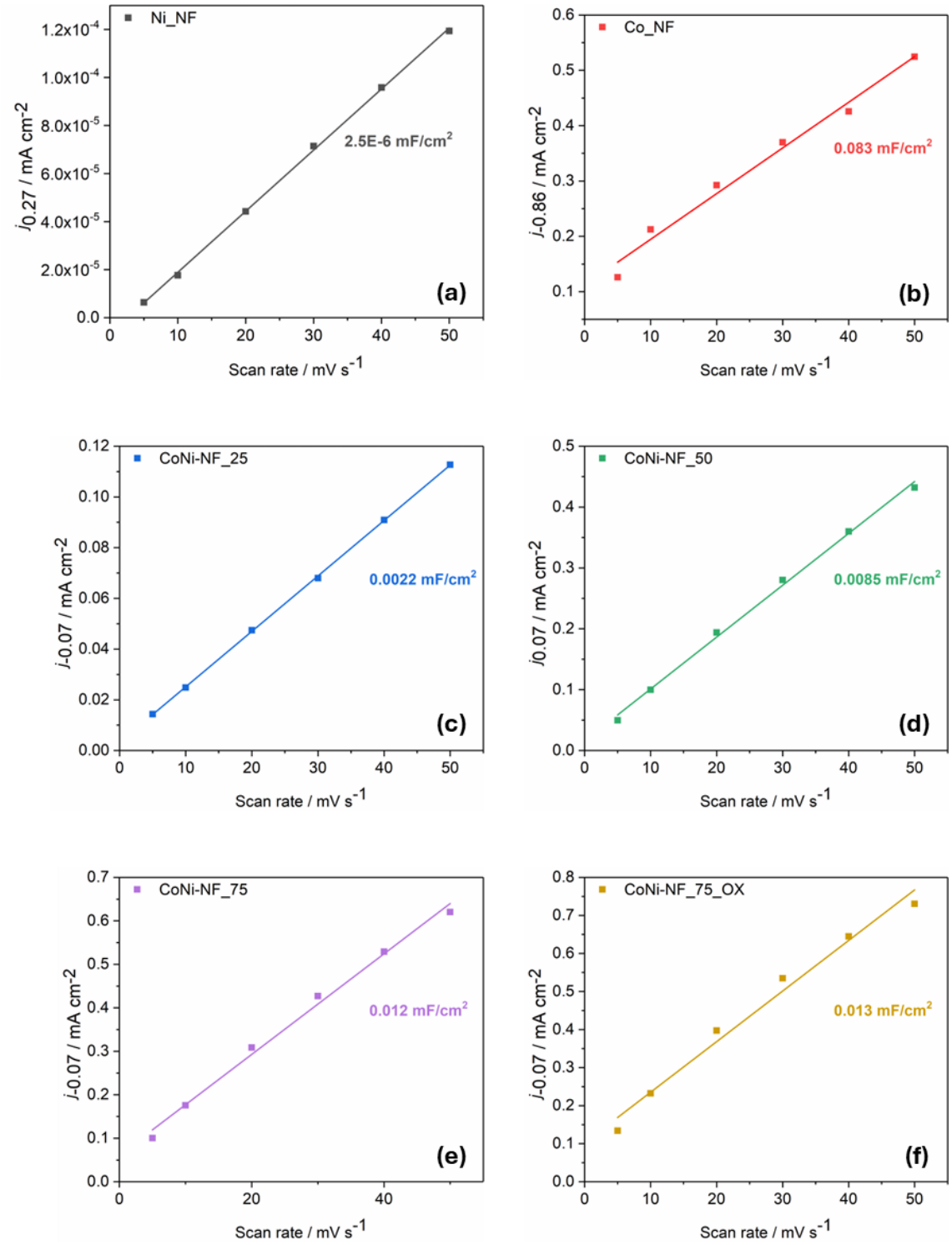



Figure 5S9 - Current density-scan rate linear fitting plots for all nanofoams. Numeric values correspond to the double-layer capacitances ($C_{dl}$) for each nanofoam.

Table S5.1 - The performance for Ni-NF and Co-NF as OER/HER electrocatalysts compared with published work.

| Electrocatalysts | HER $\eta_{10}$ (mV) | OER $\eta_{10}$ (mV) | Ref. |
|---|---|---|---|
| Ni-NF | 142 | 323 | This work |
| Co-NF | 32 | 321 | This work |
| $Co(OH)_2$@NiFe/NF | 87 | 191 | [71] |
| Ni-Fe | 124 | 271 | [72] |
| NiFe | 120 | 220 | [73] |
| FeNiOH/NF | 160 | - | [74] |
| $Fe_{1-x}Co_xSe_2$/RGO | 166 | - | [75] |
| CoPt@$Co(OH)_2$ | - | 334 | [76] |

Table S5.2 - The performance for Ni-NF and Co-NF as OER/HER electrocatalysts compared with published work.

| Electrocatalysts | HER $\eta_{10}$ (mV) | OER $\eta_{10}$ (mV) | Ref. |
|---|---|---|---|
| Ni-NF | 142 | 323 | This work |
| Co-NF | 32 | 321 | This work |
| $Co(OH)_2$@NiFe/NF | 87 | 191 | [71] |
| Ni-Fe | 124 | 271 | [72] |
| NiFe | 120 | 220 | [73] |
| FeNiOH/NF | 160 | - | [74] |
| $Fe_{1-x}Co_xSe_2$/RGO | 166 | - | [75] |
| CoPt@$Co(OH)_2$ | - | 334 | [76] |

Table S5.3 - The performance for Ni-NF and Co-NF as OER/HER electrocatalysts compared with published work.

| Electrocatalysts | Specific capacitance (F $g^{-1}$) | Ref. |
|---|---|---|
| CoNi-NF_75_OX | 345.5 (1 A $g^{-1}$) | This work |
| Graphene hydrogel | 220 (1 A $g^{-1}$) | [77] |
| Graphene aerogel | 325 (1 A $g^{-1}$) | [78] |
| $NiO_x$/CNF | 150 (1 A $g^{-1}$) | [79] |
| P-NCO NWs/NF | 2747.8 (1 A $g^{-1}$) | [18] |
| C7N3 (Co:Ni) | 750 (1 A $g^{-1}$) | [80] |
| $CuCo_2O_4$@$MnO_2$ | 327 (1.25 A $g^{-1}$) | [81] |

## 5.8. Declarations

**Authors' contributions:** The synthesis and characterisation of the foams was performed by H.C.N.; The electrochemical experiments were conducted by H.C.N. Raman analysis was conducted by A.J.S.F. The research was supervised by M.F.M. and D.M.F.; H.C.N was responsible for writing up the manuscript, which was proofread by D.M.F, M.F.M. and C.F. All authors have read and agreed to the published version of the manuscript.

**Funding:** This work was financially supported by FCT/MCTES through project FOAM4ENER
476 PTDC/QUI-ELT/28299/2017.

**Acknowledgments:** This work received support and help from FCT/MCTES (LA/P/0008/2020 DOI 10.54499/LA/P/0008/2020, UIDP/50006/2020 DOI 10.54499/UIDP/50006/2020 and UIDB/50006/2020 DOI 10.54499/UIDB/50006/2020), through national funds. CQE Research Unit was funded by FCT through projects DOI 10.54499/UIDP/00100/2020 and DOI 10.54499/UIDP/00100/2020. Institute of Molecular Sciences Associate Laboratory was funded by FCT through project DOI 10.54499/LA/P/0056/2020. The authors thank the FCT for the financial support under the projects DOI 10.54499/PTDC/QUI-ELT/2075/2020. H.C.N. thanks the FCT through

ChemMat program for his PhD grant PD/BD/143095/2018. D.M.F. thanks FCT/MCTES for funding through the Individual Call to Scientific Employment Stimulus (2021.00771.CEECIND/CP1662/CT0007).

**Conflict of interest:** The authors declare that they have no conflict of interest.

## 5.9. References

[1] Siwek KI, Eugénio S, Santos DMF, Silva MT, Montemor MF. 3D nickel foams with controlled morphologies for hydrogen evolution reaction in highly alkaline media. International Journal of Hydrogen Energy. 2019;44:1701-9.

[2] Fu H, Liu Y, Chen L, Shi Y, Kong W, Hou J, et al. Designed formation of NiCo2O4 with different morphologies self-assembled from nanoparticles for asymmetric supercapacitors and electrocatalysts for oxygen evolution reaction. Electrochimica Acta. 2019;296:719-29.

[3] Wang F, Zhu Y, Tian W, Lv X, Zhang H, Hu Z, et al. Co-doped Ni3S2@CNT arrays anchored on graphite foam with a hierarchical conductive network for high-performance supercapacitors and hydrogen evolution electrodes. Journal of Materials Chemistry A. 2018;6:10490-6.

[4] Novais HC, Jarrais B, Mbomekallé I-M, Teillout A-L, de Oliveira P, Freire C, et al. Enhanced Oxygen Reduction Reaction Activity of the Wells-Dawson Polyoxometalate P2W12Mo6 Immobilised in Nitrogen and Sulphur-Doped Carbon Nanomaterials. ChemElectroChem. 2024;11:e202300622.

[5] Saxena S, Le Floch C, MacDonald J, Moura S. Quantifying EV battery end-of-life through analysis of travel needs with vehicle powertrain models. Journal of Power Sources. 2015;282:265-76.

[6] Simon P, Gogotsi Y, Dunn B. Where Do Batteries End and Supercapacitors Begin? Science. 2014;343:1210-1.

[7] Conway BE. Transition from “Supercapacitor” to “Battery” Behavior in Electrochemical Energy Storage. Journal of The Electrochemical Society. 1991;138:1539.

[8] Gogotsi Y, Penner RM. Energy Storage in Nanomaterials – Capacitive, Pseudocapacitive, or Battery-like? ACS Nano. 2018;12:2081-3.

[9] Liu L, Hou Y, Gao Y, Yang N, Liu J, Wang X. Co doped α-Ni(OH)2 multiple-dimensional structure electrode material. Electrochimica Acta. 2019;295:340-6.

[10] Adán-Más A, Duarte RG, Silva TM, Guerlou-Demourgues L, Montemor MFG. Enhancement of the Ni-Co hydroxide response as Energy Storage Material by Electrochemically Reduced Graphene Oxide. Electrochimica Acta. 2017;240:323-40.

[11] Nguyen VH, Shim J-J. Three-dimensional nickel foam/graphene/NiCo2O4 as high-performance electrodes for supercapacitors. Journal of Power Sources. 2015;273:110-7.

[12] Huang S, Zhu X, Sarkar S, Zhao Y. Challenges and opportunities for supercapacitors. APL Materials. 2019;7.
[13] Cherevko S, Geiger S, Kasian O, Kulyk N, Grote J-P, Savan A, et al. Oxygen and hydrogen evolution reactions on Ru, RuO2, Ir, and IrO2 thin film electrodes in acidic and alkaline electrolytes: A comparative study on activity and stability. Catalysis Today. 2016;262:170-80.
[14] Freire C, Fernandes DM, Nunes M, Abdelkader VK. POM & MOF-based Electrocatalysts for Energy-related Reactions. ChemCatChem. 2018;10:1703-30.
[15] Limani N, Marques IS, Jarrais B, Fernandes AJ, Freire C, Fernandes DM. Cobalt phosphotungstate-based composites as bifunctional electrocatalysts for oxygen reactions. Catalysts. 2022;12:357.
[16] Nunes M, Fernandes DM, Morales MV, Rodríguez-Ramos I, Guerrero-Ruiz A, Freire C. Cu and Pd nanoparticles supported on a graphitic carbon material as bifunctional HER/ORR electrocatalysts. Catalysis Today. 2020;357:279-90.
[17] Fernandes DM, Araújo MP, Haider A, Mougharbel AS, Fernandes AJS, Kortz U, et al. Polyoxometalate-graphene Electrocatalysts for the Hydrogen Evolution Reaction. ChemElectroChem. 2018;5:273-83.
[18] Chu W, Shi Z, Hou Y, Ma D, Bai X, Gao Y, et al. Trifunctional of Phosphorus-Doped NiCo2O4 Nanowire Materials for Asymmetric Supercapacitor, Oxygen Evolution Reaction, and Hydrogen Evolution Reaction. ACS Applied Materials & Interfaces. 2020;12:2763-72.
[19] Nguyen T, Boudard M, João Carmezim M, Fátima Montemor M. NixCo1-x(OH)2 nanosheets on carbon nanofoam paper as high areal capacity electrodes for hybrid supercapacitors. Energy. 2017;126:208-16.
[20] Nguyen T, Boudard M, Carmezim MJ, Montemor MF. Layered Ni(OH)2-Co(OH)2 films prepared by electrodeposition as charge storage electrodes for hybrid supercapacitors. Scientific Reports. 2017;7:39980.
[21] Cardoso DSP, Eugénio S, Silva TM, Santos DMF, Sequeira CAC, Montemor MF. Hydrogen evolution on nanostructured Ni–Cu foams. RSC Advances. 2015;5:43456-61.
[22] Abdel Maksoud MIA, Fahim RA, Shalan AE, Abd Elkodous M, Olojede SO, Osman AI, et al. Advanced materials and technologies for supercapacitors used in energy conversion and storage: a review. Environmental Chemistry Letters. 2021;19:375-439.
[23] Li S, Hao X, Abudula A, Guan G. Nanostructured Co-based bifunctional electrocatalysts for energy conversion and storage: current status and perspectives. Journal of Materials Chemistry A. 2019;7:18674-707.

[24] Zhang Q, Guan J. Atomically dispersed catalysts for hydrogen/oxygen evolution reactions and overall water splitting. Journal of Power Sources. 2020;471:228446.
[25] Zare N, Karimi F, Altuner EE, Mashkoor H, Tiri RNE, Gulbagca F, et al. Synthesis of Bimetallic Nickel-Cobalt Nanoparticles Supported by Functional Multi-Walled Carbon Nanotubes by Chemical Methods: Characterization and Hydrogen Energy Generation. Topics in Catalysis. 2024;67:606-14.
[26] Adán-Más A, Silva TM, Guerlou-Demourgues L, Bourgeois L, Labrugere-Sarroste C, Montemor MF. Nickel-cobalt oxide modified with reduced graphene oxide: Performance and degradation for energy storage applications. Journal of Power Sources. 2019;419:12-26.
[27] Nayak S, Joshi DR, Kittur AA, Nayak S. Synthesis, Fabrication, and Performance Evaluation of Nickel-Cobalt Sulfide Nanostructures for Enhancing Energy Density of Supercapacitors in Energy Storage Applications. Journal of Electronic Materials. 2024;53:3276-88.
[28] Marozzi CA, Chialvo AC. Development of electrode morphologies of interest in electrocatalysis. Part 1: Electrodeposited porous nickel electrodes. Electrochimica Acta. 2000;45:2111-20.
[29] Eugénio S, Cardoso DSP, Santos DMF, Šljukić B, Montemor MF. Nanostructured 3D metallic foams for H2O2 electroreduction. International Journal of Hydrogen Energy. 2016;41:14370-6.
[30] Fathollahi A, Shahrabi T, Darband GB. Modulation of active surface sites on Ni–Fe–S by the dynamic hydrogen bubble template method for energy-saving hydrogen production. Journal of Materials Chemistry A. 2024;12:9038-54.
[31] Plowman BJ, Jones LA, Bhargava SK. Building with bubbles: the formation of high surface area honeycomb-like films via hydrogen bubble templated electrodeposition. Chemical Communications. 2015;51:4331-46.
[32] Arévalo-Cid P, Adán-Más A, Silva T, Rodrigues JA, Maçôas E, Vaz M, et al. On the growth and mechanical properties of nanostructured cobalt foams by dynamic hydrogen bubble template electrodeposition. Materials Characterization. 2020;169:110598.
[33] Yuan C, Yang L, Hou L, Shen L, Zhang X, Lou XW. Growth of ultrathin mesoporous Co3O4 nanosheet arrays on Ni foam for high-performance electrochemical capacitors. Energy & Environmental Science. 2012;5:7883-7.
[34] Nguyen T, Carmezim MJ, Montemor MF. Current transient and in situ AFM studies of initial growth stages of electrochemically deposited nickel cobalt hydroxide nanosheet films. Physical Chemistry Chemical Physics. 2016;18:12368-74.

[35] Arévalo-Cid P, Adán-Más A, Silva TM, Rodrigues JA, Maçôas E, Vaz MF, et al. On the growth and mechanical properties of nanostructured cobalt foams by dynamic hydrogen bubble template electrodeposition. Materials Characterization. 2020;169:110598.

[36] Mathiazhagan N, Kumar TS, Balasubramanian V, Gandhi V. Performance study of medium carbon steel and austenitic stainless steel joints: friction welding process. Oxidation Communications. 2015;38:2123-34.

[37] Jafarzadegan M, Feng A, Abdollah-Zadeh A, Saeid T, Shen J, Assadi H. Microstructural characterization in dissimilar friction stir welding between 304 stainless steel and st37 steel. Materials characterization. 2012;74:28-41.

[38] Wang L, Sun J. Molybdenum modified AISI 304 stainless steel bipolar plate for proton exchange membrane fuel cell. Journal of Renewable and Sustainable Energy. 2013;5.

[39] Krawczyk B, Cook P, Hobbs J, Engelberg DL. Corrosion behavior of cold rolled type 316L stainless steel in HCl-containing environments. Corrosion. 2017;73:1346-58.

[40] Eidelman O, Friedman H, Rosentsveig R, Moshkovith A, Perfiliev V, Cohen S, et al. Chromium-rich coatings with WS2 nanoparticles containing fullerene-like structure. Nano. 2011;6:313-24.

[41] Mo S, Zhang Q, Li S, Ren Q, Zhang M, Xue Y, et al. Integrated Cobalt Oxide Based Nanoarray Catalysts with Hierarchical Architectures: In Situ Raman Spectroscopy Investigation on the Carbon Monoxide Reaction Mechanism. ChemCatChem. 2018;10:3012-26.

[42] Li HB, Liu P, Liang Y, Xiao J, Yang GW. Amorphous cobalt hydroxide nanostructures and magnetism from green electrochemistry. RSC Advances. 2013;3:26412-7.

[43] Kettaf S, Guellati O, Harat A, Kennaz H, Momodu D, Dangbegnon J, et al. Electrochemical measurements of synthesized nanostructured β-Ni(OH)2 using hydrothermal process and activated carbon based nanoelectroactive materials. SN Applied Sciences. 2018;1:34.

[44] Xiong D, Li W, Liu L. Vertically Aligned Porous Nickel(II) Hydroxide Nanosheets Supported on Carbon Paper with Long-Term Oxygen Evolution Performance. Chemistry – An Asian Journal. 2017;12:543-51.

[45] Wang G, Ling Y, Lu X, Zhai T, Qian F, Tong Y, et al. A mechanistic study into the catalytic effect of Ni(OH)2 on hematite for photoelectrochemical water oxidation. Nanoscale. 2013;5:4129-33.

[46] Laïk B, Richet M, Emery N, Bach S, Perrière L, Cotrebil Y, et al. XPS Investigation of Co–Ni Oxidized Compounds Surface Using Peak-On-Satellite Ratio. Application to Co20Ni80 Passive Layer Structure and Composition. ACS Omega. 2024;9:40707-22.
[47] Cabrera-German D, Gomez-Sosa G, Herrera-Gomez A. Accurate peak fitting and subsequent quantitative composition analysis of the spectrum of Co 2p obtained with Al Kα radiation: I: cobalt spinel. Surface and Interface Analysis. 2016;48:252-6.
[48] Wu Y, Zhao M-J, Li F, Xie J, Li Y, He J-B. Trace Fe Incorporation into Ni-(oxy)hydroxide Stabilizes Ni3+ Sites for Anodic Oxygen Evolution: A Double Thin-Layer Study. Langmuir. 2020;36:5126-33.
[49] Goldsmith ZK, Harshan AK, Gerken JB, Vörös M, Galli G, Stahl SS, et al. Characterization of NiFe oxyhydroxide electrocatalysts by integrated electronic structure calculations and spectroelectrochemistry. Proceedings of the National Academy of Sciences. 2017;114:3050-5.
[50] Trotochaud L, Young SL, Ranney JK, Boettcher SW. Nickel–Iron Oxyhydroxide Oxygen-Evolution Electrocatalysts: The Role of Intentional and Incidental Iron Incorporation. Journal of the American Chemical Society. 2014;136:6744-53.
[51] Sun F, Wang S, Wang Y, Zhang J, Yu X, Zhou Y, et al. Synthesis of Ni-Co Hydroxide Nanosheets Constructed Hollow Cubes for Electrochemical Glucose Determination. Sensors (Basel). 2019;19.
[52] Wang L, Zhang H, Li Y, Xiao S, Bi F, Zhao L, et al. Construction of bundle-like cobalt/nickel hydroxide nanorods from metal organic framework for high-performance supercapacitors. Journal of Materials Science: Materials in Electronics. 2022;33:10540-50.
[53] Su Y-Z, Xiao K, Li N, Liu Z-Q, Qiao S-Z. Amorphous Ni(OH)2 @ three-dimensional Ni core–shell nanostructures for high capacitance pseudocapacitors and asymmetric supercapacitors. Journal of Materials Chemistry A. 2014;2:13845-53.
[54] Allison A, Andreas HA. Minimizing the Nyquist-plot semi-circle of pseudocapacitive manganese oxides through modification of the oxide-substrate interface resistance. Journal of Power Sources. 2019;426:93-6.
[55] Huang J, Yuan K, Chen Y. Wide Voltage Aqueous Asymmetric Supercapacitors: Advances, Strategies, and Challenges. Advanced Functional Materials. 2021;32.
[56] Laschuk NO, Easton EB, Zenkina OV. Reducing the resistance for the use of electrochemical impedance spectroscopy analysis in materials chemistry. RSC Advances. 2021;11:27925-36.
[57] Yang B, Li B, Xiang Z. Advanced MOF-based electrode materials for supercapacitors and electrocatalytic oxygen reduction. Nano Research. 2023;16:1338-61.

[58] Liu J, Wang X, Min Y, Li Q, Xu Q. Defect-rich carbon-coated nickel–cobalt alloy nanoparticles enhanced the OER catalytic activity through surface reconstruction. New Journal of Chemistry. 2023;47:16539-50.
[59] Benck JD, Hellstern TR, Kibsgaard J, Chakthranont P, Jaramillo TF. Catalyzing the Hydrogen Evolution Reaction (HER) with Molybdenum Sulfide Nanomaterials. ACS Catalysis. 2014;4:3957-71.
[60] Yu X, Zhao J, Zheng L-R, Tong Y, Zhang M, Xu G, et al. Hydrogen Evolution Reaction in Alkaline Media: Alpha- or Beta-Nickel Hydroxide on the Surface of Platinum? ACS Energy Letters. 2018;3:237-44.
[61] Zheng Y, Jiao Y, Vasileff A, Qiao S-Z. The Hydrogen Evolution Reaction in Alkaline Solution: From Theory, Single Crystal Models, to Practical Electrocatalysts. Angewandte Chemie International Edition. 2018;57:7568-79.
[62] Lasia A. Mechanism and kinetics of the hydrogen evolution reaction. International Journal of Hydrogen Energy. 2019;44:19484-518.
[63] Salvi P, Nelli P, Villa M, Kiros Y, Zangari G, Bruni G, et al. Hydrogen evolution reaction in PTFE bonded Raney-Ni electrodes. International Journal of Hydrogen Energy. 2011;36:7816-21.
[64] Kellenberger A, Vaszilcsin N, Brandl W, Duteanu N. Kinetics of hydrogen evolution reaction on skeleton nickel and nickel–titanium electrodes obtained by thermal arc spraying technique. International Journal of Hydrogen Energy. 2007;32:3258-65.
[65] Dong H, Lei T, He Y, Xu N, Huang B, Liu CT. Electrochemical performance of porous Ni3Al electrodes for hydrogen evolution reaction. International Journal of Hydrogen Energy. 2011;36:12112-20.
[66] Xie R-C, Batchelor-McAuley C, Rauwel E, Rauwel P, Compton RG. Electrochemical Characterisation of Co@Co(OH)2 Core-Shell Nanoparticles and their Aggregation in Solution. ChemElectroChem. 2020;7:4259-68.
[67] Hu J, Al-Salihy A, Wang J, Li X, Fu Y, Li Z, et al. Improved Interface Charge Transfer and Redistribution in CuO-CoOOH p-n Heterojunction Nanoarray Electrocatalyst for Enhanced Oxygen Evolution Reaction. Adv Sci (Weinh). 2021;8:e2103314.
[68] Chen Z, Kronawitter CX, Yeh Y-W, Yang X, Zhao P, Yao N, et al. Activity of pure and transition metal-modified CoOOH for the oxygen evolution reaction in an alkaline medium. Journal of Materials Chemistry A. 2017;5:842-50.
[69] Burke MS, Kast MG, Trotochaud L, Smith AM, Boettcher SW. Cobalt–Iron (Oxy)hydroxide Oxygen Evolution Electrocatalysts: The Role of Structure and Composition on Activity, Stability, and Mechanism. Journal of the American Chemical Society. 2015;137:3638-48.

[70] Bhattacharyya K, Auer AA. Oxygen Evolution Reaction Electrocatalysis on Cobalt(oxy)hydroxide: Role of Fe Impurities. The Journal of Physical Chemistry C. 2022;126:18623-35.
[71] Wang H, Yan Y, Zhang W, Sun S, Yao S. Preparation of Co(OH)2@NiFe/NF bifunctional electrocatalyst by electrodeposition for efficient water splitting. Journal of Solid State Chemistry. 2023;323:124048.
[72] Hatami E, Toghraei A, Darband GB. Electrodeposition of Ni–Fe micro/nano urchin-like structure as an efficient electrocatalyst for overall water splitting. International Journal of Hydrogen Energy. 2021;46:9394-405.
[73] Zhang H, Li X, Hähnel A, Naumann V, Lin C, Azimi S, et al. Bifunctional heterostructure assembly of NiFe LDH nanosheets on NiCoP nanowires for highly efficient and stable overall water splitting. Advanced Functional Materials. 2018;28:1706847.
[74] Ren J-T, Yuan G-G, Weng C-C, Chen L, Yuan Z-Y. Uniquely integrated Fe-doped Ni (OH) 2 nanosheets for highly efficient oxygen and hydrogen evolution reactions. Nanoscale. 2018;10:10620-8.
[75] Xu X, Ge Y, Wang M, Zhang Z, Dong P, Baines R, et al. Cobalt-doped FeSe2-RGO as highly active and stable electrocatalysts for hydrogen evolution reactions. ACS Applied Materials & Interfaces. 2016;8:18036-42.
[76] Malik B, Anantharaj S, Karthick K, Pattanayak DK, Kundu S. Magnetic CoPt nanoparticle-decorated ultrathin Co (OH) 2 nanosheets: an efficient bi-functional water splitting catalyst. Catalysis Science & Technology. 2017;7:2486-97.
[77] Zhang L, Shi G. Preparation of highly conductive graphene hydrogels for fabricating supercapacitors with high rate capability. The Journal of Physical Chemistry C. 2011;115:17206-12.
[78] Jung SM, Mafra DL, Lin C-T, Jung HY, Kong J. Controlled porous structures of graphene aerogels and their effect on supercapacitor performance. Nanoscale. 2015;7:4386-93.
[79] Della Noce R, Eugénio S, Boudard M, Rapenne L, Silva TM, Carmezim MJ, et al. One-step process to form a nickel-based/carbon nanofoam composite supercapacitor electrode using Na2SO4 as an eco-friendly electrolyte. RSC Advances. 2016;6:15920-8.
[80] Zhang J, Liu F, Cheng JP, Zhang XB. Binary Nickel–Cobalt Oxides Electrode Materials for High-Performance Supercapacitors: Influence of its Composition and Porous Nature. ACS Applied Materials & Interfaces. 2015;7:17630-40.

[81] Wang Q, Xu J, Wang X, Liu B, Hou X, Yu G, et al. Core–Shell CuCo2O4@MnO2 Nanowires on Carbon Fabrics as High-Performance Materials for Flexible, All-Solid-State, Electrochemical Capacitors. ChemElectroChem. 2014;1:559-64.

Chapter 6

# General Conclusions and Future Perspectives

# 6

# General Conclusions and Future Perspectives

In the concluding chapter of this thesis, the primary conclusions and most significant achievements are presented. Moreover, new perspectives for future work are proposed.

## 6.1. Final conclusions

The objective of the research presented in this doctoral thesis was to address some of the most pressing challenges in energy conversion and storage by developing novel materials for electrocatalytic and electrochemical applications. The primary focus was on the design, synthesis, and characterisation of hybrid materials based on polyoxometalates (POMs), carbon nanostructures, and 3D metallic nanofoams, with particular emphasis on their performance towards the oxygen reduction reaction (ORR), the oxygen and hydrogen evolution reactions (OER and HER), and their potential in supercapacitor applications.

A unifying theme has been identified across the various studies undertaken: the utilisation of molecular-level design and nanostructuring strategies to fine-tune the electrochemical performance of these materials. This offers promising, cost-effective, and noble-metal-free alternatives for energy-related devices.

The initial part of the work focused on exploring the electrocatalytic potential of the 48-tungsto-8-phosphate wheel-shaped polyoxometalate, $[H_7P_8W_{48}O_{184}]^{33-}$, ($P_8W_{48}$). This investigation involved the anchoring of the polyoxometalate on diverse carbonaceous supports, including graphene flakes (GF), single-walled carbon nanotubes (SWCNTs), multi-walled carbon nanotubes (MWCNTs), and nitrogen-doped MWCNTs (N-MWCNTs). These composites were synthesised through simple impregnation techniques in aqueous media, thus avoiding the use of linker molecules or binders that could impede electron transfer.

Detailed characterisation was carried out using Fourier transform infrared spectroscopy (FTIR), scanning electron microscopy (SEM), energy dispersive X-ray spectroscopy (EDX) and X-ray photoelectron spectroscopy (XPS), confirming successful immobilisation of the POM and preservation of its structural integrity. The electrochemical performance was evaluated using linear sweep voltammetry (LSV) with a rotating disc electrode (RDE) in alkaline media.

The second major study shifted focus to another POM architecture: the Wells–Dawson-type $[P_2W_{17}FeO_{61}]^{7-}$anion ($P_2W_{17}Fe$). This iron-substituted POM was immobilised onto nitrogen-doped graphene flakes (GF_N) and nitrogen-doped MWCNTs (MWCNT_N), and once more synthesised without the use of a binder or linking agent to maximise conductivity.

Characterisation confirmed the structural incorporation of the Fe-substituted POM onto the carbon nanostructures. Among the resulting composites, $P_2W_{17}Fe$@MWCNT_N8 displayed the most favourable electrochemical behaviour, with an $E_{onset}$ of 0.84 V and a diffusion-limited current density of −3.9 mA·cm$^{-2}$. RRDE analyses and Koutecky-Levich plots supported a near four-electron pathway with $n_{O2}$ values close to 3.4, indicating high selectivity for the complete reduction of oxygen to water and minimal peroxide generation. A direct comparison between $P_2W_{17}Fe$@MWCNT_N8 and $P_2W_{12}Mo_6$@MWCNT_N8 provided further insights into the influence of POM composition on ORR performance. Despite having identical onset potentials (0.84 V vs. RHE), the two hybrids exhibited distinct electrochemical behaviours. $P_2W_{12}Mo_6$@MWCNT_N8 showed superior reaction kinetics, with a lower Tafel slope (42 vs. 48 mV·dec$^{-1}$), suggesting more efficient electron transfer at low overpotentials. On the other hand, $P_2W_{17}Fe$@MWCNT_N8 achieved a slightly higher diffusion-limited current density (3.9 vs. 3.7 mA·cm$^{-2}$), indicative of improved mass transport or a higher number of active sites under diffusion-controlled conditions. These complementary behaviours reflect the subtle but significant effects of metal substitution within the POM framework.

Among the studied composites, $P_8W_{48}$@N-MWCNT showed the best ORR activity, achieving an onset potential ($E_{onset}$) of 0.94 V vs. RHE, comparable to commercial Pt/C catalysts. It also exhibited the highest limiting current density (-3.7 mA-cm$^{-2}$), which is attributed to the synergistic effects between the POM and the N-doped carbon support. The presence of nitrogen functionalities probably facilitated enhanced oxygen adsorption and modified the electronic structure, thus improving the kinetics of ORR. Furthermore, the number of electrons transferred per $O_2$ molecule ($n_{O2}$) ranged

from 2.2 to 3.0 across the materials, indicating a mixed 2- and 4-electron reduction pathway.

These results demonstrate that careful selection of carbon supports, particularly heteroatom-doped structures, plays a critical role in maximising the electrocatalytic capabilities of POM-based composites. The results support the view that POM-carbon hybrids represent a viable class of catalysts for ORR in alkaline fuel cell environments, combining high activity, selectivity and stability with earth-abundant materials.

The third line of investigation explored the impact of molybdenum substitution in the Wells–Dawson-type POM framework, focusing on $[P_2W_{12}Mo_6]^{6-}$ ($P_2W_{12}Mo_6$). This POM was immobilised onto a series of carbon nanomaterials doped with nitrogen (MWCNT_N), sulphur (MWCNT_S and GF_S). The doped supports were prepared via ball milling and thermal treatment using melamine or sulphur as precursors.

The $P_2W_{12}Mo_6$@MWCNT_N8 hybrid demonstrated the optimal electrocatalytic activity, exhibiting an onset potential of 0.84 V and a limiting current density of -3.7 $mA \cdot cm^{-2}$. The integration of heteroatoms into the carbon lattice has been demonstrated to enhance the electrochemical surface area and provide additional active sites, as evidenced by the augmentation in specific capacitance and the acceleration of ORR kinetics.

Electrochemical analysis confirmed a mixed ORR mechanism ($n_{O2} \approx 3.3$) and a very low hydrogen peroxide yield, reaffirming the high selectivity and catalytic efficiency of the composite. The catalyst also exhibited excellent durability and resistance to methanol crossover. This study thus confirms the beneficial effect of heteroatom doping in creating synergistic effects between POMs and carbonaceous supports, further establishing the role of tailored hybrid materials in enhancing catalytic properties for energy conversion applications. The collective findings indicate that nitrogen doping exerts a pronounced efficacy in activating carbon-based materials for ORR, culminating in substantial enhancements in onset potential, limiting current, and reaction selectivity. This enhanced performance is attributed to the introduction of nitrogen functionalities, particularly pyridinic and quaternary nitrogen, which directly influence the electronic structure and facilitate $O_2$ adsorption. In contrast, while sulphur doping contributes to catalytic activity, primarily through alterations in spin density and the presence of thiophene-S and oxidised sulphur species, its impact is comparatively less pronounced. This is likely due to the minimal change in charge density resulting from sulphur's electronegativity being close to that of carbon. Consequently, nitrogen doping emerges as the most effective strategy among those studied to enhance the electrocatalytic performance of POM–carbon hybrids for ORR applications.

The final component of the thesis involved the synthesis and characterisation of three-dimensional cobalt and nickel nanofoams (Co-NF, Ni-NF, and CoNi-NF) using the dynamic hydrogen bubble templating (DHBT) method. This technique enabled the formation of porous, interconnected metal networks with high conductivity and surface area, ideal for applications in water splitting and energy storage.

Electrochemical testing in 1 $mol \cdot dm^{-3}$ KOH demonstrated that Co-NF exhibited remarkable HER performance, requiring a mere 32 mV overpotential to achieve 10 $mA \cdot cm^{-2}$. For the OER, both Co-NF and Ni-NF delivered excellent results with overpotentials of 321 mV and 323 mV, respectively. The Tafel slopes ranged from 98 to 156 $mV \cdot dec^{-1}$ for HER and 102 to 204 $mV \cdot dec^{-1}$ for OER, confirming favourable reaction kinetics.

When evaluated as supercapacitor electrodes, the oxidised bimetallic CoNi-NF_75_OX demonstrated superior performance in comparison to its mono-metallic analogues, achieving a specific capacitance of 345.5 $F \cdot g^{-1}$ at 1 $A \cdot g^{-1}$. Remarkably, it retained more than 300 $F \cdot g^{-1}$ after 3000 cycles, demonstrating excellent electrochemical stability. The decline observed beyond this point was largely attributed to minor mechanical detachment rather than chemical degradation.

These findings thus validate the multifunctional nature of these 3D nanoarchitectures, offering dual performance as electrocatalysts and high-capacitance electrodes. The versatility and scalability of these 3D nanoarchitectures renders them suitable candidates for integration into next-generation energy conversion and storage platforms.

## 6.2. Final perspectives

This PhD thesis has shown that the rational design of hybrid electrocatalysts, combining POMs, doped nanostructured carbon supports and 3D metallic foams, can lead to improved electrochemical performance in various energy conversion and storage applications. By systematically investigating how the structure, composition and electronic properties of the POM and support materials affect the performance of ORR, new insights were gained into the relationship between catalyst design and electrocatalytic behaviour.

Future research could further explore the role of POM composition and electronic configuration, in particular by incorporating mixed-additive and lacunar structures, or by fine-tuning the redox active centres within the Dawson framework to favour specific ORR

pathways or to increase selectivity. Building on the results obtained with $P_2W_{12}Mo_6$ and $P_2W_{17}Fe$, it would be valuable to investigate the effect of other transition metal substitutions (e.g. Co, Mn, Cu) in modulating catalytic activity, stability and peroxide selectivity.

Furthermore, while this work has shown that nitrogen doping significantly enhances the ORR performance of carbon materials, future studies could explore co-doping strategies, such as N/S or N/P, to evaluate potential synergistic effects on electronic structure and $O_2$ adsorption. The incorporation of hierarchically structured or porous carbons, such as hollow nanospheres or 3D graphene networks, may also provide enhanced mass transport and accessible active sites.

The development of nickel- and cobalt-based metallic foams using DHBT method has been shown to be an efficient approach to obtaining 3D porous electrodes with high electrical conductivity and a large electrochemically active surface area. These materials demonstrated good performance as bifunctional electrocatalysts for HER and OER, and also showed significant capacitance and cycling stability when evaluated as electrodes for supercapacitors.

In future work, the optimisation of the morphological properties of the foams, such as pore size and interconnectivity, could further improve ionic transport and mechanical durability under operating conditions. Adjusting synthesis parameters (such as current density, deposition time, and electrolyte composition) or using pulsed or alternating current instead of constant current may allow finer control over foam architecture.

Another promising direction involves the incorporation of conductive carbon materials, such as carbon nanotubes, graphene, or carbon black, into or onto the metallic foams. This hybrid approach has the potential to combine the pseudocapacitive behaviour and redox activity of the metal with the double layer capacitance, stability and high surface area of carbon. This integration may also enhance electrical conductivity and mitigate degradation over prolonged cycling.

The results and methodologies established in this thesis thus offer a solid foundation for future innovations in electrochemical energy conversion and storage, contributing to the ongoing transition toward sustainable and scalable technologies.

# Appendices

# Appendix A: Published Scientific Articles

Electrocatalysis (2023) 14:294–305
https://doi.org/10.1007/s12678-022-00792-w

RESEARCH



## Electrocatalytic Oxygen Reduction Reaction on 48-Tungsto-8-Phosphate Wheel Anchored on Carbon Nanomaterials

**Hugo C. Novais[1] · Bruno Jarrais[1] · Ali Haider[2,3] · Ulrich Kortz[2] · Antonio Guerrero-Ruiz[4] · Inmaculada Rodríguez-Ramos[5] · Cristina Freire[1] · Diana M. Fernandes[1]**

Accepted: 6 November 2022 / Published online: 22 November 2022
© The Author(s), under exclusive licence to Springer Science+Business Media, LLC, part of Springer Nature 2022

**Abstract**
Regardless of great efforts, the development of novel low cost electrocatalysts with high electrocatalytic activity for the oxygen reduction reaction (ORR) remains a real challenge. This is a setback for the mass commercialization of one of the eco-friendliest alternative power sources: fuel cells (FCs). Thus, this work describes the preparation of four composites based on the 48-tungsto-8-phosphate polyanion salt $K_{28}Li_5[H_7P_8W_{48}O_{184}]\cdot 92H_2O$ ($KLi\text{-}P_8W_{48}$) immobilized on four distinct carbon materials, namely graphene flakes (GF), single-walled carbon nanotubes (SWCNT), multi-walled carbon nanotubes (MWCNT), and N-doped multi-walled carbon nanotubes (N-MWCNT), and their application as ORR electrocatalysts. In alkaline medium, all composites exhibited electrocatalytic activity with onset potentials between 0.71 and 0.94 V vs. RHE, while $P_8W_{48}$@N-MWCNT presented superior current density ($-3.3$ mA $cm^{-2}$). A mixed electron process of 2- and 4-electrons is observed for all the composites, supporting the results of % $H_2O_2$ production. Additionally, low Tafel slopes were obtained (43–82 mV $dec^{-1}$) for all composites. The electrocatalysts also showed excellent tolerance to methanol, with current retentions of 91–93%, and good electrochemical stability with current retentions between 67 and 82% after 36,000 s.

**Keywords** Oxygen reduction reaction · Electrocatalysis · Carbon materials · Polyoxometalate

### Introduction

In the last decades, the abrupt growth of world population and industrial processes has had a profound impact on the environment and health, increasing the urgency to substitute the use of fossil fuels with alternative energy sources and conversion devices [1]. One of the most common eco-friendly options are fuel cells (FCs), which commercialization is on hold due to the high cost of hydrogen storage and noble metal-based state-of-the-art electrocatalysts. The current use of precious Pt and Pd–based electrocatalysts is a major drawback for the economic viability of most fuel cells [2]. Proton exchange membrane (PEM) systems despite being the most technologically mature, rely on expensive acid membranes and ionomers [3] and platinum group metal-based electrocatalysts which are expensive, have restricted durability, and scarce availability [4]. To increase the oxygen reduction reaction (ORR) performance, Pt and Pd have been combined with other transition metals, such as Ru [5], Ni [6], Ag [6] or Co [7, 8]. In the case of anion exchange membrane fuel cells (AEMFCs), their intrinsically noncorrosive environment allows the use of less noble ORR electrocatalysts than Pt [9]. Therefore, materials from families of base metal oxides ($MnO_x$, mixed oxides, spinels) [10], M–N–Cs (where M = Fe, Co, Mn) [11], and Ni-based materials [12] have been extensively studied as ORR electrocatalysts in alkaline media with some excellent results.

✉ Diana M. Fernandes
diana.fernandes@fc.up.pt

[1] REQUIMTE/Departamento de Química e Bioquímica, Faculdade de Ciências, Universidade do Porto, 4169-007 Porto, Portugal

[2] Department of Life Sciences and Chemistry, Jacobs University, 28759 Bremen, Germany

[3] Department of Chemistry, Quaid-i-Azam University, Islamabad 45320, Pakistan

[4] Dpto. Química Inorgánica y Técnica, Facultad de Ciencias, UNED, Senda del Rey 9, 28040 Madrid, Spain

[5] Instituto de Catálisis y Petroleoquímica, CSIC, Cantoblanco, Marie Curie 2, 28049 Madrid, Spain

For example, pyrolyzed M–N–Cs electrocatalysts have shown ORR activities comparable to that of Pt-based catalysts in basic media [9]. As the ORR has a crucial function as the cathode reaction in these energy-converting systems, it is imperative to find new electrocatalysts with high performance and at the same time less expensive [13–16].

Polyoxometalates (POMs) exhibit a wide range of chemical and electrochemical properties that make them promising electrocatalysts for replacing platinum in the ORR. With a wide variety of sizes, compositions and shapes, POMs have the ability to undergo reversible multi-electron reductions/oxidations leading to the formation of mixed-valence species. Moreover, POMs have electron and proton transfer capabilities, and therefore, can act as acceptors/donors of a large number of electrons, without any significant structural changes.

Due to the high surface area, stability, and conductivity, combined with low cost, carbon materials have been the subject of several studies such as the degradation of organic pollutants [17], hydrogen storage [18], supercapacitors [19], batteries [20, 21] as well as their application in ORR [22, 23]. It is imperative to find and choose carbon materials that have additional anchoring positions where other active materials can be attached. For applications such as ORR, several carbon–based materials, such as graphene [24–26], carbon nanotubes [27], and respective doped carbon materials [28] have been proposed. One way to improve the electrocatalytic performance of carbon materials is through doping with different elements, nitrogen being one of the most used and with the most potential [29–31]. It has been shown that nitrogen-doped carbon materials show an increase in electrocatalytic activity towards ORR [32, 33]. Different forms of nitrogen species can be incorporated on the graphitic network, such as, pyridinic, pyrrolic, graphitic (quaternary) and oxidized nitrogen [34].

The individual use of polyoxometalates has not been very promising for reactions related to energy applications [35, 36]. However, these materials show higher performances when coupled with carbon supports [37–39]. Taking advantage of their high stability, good redox properties, and the ability to transfer electrons, POMs are excellent candidates to be coupled with carbon materials for subsequent application as ORR electrocatalysts [39, 40].

Herein, we report on the preparation of composites based on the incorporation of the 48-tungsto-8-phosphate $[H_7P_8W_{48}O_{184}]^{33-}$ ($P_8W_{48}$) onto four distinct carbon materials: graphene flakes (GF), single-walled carbon nanotubes (SWCNT), multi-walled carbon nanotubes (MWCNT), and N-doped multi-walled carbon nanotubes (N-MWCNT), and their application as ORR electrocatalysts.

## Experimental Section

### Materials Preparation and Characterization Methods

The materials and solvents used in the preparation of the composites and in the ORR studies are described in detail in the Supplementary information (SI). All carbon materials used in the preparation of the composites were commercially available, and used as received, with the exception of N-MWCNT, which was produced by catalytic chemical vapour decomposition using a previously described method [41]. The nitrogen content (4.1%) was determined by elemental analysis using a LECO CHNS-932 equipment. The rest of the N-MWCNTN-MWCNT characterization is described elsewhere [41].

The composites were prepared using an adapted procedure [42]. An aqueous dispersion of the selected carbon material (15 mL $H_2SO_4$, pH = 1.0, 3.3 mg $mL^{-1}$) was mixed with a solution of $P_8W_{48}$ ($0.5 \times 10^{-3}$ mol $dm^{-3}$ in 15 mL $H_2SO_4$, pH = 1.0) using an ultrasonic homogenizer for 15 min. Then, the grafting of $P_8W_{48}$ onto the carbon materials was achieved through controlled potential coulometry at − 0.65 V vs. SCE. For this purpose, a conventional three-electrode compartment cell was used, comprising of a glassy carbon electrode (GCE, 3 mm diameter, ALS Co., Ltd) as working electrode, a platinum wire with a large surface area as the auxiliary electrode, and a purged calomel electrode (SCE) as reference electrode, with the latter two separated from the electrolyte by a glass frit. The electrolyte was purged with ultrahigh-purity $N_2$ for at least 30 min and kept under a positive pressure of this gas during the experiments. In the end, the suspension obtained was filtered and washed with ultra-pure water and the composites were dried in an oven overnight at 80 °C.

Prior to their use in the electrocatalytic studies, all composites prepared ($P_8W_{48}$@GF, $P_8W_{48}$@SWCNT, $P_8W_{48}$@MWCNT and $P_8W_{48}$@N-MWCNT) were characterized by different techniques: Fourier-transformed infrared spectroscopy (FTIR), scanning electron microscopy (SEM), energy dispersive X-ray spectroscopy (EDS) and X-ray photoelectron spectroscopy (XPS). The methods and equipment used are detailed in the SI. Electrocatalytic performances towards ORR were evaluated using a PGSTAT 302 N potentiostat (Metrohm Autolab B.V., Utrecht, The Netherlands) controlled by NOVA 2.1 and using a conventional 3-electrode system. For all details regarding electrodes, electrode conditioning and modification, see the Supplementary information.

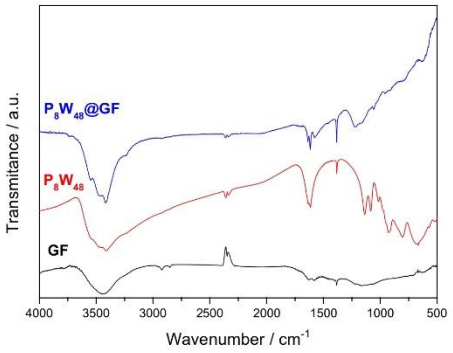



**Fig. 1** Overlaid FTIR spectra in the 4000–400 $cm^{-1}$ range of GF (black), KLi-$P_8W_{48}$ (red), and $P_8W_{48}$@GF composite (blue)

## Results and Discussion

### Materials Characterization

The infrared spectra for all prepared composites can be observed in Figs. 1 and S1 (Supplementary information). Figure 1 shows, as an example, the FTIR spectra for $P_8W_{48}$@GF, $P_8W_{48}$ and GF. The FTIR spectrum of $P_8W_{48}$ shows the typical POM vibrational bands between 1150 and 500 $cm^{-1}$. The two bands at 1134 and 1081 $cm^{-1}$ are attributed to the splitting of the $\nu_{as}$P-O stretching vibration. The $\nu_{as}W=O_t$ vibration band is detected at 1017 $cm^{-1}$ and the vibrational bands at 929 and 803 $cm^{-1}$ are assigned to $\nu_{as}$W-$O_b$-W and $\nu_{as}$W-$O_c$-W stretching modes, respectively [42, 43].

The FTIR spectrum of GF (Fig. 1, black) reveals some vibrational bands at 3433, 2921, 2853, 1633, 1580, 1384, 1165 and 1059 $cm^{-1}$, but some of the vibration bands are very weak and poorly resolved. The representative vibrational bands of OH groups are observed at 3433 and 1384 $cm^{-1}$, which are due to O–H stretching and bending modes, respectively from residual adsorbed water and to the hydroxyl groups [44, 45]. At 1580 and 1165 $cm^{-1}$, the bands are assigned to the C=C stretching mode of skeletal vibrations from non-oxidized domains and to the influence of phenolic groups vibration modes, respectively [44, 46, 47]. The two bands at 2921 and 2853 $cm^{-1}$ correspond, respectively, to the C-H stretching modes that can be due to the existence of defects in the $sp^2$ hybridized domains, and the band at 1633 $cm^{-1}$ can be assigned to the C=O stretching mode of carboxylic acid, carbonyl, ketone and quinone groups [44, 45]. The band at 1059 $cm^{-1}$ is assigned to C–O–C and C-O stretching modes and C-O–H bending mode [44, 46, 47].

The vibrational spectra of single- and multi-walled were very identical (Fig. S1 blue line) with weak bands. However, the SWCNT spectrum shows bands assigned to O–H stretching and bending modes at ~ 3437 and 1384 $cm^{-1}$, respectively [44, 45]. The band corresponding to the C=C stretching vibrations of the aromatic carbon is found at 1579 $cm^{-1}$, the band at 1628 $cm^{-1}$ is attributed to C=O stretching vibration, and the band at 1383 $cm^{-1}$ to the phenol groups [45]. Finally, the band at 1174 $cm^{-1}$ is assigned to the C-O stretching vibrations of oxygen groups [39].

The vibrational bands of N-MWCNT (Fig. S1(c)) can be observed at 3422, 1565, 1383 and 1118 $cm^{-1}$, corresponding to the O–H groups stretching vibrations, the stretching vibrations of C=N and C=C, and the C-N and C-O stretching vibrations, respectively [48, 49].

The FTIR spectra of $P_8W_{48}$@carbon materials (CM) shown in Fig. 1 for $P_8W_{48}$@GF and in Fig. S1 for the other three composites show very week and poorly resolved bands sill it confirms the immobilization of the POM onto the carbon materials, as it exhibits the typical bands from the POM in addition to the bands from the carbon material. After adsorption of the $P_8W_{48}$ onto the carbon materials, the positions of the vibration modes are slightly shifted to lower wavenumbers. Reported changes are likely to reflect weakening bonds [50, 51]. Similar results were observed for the other three composites.

All composites were characterized by XPS, and the surface atomic percentages are summarised in Table 1. This technique was used to probe the chemical environments of the elemental surface species, showing that the immobilization of the POM (O, P and W elements) onto the carbon materials was successful. The atomic ratios obtained for $P_8W_{48}$@N-MWCNT and $P_8W_{48}$@MWCNT of 1:6 (P/W) suggest that the POM structured is maintained as this value is equal to the theoretical one. Still, for the other two materials prepared, namely for $P_8W_{48}$@GF and $P_8W_{48}$@

**Table 1** XPS surface atomic percentages for the pristine carbon materials and the prepared composites

| Material | XPS Atomic %[a] | | | | |
|---|---|---|---|---|---|
| | C1s | O1s | N1s | P2p | W4f |
| GF | 96.8 | 3.2 | - | - | - |
| SWCNT | 98.4 | 1.6 | - | - | - |
| MWCNT | 98.9 | 1.1 | - | - | - |
| N-MWCNT | 90.4 | 5.2 | 4.4 | - | - |
| $P_8W_{48}$@GF | 92.2 | 6.8 | 0.6 | 0.1 | 0.3 |
| $P_8W_{48}$@SWCNT | 89.9 | 8.5 | 0.7 | 0.2 | 0.7 |
| $P_8W_{48}$@MWCNT | 87.6 | 10.6 | 1.1 | 0.1 | 0.6 |
| $P_8W_{48}$@N-MWCNT | 78.6 | 15.3 | 4.0 | 0.3 | 1.8 |

[a]Determined by the areas of the respective bands in the high-resolution XPS spectra

SWCNT the ratios are close (1:3 and 1:3.5, respectively). In Figs. S2–S8, all the deconvoluted XPS spectra are shown.

Figure 2(a) shows the C1s high-resolution spectra of $P_8W_{48}$@N-MWCNT, fitted with seven peaks: a main peak at 284.6 eV assigned to the graphitic structure ($sp^2$, C = C), a peak at approximately 285.6 eV attributed to a $sp^3$ hybridized carbon and C-N bonding, a peak at 285.9 eV assigned to C-N and C–OH bonding, a peak at approximately 286.9 eV attributed to C–O–C groups, a peak at 288.2 eV assigned to C = O groups (ketones, quinones, aldehydes), a peak at ~ 289.3 eV ascribed to COOH (carboxylic acids, esters), and a peak at 291.0 eV attributed to π–π* transitions [52]. The C1s high-resolution spectra of the remaining composites and pristine carbon materials are similar to that for $P_8W_{48}$@N-MWCNT, as can be seen in the SI file.

The N1s XPS spectrum (Fig. 2(b)) was deconvoluted onto two main peaks at 398.5 eV and 401.6 eV, attributed to pyridinic and quaternary N, respectively. This is consistent with the results obtained for the pristine N-MWCNT, which also contains a peak corresponding to pyridinic N. Different sets of peaks are observed for the other N-containing compounds, which show additional peaks referring to pyrrolic and quaternary N at 400.1 eV and 401.6 eV, respectively [53–55]. The rest of the starting carbon materials do not show any presence of nitrogen, as expected. Nevertheless, it is possible to see a small amount of nitrogen in the rest of the composites (Table 1). This is explained from the alkaline degradation in the presence of amine to obtain the polyoxometalate salt throughout the synthesis of the POM [56].

In the high resolution O1s spectra (Fig. 2(c)), the peak at 530.7 eV is ascribed to oxygen in C = O (ketones, quinones, aldehydes), and COOH groups (carboxylic acids, esters) and oxygen atoms belonging to the POM. The peak at 532.8 eV is attributed to O in HO-C groups (phenols) [39, 57]. These two peaks are observed throughout all materials, with material MWCNT having an extra peak from O of water at 536.0 eV, due to fortuitous contamination [55].

The P2p high-resolution spectra of $P_8W_{48}$@GF is shown in Fig. 2(d) and the observed peaks can be resolved as $2p_{3/2}$ and $2p_{1/2}$ doublets at 133.4 and 134 eV, respectively. Finally, in Fig. 2(e), the peaks found in the high-resolution spectra of W4f are attributed to $4f_{7/2}$ (35.4 eV) and $4f_{5/2}$ (37.6 eV), due to spin-orbital coupling.

The morphology of all composites was assessed by SEM and Fig. 3 shows the SEM images for $P_8W_{48}$@GF(a), $P_8W_{48}$@SWCNT (b), $P_8W_{48}$@MWCNT (c), and $P_8W_{48}$@N-MWCNT (d). In Fig. 3(a), it is possible to observe the folded graphene sheets completely covered with $P_8W_{48}$ clusters which leads to this roughened texture. For the other three images, the morphology is quite different, being possible to observe the carbon nanotubes with diverse widths. The measured diameter of the nanotubes is approximately $d = 12$ nm for the single-walled, and between $d = 12$–22 nm for the multi-walled nanotubes. The N-MWCNTs are much larger in size, with diameters ranging from 90 to 190 nm. A possible reason for such a large difference in diameter is the fact that the MWCNT were commercially available while the N-MWCNT were prepared by chemical vapour decomposition (CVD). This can lead to different sizes and shapes.

EDX analysis was conducted to assess the distribution of $P_8W_{48}$ throughout the carbon materials. Figure 4 shows the SEM and EDX elemental mapping images for $P_8W_{48}$@GF, while the images for the other composites can be found in Figs. S5 to S7. The EDX spectra of the composites show the presence of C and O from the carbon materials, and P, W and O from the POMs. The elemental mapping analysis also revealed a homogeneous distribution of all the elements throughout the sample, which indicates that the $P_8W_{48}$ polyanions are well distributed throughout the carbon materials.

### Electrochemical Performance Towards ORR

The electrocatalytic activity of all composites prepared was evaluated by cyclic voltammetry (CV) in $N_2$- and $O_2$-satured KOH solution (0.1 mol $dm^{-3}$) and the CVs obtained are shown in Fig. 5. In $N_2$-purged electrolyte no peaks are observed except for $P_8W_{48}$@MWCNT where two pairs of peaks can be identified at $E_{pc1} = 0.79$ V, $E_{pa1} = 0.90$ V, $E_{pc2} = 0.46$ V, and $E_{pa2} = 0.51$ V, corresponding to the two consecutive 4-electron redox processes of tungsten [42]. In $O_2$-purged electrolyte, all composites exhibit an irreversible reduction peak corresponding to oxygen reduction at $E_{pc} = 0.72$, 0.70, 0.69 and 0.83 V vs. RHE for $P_8W_{48}$@GF, $P_8W_{48}$@SWCNT, $P_8W_{48}$@MWCNT and $P_8W_{48}$@N-MWCNT, respectively. The Pt/C (20 wt.%) was also evaluated in the same experimental conditions (Figure S8(a) in the SI) and it presented an $E_{pc} = 0.86$ V vs. RHE.

Linear sweep voltammetry (LSV) at different rotation speeds was further used to evaluate the performance of the composites prepared (Fig. S12). For comparison, the LSV studies were also performed for the carbon supports (GF, SWCNT, MWCNT and N-MWCNT) in order to determine their contribution to the overall ORR electroactivity (Fig. S13) and for Pt/C (Fig. S14). The LSV curves of the composites, obtained at 1600 rpm in $O_2$-purged KOH solution (0.1 mol $dm^{-3}$), are shown in Fig. 6 and Table 2 presents the main ORR parameters obtained—onset potential ($E_{onset}$), diffusion-limiting current density values ($j_{L,\ 0.26\ V,\ 1600\ rpm}$), Tafel slopes (TS) and the number of electrons transferred per oxygen molecule ($n_{O2}$).

The results obtained for the carbon supports show that all materials present similar $E_{onset}$ values (between 0.72 and 0.69 V vs RHE) except for N-MWCNT that presented an

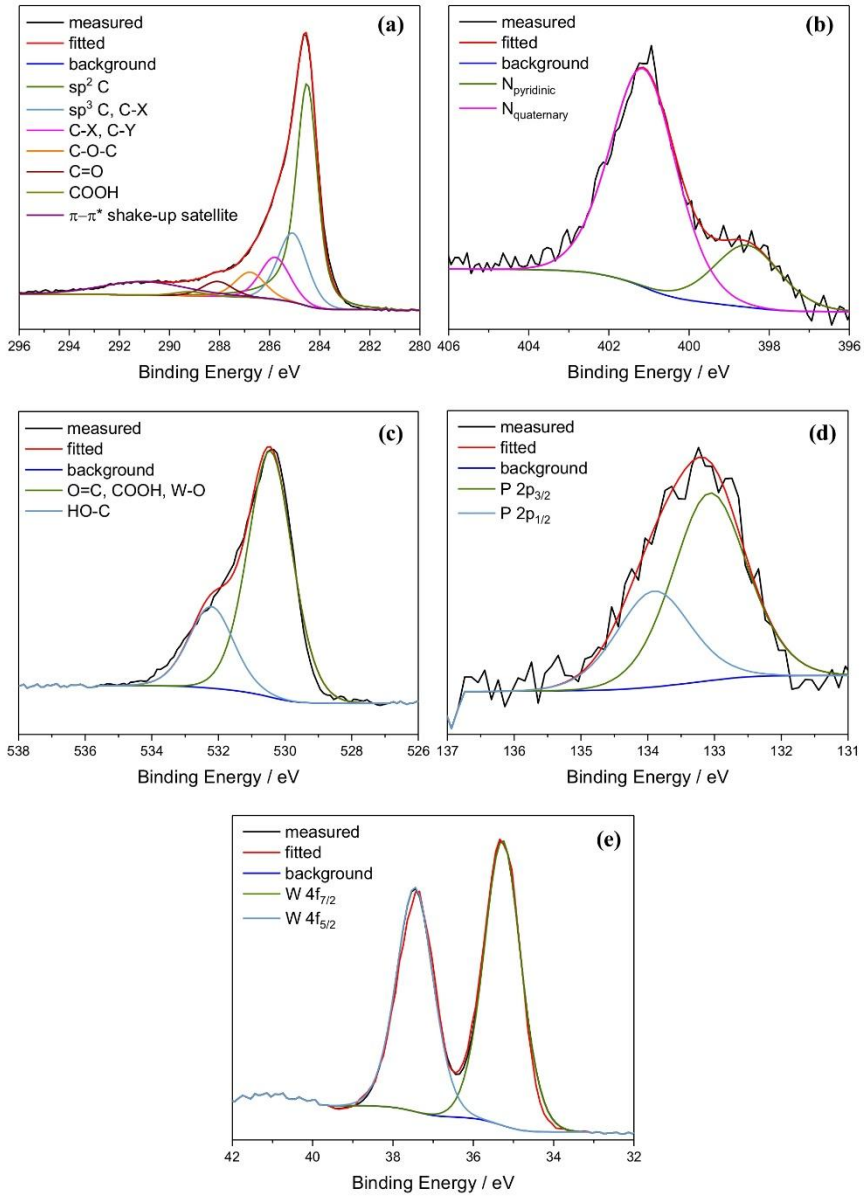



**Fig. 2** XPS deconvoluted spectra of corresponding elements in $P_8W_{48}$@N-MWCNT composite

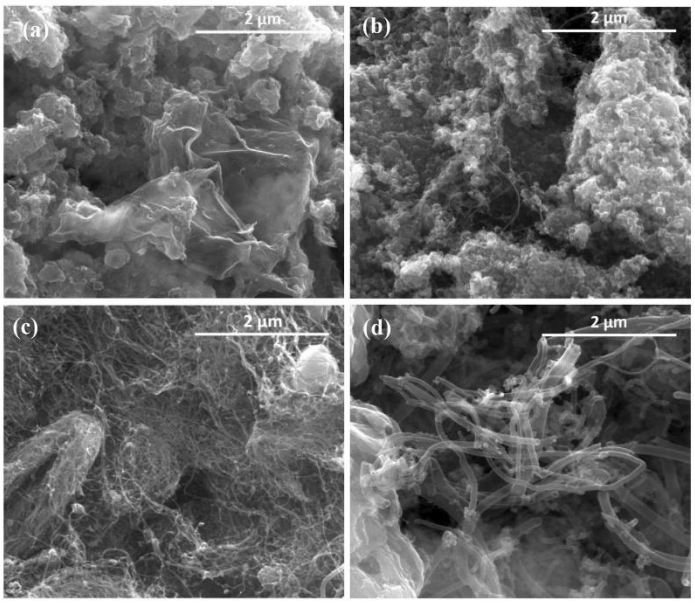



**Fig. 3** SEM images of $P_8W_{48}$@GF (**a**), $P_8W_{48}$@SWCNT (**b**), $P_8W_{48}$@MWCNT (**c**) and $P_8W_{48}$@N-MWCNT (**d**) at 50,000 × magnification

$E_{onset}$ value of 0.90 V vs RHE being just 0.04 V lower than that obtained for Pt/C. Moreover, N-MWCNT presented the highest $j_L$ value (−3.2 mA cm$^{-2}$) compared with the other carbon supports where $-2.6 \geq j_L \geq 2.0$ mA cm$^{-2}$. In the same condition, Pt/C presented a $j_L = -4.7$ mA cm$^{-2}$. The doping process of MWCNT led to an improvement of ORR electrocatalytic activity owing to the presence of nitrogen atoms, which is in agreement with several already reported works [39, 58] where N-doping led to an enhancement of ORR electrocatalytic activity. After doping, the $E_{onset}$ value of MWCNT shifted 21 mV to more positive potentials, and the $j_L$ increases 60%.

Then the ORR performance of the POM-based composites was evaluated. It can be clearly seen that the immobilization of $P_8W_{48}$ onto the different carbon nanomaterials leads to an improvement of the ORR electrocatalytic performance (more positive $E_{onset}$ values and higher $j_L$). It is also possible to observe that $P_8W_{48}$@GF, $P_8W_{48}$@SWCNT and $P_8W_{48}$@MWCNT composites present a similar behaviour with comparable $E_{onset}$ values (0.75, 0.76, 0.77 respectively). However, $P_8W_{48}$@N-MWCNT presents an $E_{onset}$ value shifted to more positive potentials (0.93 V vs. RHE) which is equal to the value obtained for Pt/C. This suggests an enhancement of the ORR electrocatalytic performance for the $P_8W_{48}$@N-MWCNT composite. This is also confirmed by the higher value of $j_L$ obtained for the later composite (−3.7 mA cm$^{-2}$) compared to those obtained for the other composites (−3.0, −3.0 and −2.4 mA cm$^{-2}$ for $P_8W_{48}$@GF, SWCNT and MWCNT, respectively).

This behaviour might be explained because of the nitrogen atom presence leading to a better electrocatalytic performance [59]. Due to its high electronegativity, it may be allowing greater interaction between $O_2$ molecules and thus restructuring the electronic structure of neighbouring atoms, promoting the ORR mechanism [60]. Hereupon, all the composites are implicated in a mixed electron process of 2- and 4-electrons, confirmed by the $n_{O2}$ values occurred between 2.2 and 3.0 (Fig. 6(b)).

Using Eq. (4) (SI) the percentage of $H_2O_2$ produced was calculated and is shown in Fig. 7 at various potential values. Thus, as expected, $P_8W_{48}$@N-MWCNT got the lowest percentage of $H_2O_2$ among the analysed composites. This behaviour was anticipated [61] towards ORR applications once this composite got the highest number of transferred electrons ($n_{O2} = 3.0$). The composites $P_8W_{48}$@GF, $P_8W_{48}$@SWCNT and $P_8W_{48}$@MWCNT with the lowest number of transferred electrons feature a higher production of $H_2O_2$ obtaining respectively, 84, 86 and 54% in about the same potential range.

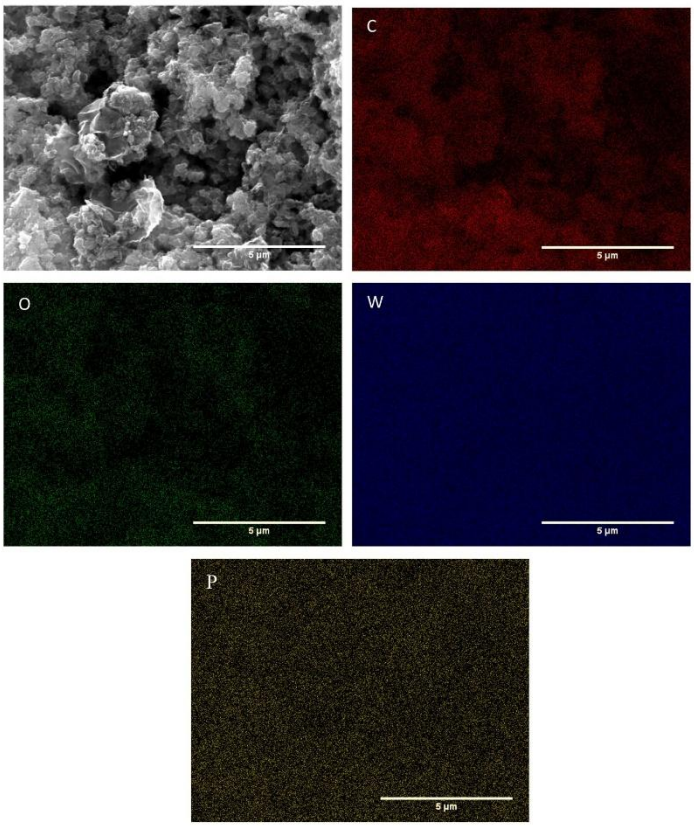



**Fig. 4** SEM and EDX elemental mapping images of $P_8W_{48}$@GF, at 10,000 × magnification for the elements C (red), O (green), W (blue) and P (yellow)

The Tafel plots of the prepared electrocatalysts and of the Pt/C reference were obtained from the LSV curves in $O_2$-purged KOH at 1600 rpm and are shown in Fig. 8. $P_8W_{48}$@GF, $P_8W_{48}$@MWCNT and $P_8W_{48}$@SWCNT showed very similar Tafel slopes between 44 and 48 mV $dec^{-1}$ while $P_8W_{48}$@N-MWCNT slightly higher value (72 mV $dec^{-1}$). The proposed mechanism for all compounds suggests the overall reaction rate is probably determined by the elementary step that involves the conversion the intermediate surface adsorbed specie $MOO^-$ to MOOH (M is an empty site on the electrocatalyst surface) [62].

To get more information about the effect of POM immobilization onto the carbon supports used on the intrinsic ORR performance, the current values were normalized to the double-layer capacitances ($C_{dl}$) used as an approximated estimation of the electrochemically active surface areas (ECSAs) (Fig. S15). This is only possible due to the similar nature of the materials tested and the proportional relationship between $C_{dl}$ and ECSAs [58, 63].

The $C_{dl}$ values (see Table 3) were determined by performing CV measurements at increasing scan rates (see full details in Supplementary information file and Fig. S16). So, $C_{dl}$ values

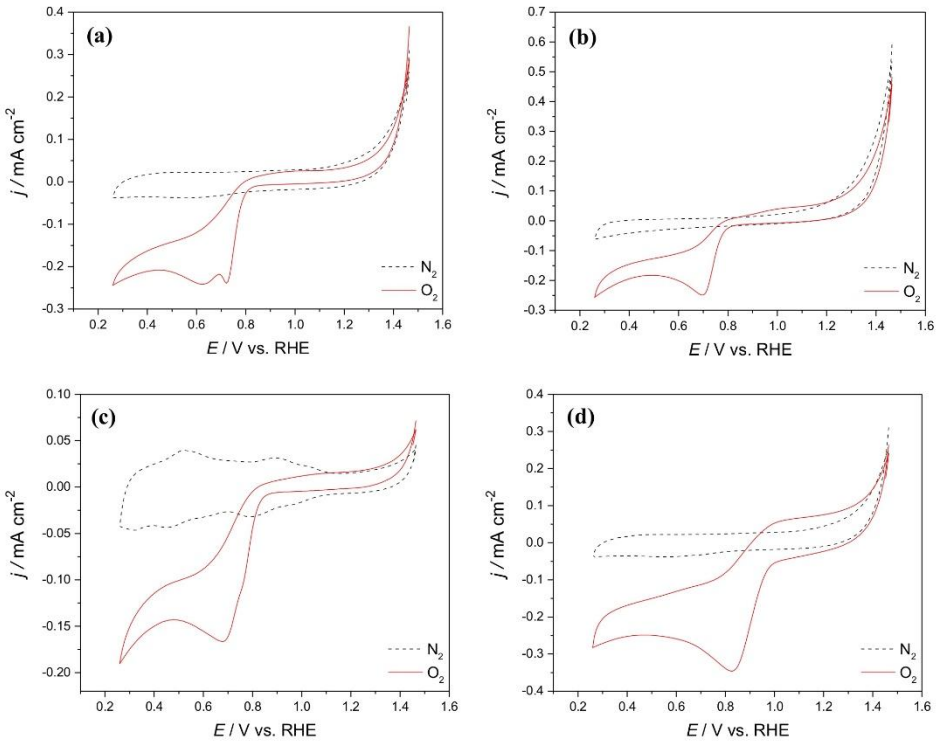



**Fig. 5** CVs of $P_8W_{48}$@GF (**a**), $P_8W_{48}$@SWCNT (**b**), $P_8W_{48}$@MWCNT (**c**) and $P_8W_{48}$@N-MWCNT (**d**) modified electrodes in $N_2$-purged (dash line) and $O_2$-purged (full line) 0.1 mol $dm^{-3}$ KOH solution at 0.005 V $s^{-1}$

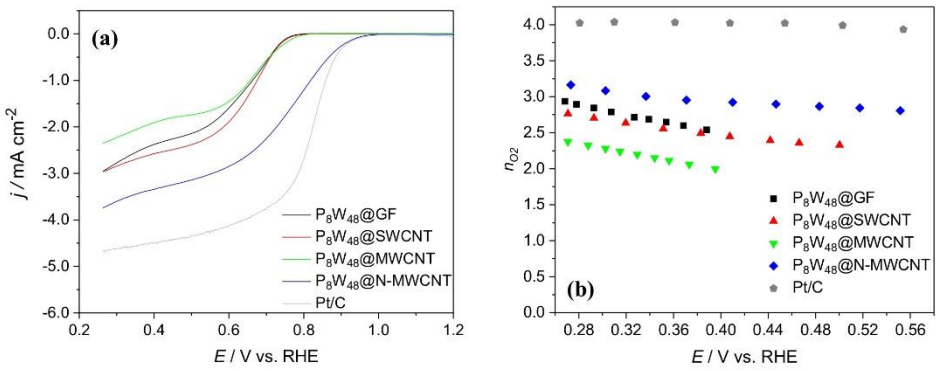



**Fig. 6** ORR LSV curves acquired using an RDE in $O_2$-purged KOH solution (0.1 mol $dm^{-3}$) at 1600 rpm and 0.005 V $s^{-1}$ of commercial Pt/C (20 wt.%) and $P_8W_{48}$@CM composites (**a**); $n_{O2}$ at several potential values (**b**)

**Table 2** Onset Potentials ($E_{onset}$), diffusion-limiting current density values ($j_{L\text{-}0.26\ V,1600\ rpm}$) derived from the ORR polarization curves in $O_2$-purged 0.1 mol $dm^{-3}$ KOH solution for commercial Pt/C, carbon materials and composites prepared and Tafel and $n_{O2}$values

| Samples | $E_{onset}$vs RHE | $j_L$ (mA $cm^{-2}$) | Tafel (mV $dec^{-1}$) | $n_{O2}$ |
|---|---|---|---|---|
| Pt/C | 0.94 | −4.7 | 89 | 4.0 |
| GF | 0.72 | −2.0 | 63 | 2.4 |
| SWCNT | 0.72 | −2.6 | 60 | 3.0 |
| MWCNT | 0.69 | −2.0 | 54 | 2.1 |
| N-MWCNT | 0.90 | −3.2 | 125 | 2.5 |
| $P_8W_{48}$@GF | 0.75 | −3.0 | 44 | 2.7 |
| $P_8W_{48}$@SWCNT | 0.76 | −3.0 | 48 | 2.7 |
| $P_8W_{48}$@MWCNT | 0.77 | −2.4 | 47 | 2.2 |
| $P_8W_{48}$@N-MWCNT | 0.94 | −3.7 | 72 | 3.0 |

were calculated from the slopes of the linear fittings of CV current densities (measured at the same potential of 1.13 V vs. RHE) reached at different scan rates (Fig. S17). However, as some faradaic contributions can be seen in the CV plots of the charge–discharge tests, these calculated capacitance values must be seen as estimated values. Therefore, the $C_{dl}$ can be considered as an estimate of the number of electrocatalytically accessible sites for a given electrocatalyst [64]. Results show that there is a significant increase in the number of active sites after the immobilization of POM for GF and a less significant one for MWCNT. For SWCNT and N-MWCNT the number of active sites decreases after POM immobilization. As can be observed in Fig. S15, the electroactive surface area has a significant impact on the ORR performance with $P_8W_{48}$@

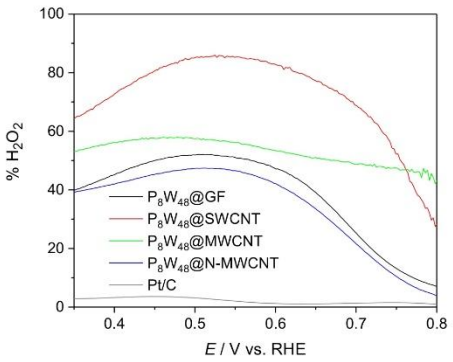



**Fig. 7** Estimated percentage of $H_2O_2$ produced with RRDE in $O_2$-purged 0.1 mol $dm^{-3}$ KOH solution, at 1600 rpm; the disk potential was swept at v = 0.005 V $s^{-1}$ and the ring potential was kept at $E$ = 0.2 V versus Ag/AgCl for $P_8W_{48}$@GF, $P_8W_{48}$@MWCNT, $P_8W_{48}$@SWCNT, $P_8W_{48}$@N-MWCNT and Pt/C (20 wt.%)

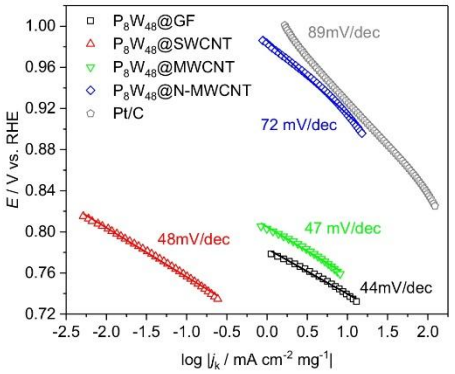



**Fig. 8** ORR Tafel plots obtained from LSV data in Fig. 6 where current densities are normalized to the mass of each ECs

SWCNT and $P_8W_{48}$@MWCNT showing the best ORR intrinsic activity. Results also show that apparent better performance of N-MWCNT (nominal activity) is due to the higher number of active sites when compared with the other composites.

Another crucial parameter when assessing potential electrocatalysts for ORR is their stability. Therefore, chronoamperometric studies were performed at $E$ = 0.46 V vs. RHE for 36,000 s at 1600 rpm, in oxygen-purged alkaline electrolyte (Fig. 9(a)). The composite that shows better stability is $P_8W_{48}$@N-MWCNT with a current retention of 82%, while the other electrocatalysts showed slightly lower values, of 75%, 67% and 69% for $P_8W_{48}$@GF, $P_8W_{48}$@SWCNT and $P_8W_{48}$@MWCNT, respectively. The higher current retention obtained for $P_8W_{48}$@N-MWCNT may be due to the stronger interaction between the POM and this particular carbon material as a result of N-doping process. Still, the decrease in stability for all composites may be a consequence of depletion of catalyst from the electrode surface over time. Nevertheless, the value obtained for the $P_8W_{48}$@N-MWCNT is very close to that obtained by us for commercial Pt/C catalysts (87%) which is consistent with the literature [39].

In methanol fuel cells, the study of the methanol tolerance is very important because it can lead to a drastic drop in cathodic performance if the electrocatalysts are sensitive to it [65]. For this reason, chronoamperometry (CA) was evaluated for the methanol tolerance of $P_8W_{48}$@CM composites. CA were obtained in $O_2$-purged 0.1 mol $dm^{-3}$ KOH (0.1 mol $dm^{-3}$), in presence of methanol (0.5 mol $dm^{-3}$) for Pt/C and $P_8W_{48}$@CM composites (Fig. 9(b)) during 2500 s. The methanol was added after 500 s since the beginning of the CA. The Pt/C electrocatalyst retains ~ 70% of its current density. On the other hand, the composites retain between ~ 91–93% of their initial current density.

**Table 3** Electrocatalytically active surface area (ECSA) values of the carbon supports and the corresponding POM-based composites

| CM support | $C_{dl}$ mF cm$^{-2}$ | Composite | $C_{dl}$ mF cm$^{-2}$ | Composite/carbon support $C_{dl}$ ratio |
|---|---|---|---|---|
| GF | 0.0048 | $P_8W_{48}$@GFx | 0.0762 | 15.8 |
| SWCNT | 0.0039 | $P_8W_{48}$@SWCNT | 0.0032 | 0.813 |
| MWCNT | 0.0023 | $P_8W_{48}$@MWCNT | 0.0035 | 1.53 |
| N-MWCNT | 0.0685 | $P_8W_{48}$@N-MWCNT | 0.0609 | 0.889 |

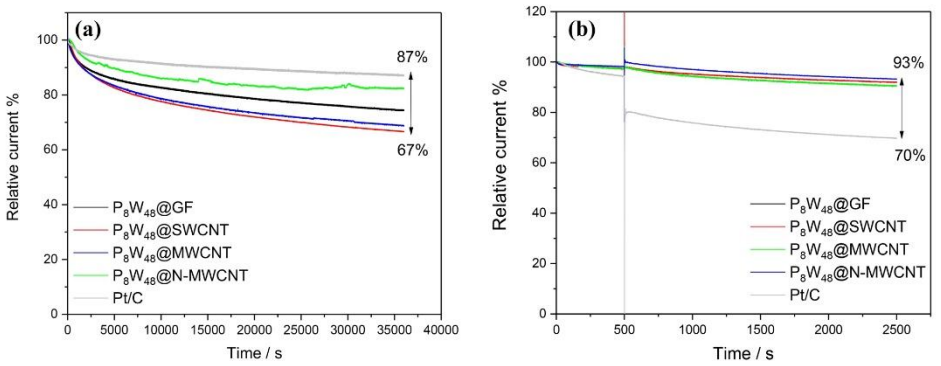



**Fig. 9** Chronoamperometric response of the ECs at 1600 rpm, in 0.1 mol dm$^{-3}$ $O_2$-purged KOH at: **a** $E = 0.46$ V vs. RHE for 36000 s and **b** $E = 0.46$ V vs. RHE with the addition of 0.5 mol dm$^{-3}$ methanol after ≈ 500 s

## Conclusions

This work introduces $P_8W_{48}$/carbon-based nanomaterials as alternative electrocatalysts for ORR with good activity and stability, including high selectivity towards the ORR in the presence of methanol. Throughout various characterization techniques such as FTIR, XPS and SEM analysis, it was proven that all composites ($P_8W_{48}$@GF, $P_8W_{48}$@SWCNT, $P_8W_{48}$@MWCNT, $P_8W_{48}$@N-MWCNT) were successfully synthesized. All nanocomposites showed ORR electroactivity in alkaline medium with onset potential values ranging from 0.71 and 0.94 V vs. RHE, low Tafel slopes (44–72 mV dec$^{-1}$), good $j_L$ values (−2.4 to −3.7 mA cm$^{-2}$), and a mixed electron process of 2- and 4 electrons confirmed by the results of $\%H_2O_2$ production. Still, the $P_8W_{48}$@N-MWCNT showed the best ORR electrocatalytic activity out of all materials prepared. Additionally, all nanocomposites showed robust electrocatalytic performance over 36,000 s, exhibiting high current retention values (~91–93%) and excellent methanol tolerance, suggesting high selectivity to ORR, overcoming one of the major limitations of the Pt/C electrocatalyst. Globally, this study is a step forward towards novel cheap and durable electrocatalysts, which are noble metal-free and offer great potential for energy-related reactions.

**Supplementary Information** The online version contains supplementary material available at https://doi.org/10.1007/s12678-022-00792-w.

**Acknowledgements** Thanks are also due to PT national funds FCT/MCTES through the projects UIDB/50006/2020 and UIDP/50006/2020. HCN thanks FCT through ChemMat program for his PhD grant PD/BD/143095/2018. DMF thanks FCT/MCTES for funding through the Individual Call to Scientific Employment Stimulus (2021.00771.CEECIND/CP1662/CT0007). UK thanks the German Science Foundation (DFG) and Jacobs University for support.

**Author Contribution** The synthesis and characterization of: POM was performed by A.H., N-MWCNT by A.G-R and I.R-R, composite materials by D.M.F, H.C.N and B.J. The electrocatalytic experiments were conducted by H.C.N. The research was supervised by D.M.F., U.K. and C.F. and H.C.N was responsible for writing up the manuscript, which was proofread by D.M.F and U.K.

**Funding** This work was financially supported by: Project FOAM-4NER (PTDC/QUI-ELT/28299/2017) (FOAM4NER) funded by (FCT/MCTES, Fundação para a Ciência e Tecnologia and Ministério da Ciência, Tecnologia e Ensino Superior) through national funds.

**Data Availability** The following are available online. It includes: 1. Experimental with 1.1. Materials and solvents, 1.2. Physicochemical characterization, 1.3. ORR electrochemical tests. Figure S1 Infrared spectra in the range of 4000–400 cm-1 for $P_8W_{48}$ (red), carbon material (black) and composite (blue) for: SWCNT (a), MWCNT (b) and N-MWCNT (c), Fig. S2. XPS deconvoluted spectra of corresponding elements in $P_8W_{48}$@GF composite, Fig. S3. XPS deconvoluted

spectra of corresponding elements in $P_8W_{48}$@SWCNT composite, Fig. S4. XPS deconvoluted spectra of corresponding elements in $P_8W_{48}$@MWCNT composite, Fig. S5. XPS deconvoluted spectra of corresponding elements in GF composite, Fig. S6. XPS deconvoluted spectra of corresponding elements in SWCNT composite, Fig. S7. XPS deconvoluted spectra of corresponding elements in MWNT composite, Fig. S8. XPS deconvoluted spectra of corresponding elements in N-MWCNT composite, Fig. S9. SEM and EDS elemental mapping images of $P_8W_{48}$@SWCNT at magnification 5000× for the elements C, O, W and P., Fig. S10. SEM and EDS elemental mapping images of $P_8W_{48}$@MWCNT at magnification 5000× for the elements C, O, W and P., Fig. S11. SEM and EDS elemental mapping images of $P_8W_{48}$@N-MWCNT at magnification 5000× for the elements C, O, W and P., Fig. S12. ORR polarization curves of $P_8W_{48}$@GF (a), $P_8W_{48}$@SWCNT (c), $P_8W_{48}$@MWCNT (e) and $P_8W_{48}$@N-MWCNT (g) at different rotation rates in $O_2$-saturated 0.1 mol $dm^{-3}$ KOH solution at 0.005 V $s^{-1}$ and the corresponding Koutecky-Levich (K-L) plots (b, d, f and h)., Fig. S13. ORR polarization curves of GF (a), SWCNT (c), MWCNT (e) and N-MWCNT (g) modified electrodes, acquired at different rotation rates in $O_2$-saturated 0.1 mol $dm^{-3}$ KOH solution at 0.005 V $s^{-1}$ and the corresponding Koutecky-Levich (K-L) plots (b, d, f and h)., Fig. S14. ORR polarization curves for Pt/C at different rotation rates in $O_2$-saturated 0.1 mol $dm^{-3}$ KOH solution at 0.005 V $s^{-1}$ (a) and the corresponding Koutecky-Levich (K-L) plots (b)., Fig. S15. ORR LSV curves obtained in KOH (0.1 M) saturated with $O_2$ at 1600 rpm and 0.005 V $s^{-1}$ with current densities normalized to the respective double-layer capacitance values., Fig. S16. CVs at different scan rates for GF (a), SWCNT (b), MWCNT (c), N-MWCNT (d), $P_8W_{48}$@GF (e), $P_8W_{48}$@SWCNT (f), $P_8W_{48}$@MWCNT (g), $P_8W_{48}$@N-MWCNT (h) and Pt/C (i) in $N_2$-saturated KOH (0.1 M)., Fig. S17. Current density-scan rate linear fitting plots for all materials. Numeric values correspond to the double-layer capacitances ($C_{dl}$) for each material.

## Declarations

**Conflict of Interest** The authors declare no competing interests.

## References

1. F. Perera, Int. J. Environ. Res. Public Health **15**, 16 (2018)
2. M. Kuang, G. Zheng, Small **12**, 5656 (2016)
3. A.M. Samsudin, M. Bodner, V. Hacker, Polymers **14**, 3565 (2022)
4. D.M. Fernandes, A.F. Peixoto, C. Freire, Dalton Trans. **48**, 13508 (2019)
5. E.H. Yu, K. Scott, R.W. Reeve, Fuel Cells **3**, 169 (2003). https://doi.org/10.1002/fuce.200330129
6. H. Yin, S. Liu, C. Zhang et al., ACS Appl. Mater. Interfaces. **6**, 2086 (2014). https://doi.org/10.1021/am405164f
7. F.H.B. Lima, E.A. Ticianelli, Electrochim. Acta **49**, 4091 (2004). https://doi.org/10.1016/j.electacta.2004.04.002
8. N. Todoroki, T. Wadayama, Electrochemistry advpub. (2018). https://doi.org/10.5796/electrochemistry.18-00024
9. M. Hren, M. Božič, D. Fakin, K.S. Kleinschek, S. Gorgieva, Sustainable Energy Fuels **5**, 604 (2021). https://doi.org/10.1039/D0SE01373K
10. J.S. Spendelow, A. Wieckowski, Phys. Chem. Chem. Phys. **9**, 2654 (2007). https://doi.org/10.1039/B703315J
11. M.M. Hossen, K. Artyushkova, P. Atanassov, A. Serov, J. Power Sources **375**, 214 (2018). https://doi.org/10.1016/j.jpowsour.2017.08.036
12. X. Song, D. Zhang, Energy **70**, 223 (2014). https://doi.org/10.1016/j.energy.2014.03.116
13. A.S. Arico, P. Bruce, B. Scrosati, J.-M. Tarascon, W. Van Schalkwijk, Materials for sustainable energy: a collection of peer-reviewed research and review articles from Nature Publishing GroupWorld Scientific, (2011)
14. C. Freire, D.M. Fernandes, M. Nunes, V.K. Abdelkader, ChemCatChem **10**, 1703 (2018). https://doi.org/10.1002/cctc.201701926
15. H. Qin, Y. Wang, B. Wang et al., J. Energy Chem. **53**, 77 (2021). https://doi.org/10.1016/j.jechem.2020.05.015
16. C.-X. Zhao, B.-Q. Li, J.-N. Liu, J.-Q. Huang, Q. Zhang, Chin. Chem. Lett. **30**, 911 (2019). https://doi.org/10.1016/j.cclet.2019.03.026
17. A. Rodríguez, G. Ovejero, J.L. Sotelo, M. Mestanza, J. García, Ind. Eng. Chem. Res. **49**, 498 (2010). https://doi.org/10.1021/ie901212m
18. M. Mohan, V.K. Sharma, E.A. Kumar, V. Gayathri, Energy Storage **1**, e35 (2019). https://doi.org/10.1002/est2.35
19. Y. Gong, Q. Fu, C. Pan, MRS Advances **2**, 3283 (2017). https://doi.org/10.1557/adv.2017.385
20. J. Lach, K. Wróbel, J. Wróbel, P. Podsadni, A. Czerwiński, J. Solid State Electrochem. **23**, 693 (2019). https://doi.org/10.1007/s10008-018-04174-5
21. W. Yuan, Y. Zhang, L. Cheng, H. Wu, L. Zheng, D. Zhao, Journal of Materials Chemistry A **4**, 8932 (2016). https://doi.org/10.1039/C6TA01546H
22. L. Yang, J. Shui, L. Du et al., Adv. Mater. **31**, 1804799 (2019)
23. Q. Wu, L. Yang, X. Wang, Z. Hu, Acc. Chem. Res. **50**, 435 (2017)
24. Y. Liang, H. Wang, J. Zhou et al., J. Am. Chem. Soc. **134**, 3517 (2012)
25. Y. Liang, Y. Li, H. Wang et al., Nat. Mater. **10**, 780 (2011)
26. M.P. Araújo, M. Nunes, I.M. Rocha, M. Pereira, C. Freire, ChemistrySelect **3**, 10064 (2018)
27. Y. Liang, H. Wang, P. Diao et al., J. Am. Chem. Soc. **134**, 15849 (2012)
28. G. Zhang, C. Li, J. Liu et al., Journal of Materials Chemistry A **2**, 8184 (2014)
29. A. Sarapuu, E. Kibena-Põldsepp, M. Borghei, K. Tammeveski, J. Mater. Chem. A **6**, 776 (2018)
30. J. Masa, W. Xia, M. Muhler, W. Schuhmann, Angew. Chem. Int. Ed. **54**, 10102 (2015)
31. Z. Yang, H. Nie, X. Chen, S. Huang, J. Power Sources **236**, 238 (2013)
32. N.-T. Suen, S.-F. Hung, Q. Quan, N. Zhang, Y.-J. Xu, H.M. Chen, Chem. Soc. Rev. **46**, 337 (2017)
33. X. Wang, X. Fan, H. Lin et al., RSC Adv. **6**, 37965 (2016). https://doi.org/10.1039/C6RA04771H
34. M. Vikkisk, I. Kruusenberg, S. Ratso et al., RSC Adv. **5**, 59495 (2015)
35. E. Naseri, R. Khoshnavazi, RSC Adv. **8**, 28249 (2018)
36. Y. Ji, L. Huang, J. Hu, C. Streb, Y.-F. Song, Energy Environ. Sci. **8**, 776 (2015)
37. M. Skunik, B. Baranowska, D. Fattakhova et al., J. Solid State Electrochem. **10**, 168 (2006)
38. S. Aguado-Ureta, J. Rodríguez-Hernández, A. Del Campo et al., Nanomaterials **8**, 142 (2018)
39. D.M. Fernandes, H.C. Novais, R. Bacsa et al., Langmuir **34**, 6376 (2018). https://doi.org/10.1021/acs.langmuir.8b00299
40. T.C. Nagaiah, D. Gupta, S.D. Adhikary, A. Kafle, D. Mandal, Journal of Materials Chemistry A **9**, 9228 (2021). https://doi.org/10.1039/D0TA10423J
41. L. Faba, Y.A. Criado, E. Gallegos-Suárez et al., Appl. Catal. A **458**, 155 (2013)
42. R. Liu, G. Zhang, H. Cao et al., Energy Environ. Sci. **9**, 1012 (2016). https://doi.org/10.1039/C5EE03503A
43. D.M. Fernandes, M.P. Araújo, A. Haider et al., ChemElectroChem **5**, 273 (2018). https://doi.org/10.1002/celc.201701210
44. A. Navaee, A. Salimi, S. Soltanian, P. Servati, J. Power Sources **277**, 268 (2015). https://doi.org/10.1016/j.jpowsour.2014.11.117
45. B. Olalde, J.M. Aizpurua, A. García, I. Bustero, I. Obieta, M.J. Jurado, The Journal of Physical Chemistry C **112**, 10663 (2008). https://doi.org/10.1021/jp800266j

46. D.W. Lee, L.V. De Los Santos, J.W. Seo et al., J. Phys. Chem. B **114**, 5723 (2010). https://doi.org/10.1021/jp1002275
47. A.R. Kumarasinghe, L. Samaranayake, F. Bondino et al., J. Phys. Chem. C **117**, 9507 (2013). https://doi.org/10.1021/jp402428j
48. D.M. Fernandes, C. Freire, ChemElectroChem **2**, 269 (2015). https://doi.org/10.1002/celc.201402271
49. N. Daems, X. Sheng, I.F.J. Vankelecom, P.P. Pescarmona, J. Mater. Chem. A **2**, 4085 (2014). https://doi.org/10.1039/C3TA14043A
50. M. Skunik, M. Chojak, I.A. Rutkowska, P.J. Kulesza, Electrochim. Acta **53**, 3862 (2008)
51. N. Mizuno, K. Katamura, Y. Yoneda, M. Misono, J. Catal. **83**, 384 (1983)
52. H. Estrade-Szwarckopf, Carbon **42**, 1713 (2004)
53. W. Ai, Z. Luo, J. Jiang et al., Adv. Mater. **26**, 6186 (2014)
54. Y. Liu, Y. Qiao, G. Wei et al., Energy Storage Mater. **11**, 274 (2018)
55. B. Jarrais, A. Guedes, C. Freire, ChemistrySelect **3**, 1737 (2018). https://doi.org/10.1002/slct.201702706
56. R. Contant, A. Teze, Inorg. Chem. **24**, 4610 (1985). https://doi.org/10.1021/ic00220a036
57. M.E. Lipińska, S.L. Rebelo, M.F.R. Pereira, J. Gomes, C. Freire, J. Figueiredo, Carbon **50**, 3280 (2012)
58. N. Limani, I.S. Marques, B. Jarrais, A.J.S. Fernandes, C. Freire, D.M. Fernandes, Catalysts **12**, 357 (2022)
59. L. Dai, Y. Xue, L. Qu, H.-J. Choi, J.-B. Baek, Chem. Rev. **115**, 4823 (2015). https://doi.org/10.1021/cr5003563
60. S. Ni, Z. Li, J. Yang, Nanoscale **4**, 1184 (2012). https://doi.org/10.1039/C1NR11086A
61. X. Wang, H. Fu, W. Li, J. Zheng, X. Li, RSC Adv. **4**, 37779 (2014). https://doi.org/10.1039/C4RA05961A
62. T. Shinagawa, A.T. Garcia-Esparza, K. Takanabe, Sci. Rep. **5**, 13801 (2015). https://doi.org/10.1038/srep13801
63. I.S. Marques, B. Jarrais, I.-M. Mbomekallé et al., Catalysts **12**, 440 (2022)
64. V.K. Abdelkader-Fernández, D.M. Fernandes, S.S. Balula, L. Cunha-Silva, C. Freire, J. Mater. Chem. A **8**, 13509 (2020). https://doi.org/10.1039/D0TA03898A
65. C. Lo Vecchio, D. Sebastián, M. Lázaro, A. Aricò, V. Baglio, Catalysts **8**, 650 (2018)

**Publisher's Note** Springer Nature remains neutral with regard to jurisdictional claims in published maps and institutional affiliations.

Springer Nature or its licensor (e.g. a society or other partner) holds exclusive rights to this article under a publishing agreement with the author(s) or other rightsholder(s); author self-archiving of the accepted manuscript version of this article is solely governed by the terms of such publishing agreement and applicable law.

*inorganics*

MDPI

*Article*

# Hybrids Composed of an Fe-Containing Wells–Dawson Polyoxometalate and Carbon Nanomaterials as Promising Electrocatalysts for the Oxygen Reduction Reaction

**Hugo C. Novais [1], Bruno Jarrais [1], Israël-Martyr Mbomekallé [2], Anne-Lucie Teillout [2], Pedro de Oliveira [2], Cristina Freire [1] and Diana M. Fernandes [1,*]**

[1] LAQV-REQUIMTE/Department of Chemistry and Biochemistry, Faculty of Sciences, University of Porto, 4169-007 Porto, Portugal; hugodcnt@gmail.com (H.C.N.); bjarrais@gmail.com (B.J.); acfreire@fc.up.pt (C.F.)
[2] Equipe d'Electrochimie et de Photo-Électrochimie, Institut de Chimie Physique, UMR 8000 CNRS, Faculté des Sciences d'Orsay, Université Paris-Saclay, F-91405 Orsay, France; israel.mbomekalle@universite-paris-saclay.fr (I.-M.M.); anne-lucie.teillout@universite-paris-saclay.fr (A.-L.T.); pedro.almeida-de-oliveira@universite-paris-saclay.fr (P.d.O.)
* Correspondence: diana.fernandes@fc.up.pt

**Abstract:** The oxygen reduction reaction (ORR) is a key cathodic reaction in energy-converting systems, such as fuel cells (FCs). Thus, it is of utmost importance to develop cost-effective and efficient electrocatalysts (ECs) without noble metals to substitute the Pt-based ones. This study focuses on polyoxometalate (POM)-based ECs for ORR applications. A Wells–Dawson POM salt $K_7$ [$P_2W_{17}(FeOH_2)O_{61}$].·$20H_2O$ was immobilised onto graphene flakes and multiwalled carbon nanotubes doped with nitrogen, denominated as $P_2W_{17}$Fe@GF_N8 and $P_2W_{17}$Fe@MWCNT_N8. The successful preparation of the composites was proved with various characterisation techniques, including FTIR, XPS and SEM. Both materials showed good ORR performance in an alkaline medium with similar potential onset values of ~0.84 V vs. RHE and diffusion-limiting current densities of −3.9 and −3.3 mA $cm^{-2}$ for $P_2W_{17}$Fe@MWCNT_N8 and $P_2W_{17}$Fe@GF_N8, respectively. Furthermore, both composites presented low Tafel slopes (48–58 mV $dec^{-1}$). Chronoamperometric tests revealed that the as-prepared nanocomposites rendered a significant improvement achieving between 90 and 94% of current retention in tolerance to methanol in comparison with Pt/C, and moderate to good long-term electrochemical stability with current retentions comprised between 68 and 88%. This work reinforces the use of POMs as important electroactive species for the preparation of alternative ORR electrocatalysts, exhibiting good activity, stability and selectivity towards the ORR in the presence of methanol.

**Keywords:** oxygen reduction reaction; electrocatalysis; carbon-based electrocatalyst; polyoxometalates; N-doping

check for updates

**Citation:** Novais, H.C.; Jarrais, B.; Mbomekallé, I.-M.; Teillout, A.-L.; Oliveira, P.d.; Freire, C.; Fernandes, D.M. Hybrids Composed of an Fe-Containing Wells–Dawson Polyoxometalate and Carbon Nanomaterials as Promising Electrocatalysts for the Oxygen Reduction Reaction. *Inorganics* **2023**, *11*, 388. https://doi.org/10.3390/inorganics11100388

Academic Editors: Pavel A. Abramov and Kirill Grzhegorzhevskii

Received: 6 September 2023
Revised: 25 September 2023
Accepted: 26 September 2023
Published: 29 September 2023

**Copyright:** © 2023 by the authors. Licensee MDPI, Basel, Switzerland. This article is an open access article distributed under the terms and conditions of the Creative Commons Attribution (CC BY) license (https://creativecommons.org/licenses/by/4.0/).

## 1. Introduction

The population growth has resulted in a steep rise in energy demand, which has raised concerns about the security of our energy supplies in the midterm future. It is, therefore, of the highest urgency to develop sustainable alternative energy sources and conversion devices in order to reduce carbon emissions [1]. Fuel cells (FCs) present themselves as one of the most promising green options and sustainable technologies available. A key feature of these systems is the oxygen reduction reaction (ORR) that occurs at the cathode and generally exhibits slow kinetics [2–4]. Electrocatalysts (ECs) play a major role in most energy conversion devices, including FCs, because they enhance the selectivity and efficiency of the chemical reactions involved. Thus far, the most effective ECs for ORR, to date, have been derived from noble metals, like platinum and palladium [5]. The latter have several drawbacks, including expensive price, limited availability and a lack of

tolerance towards fuel crossover (such as methanol and CO) [5]. Since the discovery of the ORR in fuel cells, researchers have been working to improve the efficiency and stability of the electrocatalysts used in this process. In recent years, there have been significant advances in the development of ORR electrocatalysts, particularly in the use of iron-based catalysts [6]. Additionally, surface science studies have been conducted to understand better the electronic structure, stability and electrocatalytic properties of various catalysts [7,8]. In addition, computational methods have been developed to aid in the design of solid catalysts, which has opened up new possibilities for ORR electrocatalyst research [9]. Over recent years, several studies have been carried out with the objective of designing high-performance ECs based on earth-abundant elements to overcome the referred limitations associated with Pt- and Pd-based electrocatalysts [2,4,10]. The development of efficient and cost-effective catalysts for the ORR is of critical importance for the widespread adoption of fuel cells. Plus, significant progress has been achieved towards the design of ORR catalysts based on earth-abundant elements [11]. However, despite these advances, the search for efficient and stable ORR catalysts remains a topic of active research. One of the first catalysts tested for the ORR was cobalt phthalocyanine (CoPc) [11]. Jasinski's seminal work published in *Nature* in 1964 demonstrated that CoPc can catalyse ORR in acidic media. This work laid the foundation for the development of metal–phthalocyanine-based catalysts for fuel cells. Currently, the FCs that have received the most attention are proton exchange membrane fuel cells (PEMFCs) [12]. Although these systems are considered the most technologically advanced, they depend on pricey acid membranes and ionomers [13] and on platinum group metal-based electrocatalysts, which are costly, show limited durability and are scarcely available [14]. In order to enhance the electrocatalytic behaviour of the ORR, Pt and Pd have been incorporated with several transition metals, such as Ru [15], Ni [16], Ag [16] or Co [17,18].

Carbon nanomaterials (CMs), including graphene (GF) and carbon nanotubes (CNT), show great promise as efficient ORR electrocatalysts due to their high stability, conductivity, low cost and large surface area [19]. These materials demonstrate an exceptional high chemical and thermal stability, favourable electrical properties, high porosity and a large surface area [20]. Nanotubes and graphene are among the most widely applied materials in the ORR, employed as metal-free ECs in alkaline media and supporting materials for electrocatalysts in hybrid nanocomposites [21,22]. In addition, doping the material with heteroatoms, such as nitrogen, sulphur and phosphorus, could enhance its electrocatalytic activity [21–26]. Regarding nitrogen species, different forms can be incorporated into the graphitic network, including pyridinic, pyrrolic, graphitic (quaternary) and oxidized nitrogen, and these variations can significantly affect the electrocatalytic performance of the material. Artyushkova et al. showed that pyridinic and graphitic (quaternary) nitrogen species can act as highly active sites for the ORR due to their ability to stabilize the adsorption of reaction intermediates [26]. On the other hand, pyrrolic and oxidized nitrogen species have been found to exhibit lower activity for the ORR. Therefore, it is important to carefully consider the type and concentration of nitrogen species when designing doped carbon catalysts for the ORR. Incorporating nitrogen in the $sp^2$ carbon allows for the improvement of the electronic properties of pristine carbons, which gives rise to an enhanced electrocatalytic performance towards the ORR [21,22,27–29]. Over the years, several studies have reported progress in the performance of pyrolyzed catalysts for the ORR [30,31]. In 2009, Lefèvre et al. disclosed the utilisation of polymers as carbon–nitrogen sources for the synthesis of ORR catalysts [32]. The sacrificial support method (SSM) has also been shown to be an effective strategy for the preparation of ORR catalysts [33]. In 2011, Zelenay reported on a significant improvement in the durability of ORR catalysts based on nonprecious metals [34].

Furthermore, it has been proposed that creating composite electrocatalysts, which combine the exceptional properties of carbon nanomaterials with the vast stability and abundant redox characteristics of polyoxometalates (POMs), could be a feasible approach to increase the proficiency of various energy-linked reactions [28,35–38]. The POM used

in this work belongs to the Wells–Dawson family ($[(P_2W_{17}O_{61})Fe^{III}(H_2O)]^{7-}$). The iron-substituted POMs are of particular interest, as they may act either as oxidation or as reduction electrocatalysts [12]. Fe-substituted polyoxometalates (Fe-POMs) have emerged as a promising candidate amidst various catalysts due to their distinctive characteristics. These offer a cost-effective alternative to expensive Pt-based catalysts, making them a potential substitute for the ORR [39]. Moreover, the use of Fe in these catalysts adds to their sustainability. Iron is one of the most abundant elements on Earth, making it a readily available resource. It is also widely recycled, and its extraction and processing require less energy compared to other metals like cobalt [40].

This report details the preparation of composites by incorporating $K_7[P_2W_{17}(FeOH_2)O_{61}]\cdot 20H_2O$, a salt of Wells-Danson POM, onto two distinct nitrogen-doped carbon materials (nitrogen-doped graphene flakes—GF_N8; nitrogen-doped multiwalled carbon nanotubes—MWCNT_N8. The resulting composites were then applied as electrocatalysts for the ORR.

## 2. Experimental Section

*Materials Preparation and Characterisation Methods*

The preparation of the composites and ORR studies' solvents and materials are extensively described in the Supplementary Information (SI). Nitrogen doping of the carbon materials (0.60 g) was achieved with the mechanical ball-milling treatment during 5 h at a constant frequency of 15 vibrations $s^{-1}$ with Retsch MM200 equipment using melamine (0.26 g) as a precursor. Then, the materials that resulted underwent a thermal treatment under a $N_2$ flow (100 $cm^3$ $min^{-1}$) at a rate of 10 °C $min^{-1}$ until reaching the final temperature of 800 °C and kept at these temperature during 1 h; they were then cooled to room temperature under a nitrogen atmosphere and stored in a desiccator [41]. The $P_2W_{17}Fe$@CM composites were then prepared through the immobilization of $P_2W_{17}Fe$ onto previously prepared MWCNT_N8 and GF_N8. The immobilization of the POM was achieved as follows: a 5 mL acetate buffer solution (pH = 4.0) containing 50 mg of $P_2W_{17}Fe$ was added to a 20 mL acetate buffer solution (pH = 4.0) containing 25 mg of CM. The mixture was dispersed for 15 min in an ultrasonic bath and then left to stir for 2 h at 400 rpm. Then, the resulting composites were filtered, washed and left to dry at 60 °C under vacuum overnight. The composites were labelled as $P_2W_{17}Fe$@GF_N8 and $P_2W_{17}Fe$@MWCNT_N8.

Before use in the electrocatalytic studies, the composites prepared were characterized using different techniques: Fourier-transformed infrared spectroscopy (FTIR), scanning electron microscopy (SEM), energy-dispersive X-ray spectroscopy (EDS) and X-ray photoelectron spectroscopy (XPS). The methods and equipment used are detailed in the Supplementary Materials. Electrocatalytic performances towards the ORR were evaluated using a PGSTAT 302N potentiostat (Metrohm Autolab B.V., Utrecht, The Netherlands) controlled with NOVA 2.1 software and using a conventional 3-electrode system. For all details regarding electrodes, electrode conditioning and modification, see the Supplementary Materials.

## 3. Results and Discussion

### *3.1. Materials Characterisation*

All the prepared materials were initially characterized with infrared spectroscopy (Figure 1). The FTIR spectra of the nitrogen-doped carbon materials are shown in Figure S1. The MWCNT_N8 spectrum revealed several vibrational bands at 3436, 2928, 2846, 1641, 1383 and 1124 $cm^{-1}$, but some of these bands appeared quite weak and poorly resolved. This may have arisen from the low loading of the POMs onto the carbon material or their interaction with the graphene and carbon nanotube matrix that hindered their identification. The vibrational bands of the OH groups could be observed at 3436 $cm^{-1}$, and were due to the O-H stretching and bending modes from the adsorbed residual water and hydroxyl groups [42,43]. The C-N stretching vibration band was shown at 1383 $cm^{-1}$ [44,45]. The band at 1124 $cm^{-1}$ was assigned to the phenolic groups' vibration modes [42,46,47]. Lastly, the two bands at 2928 and 2846 $cm^{-1}$ corresponded to the C-H stretching modes, possibly caused by defects in the $sp^2$ hybridised domains. The band located at 1641 $cm^{-1}$ could be

attributed to the C=N and C=O stretching modes of carboxylic acid, carbonyl, ketone and quinone groups [42,44–47]. The vibrational spectra of GF_N8 were similar (Figure S1, black line), showing vibrational bands assigned to O-H stretching and bending modes at ~3410 and 1386 $cm^{-1}$, respectively [42,43]. The observed vibrations at 1630 $cm^{-1}$ represented the C=N and C=O stretching modes, while the phenol groups displayed vibrations at 1387 $cm^{-1}$ and the C-O stretching modes of oxygen groups could be observed at 1142 $cm^{-1}$ [38,42–45]. Finally, the band associated with the C-O-C and the C-O stretching modes and the C-O-H bending mode was observed at 1070 $cm^{-1}$ [42,46,47].

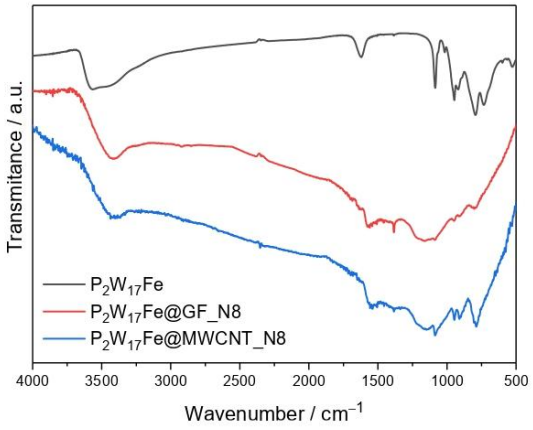



**Figure 1.** FTIR spectra in the 4000–500 $cm^{-1}$ range of $K_7$ [$P_2W_{17}(FeOH_2)O_{61}$] (black) and of the composites $P_2W_{17}$Fe@GF_N8 (red) and $P_2W_{17}$Fe@MWCNT_N8 (blue).

Figure 1 (black) shows the FTIR spectrum of $P_2W_{17}Fe$, where the typical vibrational bands of the POMs could be observed between 1100 and 700 $cm^{-1}$. The band at 1085 $cm^{-1}$ was assigned to the splitting of the $\nu_{as}$P-O stretching vibration and the three vibration bands at 947, 917 and 793 $cm^{-1}$ were assigned to the $\nu_{as}$W=$O_t$, $\nu_{as}$W-$O_b$-W and $\nu_{as}$W-$O_c$-W stretching modes (corner and edge sharing W-O-W), respectively [48,49]. The infrared spectra of the composites $P_2W_{17}$Fe@GF_N8 (red) and $P_2W_{17}$Fe@MWCNT_N8 (blue) showed weaker bands when compared with the spectrum of the POM; still, it was possible to confirm its immobilization onto the carbon materials. Additionally, bands arising from the nitrogen-doped carbon materials were also observed. After the immobilization of $P_2W_{17}Fe$ onto the carbon materials, a small shift in the position of the characteristic bands of the POM to shorter wavelengths could be verified. The reported changes were likely due to reflect the weakening (stretching) of the W-O bonds as a result of possible changes in electron densities (or strengthening of repulsive interactions between oxygen atoms), following the adsorption of the POM on the surfaces of the carbon materials [28,50].

The XPS characterisation of the starting nitrogen-doped materials GF_N8 and MWCNT_N8 was already published by Bruno Jarrais et al. [41]. Still, for a proper comparison with the composite materials, the main peaks were recalled here. Both composites were also characterised with XPS to assess their composition. The relative amounts of the different elements were calculated through the peak areas and are presented in Table 1.

**Table 1.** XPS surface atomic percentages for the pristine carbon materials, the doped carbon materials and the prepared composites.

| Material | XPS Atomic % [a] | | | | | |
|---|---|---|---|---|---|---|
| | C1s | O1s | N1s | P2p | W4f | Fe 2p |
| GF | 96.8 | 3.2 | - | - | - | -- |
| MWCNT | 98.9 | 1.1 | - | - | - | - |
| GF_N8 | 97.0 | 2.0 | 1.0 | - | - | - |
| MWCNT_N8 | 98.0 | 1.0 | 1.0 | - | - | - |
| $P_2W_{17}Fe$@GF_N8 | 92.6 | 6.0 | 0.62 | 0.10 | 0.61 | 0.16 |
| $P_2W_{17}Fe$@MWCNT_N8 | 95.0 | 3.4 | 0.68 | 0.12 | 0.63 | 0.12 |

[a] Calculated based on the areas of the corresponding bands in the high-resolution XPS spectra.

As can be seen in Figures S2a and S3a in the Supplementary Materials file, the presence of nitrogen in the heteroatom-doped carbon materials (GF_N8 and MWCNT_N8) was found, which suggested that the doping procedure was successful. The XPS N1s spectra of the nitrogen-doped carbon materials were deconvoluted into three primary peaks, corresponding to pyridinic N at 398.2 eV, pyrrolic N at 399.6 eV and quaternary N at 401.0 eV [51,52]. For MWCNT_N8, a fourth peak at 404.1 eV was found and attributed to nitrogen oxide and/or nitrate species [51,53]. For both N-doped materials, the relative amounts of N functionalities showed the same pattern, increasing in the same order: (quaternary N) < (pyrrolic N) < (pyridinic N). The C1's high-resolution spectra (Figures S2b and S3b) were fitted with seven peaks: one at 284.6 eV, attributed to the graphitic structure ($sp^2$ and C=C), $sp^3$ hybridized carbon and C-N bonding at 285.2 eV, C-N and C-OH bonding at 285.9 eV, C-O-C groups at 286.9 eV, C=O groups (ketones, quinones and aldehydes) at 288.2 eV, COOH (carboxylic acids and esters) at 289.3 eV and a peak at 291.0 eV, attributed to $\pi$–$\pi^*$ transitions [41,54]. The O1's high-resolution spectra of the GF_N8 (Figure S2c) were fitted with one peak at 531.9 eV, attributed to C=O and COOH. However, MWCNT_N8 (Figure S3c), upon deconvolution, presented two peaks, one at 531.7 eV, assigned to C=O and COOH, and another at 533.1 eV, attributed to HO-C [38,41,55].

The XPS spectra of $P_2W_{17}Fe$@MWCNT_N8 are presented in Figure 2. The N1's XPS spectrum of the $P_2W_{17}Fe$@MWCNT_N8 composite (Figure 2a) had four main peaks at 398.5, 399.8, 401 and 402.2 eV, attributed to pyridinic, pyrrolic, quaternary N and to nitrogen oxide and/or nitrate species, respectively [41,52,56,57]. The XPS fitting of the N1's spectrum for the composite $P_2W_{17}Fe$@GF_N8 (Figure S2a) was very similar to that of GF_N8, presenting peaks at 398.1, 399.8 and 401.1 eV, corresponding to pyridinic, pyrrolic and quaternary N, respectively.

Figure 2b displayed the C1's high-resolution XPS spectrum of the $P_2W_{17}Fe$@MWCNT_N8 composite. It exhibited seven peaks in total, the primary peak at 284.6 eV ($sp^2$ graphitic structure and C=C), a peak at approximately 285.1 eV ($sp^3$ hybridized carbon and C-N bonding), a peak at 285.8 eV (C-N and C-OH bonding), a peak at approximately 286.8 eV (C-O-C groups), a peak at 288.1 eV (C=O groups, such as ketones, quinones and aldehydes), a peak at ~289.2 eV (COOH, such ascarboxylic acids and esters) and a peak at 291.0 eV ($\pi$–$\pi^*$ transitions) [41,54]. The fitting of the C1's XPS spectrum of $P_2W_{17}Fe$@GF_N8 was very similar, as can be seen in Figure S4a of the Supplementary Materials file.

Figure 2c shows the high-resolution O1's spectrum for $P_2W_{17}Fe$@MWCNT_N8, which was deconvoluted into two main peaks: one at 530.7 eV, assigned to oxygen in C=O (ketones, quinones and aldehydes) and COOH (carboxylic acids and esters) groups and oxygen atoms belonging to the POM, and another at 532.6 eV, attributed to O in the HO-C groups (phenols) [38,41,55]. These two peaks were observed for MWCNT_N8 and in the O1's spectrum of $P_2W_{17}Fe$@GF_N8. It is important to refer that, after the immobilisation of the POM on the carbon materials, there was a significant increase (approximately three-fold)

in the percentage of oxygen O1s in the final composites. This was due to a contribution of the POM to the O1's percentages of the composite.

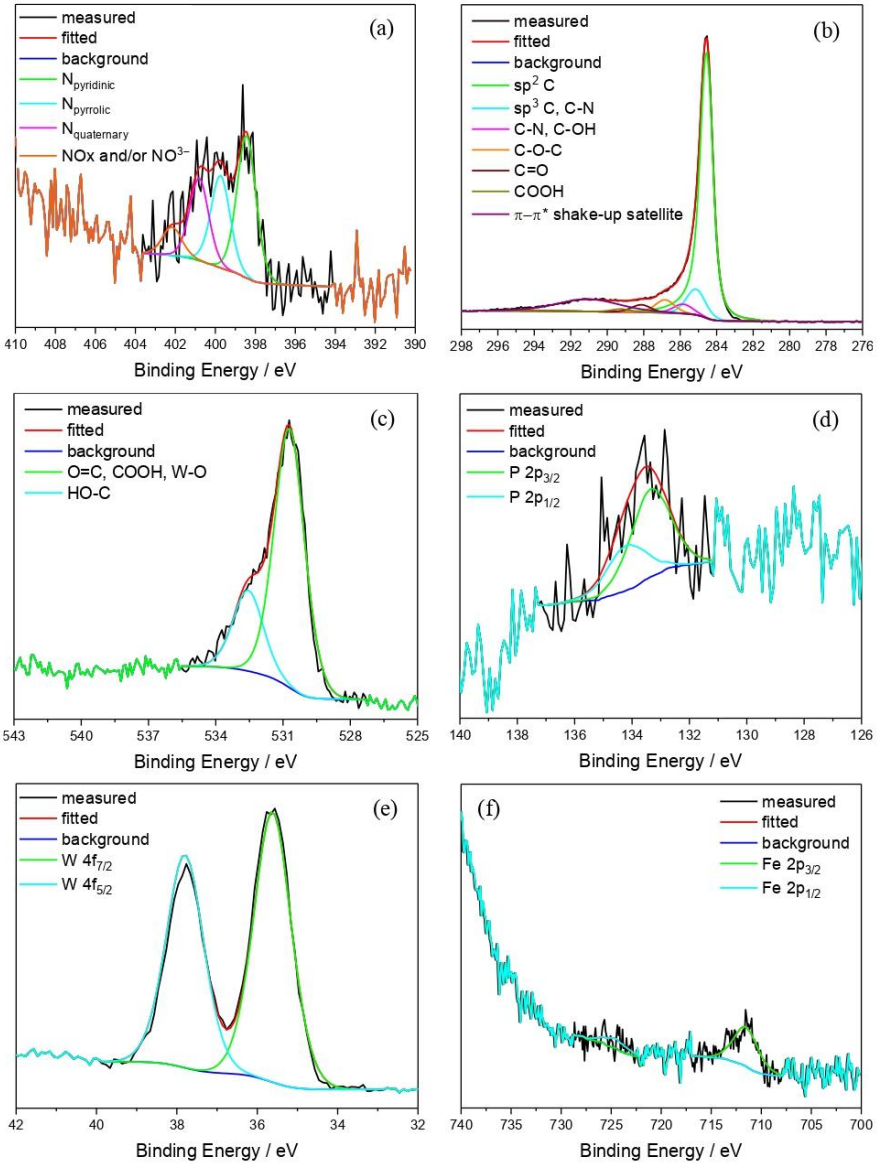
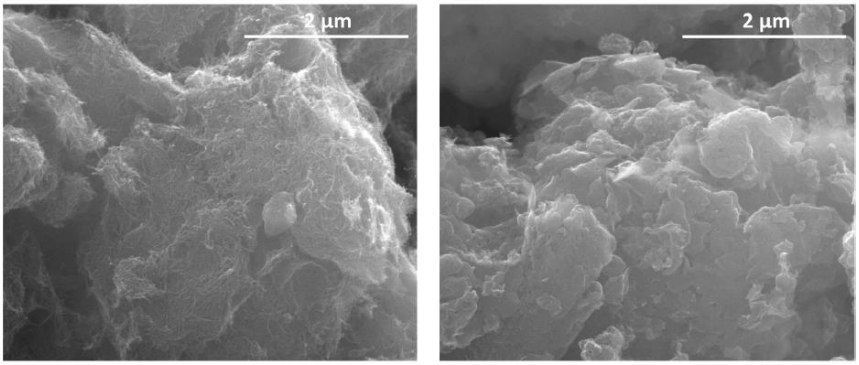



**Figure 2.** XPS deconvoluted spectra of corresponding elements in the $P_2W_{17}Fe$@MWCNT_N8 composite.

The P2p high-resolution spectra of $P_2W_{17}Fe$@CM are shown in Figures 2d and S4d. The observed peaks could be resolved as $2p_{3/2}$ and $2p_{1/2}$ doublets at ~133.4 and ~134.2 eV, respectively [58]. In Figures 2e and S4e, the peaks found in the high-resolution spectra of W4f were attributed to $4f_{7/2}$ (~35.6 eV) and $4f_{5/2}$ (~37.8 eV) due to spin-orbital coupling [58]. Finally, in Figure 2f and Figure S4f, the Fe2p could be divided into Fe $2p_{3/2}$ and Fe $2p_{1/2}$ with the binding energies of ~711.6 eV and ~724.7 eV associated with $Fe^{3+}$, respectively [59,60].

Assuming that XPS is a surface technique that scans sample depths down to 10 nm, this may have prevented us from reaching the expected P/W ratio. Still, the experimental value of the P/W ratio of both composites was very close to the theoretical value, thus, confirming the preservation of the polyoxometalate structure.

The morphology of all the materials underwent an assessment through scanning electron microscopy (SEM), and Figure 3 demonstrates the SEM images for $P_2W_{17}Fe$@MWCNT_N8 (a) and $P_2W_{17}Fe$@GF_N8 (b) at a 50,000× magnification. As can be seen, the morphologies of $P_2W_{17}Fe$@MWCNT_N8 and $P_2W_{17}Fe$@GF_N8 differed significantly. $P_2W_{17}Fe$@MWCNT_N8 exhibited a needle-like structure characteristic of multiwalled carbon nanotubes, whereas $P_2W_{17}Fe$@GF_N8 showed thin and flat flakes of carbon layers. Both composites were decorated with lighter microsized spots that corresponded to $P_2W_{17}Fe$ clusters, which led to this roughened texture. In Figure 3a, the widths of the carbon nanotubes showed clear uniformity with a range of diameters between 8 and 20 nm wide. Figure 3b displays folded graphene sheets and a less rough texture. The SEM images of MWCNT_N8 and GF_N8, exhibiting the same morphological characteristics as described above, are shown in Figure S5.




(**a**) (**b**)

**Figure 3.** SEM images of $P_2W_{17}Fe$@MWCNT_N8 (**a**) and $P_2W_{17}Fe$@GF_N8 (**b**) at 50,000× magnification.

An EDX analysis was conducted to assess the distribution of $P_2W_{17}Fe$ throughout the composites. Figure 4 shows the SEM and EDX elemental mapping images for $P_2W_{17}Fe$@MWCNT_N8, while the images of the $P_2W_{17}Fe$ @GF_N8 composite can be found in Figure S6. The elemental mapping analysis showed, in general, a homogenous distribution of the POM elements (W, P, Fe and O), suggesting that the POM was uniformly immobilized throughout the carbon material. The lighter shades on the EDX elemental mapping images of the W, P, Fe and O elements refer to the POM clusters.

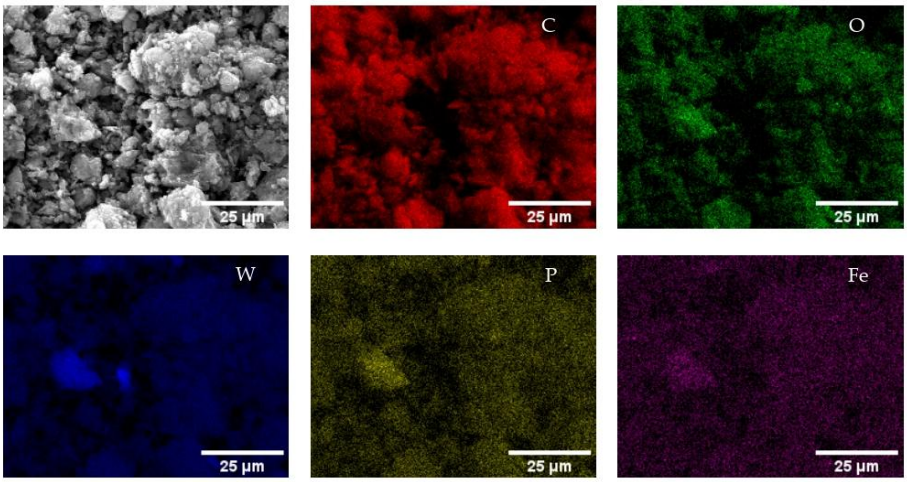



**Figure 4.** SEM and EDX elemental mapping images of $P_2W_{17}Fe$@MWCNT_N8 at 5000× magnification for the elements C (red), O (green), W (blue), P (yellow) and Fe (purple).

*3.2. Electrochemical Performance towards the ORR*

The electrocatalytic activity towards the ORR of both composites was firstly studied with cyclic voltammetry (CV) in $N_2$- and $O_2$-saturated KOH solutions (0.1 mol $dm^{-3}$). The N-doped carbon materials were also evaluated in identical experimental conditions for comparison. Figure 5 presents the CVs in $N_2$- and $O_2$-saturated solutions for the two nanocomposites prepared, where it could be clearly observed that in the $N_2$-saturated electrolyte, no peak was detected, while in the $O_2$-purged electrolyte, both composites exhibited an irreversible peak corresponding to oxygen reduction at $E_{pc}$ = 0.82 and 0.79 V vs. RHE for $P_2W_{17}Fe$@MWCNT_N8 and $P_2W_{17}Fe$@GF_N8, respectively. The electrochemical study of the starting nitrogen-doped materials—GF_N8 and MWCNT_N8—was published by Limani et al. [53], but was replicated here for comparison. MWCNT_N8 and GF_N8 underwent an assessment under identical experimental circumstances (refer to Figure S7a,b within the Supplementary Materials), and they exhibited reduction peaks at $E_{pc}$ = 0.74 and 0.80 V vs. RHE, respectively. The performance of Pt/C (20 wt %) was also tested under the same experimental conditions (Figure S7c), exhibiting the ORR peak at $E_{pc}$ = 0.86 V vs. RHE.

To gain a deeper understanding of the electrocatalytic performance of the $P_2W_{17}Fe$@CM nanocomposites towards the ORR, linear sweep voltammetry (LSV) was carried out at 1600 rpm in an $O_2$-saturated KOH solution (0.1 mol $dm^{-3}$). The LSV curves shown in Figure 6a were obtained by subtracting the blanks (the latter recorded in a $N_2$-saturated KOH solution) from the ones saved in the $O_2$-saturated KOH. Table 2 displays the key ORR parameters acquired—the onset potential ($E_{onset}$), the diffusion-limiting current density values ($j_{L,\ 0.26\ V,\ 1600\ rpm}$), the Tafel slopes (TS) and the number of electrons transferred per oxygen molecule ($n_{O2}$).

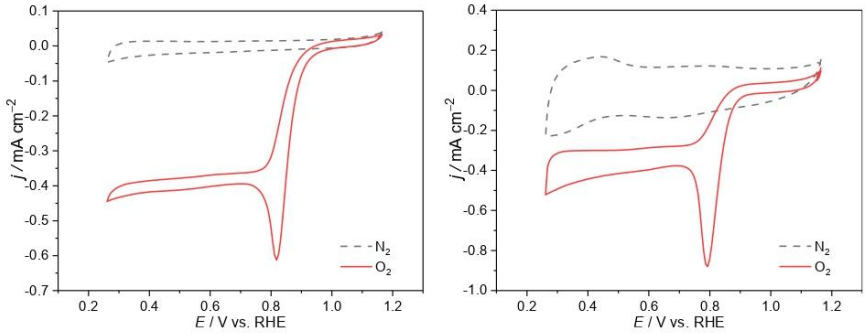



**Figure 5.** CVs of $P_2W_{17}Fe$@MWCNT_N8 (**a**) and $P_2W_{17}Fe$@GF_N8 (**b**) modified electrodes in $N_2$-saturated (dash line) and $O_2$-saturated (full line) 0.1 mol dm$^{-3}$ KOH solution at 0.005 V s$^{-1}$.

**Table 2.** Main ORR parameters obtained from polarisation curves recorded in $O_2$-saturated 0.1 mol dm$^{-3}$ KOH solution for the different materials tested.

| Samples | $E_{onset}$ vs. RHE (V) | $j_L$ (mA cm$^{-2}$) | Tafel Slope (mV dec$^{-1}$) | $n_{O2}$ |
|---|---|---|---|---|
| Pt/C | 0.94 | −4.7 | 89 | 4.0 |
| GF | 0.72 | −2.0 | 63 | 2.4 |
| MWCNT | 0.69 | −2.0 | 54 | 2.1 |
| GF_N8 | 0.83 | −3.3 | 70 | 2.5 |
| MWCNT_N8 | 0.83 | −4.0 | 47 | 3.5 |
| $P_2W_{17}Fe$@GF_N8 | 0.83 | −3.3 | 58 | 3.1 |
| $P_2W_{17}Fe$@MWCNT_N8 | 0.84 | −3.9 | 48 | 3.4 |

The $E_{onset}$ values of the $P_2W_{17}Fe$@CM nanocomposites and N-doped carbon materials were very similar, ranging from 0.83 to 0.84 V vs. RHE. $P_2W_{17}Fe$@MWCNT_N8 had the closest $E_{onset}$ value to the one obtained for Pt/C (0.94 V vs. RHE). Furthermore, all electrocatalysts showed $j_L$ values between −4.0 and −3.3 mA cm$^{-2}$, but did not reach the value obtained for Pt/C (−4.7 mA cm$^{-2}$). Still, these nanocomposites performed well compared to other similar electrocatalysts, as can be observed in Table S2. It is also important to highlight that the ORR electrocatalytic activity of the pristine carbon materials greatly improved after nitrogen doping, which agreed with various studies that reported an enhancement in the ORR electrocatalytic performance after the N-doping of similar carbon materials [53,61]. After N-doping, the $E_{onset}$ potential of MWCNT shifted by 14 mV towards positive values, and the value of $j_L$ doubled, whereas GF presented a positive shift of 11 mV and a $j_L$ 1.3 times higher (in magnitude of $j_L$). As nitrogen atoms have a high electronegativity, there may have contributed to an increased favourable interaction between $O_2$ molecules promoting the ORR mechanism through a rearrangement of the electronic structure of the neighbouring atoms [62].

Based on the XPS results in Table 1, it was not possible to directly link the superior performance of MWCNT_N8 with N%, as both the nitrogen-doped carbon materials had the same total percentage. Therefore, Table S1 presents the relative atomic percentages of nitrogen in the prepared carbon materials. According to the literature, the most active N species for the ORR are the pyridinic and quaternary ones. Pyridinic nitrogen atoms, due to their electron donation to the conjugated p bond of graphene and to the lone pair of electrons, have been identified as electroactive sites for the ORR through their ability to facilitate reductive oxygen adsorption [62,63]. Similarly, quaternary nitrogen is also recognised as an electroactive site for the ORR [63,64]. Even though our previous work [58]

showed that the amount of pyridinic nitrogen is positively correlated with the ORR activity in nitrogen-doped carbon materials, here, it seems that quaternary nitrogen was more relevant. If we compare MWCNT_N8 and GF_N8, the best performing electrocatalysts was the former presenting higher quaternary N (16.9%). The same applied for the composite material.

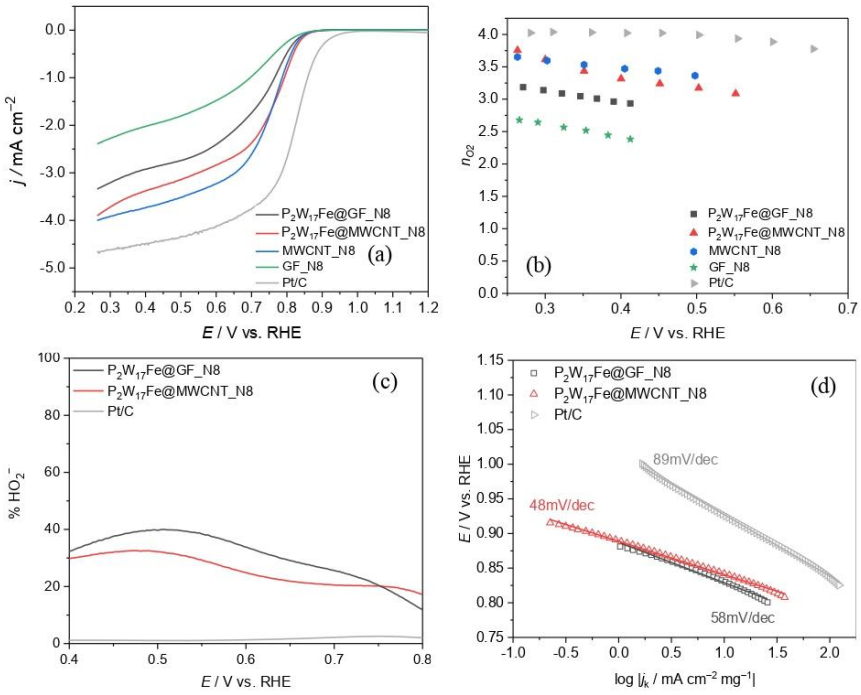



**Figure 6.** ORR LSV curves acquired using an RDE in $O_2$-saturated KOH solution (0.1 mol $dm^{-3}$) at 1600 rpm and 0.005 V $s^{-1}$ of commercial Pt/C (20 wt %), $P_2W_{17}Fe$@CM nanocomposites and nitrogen-doped carbon materials (**a**); $n_{O2}$ at several potential values (**b**); estimated percentage of $HO_2^-$ produced with RRDE for $P_2W_{17}Fe$@CM and Pt/C (20 wt %) in $O_2$-saturated 0.1 mol $dm^{-3}$ KOH solution at 1600 rpm; the disk potential was swept at v = 0.005 V $s^{-1}$ and the ring potential was kept at E = 0.2 V versus Ag/AgCl (**c**); ORR Tafel plots for $P_2W_{17}Fe$@CM obtained from LSV data in Figure 6a, where current densities were normalized to the mass of each EC (**d**).

On the other hand, we had the incorporation of POMs, which are known for their excellent ORR activity. POMs have multiple redox-active sites that can facilitate an electron transfer during the ORR. In previous studies, including ours, POMs have been suggested to interact with nitrogen-doped carbon materials to form composite catalysts that exhibit enhanced ORR activity.

Figure 6b depicts the quantity of electrons transferred per oxygen molecule for the N-doped CM and the respective composites. The results obtained with $P_2W_{17}Fe$@MWCNT_N8 and MWCNT_N8 suggested that the redox processes were very close to being four-electron ones. On the other hand, $P_2W_{17}Fe$@GF_N8 and GF_N8 participated in a mixed redox process involving two and four electrons, as confirmed with the $n_{O2}$ values. Based on these parameters, the behaviour after POM immobilisation appeared to be very similar to the

nitrogen-doped carbon materials. A possible explanation is that the active sites originating from the POM immobilisation did not offset for the eventual loss of N-induced active sites [38,53].

In an alkaline medium, the oxygen reduction reaction can take either an indirect (two-electron) pathway, which involves reducing $O_2$ to $HO_2^-$ and then reducing the intermediate to $H_2O/HO^-$, or a more desirable process, where $O_2$ is directly reduced to $H_2O/HO^-$ [65]. Thus, for a more complete examination of the ECs, it is of utmost importance to estimate the percentage of $HO_2^-{}_2$ produced during the ORR process. The percentage of $HO_2^-$ produced was calculated using Equation (S4) (Supplementary Materials) to various potential values (Figure 6c). The $P_2W_{17}Fe$@MWCNT_N8 composite showed the lowest percentage of $HO_2^-$ produced (33%), which corresponded to the $n_{O2}$ value ($n_{O2}$ = 3.4). For the $P_2W_{17}Fe$@GF_N8 composite, the values of $HO_2^-$ produced (40%) were also in accordance with the $n_{O2}$ value obtained (3.1). Despite the agreement of the results, care should be taken when a direct comparison between these two methods is attempted, as both present limitations [61,66–68]. Firstly, the oxidation process of hydrogen peroxide on the platinum electrocatalyst was not a mass-transfer-limited process. Secondly, as can be seen in the SEM images, these prepared electrocatalysts presented a rough structure of the support material and a heterogeneity of clusters of the immobilised POM. This may have altered the electrode geometry and introduced turbulence in the electrolyte flow, resulting in approximate $n_{O2}$ measurements that may not accurately portray the true electrocatalytic performance of the ORR [53].

In order to obtain more information about the kinetics of the reaction, we extracted the Tafel plots for the prepared nanocomposites and the Pt/C reference from the LSV curves in $O_2$-saturated KOH at 1600 rpm. These plots are presented in Figure 6d. The nanocomposite $P_2W_{17}Fe$@GF_N8 had a slightly higher Tafel slope value (58 mV $dec^{-1}$) when compared with $P_2W_{17}Fe$@MWCNT_N8 (48 mV $dec^{-1}$), but both nanocomposites showed a lower Tafel slope compared with Pt/C (89 mV $dec^{-1}$). These results indicated that oxygen molecules were readily adsorbed and activated on the surface of these materials. In general, the ORR process can follow different mechanisms in a high-pH environment. One is the well-known electrocatalytic inner-sphere electron transfer mechanism, where molecular $O_2$ undergoes direct chemisorption on the catalyst site, leading to a direct/series $4e^-$ pathway without the desorption of reaction intermediates (such as peroxide) from the surface [69–71]. Normally, metal-containing materials follow a dissociative four-electron pathway, facilitated by their excellent $O_2$ adsorption ability. This process involves the initial adsorption of $O_2$, followed by breakage of the O-O bond, forming adsorbed O* species ($O_2 + 2^* \rightarrow 2O^*$, where $^*$ denotes a surface catalytic site). The species then gains two electrons and two protons to produce the final product OH- ($2O^* + 2e^- + 2H_2O \rightarrow 2OH^* + 2OH^-$; $2OH^* + 2e^- \rightarrow 2OH^- + 2^*$) [72].

Our Tafel slope values suggested that for $P_2W_{17}Fe$@CM, the global reaction rate was ruled by the conversion of a species $MOO^-$ to MOOH (where M denotes an empty site on the electrocatalyst surface) or by the first discharge step [38,53].

The proportional relationship between the double-layer capacitance ($C_{dl}$) and the electrochemically active surface areas (ECSAs), as well as the similarity between the electrocatalysts used in this study, allowed for a direct comparison of the obtained $C_{dl}$ values of the composites [73–76]. By conducting CV measurements at varying scan rates, it was possible to estimate $C_{dl}$ values from the slopes of the linear fittings of the CV current densities (measured at the same potential of 1.13 V vs. RHE in a nonfaradaic region), obtained at different scan rates for the composites and their nitrogen-doped carbon materials (see experimental details in Supplementary Materials file Section S1.4 and Figures S13 and S14). Still, the $C_{dl}$ should be interpreted as an estimation of the number of accessible electrocatalytically active sites for a specific electrocatalyst [77]. Table 3 clearly shows a notable increase in the count of active sites, following the immobilisation of the POM ($P_2W_{17}Fe$) on both nitrogen-doped carbon materials. This increase was higher for the $P_2W_{17}Fe$@MWCNT_N8 composite, with a composite/carbon support $C_{dl}$ ratio of 3.98 vs. 1.39 for $P_2W_{17}Fe$@GF_N8.

**Table 3.** Electrocatalytically active surface area (ECSA) values of the carbon supports and their corresponding POM-based composites.

| CM Support | $C_{dl}$ (mF cm$^{-2}$) | Composite | $C_{dl}$ (mF cm$^{-2}$) | Composite/Carbon Support $C_{dl}$ Ratio |
|---|---|---|---|---|
| GF_N8 | 0.0228 | $P_2W_{17}Fe$@GF_N8 | 0.0317 | 1.39 |
| MWCNT_N8 | 0.0203 | $P_2W_{17}Fe$@MWCNT_N8 | 0.0808 | 3.98 |

When evaluating the potential of an electrocatalyst for the ORR, it is of utmost importance to assess its stability. This was carried out with chronoamperometry (CA) at $E$ = 0.46 V vs. RHE for 36,000 s at 1600 rpm in an oxygen-saturated alkaline electrolyte (Figure 7a). The nanocomposite $P_2W_{17}Fe$@MWCNT_N8 showed superior stability with an 88% current retention, surpassing the results achieved for Pt/C (86%), while $P_2W_{17}Fe$@GF_N8 showed a lower current retention value (68%). The increased current retention observed for $P_2W_{17}Fe$@MWCNT_N8 could be attributed to the stronger interaction between the POM and its highly ordered nitrogen-doped MWCNT. Still, the good stability of the composites was mainly due to the trapping of the POM particles in the nanonetworks of the carbon materials, avoiding (or at least limiting) their migration, aggregation and leaching towards the electrolyte, not adversely affecting the corresponding support stabilities. In addition, the high degree of graphitisation and/or ordered wall structure of the carbon materials could reduce a possible degradation of the composite, which could be another cause of the increased durability [78–80].

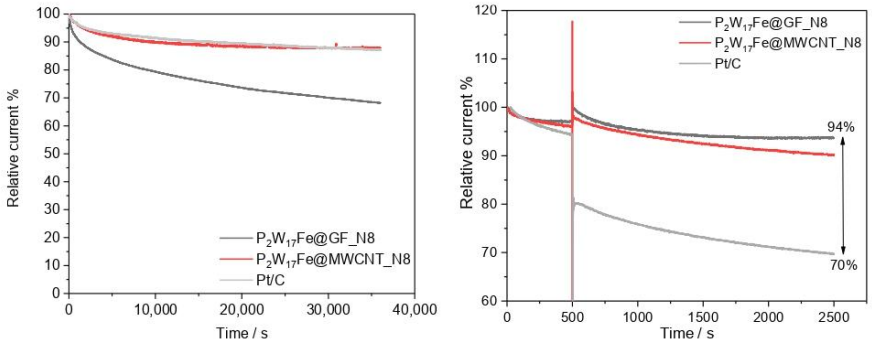



**Figure 7.** Chronoamperometric response of the ECs at 1600 rpm in 0.1 mol dm$^{-3}$ $O_2$-saturated KOH at E = 0.46 V vs. RHE for 36,000 s (**a**) and E = 0.46 V vs. RHE with the addition of 0.5 mol dm$^{-3}$ methanol after ≈ 500 s (**b**).

Methanol is an excellent hydrogen carrier fuel, and can also be produced from sustainable and green pathways to allow it to be a carrier of low carbon and potentially carbon-neutral hydrogen [81,82]. As such, the study of the methanol tolerance of electrocatalysts in methanol fuel cells is extremely important, since the methanol crossover from the anode to the cathode can lead to a significantly decrease in the cathodic performance, if the electrocatalysts is sensitive to it [83]. The Pt-based materials are handicapped by their high sensitivity to the methanol oxidation reaction, despite their better performance in alkaline medium compared most of the studied electrocatalysts [84]. This situation affected their performance in the ORR, lowering the current density obtained. Thus, the tolerance of methanol was assessed through chronoamperometry in $O_2$-saturated 0.1 mol dm$^{-3}$ KOH in the presence of methanol (0.5 mol dm$^{-3}$) for the Pt/C and $P_2W_{17}Fe$@CM composites during

2500 s (Figure 7b). Methanol was added 500 s after the beginning of the CA. The Pt/C electrocatalyst maintained only ~70% of its initial current density, whereas the composites retained between ~90 and 94%, being one of the advantages of using this type of material.

## 4. Conclusions

In this work, it was possible to successfully immobilise the Wells–Dawson POM $[P_2W_{17}(FeOH_2)O_{61}]^{7-}$ onto graphene flakes and carbon nanotubes doped with nitrogen ($P_2W_{17}$Fe@GF_N8 and $P_2W_{17}$Fe@MWCNT_N8) without the need for linker molecules. It was proven that both composites were successfully synthesised using several characterisation techniques, such as FTIR, XPS and SEM analysis. The prepared composites showed intrinsic electroactivity towards the ORR in an alkaline medium, displaying onset potential values varying between 0.83 and 0.84 V vs. RHE. Furthermore, the nanocomposites demonstrated low Tafel slopes (47–70 mV $dec^{-1}$) and commendable $j_L$ values (−3.3–−4.0 mA $cm^{-2}$). The analysis of the Koutecky−Levich plots revealed that the ORR process occurred through a mixed electron process for $P_2W_{17}$Fe@GF_N8 and a process involving four electrons for $P_2W_{17}$Fe@MWCNT_N8, also confirmed with the results of the $\%HO_2^-$ production. The composite $P_2W_{17}$Fe@MWCNT_N8 demonstrated a sturdy electrocatalytic performance over 36,000 s, revealing a high retention value of 88%—surpassing the commercial Pt/C, which achieved 86%. Additionally, both composites had an excellent methanol tolerance (90–94%), evincing high selectivity for the OR and, thus, overcoming a significant limitation of the Pt/C electrocatalyst. This study was a significant stride towards creating new, inexpensive and sturdy electrocatalysts that are free of noble metals, with immense potential for energy-related reactions.

**Supplementary Materials:** The following supporting information can be downloaded at: https://www.mdpi.com/article/10.3390/inorganics11100388/s1, Figure S1: FTIR spectra in the 4000–500 $cm^{-1}$ range of the nitrogen-doped carbon materials GF_N8 (black) and MWCNT_N8 (red), Figure S2: XPS deconvoluted spectra of corresponding elements of GF_N8, Figure S3: XPS deconvoluted spectra of corresponding elements of MWCNT_N8, Figure S4: XPS deconvoluted spectra of corresponding elements in the $P_2W_{17}$Fe@GF_N8 composite, Figure S5: SEM images of MWCNT_N8 (a) and GF_N8 (b) at 50,000× magnification, Figure S6: SEM and EDX elemental mapping images of $P_2W_{17}$Fe @GF_N8 at 5000× magnification for the elements C (red), O (green), W (blue), P (yellow) and Fe (purple), Figure S7: CVs of MWCNT_N8 (a), GF_N8 (b) and Pt/C (20 wt. %) (c) modified electrodes in $N_2$-saturated (dash line) and $O_2$-saturated (full line) 0.1 mol $dm^{-3}$ KOH solution at 0.005 V, Figure S8: ORR LSV polarization curves for Pt/C (20 wt. %) at different rotation rates in $O_2$-saturated 0.1 mol $dm^{-3}$ KOH solution at 0.005 V $s^{-1}$ (a), and the corresponding Koutecky–Levich (K-L) plots (b), Figure S9: ORR LSV polarization curves for MWCNT_N8 at different rotation rates in $O_2$-saturated 0.1 mol $dm^{-3}$ KOH solution at 0.005 V $s^{-1}$ (a) and the corresponding Koutecky–Levich (K-L) plots (b), Figure S10: ORR polarization curves for GF_N8 at different rotation rates in $O_2$-saturated 0.1 mol $dm^{-3}$ KOH solution at 0.005 V $s^{-1}$ (a) and the corresponding Koutecky–Levich (K-L) plots (b), Figure S11: ORR LSV polarization curves for $P_2W_{17}$Fe@MWCNT_N8 at different rotation rates in $O_2$-saturated 0.1 mol $dm^{-3}$ KOH solution at 0.005 V $s^{-1}$ (a) and the corresponding Koutecky–Levich (K-L) plots (b), Figure S12: ORR LSV polarization curves for $P_2W_{17}$Fe@GF_N8 at different rotation rates in $O_2$-saturated 0.1 mol $dm^{-3}$ KOH solution at 0.005 V $s^{-1}$ (a) and the corresponding Koutecky–Levich (K-L) plots (b), Figure S13: CVs at different scan rates for GF_N8 (a), MWCNT_N8 (b), P2W17Fe@GF_N8 (c), $P_2W_{17}$Fe@MWCNT_N8 (d) and Pt/C (e) in $N_2$-saturated KOH (0.1 M), Figure S14: current density-scan rate linear fitting plots for all materials. Numeric values correspond to the double-layer capacitances ($C_{dl}$) for each material, Table S1: relative atomic percentages of nitrogen presented in the XPS high-resolution N1s spectra of the prepared carbon materials, Table S2: ORR performance of transition metal carbon hybrid electrocatalysts obtained from the literature. References [38,45,48,53,58,85–97] cited in Supplementary Materials.

**Author Contributions:** Conceptualization, D.M.F. and P.d.O.; methodology, H.C.N., B.J., I.-M.M. and A.-L.T.; validation, D.M.F.; writing—original draft preparation, H.C.N.; writing—review and editing, D.M.F. and P.d.O.; supervision, D.M.F. and C.F.; funding acquisition, C.F. All authors have read and agreed to the published version of the manuscript.

**Funding:** This work was financially supported by project UNIRCELL POCI-01-0145-FEDER-16422 and funded by FEEI through Programa operacional Competitividade e Internacionalização-COMPETE2020 and by national funds through FCT—Fundação para a Ciência e a Tecnologia, I.P.

**Data Availability Statement:** The data presented in this study are available on request from the corresponding author. The data are not publicly available due to institutions policies.

**Acknowledgments:** Thanks are due to the PT national funds FCT/MCTES through the projects UIDB/50006/2020 and UIDP/50006/2020, as well as to Campus France—project PHC Pessoa 42341RM (O2@nanoCPOM). Thanks are also due to the FCT project FOAM4ENER PTDC/QUI-ELT/28299/2017. H.C.N. thanks the FCT through the ChemMat program for his PhD grant PD/BD/143095/2018. D.M.F. thanks FCT/MCTES for funding through the Individual Call to Scientific Employment Stimulus (2021.00771.CEECIND/CP1662/CT0007). I.-M M., A.-L.T. and P.d.O. thank the CNRS (namely, its IEA programme) and the Université Paris-Saclay for financial support.

**Conflicts of Interest:** The authors declare that they have no conflict of interest.

## References

1. Perera, F. Pollution from Fossil-Fuel Combustion is the Leading Environmental Threat to Global Pediatric Health and Equity: Solutions Exist. *Int. J. Environ. Res. Public Health* **2018**, *15*, 16. [CrossRef] [PubMed]
2. Nie, Y.; Li, L.; Wei, Z. Recent advancements in Pt and Pt-free catalysts for oxygen reduction reaction. *Chem. Soc. Rev.* **2015**, *44*, 2168–2201. [CrossRef] [PubMed]
3. Stacy, J.; Regmi, Y.N.; Leonard, B.; Fan, M. The recent progress and future of oxygen reduction reaction catalysis: A review. *Renew. Sustain. Energy Rev.* **2017**, *69*, 401–414. [CrossRef]
4. Xia, W.; Mahmood, A.; Liang, Z.; Zou, R.; Guo, S. Earth-Abundant Nanomaterials for Oxygen Reduction. *Angew. Chem. Int. Ed.* **2016**, *55*, 2650–2676. [CrossRef]
5. Kuang, M.; Zheng, G. Nanostructured Bifunctional Redox Electrocatalysts. *Small* **2016**, *12*, 5656–5675. [CrossRef]
6. Parvez, K.; Yang, S.; Hernandez, Y.; Winter, A.; Turchanin, A.; Feng, X.; Müllen, K. Nitrogen-Doped Graphene and Its Iron-Based Composite As Efficient Electrocatalysts for Oxygen Reduction Reaction. *ACS Nano* **2012**, *6*, 9541–9550. [CrossRef]
7. Stamenkovic, V.R.; Mun, B.S.; Mayrhofer, K.J.J.; Ross, P.N.; Markovic, N.M. Effect of Surface Composition on Electronic Structure, Stability, and Electrocatalytic Properties of Pt-Transition Metal Alloys: Pt-Skin versus Pt-Skeleton Surfaces. *J. Am. Chem. Soc.* **2006**, *128*, 8813–8819. [CrossRef]
8. Marković, N.M.; Ross, P.N. Surface science studies of model fuel cell electrocatalysts. *Surf. Sci. Rep.* **2002**, *45*, 117–229. [CrossRef]
9. Nørskov, J.K.; Bligaard, T.; Rossmeisl, J.; Christensen, C.H. Towards the computational design of solid catalysts. *Nat. Chem.* **2009**, *1*, 37–46. [CrossRef]
10. Cao, R.; Lee, J.-S.; Liu, M.; Cho, J. Recent Progress in Non-Precious Catalysts for Metal-Air Batteries. *Adv. Energy Mater.* **2012**, *2*, 816–829. [CrossRef]
11. Jasinski, R. A New Fuel Cell Cathode Catalyst. *Nature* **1964**, *201*, 1212–1213. [CrossRef]
12. Kuo, M.-C.; Stanis, R.J.; Ferrell, J.R., III; Turner, J.A.; Herring, A.M. Electrocatalyst materials for fuel cells based on the polyoxometalates—$K_7$ or $H_7[(P_2W_{17}O_{61})Fe^{III}(H_2O)]$ and $Na_{12}$ or $H_{12}[(P_2W_{15}O_{56})_2Fe^{III}{}_4(H_2O)_2]$. *Electrochim. Acta* **2007**, *52*, 2051–2061. [CrossRef]
13. Samsudin, A.M.; Bodner, M.; Hacker, V. A Brief Review of Poly(Vinyl Alcohol)-Based Anion Exchange Membranes for Alkaline Fuel Cells. *Polymers* **2022**, *14*, 3565. [CrossRef]
14. Zhang, X.; Li, H.; Yang, J.; Lei, Y.; Wang, C.; Wang, J.; Tang, Y.; Mao, Z. Recent advances in Pt-based electrocatalysts for PEMFCs. *RSC Adv.* **2021**, *11*, 13316–13328. [CrossRef] [PubMed]
15. Yu, E.H.; Scott, K.; Reeve, R.W. Electrochemical Reduction of Oxygen on Carbon Supported Pt and Pt/Ru Fuel Cell Electrodes in Alkaline Solutions. *Fuel Cells* **2003**, *3*, 169–176. [CrossRef]
16. Yin, H.; Liu, S.; Zhang, C.; Bao, J.; Zheng, Y.; Han, M.; Dai, Z. Well-Coupled Graphene and Pd-Based Bimetallic Nanocrystals Nanocomposites for Electrocatalytic Oxygen Reduction Reaction. *ACS Appl. Mater. Interfaces* **2014**, *6*, 2086–2094. [CrossRef]
17. Lima, F.H.B.; Ticianelli, E.A. Oxygen electrocatalysis on ultra-thin porous coating rotating ring/disk platinum and platinum–cobalt electrodes in alkaline media. *Electrochim. Acta* **2004**, *49*, 4091–4099. [CrossRef]
18. Todoroki, N.; Wadayama, T. Oxygen Reduction Reaction Activity for Cobalt-Deposited Pt(111) Model Catalyst Surfaces in Alkaline Solution. *Denki Kagaku Oyobi Kōgyō Butsuri Kagaku* **2018**, *86*, 243–245. [CrossRef]
19. Wohlgemuth, S.-A.; White, R.J.; Willinger, M.-G.; Titirici, M.-M.; Antonietti, M. A one-pot hydrothermal synthesis of sulfur and nitrogen doped carbon aerogels with enhanced electrocatalytic activity in the oxygen reduction reaction. *Green Chem.* **2012**, *14*, 1515–1523. [CrossRef]
20. Zheng, Y.; Jiao, Y.; Jaroniec, M.; Jin, Y.; Qiao, S.Z. Nanostructured Metal-Free Electrochemical Catalysts for Highly Efficient Oxygen Reduction. *Small* **2012**, *8*, 3550–3566. [CrossRef]
21. Qu, L.; Liu, Y.; Baek, J.-B.; Dai, L. Nitrogen-Doped Graphene as Efficient Metal-Free Electrocatalyst for Oxygen Reduction in Fuel Cells. *ACS Nano* **2010**, *4*, 1321–1326. [CrossRef] [PubMed]

22. Chen, Z.; Higgins, D.; Chen, Z. Nitrogen doped carbon nanotubes and their impact on the oxygen reduction reaction in fuel cells. *Carbon* **2010**, *48*, 3057–3065. [CrossRef]
23. Debe, M.K. Electrocatalyst approaches and challenges for automotive fuel cells. *Nature* **2012**, *486*, 43–51. [CrossRef] [PubMed]
24. Steele, B.C.H.; Heinzel, A. Materials for fuel-cell technologies. *Nature* **2001**, *414*, 345–352. [CrossRef] [PubMed]
25. Gasteiger, H.A.; Kocha, S.S.; Sompalli, B.; Wagner, F.T. Activity benchmarks and requirements for Pt, Pt-alloy, and non-Pt oxygen reduction catalysts for PEMFCs. *Appl. Catal. B Environ.* **2005**, *56*, 9–35. [CrossRef]
26. Wang, H.; Grabstanowicz, L.R.; Barkholtz, H.M.; Rebollar, D.; Kaiser, Z.B.; Zhao, D.; Chen, B.-H.; Liu, D.-J. Impacts of Imidazolate Ligand on Performance of Zeolitic-Imidazolate Framework-Derived Oxygen Reduction Catalysts. *ACS Energy Lett.* **2019**, *4*, 2500–2507. [CrossRef]
27. Wang, X.; Fan, X.; Lin, H.; Fu, H.; Wang, T.; Zheng, J.; Li, X. An efficient Co–N–C oxygen reduction catalyst with highly dispersed Co sites derived from a ZnCo bimetallic zeolitic imidazolate framework. *RSC Adv.* **2016**, *6*, 37965–37973. [CrossRef]
28. Freire, C.; Fernandes, D.M.; Nunes, M.; Abdelkader, V.K. POM & MOF-based Electrocatalysts for Energy-Related Reactions. *ChemCatChem* **2018**, *10*, 1703–1730. [CrossRef]
29. Vikkisk, M.; Kruusenberg, I.; Ratso, S.; Joost, U.; Shulga, E.; Kink, I.; Rauwel, P.; Tammeveski, K. Enhanced electrocatalytic activity of nitrogen-doped multi-walled carbon nanotubes towards the oxygen reduction reaction in alkaline media. *RSC Adv.* **2015**, *5*, 59495–59505. [CrossRef]
30. Jahnke, H.; Schönborn, M.; Zimmermann, G. Organic dyestuffs as catalysts for fuel cells. *Top. Curr. Chem.* **1976**, *61*, 133–181. [CrossRef]
31. Gupta, S.; Tryk, D.; Bae, I.; Aldred, W.; Yeager, E. Heat-Treated Polyacrylonitrile-Based Catalysts for Oxygen Electroreduction. *J. Appl. Electrochem.* **1989**, *19*, 19–27. [CrossRef]
32. Lefèvre, M.; Proietti, E.; Jaouen, F.; Dodelet, J.P. Iron-based catalysts with improved oxygen reduction activity in polymer electrolyte fuel cells. *Science* **2009**, *324*, 71–74. [CrossRef] [PubMed]
33. Pylypenko, S.; Mukherjee, S.; Olson, T.S.; Atanassov, P. Non-platinum oxygen reduction electrocatalysts based on pyrolyzed transition metal macrocycles. *Electrochim. Acta* **2008**, *53*, 7875–7883. [CrossRef]
34. Wu, G.; More, K.L.; Johnston, C.M.; Zelenay, P. High-performance electrocatalysts for oxygen reduction derived from polyaniline, iron, and cobalt. *Science* **2011**, *332*, 443–447. [CrossRef] [PubMed]
35. Lin, H.; Wang, J.-W.; Guo, X.-W.; Yao, S.; Liu, M.; Zhang, Z.-M.; Lu, T.-B. Phosphorized polyoxometalate-etched iron-hydroxide porous nanotubes for efficient electrocatalytic oxygen evolution. *J. Mater. Chem. A* **2018**, *6*, 24479–24485. [CrossRef]
36. Zhang, S.; Oms, O.; Hao, L.; Liu, R.; Wang, M.; Zhang, Y.; He, H.-Y.; Dolbecq, A.; Marrot, J.; Keita, B.; et al. High Oxygen Reduction Reaction Performances of Cathode Materials Combining Polyoxometalates, Coordination Complexes, and Carboneous Supports. *ACS Appl. Mater. Interfaces* **2017**, *9*, 38486–38498. [CrossRef]
37. Fernandes, D.M.; Araújo, M.P.; Haider, A.; Mougharbel, A.S.; Fernandes, A.J.S.; Kortz, U.; Freire, C. Polyoxometalate-graphene Electrocatalysts for the Hydrogen Evolution Reaction. *ChemElectroChem* **2018**, *5*, 273–283. [CrossRef]
38. Fernandes, D.M.; Novais, H.C.; Bacsa, R.; Serp, P.; Bachiller-Baeza, B.; Rodríguez-Ramos, I.; Guerrero-Ruiz, A.; Freire, C. Polyoxotungstate@Carbon Nanocomposites As Oxygen Reduction Reaction (ORR) Electrocatalysts. *Langmuir* **2018**, *34*, 6376–6387. [CrossRef]
39. He, S.; Liu, Q.; Wang, X. Polyoxometalate-based materials: Quasi-homogeneous single-atom catalysts with atomic-precision structures. *J. Mater. Chem. A* **2022**, *10*, 5758–5770. [CrossRef]
40. Shen, H.; Thomas, T.; Rasaki, S.A.; Saad, A.; Hu, C.; Wang, J.; Yang, M. Oxygen Reduction Reactions of Fe–N–C Catalysts: Current Status and the Way Forward. *Electrochem. Energy Rev.* **2019**, *2*, 252–276. [CrossRef]
41. Jarrais, B.; Guedes, A.; Freire, C. Heteroatom-Doped Carbon Nanomaterials as Metal-Free Catalysts for the Reduction of 4-Nitrophenol. *ChemistrySelect* **2018**, *3*, 1737–1748. [CrossRef]
42. Navaee, A.; Salimi, A.; Soltanian, S.; Servati, P. Facile one-pot synthesis of platinum nanoparticles decorated nitrogen-graphene with high electrocatalytic performance for oxygen reduction and anodic fuels oxidation. *J. Power Sources* **2015**, *277*, 268–276. [CrossRef]
43. Olalde, B.; Aizpurua, J.M.; García, A.; Bustero, I.; Obieta, I.; Jurado, M.J. Single-Walled Carbon Nanotubes and Multiwalled Carbon Nanotubes Functionalized with Poly(l-lactic acid): A Comparative Study. *J. Phys. Chem. C* **2008**, *112*, 10663–10667. [CrossRef]
44. Fernandes, D.M.; Freire, C. Carbon Nanomaterial–Phosphomolybdate Composites for Oxidative Electrocatalysis. *ChemElectroChem* **2015**, *2*, 269–279. [CrossRef]
45. Daems, N.; Sheng, X.; Vankelecom, I.F.J.; Pescarmona, P.P. Metal-free doped carbon materials as electrocatalysts for the oxygen reduction reaction. *J. Mater. Chem. A* **2014**, *2*, 4085–4110. [CrossRef]
46. Lee, D.W.; De Los Santos, V.L.; Seo, J.W.; Felix, L.L.; Bustamante, D.A.; Cole, J.M.; Barnes, C.H.W. The Structure of Graphite Oxide: Investigation of Its Surface Chemical Groups. *J. Phys. Chem. B* **2010**, *114*, 5723–5728. [CrossRef]
47. Kumarasinghe, A.R.; Samaranayake, L.; Bondino, F.; Magnano, E.; Kottegoda, N.; Carlino, E.; Ratnayake, U.N.; de Alwis, A.A.P.; Karunaratne, V.; Amaratunga, G.A.J. Self-Assembled Multilayer Graphene Oxide Membrane and Carbon Nanotubes Synthesized Using a Rare Form of Natural Graphite. *J. Phys. Chem. C* **2013**, *117*, 9507–9519. [CrossRef]
48. Lyon, D.K.; Miller, W.K.; Novet, T.; Domaille, P.J.; Evitt, E.; Johnson, D.C.; Finke, R.G. Highly oxidation resistant inorganic-porphyrin analog polyoxometalate oxidation catalysts. 1. The synthesis and characterization of aqueous-soluble potassium salts of $\alpha_2$-$P_2W_{17}O_{61}(M^{n+}{\cdot}OH_2)^{(n-10)}$ and organic solvent soluble tetra-n-butylammonium salts of $\alpha_2$-$P_2W_{17}O_{61}(M^{n+}{\cdot}Br)^{(n-11)}$ (M = $Mn^{3+}$, $Fe^{3+}$, $Co^{2+}$, $Ni^{2+}$, $Cu^{2+}$). *J. Am. Chem. Soc.* **1991**, *113*, 7209–7221. [CrossRef]

49. Amiri, A.; Saadati-Moshtaghin, H.R.; Zonoz, F.M.; Targhoo, A. Preparation and characterization of magnetic Wells–Dawson heteropoly acid nanoparticles for magnetic solid-phase extraction of aromatic amines in water samples. *J. Chromatogr. A* **2017**, *1483*, 64–70. [CrossRef]
50. Aricò, A.S.; Bruce, P.; Scrosati, B.; Tarascon, J.-M.; van Schalkwijk, W. Nanostructured materials for advanced energy conversion and storage devices. *Nat. Mater.* **2005**, *4*, 366–377. [CrossRef]
51. Huang, M.-C.; Teng, H. Nitrogen-containing carbons from phenol–formaldehyde resins and their catalytic activity in NO reduction with NH3. *Carbon* **2003**, *41*, 951–957. [CrossRef]
52. Artyushkova, K.; Serov, A.; Rojas-Carbonell, S.; Atanassov, P. Chemistry of Multitudinous Active Sites for Oxygen Reduction Reaction in Transition Metal–Nitrogen–Carbon Electrocatalysts. *J. Phys. Chem. C* **2015**, *119*, 25917–25928. [CrossRef]
53. Limani, N.; Marques, I.S.; Jarrais, B.; Fernandes, A.J.S.; Freire, C.; Fernandes, D.M. Cobalt Phosphotungstate-Based Composites as Bifunctional Electrocatalysts for Oxygen Reactions. *Catalysts* **2022**, *12*, 357. [CrossRef]
54. Estrade-Szwarckopf, H. XPS photoemission in carbonaceous materials: A "defect" peak beside the graphitic asymmetric peak. *Carbon* **2004**, *42*, 1713–1721. [CrossRef]
55. Lipińska, M.E.; Rebelo, S.L.H.; Pereira, M.F.R.; Gomes, J.A.N.F.; Freire, C.; Figueiredo, J.L. New insights into the functionalization of multi-walled carbon nanotubes with aniline derivatives. *Carbon* **2012**, *50*, 3280–3294. [CrossRef]
56. Ai, W.; Luo, Z.; Jiang, J.; Zhu, J.; Du, Z.; Fan, Z.; Xie, L.; Zhang, H.; Huang, W.; Yu, T. Nitrogen and Sulfur Codoped Graphene: Multifunctional Electrode Materials for High-Performance Li-Ion Batteries and Oxygen Reduction Reaction. *Adv. Mater.* **2014**, *26*, 6186–6192. [CrossRef]
57. Liu, Y.; Qiao, Y.; Wei, G.; Li, S.; Lu, Z.; Wang, X.; Lou, X. Sodium storage mechanism of N, S co-doped nanoporous carbon: Experimental design and theoretical evaluation. *Energy Storage Mater.* **2018**, *11*, 274–281. [CrossRef]
58. Novais, H.C.; Jarrais, B.; Haider, A.; Kortz, U.; Guerrero-Ruiz, A.; Rodríguez-Ramos, I.; Freire, C.; Fernandes, D.M. Electrocatalytic Oxygen Reduction Reaction on 48-Tungsto-8-Phosphate Wheel Anchored on Carbon Nanomaterials. *Electrocatalysis* **2022**, *14*, 294–305. [CrossRef]
59. Imar, S.; Yaqub, M.; Maccato, C.; Dickinson, C.; Laffir, F.; Vagin, M.; McCormac, T. Nitrate and Nitrite Electrocatalytic Reduction at Layer-by-Layer Films Composed of Dawson-Type Heteropolyanions Mono-Substituted with Transitional Metal Ions and Silver Nanoparticles. *Electrochim. Acta* **2015**, *184*, 323–330. [CrossRef]
60. Li, X.-H.; Chen, W.-L.; He, P.; Wang, T.; Liu, D.; Li, Y.-W.; Li, Y.-G.; Wang, E.-B. Dawson-type polyoxometalate-based vacancies g-$C_3N_4$ composite-nanomaterials for efficient photocatalytic nitrogen fixation. *Inorg. Chem. Front.* **2019**, *6*, 3315–3326. [CrossRef]
61. Dai, L.; Xue, Y.; Qu, L.; Choi, H.-J.; Baek, J.-B. Metal-free catalysts for oxygen reduction reaction. *Chem. Rev.* **2015**, *115*, 4823–4892. [CrossRef] [PubMed]
62. Ni, S.; Li, Z.; Yang, J. Oxygen molecule dissociation on carbon nanostructures with different types of nitrogen doping. *Nanoscale* **2012**, *4*, 1184–1189. [CrossRef] [PubMed]
63. Subramanian, N.P.; Li, X.; Nallathambi, V.; Kumaraguru, S.P.; Colon-Mercado, H.; Wu, G.; Lee, J.-W.; Popov, B.N. Nitrogen-modified carbon-based catalysts for oxygen reduction reaction in polymer electrolyte membrane fuel cells. *J. Power Sources* **2009**, *188*, 38–44. [CrossRef]
64. Fernandes, D.M.; Mathumba, P.; Fernandes, A.J.S.; Iwuoha, E.I.; Freire, C. Towards efficient oxygen reduction reaction electrocatalysts through graphene doping. *Electrochim. Acta* **2019**, *319*, 72–81. [CrossRef]
65. Kakaei, K.; Esrafili, M.D.; Ehsani, A. (Eds.) Chapter 6—Oxygen Reduction Reaction. In *Interface Science and Technology*; Elsevier: Amsterdam, The Netherlands, 2019; Volume 27, pp. 203–252.
66. Zheng, Y.; Jiao, Y.; Ge, L.; Jaroniec, M.; Qiao, S.Z. Two-step boron and nitrogen doping in graphene for enhanced synergistic catalysis. *Angew. Chem.* **2013**, *125*, 3192–3198. [CrossRef]
67. Mamlouk, M.; Kumar, S.S.; Gouerec, P.; Scott, K. Electrochemical and fuel cell evaluation of Co based catalyst for oxygen reduction in anion exchange polymer membrane fuel cells. *J. Power Sources* **2011**, *196*, 7594–7600. [CrossRef]
68. Zhou, R.; Zheng, Y.; Jaroniec, M.; Qiao, S.-Z. Determination of the electron transfer number for the oxygen reduction reaction: From theory to experiment. *ACS Catal.* **2016**, *6*, 4720–4728. [CrossRef]
69. Ramaswamy, N.; Mukerjee, S. Fundamental mechanistic understanding of electrocatalysis of oxygen reduction on Pt and non-Pt surfaces: Acid versus alkaline media. *Adv. Phys. Chem.* **2012**, *2012*, 491604. [CrossRef]
70. Fletcher, S. Tafel slopes from first principles. *J. Solid State Electrochem.* **2009**, *13*, 537–549. [CrossRef]
71. Zúñiga, C.; Candia-Onfray, C.; Venegas, R.; Muñoz, K.; Urra, J.; Sánchez-Arenillas, M.; Marco, J.F.; Zagal, J.H.; Recio, F.J. Elucidating the mechanism of the oxygen reduction reaction for pyrolyzed Fe–N–C catalysts in basic media. *Electrochem. Commun.* **2019**, *102*, 78–82. [CrossRef]
72. Jiao, Y.; Zheng, Y.; Jaroniec, M.; Qiao, S.Z. Design of electrocatalysts for oxygen- and hydrogen-involving energy conversion reactions. *Chem. Soc. Rev.* **2015**, *44*, 2060–2086. [CrossRef] [PubMed]
73. Liu, X.; Liu, Y.; Fan, L.-Z. MOF-derived $CoSe_2$ microspheres with hollow interiors as high-performance electrocatalysts for the enhanced oxygen evolution reaction. *J. Mater. Chem. A* **2017**, *5*, 15310–15314. [CrossRef]
74. Liu, S.; Wang, Z.; Zhou, S.; Yu, F.; Yu, M.; Chiang, C.Y.; Zhou, W.; Zhao, J.; Qiu, J. Metal–organic-framework-derived hybrid carbon nanocages as a bifunctional electrocatalyst for oxygen reduction and evolution. *Adv. Mater.* **2017**, *29*, 1700874. [CrossRef] [PubMed]

75. Lach, J.; Wróbel, K.; Wróbel, J.; Podsadni, P.; Czerwiński, A. Applications of carbon in lead-acid batteries: A review. *J. Solid State Electrochem.* **2019**, *23*, 693–705. [CrossRef]
76. Liang, Y.; Wang, H.; Zhou, J.; Li, Y.; Wang, J.; Regier, T.; Dai, H. Covalent Hybrid of Spinel Manganese–Cobalt Oxide and Graphene as Advanced Oxygen Reduction Electrocatalysts. *J. Am. Chem. Soc.* **2012**, *134*, 3517–3523. [CrossRef]
77. Araújo, M.P.; Nunes, M.; Rocha, I.M.; Pereira, M.F.R.; Freire, C. $Co_3O_4$ Nanoparticles Anchored on Selectively Oxidized Graphene Flakes as Bifunctional Electrocatalysts for Oxygen Reactions. *ChemistrySelect* **2018**, *3*, 10064–10076. [CrossRef]
78. Lei, Z.; Feng, W.; Feng, C.; Zhou, W.; Wei, C.; Wang, X. Nitrified coke wastewater sludge flocs: An attractive precursor for N,S dual-doped graphene-like carbon with ultrahigh capacitance and oxygen reduction performance. *J. Mater. Chem. A* **2017**, *5*, 2012–2020. [CrossRef]
79. Wang, Z.; Lu, Y.; Yan, Y.; Larissa, T.Y.P.; Zhang, X.; Wuu, D.; Zhang, H.; Yang, Y.; Wang, X. Core-shell carbon materials derived from metal-organic frameworks as an efficient oxygen bifunctional electrocatalyst. *Nano Energy* **2016**, *30*, 368–378. [CrossRef]
80. Xia, S.; Guo, W.; Cai, N.; Sun, L.; Zhou, H.; Lu, W.; Chen, X.; Zhang, J.; Chen, Y.; Yang, H.; et al. Synthesis and application in oxygen reduction reaction of N-doping porous graphitic carbon from biomass waste. *Fuel Process. Technol.* **2021**, *224*, 107028. [CrossRef]
81. Olah, G.A. Towards Oil Independence Through Renewable Methanol Chemistry. *Angew. Chem. Int. Ed.* **2013**, *52*, 104–107. [CrossRef]
82. Kumar, A.; Daw, P.; Milstein, D. Homogeneous Catalysis for Sustainable Energy: Hydrogen and Methanol Economies, Fuels from Biomass, and Related Topics. *Chem. Rev.* **2022**, *122*, 385–441. [CrossRef] [PubMed]
83. Lo Vecchio, C.; Sebastián, D.; Lázaro, M.J.; Aricò, A.S.; Baglio, V. Methanol-Tolerant M–N–C Catalysts for Oxygen Reduction Reactions in Acidic Media and Their Application in Direct Methanol Fuel Cells. *Catalysts* **2018**, *8*, 650. [CrossRef]
84. Mathumba, P.; Fernandes, D.M.; Matos, R.; Iwuoha, E.I.; Freire, C. Metal Oxide ($Co_3O_4$ and $Mn_3O_4$) Impregnation into S, N-doped Graphene for Oxygen Reduction Reaction (ORR). *Materials* **2020**, *13*, 1562. [CrossRef] [PubMed]
85. Hoang, S.; Guo, S.; Hahn, N.T.; Bard, A.J.; Mullins, C.B. Visible Light Driven Photoelectrochemical Water Oxidation on Nitrogen-Modified $TiO_2$ Nanowires. *Nano Lett.* **2012**, *12*, 26–32. [CrossRef]
86. Tuci, G.; Zafferoni, C.; Rossin, A.; Milella, A.; Luconi, L.; Innocenti, M.; Phuoc, L.T.; Duong-Viet, C.; Pham-Huu, C.; Giambastiani, G. Chemically functionalized carbon nanotubes with pyridine groups as easily tunable N-decorated nanomaterials for the oxygen reduction reaction in alkaline medium. *Chem. Mater.* **2014**, *26*, 3460–3470. [CrossRef]
87. Muthuswamy, N.; Buan, M.E.M.; Walmsley, J.C.; Rønning, M. Evaluation of ORR active sites in nitrogen-doped carbon nanofibers by KOH post treatment. *Catal. Today* **2018**, *301*, 11–16. [CrossRef]
88. Chen, X.; Zhang, W.; Qu, Y.; Chen, X.; Liu, Y.; Lu, C. Solvent-free synthesis of honeycomb-like N-doped porous carbon derived from biomass pine sawdust as an efficient metal-free electrocatalyst for oxygen reduction reaction. *J. Electroanal. Chem.* **2022**, *926*, 116909. [CrossRef]
89. Ingavale, S.; Patil, I.; Prabakaran, K.; Swami, A. Microwave-assisted synthesis of cobalt-polyoxometalate@ carbon black nanocomposites and their electrocatalytic ability toward oxygen reduction reaction. *Int. J. Energy Res.* **2021**, *45*, 7366–7379. [CrossRef]
90. Fernandes, D.M.; Mestre, A.S.; Martins, A.; Nunes, N.; Carvalho, A.P.; Freire, C. Biomass-derived nanoporous carbons as electrocatalysts for oxygen reduction reaction. *Catal. Today* **2020**, *357*, 269–278. [CrossRef]
91. Nunes, M.; Fernandes, D.M.; Rocha, I.M.; Pereira, M.F.; Mbomekalle, I.M.; de Oliveira, P.; Freire, C. Phosphomolybdate@ Carbon-Based Nanocomposites as Electrocatalysts for Oxygen Reduction Reaction. *ChemistrySelect* **2016**, *1*, 6257–6266. [CrossRef]
92. Su, Y.; Jiang, H.; Zhu, Y.; Yang, X.; Shen, J.; Zou, W.; Chen, J.; Li, C. Enriched graphitic N-doped carbon-supported $Fe_3O_4$ nanoparticles as efficient electrocatalysts for oxygen reduction reaction. *J. Mater. Chem. A* **2014**, *2*, 7281–7287. [CrossRef]
93. Zhang, H.; Li, H.; Wang, H.; He, K.; Wang, S.; Tang, Y.; Chen, J. $NiCo_2O_4$/N-doped graphene as an advanced electrocatalyst for oxygen reduction reaction. *J. Power Sources* **2015**, *280*, 640–648. [CrossRef]
94. Yang, Z.; Wu, J.; Zheng, X.; Wang, Z.; Yang, R. Enhanced catalytic activity for the oxygen reduction reaction with co-doping of phosphorus and iron in carbon. *J. Power Sources* **2015**, *277*, 161–168. [CrossRef]
95. Ning, R.; Tian, J.; Asiri, A.M.; Qusti, A.H.; Al-Youbi, A.O.; Sun, X. Spinel $CuCo_2O_4$ nanoparticles supported on N-doped reduced graphene oxide: A highly active and stable hybrid electrocatalyst for the oxygen reduction reaction. *Langmuir* **2013**, *29*, 13146–13151. [CrossRef]
96. Hossen, M.M.; Artyushkova, K.; Atanassov, P.; Serov, A. Synthesis and characterization of high performing Fe-NC catalyst for oxygen reduction reaction (ORR) in Alkaline Exchange Membrane Fuel Cells. *J. Power Sources* **2018**, *375*, 214–221. [CrossRef]
97. Lu, F.; Fan, K.; Cui, L.; Li, B.; Yang, Y.; Zong, L.; Wang, L. Engineering $FeN_4$ active sites onto nitrogen-rich carbon with tubular channels for enhanced oxygen reduction reaction performance. *Appl. Catal. B Environ.* **2022**, *313*, 121464. [CrossRef]

**Disclaimer/Publisher's Note:** The statements, opinions and data contained in all publications are solely those of the individual author(s) and contributor(s) and not of MDPI and/or the editor(s). MDPI and/or the editor(s) disclaim responsibility for any injury to people or property resulting from any ideas, methods, instructions or products referred to in the content.

Check for updates
ChemElectroChem
Research Article
doi.org/10.1002/celc.202300622
Chemistry Europe
European Chemical Societies Publishing
www.chemelectrochem.org

# Enhanced Oxygen Reduction Reaction Activity of the Wells-Dawson Polyoxometalate $P_2W_{12}Mo_6$ Immobilised in Nitrogen and Sulphur-Doped Carbon Nanomaterials

Hugo C. Novais,[a] Bruno Jarrais,[a] Israël-Martyr Mbomekallé,[b] Anne-Lucie Teillout,[b] Pedro de Oliveira,[b] Cristina Freire,[a] and Diana M. Fernandes*[a]

As the world faces an escalating energy crisis, the necessity of adopting alternative energy sources becomes increasingly evident. Despite challenges, the imperative to prioritise these eco-friendly alternatives remains paramount in paving the way for a more sustainable and resilient future for our planet and its inhabitants. The pursuit of sustainable energy sources has brought the oxygen reduction reaction (ORR) into the spotlight as a crucial cathodic reaction in energy-converting systems, notably fuel cells (FCs). These FCs hold tremendous promise in providing an eco-friendly and efficient energy supply. However, the widespread implementation of FCs is hindered by their reliance on expensive and scarce noble metal catalysts, such as platinum (Pt), which pose economic and environmental challenges. Hence, this work reports the preparation, characterisation (FTIR, XPS, SEM and EDX) and application of four composites based on doped-carbon materials (CM) and on the Wells-Dawson POM salt $K_6$-α-$[P_2W_{12}Mo_6O_{62}]\cdot 19H_2O$ ($P_2W_{12}Mo_6$@MWCNT_N8, $P_2W_{12}Mo_6$@MWCNT_N6, $P_2W_{12}Mo_6$@MWCNT_S6, and $P_2W_{12}Mo_6$@GF_S6) as ORR electrocatalysts in alkaline medium (pH = 13). The successful doping of the carbon materials with nitrogen (N) and sulphur (S) and the incorporation of the polyoxometalate were verified through comprehensive structural characterisation. Overall, $P_2W_{12}Mo_6$@MWCNT_N8 exhibited favourable onset potentials of 0.84 V vs. RHE, highlighting its high catalytic activity. Additionally, the catalyst showed excellent tolerance to methanol crossover, retaining 91% of initial current, which is crucial for practical fuel cell applications. Furthermore, the $P_2W_{12}Mo_6$@MWCNT_N8 catalyst showed commendable stability, retaining 81% of its initial current after 36000 seconds at an operating potential of $E = 0.46$ V vs. RHE. These encouraging results denote the significant potential of this electrocatalyst in advancing sustainable energy conversion technologies.

## Introduction

There is an increasing need for sustainable and ecologically friendly energy sources with a more balanced and practical approach to tackling environmental difficulties as civilisations around the world struggle with the repercussions of global environmental concerns.[1,2] The exploration of alternative clean energy technologies has been sparked by the depletion of traditional fossil fuels and the unfavourable consequences of energy consumption, which emphasise the need to take into account human welfare, economic development, and the potential benefits of technology in environmental solutions.[3] Among these, fuel cells have emerged as a promising avenue for clean energy conversion, offering a viable solution to mitigate the negative environmental impacts associated with traditional energy sources. The cathode's oxygen reduction reaction stands out as a critical feature of FCs. However, the reaction kinetics are typically slow, presenting a challenge that requires resolution.[4–7] Fuel cells and other energy conversion devices, rely heavily on electrocatalysts (ECs) because they greatly improve the selectivity and efficiency of critical chemical reactions. The ORR's most active ECs, however, are mostly dependent on noble metals like platinum and palladium.[8] While effective, these ECs have several drawbacks, including high cost, low abundance and intolerance to fuel crossover (such as methanol and CO).[8] Therefore, it is imperative to search for other electrocatalysts that can lessen these drawbacks and provide more practical and affordable options. Moreover, the emergence of computational methods has revolutionised the field of solid catalyst design, offering exciting prospects for advancing research in ORR electrocatalysts.[9]

The molybdenum (Mo) based electrocatalyst has shown great promise as a viable alternative to address the sluggish ORR at the cathode, leading to significant improvements in overall ORR performance. However, its use in ORR has been limited by the unfavourable energy level of the Mo d-band for this particular reaction, as well as the lack of a suitable coordination environment.[10] In ORR catalytic activity, the process involves the activation of $O_2$ and the adsorption of

[a] H. C. Novais, B. Jarrais, C. Freire, D. M. Fernandes
LAQV-REQUIMTE/Departamento de Química e Bioquímica, Faculdade de Ciências, Universidade do Porto, 4169-007 Porto, Portugal
E-mail: diana.fernandes@fc.up.pt
[b] I.-M. Mbomekallé, A.-L. Teillout, P. de Oliveira
Equipe d'Electrochimie et de Photo-électrochimie, Institut de Chimie Physique, Université Paris-Saclay, UMR 8000 CNRS, Orsay F-91405, France
Supporting information for this article is available on the WWW under https://doi.org/10.1002/celc.202300622
© 2024 The Authors. ChemElectroChem published by Wiley-VCH GmbH. This is an open access article under the terms of the Creative Commons Attribution License, which permits use, distribution and reproduction in any medium, provided the original work is properly cited.

ChemElectroChem | Research Article
doi.org/10.1002/celc.202300622
Chemistry Europe
European Chemical Societies Publishing

21960216, 2024, 4, Downloaded from https://chemistry-europe.onlinelibrary.wiley.com/doi/10.1002/celc.202300622 by Cochrane Portugal, Wiley Online Library on [02/04/2025]. See the Terms and Conditions (https://onlinelibrary.wiley.com/terms-and-conditions) on Wiley Online Library for rules of use; OA articles are governed by the applicable Creative Commons License

reaction intermediates onto the electrocatalyst surface. These interactions are strongly influenced by the geometric and electronic structures of the catalyst.[9,11] The strength of adsorption of oxygen-containing intermediates (O*, OH*, and OOH*) is particularly crucial and depends on the position of the d-band centre for the transition metal in the catalyst.[12–14] The design and employment of composite electrocatalysts has been proposed as a promising way to improve the efficiency of various energy-related reactions. These hybrids combine the exceptional properties of carbon nanomaterials with the high stability and rich redox properties of polyoxometalates (POMs).[15–19] The specific POM used belongs to the Wells-Dawson family ($[(P_2W_{12}Mo_6O_{62})^{6-}$). In particular, the molybdenum-substituted POMs have attracted considerable interest due to their dual ability to act as either oxidation or reduction electrocatalysts.[10]

Promising ORR electrocatalysts have emerged in the form of carbon nanomaterials (CMs), including graphene (GF) and carbon nanotubes (CNT). These materials have remarkable properties such as low cost, high surface area, excellent conductivity, and superior stability.[20] In particular, they have high chemical and thermal stability, desirable electrical properties, significant porosity, and large surface area. Both nanotubes and graphene have found widespread applications in ORR, serving as metal-free electrocatalysts in alkaline media and as supports for electrocatalysts in hybrid nanocomposites.[15,21–23] In addition, their electrocatalytic activity can be further enhanced by doping with various heteroatoms such as nitrogen, sulphur, and phosphorus.[21,22,24–27] By introducing nitrogen and sulphur into the $sp^2$ carbon structure, the electronic properties of the original carbons can be enhanced, resulting in improved electrocatalytic performance for ORR.[28,29] Various nitrogen and sulphur species can be incorporated into the graphitic network, including pyridinic, pyrrolic, graphitic (quaternary) and thiol groups, further enhancing their catalytic activity.[19,30–34]

Following the pioneering work of Hu et al.[35] and Girault *et al*.[12] our group have demonstrated that hybrids composed of the molybdotungstophosphate polyoxometalate ($P_2W_{12}Mo_6$) considered in this work immobilised in nitrogen and sulphur-doped carbon nanomaterials are active catalysts for the oxygen reduction reaction on modified electrodes. Herein, we report on the preparation of composites based on the incorporation of the Wells-Danson POM's salt $K_6 \cdot \alpha$-$[P_2W_{12}Mo_6O_{62}] \cdot 19H_2O$ onto distinct nitrogen and sulphur-doped carbon materials (sulphur-doped graphene flakes and multi-walled carbon nanotubes, nitrogen-doped multi-walled carbon nanotubes) and their application as ORR electrocatalysts.

## Experimental Section

### Materials preparation and characterization methods

A full description of the materials and solvents used in the preparation of the composites and in the ORR studies can be found in the Supplementary Information (SI). A mixture of 0.60 g of the carbon materials (multi-walled carbon nanotubes and graphene flakes) and 0.26 g of the doping element was prepared using an appropriate precursor (melamine as nitrogen precursor and molecular sulphur as sulphur precursor) via a 5-hour mechanical ball milling procedure utilizing a Retsch MM200 apparatus operating at a consistent frequency of 15 vibrations per second. In the next step, the materials were exposed to a thermal process with a nitrogen flow rate of 100 $cm^3\,min^{-1}$. The temperature was subsequently raised by 10 °C per minute until it reached 800 °C for MWCNT_N8 preparation and 600 °C for MWCNT_N6, MWCNT_S6 and GF_S6 preparation. The attained temperature was then sustained for an hour before the materials were cooled down to room temperature in a nitrogen atmosphere. Finally, the components were preserved in a desiccator. The $P_2W_{12}Mo_6$@CM composites were then prepared by immobilising $P_2W_{12}Mo_6$ onto previously prepared MWCNT_N8, MWCNT_N6, MWCNT_S6, and GF_S6. The immobilisation of POM was accomplished by mixing a 5 mL $H_2SO_4/Na_2SO_4$ solution (pH = 2.0) containing 50 mg of $P_2W_{12}Mo_6$ with 50 mg of CM in 20 mL of the same solution. The mixture was dispersed for 15 minutes in an ultrasonic bath and then stirred for 2 hours at 400 rpm. The resulting composites were subsequently filtered, washed, and dried at 60 °C under vacuum overnight. The composites were labelled as $P_2W_{12}Mo_6$@MWCNT_N8, $P_2W_{12}Mo_6$@MWCNT_N6, $P_2W_{12}Mo_6$@MWCNT_S6, and $P_2W_{12}Mo_6$@GF_S6.

Prior to their utilization in electrocatalytic studies, the composites were characterized using Fourier-transformed infrared spectroscopy (FTIR), scanning electron microscopy (SEM), energy-dispersive X-ray spectroscopy (EDS), and X-ray photoelectron spectroscopy (XPS). The methodologies and instrumentation used for the characterization are expounded in the SI. Electrochemical performances towards ORR were assessed using a conventional 3-electrode system with a PGSTAT 302N potentiostat (Metrohm Autolab B.V., Utrecht, The Netherlands) controlled by NOVA 2.1. Complete details of the electrodes, electrode conditioning, and modification are provided in the SI.

## Results and Discussion

### Materials characterisation

The prepared composite materials were subjected to initial characterisation via infrared spectroscopy, as depicted in Figure 1. The nitrogen-doped multi-walled carbon nanotubes synthesised at two different calcination temperatures of 600 and 800 °C (MWCNT_N6 and MWCNT_N8, respectively) as well as sulphur-doped multi-walled carbon nanotubes (MWCNT_S6) and sulphur-doped graphene (GF_S6) at 600 °C were also characterised by FTIR and the spectra are presented in Figure S1 (N-doped) and Figure S2 (S-doped).

The spectrum of MWCNT_N8 displayed several vibrational bands at 3436, 2928, 2846, 1641, 1383, and 1124 $cm^{-1}$, even though some of these bands were weak and poorly resolved. This may be attributed to the low loading of POMs on the carbon material or their interaction with the graphene and carbon nanotube matrix, which may impede their detection. The OH groups' vibrational bands appeared at 3436 $cm^{-1}$, resulting from the O–H stretching and bending modes from adsorbed residual water and hydroxyl groups.[36,37] The C–N stretching vibration band appeared at 1383 $cm^{-1}$,[38,39] and the band at 1124 $cm^{-1}$ was assigned to the phenolic groups' vibration modes.[39,41] The bands at 2928 and 2846 $cm^{-1}$


© 2024 The Authors. ChemElectroChem published by Wiley-VCH GmbH

ChemElectroChem
Research Article
doi.org/10.1002/celc.202300622
Chemistry Europe
European Chemical Societies Publishing

21960216, 2024, 4, Downloaded from https://chemistry-europe.onlinelibrary.wiley.com/doi/10.1002/celc.202300622 by Cochrane Portugal, Wiley Online Library on [02/04/2025]. See the Terms and Conditions (https://onlinelibrary.wiley.com/terms-and-conditions) on Wiley Online Library for rules of use; OA articles are governed by the applicable Creative Commons License

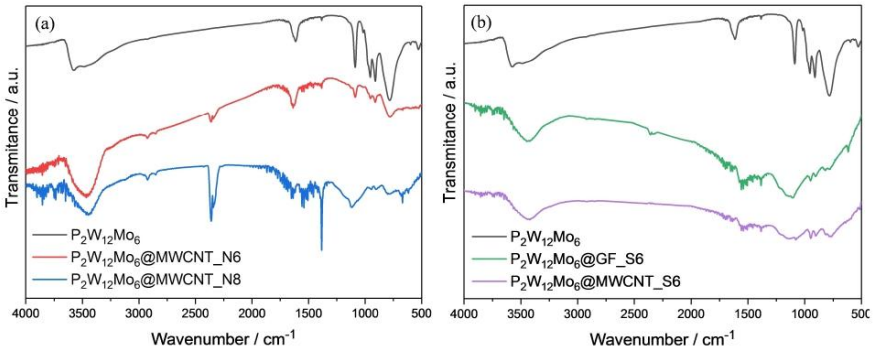



**Figure 1.** FTIR spectra in the 4000–500 $cm^{-1}$ range of $K_6 \cdot \alpha$-$[P_2W_{12}Mo_6O_{62}] \cdot 19H_2O$ (black), and of the composites $P_2W_{12}Mo_6$@MWCNT_N6 (red), $P_2W_{12}Mo_6$@MWCNT_N8 (blue) (a) and $P_2W_{12}Mo_6$@MWCNT_S6 (green) and $P_2W_{12}Mo_6$@GF_S6 (purple) (b).

corresponded, respectively, to the C–H stretching modes, which may be attributed to the presence of defects in the $sp^2$ hybridised domains. Additionally, the band at 1641 $cm^{-1}$ could be attributed to the C=N and the C=O stretching mode of the carboxylic acid, carbonyl, ketone, and quinone groups.[36,38,41] Our results show that MWCNTs doped with nitrogen at 600 °C (MWCNT_N6) exhibit similar vibrational bands to those of MWCNTs doped with nitrogen at 800 °C (MWCNT_N8). However, it is observed mainly two additional vibrational bands in the spectra of MWCNT_N6: a C=O stretching mode at 1710 $cm^{-1}$ and a C–N stretching mode at 1224 $cm^{-1}$. The presence of the C=O stretching mode in the spectrum of MWCNT_N6 indicates the presence of carboxylic acid, carbonyl, ketone or quinone groups.[36,42] The C–N stretching mode at 1224 $cm^{-1}$ suggests the presence of amine or amide groups, which are also likely introduced during the nitrogen doping process.[36,42]

In the FTIR analysis of sulphur-doped carbon nanomaterials, it is important to consider the potential overlap of vibrational bands associated with sulphur and carbon bonds. Due to the presence of sulphur atoms in the carbon nanotube structure, certain vibrational modes may exhibit overlapping peaks, making it challenging to directly assign specific bands to either sulphur or carbon bonds based solely on their positions. The FTIR spectrum of sulphur-doped multi-walled carbon nanotubes (MWCNT_S6), as such, is expected to show similar vibrational bands as those of nitrogen-doped MWCNTs, but with some differences due to the presence of sulphur. MWCNT_S6 (Figure S2 black line) shows vibrational bands assigned to O–H stretching and bending modes at ~3436 and 1363 $cm^{-1}$, respectively.[36,43,44] The presence of peaks between 1122 and 1515 $cm^{-1}$ in the FTIR spectrum of sulphonated multi-walled carbon nanotubes can be attributed to the C–S (carbon-sulphur), S=O (sulphone/sulphite) and S–O stretching bonds.[45] Figure S2 also shows an intense band at a wavelength of 1224 $cm^{-1}$ which corresponds to the presence of the S–O vibration related to the absorption of sulphonate.[46] Nevertheless, the band at 1118 $cm^{-1}$ may be assigned to the phenolic groups' vibration modes[39,41], and the two bands at 2921 and 2853 $cm^{-1}$ correspond, respectively, to the C–H stretching modes, the band at 1641 $cm^{-1}$ can be attributed to the C=N and the C=O stretching mode of the carboxylic acid, carbonyl, ketone, and quinone groups.[36,38,41] Both GF_S6 and MWCNT_S6 exhibit similar vibrational bands related to the presence of sulphur in the nanomaterial and its carbon structure. In the infrared spectrum of GF_S6 (Figure S2 red line), prominent bands are observed at 3434, 2922, 2856, 1639, 1387, and 1135 $cm^{-1}$, which can be attributed to specific molecular vibrations. The O–H stretching and bending modes are observed at approximately 3410 $cm^{-1}$ and 1386 $cm^{-1}$, respectively.[36,43] The presence of C=N and the C=O stretching vibrations are observed at 1630 $cm^{-1}$, the phenol groups at 1387 $cm^{-1}$ and the C–O stretching vibrations of oxygen groups at 1142 $cm^{-1}$.[36,38,43,47,48] Furthermore, a band assigned to the C–O–C and C–O stretching modes, along with the C–O–H bending mode, is observed at 1070 $cm^{-1}$.[36,49,50] Notably, these bands closely resemble the corresponding bands in the infrared spectrum of MWCNT_S6. The resemblance in the infrared spectra of GF_S6 and MWCNT_S6 suggests the presence of similar sulphur-related functional groups in both materials. These functional groups may include sulphur-oxygen (S=O/S–O) bonds or sulphur-carbon (S–C) bonds.

Figure 1 depicts the FTIR spectrum of $P_2W_{12}Mo_6$ (black), wherein the typical vibrational bands associated with polyoxometalates are evident within the range of 1100 to 700 $cm^{-1}$. The band observed at 1088 $cm^{-1}$ is attributed to the splitting of the $\nu_{as}$P–O stretching vibration, while the three vibration bands located at 955, 910, and 781 $cm^{-1}$ correspond to the $\nu_{as}$W=$O_t$, $\nu_{as}$W–$O_b$–W and $\nu_{as}$W–$O_c$–W stretching modes (corner and edge sharing W–O–W), respectively.[51,52] In the infrared spectra of the composites $P_2W_{12}Mo_6$@MWCNT_N6 (red line), $P_2W_{12}Mo_6$@MWCNT_N8 (blue line) and $P_2W_{12}Mo_6$@MWCNT_S6 (green line) and $P_2W_{12}Mo_6$@GF_S6 (purple line), the intensity of the bands appears weaker compared to that of the pure POM spectrum. However, the immobilisation of $P_2W_{12}Mo_6$ onto the


© 2024 The Authors. ChemElectroChem published by Wiley-VCH GmbH

ChemElectroChem
Research Article
doi.org/10.1002/celc.202300622
Chemistry Europe
European Chemical Societies Publishing

21960216, 2024, 4, Downloaded from https://chemistry-europe.onlinelibrary.wiley.com/doi/10.1002/celc.202300622 by Cochrane Portugal, Wiley Online Library on [02/04/2025]. See the Terms and Conditions (https://onlinelibrary.wiley.com/terms-and-conditions) on Wiley Online Library for rules of use; OA articles are governed by the applicable Creative Commons License

carbon materials can still be confirmed. Notably, the bands arising from the nitrogen-doped carbon materials are also observed. Interestingly, the characteristic bands of the POM experience a small shift in the position towards shorter wavelengths upon immobilisation, suggesting potential changes in electron densities or increased repulsive interactions between oxygen atoms on the carbon material surfaces likely to reflect the weakening (stretching) of the W–O bonds.[19,53,54]

The XPS characterisation of the initial nitrogen-doped materials, MWCNT_N8 and MWCNT_N6, as well as the sulphur-doped materials, MWCNT_S6 and GF_S6, has been previously reported by Bruno Jarrais et al..[55] However, to facilitate a comprehensive comparison with the composite materials, we present a concise summary of the main peaks observed in the XPS spectra. The relative amounts of the different elements were calculated through the peak areas and are presented in Table 1.

The successful incorporation of nitrogen and sulphur in the N, S-doped materials (MWCNT_N6, MWCNT_N8, GF_S6, and MWCNT_S6) was confirmed, validating the effectiveness of the doping procedure. The analysis of the atomic percentages of the composite materials further demonstrated the presence of the POM. Substantial increase in the oxygen percentage was observed following the immobilisation of the POM, providing strong evidence for its presence in the composite materials. Furthermore, following the immobilisation of the POM, the composite materials containing sulphur ($P_2W_{12}Mo_6$@GF_S6 and $P_2W_{12}Mo_6$@MWCNT_S6) exhibited a marginal change in the atomic percentages of S2p, falling well within the range of experimental uncertainty. The observed increase of sulphur in the sample could potentially be linked to its surface heterogeneity, which allowed for the detection of areas with varying concentrations that may have hindered sulphur detection. The coexistence of overlapping N1s and Mo3p peaks presents a notable obstacle in precisely discerning the individual contributions of nitrogen in the XPS analysis. Therefore, discrepancies may arise in the atomic percentage of nitrogen in the resulting composites when compared to the nitrogen content in the initial materials due to the surface limit of XPS analysis, which analyses depths up to 10 nm.

In the Supplementary Information (SI), Figure S3 to S6 (a) clearly demonstrate the presence of nitrogen and sulphur in the heteroatom-doped carbon materials (MWCNT_N8, MWCNT_N6, MWCNT_S6, and GF_S6). This observation strongly indicates the successful implementation of the doping procedure. The XPS spectra of the nitrogen-doped carbon materials revealed distinct peaks corresponding to different nitrogen functionalities. Deconvolution of the N1s spectra resulted in three prominent peaks assigned to specific nitrogen species: pyridinic N at ~398.3 eV, pyrrolic N at ~400.0 eV, and quaternary N at ~401.6 eV.[19,56,57] Additionally, a fourth peak observed at 404.2 eV was attributed to nitrogen oxide and/or nitrate species.[19,33,56] The relative quantities of these nitrogen functionalities followed a consistent trend across both N-doped materials (MWCNT_N8 and MWCNT_N6), with increasing proportions in the order: [quaternary N] < [pyrrolic N] < [pyridinic N]. The deconvolution analysis of the S-doped carbon materials, MWCNT_S6 and GF_S6, revealed the presence of characteristic peaks common to both samples. In particular, two peaks observed at ~164.1 and ~165.3 eV assigned to the doublet of $S2p_{3/2}$ and $S2p_{1/2}$ in thiophene-S, indicating the presence of thiophene-like sulphur functionalities.[55,58–60] Additionally, a peak identified at ~162.3 eV was assigned to thiol groups.[55,58–60] For material GF_S6, a fourth peak at 166.7 eV was found, which corresponds to sulphate species.[61] These results provide clear evidence of the successful incorporation of sulphur into the carbon matrix of the composite materials, highlighting the specific sulphur species present and their respective chemical environments. The C1s high-resolution spectra (Figure S3 to S6 (b)) were also subjected to fitting analysis, resulting in the identification of seven distinct peaks. At 284.6 eV, a peak corresponding to the graphitic structure ($sp^2$, C=C) was observed. Then, $sp^3$ hybridised carbon and C–N bonding at ~285.2 eV indicated the incorporation of nitrogen in the materials, as seen in MWCNT_N8 and MWCNT_N6, as well the presence of C–S bonding in MWCNT_S6 and GF_S6, alongside

**Table 1.** XPS surface atomic percentages for the pristine carbon materials, the doped carbon materials and the prepared composites.

| Material | XPS Atomic %[a] | | | | | | |
|---|---|---|---|---|---|---|---|
| | C1s | O1s | N1s | S2p | P2p | W4f | Mo3d |
| **GF** | 96.8 | 3.2 | – | – | – | – | – |
| **MWCNT** | 98.9 | 1.1 | – | – | – | – | – |
| **MWCNT_N6** | 94.9 | 3.3 | 1.8 | – | – | – | – |
| **MWCNT_N8** | 98.0 | 1.0 | 1.0 | – | – | – | – |
| **GF_S6** | 96.2 | 2.0 | – | 0.8 | – | – | – |
| **MWCNT_S6** | 98.6 | 0.7 | – | 0.7 | – | – | – |
| **$P_2W_{12}Mo_6$@MWCNT_N6** | 90.2 | 6.1 | 2.7 | – | 0.1 | 0.6 | 0.3 |
| **$P_2W_{12}Mo_6$@MWCNT_N8** | 86.1 | 10.9 | 1.7 | – | 0.2 | 0.6 | 0.5 |
| **$P_2W_{12}Mo_6$@GF_S6** | 91.6 | 6.1 | – | 1.0 | 0.2 | 0.8 | 0.4 |
| **$P_2W_{12}Mo_6$@MWCNT_S6** | 94.2 | 3.9 | – | 0.9 | 0.1 | 0.6 | 0.3 |

[a] Determined by the areas of the respective bands in the high-resolution XPS spectra.


© 2024 The Authors. ChemElectroChem published by Wiley-VCH GmbH

ChemElectroChem
Research Article
doi.org/10.1002/celc.202300622
Chemistry Europe
European Chemical Societies Publishing

21960216, 2024, 4, Downloaded from https://chemistry-europe.onlinelibrary.wiley.com/doi/10.1002/celc.202300622 by Cochrane Portugal, Wiley Online Library on [02/04/2025]. See the Terms and Conditions (https://onlinelibrary.wiley.com/terms-and-conditions) on Wiley Online Library for rules of use; OA articles are governed by the applicable Creative Commons License

the C–N bonding, with additionally peaks at ~285.9 eV attributed to C–N/C–S and C–OH bonding. The presence of C–O–C groups was indicated by a peak at ~286.9 eV, C=O groups at ~288.2 eV encompassing ketones, quinones, and aldehydes, the occurrence of COOH functional groups, including carboxylic acids and esters, was observed at ~289.3 eV, and finally, a peak at ~291.0 eV was attributed to $\pi$–$\pi$* transitions.[19,55,62] The high-resolution O1s spectra of MWCNT_N6 (Figure S4 (c)) did not allow for precise peak deconvolution. However, the peak observed at ~532.7 eV was attributed to the contributions of oxygen in the form of C=O, COOH, and C–OH groups.[19] In contrast, the O1s spectra of MWCNT_N8, MWCNT_S6, and GF_S6 (Figure S3 (c), S5 (c), and S6 (c)) showed a distinct two-peak structure upon deconvolution. The first peak, located at ~531.7 eV, was attributed to C=O and COOH functionalities and a second peak at ~533.1 eV could be attributed to the presence of HO–C species.[19,38,55,63]

The N1s XPS spectrum of the $P_2W_{12}Mo_6$@MWCNT_N8 composite (Figure 2(a)) exhibits four prominent peaks at 398.3, 399.8, 400.0, and 405.2 eV, which are assigned to pyridinic, pyrrolic, quaternary N, and nitrogen oxide and/or nitrate species, respectively.[19,55,57,64,65] Similarly, the N1s spectrum fitting of the $P_2W_{12}Mo_6$@MWCNT_N6 composite (Figure S7(a)) shows peaks at 398.5, 400.4, 402.8, and 406.3 eV, corresponding to pyridinic, pyrrolic, quaternary N, and nitrogen oxide and/or nitrate species, respectively. The S2p XPS spectrum of the $P_2W_{12}Mo_6$@MWCNT_S6 composite (Figure S8(a)) reveals distinct peaks at 163.8 and 165.0 eV, corresponding to the $S2p_{3/2}$ and $S2p_{1/2}$ doublet, which can be attributed to the presence of sulphur in thiophene-S.[55,58–60] Additionally, a peak at 169.0 eV is observed, which corresponds to sulphate species.[61] Similarly, in the case of the $P_2W_{12}Mo_6$@GF_S6 composite (Figure S9 (a)), the deconvolution of the S2p spectrum exhibits peaks at 163.9 and 165.1 eV, representing the $S2p_{3/2}$ and $S2p_{1/2}$ doublet, associated with thiophene-S. Furthermore, as for the previous composite, a distinct peak at 168.6 eV is observed, indicative of the presence of sulphate species.

The C1s high-resolution XPS spectra of the $P_2W_{12}Mo_6$@MWCNT_N8, $P_2W_{12}Mo_6$@MWCNT_N6, $P_2W_{12}$Mo6@MWCNT_S6, and $P_2W_{12}Mo_6$@GF_S6 composites are depicted in Figure 2(b) and Figures S7–S9(b), respectively. Each spectrum displays a total of seven distinct peaks, with the main peak observed at 284.6 eV representing the graphitic structure ($sp^2$, C=C), a peak at around 285.1 eV attributed to $sp^3$ hybridised carbon and C–N bonding, a peak at 285.8 eV assigned to C–N and C–OH bonding, a peak at approximately 286.8 eV attributed to C–O–C groups, a peak at 288.1 eV assigned to C=O groups including ketones, quinones, and aldehydes, a peak at 289.2 eV corresponding to COOH functional groups, namely carboxylic acids and esters, and a peak at 291.0 eV ascribed to $\pi$–$\pi$* transitions.[19,55,62] The similarity between the C1s XPS spectra of $P_2W_{12}Mo_6$@MWCNT_N8, $P_2W_{12}Mo_6$@MWCNT_N6, $P_2W_{12}$Mo6@MWCNT_S6, and $P_2W_{12}Mo_6$@GF_S6 indicates consistent carbon functionalisation patterns in these composite materials.

Figure 2 (c) and Figures S7–S9 (c) display the high-resolution O1s spectra for $P_2W_{12}Mo_6$@CM, which has been deconvoluted into two primary peaks: one at 530.7 eV assigned to oxygen in C=O (ketones, quinones, aldehydes) and COOH (carboxylic acids, esters) groups, along with oxygen atoms originating from the POM, and another at 532.7 eV attributed to O in HO–C groups (phenols).[19,38,55,63] These two peaks are also evident in the remaining composites. It is noteworthy that the immobilisation of the POM on the carbon materials led to a significant increase in the percentage of O1s in the final composites. This increase can be attributed to the contribution of the POM to the O1s percentages of the composite materials. The P2p high-resolution spectra of $P_2W_{12}Mo_6$@CM are depicted in Figure 2 (d) and Figures S7–S9 (d). The observed peaks exhibit distinct $2p_{3/2}$ and $2p_{1/2}$ doublets, with energies approximately at ~133.5 and ~134.4 eV, respectively.[19] In Figure 2 (e) and Figures S7–S9 (e) the peaks observed in the high-resolution spectra of W4f are attributed to $4f_{7/2}$ (~35.6 eV) and $4f_{5/2}$ (~37.8 eV), resulting from spin-orbital coupling.[19,66] Lastly, in Figure 2(f) and Figures S7–S9(f), the Mo3d spectrum can be divided into $Mo3d_{5/2}$ and $Mo3d_{3/2}$ regions. The dominant doublet (with higher intensity) at ~233.0 and ~235.7 eV corresponds to the $Mo^{6+}$ oxidation state, while the minor doublet (with lower intensity) at ~231.5 and ~234.2 eV corresponds to the $Mo^{5+}$ oxidation state.[67,70]

The morphology of all the materials was examined using scanning electron microscopy (SEM), and Figure 3 displays the SEM images for $P_2W_{12}Mo_6$@MWCNT_N8 (a), $P_2W_{12}Mo_6$@MWCNT_N6 (b), $P_2W_{12}Mo_6$@MWCNT_S6 (c), and $P_2W_{12}Mo_6$@GF_S6 (d) at a magnification of 50,000×. As observed, the morphologies of the composites containing carbon nanotubes ($P_2W_{12}Mo_6$@MWCNT_N8, $P_2W_{12}Mo_6$@MWCNT_N6, and $P_2W_{12}$Mo6@MWCNT_S6) differ significantly from the composite containing graphene ($P_2W_{12}Mo_6$@GF_S6). Those containing carbon nanotubes exhibit a needle-like structure characteristic of multi-walled carbon nanotubes, whereas $P_2W_{12}$Mo6@GF_S6 shows thin and flat flakes of carbon layers. In all composites, lighter micro-sized spots are visible, corresponding to $P_2W_{12}Mo_6$ clusters, contributing to the overall roughened texture. Figure 3(a–c) demonstrate a clear uniformity in the widths of the carbon nanotubes, with diameters ranging between 5–22 nm. In Figure 3 (d), folded graphene sheets and a smoother texture can be observed. Supplementary Figure S10 displays SEM images of MWCNT_N8, MWCNT_N6, MWCNT_S6, and GF_S6, exhibiting similar morphological characteristics as described above.

EDX elemental mapping was employed to investigate the spatial distribution of $P_2W_{12}Mo_6$ within the composite materials. Figure 4 presents the SEM and corresponding elemental mapping images specifically for $P_2W_{12}Mo_6$@MWCNT_N8, while Supplementary Figures S11, S12, and S13 showcase the mapping images for the $P_2W_{12}Mo_6$@MWCNT_N6, $P_2W_{12}Mo_6$@MWCNT_S6, and $P_2W_{12}Mo_6$@GF_S6 composites, respectively. The elemental mapping analysis revealed a homogeneous dispersion of the POM elements (W, P, Mo, and O) throughout the carbon matrix, indicating the successful immobilisation of the POM species. The brighter regions observed in the elemental mapping images correspond to the localised accumulation of $P_2W_{12}Mo_6$ clusters.

The composites were also characterized by XRD (Figure S14). The analyzed composites present peaks at a 25.8°


© 2024 The Authors. ChemElectroChem published by Wiley-VCH GmbH

ChemElectroChem
Research Article
doi.org/10.1002/celc.202300622
Chemistry Europe
European Chemical Societies Publishing

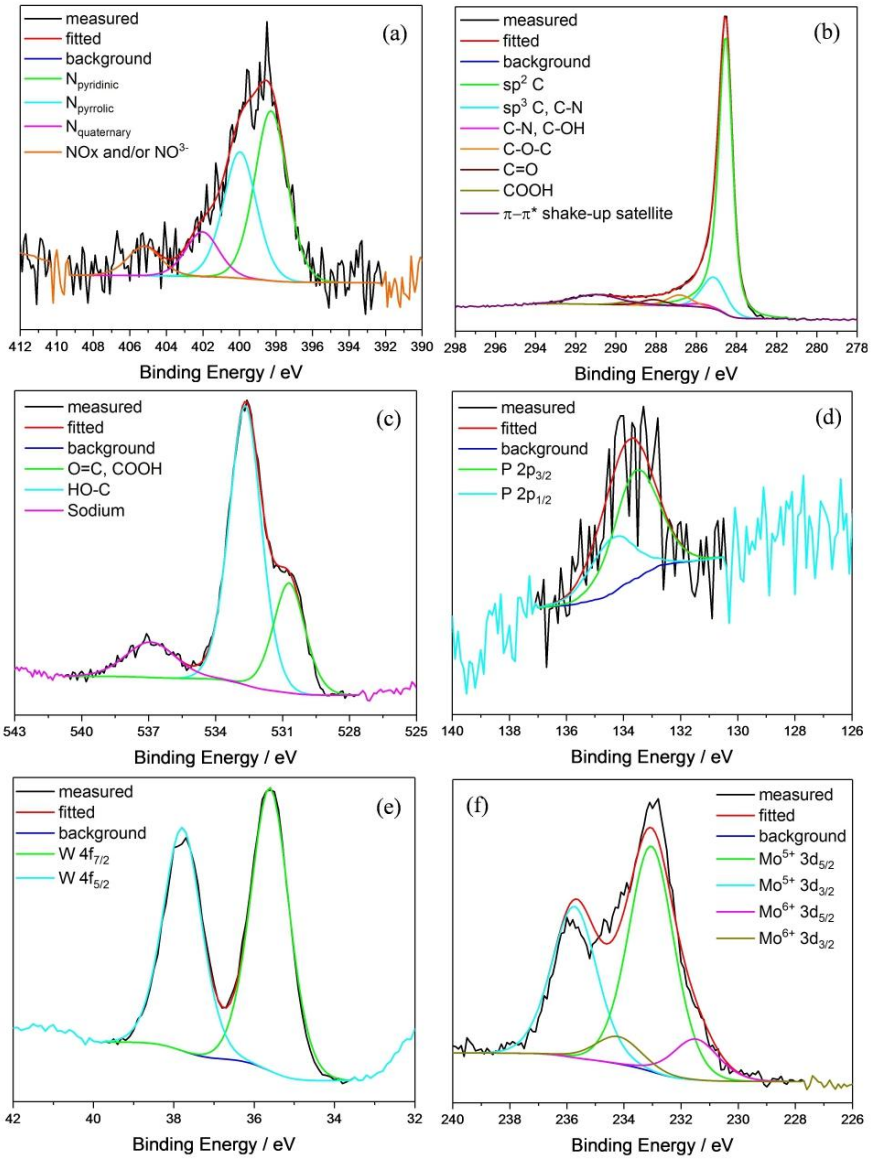



**Figure 2.** XPS deconvoluted spectra of the corresponding elements of $P_2W_{12}Mo_6$@MWCNT_N8.

angle corresponding to (002) planes of graphitic framework and at 43.1° which are indexed to the 002 graphite planes. The narrower and more prominent peak displayed in GF_S6 may indicate a higher level of crystallinity in the graphitic framework, as anticipated, contrasted with MWCNT_N8 and MWCNT_S6.


© 2024 The Authors. ChemElectroChem published by Wiley-VCH GmbH

21960216, 2024, 4, Downloaded from https://chemistry-europe.onlinelibrary.wiley.com/doi/10.1002/celc.202300622 by Cochrane Portugal, Wiley Online Library on [02/04/2025]. See the Terms and Conditions (https://onlinelibrary.wiley.com/terms-and-conditions) on Wiley Online Library for rules of use; OA articles are governed by the applicable Creative Commons License

ChemElectroChem
Research Article
doi.org/10.1002/celc.202300622
Chemistry Europe
European Chemical Societies Publishing

21960216, 2024, 4, Downloaded from https://chemistry-europe.onlinelibrary.wiley.com/doi/10.1002/celc.202300622 by Cochrane Portugal, Wiley Online Library on [02/04/2025]. See the Terms and Conditions (https://onlinelibrary.wiley.com/terms-and-conditions) on Wiley Online Library for rules of use; OA articles are governed by the applicable Creative Commons License

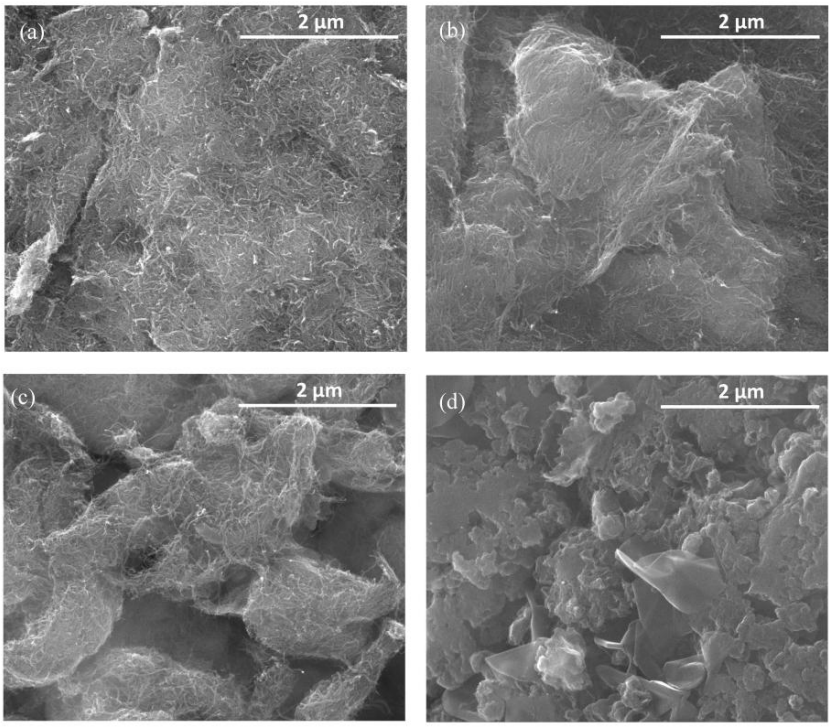



**Figure 3.** SEM images of $P_2W_{12}Mo_6$@MWCNT_N8 (a), $P_2W_{12}Mo_6$@MWCNT_N6 (b), $P_2W_{12}Mo_6$@MWCNT_S6 (c) and $P_2W_{12}Mo_6$@GF_S6 (d) at 50000× magnification.

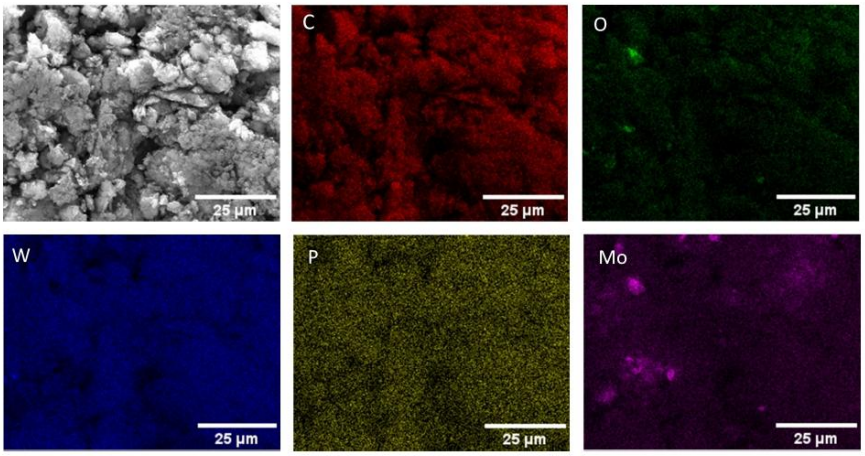



**Figure 4.** SEM and EDX elemental mapping images of $P_2W_{12}Mo_6$@MWCNT_N8, at 5000× magnification for the elements C (red), O (green), W (blue), P (yellow) and Mo (purple).


© 2024 The Authors. ChemElectroChem published by Wiley-VCH GmbH

ChemElectroChem
Research Article
doi.org/10.1002/celc.202300622
Chemistry Europe
European Chemical Societies Publishing

21960216, 2024, 4, Downloaded from https://chemistry-europe.onlinelibrary.wiley.com/doi/10.1002/celc.202300622 by Cochrane Portugal, Wiley Online Library on [02/04/2025]. See the Terms and Conditions (https://onlinelibrary.wiley.com/terms-and-conditions) on Wiley Online Library for rules of use; OA articles are governed by the applicable Creative Commons License

### Electrochemical performance towards the ORR

The electrocatalytic activity towards the ORR of the prepared composites was initially investigated using cyclic voltammetry (CV) in $N_2$- and $O_2$-saturated KOH solutions (0.1 M). The N and S-doped carbon materials were also examined under identical experimental conditions for comparative analysis. Figure 5 illustrates the CVs obtained in $N_2$- and $O_2$-saturated electrolytes for the prepared nanocomposites. It is evident that in the $N_2$-saturated electrolyte, no reduction peak associated with oxygen reduction is observed. However, in the $O_2$-saturated electrolyte, all four composites exhibit an irreversible peak corresponding to the reduction of oxygen. Specifically, the reduction peaks are observed at $E_{pc} = 0.81$, 0.79, 0.70, and 0.71 V vs. RHE for $P_2W_{12}Mo_6$@MWCNT_N8, $P_2W_{12}Mo_6$@MWCNT_N6, $P_2W_{12}Mo_6$@MWCNT_S6, and $P_2W_{12}Mo_6$@GF_S6, respectively. The CVs for MWCNT_N8, MWCNT_N6, MWCNT_S6, and GF_S6 in the same experimental conditions are shown in Figure S15(a–d) in the supplementary information. These materials exhibit ORR peaks at $E_{pc}$ values of 0.79, 0.77, 0.70, and 0.72 V vs. RHE, respectively. Furthermore, the performance of Pt/C (20 wt%) was evaluated and found to closely resemble that of the composites ($E_{pc} = 0.86$ V vs. RHE) (Figure S15(e)).

In order to gain deeper insights into the electrocatalytic performance of all carbon materials and $P_2W_{12}Mo_6$@CM nanocomposites towards the ORR, linear sweep voltammetry (LSV) was performed at 1600 rpm in an $O_2$-saturated KOH solution (0.1 mol dm$^{-3}$). The LSV curves, as depicted in Figure 6 (a), were obtained after subtracting the blanks (obtained in $N_2$-saturated KOH solution) from the corresponding $O_2$-saturated KOH curves. Table 2 presents the key ORR parameters acquired, including the onset potential ($E_{onset}$), the half-wave potential ($E_{1/2}$), the Tafel slopes (TS), and the number of electrons transferred per oxygen molecule ($n_{O2}$). Even though a diffusion-limiting current density plateau was not reached for our materials, we measured the values of current density obtained at 0.26 V vs RHE for a rotation speed of 1600 rpm ($j_{L\,0.26\,V,\,1600\,rpm}$). These are also included in Table 2. The electrocatalytic activity of the pristine carbon materials is significantly enhanced upon nitrogen and sulphur doping, corroborating the findings from various studies that have reported improved ORR performance upon N- and S-doping of similar carbon materials.[19,32,33,71–74] This observed enhancement underscores the potential of N- and S-doping as effective strategies for enhancing the ORR electrocatalytic performance of carbon-based materials. Upon N-doping, both MWCNT_N8 and MWCNT_N6 exhibited a positive shift of $E_{onset}$ by 14 mV and 12 mV, respectively, compared to pristine carbon

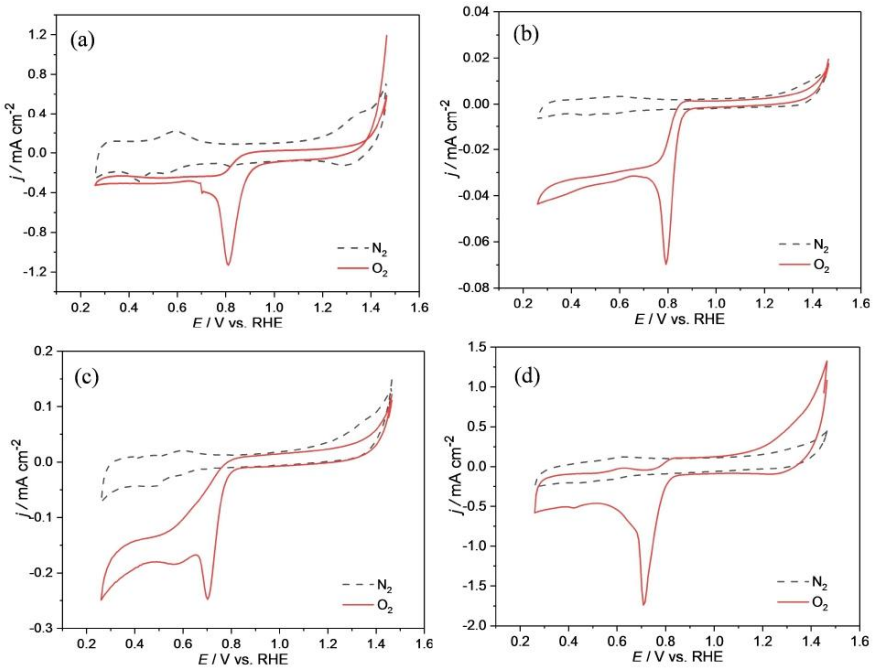



**Figure 5.** CVs of $P_2W_{12}Mo_6$@MWCNT_N8 (a), $P_2W_{12}Mo_6$@MWCNT_N6 (b), $P_2W_{12}Mo_6$@MWCNT_S6 (c) and $P_2W_{12}Mo_6$@GF_S6 (d) modified electrodes in $N_2$-saturated (dash line) and $O_2$-saturated (full line) 0.1 mol dm$^{-3}$ KOH solution at 0.005 V s$^{-1}$.


© 2024 The Authors. ChemElectroChem published by Wiley-VCH GmbH

ChemElectroChem
Research Article
doi.org/10.1002/celc.202300622
Chemistry Europe
European Chemical Societies Publishing

21960216, 2024, 4, Downloaded from https://chemistry-europe.onlinelibrary.wiley.com/doi/10.1002/celc.202300622 by Cochrane Portugal, Wiley Online Library on [02/04/2025]. See the Terms and Conditions (https://onlinelibrary.wiley.com/terms-and-conditions) on Wiley Online Library for rules of use; OA articles are governed by the applicable Creative Commons License

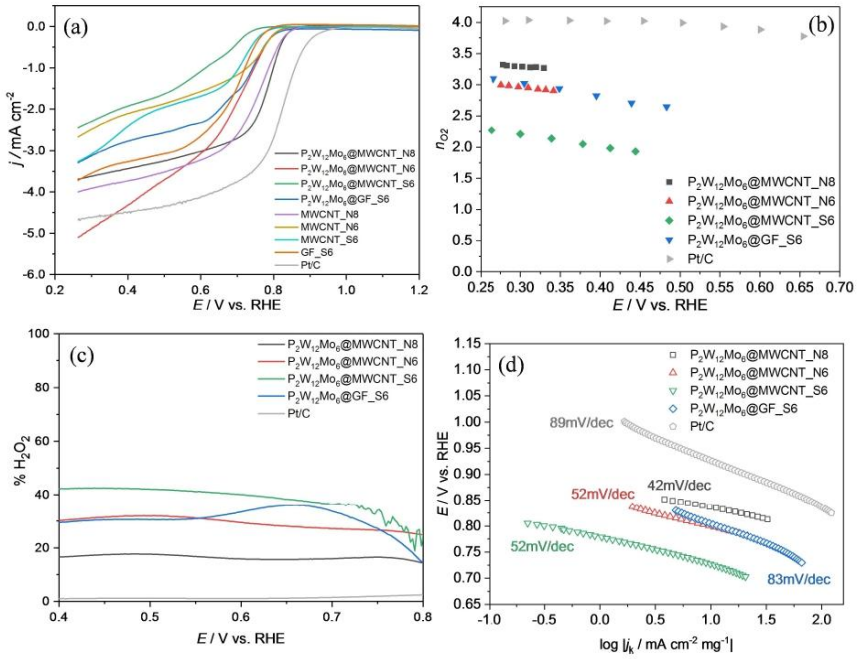



**Figure 6.** ORR LSV curves acquired using an RDE in $O_2$-saturated KOH solution (0.1 mol dm$^{-3}$) at 1600 rpm and 0.005 V s$^{-1}$ of commercial Pt/C (20 wt%), $P_2W_{12}Mo_6$@CM nanocomposites and doped-nitrogen and sulphur carbon materials (a); $n_{O2}$ at several potential values (b); estimated percentage of $H_2O_2$ produced with RRDE for $P_2W_{12}Mo_6$@CM and Pt/C (20 wt%) in $O_2$-saturated 0.1 mol dm$^{-3}$ KOH solution, at 1600 rpm; the disk potential was swept at v = 0.005 V s$^{-1}$ and the ring potential was kept at E = 0.2 V versus Ag/AgCl (c); ORR Tafel plots for $P_2W_{12}Mo_6$@CM obtained from LSV data in Figure 6 (a) where current densities are normalised to the mass of each ECs (d).

**Table 2.** Main ORR parameters obtained from polarisation curves recorded in $O_2$-saturated 0.1 mol dm$^{-3}$ KOH solution for the different materials tested.

| Samples | $E_{onset}$ vs RHE (V) | $j_L$ (mA cm$^{-2}$) | Tafel slope (mV dec$^{-1}$) | $n_{O2}$ | $E_{1/2}$ (V) |
|---|---|---|---|---|---|
| Pt/C | 0.94 | −4.7 | 89 | 4.0 | 0.82 |
| GF | 0.72 | −2.0 | 63 | 2.4 | 0.60 |
| MWCNT | 0.69 | −2.0 | 54 | 2.1 | 0.57 |
| GF_S6 | 0.77 | −3.7 | 50 | 4.0 | 0.68 |
| MWCNT_S6 | 0.77 | −3.3 | 49 | 3.0 | 0.62 |
| MWCNT_N6 | 0.81 | −2.7 | 37 | 2.3 | 0.67 |
| MWCNT_N8 | 0.83 | −4.0 | 47 | 3.5 | 0.74 |
| $P_2W_{12}Mo_6$@GF_S6 | 0.73 | −3.2 | 83 | 2.9 | 0.70 |
| $P_2W_{12}Mo_6$@MWCNT_S6 | 0.74 | −2.4 | 52 | 2.1 | 0.73 |
| $P_2W_{12}Mo_6$@MWCNT_N6 | 0.79 | −5.1 | 52 | 3.0 | 0.76 |
| $P_2W_{12}Mo_6$@MWCNT_N8 | 0.84 | −3.7 | 42 | 3.3 | 0.79 |

materials. Additionally, the diffusion-limiting current density doubled for MWCNT_N8 and increased by 1.35 times for MWCNT_N6. These enhancements suggest that the incorporation of nitrogen atoms introduced favourable interactions with $O_2$ molecules, thereby promoting the ORR mechanism through rearrangement of the neighbouring atoms' electronic structure.[75] For all of the N-doped materials tested, the proportion of N-functionalities increases in a consistent order:


© 2024 The Authors. ChemElectroChem published by Wiley-VCH GmbH

ChemElectroChem
Research Article
doi.org/10.1002/celc.202300622
Chemistry Europe
European Chemical Societies Publishing

21960216, 2024, 4, Downloaded from https://chemistry-europe.onlinelibrary.wiley.com/doi/10.1002/celc.202300622 by Cochrane Portugal, Wiley Online Library on [02/04/2025]. See the Terms and Conditions (https://onlinelibrary.wiley.com/terms-and-conditions) on Wiley Online Library for rules of use; OA articles are governed by the applicable Creative Commons License

[N-oxides/nitrates] < [quaternary N] < [pyrrolic N] < [pyridinic N]. Nitrogen species, especially pyridinic and quaternary ones, are involved in ORR. Our previous research has demonstrated a positive correlation between the quantity of pyridinic nitrogen and ORR activity in carbon materials doped with nitrogen.[19,23] Similarly, S-doping resulted in significant improvements in ORR performance. Both MWCNT_S6 and GF_S6 exhibited an $E_{onset}$ value of 0.77 V, indicating a substantial positive shift compared to the pristine materials (80 and 50 mV, respectively). A significant increase in the magnitude of the limiting current density was observed (65% for MWCNT_S6 and 85% for GF_S6), with values of 3.3 and 3.7 mA cm$^{-2}$ for MWCNT_S6 and GF_S6, respectively. The electronegativity of sulphur being close to that of carbon had a lesser influence on the charge density of the carbon framework after doping. Species containing sulphur, such as thiophene S or sulphur oxide, positioned at the boundaries of carbon structures, exhibit electrocatalytic activity, especially in the context of GF_S6. Nevertheless, the introduction of sulphur doping triggers modifications in the spin density of carbon materials, thereby generating active sites for the chemisorption of $O_2$. This leads to an enhancement in the performance of the ORR.[32,65,73,74]

The $P_2W_{12}Mo_6$@CM doped with nitrogen-based nanocomposites displayed good electrocatalytic activity. Among the $P_2W_{12}Mo_6$@CM derivatives, $P_2W_{12}Mo_6$@MWCNT_N6 and $P_2W_{12}Mo_6$@MWCNT_N8 exhibited particularly encouraging results, with $E_{onset}$ values of 0.79 V and 0.84 V vs. RHE, respectively, being the closest to the reference $E_{onset}$ value of 0.94 V vs. RHE observed for Pt/C. The difference is even smaller if the $E_{1/2}$ values are compared with 0.76 V and 0.79 V for $P_2W_{12}Mo_6$@MWCNT_N6 and $P_2W_{12}Mo_6$@MWCNT_N8 and 0.82 V for Pt/C. Moreover, among the investigated materials, $P_2W_{12}Mo_6$@MWCNT_N6 demonstrated the highest $j_L$ value of −5.1 mA cm$^{-2}$, surpassing even the Pt/C value of −4.7 mA cm$^{-2}$. This indicates its superior ability to facilitate the ORR process and sustain high current densities, thereby outperforming the benchmark catalyst in this regard. $P_2W_{12}Mo_6$@MWCNT_N8 and $P_2W_{12}Mo_6$@GF_S6 also exhibited noteworthy $j_L$ values of −3.7 mA cm$^{-2}$ and −3.2 mA cm$^{-2}$, respectively, further highlighting their good ORR activity. Finally, $P_2W_{12}Mo_6$@MWCNT_S6 showed the lowest $j_L$ value of −2.4 mA cm$^{-2}$. Figure 6 (b) shows the number of electrons transferred per oxygen molecule for the N and S-doped CMs and their respective composites. These results were obtained by applying the Koutecky-Levich (K–L) equation to the LSVs ate different rotation speeds (see Figures S16 to S20 and section 1.3 in SI file for more details). The data obtained for $P_2W_{12}Mo_6$@MWCNT_N8 and MWCNT_N8 indicate that the redox processes are nearly 4-electrons. Conversely, $P_2W_{12}Mo_6$@MWCNT_N6 and MWCNT_N6 show a mixed redox process involving 2- and 4-electrons, as confirmed by the $n_{O2}$ values. Interestingly, the POM immobilisation improved the $n_{O2}$ value in the MWCNT_N6 composite, implying an enhancement in its electrocatalytic performance. The behaviour of the doped-nitrogen carbon materials after POM immobilisation appears to be similar, with the active sites arising from the POM immobilisation possibly compensating for the loss of N-induced active sites.[19,33,38] Contrary to expectations, the immobilisation of $P_2W_{12}Mo_6$ did not lead to the expected improvement in the electrochemical parameters of GF_S6 and MWCNT_S6. This observation suggests that the immobilisation process may not have resulted in effective interactions between $P_2W_{12}Mo_6$ and the composites, potentially hindering their catalytic activity as electrocatalysts.

In an alkaline medium, the oxygen reduction reaction can proceed through either an indirect (2-electron) pathway involving the reduction of $O_2$ to $HO_2^-$ and subsequent reduction to $H_2O/HO^-$, or a more desirable direct pathway where $O_2$ is directly reduced to $H_2O/HO^-$.[76] To assess comprehensively the ECs, it is crucial to determine the percentage of $H_2O_2$ produced during the ORR process. The percentage of $H_2O_2$ was calculated using Eq. 4 (see SI) at various potential values (Figure 6(c)). Among the composites studied, $P_2W_{12}Mo_6$@MWCNT_N8 showed the lowest percentage of $H_2O_2$ produced (17.7%), which aligns with its $n_{O2}$ value ($n_{O2}$ = 3.3). $P_2W_{12}Mo_6$@MWCNT_N6, $P_2W_{12}Mo_6$@MWCNT_S6 and $P_2W_{12}Mo_6$@GF_N6 showed percentages of 32.0%, 42.4% and 36.0% respectively. While the results are consistent, caution must be exercised when directly comparing these two methods, as both have limitations.[72,77,78] Firstly, the oxidation process of hydrogen peroxide on the platinum electrocatalyst is not a mass-transfer limited process. Secondly, the SEM images reveal a rough structure of the support material and a heterogeneity of clusters of the immobilised POM in the prepared electrocatalysts. This structural variability may alter the electrode geometry and introduce turbulence in the electrolyte flow, leading to estimated $n_{O2}$ values that may not fully reflect the actual electrocatalytic performance of the ORR.[33]

To gain deeper insights into the reaction kinetics, Tafel plots of the prepared nanocomposites and the Pt/C reference were derived from the LSV curves in $O_2$-saturated KOH at 1600 rpm, as shown in Figure 6(d). Remarkably, all the investigated materials exhibited lower Tafel slopes when compared to Pt/C (89 mV dec$^{-1}$), with $P_2W_{12}Mo_6$@MWCNT_N8 displaying the most favourable Tafel value (42 mV dec$^{-1}$). These results suggest that oxygen molecules undergo facile adsorption and activation at the surface of the nanocomposites, indicating efficient catalytic sites for the ORR. The lower Tafel slopes in the prepared nanocomposites imply enhanced reaction kinetics, favouring either the conversion of $MOO^-$ species to MOOH (where M represents an empty site on the electrocatalyst surface) or the initial discharge step.[23,33,38]

The linear relationship between the double layer capacitance ($C_{dl}$) and the electrochemically active surface area (ECSA), coupled with the similar nature of the electrocatalysts used in this investigation, facilitates a direct comparison of the $C_{dl}$ values obtained for the composites.[79–82] By performing CV measurements at varying scan rates, we estimated the $C_{dl}$ values from the slopes of the linear fittings of the CV current densities (measured at the same potential of 1.13 V vs. RHE in a non-faradaic region) obtained at different scan rates for both the composites and their corresponding nitrogen and sulphur-doped carbon materials (for experimental details, see SI file section 1.4 and Figures S21 and S22). However, it is important to note that the $C_{dl}$ should be interpreted as an estimate of the


© 2024 The Authors. ChemElectroChem published by Wiley-VCH GmbH

ChemElectroChem
Research Article
doi.org/10.1002/celc.202300622
Chemistry Europe
European Chemical Societies Publishing

21960216, 2024, 4, Downloaded from https://chemistry-europe.onlinelibrary.wiley.com/doi/10.1002/celc.202300622 by Cochrane Portugal, Wiley Online Library on [02/04/2025]. See the Terms and Conditions (https://onlinelibrary.wiley.com/terms-and-conditions) on Wiley Online Library for rules of use; OA articles are governed by the applicable Creative Commons License

number of electrocatalytically active sites accessible to a specific electrocatalyst.[83] As shown in Table 3, a noticeable increase in the number of active sites was observed upon immobilisation of the POM ($P_2W_{12}Mo_6$) for all the composites. The extent of this increase was most pronounced for the $P_2W_{12}Mo_6$@MWCNT_N8 composite, with a composite/carbon support $C_{dl}$ ratio of 2.00. These findings suggest the enhanced accessibility and availability of electrocatalytically active sites resulting from the incorporation of $P_2W_{12}Mo_6$ into the nanocomposite structures.

In the evaluation of an electrocatalyst's potential for ORR, assessing its stability is of paramount importance. To investigate thoroughly this aspect, chronoamperometry (CA) was performed at E = 0.46 V vs. RHE for 36000 s at 1600 rpm in an oxygen-saturated alkaline electrolyte (Figure 7 (a)). Among the nanocomposites studied, $P_2W_{12}Mo_6$@MWCNT_N8 showed the highest stability, with a current retention of 81%. Following closely, both $P_2W_{12}Mo_6$@MWCNT_N6 and $P_2W_{12}Mo_6$@GF_S6 showed identical current retention values of 76%. In contrast, $P_2W_{12}Mo_6$@MWCNT_S6 exhibited a slightly lower current retention of 63%. This variation in stability could be attributed to the distinct interactions between the POM and its respective doped carbon supports. Still, the good stability of most composites can be attributed to the effective trapping of POM particles within the nano-networks of the carbon materials, effectively preventing (or at least limiting) their migration, aggregation, and leaching into the electrolyte. This, in turn, ensures that the stability of the corresponding support materials remains unaffected. Additionally, the high degree of graphitisation and/or ordered wall structure of the carbon materials contributes to the reduced likelihood of composite degradation, further enhancing their durability and long-term stability.[84,86]

Methanol, an excellent hydrogen carrier fuel with potential for sustainable and low-carbon pathways, holds promise as a carrier of carbon-neutral hydrogen.[87] Consequently, studying the methanol tolerance of electrocatalysts in methanol fuel cells assumes paramount importance. Methanol crossover from the anode to the cathode can severely compromise cathodic performance if the electrocatalysts are sensitive to it.[88] Although Pt-based materials offer superior performance in alkaline media compared to most electrocatalysts studied, they suffer from a significant drawback: heightened responsiveness to methanol oxidation reactions.[89] This vulnerability negatively impacts their ORR performance, leading to reduced current density outputs. Therefore, evaluating the methanol tolerance of the electrocatalysts becomes essential for their practical application. To assess methanol tolerance, CA was performed in $O_2$-saturated 0.1 mol $dm^{-3}$ KOH, in the presence of methanol (0.5 mol $dm^{-3}$) for both Pt/C and $P_2W_{12}Mo_6$@CM composites, over a period of 2500 s (Figure 7(b)). Notably, methanol was introduced 500 s after the onset of CA. The results revealed a significant difference in methanol tolerance between Pt/C and the composites. While Pt/C retained only approximately 70% of its initial current density, the composites exhibited higher retention rates, ranging from ~86% to ~92%. This enhanced methanol tolerance represents a key advantage of using this kind of composites. The improved methanol tolerance of

**Table 3.** Electrocatalytically active surface area (ECSA) values of the carbon supports and the corresponding POM-based composites.

| CM support | $C_{dl}$ (mF $cm^{-2}$) | Composite | $C_{dl}$ (mF $cm^{-2}$) | Composite/Carbon Support $C_{dl}$ Ratio |
|---|---|---|---|---|
| MWCNT_N8 | 0.0203 | $P_2W_{12}Mo_6$@MWCNT_N8 | 0.0411 | 2.00 |
| MWCNT_N6 | 0.0108 | $P_2W_{12}Mo_6$@MWCNT_N6 | 0.0105 | 0.97 |
| MWCNT_S6 | 0.0054 | $P_2W_{12}Mo_6$@MWCNT_S6 | 0.0092 | 1.80 |
| GF_S6 | 0.0138 | $P_2W_{12}Mo_6$@GF_S6 | 0.0254 | 1.70 |

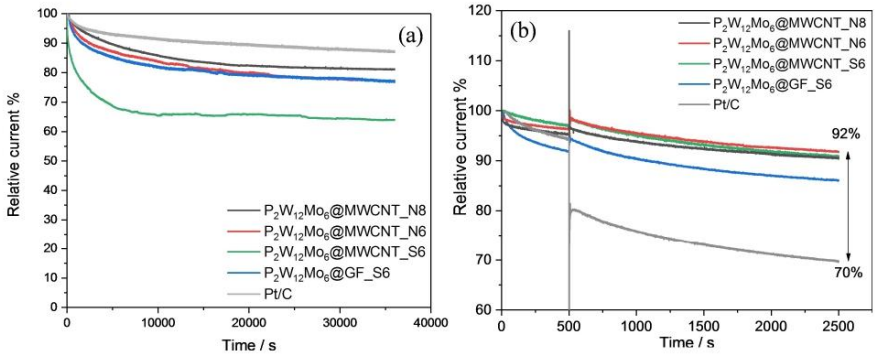



**Figure 7.** Chronoamperometric response of the ECs at 1600 rpm, in 0.1 mol $dm^{-3}$ $O_2$-saturated KOH at: $E = 0.46$ V vs. RHE for 36000s (a) and $E = 0.46$ V vs. RHE with the addition of 0.5 mol $dm^{-3}$ methanol after ≈500 s (b).


© 2024 The Authors. ChemElectroChem published by Wiley-VCH GmbH

ChemElectroChem | Research Article
doi.org/10.1002/celc.202300622
Chemistry Europe
European Chemical Societies Publishing

21960216, 2024, 4, Downloaded from https://chemistry-europe.onlinelibrary.wiley.com/doi/10.1002/celc.202300622 by Cochrane Portugal, Wiley Online Library on [02/04/2025]. See the Terms and Conditions (https://onlinelibrary.wiley.com/terms-and-conditions) on Wiley Online Library for rules of use; OA articles are governed by the applicable Creative Commons License

$P_2W_{12}Mo_6$@CM composites holds significant implications for their application in methanol fuel cells. By minimising the detrimental impact of methanol crossover on the cathodic performance, these materials pave the way for more efficient and reliable fuel cell technologies. The ability to retain higher current densities in the presence of methanol bodes well for the practical implementation of these composites in real-world energy conversion devices.

## Conclusions

The study involved the immobilisation of the POM ($P_2W_{12}Mo_6$) onto nitrogen-doped multi-walled carbon nanotubes (MWCNT_N8 and MWCNT_N6), sulphur-doped multi-walled carbon nanotubes (MWCNT_S6), and sulphur-doped graphene (GF_S6) at varying calcination temperatures. The materials were extensively characterised using various analytical techniques, including FTIR, XPS, SEM, and EDX mapping proving that all composites were successfully synthesised. Electrochemical performance towards the ORR was investigated using cyclic voltammetry and linear sweep voltammetry in $O_2$-saturated KOH solution. The nanocomposites displayed excellent electrocatalytic activity for the ORR, with some composites approaching the performance of the Pt/C catalyst. $P_2W_{12}Mo_6$@MWCNT_N8 and $P_2W_{12}Mo_6$@MWCNT_N6 showed particularly encouraging results, with onset potentials close to Pt/C, significantly high diffusion-limiting current densities and low Tafel slopes. The nitrogen and sulphur-doped carbon materials demonstrated enhanced ORR performance compared to the pristine carbon materials, validating the effectiveness of N- and S-doping strategies. Through the analysis of Koutecky-Levich plots, it was determined that the ORR follows a mixed electron process, a conclusion further supported by the $\%H_2O_2$ production results. The composite $P_2W_{12}Mo_6$@MWCNT_N8 exhibited an enduring electrocatalytic performance over 36000 seconds, retaining a high value of 81%. This achievement is quite close to the performance of the commercial Pt/C catalyst, which reached 86% retention. These findings underscore the robustness of the $P_2W_{12}Mo_6$@MWCNT_N8 composite and its potential as a viable alternative to traditional Pt/C in electrocatalytic applications. Moreover, the composites display remarkable methanol tolerance (86-92%), demonstrating a high selectivity for the ORR. This accomplishment addresses a significant limitation of the Pt/C electrocatalyst, marking a substantial advancement. The study's findings represent a significant step forward in the development of novel, cost-effective, and long-lasting electrocatalysts that are free of noble metals.

**Funding**: This work was financially supported by: Project UNIRCELL POCI-01-0145-FEDER-16422, funded by FEEI through Programa operacional Competitividade e Internacionalização-COMPETE2020 and by national funds through FCT - Fundação para a Ciência e a Tecnologia, I.P.

### Acknowledgements

Thanks are also due to PT national funds FCT/MCTES through the projects UIDB/50006/2020, UIDP/50006/2020 as well as to Campus France – project PHC Pessoa 42341RM (O2@nano-CPOM). Thanks are also due to the FCT project FOAM4ENER PTDC/QUI-ELT/28299/2017. H.C.N. thanks the FCT through ChemMat program for his PhD grant PD/BD/143095/2018. D.M.F. thanks FCT/MCTES for funding through the Individual Call to Scientific Employment Stimulus (2021.00771.CEECIND/CP1662/CT0007). I.-M M., A.-L.T. and P.d.O. thank the CNRS (namely its IEA programme) and the Université Paris-Saclay for financial support.

### Conflict of Interests

The authors declare no conflict of interest.

### Data Availability Statement

The data that support the findings of this study are available from the corresponding author upon reasonable request.

**Keywords:** Oxygen Reduction Reaction · Electrocatalysis · Carbon Materials · Polyoxometalate

[1] F. Perera, *Int. J. Environ. Res. Public Health* **2018**, *15*, 16.
[2] F. Dawood, M. Anda, G. Shafiullah, *Int. J. Hydrogen Energy* **2020**, *45*, 3847–3869.
[3] K. Alanne, S. Cao, *Appl. Energy* **2019**, *238*, 284–302.
[4] Y. Nie, L. Li, Z. Wei, *Chem. Soc. Rev.* **2015**, *44*, 2168–2201.
[5] J. Stacy, Y. N. Regmi, B. Leonard, M. Fan, *Renewable Sustainable Energy Rev.* **2017**, *69*, 401–414.
[6] W. Xia, A. Mahmood, Z. Liang, R. Zou, S. Guo, *Angew. Chem. Int. Ed.* **2016**, *55*, 2650–2676.
[7] F. Guo, M. Zhang, S. Yi, X. Li, R. Xin, M. Yang, B. Liu, H. Chen, H. Li, Y. Liu, *Nano Res. Energy* **2022**, *1*, 9120027.
[8] M. Kuang, G. Zheng, *Small* **2016**, *12*, 5656–5675.
[9] J. K. Nørskov, T. Bligaard, J. Rossmeisl, C. H. Christensen, *Nat. Chem.* **2009**, *1*, 37–46.
[10] C. Wang, D. Wang, S. Liu, P. Jiang, Z. Lin, P. Xu, K. Yang, J. Lu, H. Tong, L. Hu, W. Zhang, Q. Chen, *J. Catal.* **2020**, *389*, 150–156.
[11] V. Stamenkovic, B. S. Mun, K. J. J. Mayrhofer, P. N. Ross, N. M. Markovic, J. Rossmeisl, J. Greeley, J. K. Nørskov, *Angew. Chem. Int. Ed.* **2006**, *45*, 2897–2901.
[12] L. Liao, X. Bian, J. Xiao, B. Liu, M. D. Scanlon, H. H. Girault, *Phys. Chem. Chem. Phys.* **2014**, *16*, 10088–10094.
[13] F. H. B. Lima, J. Zhang, M. H. Shao, K. Sasaki, M. B. Vukmirovic, E. A. Ticianelli, R. R. Adzic, *J. Phys. Chem. C* **2007**, *111*, 404–410.
[14] Y. Cheng, H. Wang, H. Song, K. Zhang, G. I. N. Waterhouse, J. Chang, Z. Tang, S. Lu, *Nano Res. Energy* **2023**, *2*, e9120082.
[15] C. Freire, D. M. Fernandes, M. Nunes, V. K. Abdelkader, *ChemCatChem* **2018**, *10*, 1703–1730.
[16] H. Lin, J.-W. Wang, X.-W. Guo, S. Yao, M. Liu, Z.-M. Zhang, T.-B. Lu, *J. Mater. Chem. A* **2018**, *6*, 24479–24485.
[17] S. Zhang, O. Oms, L. Hao, R. Liu, M. Wang, Y. Zhang, H.-Y. He, A. Dolbecq, J. Marrot, B. Keita, *ACS Appl. Mater. Interfaces* **2017**, *9*, 38486–38498.
[18] D. M. Fernandes, M. P. Araujo, A. Haider, A. S. Mougharbel, A. J. Fernandes, U. Kortz, C. Freire, *ChemElectroChem* **2018**, *5*, 273–283.
[19] H. C. Novais, B. Jarrais, A. Haider, U. Kortz, A. Guerrero-Ruiz, I. Rodríguez-Ramos, C. Freire, D. M. Fernandes, *Electrocatalysis* **2023**, *14*, 294–305.


© 2024 The Authors. ChemElectroChem published by Wiley-VCH GmbH

ChemElectroChem
Research Article
doi.org/10.1002/celc.202300622
Chemistry Europe
European Chemical Societies Publishing

21960216, 2024, 4, Downloaded from https://chemistry-europe.onlinelibrary.wiley.com/doi/10.1002/celc.202300622 by Cochrane Portugal, Wiley Online Library on [02/04/2025]. See the Terms and Conditions (https://onlinelibrary.wiley.com/terms-and-conditions) on Wiley Online Library for rules of use; OA articles are governed by the applicable Creative Commons License

[20] S.-A. Wohlgemuth, R. J. White, M.-G. Willinger, M.-M. Titirici, M. Antonietti, *Green Chem.* **2012**, *14*, 1515–1523.
[21] L. Qu, Y. Liu, J.-B. Baek, L. Dai, *ACS Nano* **2010**, *4*, 1321–1326.
[22] Z. Chen, D. Higgins, Z. Chen, *Carbon* **2010**, *48*, 3057–3065.
[23] H. C. Novais, B. Jarrais, I.-M. Mbomekallé, A.-L. Teillout, P. d. Oliveira, C. Freire, D. M. Fernandes, *Inorganics* **2023**, *11*, 388.
[24] M. K. Debe, *Nature* **2012**, *486*, 43–51.
[25] B. C. Steele, A. Heinzel, *Nature* **2001**, *414*, 345–352.
[26] H. A. Gasteiger, S. S. Kocha, B. Sompalli, F. T. Wagner, *Appl. Catal. B* **2005**, *56*, 9–35.
[27] H. Wang, L. R. Grabstanowicz, H. M. Barkholtz, D. Rebollar, Z. B. Kaiser, D. Zhao, B.-H. Chen, D.-J. Liu, *ACS Energy Lett.* **2019**, *4*, 2500–2507.
[28] J. Yan, F. Ye, Q. Dai, X. Ma, Z. Fang, L. Dai, C. Hu, *Nano Res. Energy* **2023**, *2*, e9120047.
[29] W. Zhang, W. Pu, Y. Qu, H. Yang, Y. Liu, *Electrochim. Acta* **2023**, *462*, 142800.
[30] I. Kone, A. Xie, Y. Tang, Y. Chen, J. Liu, Y. Chen, Y. Sun, X. Yang, P. Wan, *ACS Appl. Mater. Interfaces* **2017**, *9*, 20963–20973.
[31] D. Xu, W. D. Wu, in *Chalcogen Chemistry*, IntechOpen, **2018**.
[32] E. M. Macias, A. M. Valenzuela-Muñiz, G. Alonso-Núñez, M. H. F. Sánchez, R. Gauvin, Y. V. Gómez, *Diamond Relat. Mater.* **2020**, *103*, 107671.
[33] N. Limani, I. S. Marques, B. Jarrais, A. J. Fernandes, C. Freire, D. M. Fernandes, *Catalysts* **2022**, *12*, 357.
[34] P. M. Gíslason, E. Skúlason, *Nanoscale* **2019**, *11*, 18683–18690.
[35] H. Vrubel, X. Hu, *Angew. Chem. Int. Ed.* **2012**, *51*, 12703–12706.
[36] A. Navaee, A. Salimi, S. Soltanian, P. Servati, *J. Power Sources* **2015**, *277*, 268–276.
[37] B. Olalde, J. M. Aizpurua, A. García, I. Bustero, I. Obieta, M. J. Jurado, *J. Phys. Chem. C* **2008**, *112*, 10663–10667.
[38] D. M. Fernandes, C. Freire, *ChemElectroChem* **2015**, *2*, 269–279.
[39] N. Daems, X. Sheng, I. F. Vankelecom, P. P. Pescarmona, *J. Mater. Chem. A* **2014**, *2*, 4085–4110.
[40] D. Lee, L. De Los Santos V, J. Seo, L. L. Felix, A. Bustamante D, J. Cole, C. Barnes, *J. Phys. Chem. B* **2010**, *114*, 5723–5728.
[41] A. Kumarasinghe, L. Samaranayake, F. Bondino, E. Magnano, N. Kottegoda, E. Carlino, U. Ratnayake, A. De Alwis, V. Karunaratne, G. A. Amaratunga, *J. Phys. Chem. C* **2013**, *117*, 9507–9519.
[42] A. Misra, P. K. Tyagi, M. K. Singh, D. S. Misra, *Diamond Relat. Mater.* **2006**, *15*, 385–388.
[43] B. Olalde, J. M. Aizpurua, A. García, I. Bustero, I. Obieta, M. J. Jurado, *J. Phys. Chem. C* **2008**, *112*, 10663–10667.
[44] Z. Tian, J. Li, G. Zhu, J. Lu, Y. Wang, Z. Shi, C. Xu, *Phys. Chem. Chem. Phys.* **2016**, *18*, 1125–1130.
[45] M. M. Doroodmand, S. Sobhani, A. Ashoori, *Can. J. Chem.* **2012**, *90*, 701–707.
[46] Y. Lou, H. Cai, X. Liu, S. Tu, K. Pei, Y. Zhao, G. Cao, S. Li, K. Qin, B. Cai, *Pharmacogn. Mag.* **2014**, *10*, S30.
[47] N. Daems, X. Sheng, I. F. J. Vankelecom, P. P. Pescarmona, *J. Mater. Chem. A* **2014**, *2*, 4085–4110.
[48] D. M. Fernandes, H. C. Novais, R. Bacsa, P. Serp, B. Bachiller-Baeza, I. Rodríguez-Ramos, A. Guerrero-Ruiz, C. Freire, *Langmuir* **2018**, *34*, 6376–6387.
[49] D. W. Lee, L. De Los Santos V, J. W. Seo, L. L. Felix, A. Bustamante D, J. M. Cole, C. H. W. Barnes, *J. Phys. Chem. B* **2010**, *114*, 5723–5728.
[50] A. R. Kumarasinghe, L. Samaranayake, F. Bondino, E. Magnano, N. Kottegoda, E. Carlino, U. N. Ratnayake, A. A. P. de Alwis, V. Karunaratne, G. A. J. Amaratunga, *J. Phys. Chem. C* **2013**, *117*, 9507–9519.
[51] R. Guerroudj, L. Dermeche, L. Mouheb, T. Mazari, C. Rabia, *Eurasia Proc. Sci. Technol. Eng. Math* **2022**, *20*, 1–9.
[52] M. R. Guerroudj, L. Dermeche, L. Mouheb, T. Mazari, S. Benadji, C. Rabia, *Bull. Chem. React. Eng. Catal* **2019**, *14*, 283–293.
[53] A. S. Aricò, P. Bruce, B. Scrosati, J.-M. Tarascon, W. van Schalkwijk, *Nat. Mater.* **2005**, *4*, 366–377.
[54] C. Freire, D. M. Fernandes, M. Nunes, V. K. Abdelkader, *ChemCatChem* **2018**, *10*, 1703–1730.
[55] B. Jarrais, A. Guedes, C. Freire, *ChemistrySelect* **2018**, *3*, 1737–1748.
[56] M.-C. Huang, H. Teng, *Carbon* **2003**, *41*, 951–957.
[57] K. Artyushkova, A. Serov, S. Rojas-Carbonell, P. Atanassov, *J. Phys. Chem. C* **2015**, *119*, 25917–25928.
[58] A. M. El-Sawy, I. M. Mosa, D. Su, C. J. Guild, S. Khalid, R. Joesten, J. F. Rusling, S. L. Suib, *Adv. Energy Mater.* **2016**, *6*, 1501966.
[59] M. Waqas, L. Wu, H. Tang, C. Liu, Y. Fan, Z. Jiang, X. Wang, J. Zhong, W. Chen, *ACS Appl. Nano Mater.* **2020**, *3*, 4788–4798.
[60] J.-J. Fan, Y.-J. Fan, R.-X. Wang, S. Xiang, H.-G. Tang, S.-G. Sun, *J. Mater. Chem. A* **2017**, *5*, 19467–19475.
[61] Y. Wang, B. Zhang, M. Xu, X. He, *RSC Adv.* **2015**, *5*, 86746–86753.
[62] H. Estrade-Szwarckopf, *Carbon* **2004**, *42*, 1713–1721.
[63] M. E. Lipińska, S. L. Rebelo, M. F. R. Pereira, J. Gomes, C. Freire, J. Figueiredo, *Carbon* **2012**, *50*, 3280–3294.
[64] W. Ai, Z. Luo, J. Jiang, J. Zhu, Z. Du, Z. Fan, L. Xie, H. Zhang, W. Huang, T. Yu, *Adv. Mater.* **2014**, *26*, 6186–6192.
[65] Y. Liu, Y. Qiao, G. Wei, S. Li, Z. Lu, X. Wang, X. Lou, *Energy Storage Mater.* **2018**, *11*, 274–281.
[66] H. C. Novais, D. M. Fernandes, C. Freire, *Appl. Surf. Sci.* **2015**, *347*, 40–47.
[67] K. Zilberberg, H. Gharbi, A. Behrendt, S. Trost, T. Riedl, *ACS Appl. Mater. Interfaces* **2012**, *4*, 1164–1168.
[68] R. Amin, M. A. Hossain, Y. Zakaria, *ACS Appl. Mater. Interfaces* **2018**, *10*, 13509–13518.
[69] H. N. Tran, S. Park, F. T. A. Wibowo, N. V. Krishna, J. H. Kang, J. H. Seo, H. Nguyen-Phu, S. Y. Jang, S. Cho, *Adv. Sci.* **2020**, *7*, 2002395.
[70] H. Wu, K. Lian, *ECS Trans.* **2014**, *58*, 67.
[71] I. M. Rocha, O. S. G. Soares, D. M. Fernandes, C. Freire, J. L. Figueiredo, M. F. R. Pereira, *ChemistrySelect* **2016**, *1*, 2522–2530.
[72] L. Dai, Y. Xue, L. Qu, H.-J. Choi, J.-B. Baek, *Chem. Rev.* **2015**, *115*, 4823–4892.
[73] G. Rambabu, Z. Turtayeva, F. Xu, G. Maranzana, M. Emo, S. Hupont, M. Mamlouk, A. Desforges, B. Vigolo, *J. Mater. Sci.* **2022**, *57*, 16739–16754.
[74] N. Yang, L. Li, J. Li, W. Ding, Z. Wei, *Chem. Sci.* **2018**, *9*, 5795–5804.
[75] S. Ni, Z. Li, J. Yang, *Nanoscale* **2012**, *4*, 1184–1189.
[76] K. Kakaei, M. D. Esrafili, A. Ehsani, in *Interface Science and Technology* eds. K. Kakaei, M. D. Esrafili, A. Ehsani, Elsevier, **2019**, vol. 27, pp. 203–252.
[77] Y. Zheng, Y. Jiao, L. Ge, M. Jaroniec, S. Z. Qiao, *Angew. Chem. Int. Ed.* **2013**, *52*, 3110–3116.
[78] R. Zhou, Y. Zheng, M. Jaroniec, S.-Z. Qiao, *ACS Catal.* **2016**, *6*, 4720–4728.
[79] X. Liu, Y. Liu, L.-Z. Fan, *J. Mater. Chem. A* **2017**, *5*, 15310–15314.
[80] S. Liu, Z. Wang, S. Zhou, F. Yu, M. Yu, C. Y. Chiang, W. Zhou, J. Zhao, J. Qiu, *Adv. Mater.* **2017**, *29*, 1700874.
[81] J. Lach, K. Wróbel, J. Wróbel, P. Podsadni, A. Czerwiński, *J. Solid State Electrochem.* **2019**, *23*, 693–705.
[82] Y. Liang, H. Wang, J. Zhou, Y. Li, J. Wang, T. Regier, H. Dai, *J. Am. Chem. Soc.* **2012**, *134*, 3517–3523.
[83] M. P. Araújo, M. Nunes, I. M. Rocha, M. Pereira, C. Freire, *ChemistrySelect* **2018**, *3*, 10064–10076.
[84] Z. Lei, W. Feng, C. Feng, W. Zhou, C. Wei, X. Wang, *J. Mater. Chem. A* **2017**, *5*, 2012–2020.
[85] Z. Wang, Y. Lu, Y. Yan, T. Y. P. Larissa, X. Zhang, D. Wuu, H. Zhang, Y. Yang, X. Wang, *Nano Energy* **2016**, *30*, 368–378.
[86] S. Xia, W. Guo, N. Cai, L. Sun, H. Zhou, W. Lu, X. Chen, J. Zhang, Y. Chen, H. Yang, *Fuel Process. Technol.* **2021**, *224*, 107028.
[87] G. A. Olah, *Angew. Chem. Int. Ed.* **2013**, *52*, 104–107.
[88] C. Lo Vecchio, D. Sebastián, M. J. Lázaro, A. S. Aricò, V. Baglio, *Catalysts* **2018**, *8*, 650.
[89] P. Mathumba, D. M. Fernandes, R. Matos, E. I. Iwuoha, C. Freire, *Materials* **2020**, *13*, 1562.

Manuscript received: November 3, 2023
Revised manuscript received: December 5, 2023
Version of record online: January 19, 2024


© 2024 The Authors. ChemElectroChem published by Wiley-VCH GmbH